2024

Benefits of quadratically tapered flexures for MEMS resonators and gyroscopes

Brian Grantham

BENEFITS OF QUADRATICALLY TAPERED FLEXURES FOR MEMS RESONATORS AND GYROSCOPES

Brian Grantham

A DISSERTATION

Submitted in partial fulfillment of the requirements
for the degree of Doctor of Philosophy
in
Electrical Engineering
to
The Graduate School
of
The University of Alabama in Huntsville
May 2024

Approved by:

Dr. Jennifer English, Research Advisor and Committee Chair
Dr. Rhonda Gaede, Committee Member
Dr. David Coe, Committee Member
Dr. David Pan, Committee Member
Dr. Robert Lindquist, Committee Member
Dr. Aleksandar Milenkovic, Electrical and Computer Engineering Department Chair
Dr. Shankar Mahalingam, Engineering College Dean
Dr. Jon Hakkila, Graduate Dean

Abstract

BENEFITS OF QUADRATICALLY TAPERED FLEXURES FOR MEMS RESONATORS AND GYROSCOPES

Brian Grantham

A dissertation submitted in partial fulfillment of the requirements for the degree of Doctor of Philosophy

Electrical and Computer Engineering

The University of Alabama in Huntsville

May 2024

An investigation into the benefits of quadratically tapered flexures for MEMS resonators and gyroscopes is performed and compared to the traditional non-tapered flexure design. Quadratically tapered flexures exhibit constant strain along the outer edge of the flexure whereas non-tapered flexures have significant stress concentration near the base of the flexure. The investigation considers peak stress, thermoelastic damping (TED), nonlinearity, and sensitivity to manufacturing variations. The impact of inside corner fillets on peak stress, TED, and resonant frequency is also investigated. Five new anti-phase lever mechanism (APLM) configurations for resonators and gyroscopes are designed and analyzed using CoventorWare 10. Fabrication experiment results are presented for an array of resonator designs to substantiate the FEA findings. Quadratically tapered flexures are found to reduce stress and thermoelastic damping while maintaining similar or slightly reducing sensitivity to manufacturing variations, but at the cost of a slight increase in nonlinearity.

Acknowledgments

Several individuals deserve recognition for their assistance and recommendations toward the completion of this thesis. Their importance cannot be overstated. The author acknowledges their contributions and extends his appreciation for their efforts. The names of these individuals and a brief description of their contributions follow.

Dr. Ryan Knight (Army Research Laboratory) is the inventor of the revised University of California anti-phase lever mechanism and co-designer of the dual mass resonator designs that were heavily leveraged in the experimental portion of this research. Dr. Knight also oversaw the production of the wafer used for the fabrication experiments. Finally, Dr. Knight is the designer of the dual mass resonator experimental test setup and provided instructions for use and data collection.

Dr. Ryan Rudy (Army Research Laboratory) is the co-designer of the dual mass resonator design that was heavily leveraged in the experimental portion of this research. Dr. Rudy also compiled the experimental designs into a wafer layout and oversaw the production of the mask.

Mr. Esmond Lau (Army Research Laboratory) provided significant assistance with experimental setup and data collection.

Dr. Dan Endean (Milwaukee Tool, formerly with Honeywell) provided several conversations that significantly impacted the direction of this research and focus on the sensitivity to manufacturing variations.

Dr. Ned Corron (Army Aviation and Missile Center, Retired) provided significant insight into the simultaneous solution of multiple non-linear equations.

Dr. Jenna Chan (Army Research Laboratory) reviewed and provided valuable constructive feedback for several abstracts, presentations, and papers.

Dr. Jonathan Hoffman (Defense Advanced Research Projects Agency) reviewed and provided valuable constructive feedback for several abstracts, presentations, and papers.

Dr. Michael Whitley (Engenius Micro, Inc.) provided a fabrication opportunity and layout assistance for an early version of the concentric proof mass resonator.

Dr. Jennifer English (University of Alabama in Huntsville) provided continuous encouragement, insightful recommendations, and technical assistance with every phase of this project as well as providing a constructive critique of the final manuscript.

The author extends his appreciation to his family, friends, and coworkers for their patience and encouragement during all stages of this research, and dedicates this document to his wife, Lynn, and wishes to express his sincere gratitude for her unending support and patience throughout the pursuit of this research.

Table of Contents

List of Figures

List of Tables

List of Acronyms

Acronym	Description
AKE	Akhiezer Effect
APLM	Anti-Phase Lever Mechanism
BMG	Bulk Metallic Glass
BOE	Buffered Oxide Etch
CDLoss	Critical Dimension Loss
CMG	Concentric Mass Gyroscope
CMOS	Complementary Metal-Oxide Semiconductor
CSP	Chip Scale Package
CVG	Coriolis Vibratory Gyroscope
CVGSAC	Coriolis Vibratory Gyro Single-Axis Controller
DRG	Disk Resonator Gyroscope
DRIE	Deep Reactive Ion Etch
FEA	Finite Element Analysis
FTR	Force To Rebalance
HRG	Hemispherical Resonator Gyroscope
IC	Integrated Circuit
LCC	Leadless Chip Carrier
LPCVD	Low-Pressure Chemical Vapor Deposition
MCM	Multi-Chip Module
MEMS	Micro-machined Electro-Mechanical Systems
μBRG	Micro Birdbath Resonator Gyroscope

MPD	Materials Properties Database
PEM	Poached Egg Molding
PZT	Lead Zirconate Titanate (Pb-Zr-Ti)
Q	Quality Factor
QMG	Quad Mass Gyroscope
QRS	Quartz Rate Sensor
RF	Radio Frequency
SCS	Single Crystal Silicon
SEM	Scanning Electron Microscope
SOC	System-on-a-Chip
SOI	Silicon On Insulator
SULEG	Sputtered ULE Glass
TED	Thermo-Elastic Damping
TFG	Tuning Fork Gyroscope
TIA	Trans-Impedance Amplifier
UAH	University of Alabama in Huntsville
ULE	Ultra Low Expansion
WA	Whole Angle

Chapter 1. Introduction

Since the first publications on the use of silicon as a micromechanical material in the 1960s by Nathanson and Wickstrom [1], and Nathanson, Newell, Wickstrom, and Davis [2], which initiated an immense amount of research superbly summarized in 1982 by Peterson [3], the mechanical properties of silicon have continuously been explored for the creation of improved sensors and actuators. The first publications to explore the use of silicon as an angular rate sensor (gyroscope) appeared over thirty years ago [4, 5, 6] and the applications using silicon Micro-Electro-Mechanical Systems (MEMS) sensors have become as prolific as Peterson predicted. These applications include hobby drone stabilization [7], cell phone motion detection [8], gaming console controllers such as the Nintendo Wii [9], and even tactical missile systems [10]. Despite their ubiquity, research into the use of MEMS for rotation rate sensing continues to be a very active with the inaugural session of the annual IEEE International Symposium on Inertial Sensors and Systems being as recent as 2014. The present investigation contributes to this ongoing research through exploring the benefits of quadratically tapered flexures for MEMS gyroscopes and resonators.

Some of the primary performance parameters of MEMS gyroscopes are input range, sensitivity, bias (or offset), noise, and bandwidth. The input range is the maximum amount of angular rate that the device can accurately measure and is typically expressed in units of degrees per second. The sensitivity of a gyroscope is the

proportionality constant that relates signal output to angular rate input and is usually expressed in volts per degree per second. Maximizing the inherent sensitivity of the gyroscope reduces the effects of noise in the associated electronics. The bias (or offset) is the amount of angular rate reported by the device when no physical angular rate is applied. Bias is generally reported in units of degrees per second and every effort is made to minimize this error during gyro design. The noise is defined as the time-varying portion of the output signal that is not correlated to applied angular rate and is often characterized by white noise in the angular rate domain. The bandwidth of the gyroscope is defined as the frequency of angular rate oscillation at which the peak angular rate reported by the device is equal to 70.7% of the applied angular rate. The incorporation of quadratically tapered flexures into the MEMS gyroscope design can offer improvements to the mechanical characteristics that impact these performance parameters and other gyroscope error sources as well.

This dissertation focuses on the mechanical characteristics of quadratically tapered flexures as they apply to a dual proof mass resonator/gyroscope configuration. The primary motivation for the work herein was to introduce potential design improvements to the dual Foucault pendulum gyroscope developed by the University of California at Irvine [11, 12] in two specific ways. The first was through the introduction of quadratically tapered flexures which will be shown to improve sensitivity while reducing bias and reducing sensitivity to manufacturing variations. The second was the introduction of a tapered-flexure-based Anti-Phase Lever Mechanism (APLM) that will couple the two proof masses more closely in anti-phase mode, which has been shown in

previous research to further improve sensitivity, reduce bias, and reduce acceleration sensitivity [28, 90].

Chapter Two of this dissertation provides background information on the operation of Coriolis-acceleration-based angular rate sensors along with a discussion of relevant error parameters, material properties, and design considerations. Chapter Three provides an investigation into the relevant characteristics of quadratically tapered flexures and includes a discussion on the sensitivity to manufacturing variations commonly found in MEMS manufacturing processes. Chapter Four documents the development of quadratically tapered flexure APLM designs and includes a comparison with the inner lever coupling APLM design from the University of California at Irvine. Chapter Five presents the results of fabrication experiments conducted on a dual proof mass resonator configuration which experimentally demonstrates the benefits of quadratically tapered flexures and the new APLM design, and compares those results with Finite Element Analysis (FEA) modeling predictions. All FEA were performed using CoventorWare 10. Chapter Six summarizes the conclusions of the analyses presented herein and includes recommendations for future research. Appendix A presents mathematical derivations too extensive for the main body. Appendix B presents the results of various FEA mesh sensitivity studies. Finally, Appendix C includes additional design images and documents the individual die locations of each design on the experimental fabrication wafer documented in Chapter Five.

Chapter 2. Background

This chapter describes the current status of research in the area of MEMS based angular rate sensors and provides context for the contributions of this dissertation to the current state of the art. In particular, these contributions are (1) investigating the benefits of quadratically tapered flexures for MEMS gyroscopes and resonators, and (2) exploring various configurations of Anti-Phase Lever Mechanisms (APLM) including two new APLM designs based on quadratically tapered flexures. These mechanical structures are analytically designed, evaluated using Finite Element Analysis (FEA), and demonstrated experimentally in a dual-mass resonator configuration.

2.1 Research Focus and Motivation

The scientific core of this research effort centers around the attributes of quadratically tapered flexures for MEMS inertial sensors. The tapered flexure design was motivated by a combination of a few papers [52, 71, 86]. First, in [71], the authors make the statement concerning their quartz tuning fork gyroscope design that "the taper, in conjunction with the [lumped] masses, distributes stress in both the drive and pickup tines in a constant manner along the tine length. In contrast, the square tines generate stress that is highly localized at the base of the tine". The authors go on to say "The tapered tine/hammerhead [*i.e.*, lumped mass] design offers higher sensitivity with a

smaller fork size… This improvement is the result of both better drive behavior, and enhanced pickup coupling. The drive system has a higher [quality factor] ... This lowers impedance allowing for higher drive current levels from a given voltage source, and decreases zero rate offset bias."

While this list of the benefits of the tapered flexure/lumped mass design was enough to warrant investigation, there were a few potential additional benefits that motivated the pursuit of this work:

1. The tapered flexure design distributes the stress equally along the length of the flexure. This should result in a lower peak stress which could enable larger displacements while maintaining better linearity.
2. The equal distribution of the stress may make the tapered flexure design more robust against manufacturing variations than the straight flexure design.
3. In [52], the authors indicate that "non-uniformity in the strain field causes temperature gradients in the solid, and an associated heat transfer; the resulting energy loss is known as thermoelastic dissipation" and [86] makes a very similar statement. Since the tapered flexure design has lower peak strain and uniform strain along the outer edges of the flexure, it was postulated that this design configuration may have lower thermoelastic dissipation than the standard straight flexure design. Indeed, while the tapered flexures investigated in [82] and [83] do not employ exactly the same quadratic taper equation that yields uniform stress, the

thermoelastic dissipation of both of those tapered flexure designs indicate lower thermoelastic dissipation than that of the equivalent straight flexure.

Although the benefits of tapered flexures were enumerated for a quartz gyroscope in 2003 [71], tapered flexures have just recently begun to be investigated for silicon MEMS inertial sensors [87, 88]. These initial studies confirmed the reduction in peak stress over an equivalent straight flexure, but experimental measurements of thermoelastic dissipation have yet to be published.

As a part of the investigation into the attributes of tapered flexures, the sensitivity of the tapered flexure to manufacturing variations as compared with that of an "equivalent" straight flexure was also investigated. An "equivalent" straight flexure was defined to be one of the same length but with a base width required to obtain the same linear deflection spring constant due to an applied force. This study was based on analytical expressions derived in this work and verified through FEA analyses. The particular focus areas investigated in this study were informed by discussions with MEMS fabrication companies as well as by literature [89]. From these, the primary issues that arise from manufacturing variations in Deep Reactive Ion Etched (DRIE) MEMS devices include:

1. Variations in corners - "rounding" of inside corners.
2. Critical Dimension Loss (CDloss) or Etch Bias - horizontal undercut of device under the mask [89].
3. Sidewall Angle - Angle deviation from vertical of the sides of the MEMS device.

Specifically, investigations were performed into the ability of tapered flexures to mitigate CDLoss variability and into the ability of radius fillets to mitigate inside corner variability. It was assumed that the performance of tapered flexures would mitigate sidewall angle variability to roughly the same extent that it mitigated CDLoss variability.

The importance of operating CVGs in anti-phase mode was highlighted in [58] which showed that anti-phase operation could increase the quality factor of the CVG by an order of magnitude over in-phase operation. This increase in quality factor increases the sensitivity of the CVG. Benefits of incorporating an APLM into CVG designs were discussed in [28] and [90], and included (1) the ability to choose the order (*i.e.*, set the relative frequencies) of a particular set of structural modes of the Quad-Mass Gyroscope (QMG) design, (2) improving quality factor of the anti-phase mode, and (3) even reducing the quality factor of the unwanted in-phase mode. The quad-mass gyroscope design includes both inner and outer anti-phase lever mechanisms, but the most substantial innovation was the design of the inner lever coupling mechanism. This work investigates several variations of APLMs consisting of straight and tapered flexures as well as the original and modified versions of that inner lever coupling mechanism. This work was performed using FEA simulations, but is supported by experimental data from fabrication experiments.

The motivation for targeting a mode-matched CVG configuration is four-fold [29]. First, mode-matched operation increases the sensitivity of the gyroscope. Second, this configuration enables the gyroscope to be operated in either the force-to-rebalance angular rate mode or whole-angle mode. Third, this configuration enables the reduction

of quadrature error using electrostatic tuning. Lastly, this configuration enables the implementation of self-calibration methods [34, 35, 36, 37].

The research will focus on implementation in Single Crystal Silicon (SCS) with a Miller Index of <100>. The choice of material is based on ease of fabrication, axial symmetry, and thermoelastic damping (TED) considerations. First, the exotic materials that can provide improved TED performance all require specialized manufacturing techniques that require significant effort to be successful and consistent. Second, the <100> SCS device should have symmetric material properties for perpendicular axes as would be used in a mode-matched gyroscope. Finally, with the exotic materials eliminated from consideration, the work reported in [53] indicates that SCS will have better TED performance than polysilicon.

2.2 Coriolis Vibratory Gyroscopes

Nearly all MEMS angular rate sensors fall under the broad category of Coriolis Vibratory Gyroscopes (CVG) [13, 14]. The IEEE defines a Coriolis Vibratory Gyroscope in [13] as "a gyro based on the coupling of a structural, driven, vibrating mode into at least one other structural mode (pickoff) via Coriolis acceleration" with a note that "CVGs may be designed to operate in open-loop, force-rebalance (*i.e.*, closed-loop), and/or whole-angle modes."

Coriolis acceleration is an acceleration that is required to maintain a linear velocity in a rotating coordinate frame. A detailed discussion and derivation of Coriolis acceleration can be found in [15] and the equation describing Coriolis acceleration is:

$$a_C = 2 \cdot \Omega \times v, \tag{2.1}$$

where a_C is the Coriolis acceleration, Ω is the angular rotation rate of the rotating coordinate frame, and v is the linear velocity of the object. All vectors in the above equation are expressed in the rotating coordinate frame.

Most MEMS CVGs are designed to operate in a geometrical configuration often referred to as a tuning fork gyroscope. Figure 2.1 presents an illustration of the operation of a tuning fork gyroscope [16]. In this illustration, the top ends of the tuning fork tines are driven to oscillate at their resonant frequency with a controlled amplitude out of phase with each other. That is, while the tine on the right is moving to the right, the tine on the left is moving to the left, and when the tine on the right is moving to the left, the tine on the left is moving to the right. This is called the "drive motion" and occurs in the "drive axis" of the sensor. When an angular rotation is applied to the device about the vertical axis, a Coriolis acceleration must be applied to the tuning fork tines in the sense axis to maintain the drive oscillation in the (now rotating) device coordinate frame. This causes the top of the tines to deflect into and out of the page of the illustration at the same frequency as the drive oscillation. This motion can be sensed and, when demodulated by the drive motion velocity, provides a signal that is proportional to the applied angular rotation rate. This motion is called the "sense motion" and occurs in the "sense axis" of the sensor. Detailed analyses of CVG operation can be found in [28] and [29].

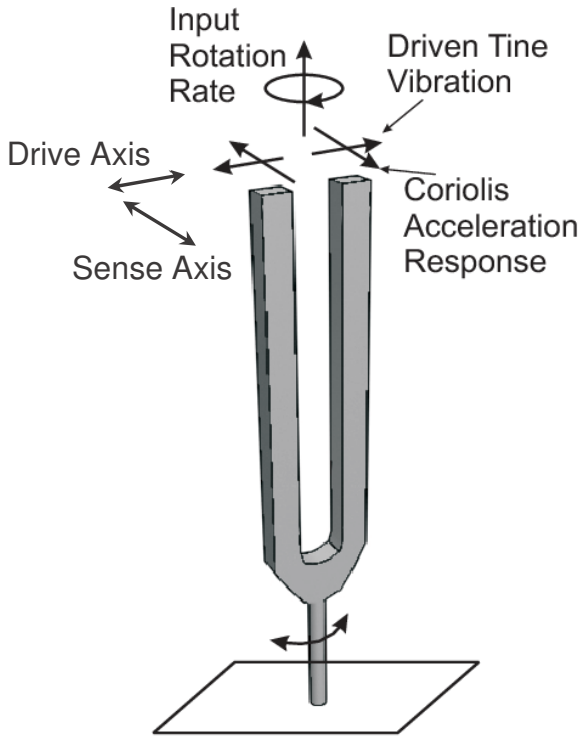

Figure 2.1 Coriolis Acceleration in a Tuning Fork Gyroscope [16].

Within the spectrum of CVGs, several physical configurations have been implemented that include, but are not limited to, an actual tuning fork configuration made in quartz [17, 18, 19, 20], a vibrating beam configuration [21], a vibrating ring configuration [22], a single plate mass configuration [23], dual plate mass configuration [24], quad mass configuration [25], and the concentric mass configuration [11]. Some configurations even allow for simultaneous sensing of two [26] or three [27] rotation axes. The work is targeted at the symmetric configurations that provide balanced anti-phase operation which are primarily the dual plate mass, quad mass, and concentric mass configurations.

CVGs typically operate in one of two modes. The first, and most common of these, is the non-mode-matched condition where the resonant frequency of the drive axis,

ω_d, is less than the resonant frequency of the sense axis, ω_s, or $\omega_d \ll \omega_s$. The second, less common mode, is the condition where $\omega_d = \omega_s$. This produces a more sensitive gyroscope that is often called the "degenerate mode" or "mode-matched" configuration.

The first configuration ($\omega_d \ll \omega_s$) essentially places the gyroscope response to the Coriolis acceleration within the mechanical response bandwidth of the sense axis structure. This results in well-behaved response characteristics of the sense axis and produces the peak sinusoidal displacement in response to applied angular rotation given in Equation (2.2):

$$y_s \approx -j\frac{2\,\omega_d\,x_d}{\omega_s^2}\,\Omega_z = -j\frac{2\,m\,\omega_d\,x_d}{k_s}\,\Omega_z\ , \tag{2.2}$$

where y_s is the peak displacement of the sense axis, x_d is the peak displacement of the drive axis, Ω_z is the rotation rate applied to the gyroscope, m is the equivalent mass of the system, and k_s is the spring constant of the system.

Noting that the sense axis resonant frequency appears as a quadratic in the denominator of the displacement equation, it is desirable for this to be as small as possible in order to maintain good gyroscope sensitivity. Therefore, it is usually designed to be just above the drive axis resonant frequency, which appears in the numerator. From this, the sensitivity of the typical non-mode-matched CVG is found to be proportional to the drive displacement amplitude and inversely proportional to the operating frequency.

The mode-matched or degenerate mode configuration has the primary advantage that the sense axis quality factor, Q_s, provides additional amplification of the Coriolis

acceleration, yielding a significantly increased sensitivity for the CVG as shown in Equation (2.3):

$$y_s \approx -\frac{2\,Q_s\,x_d}{\omega_d}\,\Omega_z\,. \tag{2.3}$$

The disadvantages of the mode-matched mode configuration include the inherent difficulty of matching the resonant frequencies of the drive and sense axes, which often requires physical or electrical trimming, as well as the bandwidth limitation that comes with operating within the resonance bandwidth of a device with a large quality factor [30]. This work focuses on mode-matched devices.

For completeness, there is a third potential configuration where $\omega_d \gg \omega_s$. This configuration operates very similar to the first configuration but with reduced sensitivity because the Coriolis acceleration is beyond the natural bandwidth of the sense axis. This also leads to a frequency dependent gain. For these reasons, this configuration has rarely been investigated in literature.

2.3 Mode-matched CVGs

The initial publication regarding the behavior of degenerate mode resonators was published in 1890 by G. H. Bryan in the Proceedings of the Cambridge Philosophical Society in a paper titled "On the Beats in the Vibrations of a Revolving Cylinder or Bell" [46]. In this paper, Bryan indicates that if a two degree of freedom degenerate mode resonator, specifically a thin ring or cylinder, is set in oscillation, and then the body of the resonator is rotated, the location of the vibration attempts to follow the rotation but

inevitably lags behind the rotation. Bryan shows that this lag is not due to imperfections in the resonator but rather a consequence of the conservation of energy. Bryan shows that the rotation of the vibration follows the rotation of the resonator body by a factor called the angular gain, k, that is calculable and defined entirely by the geometry of the resonator and is in no way dependent on the elasticity of the resonator material.

To explain the importance of minimizing resonant frequency and quality factor mismatch, a more detailed model of the mode-matched CVG must be analyzed. [47] provides a generalized model of the CVG allowing for the normal-mode axes, with resonant frequencies $\omega_1$and ω_2, to be misaligned from the drive and sense axes by an angle θ_ω, and for the principal damping axes, with damping time constants τ_1 and τ_2, to be misaligned from the drive and sense axes by an angle θ_τ. When operating the gyro in Force to Rebalance (FTR) Mode, a forcing function drives the x-axis displacement at its resonant frequency and a control loop maintains the response at a constant displacement amplitude, c_{x_0}, given by:

$$x = c_{x_0} \cos \omega_x t \ , \tag{2.4}$$

where

$$\omega_x^2 = \omega^2 - \omega \Delta\omega \cos 2\theta_\omega \ , \tag{2.5}$$

$$\omega^2 = \frac{\omega_1^2 + \omega_2^2}{2} \ , \tag{2.6}$$

and

$$\omega\Delta\omega = \frac{\omega_1^2 - \omega_2^2}{2} \quad . \tag{2.7}$$

The response displacement in the y-axis is then maintained at zero amplitude by a second control loop. The force required to maintain the zero-response amplitude condition in the y-axis, f_y, is given in the following expression:

$$\begin{aligned} f_y = -\omega_x c_{x_0} \left[2k\Omega_z + \Delta\left(\frac{1}{\tau}\right) \sin 2\theta_\tau \right] \sin \omega_x t \\ -c_{x_0} \omega\Delta\omega \sin 2\theta_\omega \cos \omega_x t \end{aligned} \quad , \tag{2.8}$$

where

$$\frac{1}{\tau} = \frac{1}{2}\left(\frac{1}{\tau_1} + \frac{1}{\tau_2}\right) , \tag{2.9}$$

and

$$\Delta\left(\frac{1}{\tau}\right) = \frac{1}{\tau_1} - \frac{1}{\tau_2} \quad . \tag{2.10}$$

The y-axis control force is used to estimate the applied rotation rate through synchronous demodulation yielding:

$$\widehat{\Omega}_z = SF \cdot demod\left(f_y\right)|_{\sin \omega_x t} + B \ , \tag{2.11}$$

where the scale factor, SF, and the bias, B, are given by:

$$SF = -\frac{1}{2k\omega_x c_{x_0}} \tag{2.12}$$

and

$$B = \frac{1}{2k}\Delta\left(\frac{1}{\tau}\right)\sin 2\theta_\tau \ . \tag{2.13}$$

Inspection of the bias equation, Equation (2.13), reveals that the bias error is directly proportional to the damping mismatch, $\Delta\left(\frac{1}{\tau}\right)$, and inversely proportional to the angular gain, k. Therefore, to reduce the bias, it is desirable to have a high angular gain. Also, recalling the general expression relating quality factor and damping time constant:

$$\tau = \frac{2Q}{\omega} \tag{2.14}$$

leads to the conclusion that it is also desirable to have very low damping (high quality factor, Q) and low damping mismatch (low quality factor mismatch, ΔQ) [35].
Section 2.4 provides information on state-of-the-art research into bias error reduction through the reduction of damping and damping mismatch and indicates how this work contributes to that research area.

The last term in Equation 2.8 gives rise to an error term known as quadrature error and indicates that it is proportional to the resonant frequency mismatch, $\omega\Delta\omega$.
Section 2.5 provides information on common techniques for reducing quadrature error through the reduction of resonant frequency mismatch and indicates how the present research contributes to that research area.

2.4 Bias Error Reduction Through Quality Factor Improvements

Aimed at reducing bias error in MEMS gyroscopes, much work has been performed in recent years to improve the quality factors of microscale resonators. There are several contributing damping mechanisms that constitute the total damping in most MEMS resonators [52]. These mechanisms include fluid losses, support losses (anchor losses), thermal energy losses, electrical damping, and surface effects. Each of these energy loss mechanisms have their own characteristic quality factor and contribute to the overall quality factor of the resonator.

The individual damping mechanisms operate in parallel such that the overall quality factor can be calculated as:

$$Q_{Tot} = \left(Q_{Fluid}^{-1} + Q_{Anchor}^{-1} + Q_{Thermal}^{-1} + Q_{Electrical}^{-1} + Q_{Surface}^{-1}\right)^{-1}. \quad (2.15)$$

The damping time constant, also referred to as the ring-down time, of a resonator is related to the quality factor by the relation given in Equation (2.14). Therefore, Equation (2.15) could alternatively be expressed as the inverse of the sum of the inverse damping time constants as shown here:

$$\tau_{Tot} = \left(\tau_{Fluid}^{-1} + \tau_{Anchor}^{-1} + \tau_{Thermal}^{-1} + \tau_{Electrical}^{-1} + \tau_{Surface}^{-1}\right)^{-1}. \quad (2.16)$$

A discussion of each of these loss mechanisms is provided below, but the present research focuses on minimizing support losses and thermal energy losses.

Generally, fluid damping effects are subdivided into two categories which are (1) shear damping, where the relative velocity of two parallel surfaces is parallel to the

surface, and (2) squeeze film damping, which is where the relative velocity of two parallel surfaces is normal to the surface. Generally speaking, for in-plane mode devices, shear damping tends to dominate the overall damping down to about 1 mTorr. Below that, other effects such as thermal or anchor losses begin to dominate [52]. For out of plane mode devices, squeeze film damping can continue to dominate to significantly lower pressures. Due to the cubic dependence of the squeeze film damping on the gap size, it is difficult to establish general design boundaries for this damping term. The devices studied in this work were all in-plane mode devices and were operated at pressures significantly below 1 mTorr to mitigate fluid damping losses.

A discussion of the importance of operating the device in anti-phase mode and incorporating an APLM to minimize support losses (anchor losses) was provided in Section 2.1. General design practices for the MEMS resonators include (1) anchoring the resonator to the substrate at locations of low stress concentrations [55, 56, 58, 60], (2) implementing long, thin flexures [59], (3) operating the resonator in an antiphase mode [28, 58, 90], and (4) when possible, anchoring with moment-based structures as opposed to linear force-based structures [57]. This work focuses on the design of several APLMs that incorporate as many of these design practices as possible including several moment-based designs and a few that minimize stress concentrations at the anchor point. All operate in anti-phase mode and incorporate long, thin flexures.

Regarding thermal losses, also called thermoelastic damping (TED) loss, Zener was the first to identify this thermal loss mechanism in long, thin reeds and derived formulas to describe this loss mechanism using classical thermodynamics [61]. In that seminal work, Zener asserted that the thermal energy loss for a long, thin reed being

driven in oscillation in steady state was dominated by heat flow across the reed. His assertion was that strain gradients across the width of the reed caused by the bending motion resulted in thermal gradients across the width of the reed. These thermal gradients subsequently resulted in heat flow, which is an energy conversion process that the Second Law of Thermodynamics indicates cannot be reconverted to kinetic energy by the mechanical system. Therefore, each oscillation of the reed permanently converts some kinetic energy to thermal energy. This conversion accounts for the majority of the thermal energy loss in the vibrating reed. He found that a material with a Poisson ratio of 0.5 would exhibit no TED loss. He also indicates that TED will be lowest in materials having a specific heat at constant pressure, C_p, very close to the specific heat at constant volume, C_v, or an adiabatic index, κ, near unity. He also found that there is an operating frequency at which the energy loss due to thermal dissipation reaches a peak, often referred to as the Debye peak or the thermal frequency.

In [62], Zener generalized his theory and reformulated his expressions [63, 64]. For operating frequencies below the Debye peak, the thermal loss, Q_{TED}^{-1}, increases linearly with increasing operating frequency, ω. This region is referred to as the iso-thermal operating region because the flexing of the material is happening slow enough for the thermal transients caused by the strain gradients to settle, thereby resulting in the material maintaining an iso-thermal condition. In this operating frequency regime, the thermal loss is proportional to the square of the beam width, implying that thicker beams have higher losses or thinner beams have lower losses.

For operating frequencies above the Debye peak, the thermal losses decrease linearly with increasing ω. This region is referred to as the adiabatic operating region

because the flexing of the material is happening so quickly that the thermal transients do not have adequate time to allow heat to flow, thereby losing only a fraction of the thermal energy and resulting in a largely adiabatic process.

While some research has suggested that MEMS resonators have found better performance operating in the adiabatic regime [65], most MEMS gyroscopes operate in the iso-thermal region and TED is often a significant energy loss mechanism [66]. Therefore, to improve quality factor and reduce thermal losses, it is generally desirable to employ long, thin flexures in the design.

In 2000, Lifshitz and Roukes [68] made a significant advancement in the analytical model for thermoelastic damping developed by Zener. In this work, the authors derive an exact expression for the thermoelastic damping which does not carry the approximation made by Zener that the vast majority of the thermal relaxation occurs in the first transverse thermal eigenmode. They did this by adding a term to Hooke's law to account for the local relative temperature field, θ, through the linear Coefficient of Thermal Expansion (CTE), α. While their resulting formula makes only a slight correction to Zener's original approximation, their reformulation of the model enables evaluation of thermal losses for more complex geometries under general motion.

Knowing that TED losses are proportional to the square of the flexure width, other researchers investigated the possibility of machining holes in locations of high strain gradients [69, 70] to mitigate the heat flow across the flexure. In these papers the authors demonstrated the ability to predict and control the quality factor of MEMS resonators that are limited by TED loss by up to a factor of four times higher than the base resonator design. This could enable quality factor tuning of a device design without

having to change the fundamental design of the device (scale, operating frequency, etc.). This significant finding, however, comes with a significant manufacturing challenge as the holes investigated were on the order of 1μm wide, which results in very high aspect ratios that are difficult to fabricate.

More recently, work has been performed to characterize thermoelastic damping for more complex geometries such as linearly tapered microbeam resonators [82] as well as exponentially tapered microbeam resonators [83]. In these two works, the authors derive analytical solutions which agree with their FEA studies that show both the linearly tapered and the exponentially tapered flexures have lower TED at low frequencies than the uniform cross section flexures but higher TED at high frequencies. This may suggest that the strain gradients arising from tapered flexures result in thermal gradients better suited for isothermal operation and may provide insight into flexure design techniques that minimize thermal losses. This work focuses on an investigation into the TED properties of quadratically tapered flexures as opposed to linearly or exponentially tapered flexures as the quadratic taper is required to achieve the uniform strain distribution along the length of the flexure reported in [71].

The dependence of the thermal loss on several material parameters, namely the linear coefficient of thermal expansion, α; the modulus of elasticity, E; the thermal conductivity, k; and the specific heat capacity, C_p or C_v; has given rise to considerable amount of research on alternate materials for MEMS gyroscope designs. In [66] the authors investigate several concentrations of boron-doped silicon and silicon-germanium and demonstrate experimentally good correlation to the theoretical predictions of Q_{TED}. In [50], the authors consider an 8mm diameter silicon Disk Resonator Gyroscope (DRG)

design and compare its expected performance based on TED losses with that of a similar fused silica (or quartz) design. The paper highlights that, based on the intrinsic material properties of silicon (high k and high α) and quartz (low k and low α), the highest quality factors using silicon will occur at the microscale in the isothermal limit while the highest quality factors using quartz will come at the mesoscale in the adiabatic limit and that the intrinsic limit of quality factor due to TED for quartz is 80 times higher than that of silicon. Researchers at the University of Michigan exploited the TED material properties of fused silica and developed a glass blowing process using a mold and a blow torch to fabricate a "Micro Birdbath Resonator Gyroscope" (μBRG), which is a hemi-toroidal resonator with a principle of operation similar to that of the HRG, and ultimately demonstrated quality factors on the order of 4.5 million [72, 38, 73, 74]. Researchers at the University of Utah explored an alternate fabrication technique in an effort to exploit the Ultra-Low Expansion (ULE) characteristics of titanium silicate glass to reduce the thermoelastic damping losses in a hemispherical shell resonator [75] but were unsuccessful at demonstrating quality factors at the theoretical limit due to fabrication and assembly issues. Borosilicate glass, or Pyrex, has been investigated by researchers at the University of California at Irvine in the development of a wafer-scale glass blowing process including a micro-scale spherical resonator used as a gyroscope which was surrounded by eight glass spheres for actuation and sense electrodes for the gyroscope [76, 77]. While the quality factors were not presented in the paper, the device was successfully demonstrated as a gyroscope. The researchers in [78] investigate the use of silicon dioxide as a gyroscope resonator material to mitigate against bulk thermoelastic dissipation loss. However, their work was limited by surface losses which prevented

measurement of TED losses. The researchers in [79, 80, 81] investigate the use of bulk metallic glass as a material for the fabrication of a hemispherical resonator gyroscope using both thermoplastic and blow molding techniques. Their published quality factors on the order of 8,000 were limited by anchor losses but they present an analytical study that indicates alternate geometries could support a TED quality factor in excess of 1 million. In [53], researchers investigate and compare the quality factors of micron and sub-micron thick cantilever beams of silicon-nitride, polysilicon, and single crystal silicon. While the primary focus of this paper was on narrower, cantilever resonators and not on realistic structures for gyroscopes, the data presented in the paper indicates that single crystal silicon has significantly higher quality factors (by orders of magnitude) than silicon nitride and polysilicon. Based on ease of fabrication, axial symmetry, and TED considerations, this work focuses on implementation in <100> SCS using a commercially available Deep Reactive Ion Etch (DRIE) fabrication process that is commonly used in mass production of MEMS devices.

The most common source of electrical loss, $Q_{Electrical}$, occurs in the signal detection circuitry whether it is capacitive, piezoelectric [71], inductive/magnetic [84], or optical [85]. Capacitive sensing is the most common for sensing the motion of MEMS gyroscopes, and is utilized in this work. To mitigate potential losses introduced by capacitive sensing, the typical Transimpedance Amplifier (TIA) circuit shown in Figure 2.2 was considered. In this circuit, a voltage source places a biasing voltage, V_B, across the variable MEMS sense capacitor, C_S. Ideally, the parasitic resistance in the circuit, R_P, is zero, but in practice it is a small but non-zero quantity due to the finite gain of the TIA and the finite conductance of the semiconductor material and conducting

metal layers. Therefore, the motion in the capacitor creates a current that is proportional to the change in capacitance and given by the solution to the differential equation:

$$I_C(t) = V_C(t)\frac{d}{dt}C_S(t) + C_S(t)\frac{d}{dt}V_C(t)\ , \tag{2.17}$$

where $I_C(t)$ is the current in the capacitor and $V_C(t)$ is the voltage across the capacitor.

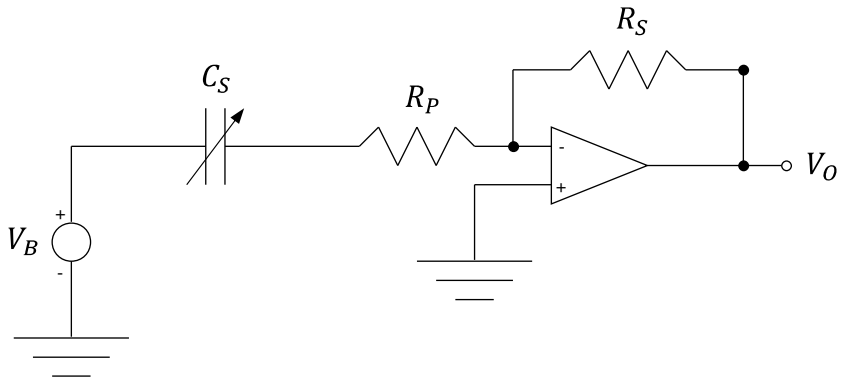

Figure 2.2 Simplified MEMS Gyroscope Capacitive Sensing TIA Circuit.

The first term of this equation is dominant if the sense capacitor is DC-biased, and the second term is dominant if the sense capacitor is AC-biased. In either case, if R_P is non-zero, then it introduces an electrical energy loss mechanism into the system. The force generated by this loss mechanism can be shown to be [52]:

$$F_x = V_x \cdot R_P\left(\frac{d}{dt}C_S\right)^2 V_B^2\ , \tag{2.18}$$

where F_x is the equivalent force generated by the parasitic resistance due to the velocity, V_x of the MEMS device. The explicit time dependence has been dropped from the equation for clarity. Since this force is proportional to the velocity, it appears in the

motion equations as a damper, which limits the quality factor of the resonator. So, care must be taken in the circuit design to ensure that this loss mechanism does not limit the quality factor measurements.

While not covered in detail here, inductive and piezoelectric sensing mechanisms carry equivalent loss mechanisms that introduce a force in opposition to the velocity. Also, while photons do carry an equivalent mass and momentum, the amount of energy transferred to optical sensing mechanisms is very small and can typically be disregarded.

Regarding surface losses, $Q_{Surface}$, as the size of a resonator or gyroscope decreases, the surface to volume ratio of the device increases. With the increasing surface to volume ratio, the impact of surface effects in the flexures begin to dominate over the bulk effects and the quality factor can ultimately be limited by surface effects, especially for very small resonators and gyroscopes [52]. There are multiple fundamental loss mechanisms that give rise to surface losses but surface asperities are the most common [78]. Some of the other sources for surface losses include loss due to electronic defects at the silicon surface, grain re-orientation, and movement of defects. For many of the mechanisms of surface loss, the quality factor can be improved using thermal annealing. For most MEMS CVGs designed to operate in the isothermal region and for the resonators studied in this dissertation, surface losses are insignificant relative to the bulk thermal losses in the flexures.

2.5 Quadrature Error Reduction Through Improved Frequency Matching

In ideal CVGs, the primary source of cross coupling between the drive axis and the sense axis is the Coriolis force. However, in actual devices, fabrication imperfections

lead to non-uniformity in support flexures and electrostatic drive elements which lead to cross coupling of the drive signal or motion into the sense axis signal. In mode-matched devices, this is often dominated by resonant frequency mismatch. Stray capacitance between the drive elements and the sense elements can also be a source of this cross coupling. All of these sources of cross coupling are generally lumped together in an error source labeled as quadrature error [31] and result in signals in the sense axis direction that are in phase quadrature with the desired signal.

Although quadrature error can be significantly mitigated through synchronous demodulation, sense axis signals arising from quadrature error can easily overwhelm and dominate analog signal processing electronics. For this reason, other allowances for quadrature error compensation are often provided in the design of the CVG itself. These include, but are not limited to, (1) additional electrostatic drive elements in the sense axis that are fed with a small portion of the drive axis signal, (2) additional DC biasing elements that enable directional electrostatic spring corrections to applied [32], and (3) drive element isolation flexures [23] and/or bridging support flexure designs [33] that significantly restrict cross-axis motion in the drive mechanism.

For mode-matched gyroscopes, resonant frequency tuning to eliminate quadrature error has been attempted in many ways. In the HRG, the hemispherical resonator is typically polished through an intense polishing process to match both the resonant frequency and the quality factor [38, 39]. In [40], the authors describe a process to perform laser trimming of a ring gyroscope to adjust the spring constants and mass distribution to match the resonant frequencies. In [39] the authors describe a process of depositing 20 µg gold balls followed by fine tuning with silver ink to match the resonant

frequencies of a disk resonator gyroscope. In [41] and [42], the authors describe geometric design approaches to compensate for known stiffness anisotropy in <100> silicon.

The most common method employed for frequency matching is electrostatic tuning through electrostatic spring softening [43, 44, 45]. This typically requires additional parallel plate capacitors to be included in the device design dedicated to this purpose. The tuning range is limited by (1) the maximum aspect ratio allowed in the fabrication process which sets the lower bound of the gap between the plates, (2) the total surface area of the parallel plate capacitor, and (3) the maximum available tuning voltage. The electrostatic spring always acts to aid motion in the direction of the displacement, which is the opposite of most mechanical springs. Therefore, the sign of the electrostatic spring is always negative regardless of whether the applied tuning voltage is positive or negative and the electrostatic spring will always work to "soften" the mechanical spring suspension. So, electrostatic spring softening must always be applied to the axis with the highest spring constant or resonant frequency. The residual demodulated quadrature signal found from synchronous demodulation of Equation (2.8) provides a convenient measurement of the quadrature error. This signal can then be used in a feedback control loop which commands an electrostatic spring softening voltage to continuously drive the residual quadrature error to zero [47].

While quadrature error can be mitigated through synchronous demodulation and frequency tuning approaches, it is still desirable to minimize the inherent resonant frequency mismatch to reduce the required amount of electrostatic tuning capacitors which consume limited silicon die area, and to reduce the initial amount of quadrature

signal in the sense channel. This work investigates if the incorporation of tapered flexures and radius fillets reduce resonant frequency variability (*i.e.*, resonant frequency mismatch) due to manufacturing variations.

Chapter 3. Relevant Characteristics of Quadratically Tapered Flexures

This chapter provides information on the investigation into the relevant characteristics of quadratically tapered flexures. It is divided into four sections. First, in Section 3.1, the derivations of the relevant mathematical expressions for quadratically tapered flexures is presented. Next, in Section 3.2, the results of the initial set of Finite Element Analysis (FEA) studies used to validate these expressions is discussed. In Section 3.3, the FEA study investigating the sensitivity of quadratically tapered flexures to common MEMS manufacturing variations is reported and offers a comparison to the sensitivities of standard straight flexures. Finally, a short summary of the overall findings is presented in Section 3.4. All tapered flexures investigated in this work are quadratically tapered and all references to "tapered flexures" imply a quadratic taper unless otherwise specified.

3.1 Relevant Quadratically Tapered Flexure Mathematical Expressions

For visual reference, a solid model rendering of a quadratically tapered flexure based tuning fork is pictured alongside a solid model rendering of a straight flexure based tuning fork in Figure 3.1. The square block at the end of the flexures is referred to as a "hammerhead" and is a necessary feature for many tapered flexure designs. The necessity and implications of the hammerhead feature is explained in more detail in

subsequent sections, but arises from the fact that the stress in the tapered flexure goes to zero at the point where the force load is applied. Since the width of the flexure is derived to maintain constant stress along the flexure length, this zero stress condition results in a flexure width of zero, which is not physically realizable and requires the inclusion of the hammerhead feature. To maintain consistency, this hammerhead feature will be included in both the tapered and straight flexure configurations studied in the chapter.

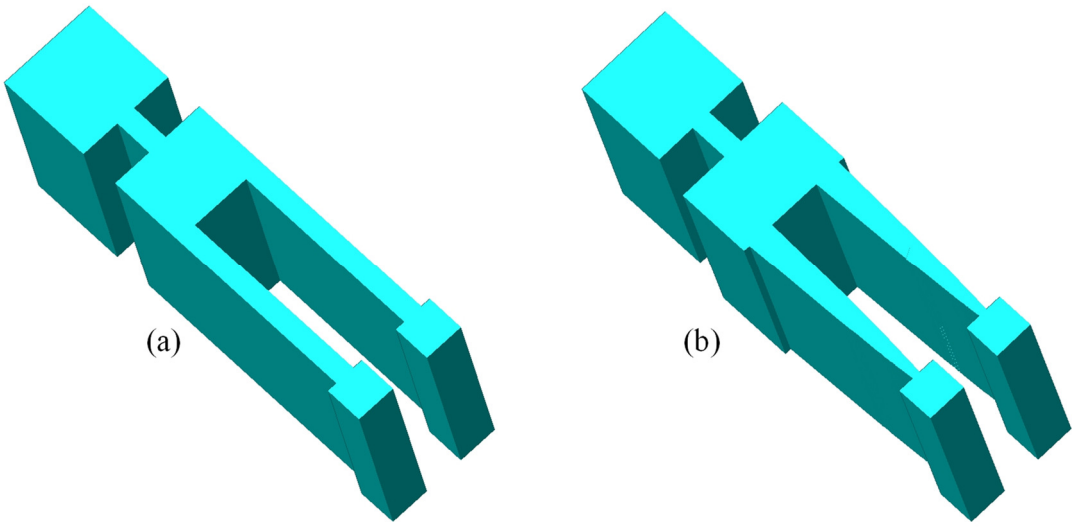

Figure 3.1 Straight Flexure (a) and Tapered Flexure (b) Tuning Forks.

This section is sub-divided into two subsections. The first presents the derivation of the equation that describes the quadratic taper of the flexure. The second section describes the derivation and summarizes many of the linear and angular deflection relationships of the quadratically tapered flexure with more detail provided in Appendix A.

3.1.1 Quadratic Taper Equation Derivation

The fundamental premise of this research effort is based on the finding presented in [71] which indicated that tapering the flexure width for constant strain on the outer edge along the entire length of the flexure provided significant benefits to the performance of their gyroscope. However, that reference does not provide the equation for the taper to achieve this condition. Therefore, it was first necessary to derive this equation and the derivation is documented here.

The problem is described graphically in Figure 3.2. In Figure 3.2, w_b is the width of the tapered flexure at the base, w_e is the width of the tapered flexure at the end, x is the axis along the length of the tapered flexure with the origin at the base, y is the transverse axis of the tapered flexure along the direction of the applied force with the origin at the center of the tapered flexure, L is the length of the tapered portion of the flexure, d is the distance between the end of the tapered flexure and the point force acting on it, and F is the point force acting on the tapered flexure. Additionally, the tapered flexure is assumed to have thickness, t, coming out of the plane of the page, which is not pictured in Figure 3.2.

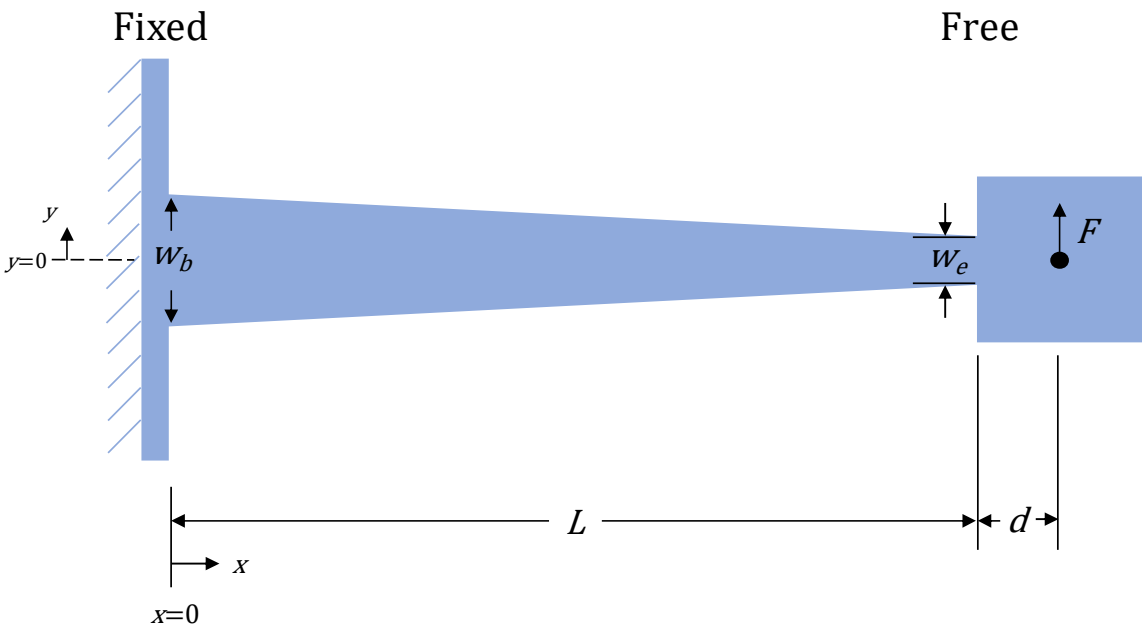

Figure 3.2 Mechanical Diagram of Tapered Flexure for Beam Width Derivation.

To derive the equation for the width of the flexure as a function of the location along the flexure, $w(x)$, we first investigate an infinitesimally small differential section at some location, l, along the length of the flexure (along the x axis). This section is shown graphically in Figure 3.3. In Figure 3.3, w_l is the width of the tapered flexure in the differential section being analyzed at x-axis coordinate l, Δx is the length of the differential flexure section, and T_{max_l} is the maximum stress at the outer edge of the differential flexure section. There are two assumptions built into Figure 3.3. Assumption 1 is that the width of the differential section, w_l, is constant throughout the width of the section, which is justified by the fact that the length of the section is infinitesimally small. Assumption 2 is that the stress in the section follows a linear distribution along the y-axis with compressive stress at the top of the flexure and tensile stress at the bottom of the flexure, which is justified by the fact that, since there is no shear in the y-axis direction

there will only be bending of the flexure. This bending will result in a small angular deflection of the faces of this differential section of the flexure. Since there is no net linear compressive or tensile force in the x-axis direction, this angular deflection can only be realized through a linear gradient of strain along the y-axis with the average strain being zero. These strain conditions imply tensile strain on one side of the flexure and an equal compressive strain on the other. Since stress and strain are linearly related through the Modulus of Elasticity (Young's Modulus) as described by Hooke's Law, then the stress must also follow a linear distribution along the y-axis with tensile stress on one side of the flexure and compressive stress on the other side.

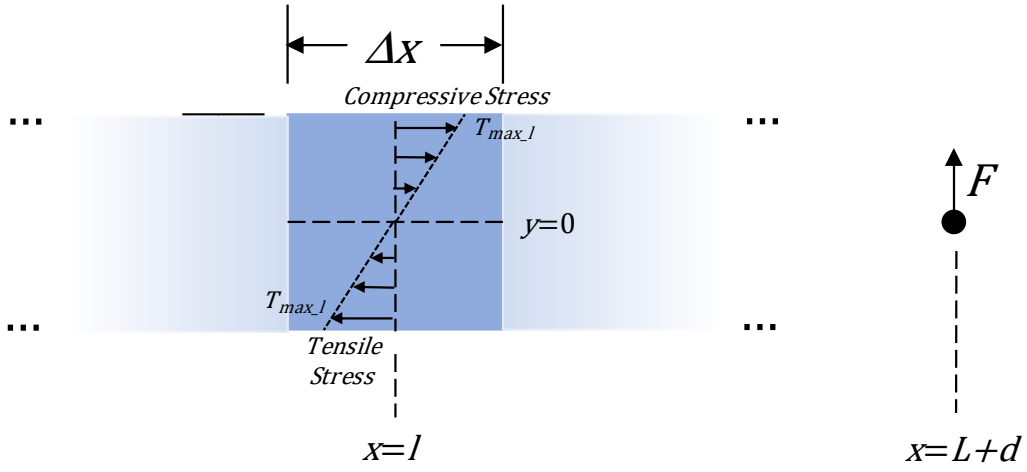

Figure 3.3 Mechanical Diagram of Differential Section of a Tapered Flexure.

Summing the moments in Figure 3.3 about the *z* axis, which is coming out of the plane of the page, around the center of the differential section, that is location (*l*, 0), yields the following equation:

$$\sum M_z = 0 = -t \cdot \int_{-\frac{w_l}{2}}^{\frac{w_l}{2}} y \cdot T_l(y)\, dy + F \cdot (L + d - l)\ , \tag{3.1}$$

where M_z is the moment about the z axis, y is a variable of integration along the y axis, and $T_l(y)$ is a function that describes the stress in the flexure as a function of y at location l. With the assumption given previously that $T_l(y)$ is linear along the y axis, $T_l(y)$ can be written by inspection as:

$$T_l(y) = T_{maxl} \frac{y}{\left(w_l/2\right)} = \frac{2 \cdot T_{maxl}}{w_l} \cdot y\ , \tag{3.2}$$

where T_{maxl} is the maximum stress at location l.

Substituting Equation 3.2 into Equation 3.1 and evaluating the integral yields:

$$\sum M_z = 0 = -t \cdot \int_{-\frac{w_l}{2}}^{\frac{w_l}{2}} \frac{2 \cdot T_{maxl}}{w_l} \cdot y^2\, dy + F \cdot (L + d - l) \tag{3.3}$$

$$F \cdot (L + d - l) = \frac{2 \cdot T_{maxl}}{w_l} \cdot t \cdot \int_{-\frac{w_l}{2}}^{\frac{w_l}{2}} y^2\, dy \tag{3.4}$$

$$F \cdot (L + d - l) = \frac{2 \cdot T_{maxl}}{w_l} \cdot t \cdot \left[\frac{y^3}{3}\right] \Bigg|_{-\frac{w_l}{2}}^{\frac{w_l}{2}} \tag{3.5}$$

$$F \cdot (L + d - l) = \frac{t \cdot T_{maxl}}{6} \cdot {w_l}^2 . \tag{3.6}$$

Solving Equation 3.6 for the maximum stress at location *l*, T_{maxl}, yields:

$$T_{maxl} = \frac{6 \cdot F \cdot (L + d - l)}{t \cdot {w_l}^2} , \tag{3.7}$$

which is consistent with the maximum stress in a non-tapered cantilever beam [30] when evaluating the stress at the base of the beam, $l=0$, and where the load is applied at the tip of the cantilever beam, $d=0$.

The purpose of the tapered beam is to provide constant stress on the outer edge of the beam along the entire length of the beam. This implies that we want the maximum stress to be a constant not dependent on the location, *l*, along the *x* axis. The maximum moment in the beam is encountered at the base of the beam since it is the greatest distance from the applied force. Therefore, we define the maximum stress in the tapered beam to be that encountered at the outer edge of the base of the beam. Setting $l=0$ and letting $w_l=w_b$, and substituting $w_l=w_b$, Equation 3.7 yields:

$$T_{max} \equiv T_{maxl}\Big|_{l = 0,\ w_l = w_b} = \frac{6 \cdot F \cdot (L + d)}{t \cdot {w_b}^2} . \tag{3.8}$$

Finally, to find the relation for the width of the tapered flexure at any location, *l*, we substitute Equation 3.8 into Equation 3.6 and solve for w_l:

$$F \cdot (L + d - l) = \frac{t \cdot \frac{6 \cdot F \cdot (L + d)}{t \cdot {w_b}^2}}{6} \cdot {w_l}^2 \tag{3.9}$$

$$w_l = w_b \sqrt{\frac{L + d - l}{L + d}}\ , \tag{3.10}$$

which is a surprisingly simple result for such a complex derivation. Clearly this equation describes a flexure that is a parabola with its origin at the point where the force is applied and opening to the left. This is why these flexures are referred to as quadratically tapered flexures. Also, from this equation it is evident that if the tapered portion of the flexure were to extend all the way to the point where the force is applied. $x=L+d$, the width of the flexure at that location would be zero. This is not a realistic flexure to fabricate and is the main reason the hammerhead feature is required.

3.1.2 Tapered Flexure Linear and Angular Deflection Equation Derivation

To enable the design of quadratically tapered flexures with desired mechanical properties, it is necessary to derive the linear and rotational deflection and spring constant equations. The mechanical system to be evaluated is pictured in Figure 3.4.

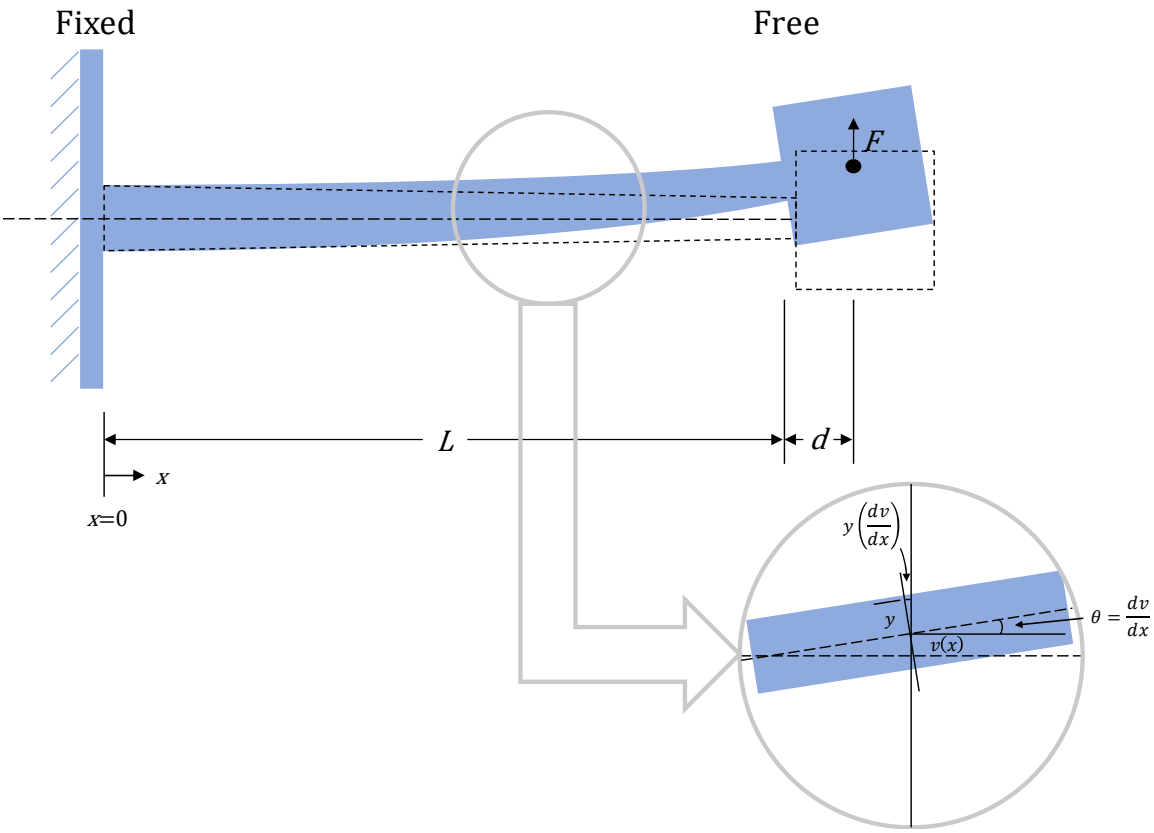

Figure 3.4 Mechanical Diagram of Tapered Flexure for Deflection Derivation.

Many references [30, 91] begin their discussion of beam deflection characteristics with the common Euler-Bernoulli beam equation given here:

$$M(x) = EI\frac{\partial^2 v(x)}{\partial x^2}\ , \tag{3.11}$$

where *M(x)* is the bending moment as a function of *x*. *E* is the modulus of elasticity (also called Young's modulus). *I* is the second moment of inertia of the beam cross-section, and *v*(*x*) is the displacement of the beam as a function of *x* shown in the inset of Figure 3.4. However, in the case of the tapered beam, the second moment of inertia, *I*, of the beam is also a function of the location along the x-axis, *x*, of that particular cross-

section. That is, for the tapered beam, *I* is a function of *x*, or $I = I(x)$. As such, it was unclear if the second moment of inertia, *I(x)*, should be pulled into the second derivative with respect to the location along the beam, *x*, in Equation 3.11 above. Therefore, the derivation of the Euler-Bernoulli beam equation was researched [92] and analyzed to ensure that the second moment of inertia could remain outside of the second derivative with respect to location along the beam, *x*. That analysis is provided in section A.1 of Appendix A and proves that the moment of inertia can remain outside of the second derivative.

Referring back to Figure 3.4, since F is the only external force acting on the beam, the moment at any point along the beam, $M(x)$, can be found as the product of that external force, F, and the distance between the external force, $L + d$, and the location, x, or:

$$M(x) = F \cdot (L + d - x). \tag{3.12}$$

Substituting Equation 3.12 into Equation 3.11 yields:

$$F \cdot (L + d - x) = E \cdot I(x) \cdot \frac{d^2 v(x)}{dx^2} \ . \tag{3.13}$$

For convenience, we introduce *N* which we will substitute back out at the end of the derivation:

$$N = L + d. \tag{3.14}$$

Substituting this into Equation 3.13 yields:

$$F \cdot (N - x) = E \cdot I(x) \cdot \frac{d^2 v(x)}{dx^2} \,. \tag{3.15}$$

We also know that the general equation for the second moment of inertia of a rectangular cross-section is given by:

$$I = \frac{t \cdot w^3}{12} \,. \tag{3.16}$$

Combining Equations 3.14 and 3.10, we obtain an expression for the width of the tapered beam as a function of x:

$$w(x) = w_b \sqrt{\frac{N - x}{N}} \,. \tag{3.17}$$

Substituting Equation 3.17 into Equation 3.16 gives the expression for the second moment of inertia of the tapered beam as a function of x:

$$I(x) = \frac{t \cdot w(x)^3}{12} = \frac{t \cdot \left(w_b \sqrt{\frac{N - x}{N}} \right)^3}{12} = \frac{t \cdot w_b^3 \left(\frac{N - x}{N} \right)^{\frac{3}{2}}}{12} \,. \tag{3.18}$$

Substituting Equation 3.18 into Equation 3.15 yields the second order differential equation that governs the deflection of the tapered beam:

$$F \cdot (N - x) = E \cdot \frac{t \cdot w_b^3 \left(\frac{N - x}{N} \right)^{\frac{3}{2}}}{12} \cdot \frac{d^2 v(x)}{dx^2} \,. \tag{3.19}$$

The solution to Equation 3.19 is found using separation of variables and is provided in section A.2 of Appendix A. This solution leads to several important relationships for the tapered flexure with a load applied to the center of the hammerhead which are summarized in Table 3.1.

It is important to note here that the hammerhead geometrical feature serves a slightly different purpose for the research presented in this dissertation than it served previously [71]. In that reference, the tapered flexure was implemented in a simple tuning fork configuration and the hammerhead primarily served as a lumped mass at the end of the flexure/tuning fork. In this work, the tapered flexure is typically employed in guided beam or folded flexure configuration where two tapered flexures are placed tip to tip. A more detailed description of this configuration is provided in Section 3.3, but as mentioned previously, if the tapered flexures were allowed to extend to the point where the force is applied ($d=0$), then the width of the flexure would go to zero. In the cantilever beam configuration, this zero-width condition occurs because there is zero moment on the beam at the location where the force is applied. In the guided beam configuration, this zero-width condition occurs in the center of the S-shaped deflection where the beam goes through a zero-moment condition as the stress in the beam changes sign from compression to tension. Therefore, the hammerhead feature is also necessary in the guided beam configuration to connect two tapered flexures together.

Table 3.1 Key Equations for the Tapered Flexure with Hammerhead Configuration.

Description	Equation	Range
Width of the Tapered Flexure	$w(x) = w_b\sqrt{\frac{(L+d)-x}{(L+d)}}$	$0 \le x \le L$
Linear Deflection of the Tapered Flexure	$v(x) = \frac{12\cdot F\cdot (L+d)^{\frac{3}{2}}}{E\cdot t\cdot w_b^3}\left\{\frac{4}{3}(L+d-x)^{\frac{3}{2}} + 2\cdot (L+d)^{\frac{1}{2}}\cdot x - \frac{4}{3}(L+d)^{\frac{3}{2}}\right\}$	$0 \le x \le L$
	$v(x) = \frac{12\cdot F\cdot (L+d)^{\frac{3}{2}}}{E\cdot t\cdot w_b^3}\left\{\left[\frac{4}{3}(d)^{\frac{3}{2}} + 2\cdot (L+d)^{\frac{1}{2}}\cdot L - \frac{4}{3}(L+d)^{\frac{3}{2}}\right] + \left[2\cdot (x-L)\cdot\left((L+d)^{\frac{1}{2}} - (d)^{\frac{1}{2}}\right)\right]\right\}$	$L < x \le L+d$
Angular Deflection of the Tapered Flexure	$\theta(x) = \frac{24\cdot F\cdot (L+d)^{\frac{3}{2}}}{E\cdot t\cdot w_b^3}\left\{(L+d)^{\frac{1}{2}} - (L+d-x)^{\frac{1}{2}}\right\}$	$0 \le x \le L$
	$\theta(x) = \theta(L) = \frac{24\cdot F\cdot (L+d)^{\frac{3}{2}}}{E\cdot t\cdot w_b^3}\left\{(L+d)^{\frac{1}{2}} - (d)^{\frac{1}{2}}\right\}$	$L < x \le L+d$
Linear Deflection at Hammerhead Center	$v(L+d) = \frac{8\cdot F}{E\cdot t\cdot w_b^3}\left\{(L+d)^3 - (L+d)^{\frac{3}{2}}(d)^{\frac{3}{2}}\right\}$	$x = L+d$
Angular Deflection at Hammerhead Center	$\theta(L+d) = \theta(L) = \frac{24\cdot F\cdot (L+d)^{\frac{3}{2}}}{E\cdot t\cdot w_b^3}\left\{(L+d)^{\frac{1}{2}} - (d)^{\frac{1}{2}}\right\}$	$x = L+d$
Linear Spring Constant at Hammerhead Center	$k_{HH} = \frac{E\cdot t\cdot w_b^3}{8\cdot\left[(L+d)^3 - (L+d)^{\frac{3}{2}}(d)^{\frac{3}{2}}\right]}$	at $x = L+d$
Angular Spring Constant at Hammerhead Center	$k_\theta = \frac{E\cdot t\cdot w_b^3}{24\cdot\left[(L+d)^2 - (L+d)^{\frac{3}{2}}(d)^{\frac{1}{2}}\right]}$	at $x = L+d$

3.2 Initial Tapered Flexure Finite Element Analyses

The goal of this work is to design a flexure that has improved properties for an in-plane resonator that can be beneficial in a MEMS gyroscope design. For ease of fabrication, it is desirable to fabricate this device out of a silicon-on-insulator (SOI) wafer using a single mask, Deep Reactive Ion Etch (DRIE) process. Therefore, the initial finite element analyses documented in this section are based on tapered flexure tuning fork designs implemented in the device layer of an SOI wafer.

All of the process modeling, device layout, meshing, and FEA were performed using the CoventorWare software package from Coventor, Inc. CoventorWare is an integrated suite of design and simulation software that has the accuracy, capacity, and speed to address real-world MEMS designs. The suite has many MEMS-specific features for modeling and simulating a wide range of MEMS devices, including inertial sensors (accelerometers and gyros), microphones, resonators, and actuators. The field solvers within CoventorWare provide comprehensive coverage of MEMS-specific multi-physics, such as electrostatics, coupled electro-mechanics, piezoelectric, piezoresistive, and damping effects, thus providing a one-stop, integrated software package for all stages of the design and modeling required for this work.

3.2.1 Initial FEA Material, Modeling, and Meshing Parameters

Implementation of a MEMS design within CoventorWare begins with the materials database. CoventorWare provides a relatively extensive database of common materials used in MEMS devices. For the purpose of the FEA presented in this section,

the design involves only 3 materials: Single Crystal Silicon <100>, Thermal Silicon Dioxide, and Bulk Silicon. The material properties used for Single Crystal Silicon <100> and Thermal Silicon Dioxide are provided in Figure 3.5 and Figure 3.6 and represent typical values of the material properties found in commercially available SOI wafers. The bulk silicon was not included in any of the finite element analyses so its material properties are not included here.

The important characteristics of the devices studied here are sensitive to several of the Single Crystal Silicon material properties listed in Figure 3.5. Specifically, the spring constant is directly proportional to the Modulus of Elasticity and the resonant frequency is proportional to the square root to the Modulus of Elasticity which can vary some across various wafer manufacturers. In addition to being sensitive to the Modulus of Elasticity, thermoelastic damping is also sensitive to Poisson's ratio, specific heat, thermal conductivity, and the thermal coefficient of expansion [61, 62]. These other material properties do not vary as much as the Modulus of Elasticity for SCS from different manufacturers. This work focuses on a side-by-side comparison of tapered flexures to straight flexures using the same material and material properties and is not attempting to predict the absolute performance of tapered flexures. Therefore, variations in the material properties are not expected to impact the comparative findings presented herein. Also, care has been taken in the design of all structures studied herein to ensure symmetry of the resonators. This symmetry should minimize the strain transmitted to the insulation layer material which, in turn, minimizes the effect of material property variations of the Silicon Dioxide in that layer.

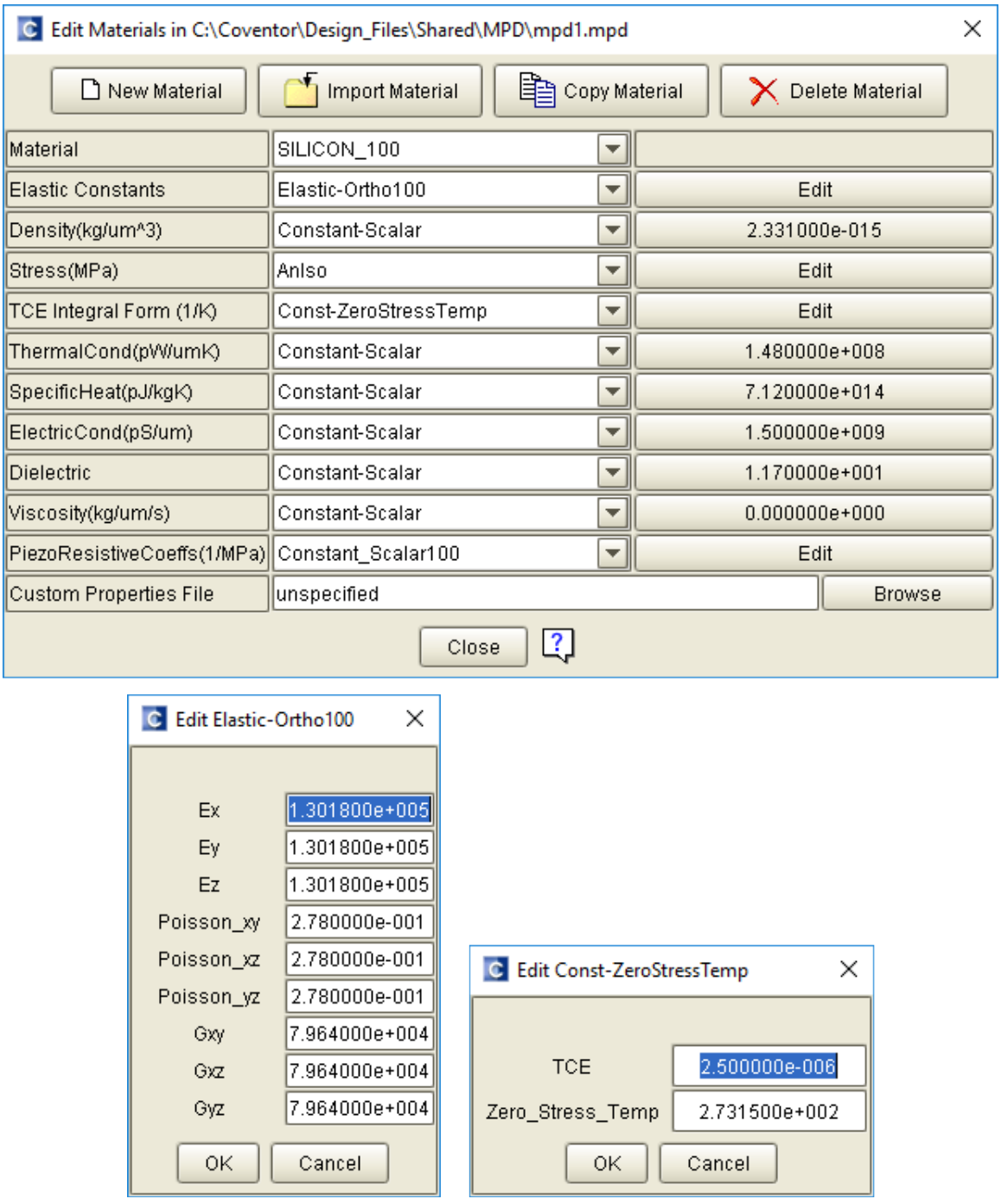

Figure 3.5 Relevant Material Properties of Single Crystal Silicon <100>.

With the materials and their relevant properties captured in the Materials Properties Database, the fabrication process is then captured in the Process Editor module

within CoventorWare. The Process Editor captures both the layer by layer structure of the wafer and the fabrication processing steps.

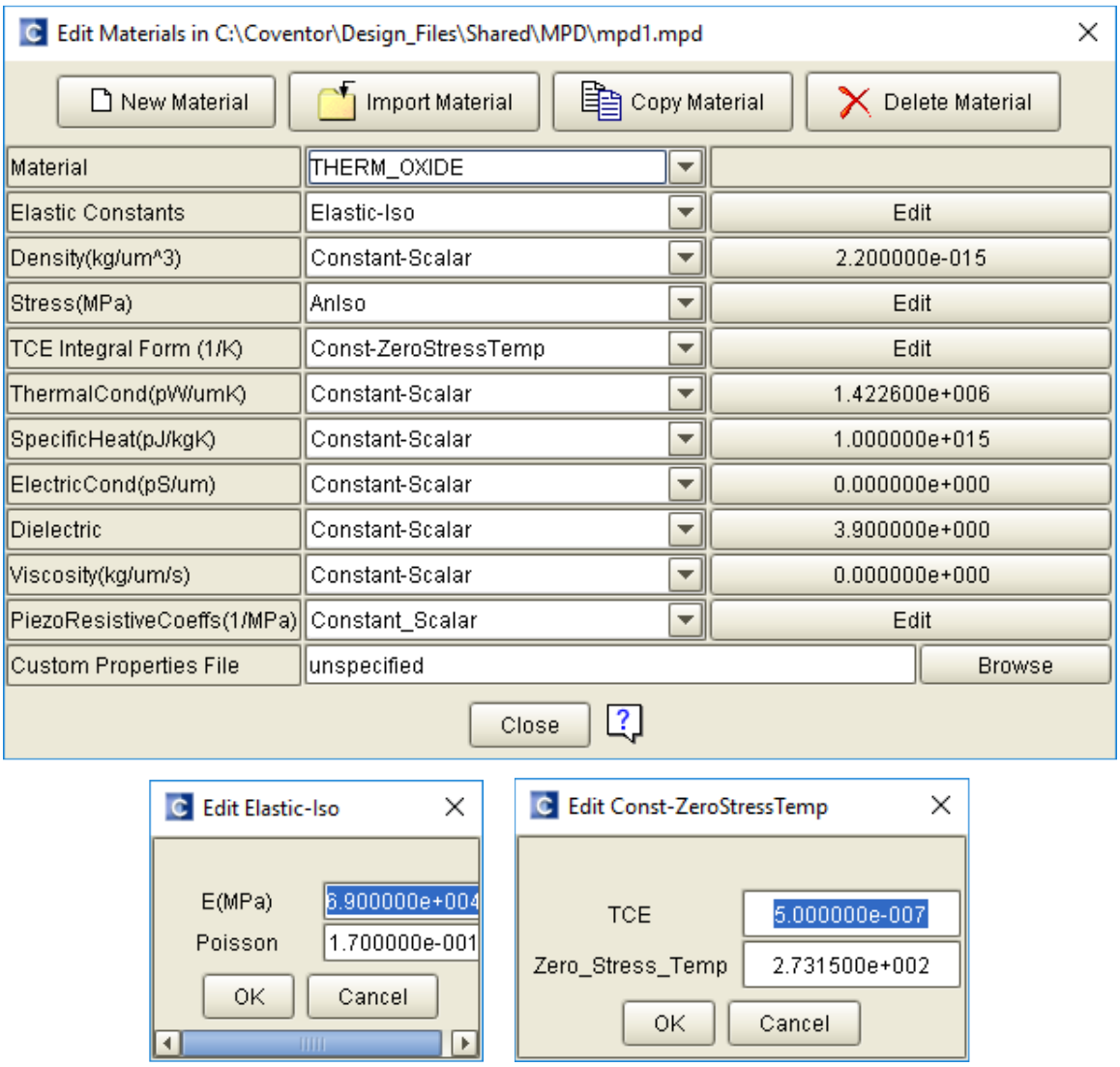

Figure 3.6 Relevant Material Properties of Thermal Silicon Dioxide.

For the designs and analyses documented in this section, the Process file is shown in Figure 3.7. This process captures the formation of the SOI wafer as well as the etching processes that form the MEMS device under analysis. The process begins on step

number zero by establishing a 500 µm thick bulk silicon layer, which is common for 150 mm SOI wafers. This step also creates a masking layer named "SubstrateMask" as shown in the "Mask Name" column. These masks are not physical layers but are virtual design layers used in the LayoutEditor to describe the outline of the etches (and subsequently the MEMS devices). In this case, the SubstrateMask is used to define the outer dimensions of the Substrate included in building the solid model of the MEMS device for subsequent modeling and analysis. The next layer forms the thermal oxide (Silicon Dioxide) and is 1 µm thick. The final layer of the SOI wafer is the Device layer and is formed as Single Crystal Silicon <100> and is 100 µm thick. The final two steps are etching process steps. The first of these, the Deep Reactive Ion Etch (DRIE) step outlined by the "DeviceMask" mask, will etch completely through the Device layer. The final step is the device release etch which is a generic wet etch of the Oxide layer outlined by the "OxideMask" mask. This is a release etch that will etch completely through the Oxide layer and the mask drawn is intended to be representative of the material left after the release step. This step does not require an actual photolithography mask for implementation.

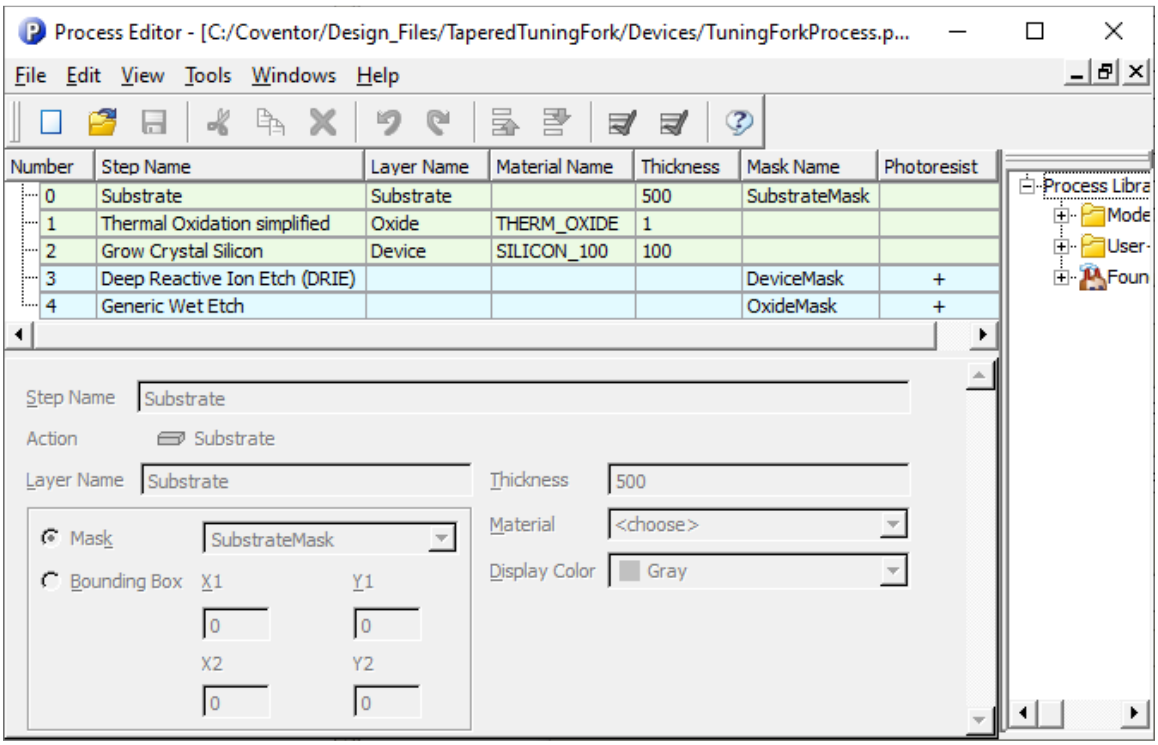

Figure 3.7 SOI Wafer Structure and Fabrication Process.

For the purposes of this initial investigation into the characteristics of the tapered flexure, the primary goal was a comparison of these characteristics against those characteristics of the straight flexure. Therefore, the absolute scale, resonant frequency, and spring constants of the flexures and the tuning forks were not as important as ensuring that these values were similar for both the straight and tapered flexure designs. However, for the purposes of shortening the FEA calculation time, it was desired to keep the device dimensions as small as possible while maintaining some reasonable size for a MEMS device. The thickness of the device layer was already set to be 100 µm and it seemed reasonable that the flexure length should not be shorter than the flexure thickness. So, the flexure length was set to 100 µm as well. For reference, please see Figure 3.1 and Figure 3.2 for the general device layout and shape. All FEA analyses were performed on

the tuning fork configuration and none were performed on just a single cantilevered beam. For the straight flexure design, the width of the flexure was set to 10 µm. To ensure a similar spring constant for the tapered flexure, the width at the base of the tapered flexure was calculated to be 13.73 µm using the equation for the spring constant for a force applied at the center of the hammerhead given in Table 3.1. It is important to note that the equations employed for the straight flexure describe its response at the end of the flexure for a force applied at the end of the flexure but the equations used for tapered flexure describe its response at the center of the hammerhead feature for a force applied at the center of the hammerhead. This causes a minor discrepancy in the results which will be discussed. In both cases the hammerhead size was 20 µm by 20 µm (d=10µm).

For the FEA analyses documented in this section, the mesher settings are presented in the screen capture images presented in Figure 3.8 and Figure 3.9, for the straight and tapered flexure tuning forks, respectively. The CoventorWare software documentation provides detailed descriptions for each of these settings [93]. The analyses contained in this section represent just the initial study of the tapered flexure design and, therefore, a formal mesh study was not completed. Instead, a limited mesh sensitivity study was performed which indicated that the mesh settings were adequate for this analysis. The mesher setting for the straight and tapered flexure tuning forks only differ in that the "small feature removal threshold" setting of 0.1 on the straight flexure tuning fork was replaced with a "minimum element size" setting of 0.2 for the tapered flexure tuning fork. This change was necessary to reduce the number of elements in the

mesh of the tapered flexure tuning fork so that the thermoelastic damping FEA would converge.

For each flexure design, three types of FEA analyses were performed. These included:

- Modal Analysis
- Spring Constant/Nonlinearity Analysis
- Quality Factor/TED Analysis

Results of these analyses are provided in the following subsections.

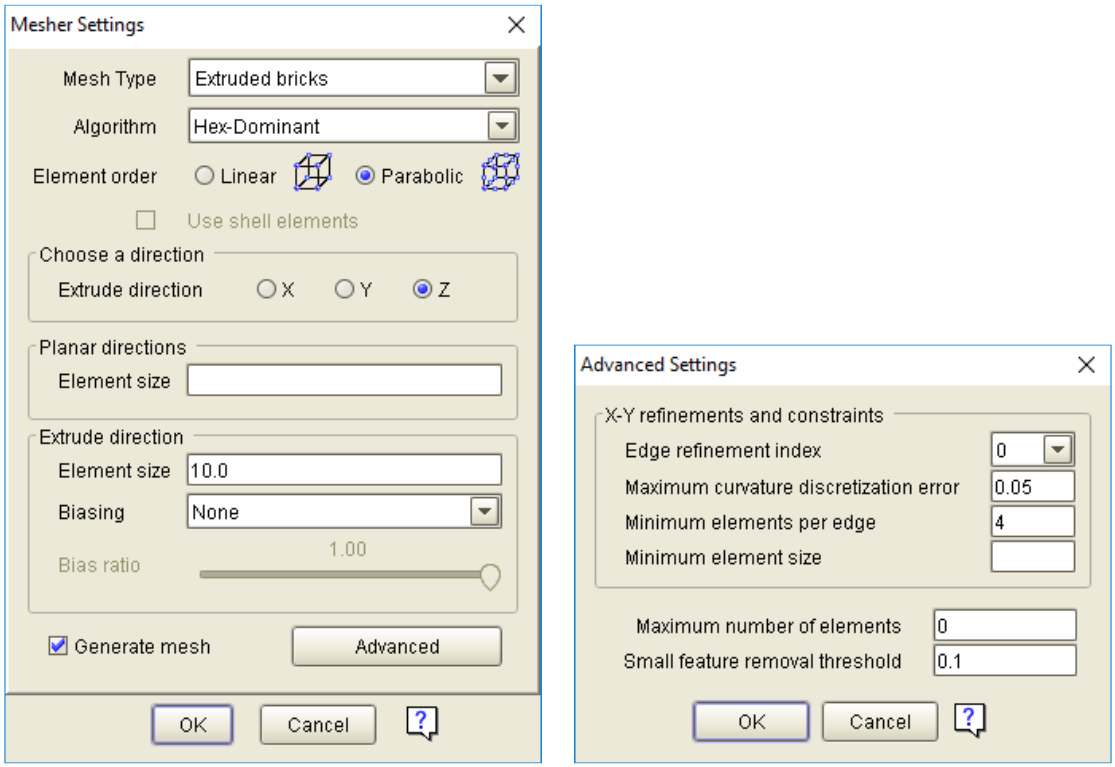

Figure 3.8 Mesher Settings for Straight Flexure Tuning Fork Initial FEA Analyses.

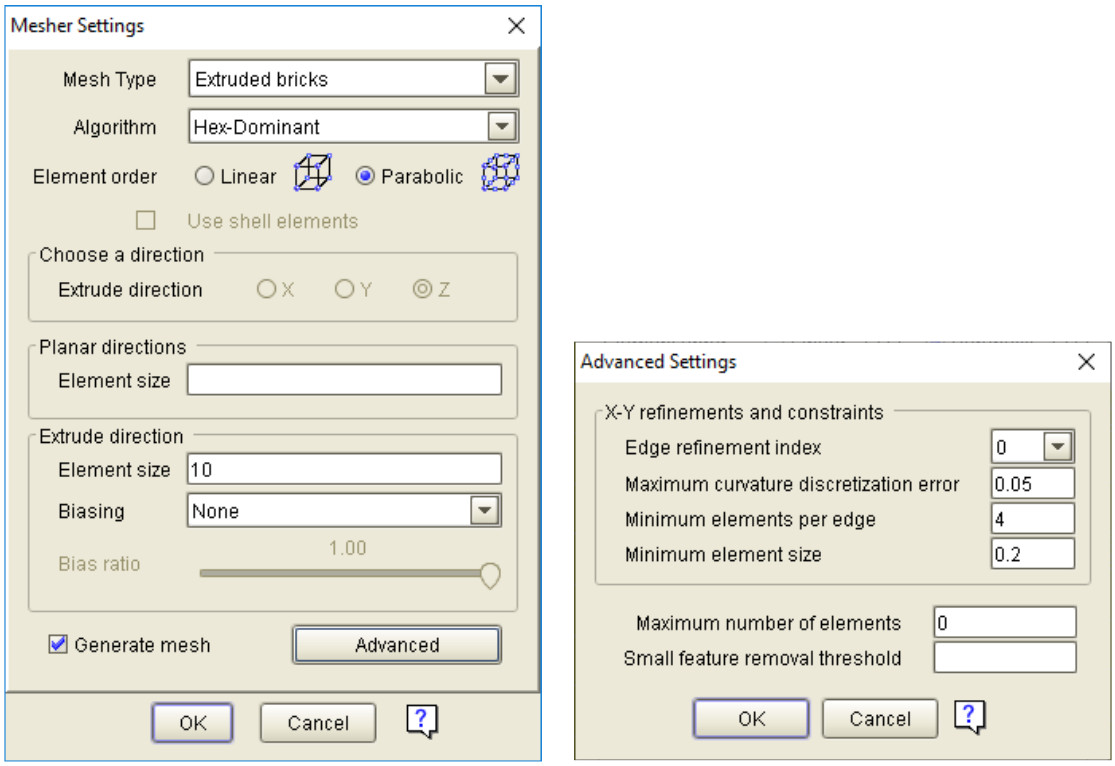

Figure 3.9 Mesher Settings for Tapered Flexure Tuning Fork Initial FEA Analyses.

3.2.2 Initial Modal Analysis

For the Modal Analysis, only one surface boundary condition was required. This was a "FixAll" boundary condition at the base of the oxide Anchor, as illustrated in Figure 3.10. The solver settings used for the Modal analyses are presented in the screen capture in Figure 3.11. It was assumed that the desired mode would be one of the first 5 modes, so only 5 modes were requested from the solver. The density of mesh elements near the end of the tapered flexure is an artifact of the combination of a rapidly changing flexure curvature in that area, the number of discrete data points chosen to define the

outer edge of the flexure, and the specific mesher algorithm settings. This type of meshing artifact appears in tapered flexure meshes periodically throughout this work.

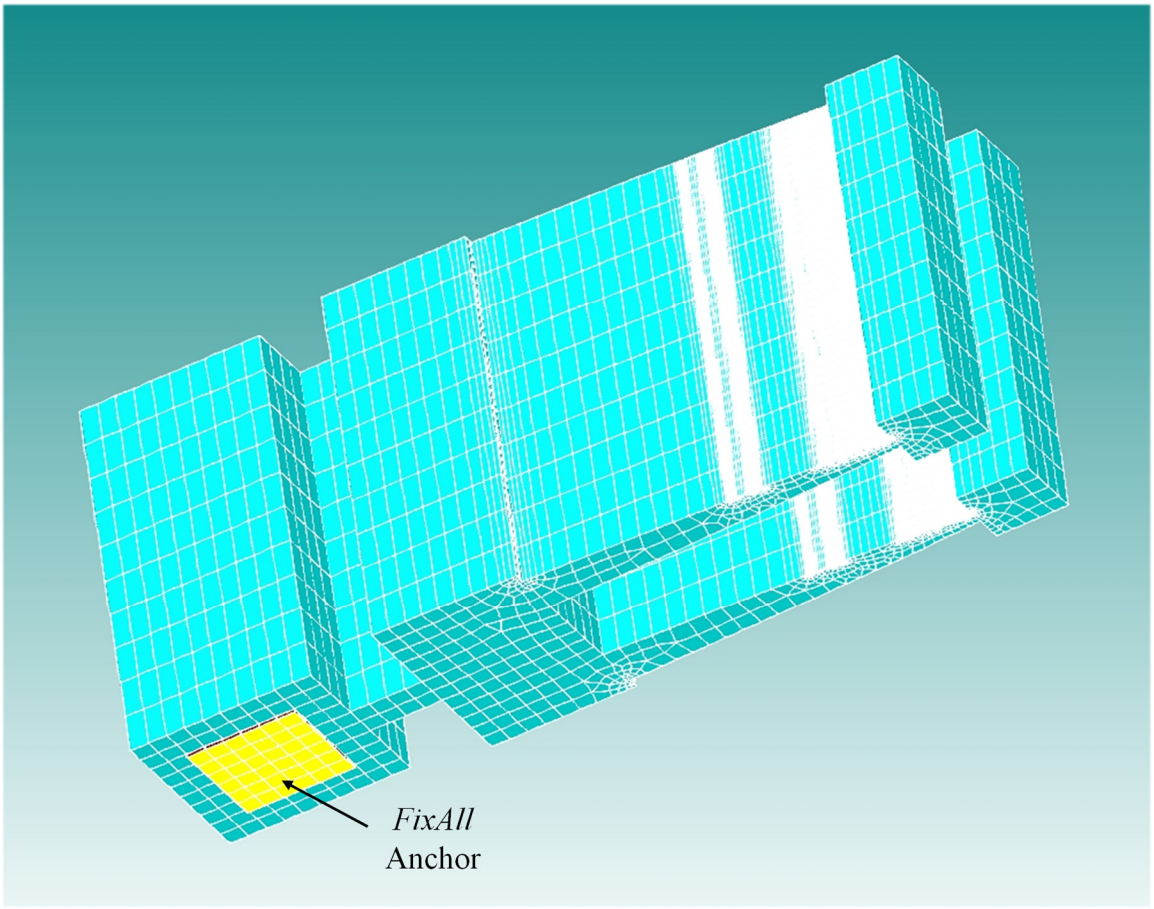

Figure 3.10 FixAll Boundary Condition Surface for Modal Analysis.

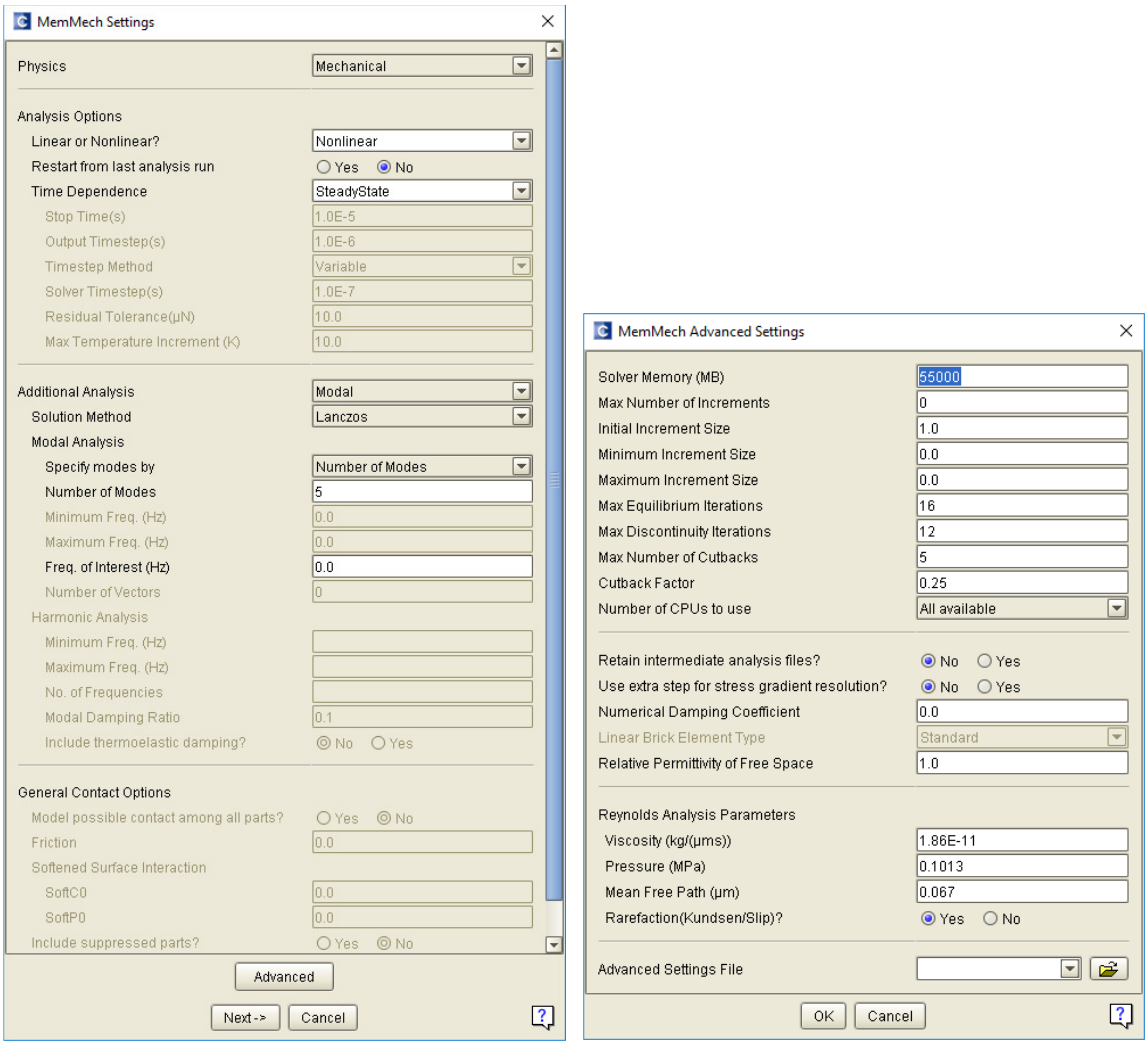

Figure 3.11 Solver Settings for Modal Analysis.

Figures 3.12 through 3.16 illustrate the first 5 modal shapes for the straight flexure design, and Figures 3.17 through 3.21 illustrate the first 5 modal shapes for the tapered flexure design. Figures 3.22 and 3.23 present the modal frequencies for the straight flexure and the tapered flexure designs. The mode 2 frequency of the straight flexure is the desired tuning fork mode where the tines are operating in anti-phase motion and is 72.315 kHz. The mode 3 frequency of the tapered flexure is the tuning fork mode and is 93.113 kHz. In general, the same modal shapes share very similar modal

frequencies between the straight and tapered flexure designs. However, the modal frequency for the tuning fork mode was shifted significantly higher (~30%) for the tapered flexure design. These flexures were designed to have similar spring constants but the mass distribution along the length of the flexure is significantly different and accounts for the majority of this shift in modal frequency.

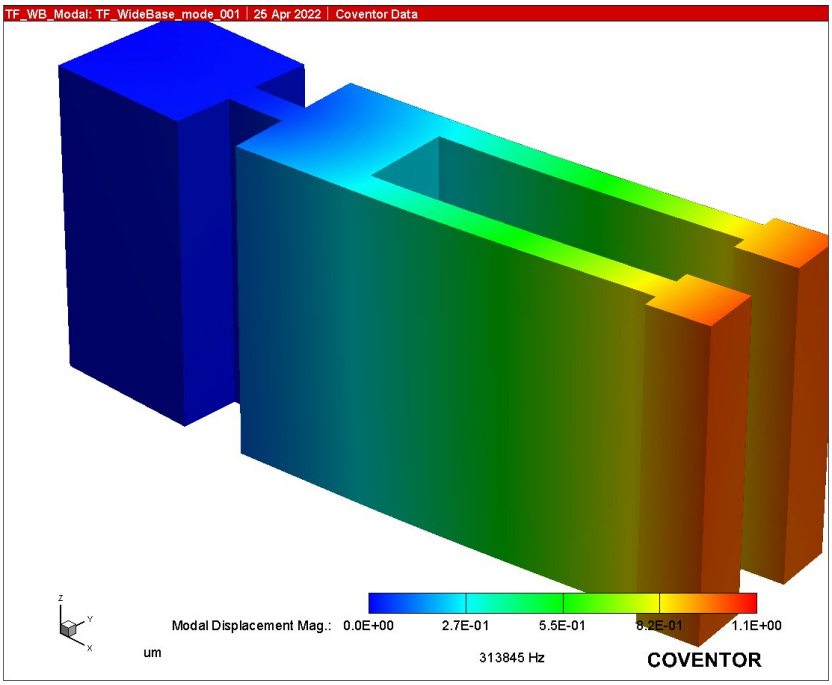

Figure 3.12 Straight Flexure Tuning Fork Mode 1.

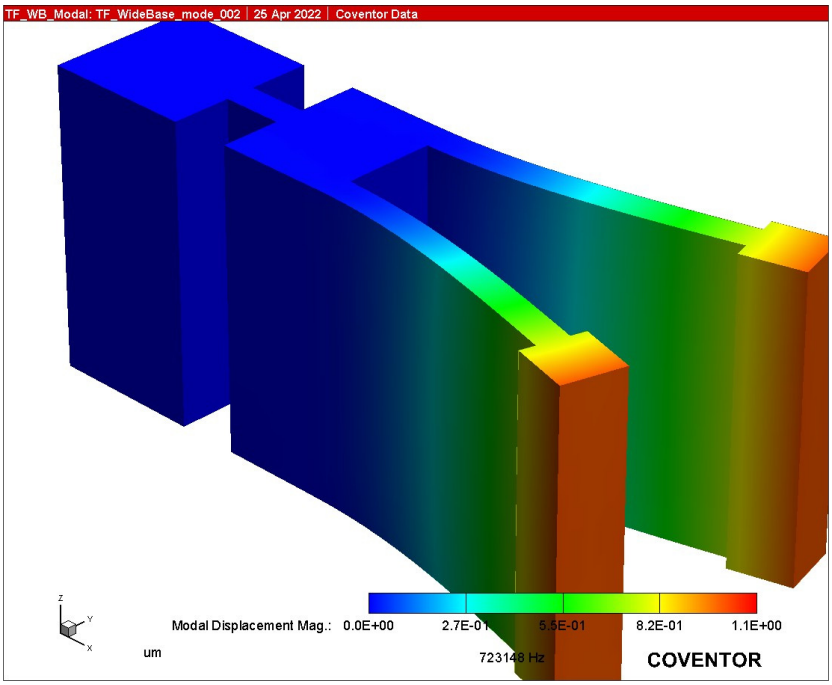

Figure 3.13 Straight Flexure Tuning Fork Mode 2.

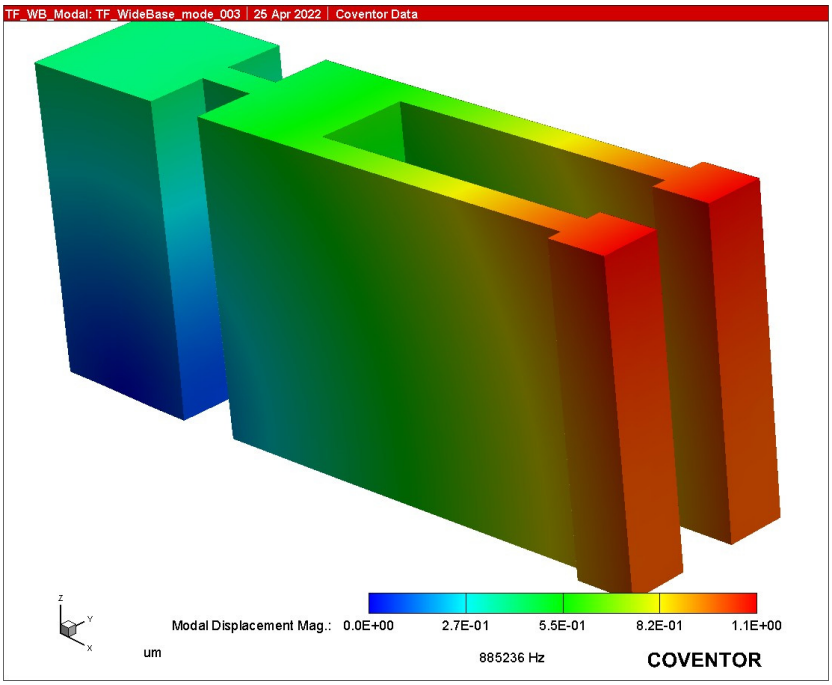

Figure 3.14 Straight Flexure Tuning Fork Mode 3.

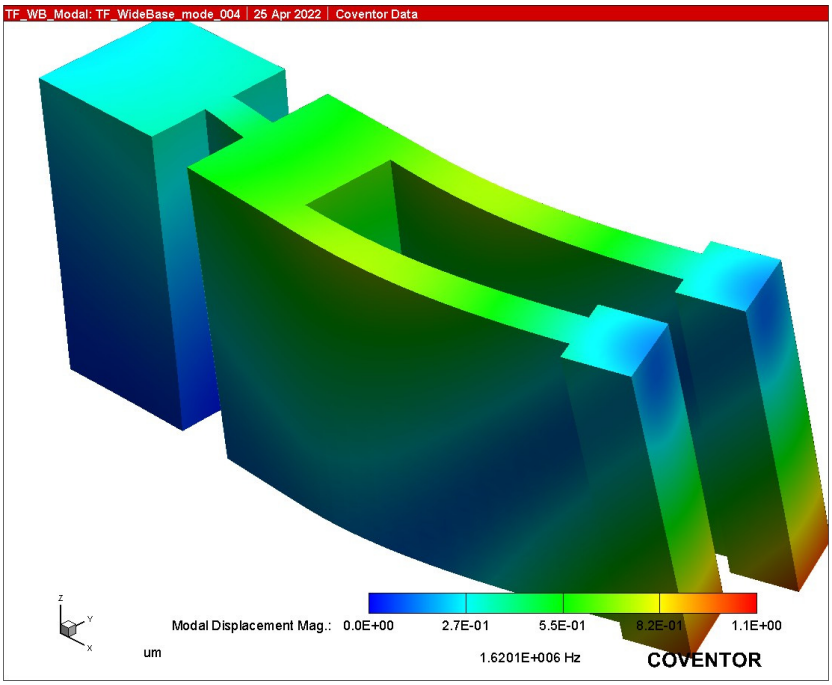

Figure 3.15 Straight Flexure Tuning Fork Mode 4.

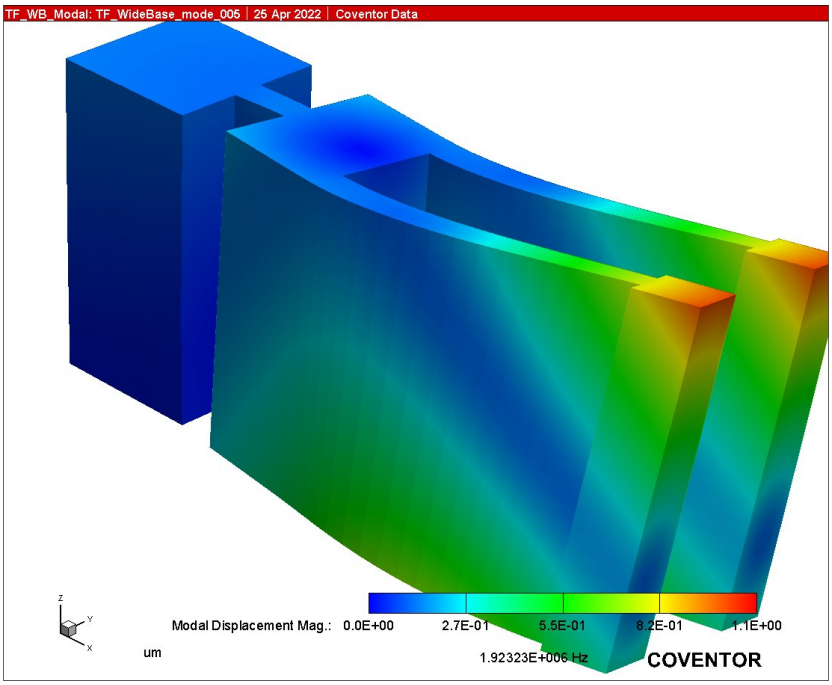

Figure 3.16 Straight Flexure Tuning Fork Mode 5.

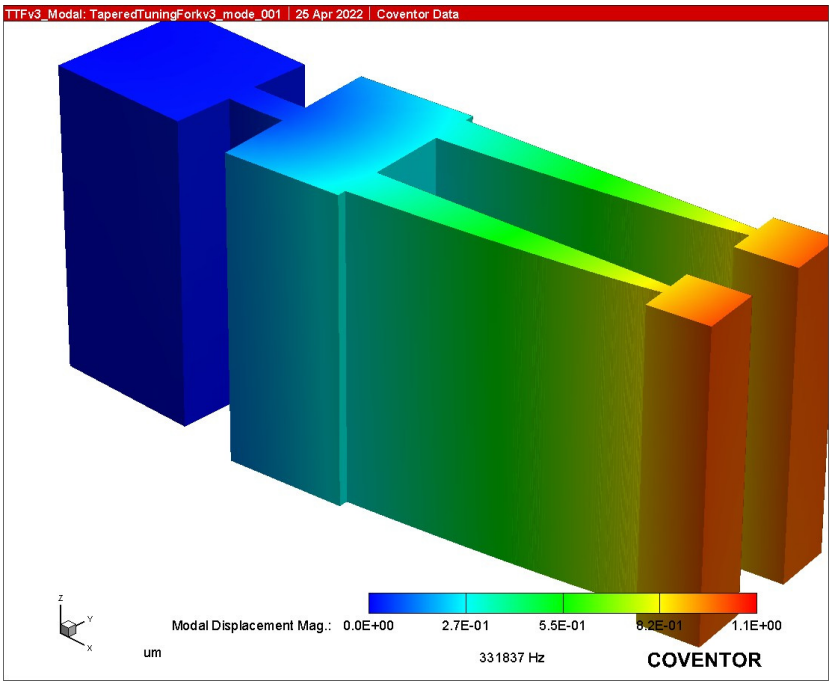

Figure 3.17 Tapered Flexure Tuning Fork Mode 1.

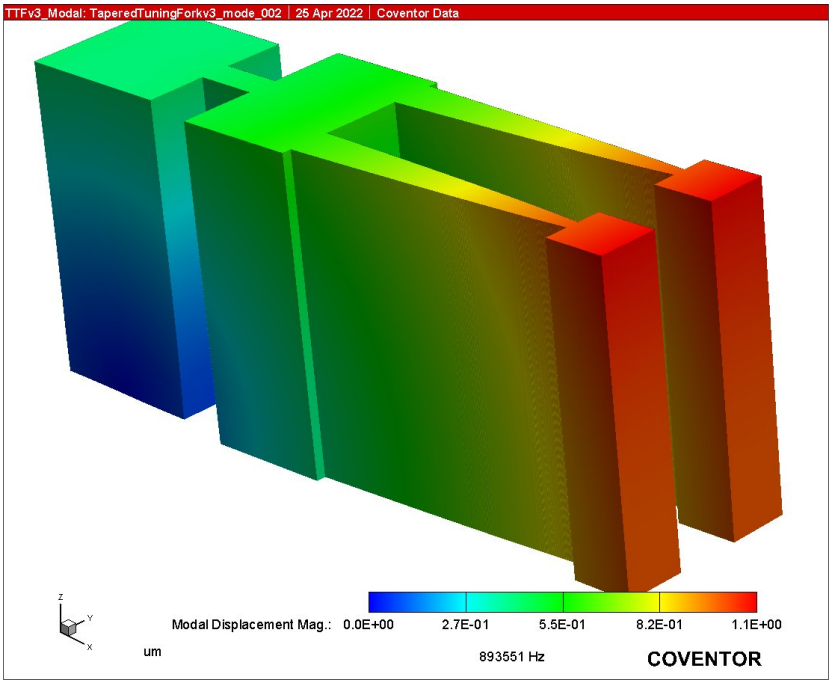

Figure 3.18 Tapered Flexure Tuning Fork Mode 2.

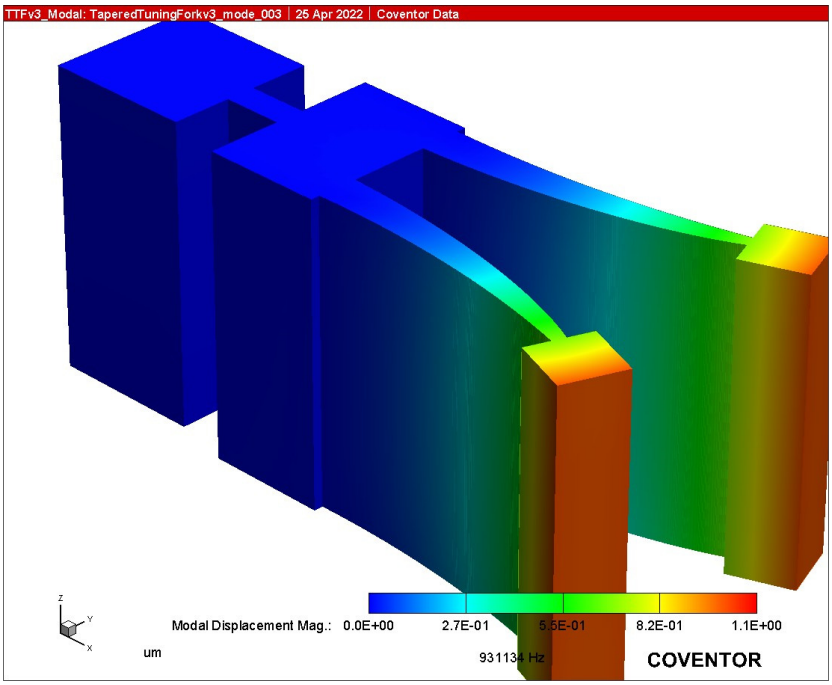

Figure 3.19 Tapered Flexure Tuning Fork Mode 3.

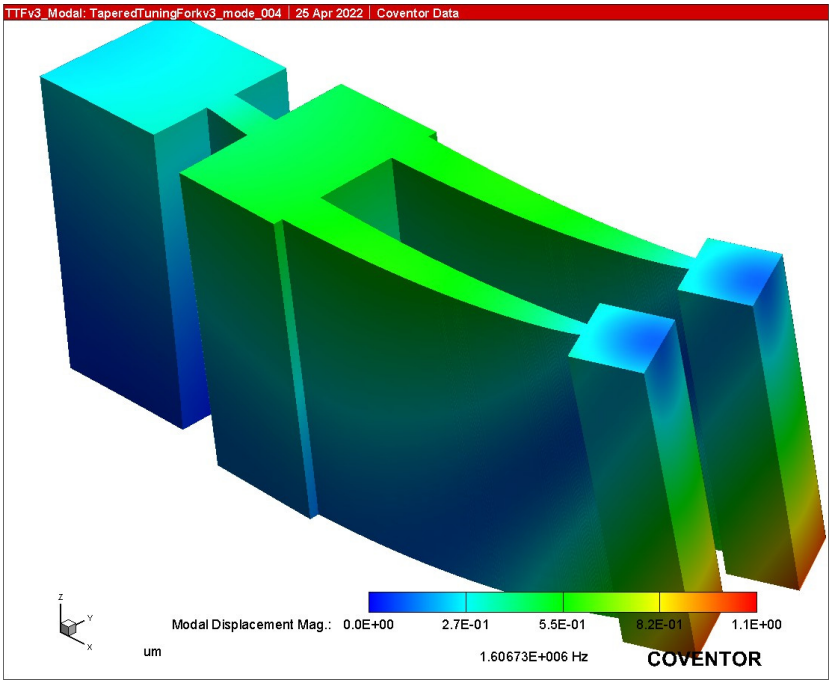

Figure 3.20 Tapered Flexure Tuning Fork Mode 4.

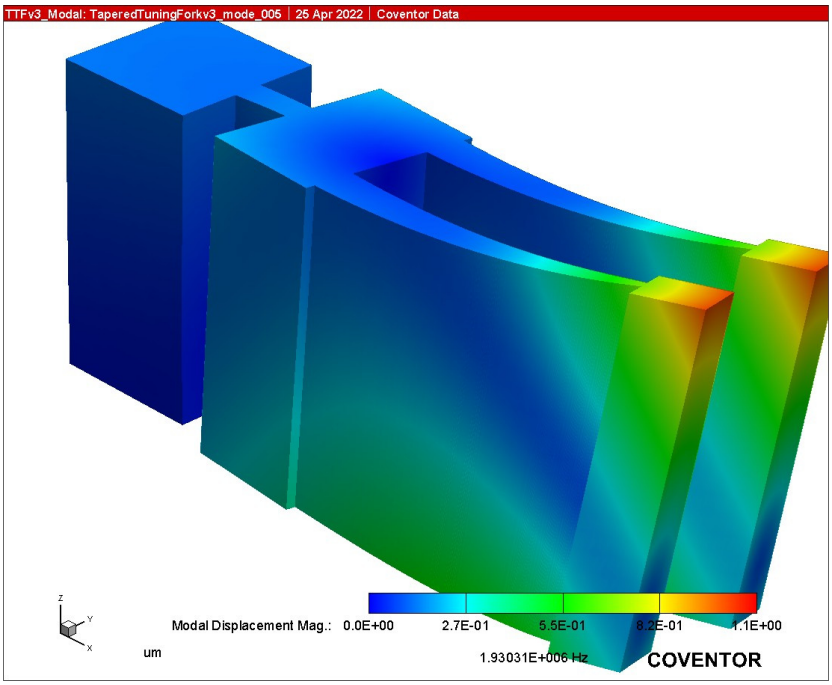

Figure 3.21 Tapered Flexure Tuning Fork Mode 5.

modeDomain

	Frequency	Generalized Mass	Damping
1	3.138446E05	3.262864E-10	0
2	7.231478E05	2.192444E-10	0
3	8.852357E05	5.139978E-10	0
4	1.620102E06	1.891266E-10	0
5	1.923234E06	1.2302E-10	0

OK

Figure 3.22 Straight Flexure Tuning Fork Modal Frequencies.

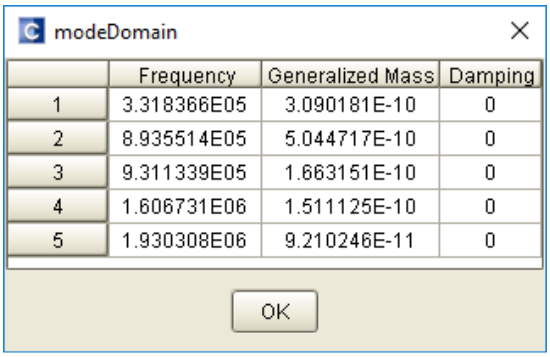

Figure 3.23 Tapered Flexure Tuning Fork Modal Frequencies.

3.2.3 Initial Spring Constant, Nonlinearity, and Stress Analysis

For the Spring Constant/Nonlinearity Analysis, two surface boundary conditions were required. Similar to the Modal Analysis, there was a "FixAll" boundary condition at the base of the oxide Anchor, as previously illustrated in Figure 3.10. Additionally, there was a "LoadPatch" surface boundary condition applied to the two outside edges of the tuning fork hammerheads as illustrated in Figures 3.24 and 3.25. Several analyses were conducted with these surfaces highlighted in yellow loaded with various pressures ranging from 1 kPa up to 10 kPa to obtain an estimate of the spring constant and estimate the nonlinearity of the response displacement. The resulting displacement values are presented in Figures 3.26 and 3.27 for the Straight Flexure and the Tapered Flexure designs, respectively.

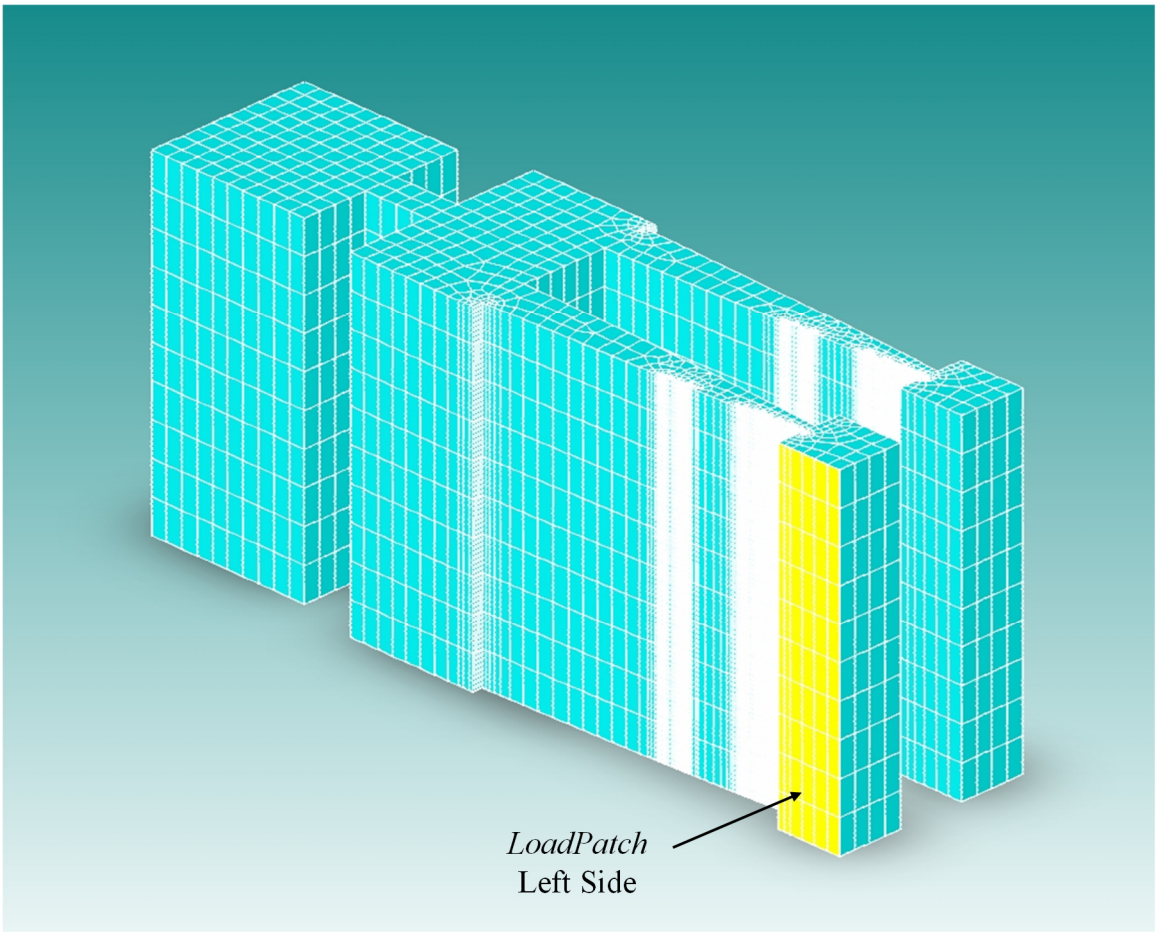

Figure 3.24 LoadPatch Boundary Condition for Spring Constant Analysis, Left Side.

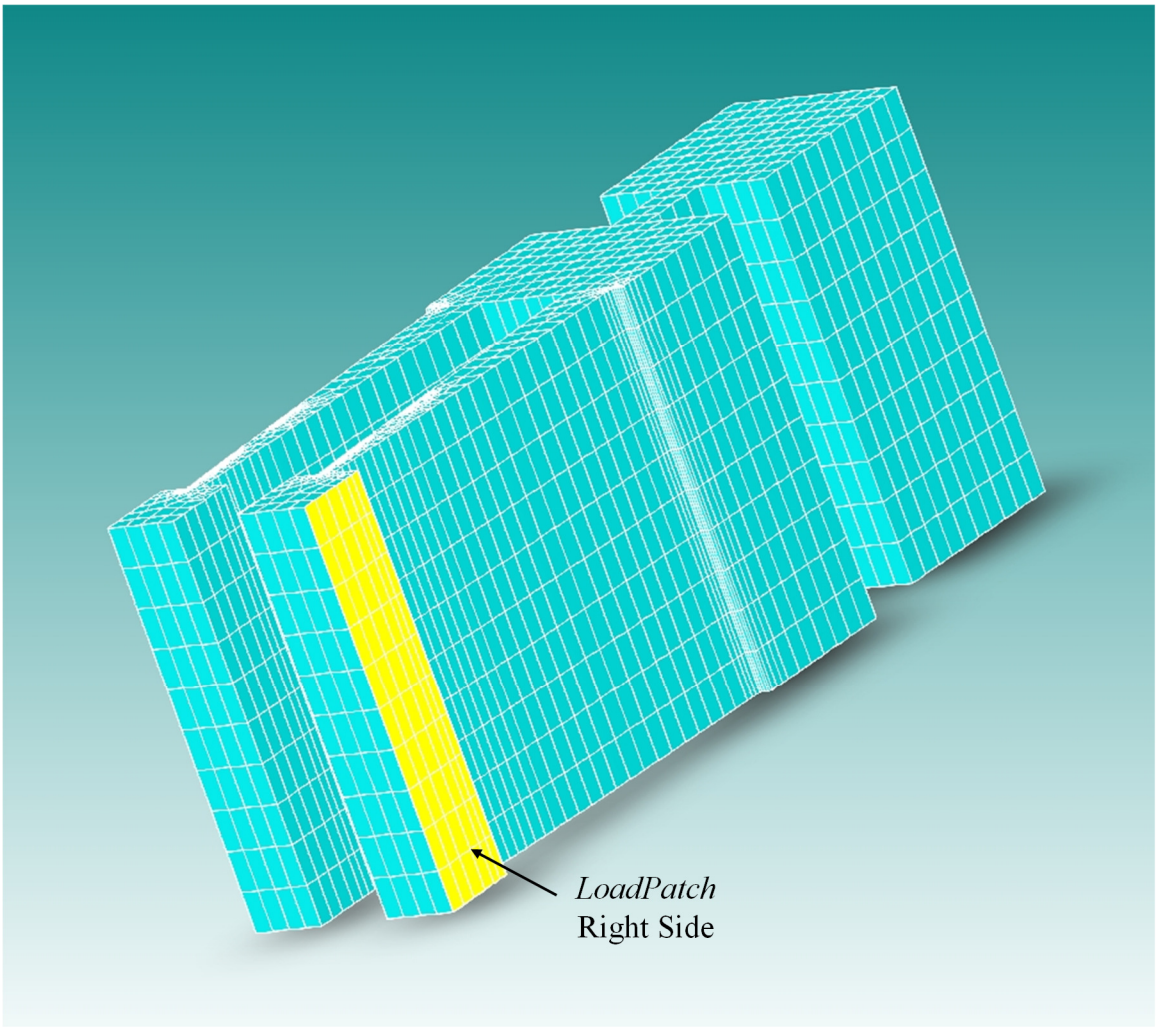

Figure 3.25 LoadPatch Boundary Condition for Spring Constant Analysis, Right Side.

mechDomain

	t1	Node Displacement_Maximum
Step 1	1.0E-03	7.976258E-04
Step 2	2.0E-03	1.595252E-03
Step 3	3.0E-03	2.392878E-03
Step 4	4.0E-03	3.190504E-03
Step 5	5.0E-03	3.98813E-03
Step 6	6.0E-03	4.785756E-03
Step 7	7.0E-03	5.583383E-03
Step 8	8.0E-03	6.381009E-03
Step 9	9.0E-03	7.178636E-03
Step 10	1.0E-02	7.976263E-03

Figure 3.26 Straight Flexure Spring Constant Analysis Displacement Results.

mechDomain

	t1	Node Displacement_Maximum
Step 1	1.0E-03	6.093814E-04
Step 2	2.0E-03	1.218763E-03
Step 3	3.0E-03	1.828145E-03
Step 4	4.0E-03	2.437527E-03
Step 5	5.0E-03	3.046909E-03
Step 6	6.0E-03	3.656291E-03
Step 7	7.0E-03	4.265674E-03
Step 8	8.0E-03	4.875057E-03
Step 9	9.0E-03	5.48444E-03
Step 10	1.0E-02	6.093823E-03

Figure 3.27 Tapered Flexure Spring Constant Analysis Displacement Results.

To obtain an estimate of the spring constant from the displacements returned by the FEA solver, several items must be taken into account. First, the applied load was given in units of pressure. These must be converted to units of force by multiplying by the area of the applied load, which was 20 µm by 100 µm, giving an area of 2000 µm².

The second item is that, for the straight flexure design, the spring constant equation given in the text is for a load applied at the end of the flexure whereas the load in this case was effectively applied 10 μm beyond the end of the flexure at the center of the hammerhead. For a cantilever beam, there is not a significant amount of additional bending that occurs near the tip of the beam. So, the application of the force just beyond the end of the flexure has approximately the same effect as increasing the effective length of the flexure by 10%. Since the length of the flexure is cubed and in the denominator of the spring constant equation, the effect is to reduce the spring constant by a factor of 1.1^3.

The final consideration is that the solver returns the maximum displacement from the very end of the hammerhead whereas the equation for the displacement of the straight flexure will be at the end of the flexure. Again, this increases the effective displacement. An estimate of this factor can be found by assuming that there is no additional bending within the hammerhead feature so that the angular displacement at the end of the flexure which also describes the angular deflection of the hammerhead feature can be used to project an additional displacement across its length. The effective linear and angular deflection spring constants for a straight cantilever beam [30] are given by:

$$k_{sc} \cong \frac{3 \cdot E \cdot I}{L_{Tot}^3} \tag{3.20}$$

and

$$k_{s\theta} \cong \frac{2 \cdot E \cdot I}{L_{Tot}^2} \ , \tag{3.21}$$

where k_{sc} is the linear deflection spring constant for the tip of the beam and $k_{s\theta}$ is the angular deflection spring constant for the tip of the beam. Using the dimensions for this

design (noting that $L_{Tot} = L + \frac{L_{HH}}{2}$) yields a k_{sc} of 3111 N/m and a $k_{s\theta}$ of 0.2282 N/rad. We extend the linear deflection expression to the end of the hammerhead feature by adding a term to perform a linear extrapolation using the angular deflection as follows:

$$k_{sce} \cong \frac{F}{\frac{F}{k_{sc}} + \frac{F}{k_{s\theta}} \cdot \frac{L_{HH}}{2}} = \frac{1}{\frac{L_{Tot}^3}{3 \cdot E \cdot I} + \frac{L_{Tot}^2}{2 \cdot E \cdot I} \cdot \frac{L_{HH}}{2}} \tag{3.22}$$

$$k_{sce} \cong \frac{6 \cdot E \cdot I}{2 \cdot L_{Tot}^3 + 3 \cdot \frac{L_{HH}}{2} \cdot L_{Tot}^2} \quad , \tag{3.23}$$

where k_{sce} is the linear deflection spring constant for the end of the hammerhead and L_{HH} is the length of the hammerhead. Using the dimensions for this design yields a k_{sce} of 2738 N/m.

In the case of the tapered flexure, the equations for force and displacement were derived assuming loads and displacement at the center of the hammerhead. Therefore, there is no need to account for the location of the applied force, but there is a need to account for the final displacement being at the end of the hammerhead instead of the center of the hammerhead. For this correction, we refer to row 3 of Table 3.1 and solve for $x = L + 2d$, or:

$$v_{HH}(L + 2 \cdot d) = \frac{12 \cdot F \cdot (L + d)^{\frac{3}{2}}}{E \cdot t \cdot w_b^3}\left\{\left[\frac{4}{3}(d)^{\frac{3}{2}} + 2 \cdot (L + d)^{\frac{1}{2}} \cdot L - \frac{4}{3}(L + d)^{\frac{3}{2}}\right] + \left[4 \cdot d \cdot \left((L + d)^{\frac{1}{2}} - (d)^{\frac{1}{2}}\right)\right]\right\} \quad \text{for } L < x \leq L + 2d, \tag{3.24}$$

which simplifies to:

$$v_{HH}(L + 2 \cdot d) = \frac{12 \cdot F}{E \cdot t \cdot w_b^3}\left\{\frac{-7}{3}(d)^{\frac{3}{2}} \cdot (L + d)^{\frac{3}{2}} + (2L + 4d) \cdot (L + d)^2 - \frac{4}{3}(L + d)^3\right\} \quad \text{for } L < x \leq L + 2d \tag{3.25}$$

and yields a spring constant of:

$$k_{HHe} = \frac{E \cdot t \cdot w_b^3}{12 \cdot \left[\frac{-7}{3}(d)^{\frac{3}{2}} \cdot (L + d)^{\frac{3}{2}} + (2L + 4d) \cdot (L + d)^2 - \frac{4}{3}(L + d)^3\right]} \quad \text{for } L < x \leq L + 2d\,, \tag{3.26}$$

where k_{HHe} is the linear deflection spring constant for the end of the hammerhead with the force applied to the center of the hammerhead. Using the dimensions for this design yields a k_{HHe} of 3422 N/m.

The FEA results from the Spring Constant analysis on the straight flexure indicated a spring constant for the applied force of 2524 N/m, which is relatively close to the approximate value of 2738 N/m calculated earlier. This is a relatively stiff beam and the bulk of the remaining difference is due to the less-than-infinite stiffness of the base where the flexure is anchored (compliance of the base). This spring constant was determined from the FEA data by calculating the linear least squares fit of the maximum Y-node displacement returned by the solver against the equivalent force applied to the center of the hammerhead. The data are plotted in Figure 3.28, which indicates very linear behavior. The error from the curve fit is plotted in Figure 3.29 and indicates that the maximum deviation from the curve fit was only a few parts per million of the actual displacement of the flexure. It is also interesting to note that the fit error follows a predominantly parabolic curve, which indicates that the error is primarily a second-order response.

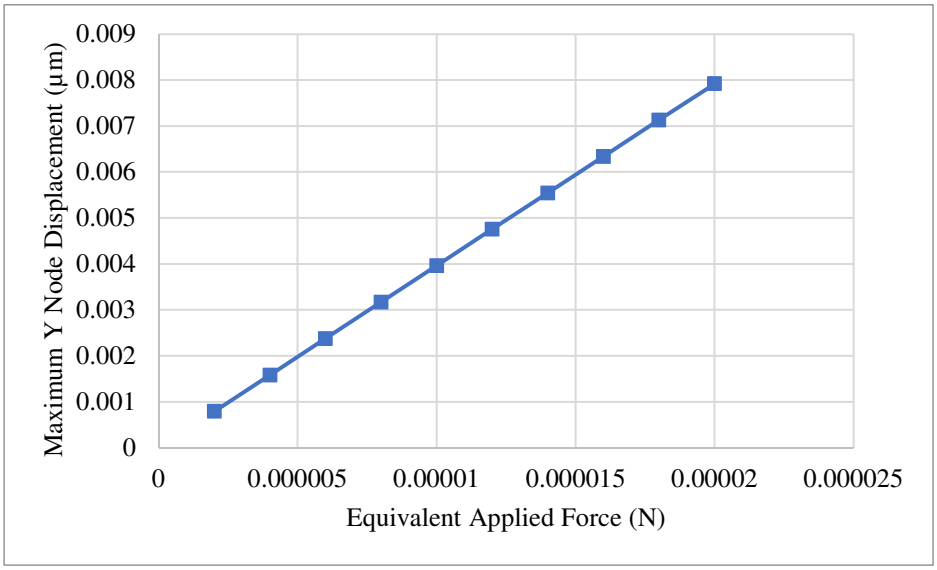

Figure 3.28 Straight Flexure Spring Constant Analysis Displacement Plot.

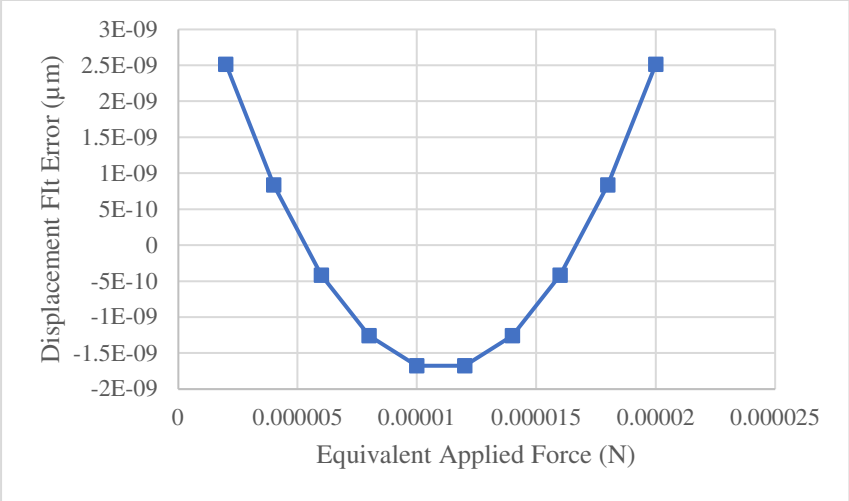

Figure 3.29 Straight Flexure Spring Constant Analysis Fit Error.

It is also instructive to perform a visual investigation into the displacement field and stress distribution. Figure 3.30 shows a visualization of the straight flexure under the largest applied force. In this figure, the color contour variable is set to the displacement with the displacement exaggerated by a factor of 2000. Similarly Figure 3.31 shows a visualization of the straight flexure under the largest applied force but in this figure, the color contour variable has been set to the principal stress with the displacement still exaggerated by a factor of 2000. From Figure 3.31, it is clear that the majority of the stress and the majority of the flexing is occurring near the base of the flexure.

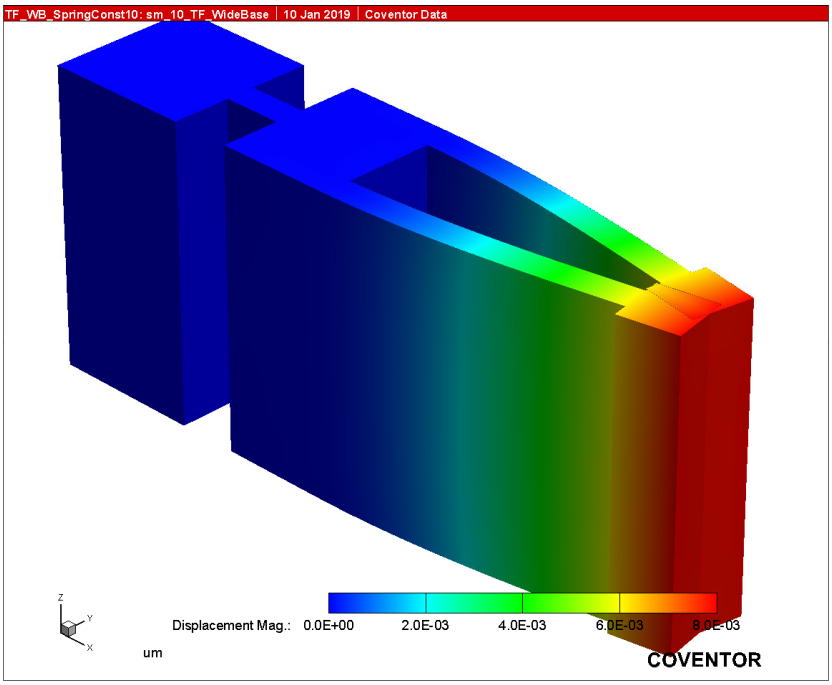

Figure 3.30 Straight Flexure Spring Constant Analysis Displacement Visualization.

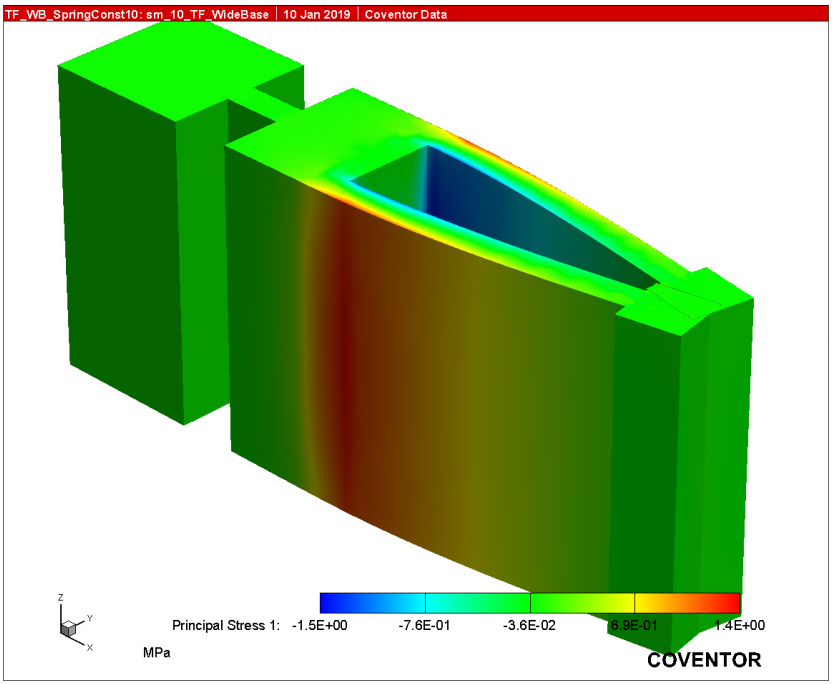

Figure 3.31 Straight Flexure Spring Constant Analysis Stress Visualization.

The FEA results from the Spring Constant analysis on the tapered flexure indicated a spring constant for the applied force of 3324 N/m. This spring constant was determined by calculating the linear least squares fit of the maximum Y node displacement returned by the solver against the equivalent force applied to the center of the hammerhead. The data are plotted in Figure 3.32, which again indicates very linear behavior. The error from the curve fit is plotted in Figure 3.33 and indicates that the maximum deviation from the curve it was only a few parts per million of the actual displacement of the flexure. It is also interesting to note that the fit error follows a predominantly parabolic curve, which indicates that the error is primarily a second-order response. This spring constant differs from the predicted value by only 2.9%. Again, this is a relatively stiff beam and the fact that the base is not infinitely stiff (compliance) where the flexure is anchored is responsible for the bulk of this difference. The impact of the compliance of the base is less than that of the straight flexure because the tapered flexure has less overall stress and is spread across a wider distance at the base because the equivalent tapered flexure is wider at the base than the straight flexure.

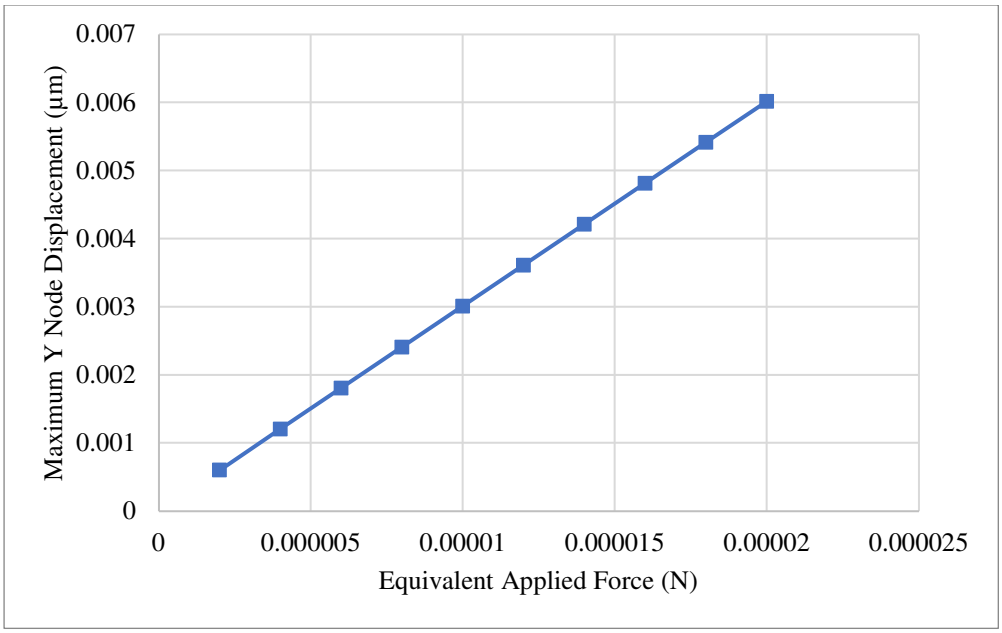

Figure 3.32 Tapered Flexure Spring Constant Analysis Displacement Plot.

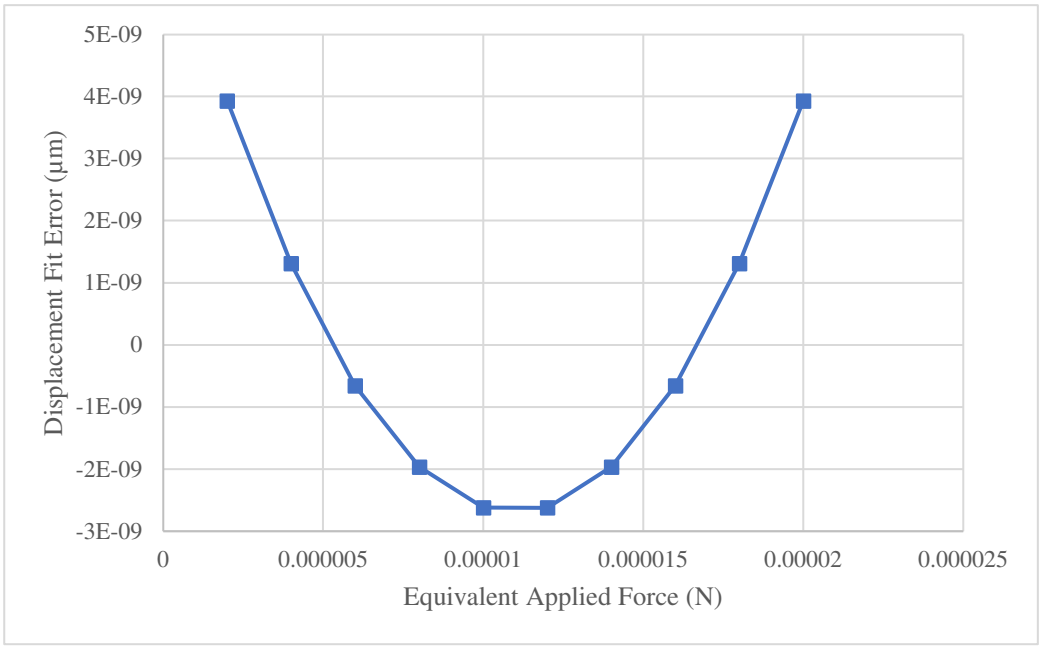

Figure 3.33 Tapered Flexure Spring Constant Analysis Fit Error.

It is also instructive to perform a visual investigation into the displacement field and stress distribution. Figure 3.34 shows a visualization of the tapered flexure under the largest applied force. In this figure, the color contour variable is set to displacement with the displacement exaggerated by a factor of 2000. Similarly Figure 3.35 shows a visualization of the tapered flexure under the largest applied force but in this figure, the color contour variable has been set to the principal stress with the displacement still exaggerated by a factor of 2000. From Figure 3.35, it is clear that the taper of the flexure did result in a constant stress along the outer edge of the flexure. This is a significant validation of the design and the equation for the width of the tapered beam.

In the original derivation of the taper equation, an assumption was made that the stress across the width of the beam would be a linear gradient as pictured in Figure 3.3. To validate this assumption, a close-up of the stress gradient in the flexure with six equally spaced stress contour bands is provided in Figure 3.36. This clearly shows very evenly spaced contour bands which indicates a linear gradient of stress across the width of the flexure, thus validating the original assumption.

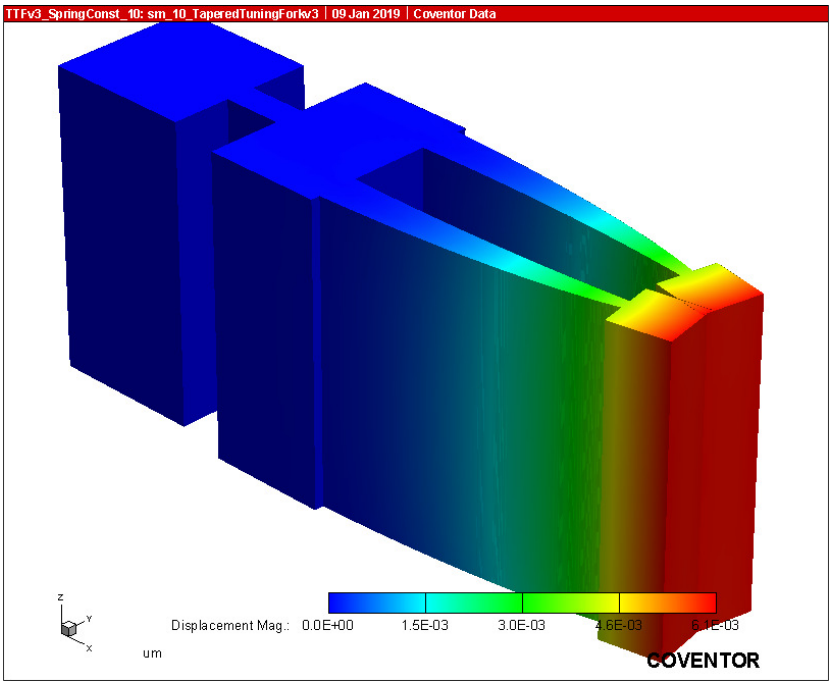

Figure 3.34 Tapered Flexure Spring Constant Analysis Displacement Visualization.

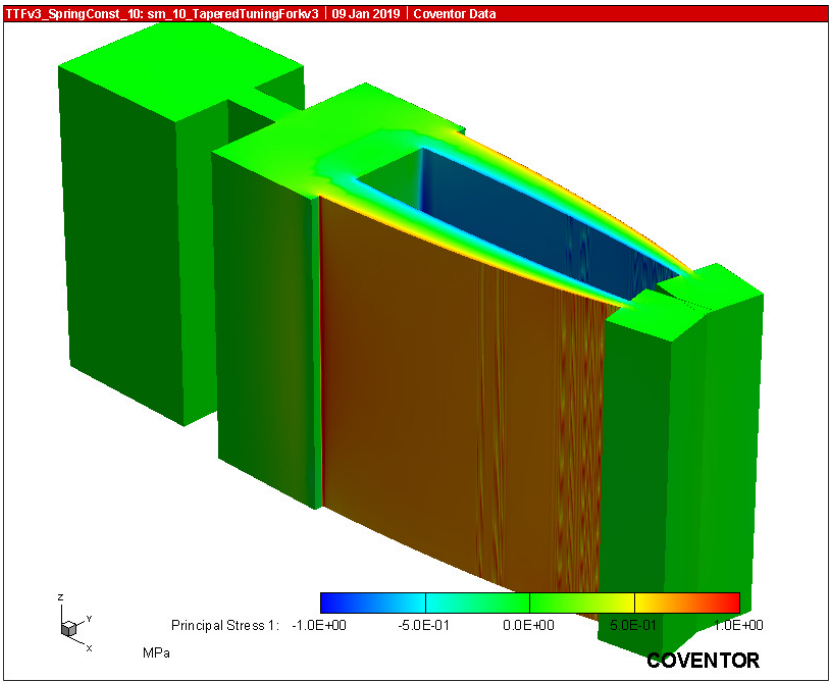

Figure 3.35 Tapered Flexure Spring Constant Analysis Stress Visualization.

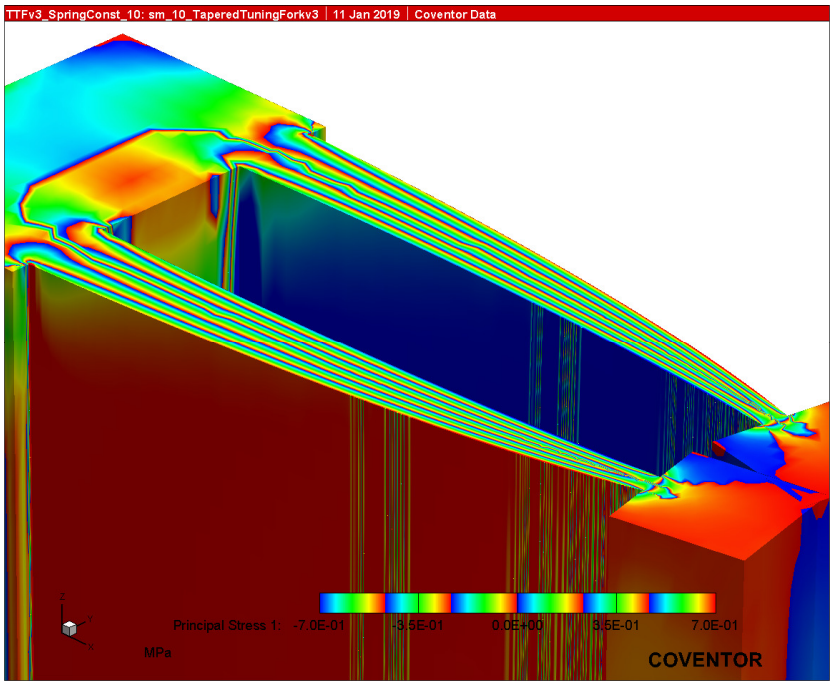

Figure 3.36 Tapered Flexure Stress Visualization with Six Contour Bands, Close-Up.

It is also important to investigate how well the maximum stress matches that predicted from Equation 3.8. Using the design parameters for this design and the boundary condition applied at the final step of the FEA analysis, the maximum stress at the outer edge of the flexures, T_{max}, is calculated from Equation 3.8 to be 0.7 MPa. The FEA indicates a maximum stress within a few percent that same value but varies a few percent around the outer surface of the flexure due to mesh variations and proximity to the edges.

Comparing the stress response of the tapered flexure against that of the straight indicates several key results. The first is that the expected/desired result that the straight flexure has its highest concentration near the base of the flexure was validated. Similarly, the stress concentration of the tapered flexure was constant along the outer edge of the entire length of the flexure. Also, the maximum stress in the tapered flexure (0.7 MPa)

was significantly less than that of the straight flexure (1.38MPa). Comparing the nonlinearity of the response of the tapered flexure to that of the straight flexure indicates that, while the nonlinearity of each of these is very small, the response of the tapered flexure displacement is slightly more nonlinear than that of the straight flexure. Since the maximum stress in the tapered flexure is roughly half that of the straight flexure, this increase in nonlinearity is likely to stem from the nonlinearity introduced by the difference in the angular deflection spring constant between these two designs rather than a nonlinearity in the material properties.

These analyses of the spring constant/nonlinearity evaluations revealed the following major findings:

- An analytic expression was correctly derived for the taper of the tapered flexure to yield constant stress on the outer edge of the flexure, which was verified by FEA.
- The predicted value for the maximum stress on the outer edge of the flexure was correct.
- The maximum stress in the tapered flexure was roughly half of the maximum stress found in the straight flexure.
- The predicted linear spring constant resulting from the tapered flexure design was in close agreement with the FEA results.
- The primary nonlinearity term in the flexure response is second-order and is on the order of ones of parts per million over the applied forces investigated here.

- The response of the tapered flexure displacement is slightly more nonlinear than that of the straight flexure. Since the maximum stress in the tapered flexure is roughly half that of the straight flexure, this increase in nonlinearity is more likely to stem from the nonlinearity introduced by the difference in the angular deflection spring constant between these two designs rather than a nonlinearity in the material properties.

3.2.4 Initial Thermo-Elastic Damping Analysis

For the Thermo-Elastic Damping (TED) Analysis, two boundary conditions were required. The first was the same "FixAll" boundary condition at the base of the oxide Anchor, as illustrated previously in Figure 3.10. The second was a Harmonic Surface Boundary Condition applied to the same two hammerhead surfaces as previously illustrated in Figure 3.24 and 3.25. Since for the straight flexure tuning fork, the Modal Analysis presented previously in Figure 3.22 indicated that the desired mode had a frequency of 723kHz, this TED analysis was set to run from 700kHz to 750kHz in steps of 1 kHz. Since for the tapered flexure tuning fork, the Modal Analysis presented previously in Figure 3.23 indicated that the desired mode had a frequency of 931kHz, this TED analysis was set to run from 900kHz to 950kHz in steps of 1 kHz.

The plot of the "material+thermal" losses represented as the inverse of the quality factor, Q_{TED}, for the straight flexure is shown in Figure 3.37. The value of $1/Q_{TED}$ is highlighted with a red marker at the resonant frequency of 723 KHz, and corresponds to a Q_{TED} of 10.9K. Figure 3.38 shows a visualization of the straight flexure with the color contour variable set to the TED Energy Density with the displacement exaggerated by a

factor of 5. Figure 3.38 clearly indicates that the majority of the TED losses in the straight flexure are occurring near the base of the flexure.

Similar to the plot shown for the straight flexure in Figure 3.37, the plot of $1/Q_{TED}$ for the tapered flexure is shown in Figure 3.39. The value of $1/Q_{TED}$ is highlighted with a red marker at the resonant frequency of 931 KHz, and corresponds to a Q_{TED} of 9.6K, which is 11.9% lower than that of the straight flexure and lower than what was expected based on the comments in previous work [71]. It was noted however, that the resonant frequency of the device was very near the thermal relaxation time of the thermoelastic dissipation, as evidenced by the fact that the curve negins to level out at this frequency [61]. It is also known [61] that operation in this frequency range causes the greatest thermoelastic energy dissipation. So, it was postulated that if the tapered tuning fork were designed to have the same resonant frequency instead of the same spring constant, then the thermal losses may indeed be lower. Therefore, a second tapered tuning fork design was modeled in an attempt to match the resonant frequency of the straight flexure tuning fork. This design had a width at the base of 11.6μm and the taper followed the prescribed equation but all other dimensions remained the same. This design yielded a resonant frequency of 745KHz, which was within a few percent of the desired resonant frequency of 723KHz. The plot of $1/Q_{TED}$ for the narrowed tapered flexure is shown in Figure 3.40. The value of $1/Q_{TED}$ is highlighted with a red marker at the resonant frequency of 745 KHz, and corresponds to a Q_{TED} of 11.5K, which is 5.5% higher than that of the straight flexure. So, the tapered flexure appears to have some marginal benefit in thermal losses over that of the straight flexure.

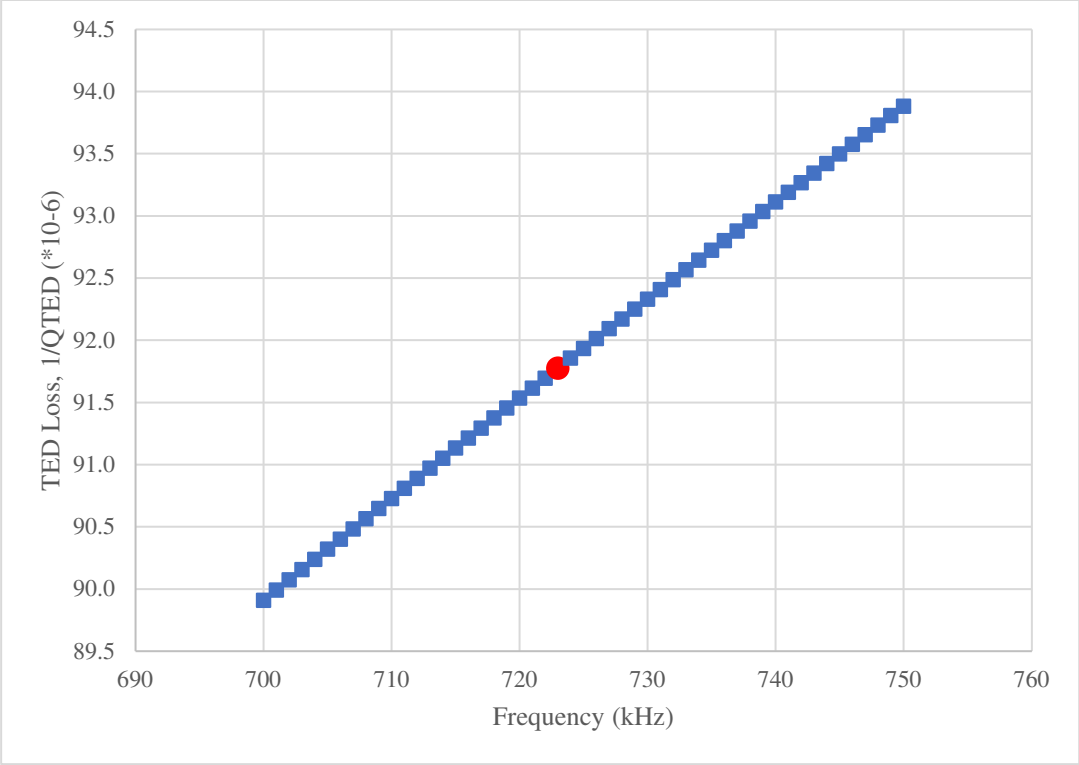

Figure 3.37 TED Loss for the Straight Flexure.

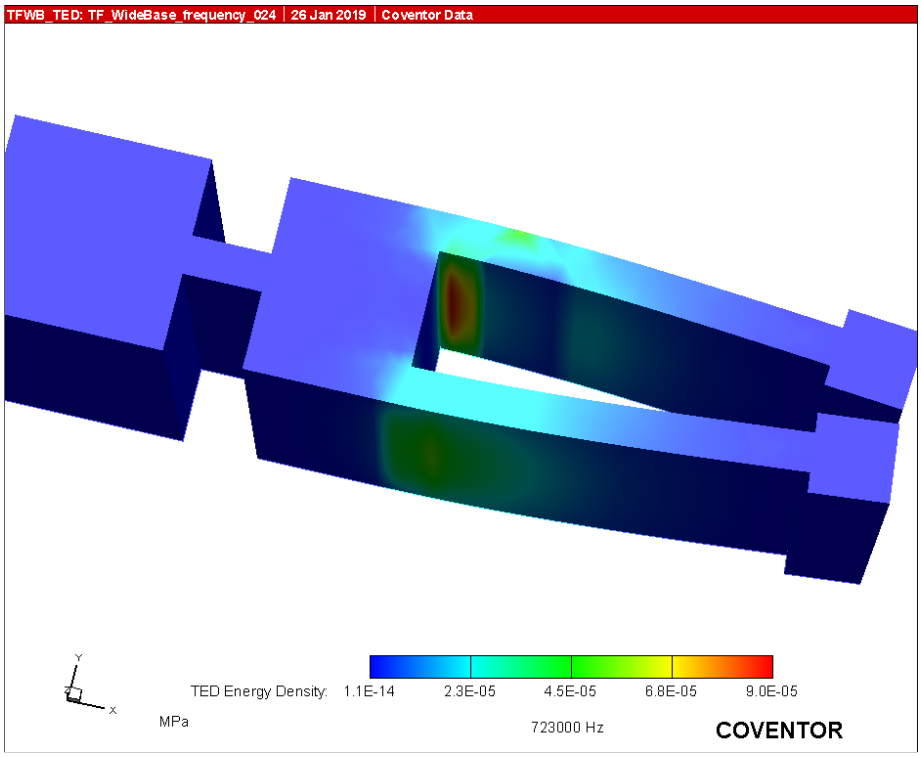

Figure 3.38 TED Energy Density for the Straight Flexure.

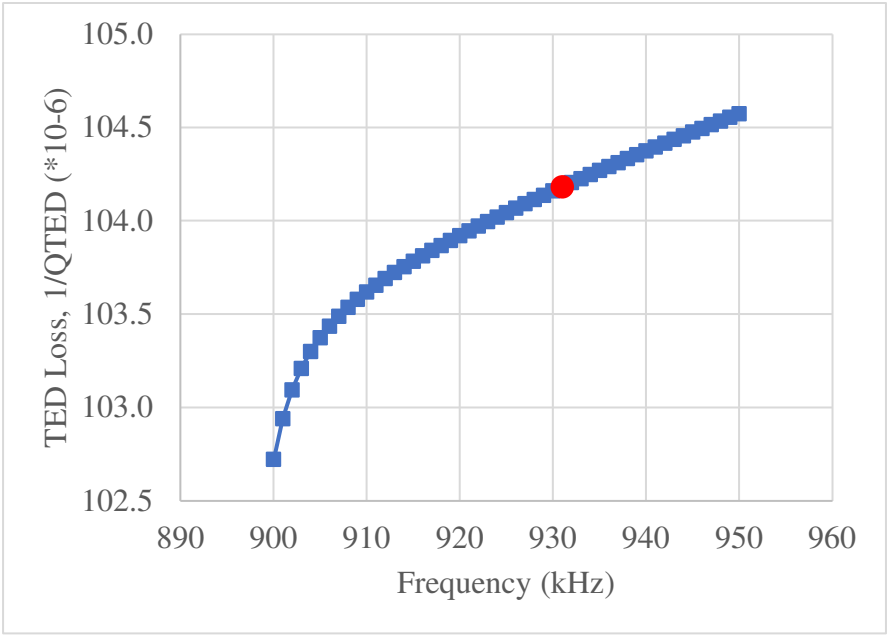

Figure 3.39 TED Loss for the Tapered Flexure.

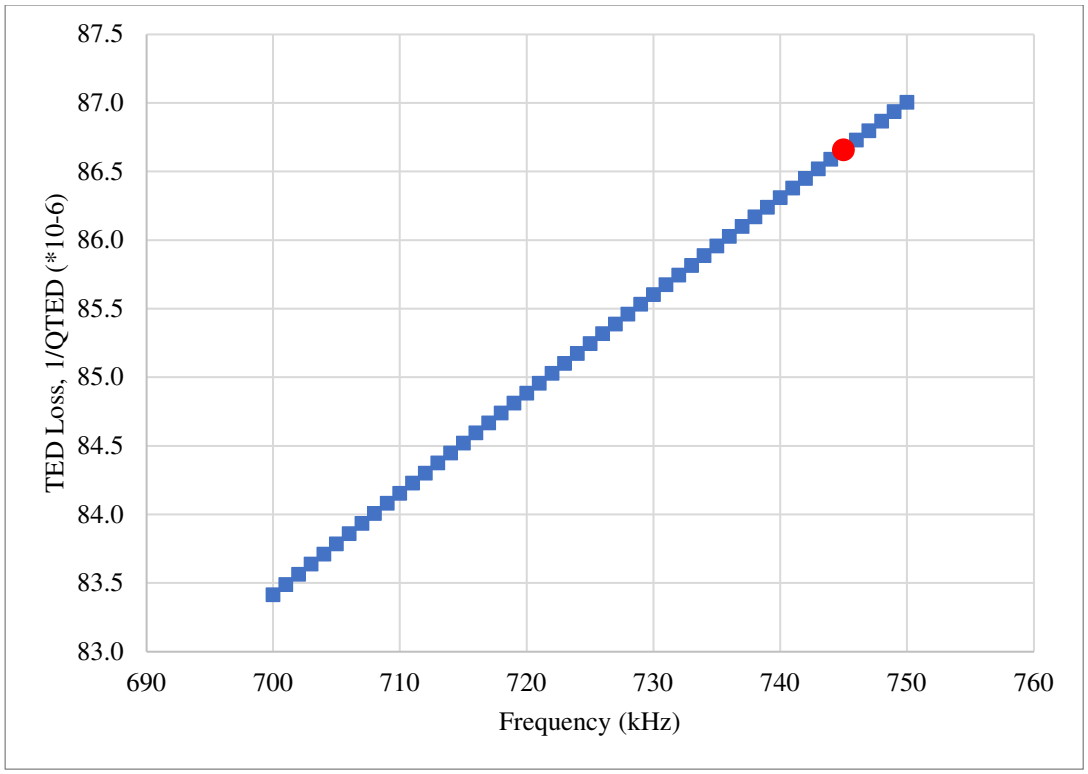

Figure 3.40 TED Loss for the Narrowed Tapered Flexure.

Figure 3.41 shows a visualization of the tapered flexure with the color contour variable set to the TED Energy Density and the displacement exaggerated by a factor of 5. Figure 3.41 clearly indicates that the TED losses in the tapered flexure design are internal to the flexure and distributed along the entire length of the flexure. Figure 3.41 also indicates that the peak TED energy density is lower than that of the straight flexure. Closer investigation into the location of the peak TED energy density reveals the peak occurs along a very narrow strip in the outside corner where the tapered flexure attaches to the base as shown in Figure 3.42. This feature was not present on the straight flexure design as the outside edge of the flexure transitioned very smoothly into the base. For completeness, Figure 3.43 shows a visualization of the narrowed tapered flexure with the color contour variable set to the TED Energy Density and the displacement exaggerated

by a factor of 5. Similarly to Figure 3.41, Figure 3.43 clearly indicates that the TED losses in the tapered flexure design are internal to the flexure and distributed along the entire length of the flexure. The peak TED energy densities displayed in Figure 3.43 within the flexures are more in line with those of the straight flexure. It is interesting to note here that a common exaggeration factor of 5 was used in each of the visualization figures, but it is clearly evident that some displaced further than others. This is due to differences in resonant frequency, differences in damping, as well as very slight differences in how close the analysis frequency is to the actual resonant frequency. Since the absolute value of the TED energy density is sensitive to the displacement, it would be wise not to read too much into the absolute values of the energy densities without normalizing them.

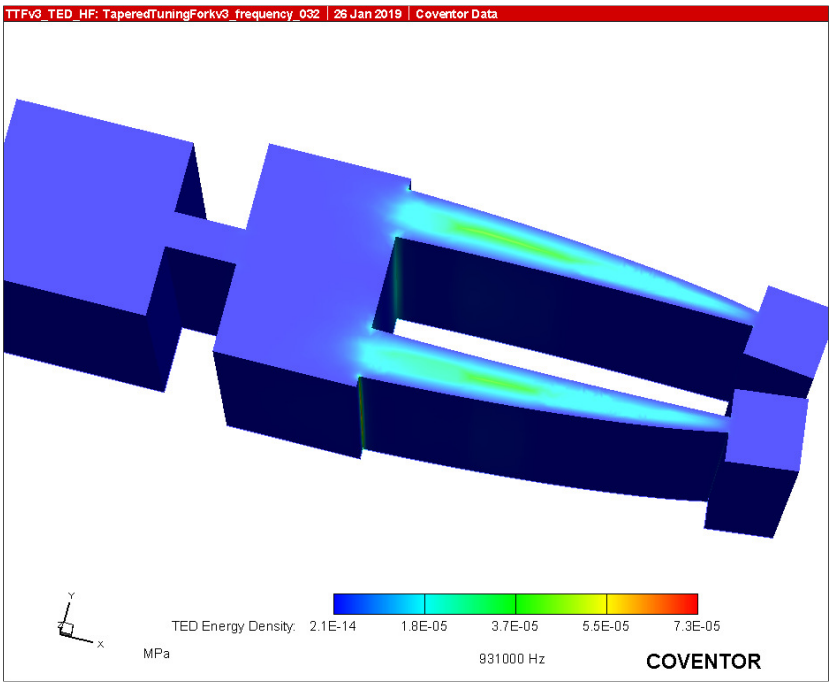

Figure 3.41 TED Energy Density for the Tapered Flexure.

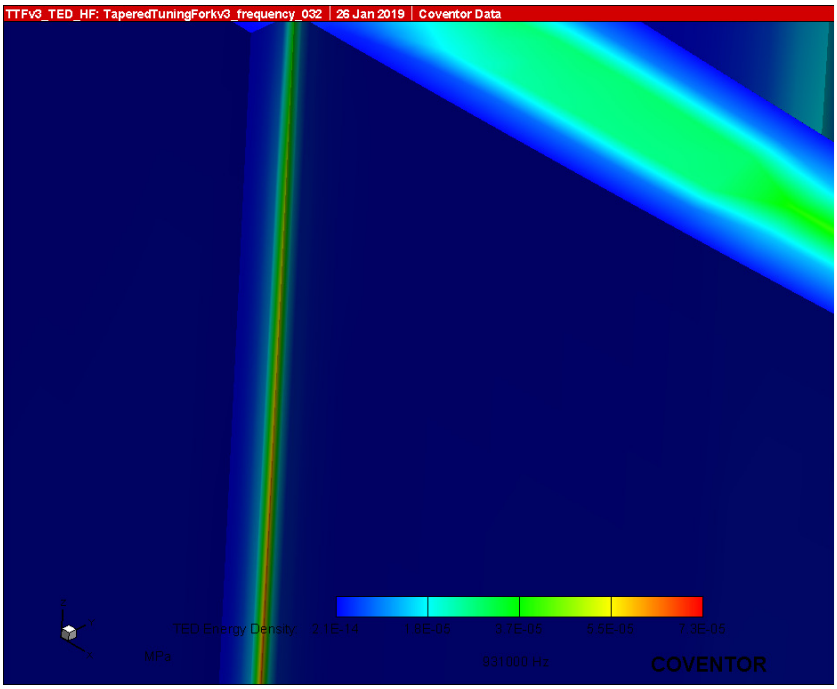

Figure 3.42 TED Energy Density Close-Up for the Tapered Flexure.

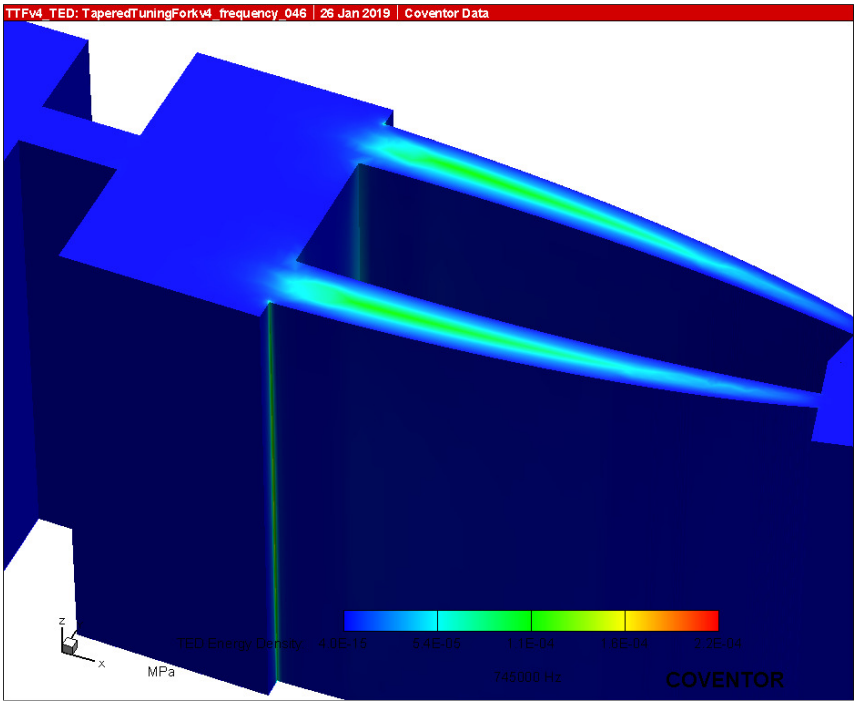

Figure 3.43 TED Energy Density for the Narrowed Tapered Flexure.

3.2.5 The Tapered Folded Flexure

To limit overall device dimensions, folded flexures are commonly incorporated into MEMS device designs. This folded flexure layout also mitigates against the rotation of the tip end of the flexure and results in a "guided" motion. Therefore, it was informative to arrange the tapered flexure into a folded flexure configuration and analyze its response characteristics.

Figure 3.44 shows a solid model of the tapered folded flexure. At the heart of this model is the tip-to-tip placement of two tapered flexures that share the same hammerhead. This element has the appearance similar to that of a bowtie, where the "knot" of the bowtie (the small, square block in the middle of the flexure) is placed at the zero-stress point along the length of the flexure. The smaller square block toward the upper left-hand corner of the figure is anchored to the substrate. The larger square block next to it is free to move in a linear "guided" fashion toward and away from the smaller, anchored block. The long rectangular beam in the lower right-hand portion of the image connects the two bowtie flexures together and is also free to move in a linear fashion parallel to that of the larger block. This rectangular beam, however, only moves half as much as that of the larger square block.

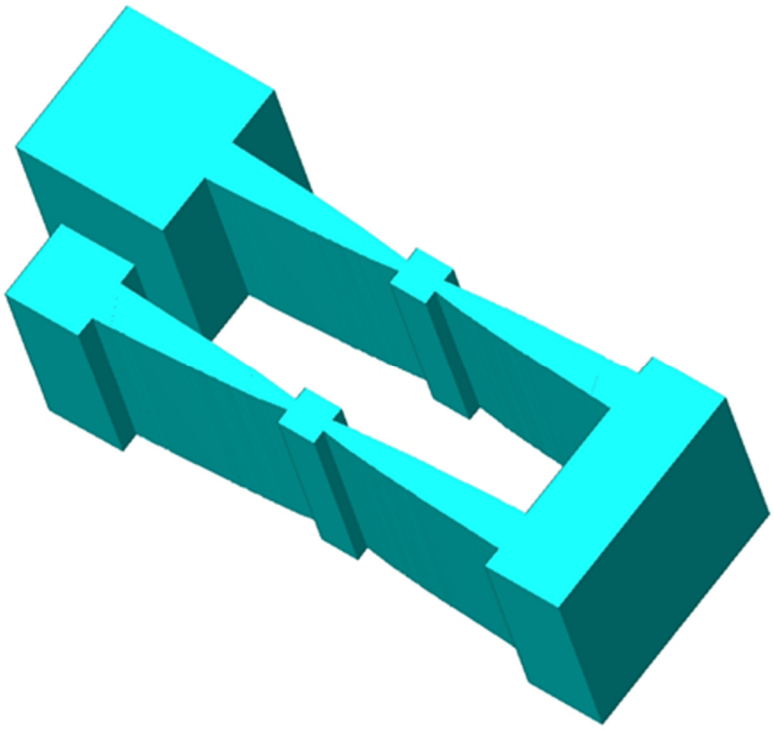

Figure 3.44 Solid Model of the Tapered Folded Flexure.

Figure 3.45 shows a solid model of a single degree of freedom shuttle design which incorporates four tapered, folded flexures. In this figure, the square block in the center is anchored to the substrate and the frame around the outer edge is free to move in a linear, "guided" fashion from the lower left-hand corner to the upper right-hand corner. Figure 3.46 shows this same model with the frame displaced toward the upper right-hand corner. In this figure, the color contour variable is showing displacement.

It can be seen from Figure 3.46 that each "bowtie" flexure in the tapered folded flexure takes on an "S" shaped deformation. This is an indication that there is a transition from compressive stress to tensile stress along the outer edge of each "bowtie" flexure in this design. Figure 3.47 shows a close-up of the stresses in the tapered folded flexures while under this deflection in the shuttle design. As can be seen from this figure, the

stresses are the same and constant along the outer edge of all flexure elements and confirms that the block at the center of each “bowtie” element is at the zero stress point.

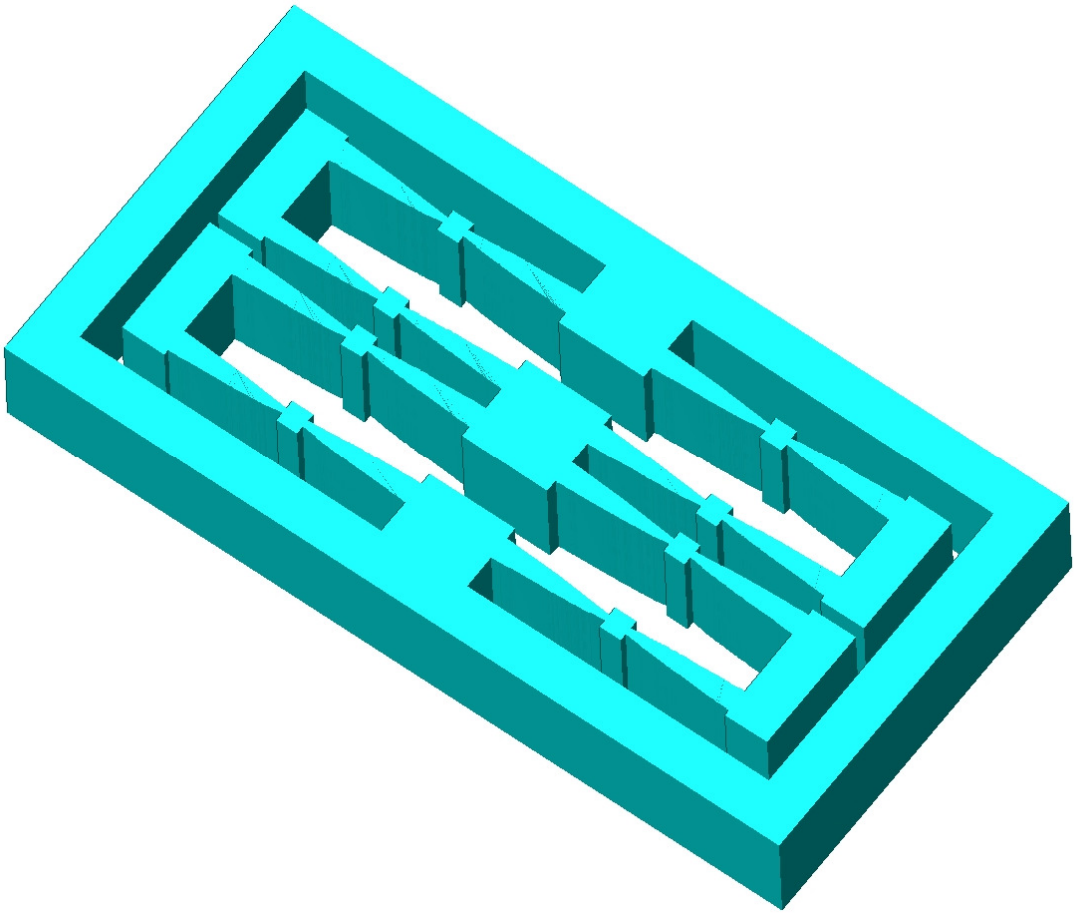

Figure 3.45 Solid Model of the Shuttle Incorporating Tapered Folded Flexures.

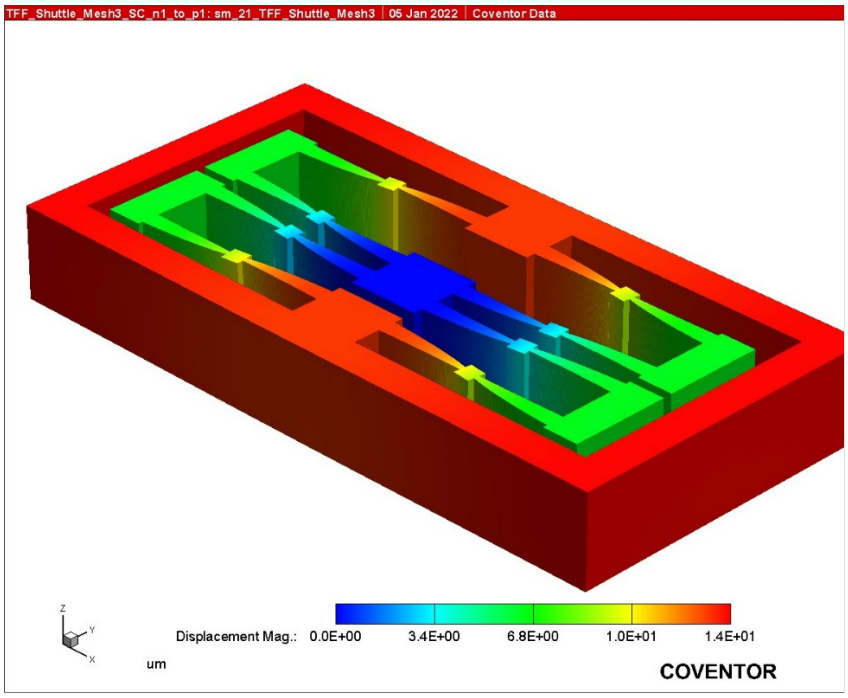

Figure 3.46 Solid Model of the Shuttle Showing Displacement.

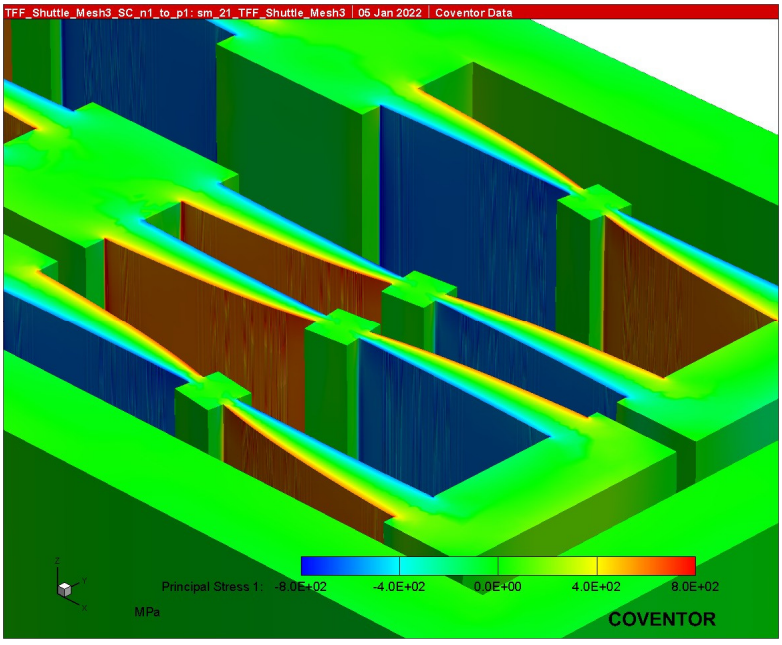

Figure 3.47 Stress Distribution in the Tapered Folded Flexure.

A spring constant analysis was performed on the shuttle design incorporating tapered folded flexures using FEA in a manner very similar to that described earlier for the tuning fork and the tapered tuning fork. The FEA results from the Spring Constant analysis on the shuttle design indicated a spring constant for the applied force of 10,484 N/m. The theoretical spring constant for this shuttle design was 12,656 N/m. The difference between the FEA predicted result and the theoretically derived value is greater than 17%, which is much higher than expected. Investigation into this discrepancy revealed that the primary cause was compliance in the structures at the base of the flexures and in the cross-member of the folded flexure, which are all assumed to be infinitely stiff in the theoretical calculations.

Spring Constant Analysis data is plotted in Figure 3.48, which again indicates very linear behavior. The error from the curve fit is plotted in Figure 3.49 and indicates that the maximum deviation from the curve was only a few nanometers of non-linear displacement while the shuttle itself was displaced up to 14 µm. It is important to note here that this level of displacement is quite extreme relative to the overall device dimensions which are on the order of 500µm. It is also interesting to note that the fit error here follows a predominantly cubic curve whereas the previous analysis on the tuning fork configuration demonstrated a mostly parabolic behavior. This is likely an artifact of the way the analyses were constructed since the one for the tuning fork applied only positive pressures and the one for the shuttle applied both positive and negative pressures which allowed the odd symmetries in the response to be more evident.

For comparison purposes, a second shuttle was designed using straight flexures. The linearity error for that design was roughly 30% lower than that of the shuttle that

incorporated tapered flexures, while the peak stresses in the straight flexures were roughly 40% higher than that of the tapered flexures. Additionally, the difference between the theoretical spring constant and the FEA predicted spring constant was even higher. This difference is caused by a combination of two factors. The first is that the peak stress in the straight flexure is higher, resulting in even more deformation of the base where the flexure attaches. The second is that the straight flexure is narrower at the base than the tapered flexure, resulting in the deformation causing a greater angular rotation of the base and exaggerated compliance of the flexure. This discovery was an unexpected attribute of the tapered flexure. That being said, for a given length, stiffer flexures can be implemented in the tapered configuration before deformation of the attachment point becomes significant.

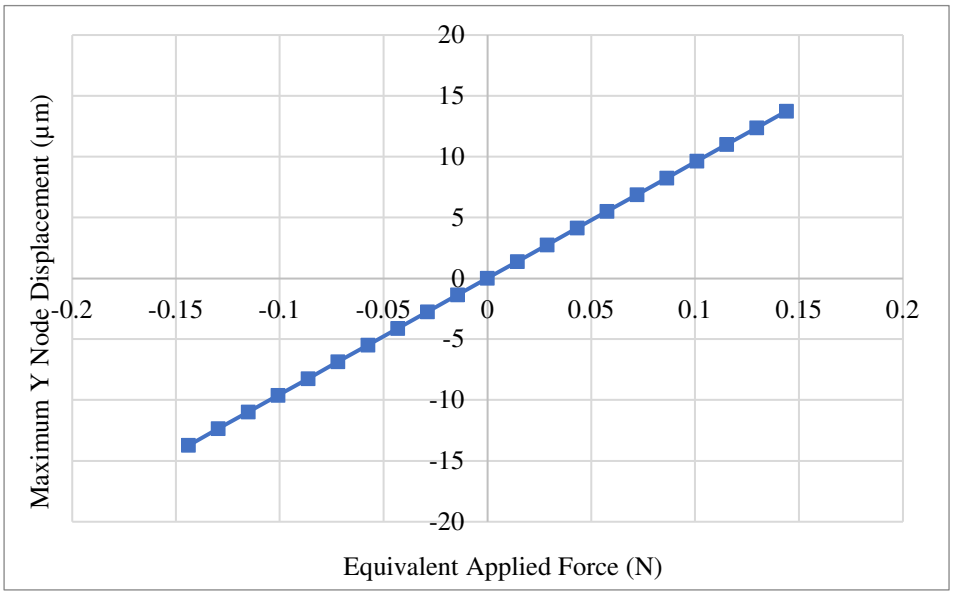

Figure 3.48 Tapered Flexure Shuttle Spring Constant Analysis Displacement Plot.

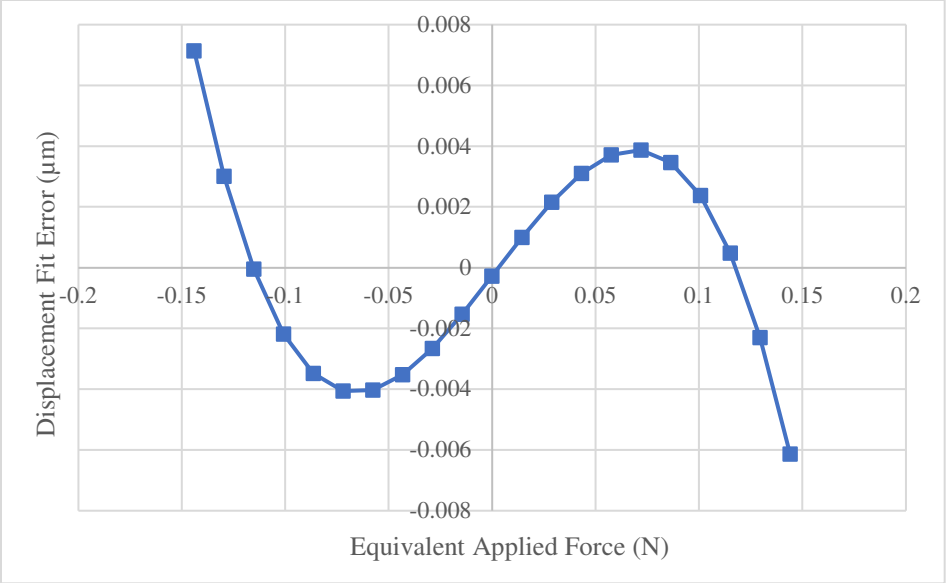

Figure 3.49 Tapered Flexure Shuttle Spring Constant Analysis Fit Error.

3.2.6 Initial FEA Results Summary

All governing equations were derived for the tapered flexure and have been documented herein. Several Finite Element Analyses (FEA) were performed to investigate the characteristics of the tapered flexure. The FEA did confirm that the tapered flexure resulted in constant stress along the outer edge of the flexure as predicted. This uniform distribution of stress resulted in approximately 40-50% lower peak stress than the straight flexure. The response of the tapered flexure was, however, slightly more non-linear than that of the straight flexure even though the peak stress was reduced. To explain this apparent discrepancy, it was noted that the equations describing the mechanical response of the tapered flexure to an applied force indicate significantly more rotational response than that of the straight flexure. It is likely that the increased nonlinearity is due to this increased rotational response as opposed to being a nonlinear

response of the material itself. The TED losses were improved by 5.5% for the tapered flexure that was designed to match the resonant frequency of the straight flexure. Finally, it was discovered that, for a given flexure length, a tapered flexure could be designed with a higher stiffness than that of a straight flexure before the compliance of the base became significant.

3.3 Sensitivity to Manufacturing Variations

An investigation was performed into the sensitivity to manufacturing variations of tapered flexures as compared with that of an "equivalent" straight flexure. This study included an extensive FEA investigation into the impact of fillets on the properties of the flexure as well as an analytical investigation into the sensitivity to flexure width variations, which is supported by FEA. Fillets, sometimes called radius fillets, are mechanical features added to the inside corners of mechanical structures (not just MEMS structures) that generally have three primary benefits. They make the structure easier to fabricate. They reduce stress peaking and associated fatigue-induced failures in inside corners, and they make the resulting structure more visually appealing. Fillets are often implemented using a constant radius which are also called radius fillets. In Figure 3.50, the same MEMS structure is shown (a) without fillets and in (b) with radius fillets. All fillets investigated in this work are radius fillets.

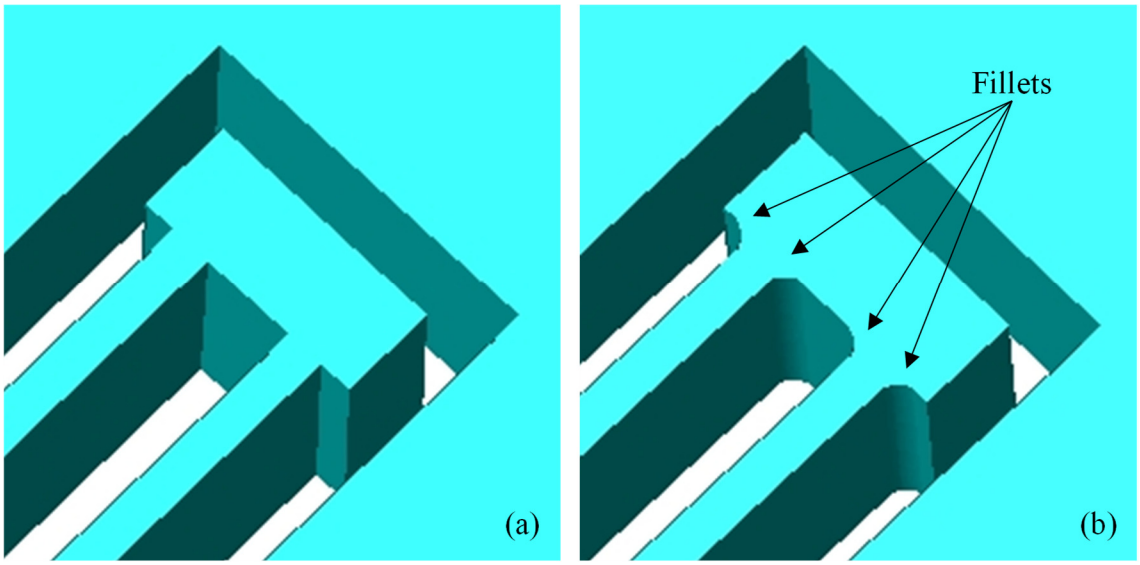

Figure 3.50 MEMS Structure (a) without Fillets, and (b) with Fillets.

The focus areas investigated in this study were informed by discussions with MEMS fabrication companies as well as by literature [89]. The primary issues that arise from manufacturing variations in Deep Reactive Ion Etched (DRIE) MEMS devices include:

1. Variability in radius of inside corners - "rounding" of inside corners.
2. Critical Dimension Loss (CDloss) or Etch Bias - horizontal undercut of device under the mask resulting in unintended variations in flexure widths.
3. Sidewall Angle - Angle deviation from vertical of the sides of the flexures.

For the purposes of this work, an "equivalent" tapered flexure was defined to be one of the same length as a straight flexure but with a width at the base required to obtain the same linear deflection spring constant due to an applied force at the center of the hammerhead. This equivalence typically results in a base width of the tapered flexure that is roughly 20-25% wider than the width of the straight flexure.

3.3.1 Sensitivity to Inside Corner Variations - Fillet Radius Study

In addition to the concerns over manufacturing variations in the inside corners, in the preliminary FEA studies reported in the previous section, it was noted that there was a significant stress rise at the inside corner locations where the flexures (straight and tapered) attached to the base as indicated in Figure 3.51. A common design technique to mitigate this stress rise is to introduce a radius fillet in the inside corners. Introducing a fillet in the inside corners also mitigates against manufacturing variations arising from the difficulties associated with etching a perfect right angle in the inside corner as well. However, the minimum radius necessary to minimize this stress peaking was not known. Additionally, the impact of the fillet on desired flexure parameters such as spring constant and thermoelastic damping (TED) was not known. Therefore, a fillet study was devised to derive some design rules for minimum fillet radius and determine its impact on desired flexure properties. This fillet study both informs the designer about the sensitivity of the design to manufacturing variations in the inside corners as well as sets some design guidelines for what size fillet should be included in future designs.

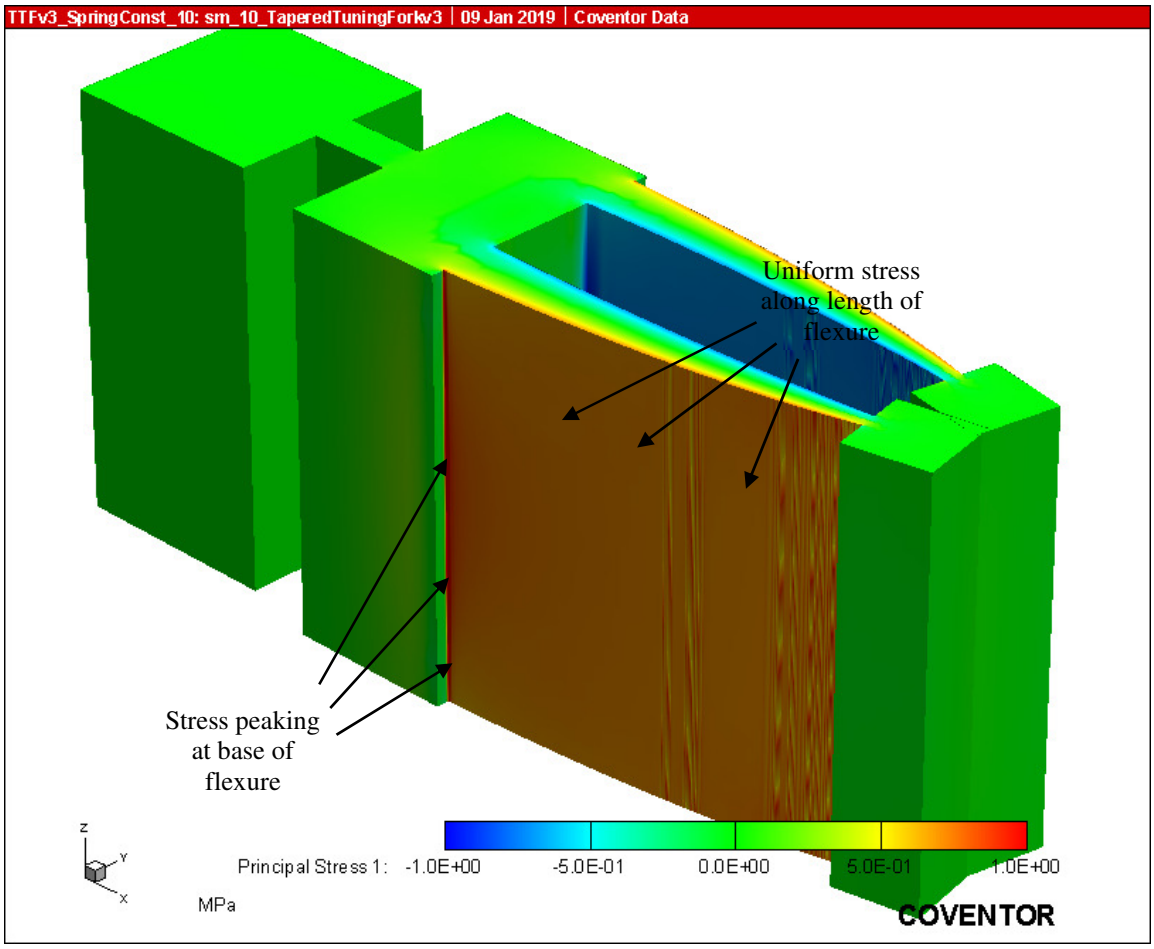

Figure 3.51 Stress Rise at the Junction Between Base and Flexure.

For the purposes of the fillet study, the test structures modeled in the FEA were all of a tuning fork design. The device thickness for all test structures was fixed at 100µm, which is a common thickness for DRIE MEMS devices. The hammerhead size was fixed at 60µm by 60µm. Three different lengths of the flexures, 300µm, 400µm, and 500µm, were investigated. Six different fillet radii, 0µm, 1µm, 2µm, 4µm, 8µm, and 16µm, were investigated. Two different types of flexure, both straight and tapered, were investigated. For the straight flexure, three different flexure widths, 10µm, 15µm, and 20µm, were investigated. For the tapered flexure, three different widths of the flexure were investigated for each flexure length. These widths were calculated based on the

width required to provide the same linear deflection spring constant as the "equivalent" straight flexure.

The equation that gives the linear spring constant for the tapered flexure at the center of the hammerhead was provided in Table 3.1. Equation 3.27 arranges that equation to provide the width of the flexure at the base given a particular desired spring constant. The widths of the tapered flexure designs are summarized in Table 3.2. This table is arranged for easy comparison of tapered vs. straight flexure widths for different lengths. From the data in this table, it is readily apparent that the tapered flexure width at the base is roughly 25% wider than the straight flexure (or the equivalent straight flexure is 20% narrower than the tapered flexure at the base) with only a small dependence on the length of the flexure over the range investigated here:

$$w_b = \sqrt[3]{\frac{k_{HHC\_T} \cdot 8 \cdot \left[(L+d)^3 - (L+d)^{\frac{3}{2}}(d)^{\frac{3}{2}}\right]}{E \cdot t}} \quad . \tag{3.27}$$

This matrix of 2 flexure types, 3 widths, 3 lengths, and 6 fillet sizes resulted in the creation of 108 solid models. For each of these solid models, FEAs were designed and conducted to investigate peak stress, spring constant, resonant frequency, and thermoelastic damping (TED), resulting in well over 300 individual FEAs conducted.

Table 3.2 Tapered Flexure Widths for Fillet Study.

Length (μm)	**Straight Flexure Width** (μm)	**Tapered Flexure Width at the Base** (μm)
300	10	12.486
400	10	12.523
500	10	12.543
300	15	18.729
400	15	18.784
500	15	18.815
300	20	24.972
400	20	25.046
500	20	25.086

At the outset of this fillet study, a mesh sensitivity study was conducted. Details of this mesh sensitivity study are provided in Section B.1 of Appendix B. The final mesh settings that were used are presented in Figure 3.52. These settings represent a combination of competing requirements that include:

1. Ensuring adequate mesh resolution to obtain accurate results,
2. Ensuring adequate mesh resolution in the fillet locations,
3. Ensuring a reasonable number of total mesh elements to have reasonable computational run time, and
4. Ensuring that the mesher algorithm would return a mesh that met all of the previously listed requirements for all of the geometries using the exact same settings.

Of these criteria, the third was the least important and the final settings employed largely resulted in relatively dense meshes. A representative mesh is shown in Figure 3.53.

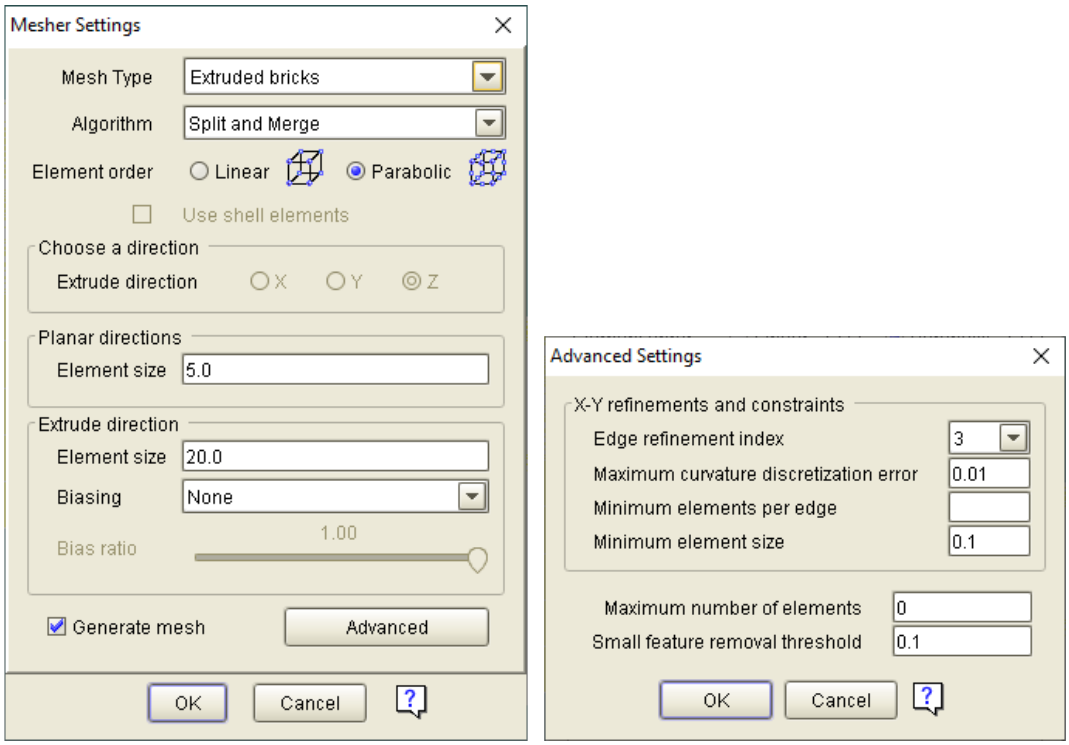

Figure 3.52 Mesher Settings for Fillet Study.

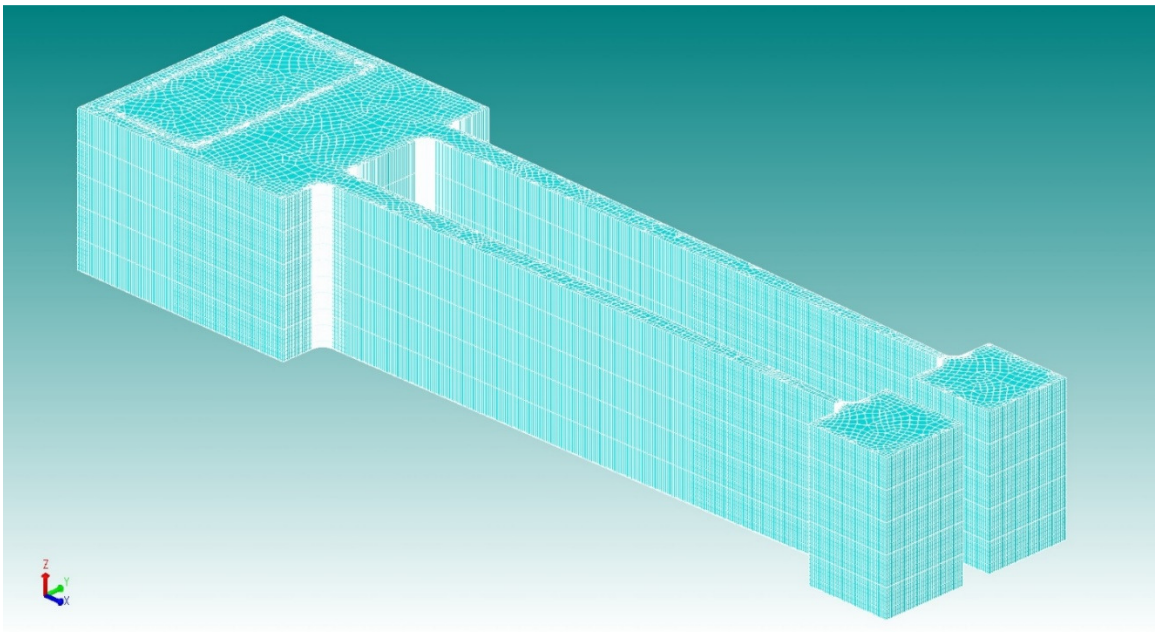

Figure 3.53 Representative Mesh for the Fillet Study.

For each of the model combinations, FEAs were performed to determine the impact the fillet has on the following parameters:

1. Linear deflection spring constant
2. Resonant frequency
3. Stress peaking
4. Thermo-Elastic Damping (TED)

The following sub-sections present the results of each of these analyses.

3.3.1.1 Impact of Fillet Radius on Linear Deflection Spring Constant

To determine the impact of the fillet radius on the linear deflection spring constant, a set of 21 linearly spaced pressure load conditions were applied to the side faces of the hammerheads. The faces that were loaded are shown in Figure 3.54. The pressure load on these faces varied from a maximum negative pressure of -1kPa up to a maximum positive pressure of +1kPa in steps of 0.1kPa.

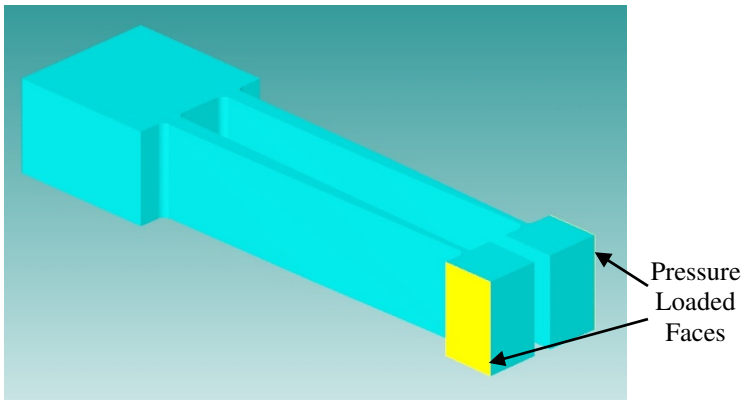

Figure 3.54 Pressure Loaded Faces for the Fillet Study.

The ideal spring constant for each base design (*i.e.*, the design with no fillet) was calculated based on the design parameters of the length and width of the flexure. However, since the load was applied at the center of the hammerhead rather than at the end of the flexure, an allowance had to be made in the calculation of the spring constant. The spring constant equation that relates the deflection at the center of the hammerhead to the applied force at the center of the hammerhead was provided in Table 3.1 for the tapered flexure, and is provided in Equation 3.28 below for the straight flexure. The derivation of this equation is provided in section A.3 of Appendix A:

$$k_{HHC\_S} = \frac{Etw^3}{4 \cdot (L^3 + 3dL^2 + 3d^2L)} \ . \tag{3.28}$$

Table 3.3 shows a comparison of the ideal spring constants to the FEA estimated spring constants with no fillet (fillet radius of zero). The data in the table indicate very good agreement between the theoretically predicted values and the FEA results. The data also indicate very good agreement between the spring constants of the straight and tapered flexures. On the stiffest of the flexures (20µm width and 300µm length), the compliance of the anchor point of the flexure is starting to become significant and once again the impact of this compliance is more severe for the straight flexure than it is for the tapered flexure.

Tables 3.4 - 3.9 present the FEA estimated spring constants for each flexure width, length, type, and fillet radius. All spring constants are presented in N/m. The right-most column in each table indicates the "span" of the spring constants expressed as a percentage of the spring constant with no fillet. That is:

$$Span = \frac{k_{HHE\_S\_F16} - k_{HHE\_S\_F1}}{k_{HHE\_S\_F0}} \times 100\% \,. \tag{3.29}$$

Table 3.3 Comparison of Theoretical and FEA Estimated Spring Constants.

Flexure Length (µm)	Straight Flexure Width (µm)	Theoretical k_{HHC_S} and k_{HHC_T} (N/m)	FEA Estimated k_{HHC_S} (N/m)	FEA Estimated k_{HHC_T} (N/m)
300	10	115.42	116.72	116.28
400	10	52.15	52.87	52.41
500	10	27.84	28.27	27.92
300	15	389.54	383.44	385.04
400	15	176.00	174.91	174.38
500	15	93.98	93.91	93.21
300	20	923.35	884.36	893.93
400	20	417.18	405.96	407.05
500	20	222.76	218.82	218.24

Table 3.4 FEA Estimated Spring Constants for 10µm Width Straight Flexure.

Length	Fillet Size (µm)						Span
µm	0	1	2	4	8	16	%
300	116.72	117.03	117.64	119.06	122.22	129.48	10.67
400	52.87	52.99	53.21	53.70	54.79	57.24	8.04
500	28.27	28.33	28.43	28.64	29.10	30.15	6.44

Table 3.5 FEA Estimated Spring Constants for 10µm Equivalent Width Tapered Flexure.

Length	Fillet Size (µm)						Span
µm	0	1	2	4	8	16	%
300	116.28	116.54	116.97	117.91	120.02	124.94	7.23
400	52.41	52.49	52.63	52.94	53.62	55.21	5.20
500	27.92	27.96	28.02	28.15	28.44	29.09	4.08

Table 3.6 FEA Estimated Spring Constants for 15μm Width Straight Flexure.

Length	Fillet Size (μm)						Span
μm	0	1	2	4	8	16	%
300	383.44	384.40	386.39	390.70	400.39	422.61	9.96
400	174.91	175.20	175.93	177.40	180.76	188.38	7.53
500	93.91	94.04	94.34	95.00	96.45	99.72	6.05

Table 3.7 FEA Estimated Spring Constants for 15μm Equivalent Width Tapered Flexure.

Length	Fillet Size (μm)						Span
μm	0	1	2	4	8	16	%
300	385.04	385.59	386.89	389.76	396.22	411.24	6.66
400	174.38	174.62	175.06	176.02	178.16	183.09	4.85
500	93.21	93.31	93.50	93.91	94.81	96.86	3.81

Table 3.8 FEA Estimated Spring Constants for 20μm Width Straight Flexure.

Length	Fillet Size (μm)						Span
μm	0	1	2	4	8	16	%
300	884.36	886.88	891.14	900.58	921.65	970.04	9.40
400	405.96	406.79	408.31	411.65	419.03	435.80	7.15
500	218.82	219.19	219.86	221.32	224.54	231.80	5.76

Table 3.9 FEA Estimated Spring Constants for 20μm Equivalent Width Tapered Flexure.

Length	Fillet Size (μm)						Span
μm	0	1	2	4	8	16	%
300	893.93	895.10	897.96	904.16	918.17	950.83	6.23
400	407.05	407.48	408.43	410.55	415.26	426.11	4.57
500	218.24	218.47	218.88	219.78	221.76	226.31	3.59

Inspection of the data indicates that, as expected, fillets of larger radii increase the stiffness of the flexure and that this effect is less pronounced for flexures of longer lengths or wider widths (relative to the fillet radius). More interesting is that the tapered flexure of "equivalent" design is consistently less sensitive, 35.5% on average, to the existence and radius of the fillet than that of the straight flexure. This result implies that

the spring constants of tapered flexures would be 35% less sensitive to manufacturing variations in the radius of inside corners than those of straight flexures.

To help visualize this reduction in sensitivity to fillet radius variations, the spring constants for each fillet radius were normalized to the value with no fillet radius for each length and width combination. These normalized spring constants are plotted in Figure 3.55. The straight flexure spring constants are shown with dashed red lines and the tapered flexure spring constants are shown with solid green lines. Figure 3.55 clearly shows that the spring constants for the tapered flexures have significantly reduced sensitivity (reduced slope) to fillet radius over that of the straight flexures. For mode-matched MEMS gyroscopes, this would improve the resonant frequency matching between the two modes thereby reducing the quadrature error in the gyroscope.

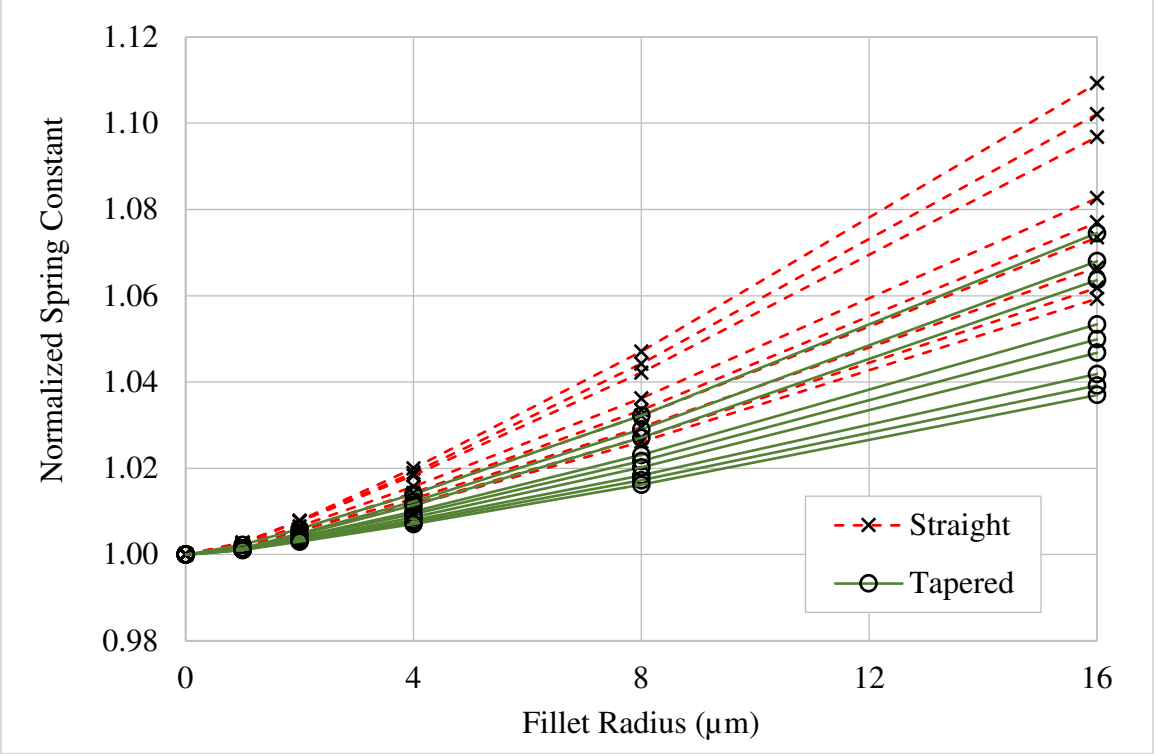

Figure 3.55 Normalized Spring Constants Versus Fillet Radius.

3.3.1.2 Impact of Fillet Radius on Resonant Frequency

A modal analysis was also performed on each of the 108 finite element models generated for the Spring Constant analysis. The primary tuning fork mode was identified and the resonant frequency extracted. Tables 3.10 - 3.15 present the FEA estimated resonant frequencies for each flexure width, length, type, and fillet radius. All resonant frequencies are presented in Hertz. The right-most column in each table indicates the "span" of the resonant frequencies expressed as a percentage of the resonant frequency with no fillet which was calculated in a similar fashion to what was calculated for the spring constants in the previous section.

Since the distributed mass of the flexures themselves were significant with respect to the mass of the hammerhead, a theoretical resonant frequency was not calculated for these designs. Also, the resonant frequencies were not expected to be identical between the straight flexure and the tapered flexure due to the differences in mass distribution along the length of the straight flexure compared to that of the tapered flexure. Had the hammerhead size been significantly larger, a theoretical calculation would have been more reasonable based on the idea that the mass distribution of the flexure was negligible compared to that of the hammerhead. However, the resonant frequencies of the straight and tapered designs are still close enough to justify a legitimate comparison of the results.

Table 3.10 FEA Estimated Resonant Frequency for 10µm Width Straight Flexure.

Length	Fillet Size (µm)						Span
µm	0	1	2	4	8	16	%
300	55150	55228	55375	55699	56368	57693	4.47
400	36220	36259	36335	36499	36820	37419	3.20
500	25837	25859	25904	25996	26176	26490	2.44

Table 3.11 FEA Estimated Resonant Frequency for 10µm Width Tapered Flexure.

Length	Fillet Size (µm)						Span
µm	0	1	2	4	8	16	%
300	56947	57008	57112	57324	57755	58563	2.73
400	38011	38037	38086	38184	38371	38668	1.66
500	27536	27552	27579	27633	27727	27844	1.06

Table 3.12 FEA Estimated Resonant Frequency for 15µm Width Straight Flexure.

Length	Fillet Size (µm)						Span
µm	0	1	2	4	8	16	%
300	96840	96961	97220	97760	98882	101115	4.29
400	63115	63174	63307	63574	64122	65149	3.13
500	44672	44707	44783	44939	45245	45793	2.43

Table 3.13 FEA Estimated Resonant Frequency for 15µm Width Tapered Flexure.

Length	Fillet Size (µm)						Span
µm	0	1	2	4	8	16	%
300	102193	102276	102447	102800	103506	104804	2.47
400	68048	68094	68177	68341	68651	69131	1.52
500	49150	49178	49225	49316	49471	49659	0.98

Table 3.14 FEA Estimated Resonant Frequency for 20µm Width Straight Flexure.

Length	Fillet Size (µm)						Span
µm	0	1	2	4	8	16	%
300	142600	142809	143173	143943	145542	148735	4.16
400	92368	92468	92654	93040	93824	95316	3.08
500	64978	65042	65149	65371	65813	66619	2.43

Table 3.15 FEA Estimated Resonant Frequency for 20µm Width Tapered Flexure.

Length	Fillet Size (µm)						Span
µm	0	1	2	4	8	16	%
300	153555	153667	153910	154406	155389	157170	2.28
400	102043	102100	102216	102453	102887	103548	1.42
500	73506	73545	73611	73740	73962	74224	0.92

Inspection of the data indicates that, as expected, fillets of larger radius increase the resonant frequency of the flexure and that the increase is less pronounced for flexures of longer lengths or wider widths (relative to the fillet radius). More interesting is that the resonant frequency of the tapered flexure of "equivalent" design is consistently 40-60% less sensitive to the existence and radius of the fillet than that of the straight flexure. This result implies that tuning fork resonant frequencies of tapered flexures would be 40-60% less sensitive to manufacturing variations in the radius of inside corners than straight flexures. Stated another way, the sensitivity of resonant frequency of the tapered flexure to variations in inside corner radius is roughly half that of the straight flexure.

Similar to what was plotted for the spring constant analysis, the resonant frequencies for each fillet radius were normalized to the 16µm fillet radius value for each length and width combination. These normalized resonant frequencies are plotted in Figure 3.56. The straight flexure normalized resonant frequencies are shown with dashed red lines and the tapered flexure normalized resonant frequencies are shown with solid

green lines. Figure 3.56 clearly shows that the normalized resonant frequencies for the tapered flexures have significantly reduced sensitivity (reduced slope) to fillet radius over that of the straight flexures. For mode-matched MEMS gyroscopes, this reduced sensitivity would improve the resonant frequency matching between the two modes thereby reducing the quadrature error in the gyroscope.

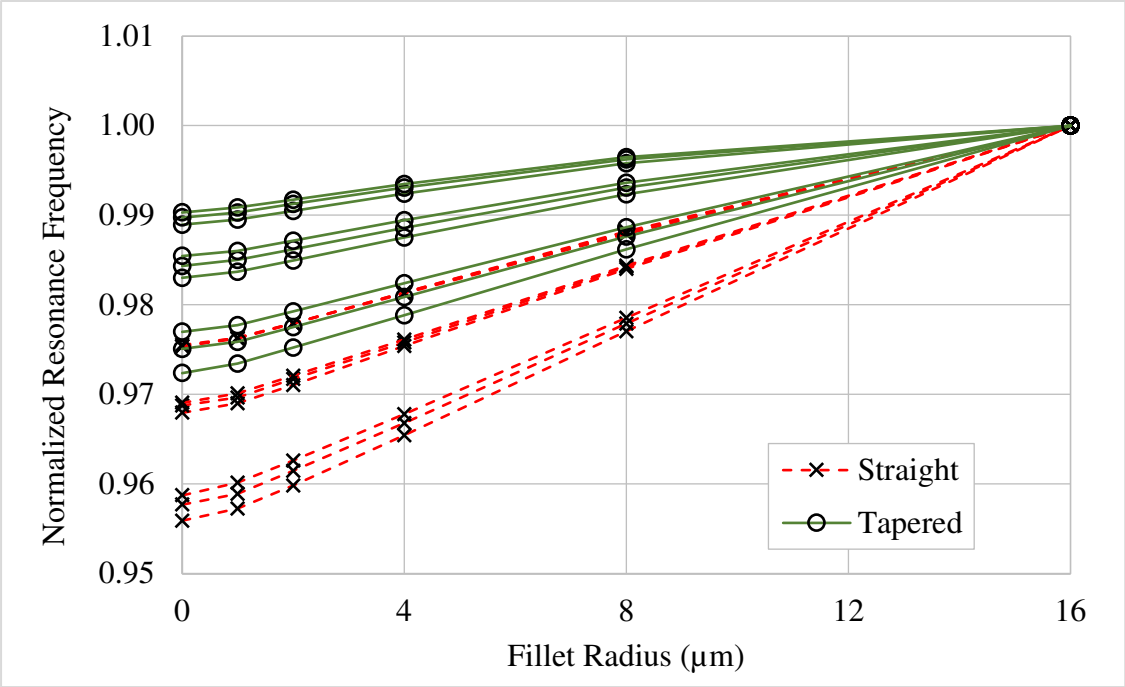

Figure 3.56 Normalized Resonant Frequency Versus Fillet Radius.

3.3.1.3 Impact of Fillet Radius on Stress Peaking

The CoventorWare software used for the fillet study provides a very nice visualization suite that provides a color contour map of any variable returned by the FEA. Figure 3.57 shows a representative visualization of the typical view of stress in a couple

of the designs (L=400µm, W=15µm, Radius = 1µm and 8µm) under similar loading conditions. Noting the scales in each figure, it is readily apparent that the peak stress is significantly higher for the 1µm fillet radius than it was for the 8µm fillet radius design. Capturing and characterizing the relationship between fillet radius and stress peaking was the object of this analysis, ultimately to inform the designer about the optimal fillet radius to mitigate stress peaking with minimal impact to design parameters such as spring constant.

While the visualization tool itself was extremely helpful in gaining insight into what was happening within the model, extracting the actual data in only the region of interest from the visualization tool was a little bit of a challenge. Visual investigation of the model revealed that the peak stress was occurring within a few microns of the edge where the flexure met the fillet in the X-Y plane. It was also determined visually that the peak stress occurred in the center of the model vertically along the Z-axis. Therefore a "Slice" was extracted from the Visualizer tool consisting of a Z-axis plane in the center of the model.

This slice, however, contained data at all X and Y values and was still a fairly large and unmanageable file. It was desirable to restrict the X-Y data set to just the region of interest. This region of interest varied for each of the designs due to varying fillet radius, flexure width and flexure length. Therefore, a Visual Basic macro was written in EXCEL to pare down the X-Y data set to the region of interest based on the fillet radius, flexure width, and flexure length. This resulted in a manageable file size that could be utilized to isolate the stress peaking location and amplitude with confidence.

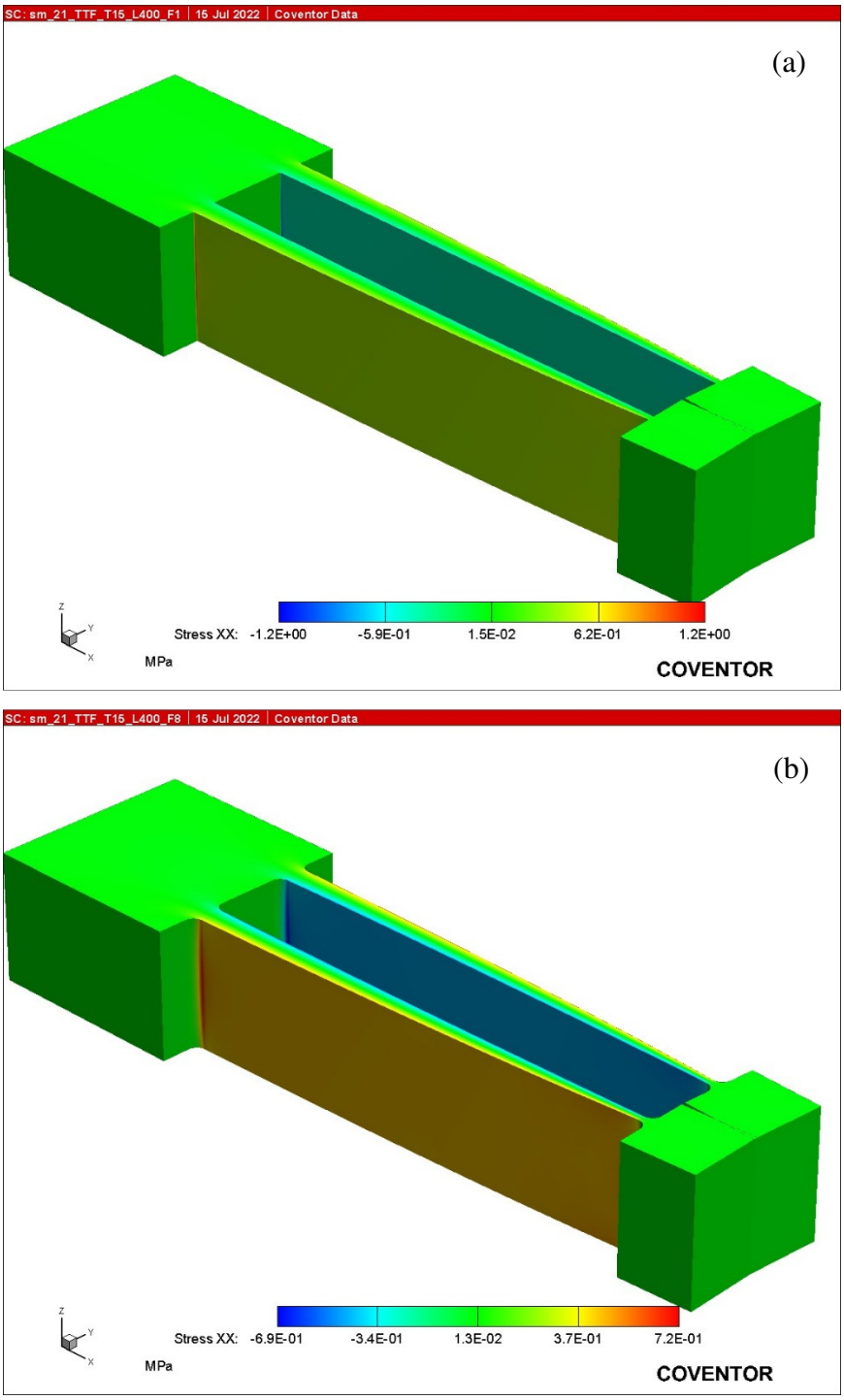

Figure 3.57 Representative Visualization of Stress Peaking for the Fillet Study. (a) 1µm Fillet Radius, (b) 8µm Fillet Radius.

It is also important to note that, while in the straight flexure the majority of the stress is near the base of the flexure, the tapered flexure is specifically tapered to maintain constant stress along the outer edge of the flexure all the way from the base to the end. Therefore, while stress peaking is only of concern at the base for straight flexures, it is of concern both at the base and at the end for tapered flexures. Therefore, for completeness of comparison, tables of stress results are provided for both designs at both the base and at the end of the flexures. These results are presented in Tables 3.16 - 3.27. All stress results are presented in units of MPa.

The solver equations are fairly ill conditioned (there is a singularity) at hard inside corner locations. Therefore, there is a wide variation in the peak stress returned for models with no fillet and, in several cases, the peak stress returned for a fillet radius of 1µm was unexpectedly 50% larger than that returned for the case where there is no fillet. Therefore, the peak stress results for the case where there is no fillet were essentially dismissed for the purposes of this analysis. This also means that the "span" of the peak stress for various fillet radii as a percentage of the peak stress with no fillet is not reported here as it has been in the previous two sections.

Table 3.16 FEA Estimated Peak Base Stress for 10µm Width Straight Flexure.

Length	Fillet Size (µm)					
µm	0	1	2	4	8	16
300	2.036	2.247	2.053	1.841	1.612	1.425
400	2.429	3.078	2.725	2.441	2.072	1.889
500	2.962	4.081	3.342	2.911	2.615	2.337

Table 3.17 FEA Estimated Peak Base Stress for 10µm Width Tapered Flexure.

Length	Fillet Size (µm)					
µm	0	1	2	4	8	16
300	1.265	1.815	1.484	1.272	1.069	0.992
400	1.649	2.413	1.946	1.670	1.446	1.316
500	2.044	3.030	2.355	1.963	1.833	1.564

Table 3.18 FEA Estimated Peak Base Stress for 15µm Width Straight Flexure.

Length	Fillet Size (µm)					
µm	0	1	2	4	8	16
300	1.265	1.815	1.484	1.272	1.069	0.992
400	1.649	2.413	1.946	1.670	1.446	1.316
500	2.044	3.030	2.355	1.963	1.833	1.564

Table 3.19 FEA Estimated Peak Base Stress for 15µm Width Tapered Flexure.

Length	Fillet Size (µm)					
µm	0	1	2	4	8	16
300	0.629	0.905	0.748	0.622	0.511	0.459
400	0.820	1.221	0.932	0.799	0.666	0.592
500	1.011	1.507	1.199	0.983	0.823	0.723

Table 3.20 FEA Estimated Peak Base Stress for 20µm Width Straight Flexure.

Length	Fillet Size (µm)					
µm	0	1	2	4	8	16
300	0.807	0.795	0.656	0.532	0.444	0.379
400	0.745	1.080	0.850	0.693	0.583	0.498
500	1.299	1.315	1.048	0.868	0.717	0.617

Table 3.21 FEA Estimated Peak Base Stress for 20µm Width Tapered Flexure.

Length	Fillet Size (µm)					
µm	0	1	2	4	8	16
300	0.386	0.579	0.440	0.358	0.305	0.263
400	0.517	0.677	0.586	0.471	0.395	0.344
500	0.582	0.864	0.704	0.575	0.486	0.417

Table 3.22 FEA Estimated Peak End Stress for 10µm Width Straight Flexure.

Length	Fillet Size (µm)					
µm	0	1	2	4	8	16
300	0.269	0.273	0.246	0.226	0.218	0.233
400	0.268	0.288	0.247	0.229	0.221	0.233
500	0.276	0.295	0.257	0.229	0.220	0.233

Table 3.23 FEA Estimated Peak End Stress for 10µm Width Tapered Flexure.

Length	Fillet Size (µm)					
µm	0	1	2	4	8	16
300	1.058	1.485	1.264	1.068	1.016	0.967
400	1.396	1.576	1.572	1.400	1.346	1.294
500	1.669	1.911	1.837	1.763	1.636	1.587

Table 3.24 FEA Estimated Peak End Stress for 15µm Width Straight Flexure.

Length	Fillet Size (µm)					
µm	0	1	2	4	8	16
300	0.095	0.144	0.117	0.106	0.098	0.101
400	0.095	0.143	0.122	0.105	0.098	0.102
500	0.095	0.143	0.119	0.105	0.098	0.102

Table 3.25 FEA Estimated Peak End Stress for 15µm Width Tapered Flexure.

Length	Fillet Size (µm)					
µm	0	1	2	4	8	16
300	0.485	0.724	0.591	0.538	0.485	0.446
400	0.628	0.827	0.742	0.647	0.616	0.567
500	0.769	1.062	0.858	0.801	0.728	0.696

Table 3.26 FEA Estimated Peak End Stress for 20µm Width Straight Flexure.

Length	Fillet Size (µm)					
µm	0	1	2	4	8	16
300	0.056	0.081	0.068	0.059	0.055	0.057
400	0.077	0.077	0.068	0.058	0.055	0.057
500	0.055	0.076	0.068	0.059	0.055	0.057

Table 3.27 FEA Estimated Peak End Stress for 20µm Width Tapered Flexure.

Length	Fillet Size (µm)					
µm	0	1	2	4	8	16
300	0.387	0.391	0.347	0.324	0.278	0.255
400	0.362	0.504	0.443	0.394	0.362	0.329
500	0.439	0.625	0.547	0.486	0.449	0.411

Inspection of the data indicates that, as expected, fillets of increasing radii mitigate the peak stress of the flexure but with diminishing effect. Since the same loading conditions were applied to the faces of the hammerhead in all designs, there is substantially more stress in the longer length and narrower width flexures. The span of peak stress appears to be roughly the same for the tapered and straight flexures for a given flexure width and length, but at the base the tapered flexure has significantly lower overall stress (generally approximately 40%) when comparing similar designs with similar radius fillets. This is consistent with the general expectation that the tapered flexure should have 40% less peak stress than a similarly loaded equivalent straight flexure. At the end, as expected, the tapered flexure exhibits stress very similar to what it has at the base while the straight flexure exhibits almost no stress at all at this location.

Since the tapered flexure was expected to have roughly 40% less stress than the straight flexure, it is difficult to draw many conclusions from the raw data. Therefore, in each case the data were normalized by the theoretical peak stress in that location to see if this yielded any additional insights. The normalized data are presented in Tables 3.28 - 3.33. Since the normalized peak stress at the end of the straight flexure results in very large and unreasonable results due to the fact that the theoretical value for stress is near zero, the stress at the end of the flexure has been omitted here.

Table 3.28 Normalized Peak Base Stress for 10µm Width Straight Flexure.

Length	Fillet Size (µm)					
µm	0	1	2	4	8	16
300	1.713	1.892	1.728	1.549	1.357	1.199
400	1.569	1.988	1.760	1.577	1.338	1.220
500	1.553	2.139	1.752	1.526	1.370	1.225

Table 3.29 Normalized Peak Base Stress for 10µm Width Tapered Flexure.

Length	Fillet Size (µm)					
µm	0	1	2	4	8	16
300	1.660	2.382	1.947	1.670	1.403	1.302
400	1.671	2.444	1.971	1.692	1.465	1.333
500	1.685	2.498	1.942	1.618	1.512	1.290

Table 3.30 Normalized Peak Base Stress for 15µm Width Straight Flexure.

Length	Fillet Size (µm)					
µm	0	1	2	4	8	16
300	2.476	2.563	2.009	1.696	1.412	1.235
400	1.760	2.571	2.038	1.698	1.439	1.248
500	2.281	2.419	1.999	1.683	1.414	1.265

Table 3.31 Normalized Peak Base Stress for 15µm Width Tapered Flexure.

Length	Fillet Size (µm)					
µm	0	1	2	4	8	16
300	1.858	2.673	2.208	1.836	1.509	1.354
400	1.868	2.783	2.124	1.821	1.519	1.349
500	1.876	2.795	2.225	1.823	1.527	1.341

Table 3.32 Normalized Peak Base Stress for 20µm Width Straight Flexure.

Length	Fillet Size (µm)					
µm	0	1	2	4	8	16
300	2.716	2.675	2.209	1.791	1.494	1.277
400	1.926	2.792	2.196	1.791	1.506	1.286
500	2.724	2.756	2.198	1.820	1.504	1.294

Table 3.33 Normalized Peak Base Stress for 20µm Width Tapered Flexure.

Length	Fillet Size (µm)					
µm	0	1	2	4	8	16
300	2.026	3.039	2.308	1.877	1.599	1.383
400	2.096	2.743	2.376	1.907	1.601	1.395
500	1.918	2.849	2.322	1.897	1.603	1.376

Four significant items were noted from this data. The first was that the normalized peak strain was consistently slightly higher for the tapered flexure than it was for the straight flexure. The second was that there did not seem to be any significant dependence on the length of the flexure. The third was that there did seem to be a dependence on the width of the flexure with that being, given the same fillet radius, normalized stress peaking was higher with increasing flexure width. Finally, the normalized stress peaking values for fillet radii of 2, 4, and 8µm for the 10µm wide straight flexure matched very closely with the values for fillet radii of 4, 8, and 16µm for the 20µm wide straight flexure. This combined with the first and third findings suggested that the real relationship may be fundamentally between the normalized stress peaking and the normalized fillet radius (the fillet radius normalized to the local flexure width).

Figure 3.58 shows a plot of the Normalized Peak Stress plotted against the Normalized Fillet Radius for both the straight and tapered flexures with a length of 400µm and the width of 15µm, which represent the center case of length and width. The overlap of these two plots is quite remarkable. This suggests that the normalized stress peaking is dependent on the fillet radius normalized to the local flexure width, regardless of whether the flexure is straight or tapered. It also suggests that there is a point of diminishing returns that occurs somewhere around a normalized fillet radius of 0.5 of the

local flexure width. Figure 3.59 plots normalized peak stress against normalized fillet radius for all designs, and the data indicate these findings are universal across all designs.

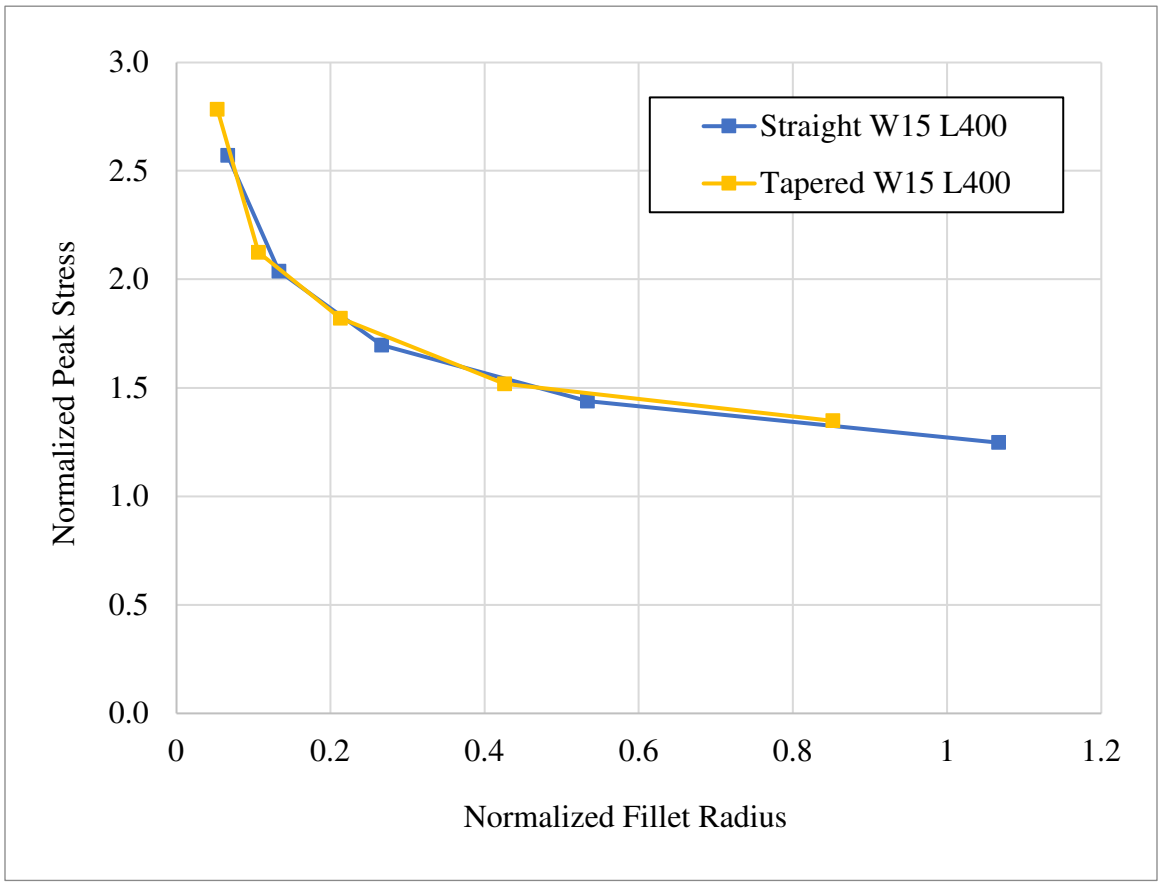

Figure 3.58 Normalized Peak Stress vs. Fillet Radius, 15µm Wide, 400µm Length.

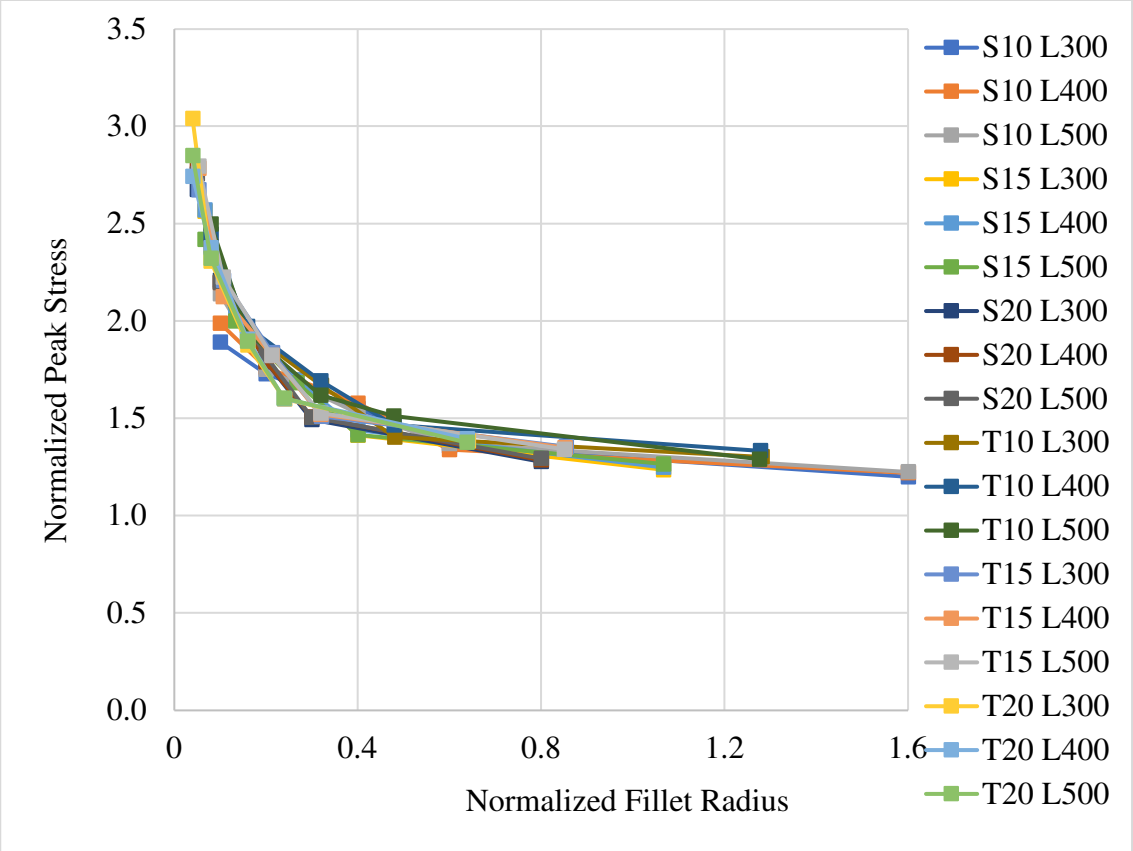

Figure 3.59 Normalized Peak Stress vs. Fillet Radius, All Designs.

Similar to what was plotted in the previous sections, the peak stress for each fillet radius was normalized to the straight flexure value with 16µm fillet radius for each length and width combinations. This normalization value was chosen to enable relative comparison of the stress peaking mitigation as a function of fillet radius as well as to show the overall reduction of peak stress in the tapered flexures. These normalized peak stresses are plotted in Figure 3.60. The straight flexure normalized peak stresses are shown with dashed red lines and the tapered flexure normalized peak stresses are shown with solid green lines. Figure 3.60 clearly shows that the normalized peak stresses for the tapered flexures are consistently 40% lower than the equivalent straight flexure for all lengths, widths, and fillet radii. The wide variation in the straight flexure peak stress

predictions (due to the ill-conditioning of the equations) for the zero fillet radius designs is also evident from the data in Figure 3.60. For MEMS gyroscopes, this would enable driving the gyroscope resonance 40% harder resulting in an increase in sensitivity of 40% over that of an equivalent straight flexure.

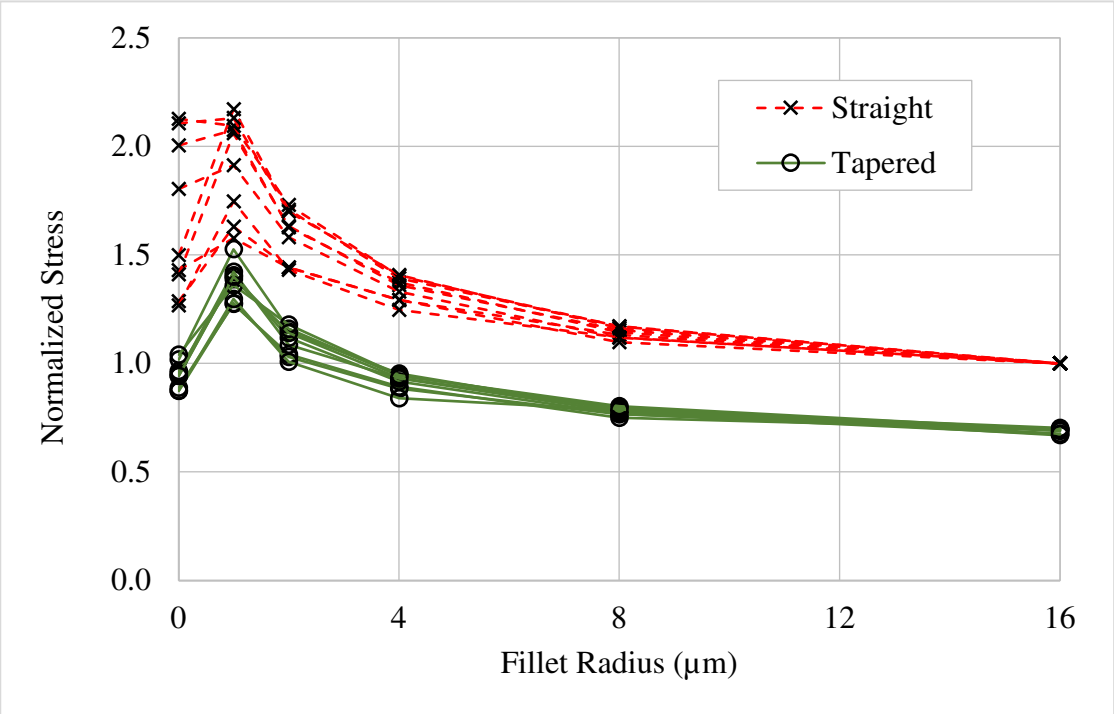

Figure 3.60 Normalized Peak Stress Versus Fillet Radius, All Designs.

3.3.1.4 Impact of Fillet Radius on Thermo-Elastic Damping

Tables 3.34 - 3.39 present FEA estimates of quality factors due to thermoelastic damping (TED), Q_{TED}, for each flexure width, length, type, and fillet radius. Quality factor is a unitless quantity. The right-most column in each table indicates the "span" of the Q_{TED} expressed as a percentage of the Q_{TED} with no fillet which was calculated in a

similar fashion to what was calculated for the spring constants in the previous section. A theoretical value for Q_{TED} was not calculated due to the complexity of the geometry associated with the tapered flexures.

Table 3.34 FEA Estimated Q_{TED} for 10μm Width Straight Flexure.

Length	Fillet Size (μm)						Span
μm	0	1	2	4	8	16	%
300	115728	115427	114772	113400	110702	105815	8.3
400	182606	182140	181339	179696	176456	170749	6.2
500	262593	261742	260806	258887	255178	248789	4.9

Table 3.35 FEA Estimated Q_{TED} for 10μm Width Tapered Flexure.

Length	Fillet Size (μm)						Span
μm	0	1	2	4	8	16	%
300	120364	120115	119676	118744	116929	113651	5.4
400	185827	185530	185083	184126	182320	179292	3.4
500	261056	260802	260279	259310	257532	254906	2.3

Table 3.36 FEA Estimated Q_{TED} for 15μm Width Straight Flexure.

Length	Fillet Size (μm)						Span
μm	0	1	2	4	8	16	%
300	31665	31584	31422	31097	30443	29326	7.1
400	49091	48995	48792	48382	47586	46208	5.7
500	70128	70009	69774	69286	68357	66743	4.7

Table 3.37 FEA Estimated Q_{TED} for 15µm Width Tapered Flexure.

Length	Fillet Size (µm)						Span
µm	0	1	2	4	8	16	%
300	32266	32214	32110	31906	31523	30894	4.1
400	48303	48242	48133	47918	47531	46946	2.7
500	66832	66769	66647	66428	66042	65550	1.8

Table 3.38 FEA Estimated Q_{TED} for 20µm Width Straight Flexure.

Length	Fillet Size (µm)						Span
µm	0	1	2	4	8	16	%
300	14550	14514	14455	14337	14129	13810	4.8
400	20927	20885	20808	20657	20375	19916	4.6
500	29039	28985	28894	28711	28365	27789	4.1

Table 3.39 FEA Estimated Q_{TED} for 20µm Width Tapered Flexure.

Length	Fillet Size (µm)						Span
µm	0	1	2	4	8	16	%
300	15229	15211	15175	15106	14991	14831	2.5
400	20574	20555	20518	20447	20330	20189	1.8
500	27143	27120	27080	27006	26889	26774	1.3

Analysis of this data is more complicated than it may seem at first because the TED was estimated at, and is dependent on, the resonant frequency of the device. So, while a cursory glance at these results may seem to indicate that a larger fillet radius decreases the Q_{TED}, factoring the increases in resonant frequency indicated in Tables 3.10 - 3.15 into the analysis, the decrease in Q_{TED} is seen to be due, at least in part, to an increasing resonant frequency.

Recalling that Zener derived a relationship between Q_{TED} and operating frequency, ω_n, for thin reeds [61], the relationship can be approximated by [64, 90]:

$$Q_{TED}^{-1} = \frac{E\alpha^2 T_0}{C_v} \frac{\omega_n \tau}{1 + \omega_n^2 \tau^2}, \tag{3.30}$$

where the characteristic time constant, τ, sometimes referred to as the Zener time constant (and its inverse sometimes referred to as the Debye frequency), is given by:

$$\tau = \frac{w^2 C_v}{\pi^2 k} \tag{3.31}$$

and where α is the linear coefficient of thermal expansion, C_v is the specific heat per unit volume, k is the thermal conductivity, T_0 is the equilibrium temperature, E is the Young's Modulus, and w is the beam width. For operating frequencies below the Debye frequency, the Q_{TED} increases linearly with decreasing ω_n. This region of frequencies below the Debye frequency is referred to as the iso-thermal operating region because the flexing of the material is happening slowly enough for the thermal transients caused by the strain transients associated with the bending motion to settle, thereby having the material remain in an iso-thermal condition. For operating frequencies above the Debye frequency, the Q_{TED} increases linearly with increasing ω_n. This region of frequencies above the Debye frequency is referred to as the adiabatic operating region because the flexing of the material is happening so quickly that the thermal transients caused by the strain transients associated with the bending motion have insufficient time to allow significant heat to flow, thereby losing essentially no energy and resulting in an adiabatic process. For the purposes of the designs evaluated in this work, all of these devices operated in the iso-thermal region. Therefore, it is reasonable to approximate that an

increase in resonant frequency should result in a decrease in Q_{TED} of a proportional percentage. That is, the $f \bullet Q_{TED}$ product should remain approximately constant.

With this relationship in mind, it is found that for smaller width flexures, increases in the fillet radius tend to decrease Q_{TED} more than what an increase in resonant frequency alone would warrant. However, for the 20µm width flexure, it is found that the decrease in Q_{TED} is just slightly larger than what would be expected from the corresponding increase in resonant frequency. This general relationship seems to hold true for both the straight flexure and the tapered flexure but it is critical to note that the overall impact of the fillet on the Q_{TED} of the tapered flexures is still roughly half of the impact on the straight flexures. This implies a significantly reduced sensitivity (roughly half) on Q_{TED} of the tapered flexures to manufacturing variations in the inside corners of the devices. This sensitivity advantage is especially relevant for mode matched gyroscopes where the bias error of the gyroscope is directly proportional to the quality factor mismatch between the two modes of the gyroscope.

For increasing lengths of the flexures, the Q_{TED} increases. This phenomenon is in agreement with the decrease in resonant frequency and is consistent with the behavior predicted by Zener's equation. It appears to hold true for both the straight and tapered flexures.

Comparing the absolute Q_{TED} performance of the straight and tapered flexures reveals that the tapered flexures have generally better performance (higher value) for Q_{TED} when considering the higher resonant frequencies associated with the tapered flexures. For example, the Q_{TED} for both the straight and tapered flexure with L=400µm, W=20µm, and Fillet = 8µm is roughly 20,300, but the resonant frequency for the tapered

flexure is roughly 10% higher than that of the straight flexure. Therefore, the tapered flexure still had higher performance than the straight flexure by about 10%. This factor of roughly 10% appears to be fairly consistent across all design veriations. Therefore, it appears that the tapered flexure has roughly 10% better TED performance than the straight flexure. This is also most relevant to mode matched gyroscope designs because their sensitivity is directly proportional to the quality factor in the sense axis.

Again, similar to what was plotted in the previous sections, the Q_{TED} for each fillet radius was first compensated for differences in resonant frequency and then normalized to the straight flexure value with fillet radius of 16μm for each length and width combination. These normalized Q_{TED} values are plotted in Figure 3.61. The straight flexure normalized Q_{TED} values are shown with dashed red lines and the tapered flexure normalized Q_{TED} values are shown with solid green lines. Figure 3.61 clearly shows that the normalized Q_{TED} values for the tapered flexures are consistently about 10% higher than the equivalent straight flexure for all lengths, widths, and fillet radii and the sensitivity to fillet radius of the tapered flexures is about half that of the straight flexures. For mode-matched MEMS gyroscopes, this implies an increase in sensitivity of about 10% due to the increased quality factor and a potential decrease in bias error of up to 50% due to the reduced sensitivity of TED to fillet radius variations.

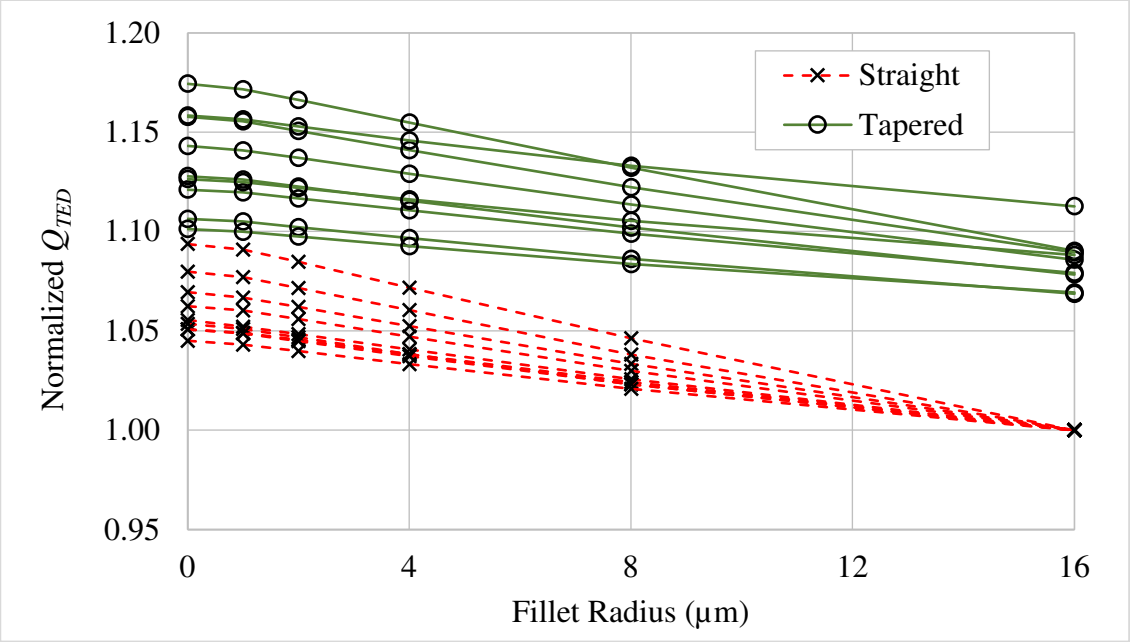

Figure 3.61 Normalized Q_{TED} Versus Fillet Radius, All Designs.

3.3.2 Critical Dimension Loss and Sidewall Angle

For the purposes of this work, a preliminary investigation was performed into the sensitivity of tapered flexures to Critical Dimension Loss (CDLoss) and Sidewall Angle variation. This study consisted of a mathematical derivation of an approximate sensitivity relationship of spring constant with respect to a constant width variation along the length of the flexure, followed by a cursory FEA to investigate the reasonableness of this approximate relationship. This result is compared with the sensitivity of the spring constant of the straight flexure to CDLoss. Sensitivity to Sidewall Angle variation is considered to be covered by this same analysis because it just represents a continuous variation of the flexure width along the height of the flexure. For relatively small

sidewall angles, the impact on spring constant can be estimated using the average flexure thickness.

The analysis begins with a look at the sensitivity of the straight flexure to CDLoss. The equation that relates the linear spring constant of straight flexure to the width of that flexure was given previously in Equation 3.28 and repeated here for convenience:

$$k_{HHC\_S} = \frac{Etw^3}{4 \cdot (L^3 + 3dL^2 + 3d^2L)} \quad . \tag{3.32}$$

Taking the partial derivative of this with respect to w provides the desired sensitivity relationship:

$$\frac{\partial k_{HHC\_S}}{\partial w} = \frac{3}{4}\frac{Etw^2}{(L^3 + 3dL^2 + 3d^2L)} \quad . \tag{3.33}$$

The procedure for deriving the corresponding relationship for the tapered flexure is much more involved. Since the width of the flexure in the tapered flexure is not a constant, the resulting spring constant equation does not result in a variable with which the desired sensitivity can be easily derived. Therefore, it was necessary to go back to the derivation of the deflection documented in Section 3.1.2 and modify the equation based on the definition of the derivative. This derivation begins with the equation for the width of the beam, w, as a function of position along the length of the beam:

$$w = w_b \sqrt{\frac{N-x}{N}} \quad , \tag{3.34}$$

where w_b is the width of the flexure at the base, N is the total length of the flexure including the length to the center of the hammerhead feature, and x is the location along the length of the flexure. A new relation must now be derived with a modified beam width equation as follows:

$$b = w + \Delta_b = w_b \sqrt{\frac{N-x}{N}} + \Delta_b \, . \tag{3.35}$$

The equation for the displacement field is then given by:

$$v(x) = \iint_0^x \frac{F(N-x)}{E \cdot I(x)} dx dx \quad , \tag{3.36}$$

where

$$I(x) = \frac{tb^3}{12} = \frac{t\left(w_b \sqrt{\frac{N-x}{N}} + \Delta_b\right)^3}{12} \tag{3.37}$$

$$I(x) = \frac{t}{12}\left[w_b^3 \left(\frac{N-x}{N}\right)^{\frac{3}{2}} + 3w_b^2 \left(\frac{N-x}{N}\right)\Delta_b + 3w_b \left(\frac{N-x}{N}\right)^{\frac{1}{2}} \Delta_b^2 + \Delta_b^3\right]. \tag{3.38}$$

A simplifying assumption was made here that only the first two terms in this equation are significant. This assumption is justified as long as $\Delta_b \ll w_b$:

$$I(x) \approx \frac{t}{12}\left[w_b^3\left(\frac{N-x}{N}\right)^{\frac{3}{2}} + 3w_b^2\left(\frac{N-x}{N}\right)\Delta_b\right]. \tag{3.39}$$

Substituting this into Equation 3.36 yields:

$$v(x) = \iint_0^x \frac{F(N-x)}{E \cdot \frac{t}{12}\left[w_b^3\left(\frac{N-x}{N}\right)^{\frac{3}{2}} + 3w_b^2\left(\frac{N-x}{N}\right)\Delta_b\right]} dxdx \tag{3.40}$$

,

which can be simplified to:

$$v(x) = \frac{12FN^{\frac{3}{2}}}{Etw_b^3}\iint_0^x \frac{1}{(N-x)^{\frac{1}{2}} + 3N^{\frac{1}{2}}\frac{\Delta_b}{w_b}} dxdx \tag{3.41}$$

.

Here a substitution of variables becomes necessary. Define:

$$y = N - x \tag{3.42}$$

$$dy = -dx \tag{3.43}$$

and

$$a = 3N^{\frac{1}{2}}\frac{\Delta_b}{w_b} \tag{3.44}$$

.

The limits of integration then become:

$$y(x = 0) = N \tag{3.45}$$

$$y(x = x) = N - x\ . \tag{3.46}$$

Equation 3.41 now becomes:

$$v(x) = \frac{12FN^{\frac{3}{2}}}{Etw_b^3} \iint_N^{N-x} \frac{1}{(y)^{\frac{1}{2}} + a} dydy \quad . \tag{3.47}$$

Performing the first integration, details of which are provided in Section A.4 of Appendix A, yields:

$$v(x) = \frac{12FN^{\frac{3}{2}}}{Etw_b^3} \int_N^{N-x} \left\{2\sqrt{y} - 2a\ \ln\left(a + \sqrt{y}\right) + C_1\right\} dy \quad , \tag{3.48}$$

where

$$C_1 = -2\sqrt{N} + 2a \ln\left(a + \sqrt{N}\right)\ . \tag{3.49}$$

Substituting Equation 3.42 back into Equation 3.48 yields:

$$v(x) = \frac{12FN^{\frac{3}{2}}}{Etw_b^3} \int_N^{N-x} \left\{2\sqrt{y} - 2a\ \ln\left(a + \sqrt{y}\right) + C_1\right\} dy\ . \tag{3.50}$$

After performing the integration and executing a relatively lengthy series of algebraic steps which are provided in section A.4 of Appendix A, the following relation is revealed:

$$v(x) = \frac{12FN^{\frac{3}{2}}}{Etw_b^3}\left\{\frac{4}{3}(N-x)^{\frac{3}{2}} + 2x\sqrt{N} - \frac{4}{3}N^{\frac{3}{2}}\right.$$
$$+ 2a\left[(N-x-a^2)\left[\ln\left(a+\sqrt{N}\right)\right.\right.$$
$$-\qquad \ln\left(a+\sqrt{N-x}\right)\Big]$$
$$+\qquad a\left(\sqrt{N}-\sqrt{N-x}\right) - \frac{x}{2}\Big]\Big\} \quad . \tag{3.51}$$

Here it is quite comforting to note that the first three terms of this equation are identical to that reported in Table 3.1 and that if Δ_b goes to zero, then the remainder of the terms in the above expression go to zero.

Extension of this relationship to the center of the hammerhead structure would be quite lengthy and only result in a slightly more accurate description of the desired relationship. Therefore, the deflection of the flexure at the end of the flexure where it connects to the hammerhead, $v(x = L)$, was investigated. First the desired sensitivity relationship, the sensitivity of the deflection with respect to a change in the width of the flexure $S\{v_t(L)\}_w$, is defined by revisiting the definition of the derivative:

$$S\{v_t(L)\}_w = \lim_{\Delta_b \to 0} \frac{v_t(L)_{\Delta_b=\Delta_b} - v_t(L)_{\Delta_b=0}}{\Delta_b} \quad . \tag{3.52}$$

Here the subscript t has been introduced to indicate tapered flexure. After another relatively lengthy series of algebraic steps and evaluating the limit, the details of which are provided in section A.4 of Appendix A, this results in the following relation:

$$S\{v_t(L)\}_w = \frac{36N^2F}{Etw_b^4}\left[-L + d\ln\left(\frac{N}{d}\right)\right] \quad . \tag{3.53}$$

This relationship is not directly comparable with the similar relationship for the straight flexure found previously in Equation 3.33. Therefore, a comparable relationship needed to be derived for the straight flexure. Beginning with the equation for the deflection of the straight flexure:

$$v_s(x = L) = \frac{12 \cdot F}{Etw^3}\left[\frac{L^3}{3} + \frac{dL^2}{2}\right] = \frac{FL^2}{Etw^3}[4L + 6d] \, . \tag{3.54}$$

To get the sensitivity of this with respect to the width it is necessary to calculate the partial with respect to the width:

$$S\{v_s(L)\}_w = -\frac{12FL^2}{Etw^4}\left[L + \frac{3}{2}d\right] \, . \tag{3.55}$$

Comparison of Equation 3.53 for the tapered flexure and Equation 3.55 for the straight flexure yields the following observations:

1. The tapered equation has a constant multiplier of 36 in the numerator whereas the straight equation has only a multiplier of 12.
2. Both equations have a width to the fourth power in the denominator. It has been mentioned previously in this report that the tapered flexure typically has a base width that is 25% wider than that of the equivalent straight flexure. Therefore, this width to the fourth power term would result in a factor of roughly 2.44 in the denominator of the tapered

equation, which comes close to, but does not completely offset, the factor of three mentioned in the above bullet.

3. The tapered equation has a factor of N^2 in the numerator whereas the straight equation has only a factor of L^2. Depending on the ratio of d to L, typically 0.1, this could easily result in another factor of 1.2 in the tapered equation.
4. The second term in the bracket has the opposite sign in the tapered equation and has a factor of $\ln\left(\frac{N}{d}\right)$ as opposed to the factor of $\frac{3}{2}$ for the straight equation. This term would tend to make the sensitivity of the tapered flexure smaller than it would for the straight flexure, which could be a factor of roughly 35% for typical designs.

When all of these factors are considered together, it appears that the sensitivity of the tapered flexure to CDLoss and sidewall angle will be roughly comparable to that of the straight flexure for typical designs. A detailed algebraic analysis of these relations indicates that the tapered flexure should be marginally less sensitive to manufacturing variations for L to d ratios below about 14.5.

A set of FEAs were performed to corroborate this finding. First, a set of FEAs were conducted with an L to d ratio of 13.3 where L =400µm and d = 30µm, which would theoretically result in approximately equivalent sensitivities. A second set of FEAs was conducted with an L to d ratio of 3, where L =150µm and d = 50µm, which is well below the ratio where the sensitivities of the tapered and straight flexures would be equivalent and should result in tapered flexure being less sensitive to CDLoss. Table 3.40 summarizes the results of these FEAs.

Table 3.40 CDLoss FEA Results.

Flexure Type	Length (µm)	Equivalent Width (µm)	Deflection (µm)	Delta (%)
Straight	400	10.0	0.098273	5.95
		9.8	0.104122	
Tapered	400	10.0	0.094660	6.79
		9.8	0.101085	
Straight	150	10.0	0.012332	3.04
		9.9	0.012707	
Tapered	150	10.0	0.010865	2.78
		9.9	0.011168	

These FEA results do generally corroborate the theoretical finding that sensitivity to CDLoss is comparable between the straight and tapered flexures, with the tapered flexure being 14% more sensitive to CDLoss for an L to d ratio of 13.3 and 9% less sensitive for an L to d ratio of 3. These results also corroborate the general trend that tapered flexures will have lower sensitivity to CDLoss than straight flexures for lower L to d ratios. Clearly the crossover point where the tapered flexure becomes less sensitive to CDLoss than the straight flexure is less than the theoretically approximated value of 14.5, but there were a lot of approximations included in that derivation and the FEA suggested value is likely somewhere around 6.9.

It is also important to recall that this sensitivity was derived for the deflection at the place where the flexure connected to the hammerhead. For the center of the hammerhead, the second set of FEAs, where the L to d ratio was set to 3, resulted in exactly the same sensitivity to CDLoss for the tapered flexure as it did for the straight flexure. Therefore, if the desired parameter of interest is the deflection of the hammerhead at its center point, then this preliminary analysis indicates that the tapered

flexures will likely have roughly the same sensitivity to manufacturing variations for L to d ratios of about 3.

3.4 Summary of Relevant Characteristics of Quadratically Tapered Flexures

In this chapter, we have performed several FEA studies that highlight several potential properties of quadratically tapered flexures. These characteristics are summarized in the list below. For the purposes of this list, an equivalent straight flexure is one that has the same length and spring constant but a constant (non-tapered) width.

- Quadratically tapered flexures exhibit approximately 40% less peak stress than an equivalent straight flexure which could mean up to 40% higher sensitivity for MEMS gyroscopes.
- Quadratically tapered flexures require a hammerhead feature to avoid sections of zero width.
- Quadratically tapered flexures exhibit more rotational deflection than an equivalent straight flexure leading to a slight increase in the nonlinearity of the deflection.
- For a given length of flexure, tapered flexures can be designed with greater stiffness than straight flexures before the compliance of the base becomes significant.
- Quadratically tapered flexures exhibit roughly 10% lower TED which could provide an additional 10% increase in sensitivity for MEMS gyroscopes.

- The use of fillets to mitigate stress peaking in the inside corners appears to follow a universal curve for both tapered and straight flexures and appears to reach a point of diminishing returns for fillet radii roughly equal to half of the local flexure width.
- The spring constants of quadratically tapered flexures exhibit significantly reduced sensitivity to variations fillet radii, which could significantly reduce quadrature error in mode-matched MEMS gyroscopes.
- The TED of quadratically tapered flexures exhibits significantly reduced sensitivity to variations fillet radii, which could significantly reduce bias error in mode-matched MEMS gyroscopes.
- The sensitivity of quadratically tapered flexures to CDLoss seems to be roughly the same as that of straight flexures for L to d ratios of about 3, with increased sensitivity for higher L to d ratios and reduced sensitivity for lower L to d ratios.
- Since lower L to d ratios leave the widest part of the tapered flexure where TED losses are greatest, the L to d ratio may provide a design variable to trade-off TED performance against the sensitivity to CDLoss.

Chapter 4. Anti-Phase Lever Mechanism Development

This chapter provides information on the development of three alternative Anti-Phase Lever Mechanism (APLM) designs based on quadratically tapered flexures and includes a comparison with the equivalent straight flexure-based designs. These include a four-flexure pivot design, a six-flexure lever design, and a revised version of the University of California at Irvine (UCI) "inner lever coupling" design [94]. The analysis provided in this chapter includes a comparison to the original UCI inner lever coupling design as well [28]. Solid model renderings of these 7 designs are presented in Figures 4.1 - 4.7. Finite Element Analyses (FEAs) were designed and conducted to investigate the performance of the seven APLM design geometries shown in Figures 4.1 - 4.7. The analyses investigated (1) peak stress under symmetric loading conditions, (2) relative displacement of the inner and outer masses under asymmetric force loading conditions, (3) separation of anti-phase and in-phase resonant modes, and (4) thermoelastic damping of each design.

First the general operation, governing equations, and design flow process for each of the APLM designs is described. Then the specific APLM design implementations that were evaluated, the Concentric Mass Resonator (CMR) configuration that was used in these evaluations, and the results of the FEA analyses will be presented. Finally, an overall discussion of the FEA results to compare the differences in the designs as well as

to compare the overall performance of tapered flexures to that of straight flexures is provided.

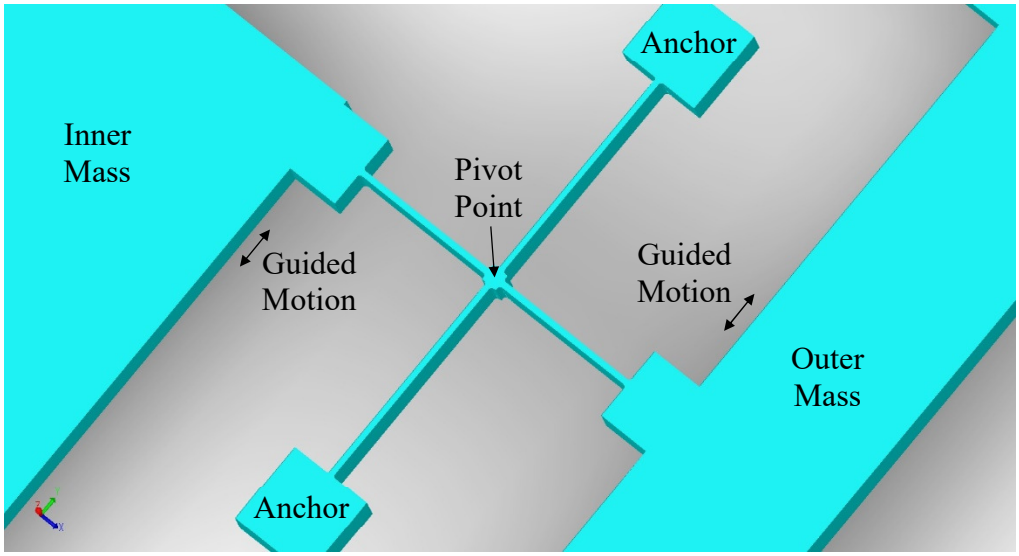

Figure 4.1 Four Straight Flexure Pivot APLM Solid Model Rendering.

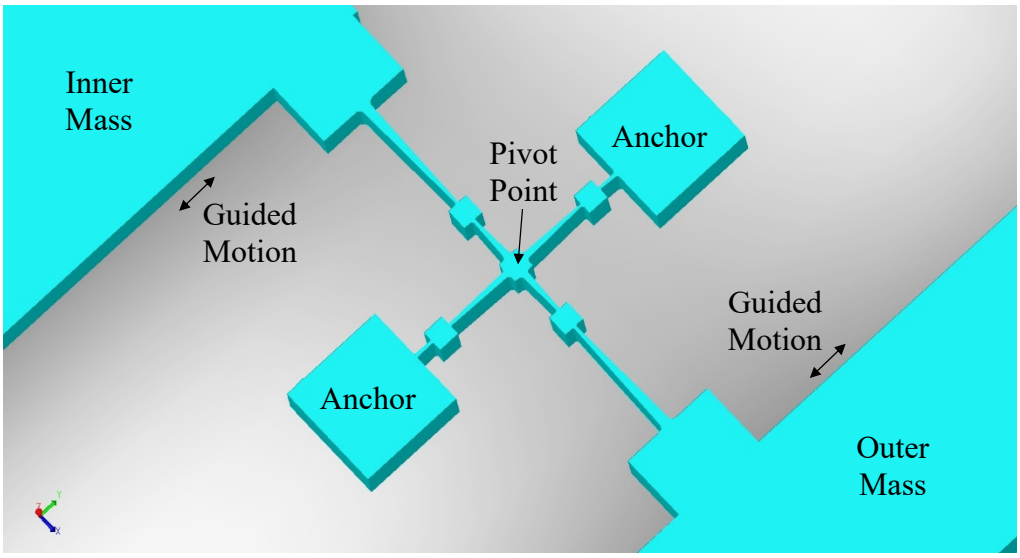

Figure 4.2 Four Tapered Flexure Pivot APLM Solid Model Rendering.

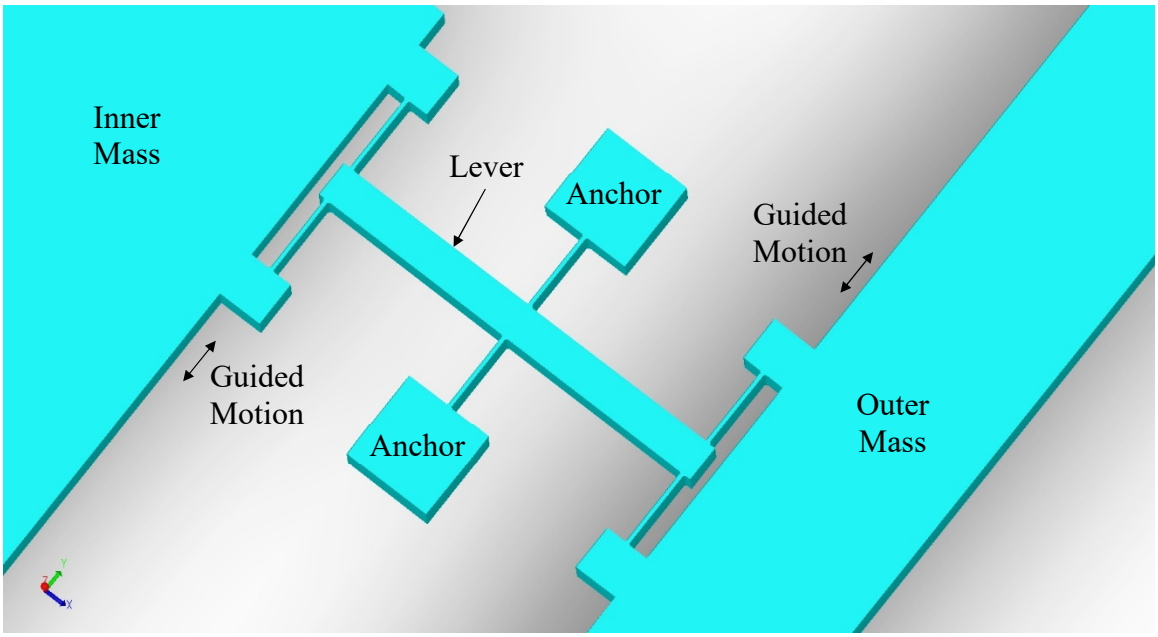

Figure 4.3 Six Straight Flexure Lever APLM Solid Model Rendering.

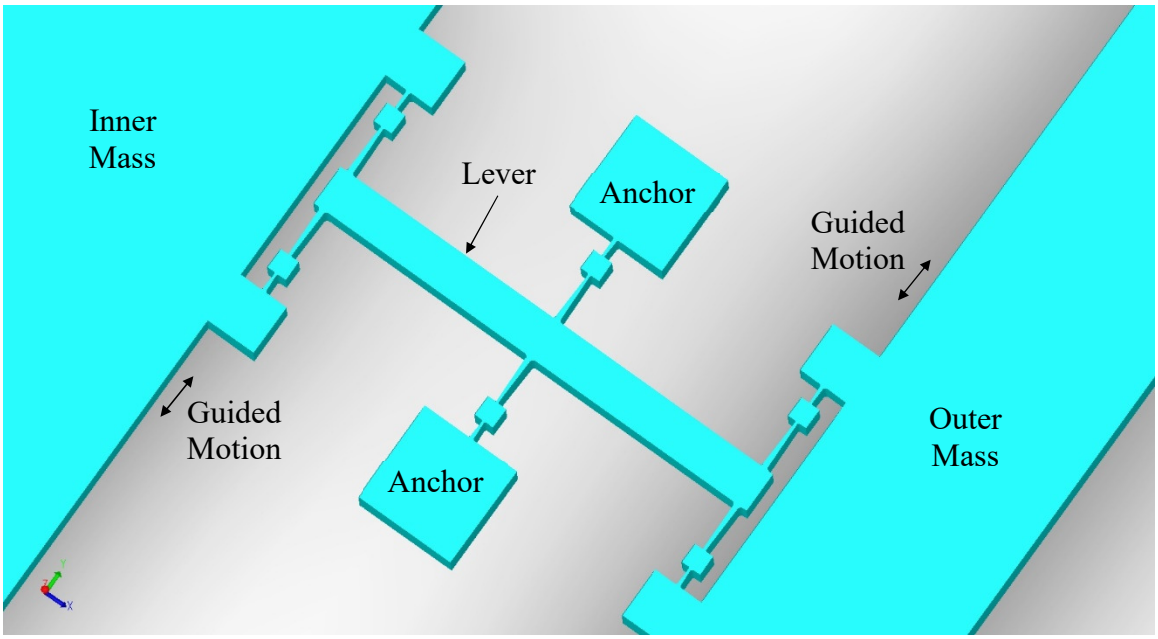

Figure 4.4 Six Tapered Flexure Lever APLM Solid Model Rendering.

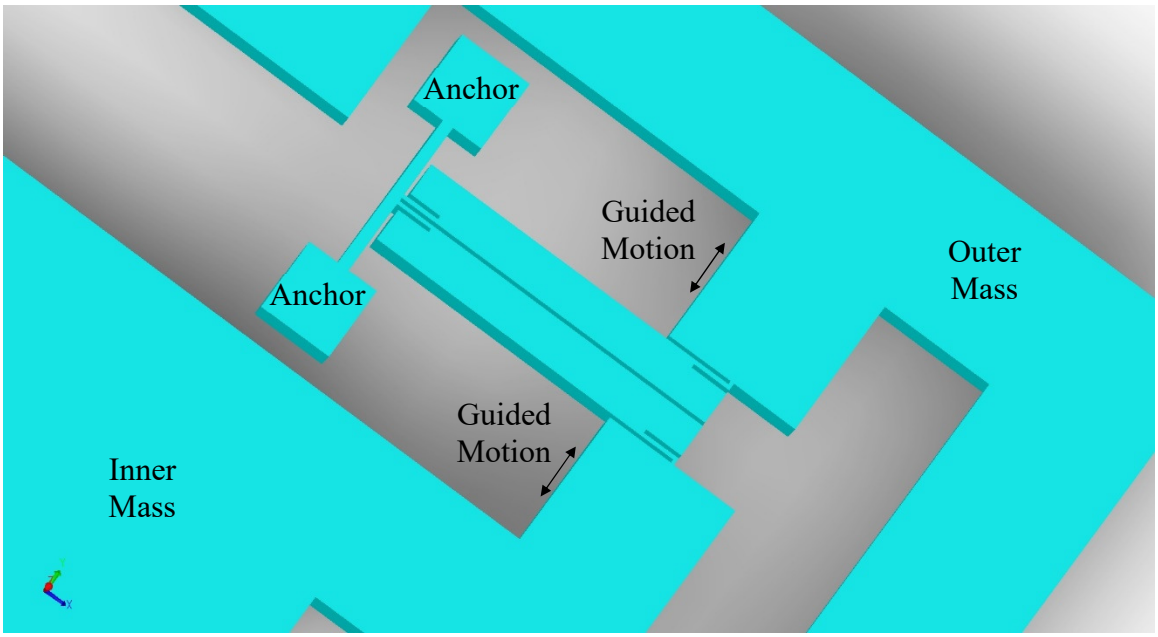

Figure 4.5 Original UCI APLM Solid Model Rendering.

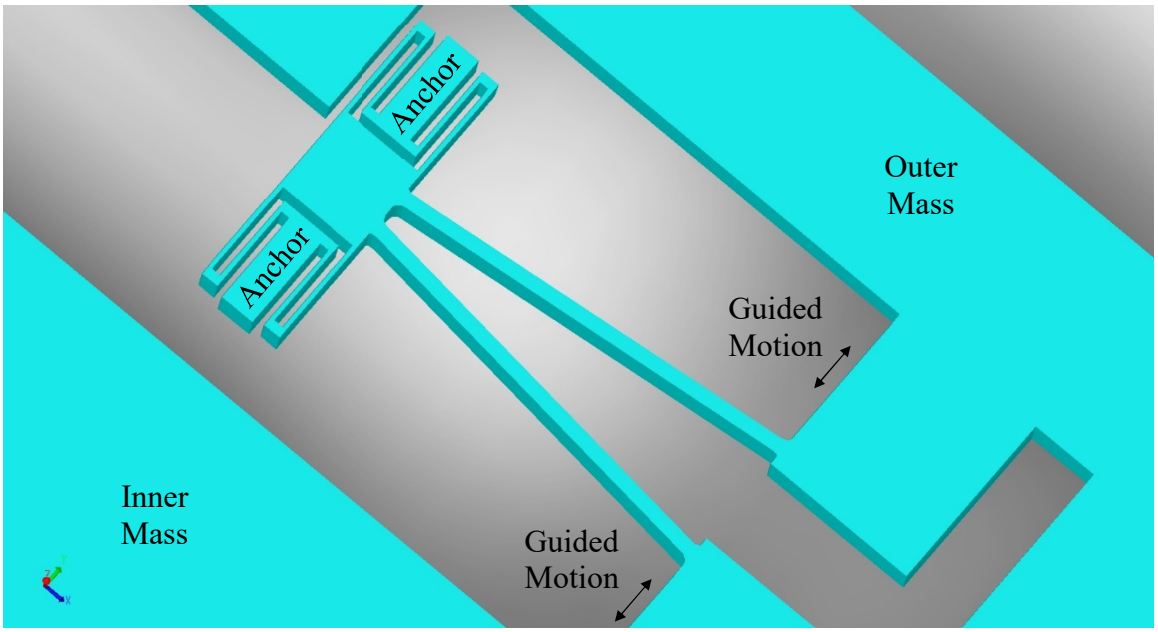

Figure 4.6 Straight Flexure Revised UCI APLM Solid Model Rendering.

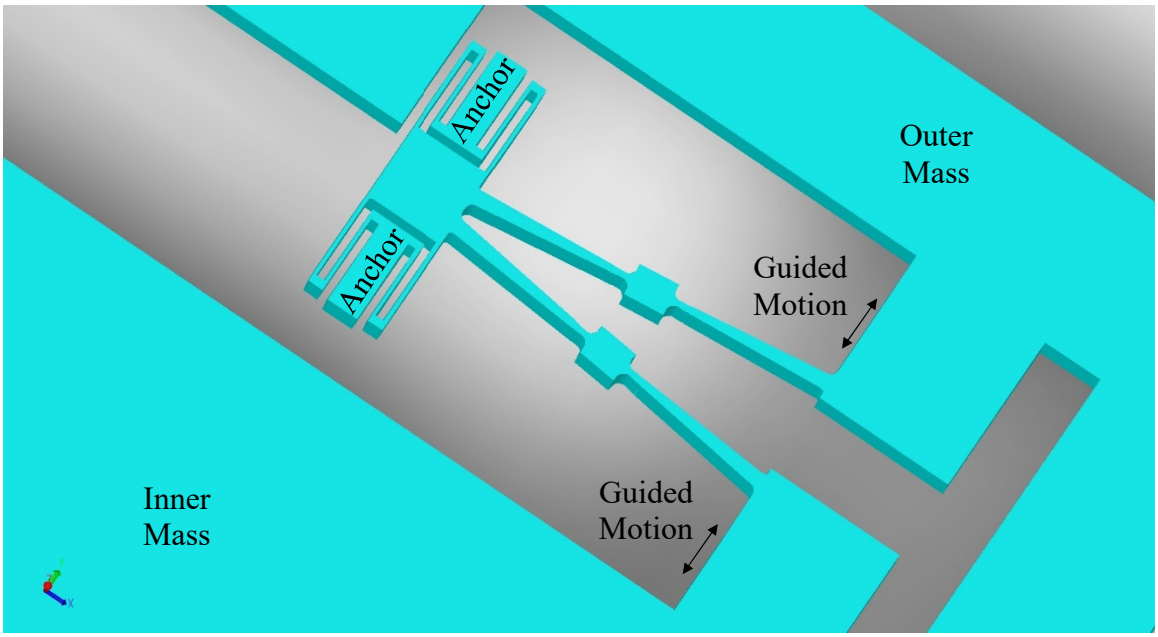

Figure 4.7 Tapered Flexure Revised UCI APLM Solid Model Rendering.

4.1 APLM Configuration Descriptions and Design Procedures

This section describes the operation of each of the APLM designs, their governing equations, and the design flow for each. The fundamental purpose of the APLM is to maintain anti-phase motion between two opposing masses in a dual mass resonator. That is, as one mass moves in one direction, the APLM will force the other mass to move in the opposite direction. For this work, straight and tapered flexures were compared in three APLM configurations.

The first configuration, pictured in Figures 4.1 - 4.2, is a four-flexure pivot design wherein four flexures are arranged at right angles around a pivot point. Two of these flexures are anchored to the substrate and the other two work as guided flexures attached to the opposing proof masses. The straight and tapered versions of the four-flexure pivot

design are shown in deflected condition in Figures 4.8 and 4.9, respectively. The straight flexure version of this configuration represents the simplest form of an APLM with the concept of operation being that motion from one mass will cause the center pivot point to rotate, which will in turn cause the other mass to move in the opposing direction. Through careful selection of the lengths and widths of the flexures in the design, the designer has control over the amount of coupling between the two masses.

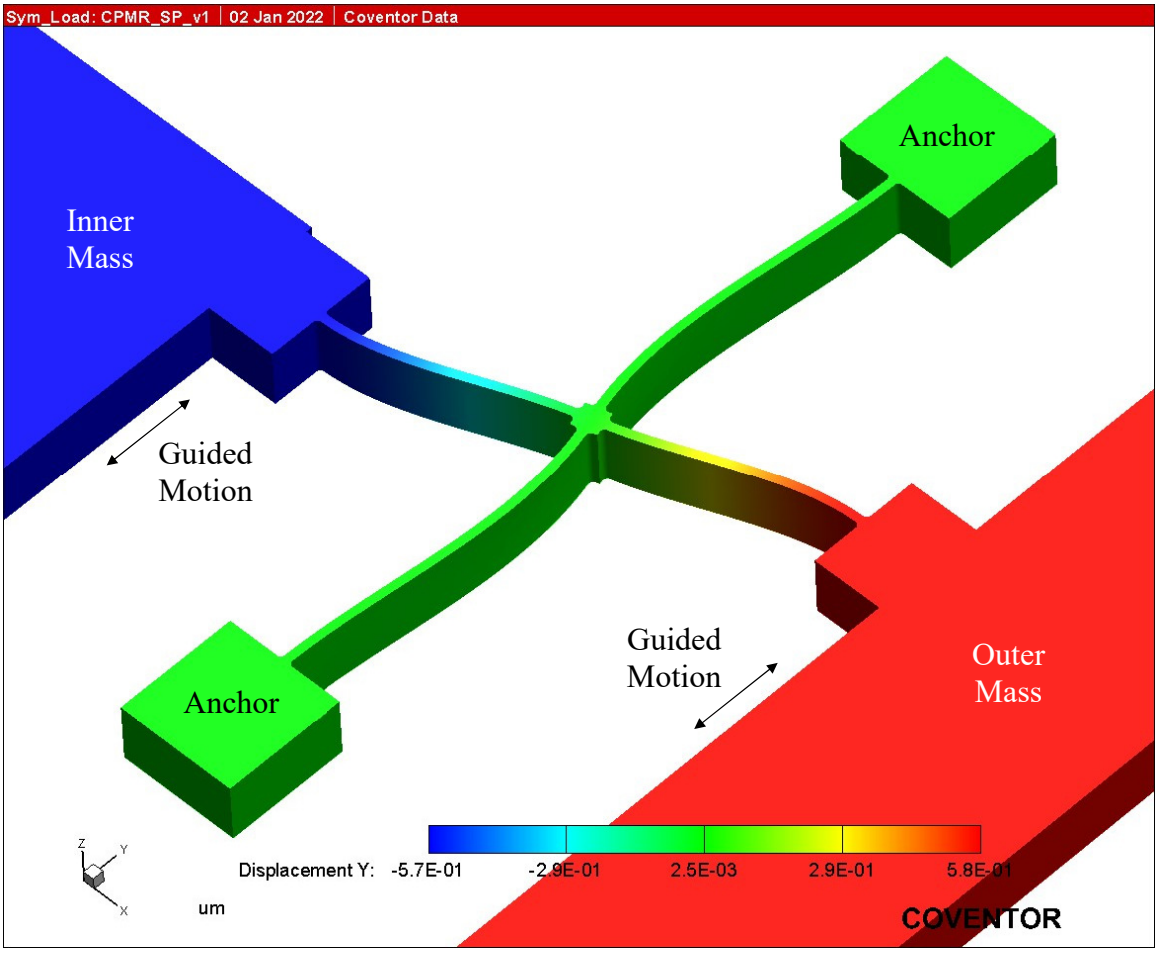

Figure 4.8 Deflected Straight Flexure Pivot APLM.

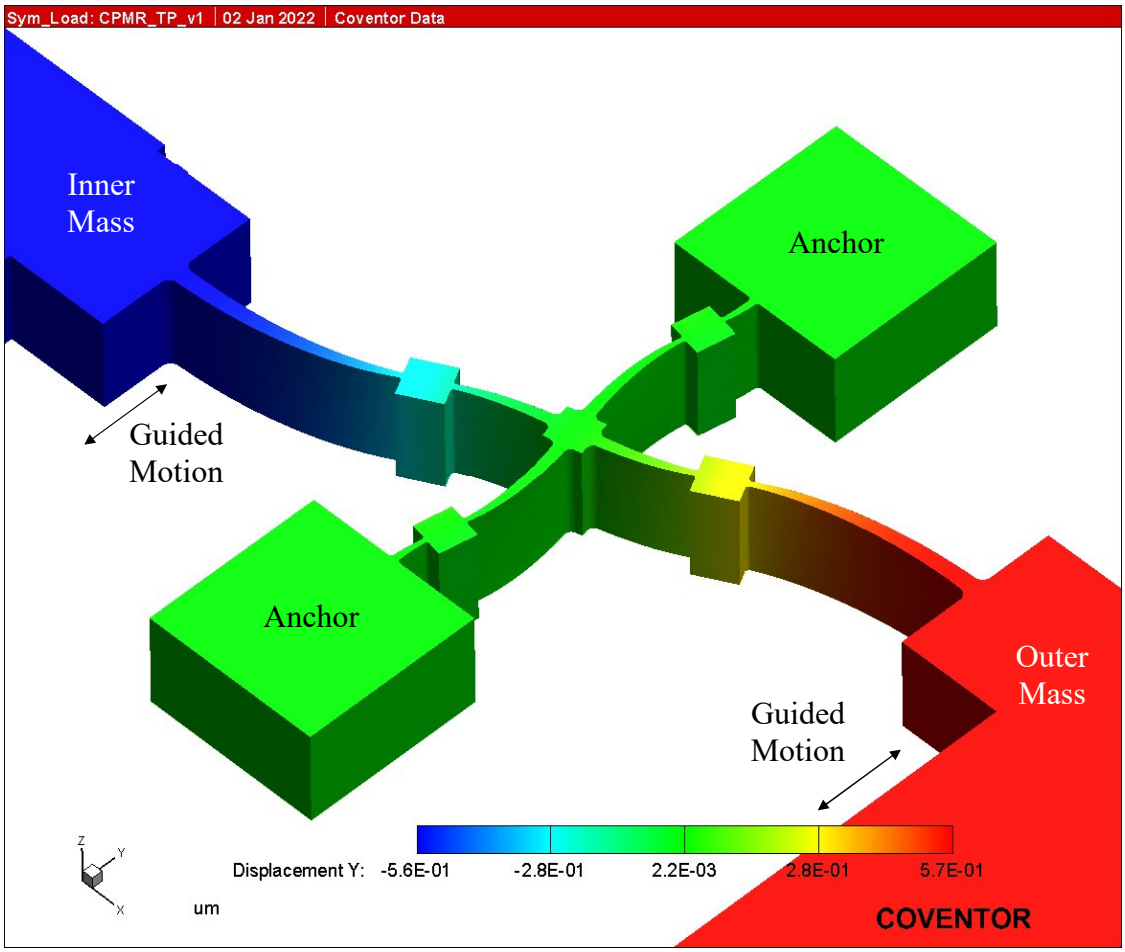

Figure 4.9 Deflected Tapered Flexure Pivot APLM.

The second configuration, pictured in Figures 4.3 and 4.4, is a six-flexure lever design wherein there is a stiff cross-element (the lever) that is anchored to the substrate in the center through two flexures that allow the lever to rotate. The lever is connected to the two opposing masses through two flexures on each end that allow the masses to translate in a guided motion. The six-flexure lever APLM designs are shown in their deflected condition in Figures 4.10 and 4.11, for the straight and tapered flexures, respectively. This configuration represents the most straightforward and rigid form of an APLM with the concept being that motion from one mass will necessarily cause the other mass to move in the opposing direction through the stiff lever arm.

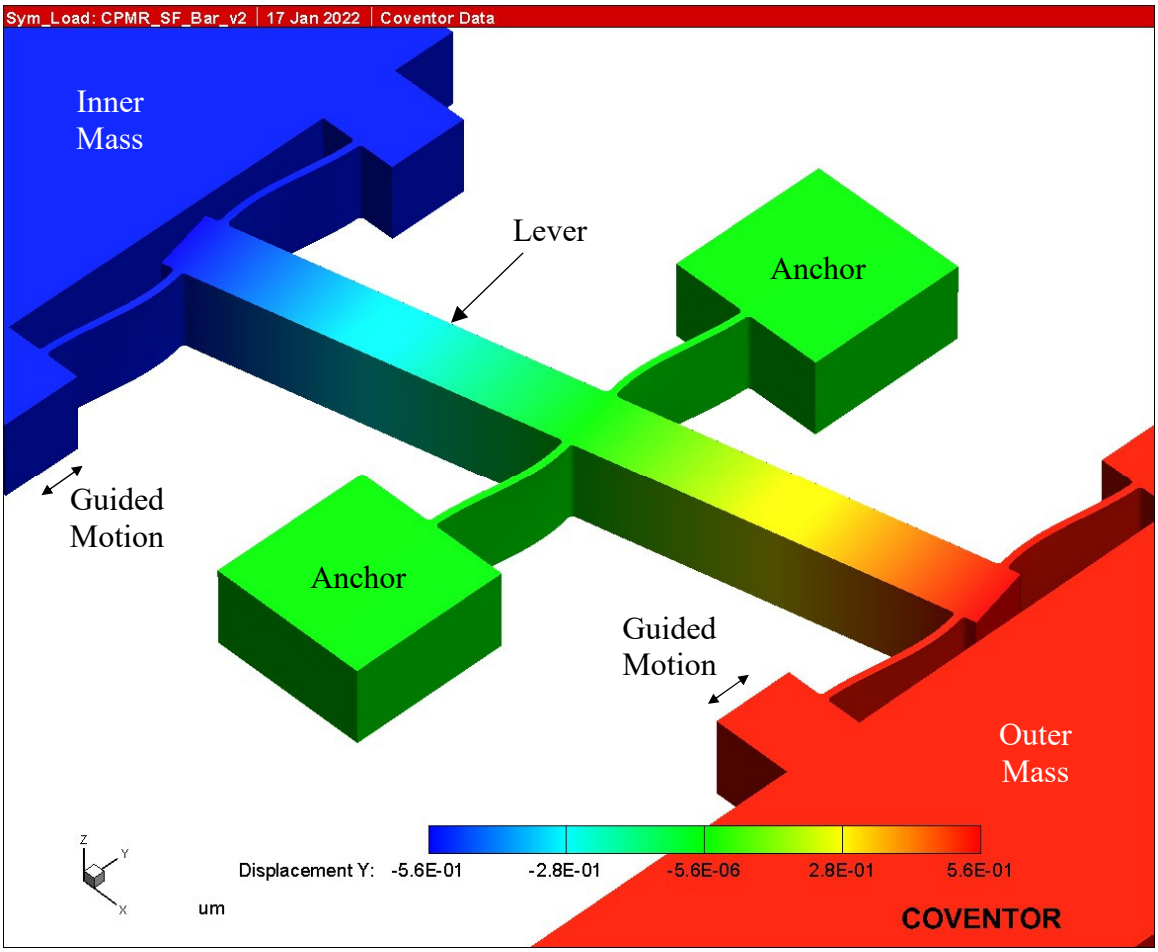

Figure 4.10 Deflected Straight Flexure Lever APLM.

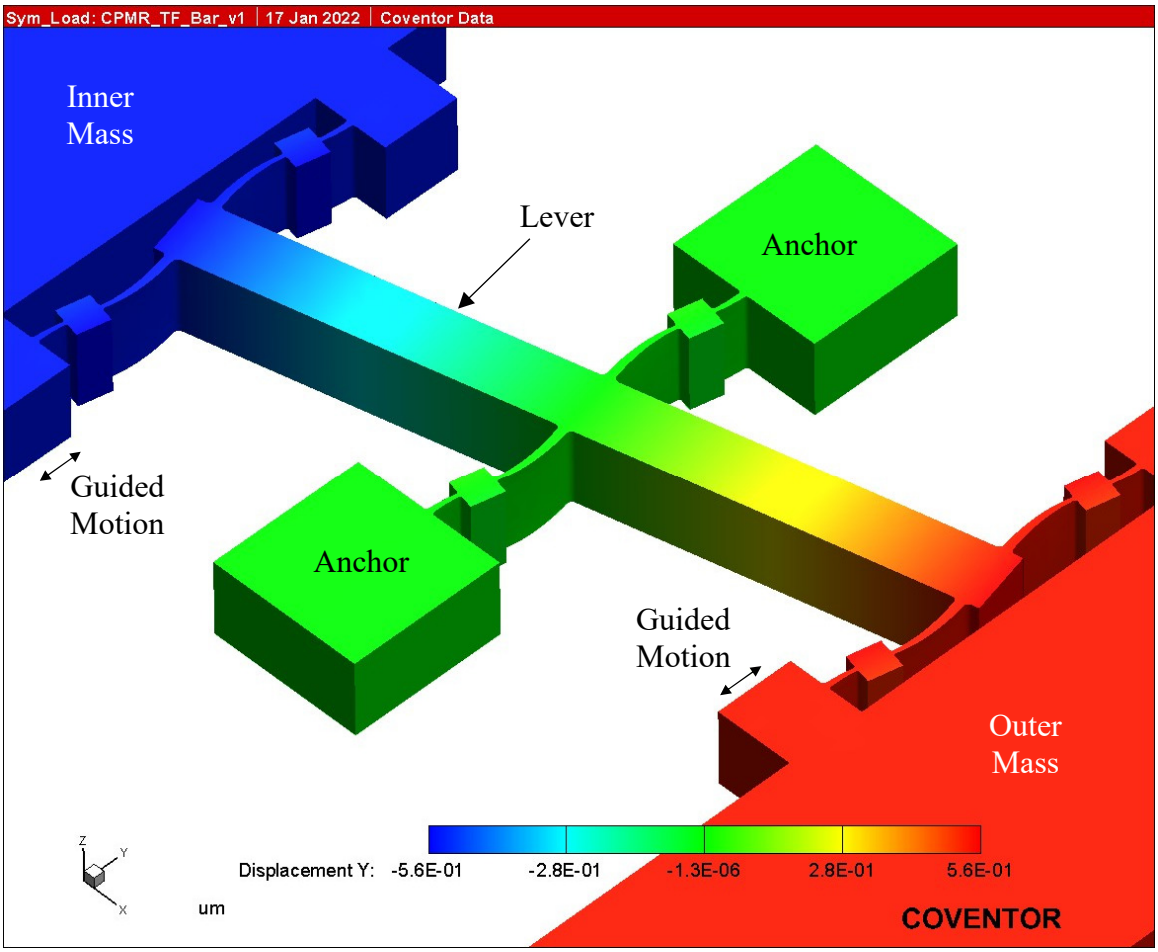

Figure 4.11 Deflected Tapered Flexure Lever APLM.

The final configuration, pictured in Figures 4.6 and 4.7, is a derivative of the inner lever coupling APLM originally developed by researchers at the University of California at Irvine (UCI) [28, 90], which is pictured in Figure 4.5. The UCI inner lever coupling APLM is an extremely innovative and effective APLM geometry in a compact space [28]. It is shown in a deflected condition in Figure 4.12. The UCI inner lever coupling APLM works by coupling the anti-phase motion of the two proof masses into the first bending mode of the clamped-clamped beam while coupling the in-phase mode of the two proof masses into the second bending mode of the clamped-clamped beam. This coupling is accomplished through the two long, stiff levers that are connected to the proof

masses on one corner and the clamped-clamped beam on the opposite corner through short, thin tethers. As pictured in Figure 4.12, the anti-phase separation of the proof masses creates a pull on the center of the clamped-clamped beam from both tethers in the same direction. This couples the anti-phase mode into the first bending mode of the clamped-clamped beam. If the proof masses attempt to deflect in the in-phase mode, one of the tethers will be pulling on the clamped-clamped beam and the other will be pushing on the clamped-clamped beam. This set of push-pull forces, coupled with the small separation of the tether attachment points, creates a moment in the center of the clamped-clamped beam, which effectively couples the in-phase mode of the proof masses into the second bending mode of the clamped-clamped beam. This forces the in-phase mode of the proof masses to be at a higher frequency than the anti-phase mode.

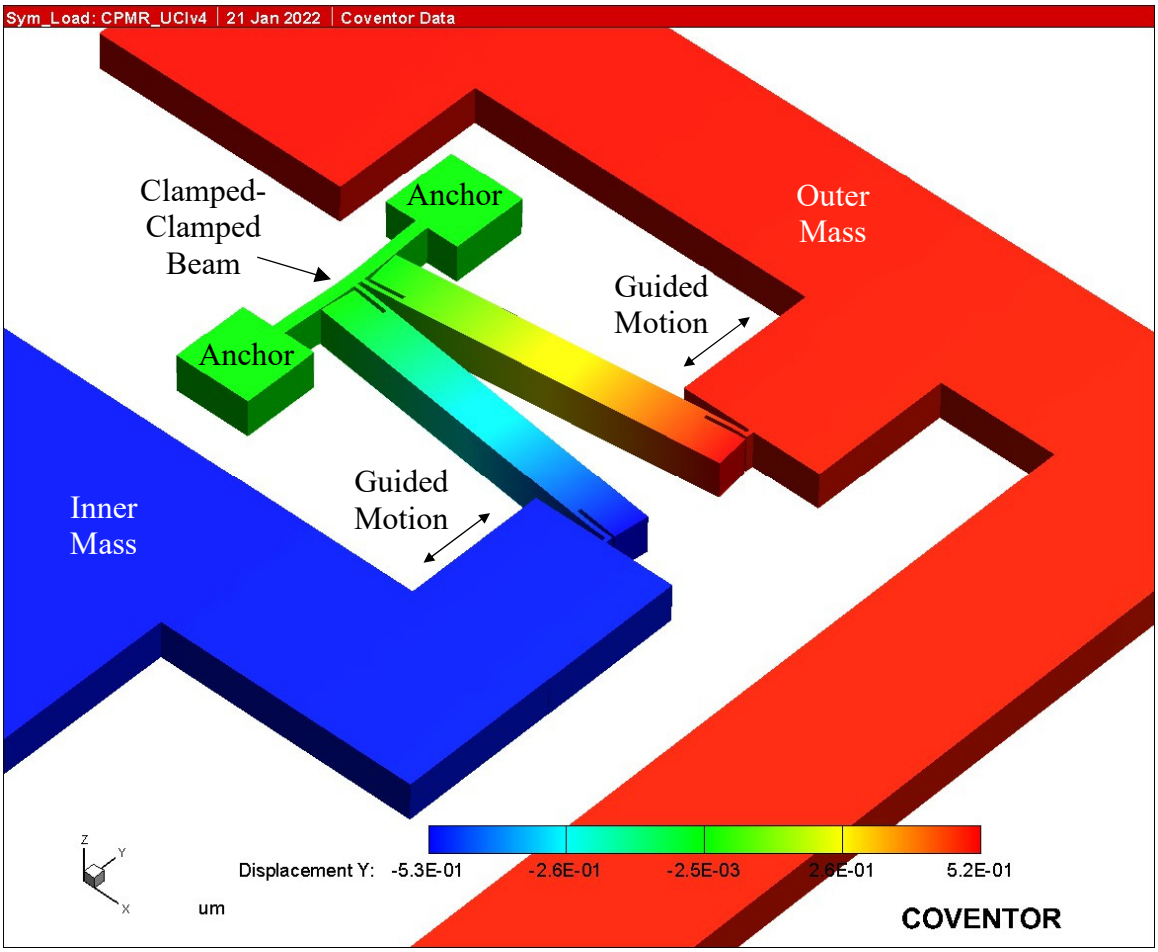

Figure 4.12 Deflected UCI Inner Lever Coupling APLM in Anti-Phase Mode.

Similar to the original UCI inner lever coupling APLM design, the operation of the revised UCI APLM design is based on coupling the guided motion of each mass to each other through a secondary resonator that has more compliance for the anti-phase mode than for the in-phase mode thereby forcing the in-phase mode frequency to be higher than that of the anti-phase mode. The revised UCI APLM designs are shown in their deflected conditions in Figure 4.13 and Figure 4.14 for the straight and tapered flexures, respectively. While the revised UCI APLM design operates in a manner very similar to that described for the original UCI inner lever coupling APLM design, it introduces three modifications which improve some performance characteristics.

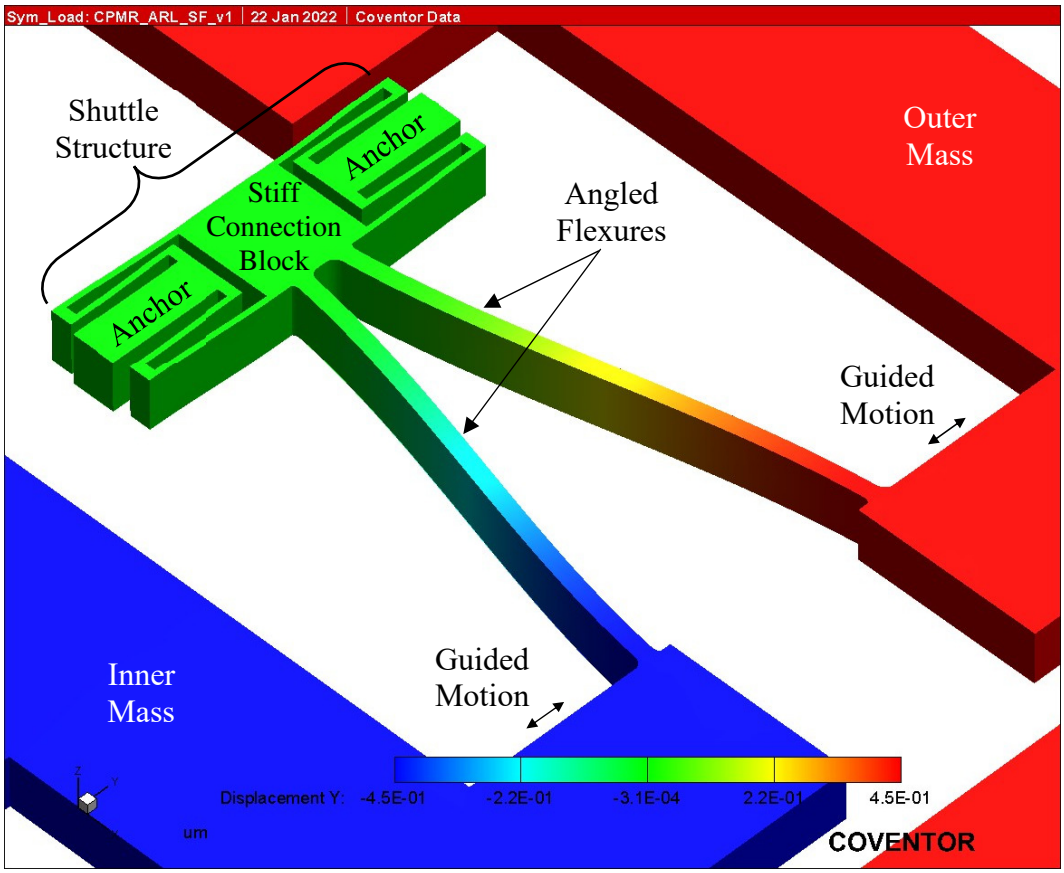

Figure 4.13 Deflected Straight Flexure Revised UCI APLM.

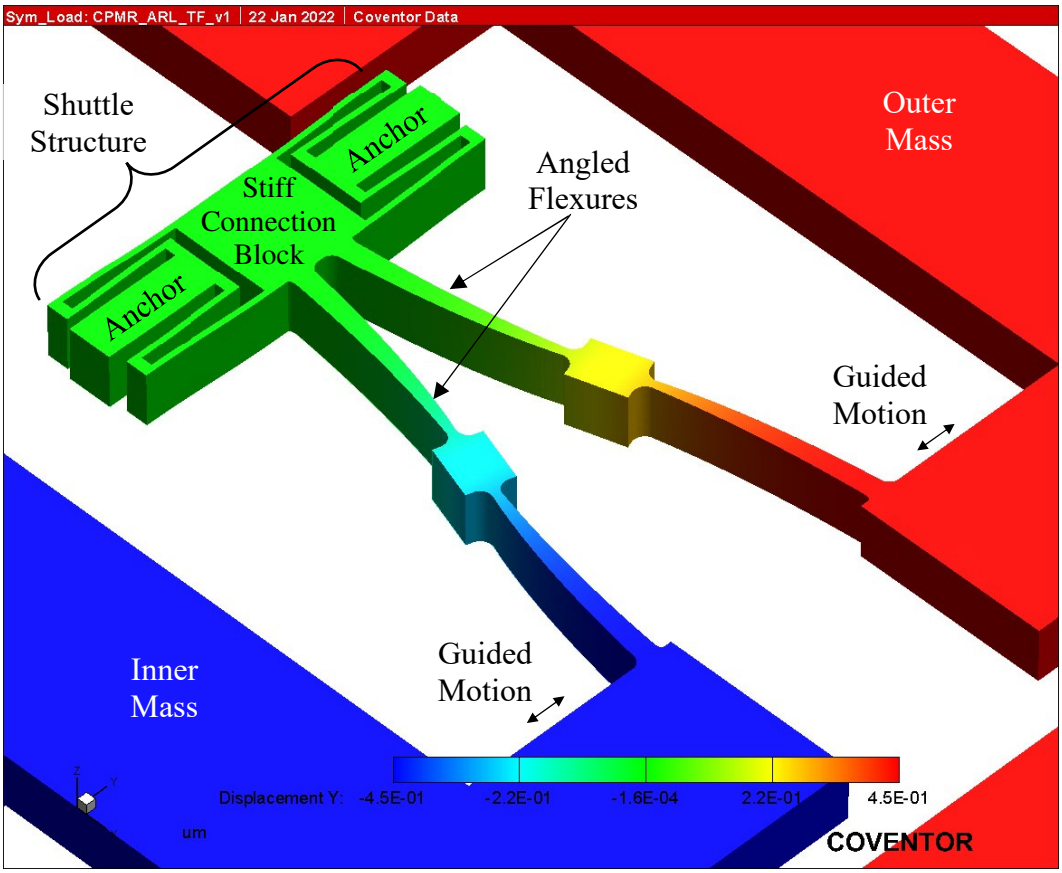

Figure 4.14 Deflected Tapered Flexure Revised UCI APLM.

The first modification is that the long stiff levers with small, thin tethers on opposing corners have been replaced with angled, moderately compliant flexures that go directly between the opposing corner locations. The compliance of these flexures creates a fundamentally different mechanism for the primary spring force than the original UCI inner lever coupling APLM design. That is, the spring constant of the original design was strongly dependent on the dimensions of the clamped-clamped beam whereas the spring constant of this revised design is dominated by the dimensions of these angled flexures.

The second modification is that the angled flexures connect to a stiff, but movable block whereas the original UCI design had the stiff levers connect near the center of the

clamped-clamped beam. This has an effect similar to allowing the gap between the attachment points, $2g$, in the original UCI design go to zero. The potential implications of letting the gap between the attachment points go to zero were discussed in reference [28]. Specifically, Dr. Simon stated, "*While it is possible to merge the connection points, this results in the motion of the proof masses not necessarily being required to transmit through the clamped-clamped beam, resulting in a break down of the analytical expressions and assumptions, deteriorating the frequency separation potential. Maximizing* $\frac{L}{g}$ *has an additional consequence of creating a stress concentration, which can both increase the chance of device fracture and greatly increase thermoelastic damping.*" These concerns are mitigated by the final modification to the structure discussed in the next paragraph.

The final modification to the original UCI design is that the clamped-clamped beam has been replaced by a relatively compliant shuttle consisting of a solid block, supported and guided by four folded flexures. This is also a major departure from the original design in that the shuttle configuration does not necessarily have a second bending mode similar to that of the clamped-clamped beam into which the in-phase mode of the proof masses can couple. Instead, the shuttle structure has more of a rotational mode into which the in-phase proof mass motion couples. This accomplishes the same goal of coupling the in-phase proof mass mode into a higher order mode, although not necessarily the second mode, of the secondary resonator which should mitigate one of the concerns identified by Dr. Simon of maintaining modal frequency separation.

The other two concerns identified by Dr. Simon are mitigated in the revised design as well. First, maintaining some separation of the connection points where they

attach to the stiff block should mitigate the concern of creating a high stress concentration and increased likelihood of fracture. Finally, the combination of introducing the compliant shuttle and the angled flexures, shifts the primary thermoelastic damping loss away from the clamped-clamped beam and into the angled flexures. This should mitigate the final concern of increased thermoelastic damping loss raised by Dr. Simon due to merging the connection points, but care must be taken in the design to ensure that the width of these flexures is sufficiently thin to mitigate thermoelastic damping loss.

The governing equations and design procedures for each APLM configuration are covered in the following subsections.

4.1.1 Straight Flexure Pivot Design

For the design of the straight flexure pivot APLM, the designer must decide how much of the total deflection of the proof mass, c, should be associated with the rotation of the pivot point,

$$a = \theta_{Tot} \cdot L_G, \tag{4.1}$$

where θ_{Tot} is the angular rotation of the pivot point and L_G is the length of the guided flexure, and how much should be associated with the deflection of the guided flexures, b. Figure 4.15 defines these quantities graphically.

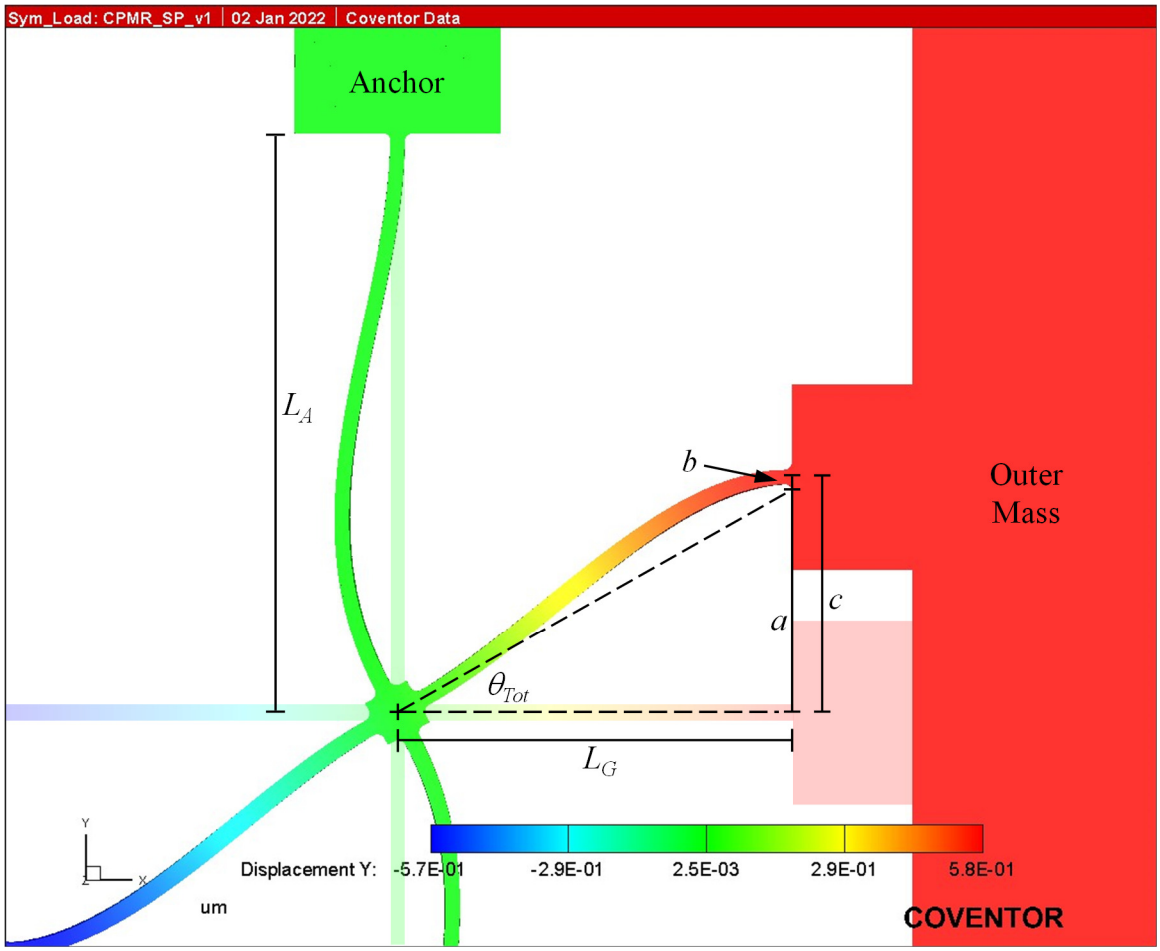

Figure 4.15 Deflections of the Straight Flexure Pivot APLM.
The solid-colored region represents the APLM in the deflected state and the shaded region represents the APLM in the undeflected state. L_A and L_G are the lengths of the anchor and guided flexures, respectively. θ_{Tot} is the angular rotation of the pivot point. The total displacement of the outer mass, c, is comprised of the displacement due to the projection of the rotation of the pivot point, $a = \theta_{Tot} \cdot L_G$, and the displacement due to the deflection, b, of the guided flexure.

Here we define the proportionality constant, P, between the deflection due to the rotation of the pivot point and the total deflection:

$$P = \frac{a}{c} = \frac{L_G \cdot \theta_{Tot}}{c} \quad , \tag{4.2}$$

where θ_{Tot} is the angular rotation of the pivot point. L_G is the length of the guided flexure and a is the displacement of the mass due to the projection of the rotation of the pivot point, *i.e.*, $a = \theta_{Tot} \cdot L_G$.

Due to the natural relationship between the linear and angular deflection spring constants of a cantilevered beam, the value of P is limited between 0 (zero) when the anchor flexures are infinitely stiff, and 1.5 when the anchor flexures have infinite compliance. The derivation of these limits is provided in Section A.5 of Appendix A. Lower values of P reduce the inter-mass coupling across the APLM that occurs through the rotation of the pivot point. Higher values of P increase the inter-mass coupling but can also result in long thin anchor flexures that may be difficult to fabricate in practice.

It is important to note here that both the anchor flexures and the guided flexures are under both a force load and a moment load applied at the center of the pivot point. When the proof masses are deflected as shown in Figure 4.15, the anchor flexure has a net rotation but does not have a net deflection. The guided flexure, however, has both a net rotation and a net deflection. The derivation of the linear spring constant of the APLM acting on the proof mass is fairly complex and requires simultaneous solution of the angular rotations and linear deflections of both the anchor and guided flexures under both force and moment loads to meet these constraints. Due to the complexity of this derivation, it is omitted here but is provided in Section A.5 of Appendix A.

The design of the straight flexure pivot APLM proceeds as follows.

1. The desired spring constant for one mass of the individual APLM, k_{v_Tot}, and the thickness of the device, t, are either given or chosen by the designer. If the designer is provided with a target resonant frequency, ω_n,

then the designer uses the mass of one proof mass, M_{PM}, and the number of APLMs in the design, Num_{APLM}, to arrive at the desired spring constant, k_{v_Tot}, using the following relation [30]:

$$k_{v\_Tot} = \frac{M_{PM} \cdot \omega_n^2}{Num_{APLM}} \ . \tag{4.3}$$

2. Choose a value for the ratio of displacements, P, between 0 (zero) and 1.5. A value around unity (1.0) is recommended to balance between inter-mass coupling and the length of the anchor flexure.
3. Choose a reasonable value for the length of the guided flexure, L_G. This value can vary widely based on the desired resonant frequency and overall dimensions of the design, but it is generally recommended that the length of the guided flexure be at least 3 times the thickness of the device, t, to ensure that the stresses along the length of the flexure are the dominant stresses.
4. Calculate the width of the guided flexure, w_G, using the following equation, which is derived in Section A.5 of Appendix A:

$$w_G = L_G \left[\frac{2 \cdot k_{v\_Tot}}{(2-P)Et}\right]^{\frac{1}{3}} \ , \tag{4.4}$$

where E is the Young's Modulus of the flexure material.

5. If w_G is not acceptable, note that L_G and w_G are linearly proportional in Equation 4.4 and scale L_G as needed to obtain an acceptable value of w_G.

If an acceptable combination cannot be obtained, then a new value for P must be selected, but note that P appears under the cubed-root in Equation 4.4. So, adjustments to P will have diminished impact on the values of L_G and w_G.

6. To maintain the same stress in the guided and anchor flexures at the pivot point, set the width of the anchor flexure, w_A, equal to the width of the guided flexure:

$$w_A = w_G. \tag{4.5}$$

7. Calculate the length of the anchor flexure, L_A, using the following equation, which is derived in Section A.5 of Appendix A:

$$L_A = L_G \frac{2P}{3 - 2P} \quad . \tag{4.6}$$

One final note is that the straight flexure pivot APLM pictured in Figure 4.15 has a small square block at the center of the pivot point which was neglected in the derivation of the design equations. There are three factors that enable this to be neglected. The first is that the moment in this region due to the force applied at the pivot point should be small due to the close proximity (short lever arm) resulting in negligible additional bending of the flexure. The second is that the moment applied from the anchor flexure is expected to be small to allow for strong coupling between the two masses, again resulting in negligible additional bending of the flexure. Finally, the size of the block is small compared to the overall lengths of the guided and anchor flexures, resulting in negligible additional deflection.

4.1.2 Tapered Flexure Pivot Design

For the tapered flexure pivot APLM design, we are also able to define a proportionality constant, *P*, similar to that of the straight flexure pivot design that describes the proportion of the total deflection that corresponds to the rotation of the pivot point, *a*, compared with the total deflection, *c*. These dimensions are shown graphically in Figure 4.16 and the expression for *P* is given by:

$$P = \frac{a}{c} = \frac{(N_{1G} + N_{2G}) \cdot \theta_{Tot}}{c} \quad , \tag{4.7}$$

where θ_{Tot} is the angular rotation of the pivot point. N_{1G} and N_{2G} are the lengths of the two elements of the guided flexure and a is the displacement of the mass due to the projection of the rotation of the pivot point, *i.e.*, $a = \theta_{Tot} \cdot (N_{1G} + N_{2G})$.

Since the tapered flexure has more rotational compliance than that of the straight flexure, the proportionality constant has a different range of possible values from 0 (zero), when the anchor flexures are infinitely stiff, to 3 when the anchor flexures have infinite compliance. The derivations of these limits are provided in Section A.6 of Appendix A. Also, since both the anchor and the guided flexures bend into an S-shape, we note that there a zero-stress point somewhere along the length of each flexure resulting in the need to place a block at the proper position along its length, but not necessarily in the center. This results in both the anchor and the guided flexures consisting of two tapered flexures, each of different lengths, and different widths. This makes the design of the tapered flexure pivot APLM more complicated than that of the

straight flexure pivot APLM. The full derivation of the design equations is provided in Section A.6 of Appendix A for reference, and only the design procedure is captured here.

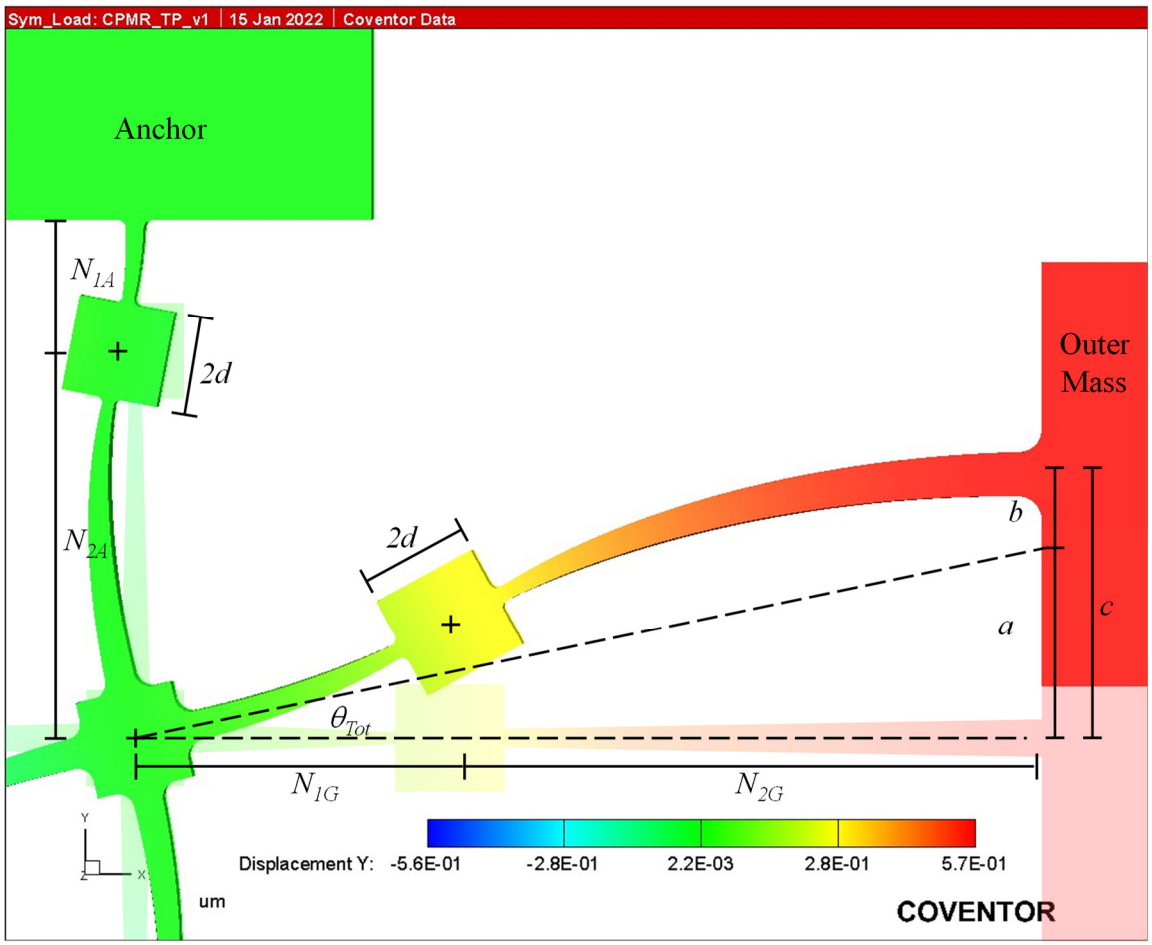

Figure 4.16 Deflections of the Tapered Flexure Pivot APLM.
The solid-colored region represents the APLM in the deflected state and the shaded region represents the APLM in the undeflected state. N_{1A} and N_{2A} are the lengths of the two elements of the anchor flexure, and N_{1G} and N_{2G} are the lengths of the two elements of the guided flexure. θ_{Tot} is the angular rotation of the pivot point. The total displacement of the outer mass, c, is comprised of the displacement due to the projection of the rotation of the pivot point, $a = \theta_{Tot} \cdot (N_{1G} + N_{2G})$, and the displacement due to the deflection, b, of the guided flexure. The size of the square blocks in the anchor and guided flexures is $2d$.

The design of the tapered flexure pivot APLM proceeds as follows:

1. The desired spring constant for one mass, k_{v_Tot}, the size of the hammerhead features, $2d$, and the thickness of the device, t, are either

given or chosen by the designer. If the designer is provided with a target resonant frequency, ω_n, then the designer uses the mass of one proof mass, M_{PM}, and the number of APLMs in that axis of the design, Num_{APLM}, to arrive at the desired spring constant, k_{v_Tot}, using the following relation [30]:

$$k_{v\_Tot} = \frac{M_{PM} \cdot \omega^2}{Num_{APLM}} . \tag{4.8}$$

2. Choose a value for the ratio of displacements, *P*, between 0 (zero) and 3. A value around unity (1.0) is recommended to balance inter-mass coupling and the length of the anchor flexure.
3. Choose a reasonable value for the length of the second element of the guided flexure, N_{2G}. This value can vary widely based on the desired resonant frequency and overall dimensions of the design, but it is generally recommended that the length of the flexure be at least 3 times the thickness of the device, t, to ensure that the stresses along the length of the flexure are the dominant stresses.
4. Calculate the length of the first element of the guided flexure, N_{1G}, by taking an initial guess ($0.355N_{2G}$ is recommended) and iterating through the following equations until the solution converges. The derivation of this is given in Section A.6 of Appendix A:

$$f(N_{1G}) = (2P-3)N_{1G}^{\frac{3}{2}} + (3-3P)N_{1G}N_{2G}^{\frac{1}{2}} - 3N_{1G}^{\frac{1}{2}}N_{2G} + (3-P)N_{2G}^{\frac{3}{2}} + 2Pd^{\frac{3}{2}} \tag{4.9}$$

$$f'(N_{1G}) = \frac{3(2P-3)}{2}N_{1G}^{\frac{1}{2}} + (3-3P)N_{2G}^{\frac{1}{2}} - \frac{3}{2}N_{1G}^{-\frac{1}{2}}N_{2G} \tag{4.10}$$

$$N_{1G_{New}} = N_{1G_{Old}} - \frac{f(N_{1G_{Old}})}{f'(N_{1G_{Old}})}\,. \tag{4.11}$$

5. Calculate the base width of the first element of the guided flexure, w_{b1G}, using the following equation, which is derived in Section A.6 of Appendix A:

$$w_{b1G} = \left\{ \frac{k_{v\_Tot} \cdot 8 \cdot N_{1G}^{\frac{3}{2}} \left[N_{2G}^{\frac{3}{2}} - 2d^{\frac{3}{2}} - 2N_{1G}^{\frac{3}{2}} + 3N_{1G}N_{2G}^{\frac{1}{2}} \right]}{E \cdot t} \right\}^{\frac{1}{3}}, \tag{4.12}$$

where E is the Young's Modulus of the flexure material.

6. Calculate the base width of the second element of the guided flexure, w_{b2G}, using the following equation, from Section A.6 of Appendix A:

$$w_{b2G} = w_{b1G}\sqrt{\frac{N_{2G}}{N_{1G}}}\,. \tag{4.13}$$

7. If any of the values for N_{1G}, N_{2G}, w_{b1G}, and w_{b2G} are not acceptable, then scale N_{2G} and repeat steps 4, 5, and 6 until all values are acceptable. While the governing equations are inherently non-linear, all widths and lengths will scale roughly in linear proportion to N_{2G} for values of P around unity. If an acceptable combination cannot be obtained, then a new value for P must be selected and the process must begin again at step 2, but note that due to the non-linear nature of the governing equations, adjustments to P will have diminished impact on the values of the lengths and widths of the flexures until P approaches the limits of its range.
8. Having fully designed the guided flexure, we now calculate the spring constant of the pivot point, $k_{M\theta_{Tot}}$, that relates the moment applied by the guided and anchor flexures, M, and the total rotation at the pivot point, θ_{Tot}, using the following equations that were derived in Section A.6 of Appendix A:

$$k_{M\theta_{Tot}} = \frac{E \cdot t \cdot w_{b1G}^3}{24 N_{1G}^{\frac{1}{2}} \left[N_{2G}^{\frac{1}{2}} - N_{1G}^{\frac{1}{2}} \right]} \quad . \tag{4.14}$$

9. To maintain the same stress in the guided and anchor flexures at the pivot point, set the base width of the second element of the anchor flexure equal to the base width of the first element of the guided flexure:

$$w_{b2A} = w_{b1G}. \tag{4.15}$$

10. Here we must employ the Multivariate Newton's Method for simultaneously solving multiple nonlinear equations for the anchor flexure lengths, which follows the general form [95]:

$$\boldsymbol{x_{n+1}} = \boldsymbol{x_n} - [\boldsymbol{DF}(\boldsymbol{x_n})]^{-1}\boldsymbol{F}(\boldsymbol{x_n}), \tag{4.16}$$

where $\boldsymbol{x_n}$ is the vector of desired variables given by:

$$\boldsymbol{x_n} = \begin{bmatrix} N_{1A_n} \\ N_{2A_n} \end{bmatrix}. \tag{4.17}$$

$\boldsymbol{F}(\boldsymbol{x_n})$ is the vector of nonlinear functions given by:

$$\boldsymbol{F}(\boldsymbol{x_n}) = \begin{bmatrix} f_A\left(N_{1A_n}, N_{2A_n}\right) \\ g_A\left(N_{1A_n}, N_{2A_n}\right) \end{bmatrix}. \tag{4.18}$$

The functions $f_A(N_{1A}, N_{2A})$ and $g_A(N_{1A}, N_{2A})$ are defined below from Section A.6 of Appendix A. $\boldsymbol{DF}(\boldsymbol{x_n})$ is the Jacobian of $\boldsymbol{F}(\boldsymbol{x_n})$ given by:

$$\boldsymbol{DF}(\boldsymbol{x_n}) = \begin{bmatrix} \dfrac{\partial f}{\partial N_{1A}} & \dfrac{\partial f}{\partial N_{2A}} \\ \dfrac{\partial g}{\partial N_{1A}} & \dfrac{\partial g}{\partial N_{2A}} \end{bmatrix} = \begin{bmatrix} a_{DF} & b_{DF} \\ c_{DF} & d_{DF} \end{bmatrix}. \tag{4.19}$$

The designer must take an initial guess for N_{1A}, and N_{2A}. Initial guesses of $N_{1A} = N_{1G}$ and $N_{2A} = N_{2G}$ are recommended. The designer must then iterate through the following equations, derived in Section A.6 of Appendix A, until the solution converges:

$$f_A(N_{1A}, N_{2A}) = \left[N_{1A}^{\frac{3}{2}} + 3N_{1A}^{\frac{1}{2}} N_{2A} - 2N_{2A}^{\frac{3}{2}} - 2d^{\frac{3}{2}} \right] \tag{4.20}$$

$$g_A(N_{1A}, N_{2A}) = k_{M\theta_{Tot}} - \frac{E \cdot t \cdot w_{b2A}^3}{24 \cdot \left\{ N_{2A} - N_{1A}^{\frac{1}{2}} \cdot N_{2A}^{\frac{1}{2}} \right\}} \tag{4.21}$$

$$a_{DF} = \frac{\partial f}{\partial N_{1A}} = \left[\frac{3}{2} N_{1A}^{\frac{1}{2}} + \frac{3}{2} N_{1A}^{-\frac{1}{2}} N_{2A} \right] \tag{4.22}$$

$$b_{DF} = \frac{\partial f}{\partial N_{2A}} = \left[3N_{1A}^{\frac{1}{2}} - 3N_{2A}^{\frac{1}{2}} \right] \tag{4.23}$$

$$c_{DF} = \frac{\partial g}{\partial N_{1A}} = -\frac{E \cdot t \cdot w_{b2A}^3}{48} \frac{N_{1A}^{-\frac{1}{2}} \cdot N_{2A}^{\frac{1}{2}}}{\left(N_{2A} - N_{1A}^{\frac{1}{2}} \cdot N_{2A}^{\frac{1}{2}} \right)^2} \tag{4.24}$$

$$d_{DF} = \frac{\partial g}{\partial N_{2A}} = \frac{E \cdot t \cdot w_{b2A}^3}{24} \frac{\left(1 - \frac{1}{2} \cdot N_{1A}^{\frac{1}{2}} \cdot N_{2A}^{-\frac{1}{2}} \right)}{\left(N_{2A} - N_{1A}^{\frac{1}{2}} \cdot N_{2A}^{\frac{1}{2}} \right)^2} \tag{4.25}$$

$$|\boldsymbol{DF}| = a_{DF} d_{DF} - b_{DF} c_{DF} \tag{4.26}$$

$$N_{1A_{n+1}} = N_{1A_n} - \frac{d_{DF} \cdot f\left(N_{1A_n}, N_{2A_n}\right) - b_{DF} \cdot g\left(N_{1A_n}, N_{2A_n}\right)}{\left|\boldsymbol{DF}\left(N_{1A_n}, N_{2A_n}\right)\right|} \tag{4.27}$$

and

$$N_{2A_{n+1}} = N_{2A_n} - \frac{c_{DF} \cdot f\left(N_{1A_n}, N_{2A_n}\right) - a_{DF} \cdot g\left(N_{1A_n}, N_{2A_n}\right)}{\left|\boldsymbol{DF}\left(N_{1A_n}, N_{2A_n}\right)\right|} \tag{4.28}$$

.

11. Calculate the base width of the first element of the anchor flexure, w_{b1A}, using the following equation from Section A.6 of Appendix A:

$$w_{b1A} = w_{b2A}\sqrt{\frac{N_{1A}}{N_{2A}}} \quad . \tag{4.29}$$

It is again important to note that the pivot APLMs pictured in Figure 4.8 and Figure 4.16 have a small square block at the center of the pivot point which was neglected in the derivation of the design equations. The assumption to neglect this block for the tapered flexure pivot APLM should be valid for the same reasons provided in the previous discussion for the straight flexure pivot APLM design. It is highlighted here that this design procedure results in the same stress (both compressive and tensile) along the entire length of every tapered flexure element of the design as shown graphically in Figure 4.17.

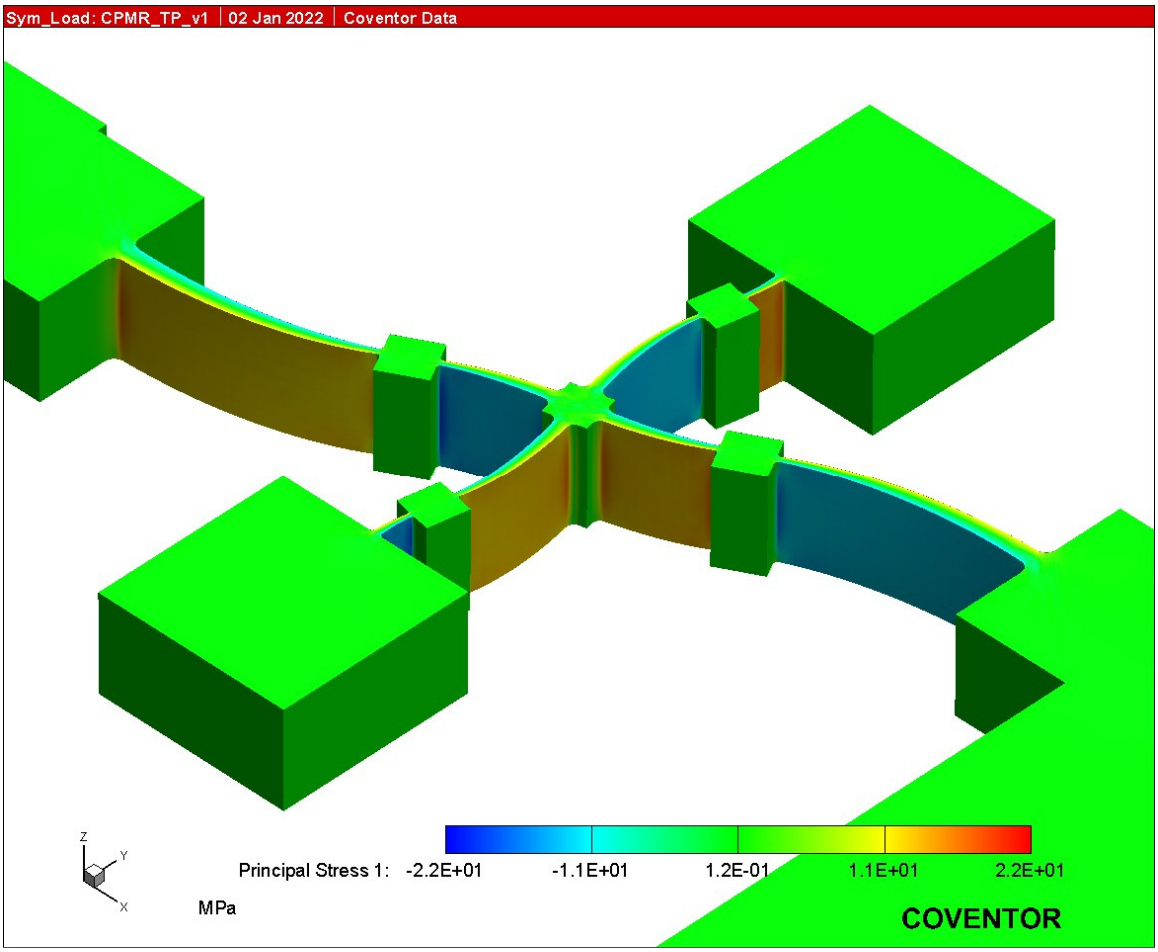

Figure 4.17 Equivalent Principle Stress in the Tapered Flexure Pivot APLM.

4.1.3 Straight Flexure Lever Design

The design and operation of the straight flexure lever APLM is relatively straightforward. It consists of two proof masses, one lever arm, and six identical flexures. Therefore, each proof mass has an effective total of three of the flexures (per APLM) acting on it. Each flexure is applying a moment to the lever which is converted to a linear force on the proof mass at the center of the location where the flexures attach to the proof mass. Figure 4.18 defines the relevant quantities graphically.

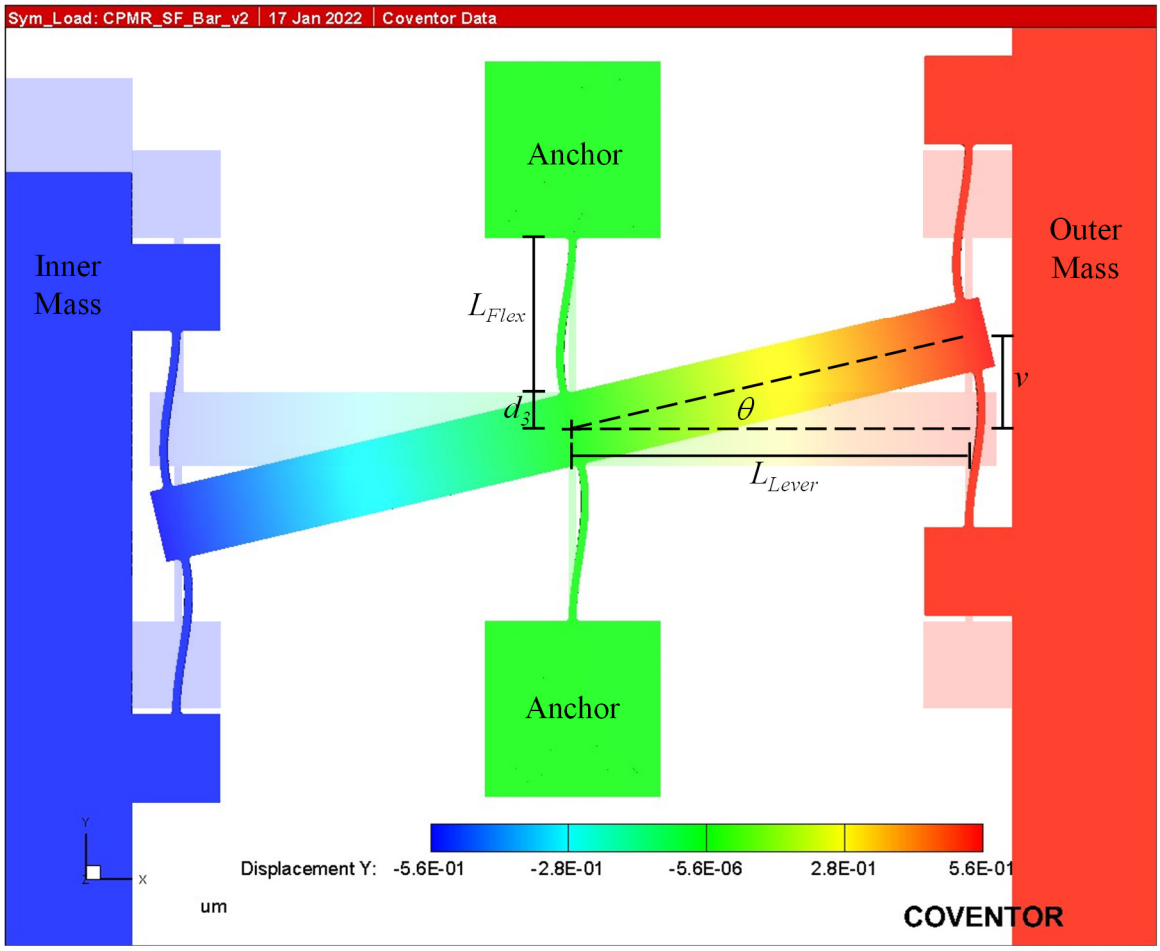

Figure 4.18 Deflections of the Straight Flexure Lever APLM.
The solid-colored region represents the APLM in the deflected state and the shaded region represents the APLM in the undeflected state. L_{Flex} and L_{Lever} are the lengths of the flexure and lever, respectively. θ is the angular rotation of the lever. The total displacement of the outer mass, v, is the product of the rotation and length of the lever, $v = \theta \cdot L_{Lever}$. The half width of the lever is d_3.

The lever is applying both a force load and a moment load to the flexures at the center of the lever which is beyond the end of the flexure. Also, while the center point of the lever is allowed to have a net rotation, it is not allowed to have a net deflection in the x-axis. The end of the flexure where it connects to the lever, however, has both a net rotation and a small net deflection. This complicates the derivation of the design equations. Therefore, the derivation of the design equations is provided in section A.7 of Appendix A and only the design procedure is captured here.

The design of the straight flexure lever APLM proceeds as follows.

1. The desired spring constant for one mass of the individual APLM, k_{v_Tot}, and the thickness of the device, *t*, are either given or chosen by the designer. If the designer is provided with a target resonant frequency, ω_n, then the designer uses the mass of one proof mass, M_{PM}, and the number of APLMs in the design, Num_{APLM}, to arrive at the desired spring constant, k_{v_Tot}, using the following relation [30]:

$$k_{v\_Tot} = \frac{M_{PM} \cdot \omega^2}{Num_{APLM}} \ . \tag{4.30}$$

2. The length of the lever arm, L_{Lever}, and the length of the flexure, L_{Flex}, are either given or can be chosen using engineering judgment. It is generally recommended that the length of the flexure, L_{Flex}, be at least 3 times the thickness of the device, t, to ensure that the stresses along the length of the flexure are the dominant stresses. It is also recommended that the length of the lever be on the order of 100 greater than the expected maximum displacement of the proof masses to keep the rotation angle of the lever to a reasonable value.
3. Choose a value for the constant, R, which relates the stiffness of the lever to the stiffness of the system. That is

$$k_{Lever} = R \cdot k_{v\_Tot}. \tag{4.31}$$

This constant relates how much displacement will occur due to the bending of lever as compared with that of the rotation of the lever. This

constant also sets the rigidity of the coupling from one mass to the other in anti-phase mode and aids in pushing the common-mode resonant to a frequency higher than that of the anti-phase mode. It is recommended that this constant be chosen between 10 and 100, with a typical value of around 50.

4. Calculate the minimum value of w_{Lever} using the equation below and select a value that is greater than or equal to that value, from Section A.7 of Appendix A:

$$w_{Lever} \geq L_{Lever}\left(\frac{4 \cdot R \cdot k_{v\_Tot}}{E \cdot t}\right)^{\frac{1}{3}}, \tag{4.32}$$

where E is the Young's Modulus of the material.

5. Since the constant d_3 was defined as the half-width of the lever, set d_3 equal to half of the desired value of w_{Lever}, from Section A.7 of Appendix A:

$$d_3 = \frac{w_{Lever}}{2} \geq \frac{L_{Lever}}{2}\left(\frac{4 \cdot R \cdot k_{v\_Tot}}{E \cdot t}\right)^{\frac{1}{3}}. \tag{4.33}$$

6. Calculate the value of the spring constant that relates the angular rotation of the lever to the total applied moment, $k_{M\theta Tot}$, from Section A.7 of Appendix A:

$$k_{M\theta Tot} = k_{v\_Tot} \cdot L_{Lever}^2. \tag{4.34}$$

7. Calculate the value of the spring constant that relates the angular rotation of the lever to the applied moment of a single flexure, $k_{M\theta Flex}$, from Section A.7 of Appendix A:

$$k_{M\theta Flex} = \frac{k_{M\theta Tot}}{3} = \frac{k_{v\_Tot} \cdot L_{Lever}^2}{3} \quad . \tag{4.35}$$

8. Calculate the width of the guided flexure, w_{Flex}, using the following equation from Section A.7 of Appendix A:

$$w_{Flex} = \left\{ k_{M\theta Flex} \frac{12 \cdot L_{Flex}}{E \cdot t} \left[1 - \frac{3}{2} \frac{(N + d_3)^2}{(2L_{Flex}^2 + 6d_3 N)} \right] \right\}^{\frac{1}{3}} , \tag{4.36}$$

where $N = (L_{Flex} + d_3)$.

9. If w_{Flex} is not acceptable, then scale L_{Flex} and/or L_{Lever} accordingly and repeat the above calculations until an acceptable value is obtained. w_{Flex} will generally scale with the cubic root of L_{Flex} and with L_{Lever} to the two-thirds power.

4.1.4 Tapered Flexure Lever Design

The tapered flexure lever APLM operates in a similar manner to that of the straight flexure lever APLM and the design is relatively straightforward. There are two proof masses, one lever arm, and six flexures. Therefore, each proof mass has an effective total of three of the flexures (per APLM) acting on it. Each flexure is applying a moment to the lever which is converted to a linear force on the proof mass at the center

of the location where the flexures attach to it. Figure 4.19 defines the relevant quantities graphically.

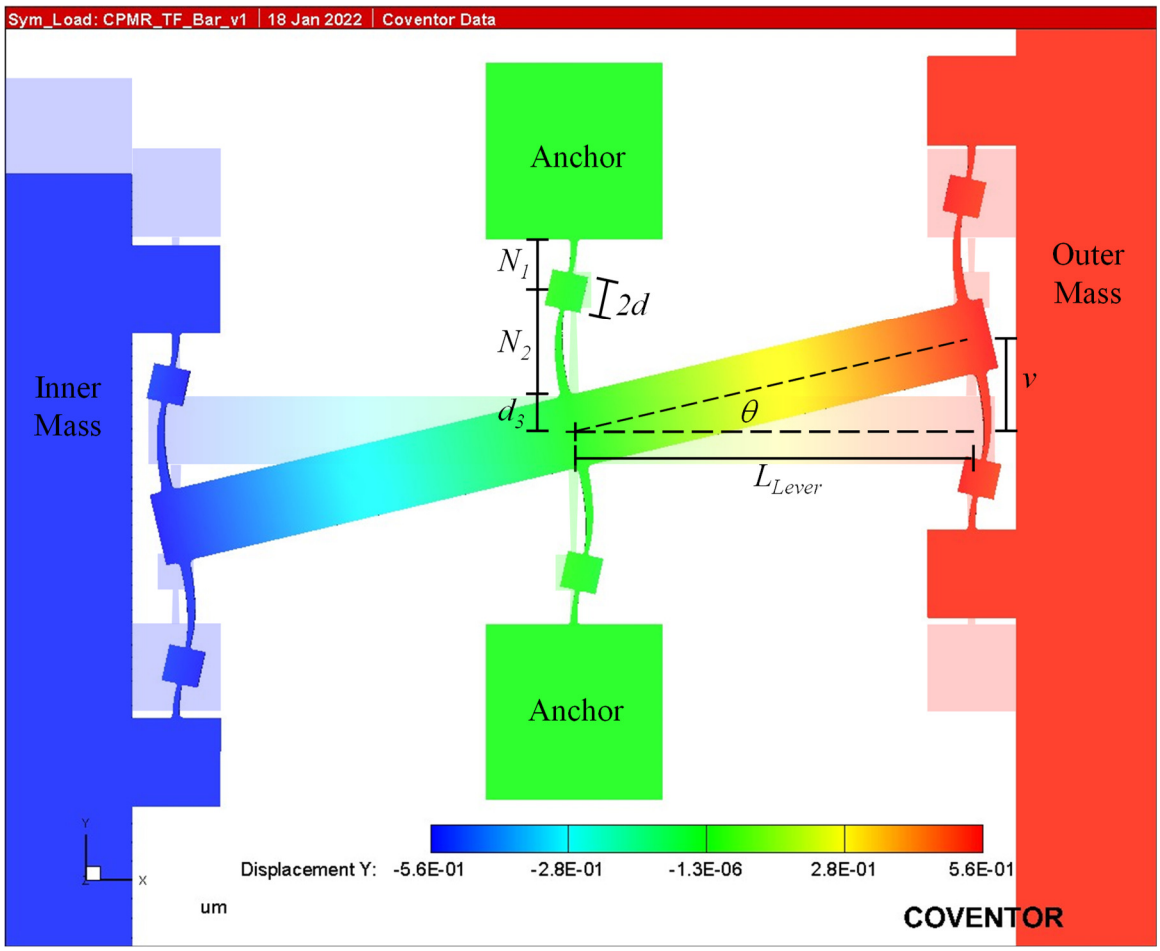

Figure 4.19 Deflections of the Tapered Flexure Lever APLM.
The solid-colored region represents the APLM in the deflected state and the shaded region represents the APLM in the undeflected state. N_1 and N_2 are the lengths of the two elements of the tapered flexures and L_{Lever} is the length of the lever. θ is the angular rotation of the lever. The total displacement of the outer mass, v, is the product of the rotation and length of the lever, $v = \theta \cdot L_{Lever}$. The half width of the lever is d_3 and the size of the small square block in the tapered flexure is $2d$.

The lever is applying a force load and a moment load to the flexures that are located on the centerline of the lever which is beyond the end of the flexure. Also, while the center of the pivot point is allowed to have a net rotation, it is constrained from

having a net deflection in the x-axis. However, the end of the flexure where it attaches to the lever has both a net rotation and a small net deflection. This complicates the derivation of the design equations quite a bit. Therefore, the detailed derivation of the design equations is provided in section A.8 of Appendix A and only the resulting design procedure is captured here.

The design of the tapered flexure lever APLM proceeds as follows.

1. The desired spring constant for one mass of the individual APLM, k_{v_Tot}, and the thickness of the device, *t*, are either given or chosen by the designer. If the designer is provided with a target resonant frequency, ω_n, then the designer uses the mass of one proof mass, M_{PM}, and the number of APLMs in that axis of the design, Num_{APLM}, to arrive at the desired spring constant, k_{v_Tot}, using the following relation [30]:

$$k_{v\_Tot} = \frac{M_{PM} \cdot \omega_n^2}{Num_{APLM}} \ . \tag{4.37}$$

2. The length of the lever arm, L_{Lever}, is either given or can be chosen using engineering judgment. It is recommended that the length of the lever be on the order of 100 greater than the expected maximum displacement of the proof masses to keep the rotation angle of the lever to a reasonable value.
3. Choose a value for the constant, R, which relates the stiffness of the lever to the stiffness of the system. That is $k_{Lever} = R \cdot k_{v\_Tot}$. Similar to that of the straight flexure lever APLM design, this constant relates how much displacement will occur due to the bending of lever as compared with that

of the rotation of the lever. This constant also sets the rigidity of the coupling from one mass to the other in anti-phase mode and aids in pushing the common-mode resonant to a frequency higher than that of the anti-phase mode. It is recommended that this constant be chosen between 10 and 100, with a typical value of around 50.

4. Calculate the minimum value of w_{Lever} using the equation below and select a value that is greater than or equal to that value, from Section A.8 of Appendix A:

$$w_{Lever} \geq L_{Lever}\left(\frac{4 \cdot R \cdot k_{v\_Tot}}{E \cdot t}\right)^{\frac{1}{3}}. \tag{4.38}$$

5. Since the constant d_3 was defined as the half-width of the lever, set d_3 equal to half of the desired value of w_{Lever}, from Section A.8 of Appendix A:

$$d_3 = \frac{w_{Lever}}{2} \geq \frac{L_{Lever}}{2}\left(\frac{4 \cdot R \cdot k_{v\_Tot}}{E \cdot t}\right)^{\frac{1}{3}}. \tag{4.39}$$

6. Calculate the value of the spring constant that relates the angular rotation of the lever to the total applied moment, $k_{M\theta Tot}$, from Section A.8 of Appendix A:

$$k_{M\theta Tot} = k_{v\_Tot} \cdot L_{Lever}^2. \tag{4.40}$$

7. Calculate the value of the spring constant that relates the angular rotation of the lever to the applied moment of a single flexure, $k_{M\theta Flex}$, from Section A.8 of Appendix A:

$$k_{M\theta Flex} = \frac{k_{M\theta Tot}}{3} = \frac{k_{v\_Tot} \cdot L_{Lever}^2}{3} \quad . \tag{4.41}$$

8. Using engineering judgement, choose a value for the size of the hammerhead, $2d$. This value can vary widely based on the overall dimensions of the design and the anticipated lengths of the flexures. It is desirable to keep the block small so that the added mass does not introduce unwanted flexural modes in the flexure itself, but it needs to be large enough to keep the narrowest part of the tapered flexure above the minimum feature size of the fabrication process employed to fabricate the device. In this work, the block size was typically between 40µm and 50µm.
9. Using engineering judgement, choose a value for the length of the second element of the flexure, N_2. This value can vary widely based on the desired resonant frequency and overall dimensions of the design, but it is generally recommended that the length of the flexure be at least 3 times the thickness of the device, t, to ensure that the stresses along the length of the flexure are the dominant stresses.
10. To determine the length of N_1, employ Newton's Method to solve the governing nonlinear equation numerically. Here we define the function, $f(N_1)$, and its derivative with respect to N_1, $f'(N_1)$, as follows, from Section A.8 of Appendix A:

$$f(N_1) = N_1^{\frac{3}{2}} - 2d^{\frac{3}{2}} - 2N_2^{\frac{3}{2}} + 3N_1^{\frac{1}{2}}N_2 - 3d_3N_2^{\frac{1}{2}} + 3d_3N_1^{\frac{1}{2}} \tag{4.42}$$

$$f'(N_1) = \frac{3}{2}N_1^{\frac{1}{2}} + \frac{3}{2}N_1^{-\frac{1}{2}}N_2 + \frac{3}{2}d_3N_1^{-\frac{1}{2}}. \tag{4.43}$$

11. Select an initial guess for N_1 and iterate using the following equation until the value has adequately converged. It is recommended that the initial guess be approximately $0.355N_2$:

$$N_{1_{New}} = N_{1_{Old}} - \frac{f(N_{1_{Old}})}{f'(N_{1_{Old}})} \ . \tag{4.44}$$

12. If the value for N_1 is not acceptable, then scale N_2 accordingly and repeat steps 9 and 10 until an acceptable value for N_1 is obtained. While the governing equations for this relationship are nonlinear, the relationship between N_1 and N_2 is approximately linear.
13. Calculate the base width of the first element of the flexure, w_{b1}, using the following equation, from Section A.8 of Appendix A:

$$w_{b1} = \left[\frac{24 \cdot k_{M\theta Flex} \cdot \left(N_1^{\frac{3}{2}} \cdot N_2^{\frac{1}{2}} - N_1^2\right)}{E \cdot t \cdot (N_2 + d_3)}\right]^{\frac{1}{3}} , \tag{4.45}$$

where E is the Young's Modulus of the material.

14. Calculate the base width of the second element of the flexure, w_{b2}, using the following equation, from Section A.8 of Appendix A:

$$w_{b2} = w_{b1}\sqrt{\frac{N_2}{N_1}}\ . \tag{4.46}$$

15. If either w_{b1} or w_{b2} are not acceptable, then scale N_2 and/or L_{Lever} accordingly and repeat the above calculations until acceptable values are obtained. Generally, the flexure base widths will be proportional to $L_{Lever}^{\frac{2}{3}}$ and to $N_2^{\frac{1}{3}}$.

4.1.5 University of California at Irvine (UCI) Inner Lever Coupling Design

Figure 4.20 shows the critical dimensions of the UCI inner lever coupling APLM design. The equations that govern the behavior of this design are documented in Reference [28] and only the final equations are included here. The anti-phase spring constant was reported to be:

$$k_{Anti-Phase} = \left\{\frac{(L-g)^2}{EI(2L)^3}\frac{h}{w}\left[\frac{wh}{w^2+h^2}\frac{2}{3}L^2(L - g)(L+3g) + h(4gL^2)\right]\right\}^{-1}, \tag{4.47}$$

[28]

where *I* refers to the moment of inertia of the clamped-clamped beam. *L* is the length of the clamped-clamped beam. The separation width of the attachment points of the two long, stiff levers to the clamped-clamed beam is $2g$, and h and w are the length and width of the long, stiff levers, respectively, as depicted in Figure 4.20.

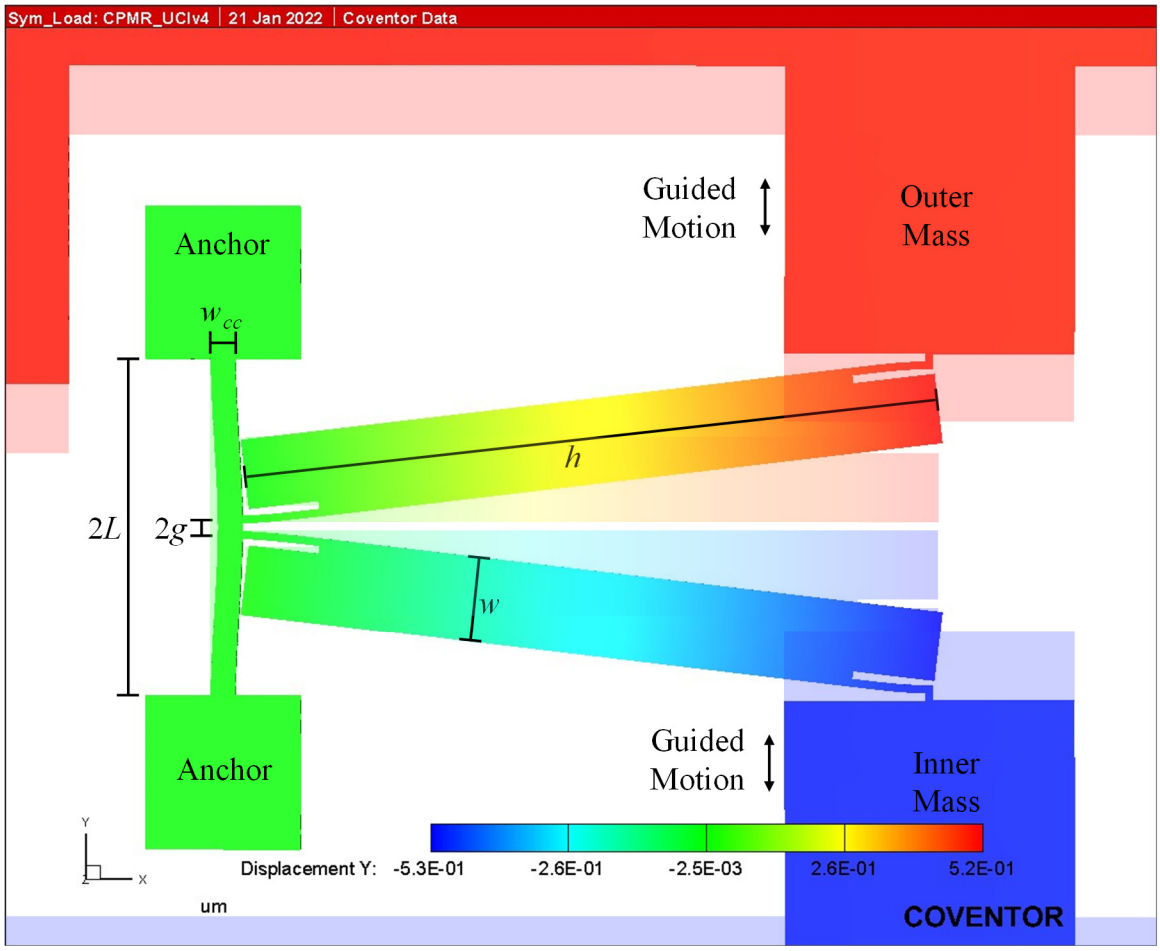

Figure 4.20 Critical Dimensions of UCI Inner Lever Coupling APLM. The solid-colored region represents the APLM in the deflected state and the shaded region represents the APLM in the undeflected state. L and w_{cc} are the length and width of the clamped-clamped beam, respectively which comprise the secondary resonator. The separation width of the attachment points of the two long, stiff levers to the clamped-clamed beam is $2g$. h and w are the length and width of the long, stiff levers, respectively.

The spring constant equation in Equation 4.47 was derived for the total differential displacement of the two proof masses. So, this value must be doubled to compare it with the spring constants that only consider the forces acting on a single proof mass as has been presented for the other APLM designs in this chapter.

Noting that the moment of inertia of the clamped-clamped beam is given by:

$$I = \frac{t \cdot w_{cc}^3}{12} \quad , \qquad [30] \qquad (4.48)$$

where t is the thickness of the device and w_{cc} is the width of the clamped-clamped beam. Substituting Equation 4.48 into Equation 4.47 yields:

$$k_{Anti-Phase} = \left\{ \frac{12(L-g)^2}{Etw_{cc}^3(2L)^3} \frac{h}{w} \left[\frac{wh}{w^2+h^2} \frac{2}{3} L^2(L - g)(L+3g) + h(4gL^2) \right] \right\}^{-1} . \qquad [28] \qquad (4.49)$$

Reference [28] provides some guidance and insight into the selection of the parameters L, g, w, and h. Here we assume that these parameters are either given or selected through engineering judgment. The final step is to solve for the width of the clamped-clamped beam. Rearranging Equation 4.49 to solve for w_{cc} we arrive at the following expression:

$$w_{cc} = \left\{ \frac{3h(L-g)^2}{2EtwL^3} \left[\frac{wh}{w^2+h^2} \frac{2}{3} L^2(L-g)(L+3g) + 4hgL^2 \right] k_{Anti-Phase} \right\}^{\frac{1}{3}} . \qquad [28] \qquad (4.50)$$

4.1.6 Straight Flexure Revised UCI Design

The design of the straight flexure revised UCI APLM is very straightforward. The critical dimensions are just the length, L_{AF}, and width, w_{AF}, of the angled flexures, which are labeled in Figure 4.21. There are several other relevant dimensions labeled in

Figure 4.21 but they do not have a dominant impact on the operation of the device as long as the folded flexures are relatively compliant. These dimensions include the width, w_{Blk}, and length, L_{Blk}, of the shuttle block; the width, w_{FF}, and length, L_{FF}, of the flexures in the folded flexure; the separation of the angled flexure attachment points to the shuttle block, d_{AF}, and the orthogonal components, a and b, of the angled flexure layout. It is important to note that higher $\frac{b}{a}$ ratios impose stronger coupling of the proof masses both to the shuttle block and to one another.

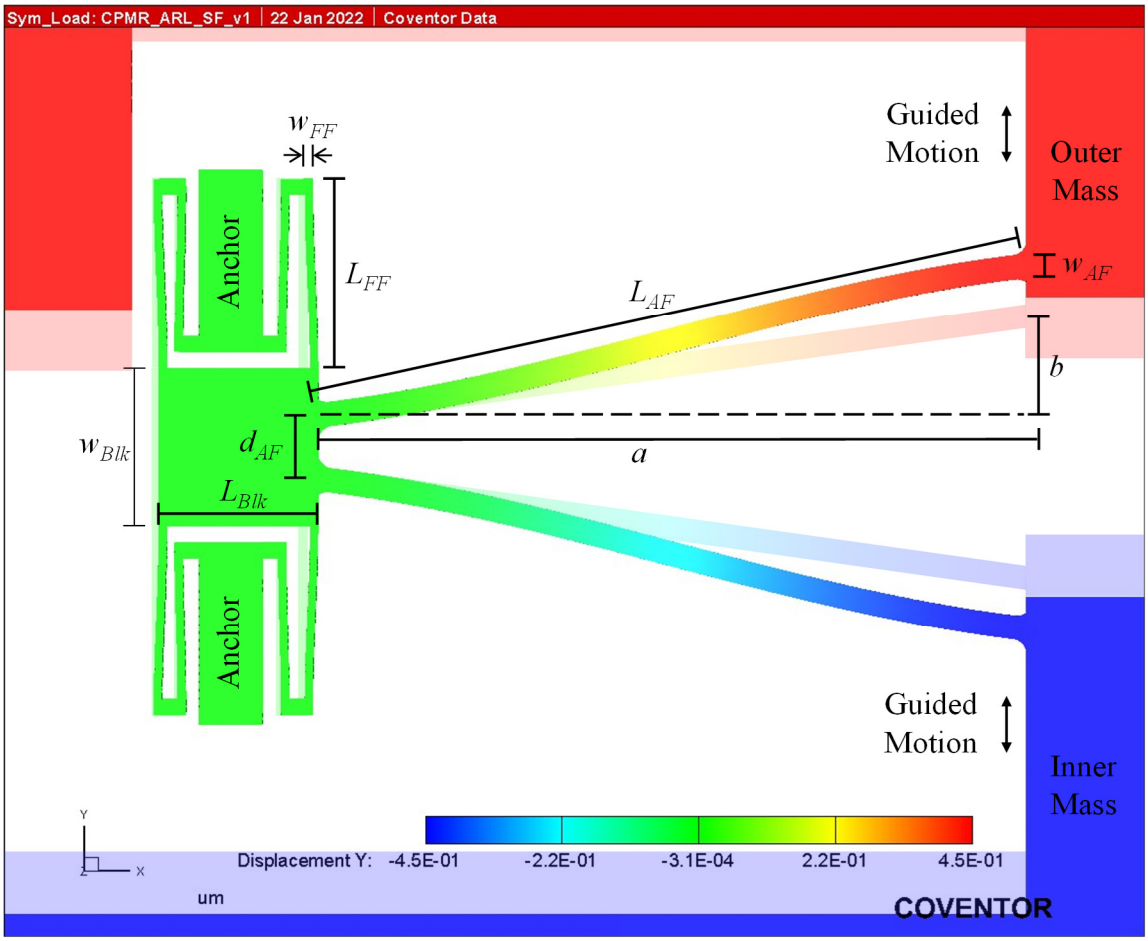

Figure 4.21 Critical Dimensions of the Straight Flexure Revised UCI APLM. The solid-colored region represents the APLM in the deflected state and the shaded region represents the APLM in the undeflected state. The length and width of the angled flexures are L_{AF} and w_{AF}, respectively. The width and length of the shuttle block is w_{Blk} and L_{Blk}, respectively. The width and length of the folded flexures are w_{FF} and L_{FF}, respectively. The separation of the angled flexure attachment points to the shuttle block is d_{AF}, and the orthogonal components of the angled flexure layout are a and b.

The design of the straight flexure revised UCI APLM proceeds as follows.

1. The desired spring constant for one mass of the individual APLM, k_{v_Tot}, and the thickness of the device, t, are either given or chosen by the designer. If the designer is provided with a target resonant frequency, ω_n, then the designer uses the mass of one proof mass, M_{PM}, and the number

of APLMs in the design, Num_{APLM}, to arrive at the desired spring constant, k_{v_Tot}, using the following relation [30]:

$$k_{v\_Tot} = \frac{M_{PM} \cdot \omega^2}{Num_{APLM}} \ . \tag{4.51}$$

2. Using engineering judgment, choose a value for the length of the angled flexure, L_{AF}. This value can vary widely based on the desired resonant frequency and overall dimensions of the design and was typically around 900μm for the designs in this dissertation, but it is generally recommended that the length of the flexure be at least 3 times the thickness of the device, t, to ensure that the stresses along the length of the flexure are the dominant stresses.
3. Calculate the width of the angled flexure, w_{AF}, using the following equation [30]:

$$w_{AF} = L_{AF}\left[\frac{k_{v\_Tot}}{E \cdot t}\right]^{\frac{1}{3}} , \tag{4.52}$$

where E is the Young's Modulus of the flexure material.

4. If w_{AF} is not acceptable, then scale L_{AF} accordingly, recalculate w_{AF} and iterate until both values are acceptable. w_{AF} should scale in direct proportion to L_{AF}. Note that the width of the angled flexure, w_{AF}, is the dominant factor in the thermoelastic damping loss. Therefore, it is desirable to keep w_{AF} to a relatively small value, which can be set through the proper selection of L_{AF} within the limits of the fabrication process.

5. The following considerations can help guide the selection of all other variables. In this design, the in-phase mode of the proof masses couples into the first rotational mode of the shuttle block. Setting the shuttle block size, L_{Blk} and w_{Blk}, to larger values (typically 200µm for the designs in this dissertation) enables greater separation of the attachment points of the folded flexures and provides increased stiffness against this mode, which will push the resonant frequency of the proof mass in-phase mode to higher frequencies. Increased separation of the angled flexure attachment points, d_{AF}, mitigates against the high stress point that Dr. Simon warned against [28] and was typically about 80µm for the designs in this dissertation. The folded flexures are not intended to contribute significantly to the operation of this design. Therefore, it is recommended that the stiffness of the folded flexures be about an order of magnitude smaller than that of the angled flexure. Therefore, it is recommended that the width of the folded flexures, w_{FF}, be set to the minimum feature size of the fabrication process and that the length of the folded flexures, L_{FF}, be guided by that stiffness. w_{FF} was typically 10µm and L_{FF} was typically 200µm for the devices modeled in this dissertation. It is recommended to select an $\frac{a}{b}$ ratio of about ten (10) to ensure good anti-phase coupling between the two proof masses and to ensure that the contribution of the folded flexures is minimized.

4.1.7 Tapered Flexure Revised UCI APLM Design

The design of the tapered flexure revised UCI APLM is also very straightforward and follows a pattern very similar to that of the straight flexure revised UCI APLM . The critical dimensions are just the length, L_{AF}, and the base width, $w_{b_{AF}}$, of the angled flexures, as well as the half length of the hammerhead feature in the angled flexure, d_{HH}, which are labeled in Figure 4.22. Similar to the straight flexure version, there are several other relevant dimensions labeled in Figure 4.22 but they do not have a dominant impact on the operation of the device as long as the folded flexures are relatively compliant. These dimensions include the width, w_{Blk}, and length, L_{Blk}, of the shuttle block; the width, w_{FF}, and length, L_{FF}, of the flexures in the folded flexure; the separation of the angled flexure attachment points to the shuttle block, d_{AF}, and the orthogonal components, a and b, of the angled flexure layout. The $\frac{b}{a}$ ratio, however, is an important design consideration as higher $\frac{b}{a}$ ratios provide stronger coupling of the proof masses to the shuttle block and to one another.

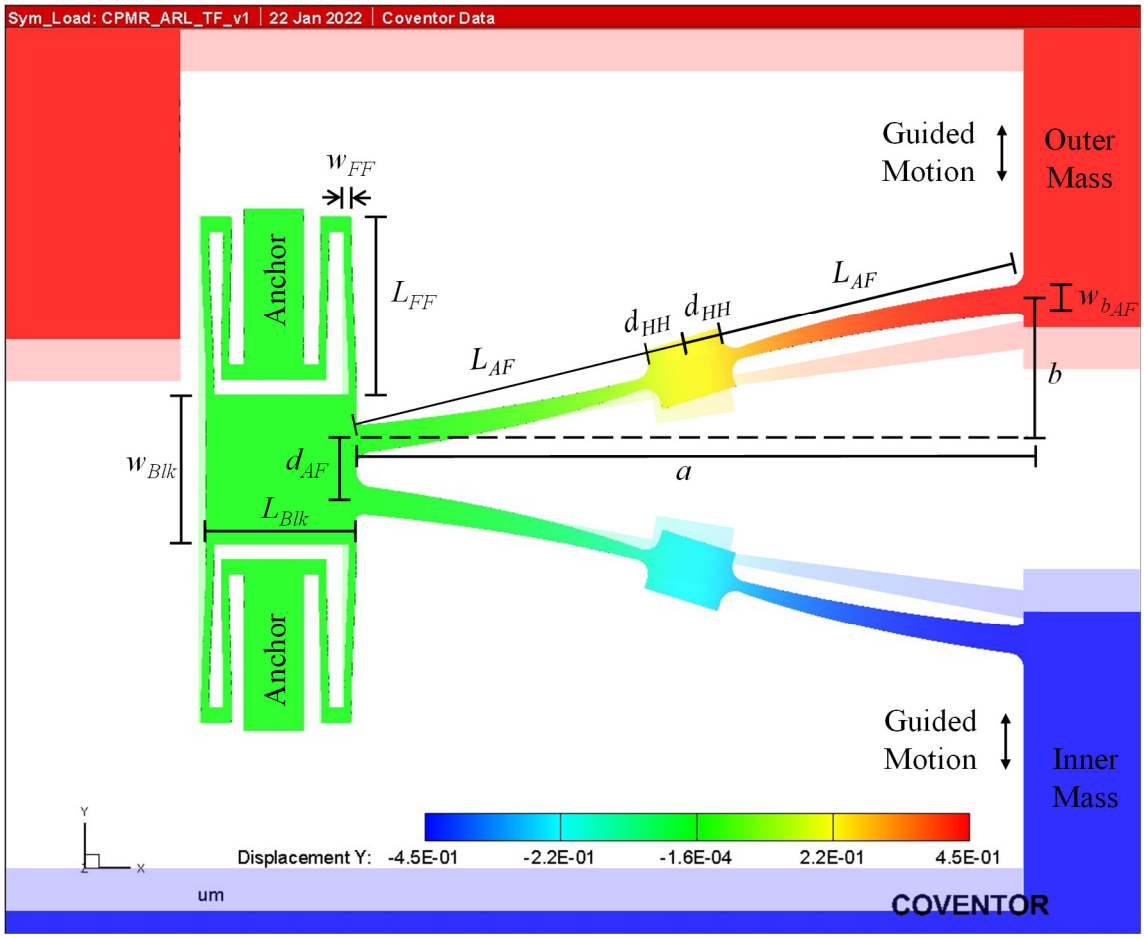

Figure 4.22 Critical Dimensions of the Tapered Flexure Revised UCI APLM. The solid-colored region represents the APLM in the deflected state and the shaded region represents the APLM in the undeflected state. The length of the two tapered flexures in the angled flexure is L_{AF} and the width of the angled flexures at their base is $w_{b_{AF}}$. The half-length of the hammerhead in the center of the angled flexure is d_{HH}. The width and length of the shuttle block is w_{Blk} and L_{Blk}, respectively. The width and length of the folded flexures are w_{FF} and L_{FF}, respectively. The separation of the angled flexure attachment points to the shuttle block is d_{AF}, and the orthogonal components of the angled flexure layout are a and b.

The design of the tapered flexure revised UCI APLM proceeds as follows.

1. The desired spring constant for one mass of the individual APLM, k_{v_Tot}, and the thickness of the device, t, are either given or chosen by the designer. If the designer is provided with a target resonant frequency, ω_n, then they use the mass of one proof mass, M_{PM}, and the number of

APLMs in that axis of the design, Num_{APLM}, to arrive at the desired spring constant, k_{v_Tot}, using the following relation [30]:

$$k_{v\_Tot} = \frac{M_{PM} \cdot \omega^2}{Num_{APLM}} \ . \tag{4.53}$$

2. Choose a value for the length of the angled flexure, L_{AF}, and the half length of the hammerhead feature, d_{HH}. The length of the angled flexure, L_{AF}, can vary widely based on the desired resonant frequency and overall dimensions of the design and was typically around 450µm for the designs in this dissertation, but it is generally recommended that the length of the flexure be at least 3 times the thickness of the device, t, to ensure that the stresses along the length of the flexure are the dominant stresses. The half length of the hammerhead feature, d_{HH}, which was typically around 50µm for the devices evaluated in this dissertation, should be chosen such that the narrowest part of the tapered flexure is still above the smallest feature size of the fabrication process. As discussed in Chapter 3, the trade-off between thermoelastic damping performance and sensitivity to critical dimension loss during fabrication is another consideration for the selection of half length of the hammerhead feature, d_{HH}.
3. Calculate the base width of the angled flexure, $w_{b_{AF}}$, using the following equation derived from Table 3.1:

$$w_{b_{AF}} = \left[\frac{8 \cdot \left(2 \cdot k_{v\_Tot}\right) \cdot \left(N_{AF}^{3} - N_{AF}^{\frac{3}{2}} \cdot d_{HH}^{\frac{3}{2}} \right)}{E \cdot t} \right]^{\frac{1}{3}}, \tag{4.54}$$

where $N_{AF} = L_{AF} + d_{HH}$ and the spring constant, k_{v_Tot}, has been multiplied by two to obtain the spring constant for one element of the angled flexure.

4. If $w_{b_{AF}}$ is not acceptable, then scale L_{AF} and/or d_{HH} accordingly, recalculate $w_{b_{AF}}$ and iterate until both values are acceptable. $w_{b_{AF}}$ should roughly scale in direct proportion to L_{AF}. Note that the width of the angled flexure, w_{AF}, is the dominant factor in the thermoelastic damping loss. Therefore, it is desirable to keep w_{AF} to a relatively small value, which can be set through the proper selection of L_{AF} within the limits of the fabrication process.
5. The following considerations can help guide the selection of all other variables. In this design, the in-phase mode of the proof masses will couple into the first rotational mode of the shuttle block. Setting the shuttle block size, L_{Blk} and w_{Blk}, to larger values (typically 200µm for the designs in this dissertation) enables greater separation of the attachment points of the folded flexures and provides increased stiffness against this mode, which will push the in-phase resonant frequency higher. Increased separation of the angled flexure attachment points, d_{AF}, mitigates against the high stress point that Dr. Simon warned against [28] and was typically

about 80μm for the designs in this dissertation. The folded flexures are not intended to contribute significantly to the operation of this design. Therefore, it is recommended that the stiffness of the folded flexures be about an order of magnitude smaller than that of the angled flexure. Therefore, it is recommended that the width of the folded flexures, w_{FF}, be set to the minimum feature size of the fabrication process and that the length of the folded flexures, L_{FF}, be guided by that stiffness. w_{FF} was typically 10μm and L_{FF} was typically 200μm for the devices modeled in this dissertation. It is recommended to select an $\frac{a}{b}$ ratio of about ten (10) to ensure good anti-phase coupling between the two proof masses and to ensure that the contribution of the folded flexures is minimized.

4.2 APLM FEA Modeling and Results

A solid model was generated for each of the design configurations described in the previous section in a Concentric Mass Resonator (CMR) configuration and a set of finite element analyses (FEA) were performed on each of these models. These FEA analyses investigated (1) peak stress under symmetric loading conditions, (2) relative displacement of the inner and outer masses under asymmetric force loading conditions, (3) separation of anti-phase and in-phase resonant modes, and (4) thermoelastic damping of each design. First a description is provided of the CMR configuration that was used in the analysis followed by the specific design details for each device configuration

investigated. Finally, a description of the FEA analyses performed and a presentation of the results are provided.

4.2.1 Concentric Mass Resonator Configuration Description

The Concentric Mass Resonator (CMR) configuration is based on a single degree of freedom resonator version of the concentric mass gyroscope configuration. For the purposes of the current investigation, no attempt was made to optimize the design of a full resonator. Rather, the CMR was a convenient configuration to investigate the properties of various APLM designs which incorporate either straight or tapered flexures. Therefore, there were no electrodes included in the models. All loads applied to the system were applied as pressure loads to the edges of the parts. A solid model of the CMR configuration incorporating the straight flexure pivot APLM design is provided in Figure 4.23. This same device is shown deflected in two extremes of the desired anti-phase mode in Figures 4.24(a) and (b). In Figure 4.24, the green blocks are anchored to the substrate. This same device is shown in the two extremes of the unwanted in-phase mode in Figures 4.25(a) and (b). Here again, the green blocks are anchored to the substrate.

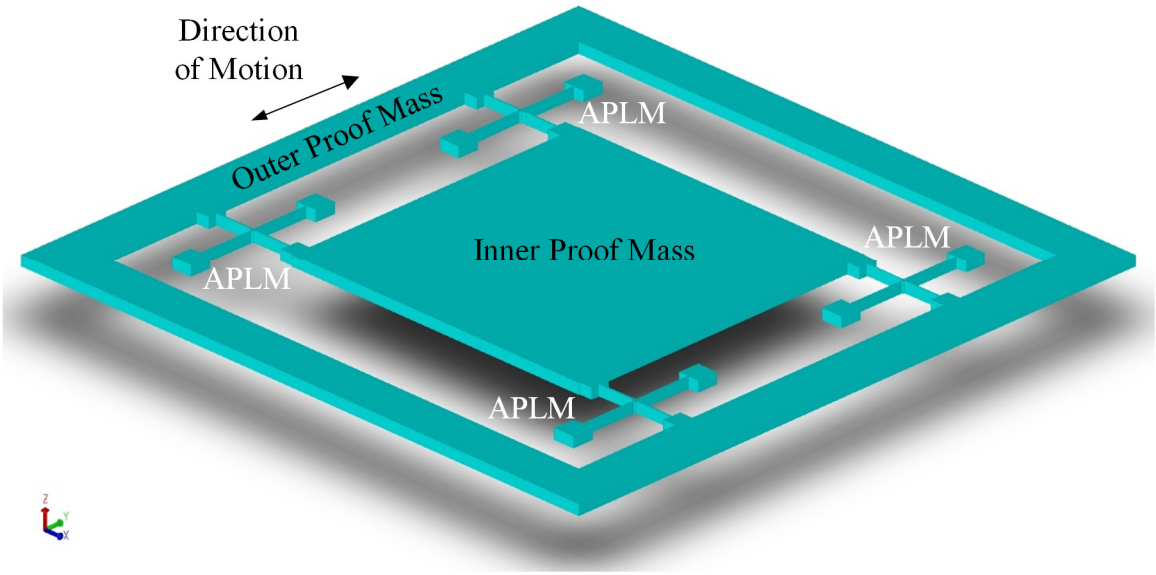

Figure 4.23 Solid Model of the Concentric Mass Resonator Configuration.

All devices were modeled in a 100µm thick <100> Single Crystal Silicon (SCS) layer using the same material properties provided previously in Figure 3.5. The insulator layer beneath the device layer was 1µm thick thermal silicon dioxide with the same material properties provided previously in Figure 3.6. The dimensions of the square inner proof mass were 3mm by 3mm. The inner dimensions of the outer proof mass were 5mm by 5mm. To maintain mass symmetry of the inner and outer masses, the outer dimensions of the outer proof mass were set to 5.831mm by 5.831mm.

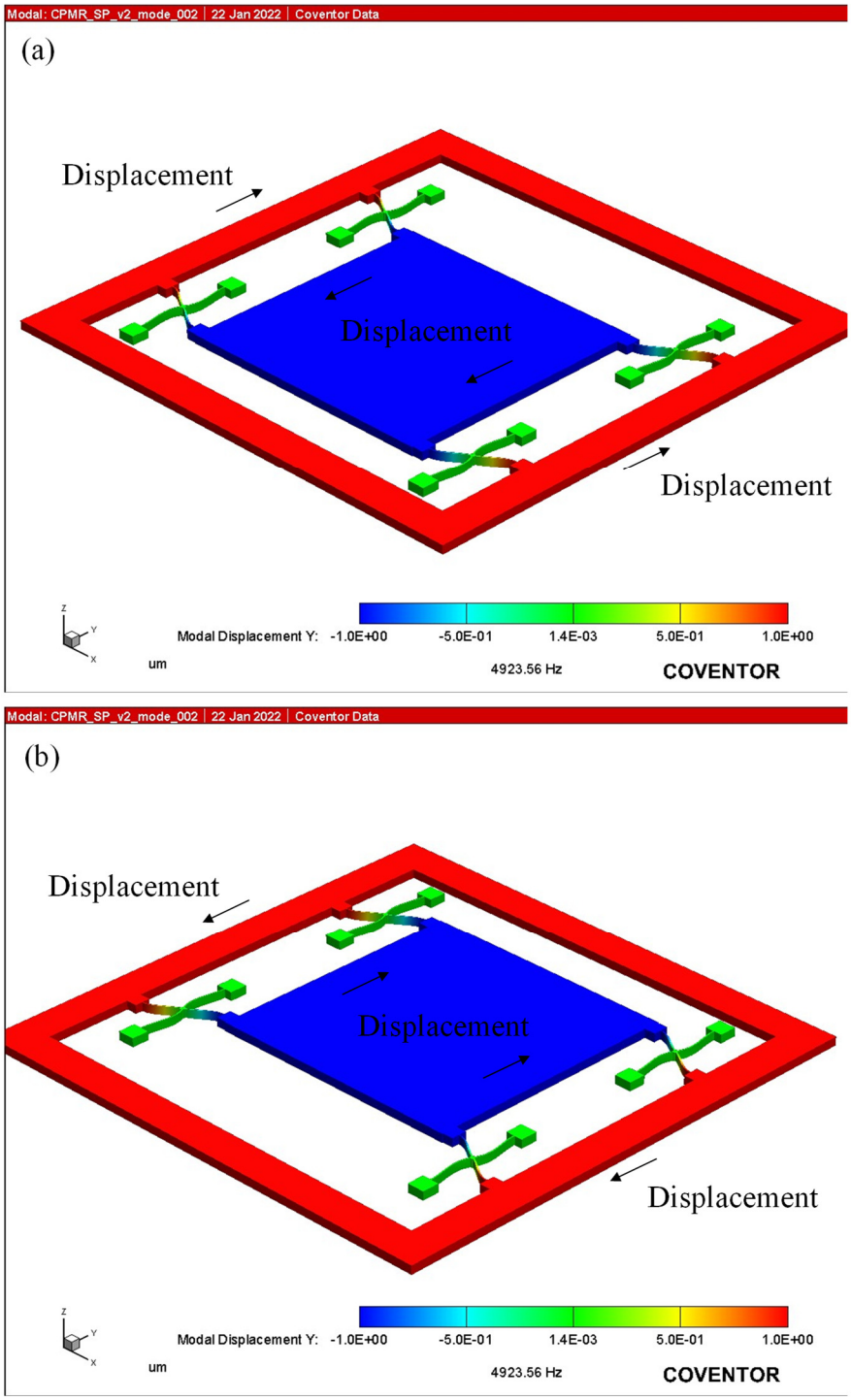

Figure 4.24 Anti-Phase Mode of the Concentric Mass Resonator Configuration. The maximum positive displacement in one half of the oscillation is shown in (a) and the maximum negative displacement in the other half of the oscillation is shown in (b) to depict the desired anti-phase mode of the concentric mass resonator configuration.

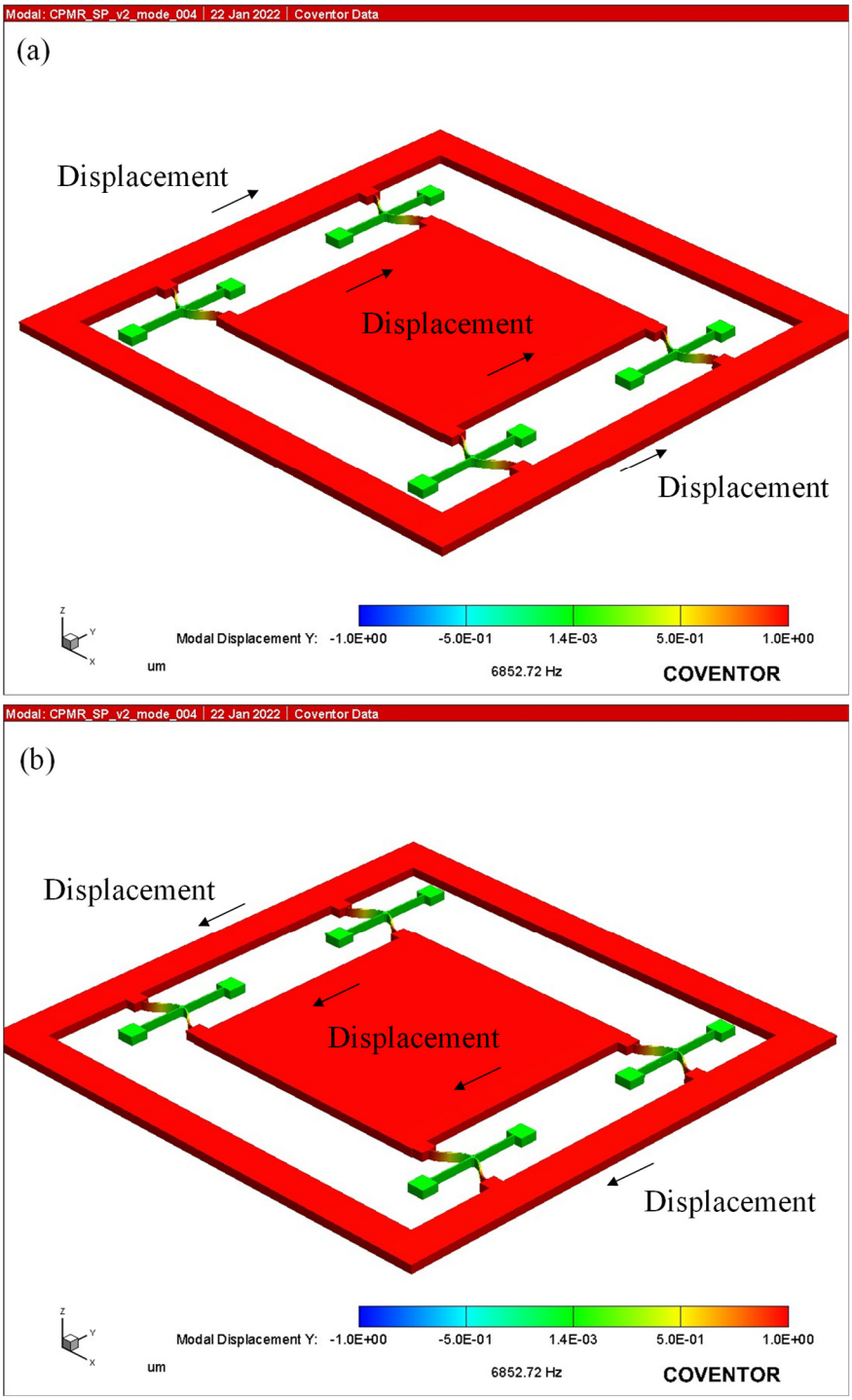

Figure 4.25 In-Phase Mode of the Concentric Mass Resonator Configuration. The maximum positive displacement in one half of the oscillation is shown in (a) and the maximum negative displacement in the other half of the oscillation is shown in (b) to depict the undesired in-phase mode of the concentric mass resonator configuration.

All designs targeted a resonant frequency of 5kHz and all designs incorporated four APLMs, one near each corner. Depending on the method of attachment of the specific APLM to the proof masses, attachment blocks were added to the proof masses as required. This led to some slight differences in the masses of each design configuration but reasonable attempts were made to ensure a fair comparison between design configurations.

4.2.2 Specific Design Details of the APLM Configurations

This section provides the specific design details for each device investigated. Based on the stress peaking results presented in Section 3.3.1.3, fillets were added to all inside corners that were approximately half of the local flexure width for all designs other than the UCI inner lever coupling design.

The design procedure documented in Section 4.1.1 for the straight flexure pivot APLM design was followed and resulted in the design specifications documented in Table 4.1. The solid model of the resulting device is pictured in Figure 4.26 and a close-up of the APLM is shown in Figure 4.27. Labels of the relevant feature sizes in Table 4.1 were defined in Section 4.1.1 but are repeated graphically in Figure 4.27 for reference.

The design procedure documented in Section 4.1.2 was also followed for the tapered flexure pivot APLM design resulted in the design specifications that are documented in Table 4.2. The solid model of the resulting device is pictured in Figure 4.28 and a close-up of the APLM is shown in Figure 4.29. Labels of the relevant feature sizes in Table 4.2 were defined in Section 4.1.2 but are repeated graphically in Figure 4.29 for reference.

To ensure a fair comparison between the straight and tapered versions of the four-flexure pivot APLM design, the tapered flexure version was actually designed first. The combined length of the N_{1G} and N_{2G} guided flexure elements was then used to set the length of the guided flexure element, L_G, of the straight flexure design to ensure that the total length of the guided flexure was the same for both designs. The value for the proportionality constant, P, was chosen to be a moderate value of 0.9 for both designs. Also, the size of the square block at the pivot point was set to the same value for both designs. These choices resulted in reasonable widths and lengths for all flexures.

Table 4.1 Straight Flexure Pivot APLM Design Specifications.

Parameter	**Label**	**Units**	**Value**
Device Thickness	t	µm	100
Proportionality Constant	P	unitless	0.9
Guided Flexure Length	L_G	µm	354.676
Guided Flexure Width	w_G	µm	13.635
Anchor Flexure Length	L_A	µm	532.014
Anchor Flexure Width	w_A	µm	13.635
Pivot Point Block Size	w_{PP}	µm	40

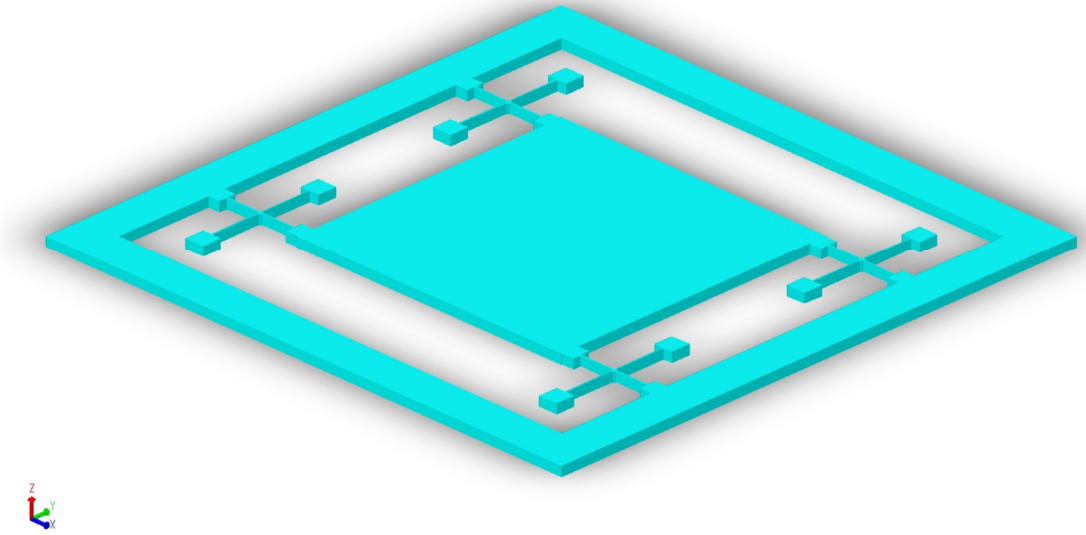

Figure 4.26 Straight Flexure Pivot CMR Solid Model.

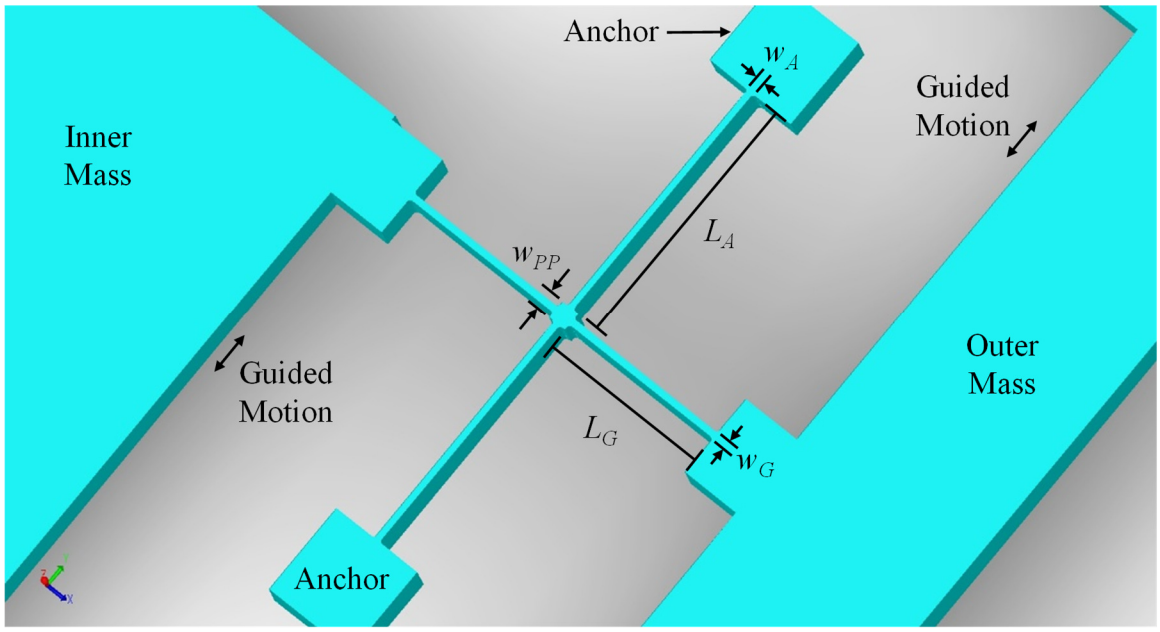

Figure 4.27 Straight Flexure Pivot APLM Close-Up.

Table 4.2 Tapered Flexure Pivot APLM Design Specifications.

Parameter	Label	Units	Value
Device Thickness	t	µm	100
Proportionality Constant	P	unitless	0.9
Guided Flexure 1st Element Length	N_{1G}	µm	104.676
Guided Flexure 1st Element Base Width	w_{b1G}	µm	12.088
Guided Flexure 2nd Element Length	N_{2G}	µm	250.000
Guided Flexure 2nd Element Base Width	w_{b2G}	µm	18.681
Anchor Flexure 1st Element Length	N_{1A}	µm	57.532
Anchor Flexure 1st Element Base Width	w_{b1A}	µm	7.493
Anchor Flexure 2nd Element Length	N_{2A}	µm	149.749
Anchor Flexure 2nd Element Base Width	w_{b2A}	µm	57.532
Tapered Flexure Hammerhead Half-Width	d	µm	20
Pivot Point Block Size	w_{PP}	µm	40

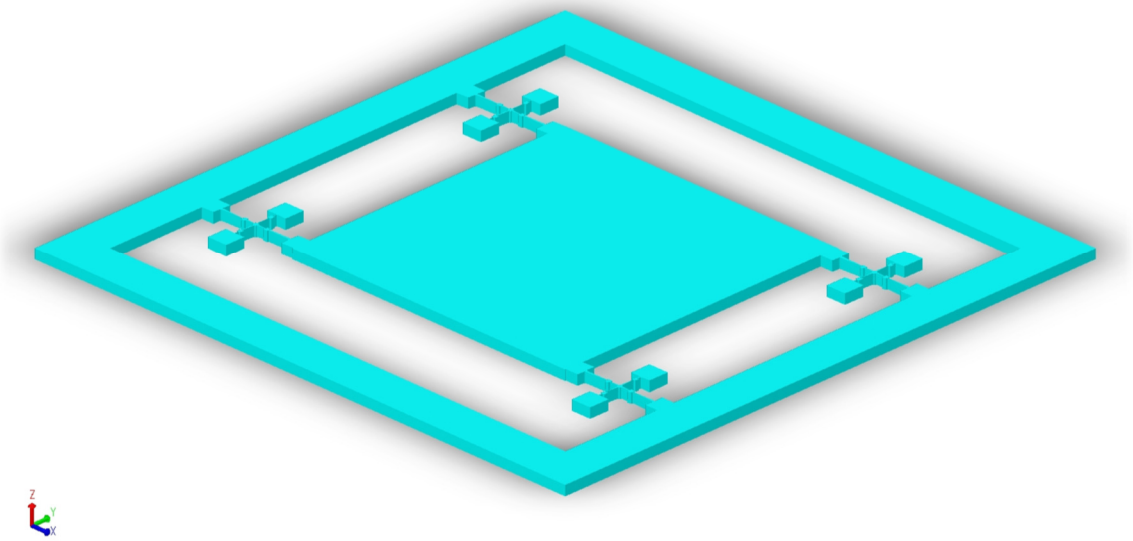

Figure 4.28 Tapered Flexure Pivot CMR Solid Model.

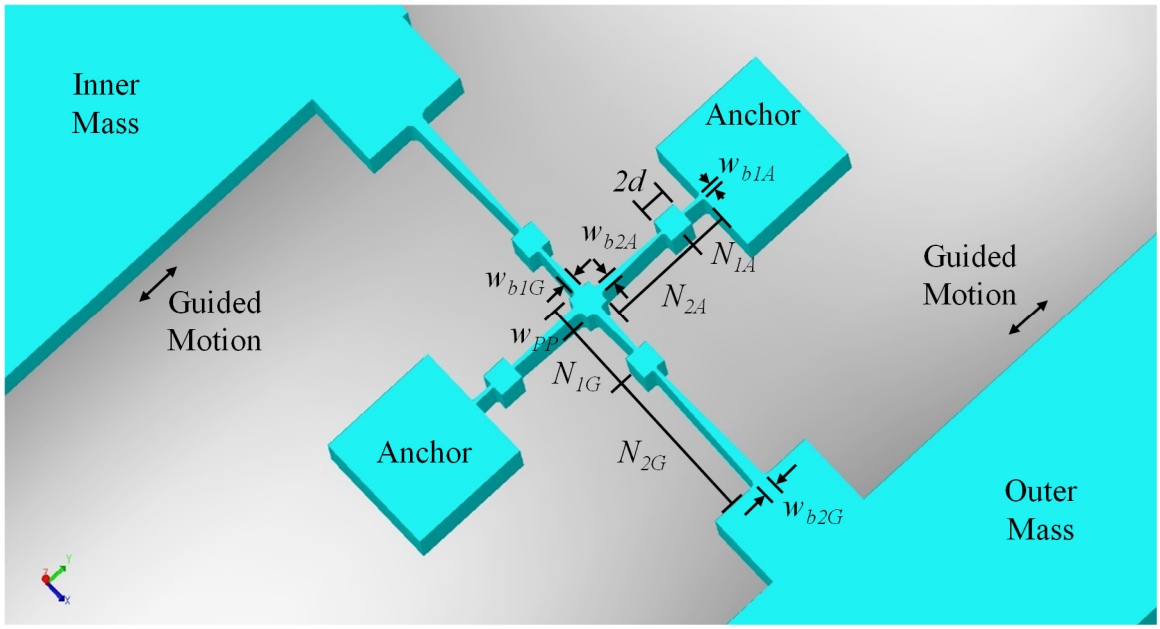

Figure 4.29 Tapered Flexure Pivot APLM Close-Up.

The design procedure documented in Section 4.1.3 for the straight flexure lever APLM design was followed and resulted in the design specifications documented in Table 4.3. The solid model of the resulting device is pictured in Figure 4.30 and a close-up of the APLM is shown in Figure 4.31. Labels of the relevant feature sizes in Table 4.3 were defined in Section 4.1.3 but are repeated here in Figure 4.31 for reference.

The design procedure documented in Section 4.1.4 was followed for the tapered flexure lever APLM design and resulted in the design specifications that are documented in Table 4.4. The solid model of the resulting device is pictured in Figure 4.32 and a close-up of the APLM is shown in Figure 4.33. Once again, labels of the relevant feature sizes in Table 4.4 were defined in Section 4.1.4 but are repeated here in Figure 4.33 for reference.

Similar to the order mentioned previously for the four-flexure pivot designs, to ensure as fair of a comparison as possible between the straight and tapered versions of the

six-flexure lever APLM designs, the tapered flexure version was actually designed first. This enabled the combined length of the N_1 and N_2 flexure elements of the tapered flexure design to be used to set the length of the flexure, L_{Flex}, of the straight flexure design.

To begin the design procedure, it was necessary to first set the length of the lever, L_{Lever}, to the same value for both the straight and tapered flexure designs. To have a reasonable comparison to the four-flexure pivot designs, it was desired to have the length of the lever be close to the total length of the guided flexure in the four-flexure pivot design, which was approximately 375 µm. However, the length of the lever impacts other elements of the six flexure lever designs including the final flexure widths, total angular deflection, and the total stress in the flexures. Considering all of these factors, the length of the lever was finally set to be 450 µm. (Note: To maintain comparability with this design, the total length of this lever was used to set critical dimensions for the UCI and revised UCI APLM designs that are discussed later.) Similarly, the relative stiffness constant, R, impacts multiple parameters beyond just the lever width, and the final value was selected to be 45, which led to an overall lever width of 80µm.

For comparison to the four-flexure pivot designs, it was also desired to have the total flexure lengths of the six-flexure lever design, including the half width of the lever, be roughly the same as the total length of the anchor flexure of the tapered flexure lever design, which was about 230µm. Therefore, N_2 of the tapered flexure was set to be 120µm. This resulted in a value of 58.588µm for N_1 and an overall length (including d_3) of 218.588µm, which was very close to the target value. All other parameters of the design resulted from these selections using the design procedure documented previously.

Table 4.3 Straight Flexure Lever APLM Design Specifications.

Parameter	Label	Units	Value
Device Thickness	t	µm	100
Lever Length	L_{Lever}	µm	450
Lever Width	w_{Lever}	µm	80
Half Lever Width	d_3	µm	40
Lever to Flexure Stiffness Ratio	R	unitless	45
Flexure Length	L_{Flex}	µm	178.588
Flexure Width	w_{Flex}	µm	10.416

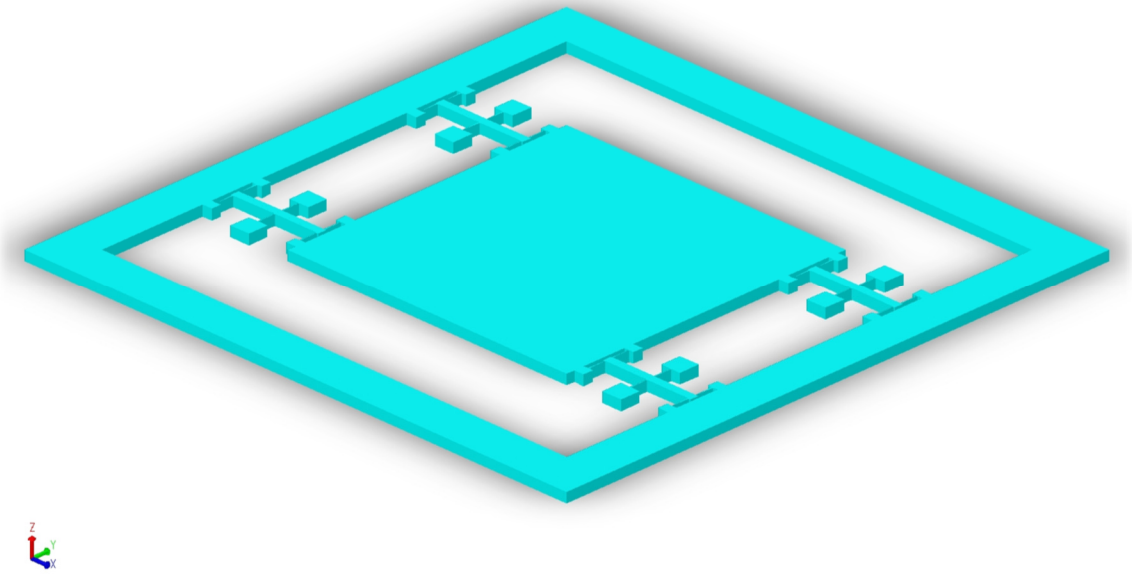

Figure 4.30 Straight Flexure Lever CMR Solid Model.

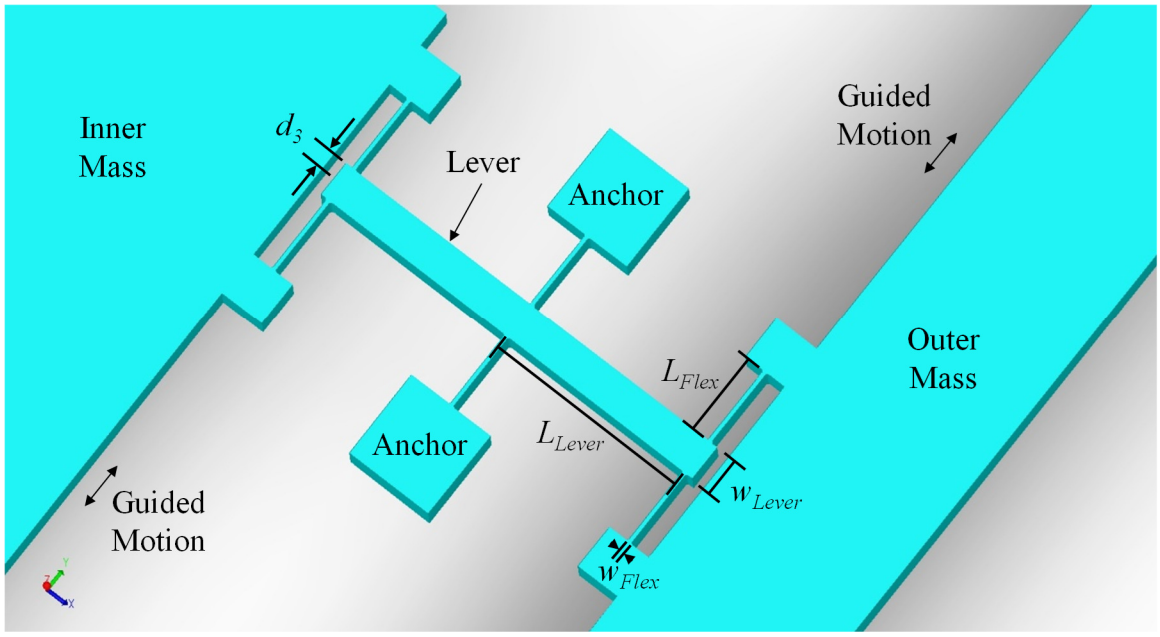

Figure 4.31 Straight Flexure Lever APLM Close-Up.

Table 4.4 Tapered Flexure Lever APLM Design Specifications.

Parameter	Label	Units	Value
Device Thickness	t	µm	100
Lever Length	L_{Lever}	µm	450
Lever Width	w_{Lever}	µm	80
Half Lever Width	d_3	µm	40
Lever to Flexure Stiffness Ratio	R	unitless	45
Flexure 1st Element Base Length	N_1	µm	58.588
Flexure 1st Element Base Width	w_{b1}	µm	7.765
Flexure 2nd Element Base Length	N_2	µm	120
Flexure 2nd Element Base Width	w_{b2}	µm	11.114
Tapered Flexure Half Hammerhead Size	d	µm	20

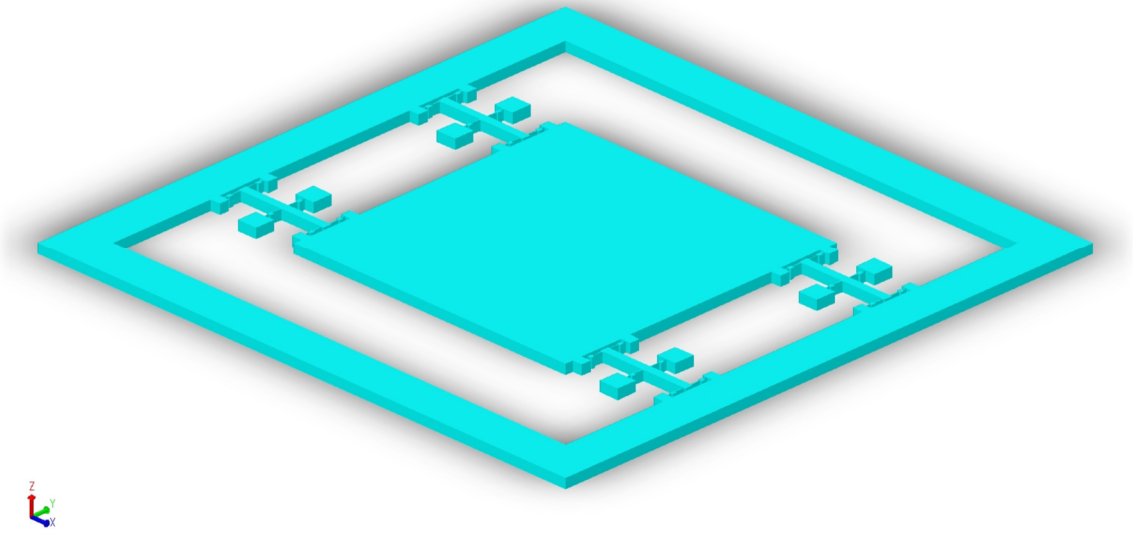

Figure 4.32 Tapered Flexure Lever CMR Solid Model.

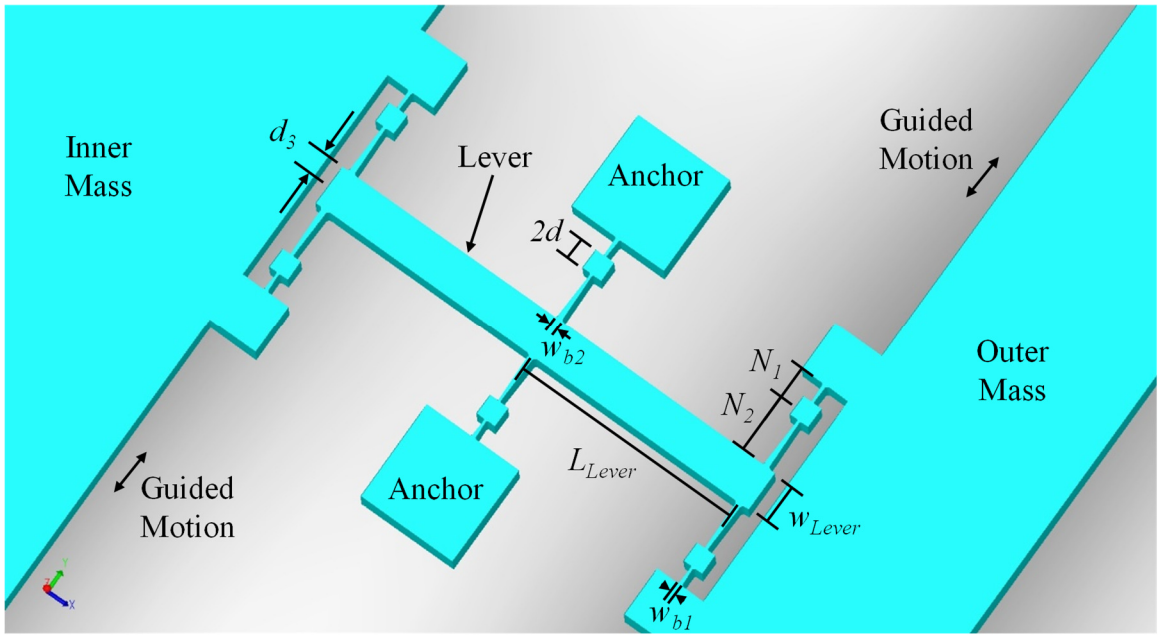

Figure 4.33 Tapered Flexure Lever APLM Close-Up.

The design procedure documented in Section 4.1.5 for the UCI inner lever coupling design was followed and resulted in the design specifications documented in Table 4.5. The solid model of the resulting device is pictured in Figure 4.34 and a close-up of the APLM is shown in Figure 4.35. Labels of the relevant feature sizes in Table 4.5 were defined in Section 4.1.5 but are repeated here in Figure 4.35 for reference.

To facilitate a reasonable comparison to the other lever-based designs, the length of the solid block, h, was chosen to be the same as the total length of the lever in the six-flexure lever designs, which was 900µm. From this value and the desire to maintain relative geometries similar to what UCI had documented in their literature [28, 90], the width of the solid block, w, was chosen to be 100µm. The length of the clamped-clamped beam, $2L$, was chosen to be the same as the total length of the flexures including the width of the lever in the six-flexure lever designs which was 218.588µm. The separation between the attachment flexures at the center of the clamped-clamped beam, $2g$, was set to be 20µm to be consistent with the values reported by UCI in the literature [28]. These values were used to calculate the width of the clamped-clamed beam according Equation 4.50 to arrive at a value of 31.681µm. No fillets were used in this design because this design incorporates only straight flexures and the motivation for the study of fillets is to compare how fillets affect the performance of tapered flexures versus that of straight flexures.

Table 4.5 UCI Inner Lever Coupling APLM Design Specifications.

Parameter	Label	Units	Value
Device Thickness	t	µm	100
Half Length of Clamped-Clamped Beam	L	µm	109.294
Width of Clamped-Clamped Beam	w_{cc}	µm	31.681
Lever Attachment Half Separation	g	µm	10
Length of Lever Block	h	µm	900
Width of the Lever Block	w	µm	100

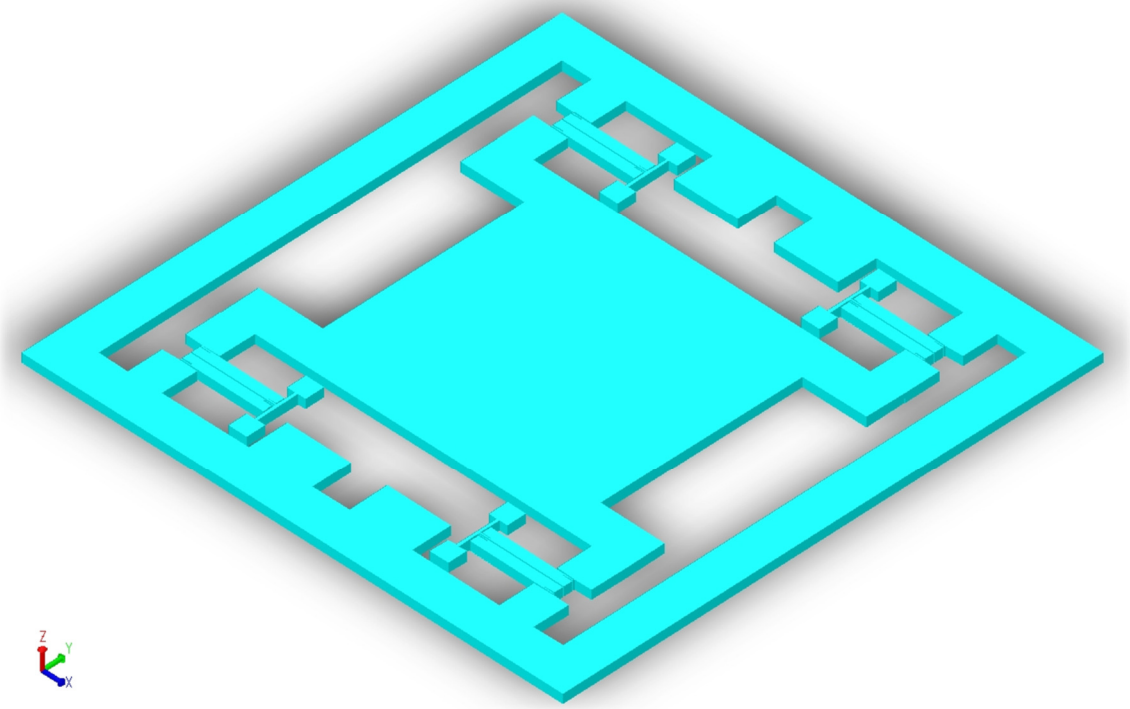

Figure 4.34 UCI Inner Lever Coupling CMR Solid Model.

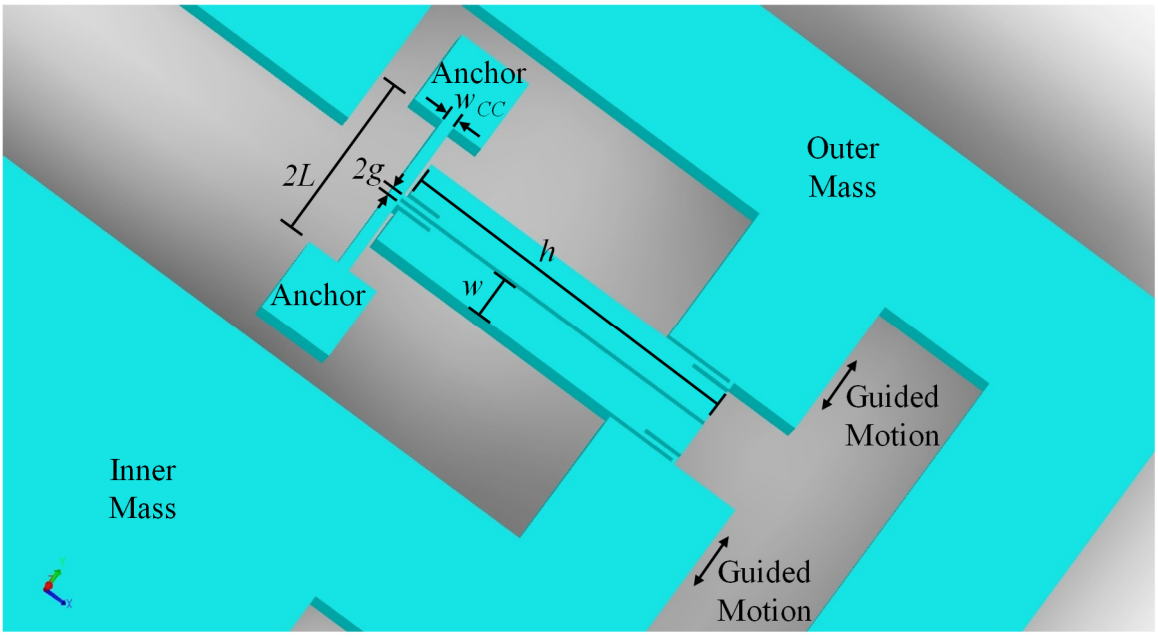

Figure 4.35 UCI Inner Lever Coupling APLM Close-Up.

The design procedure documented in Section 4.1.6 for the straight flexure revised UCI APLM design was followed and resulted in the design specifications documented in Table 4.6. The solid model of the resulting device is pictured in Figure 4.36 and a close-up of the APLM is shown in Figure 4.37. Labels of the relevant feature sizes in Table 4.6 were defined in Section 4.1.6 and are repeated in Figure 4.37 for reference.

The design procedure documented in Section 4.1.7 was also followed for the tapered flexure revised UCI APLM design and resulted in the design specifications that are documented in Table 4.7. The solid model of the resulting device is pictured in Figure 4.38 and a close-up of the APLM is shown in Figure 4.39. Once again labels of the relevant feature sizes in Table 4.7 were defined in Section 4.1.7 but are repeated in Figure 4.39 for reference.

To ensure as fair of a comparison as possible between these and the original UCI inner lever coupling design, the axial parameters of the angled flexure, *a* and *b*, were set

to the length and width of the long block in the UCI design, which were 900µm and 100µm, respectively. To accommodate the fillets and the widths of the flexures, the separation between the attachment points, d_{AF}, had to be wider than that of the original UCI design and was set to 80µm, but this difference should not be significant because the angled flexures are attaching to a solid shuttle block as opposed to a clamped-clamped beam. The dimensions of the shuttle block, L_{Blk} and w_{Blk}, were chosen to be 200µm by 200µm to accommodate the widths of the flexures and the fillets. The length of the folded flexure, L_{FF}, was set to be to be the same as the total length of the flexures including the width of the lever in the six flexure lever designs which was 218.588µm and was also the length of the clamped-clamped beam in the original UCI inner lever coupling design. The width of the folded flexures, w_{FF}, were somewhat arbitrary, but since the desire was to make these flexures relatively compliant, they were set to 10µm which is a common small feature size for Deep Reactive Ion Etch (DRIE) MEMS devices.

For the tapered flexure design, the half-length of the hammerhead feature was chosen to be relatively small, just 50µm, to highlight the thermoelastic damping performance benefit of the tapered flexure over that of the straight flexure. All other parameters of the designs followed from these dimension selections using the design procedure documented previously.

Table 4.6 Straight Flexure Revised UCI APLM Design Specifications.

Parameter	Label	Units	Straight Flexure Design
Device Thickness	t	µm	100
Angled Flexure Length	L_{AF}	µm	905.539
Angled Flexure Width	w_{AF}	µm	30.471
Shuttle Block Width	w_{Blk}	µm	200
Shuttle Block Length	L_{Blk}	µm	200
Folded Flexure Width	w_{FF}	µm	10
Folded Flexure Length	L_{FF}	µm	218.588
Angled Flexure Attachment Separation	d_{AF}	µm	80
Angled Flexure X-axis Dimension	a	µm	900
Angled Flexure Y-axis Dimension	b	µm	100

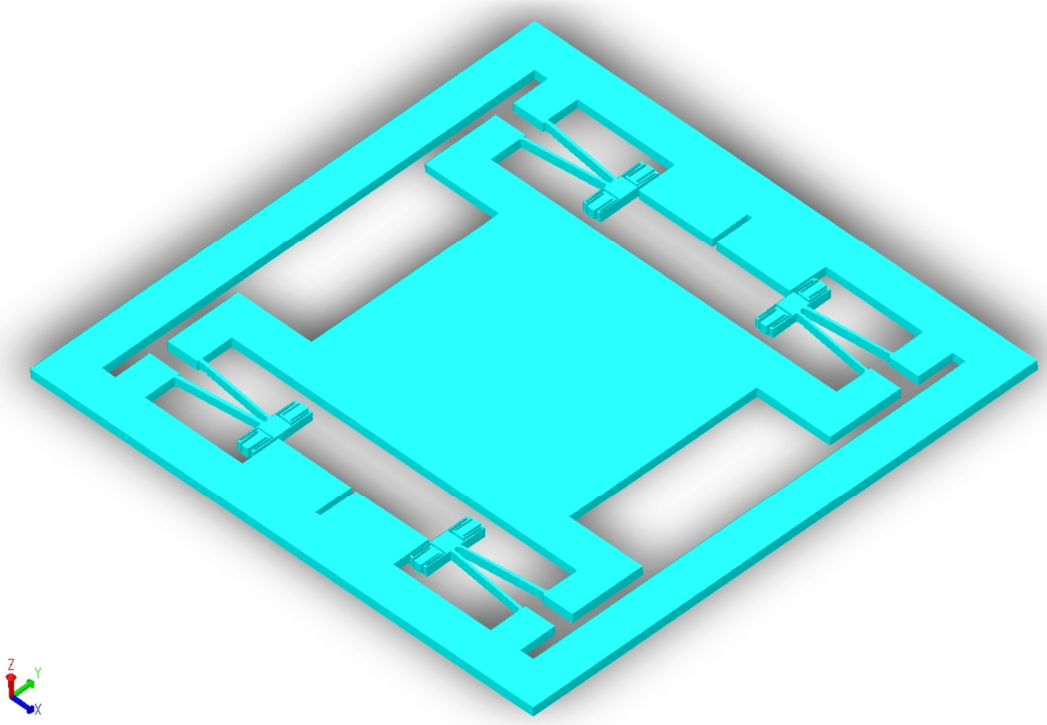

Figure 4.36 Straight Flexure Revised UCI CMR Solid Model.

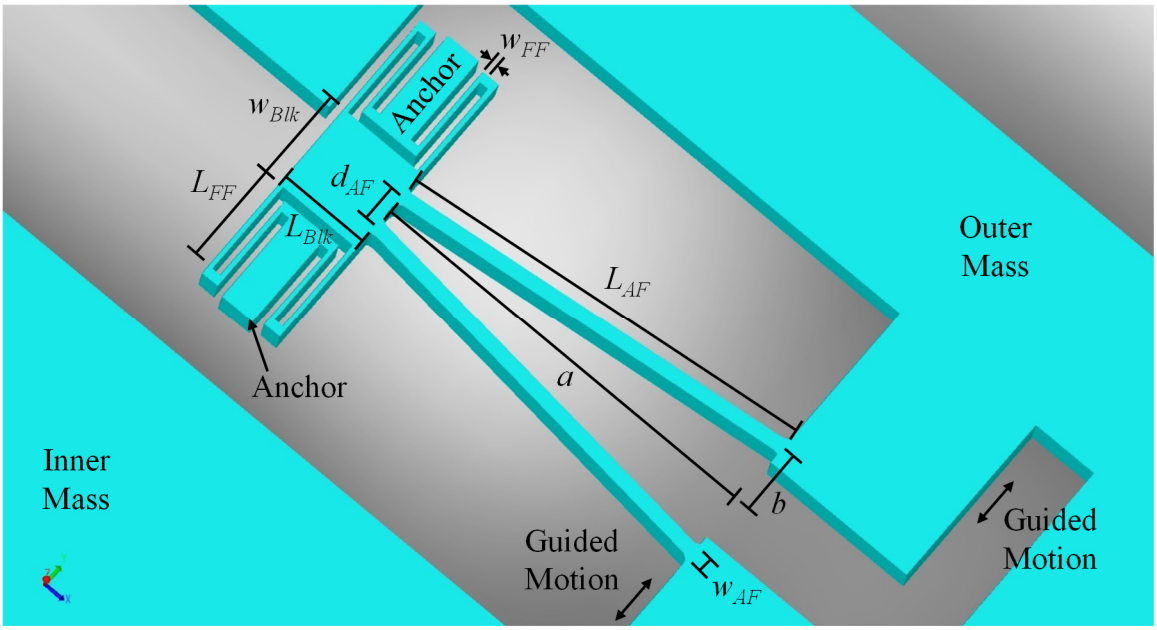

Figure 4.37 Straight Flexure Revised UCI APLM Close-Up.

Table 4.7 Tapered Flexure Revised UCI APLM Design Specifications.

Parameter	Label	Units	Tapered Flexure Design
Device Thickness	t	µm	100
Angled Flexure Length	L_{AF}	µm	402.769
Angled Flexure Width	w_{AF}	µm	37.915
Angled Flexure Hammerhead Half Width	d_{HH}	µm	50
Shuttle Block Width	w_{Blk}	µm	200
Shuttle Block Length	L_{Blk}	µm	200
Folded Flexure Width	w_{FF}	µm	10
Folded Flexure Length	L_{FF}	µm	218.588
Angled Flexure Attachment Separation	d_{AF}	µm	80
Angled Flexure X-axis Dimension	a	µm	900
Angled Flexure Y-axis Dimension	b	µm	100

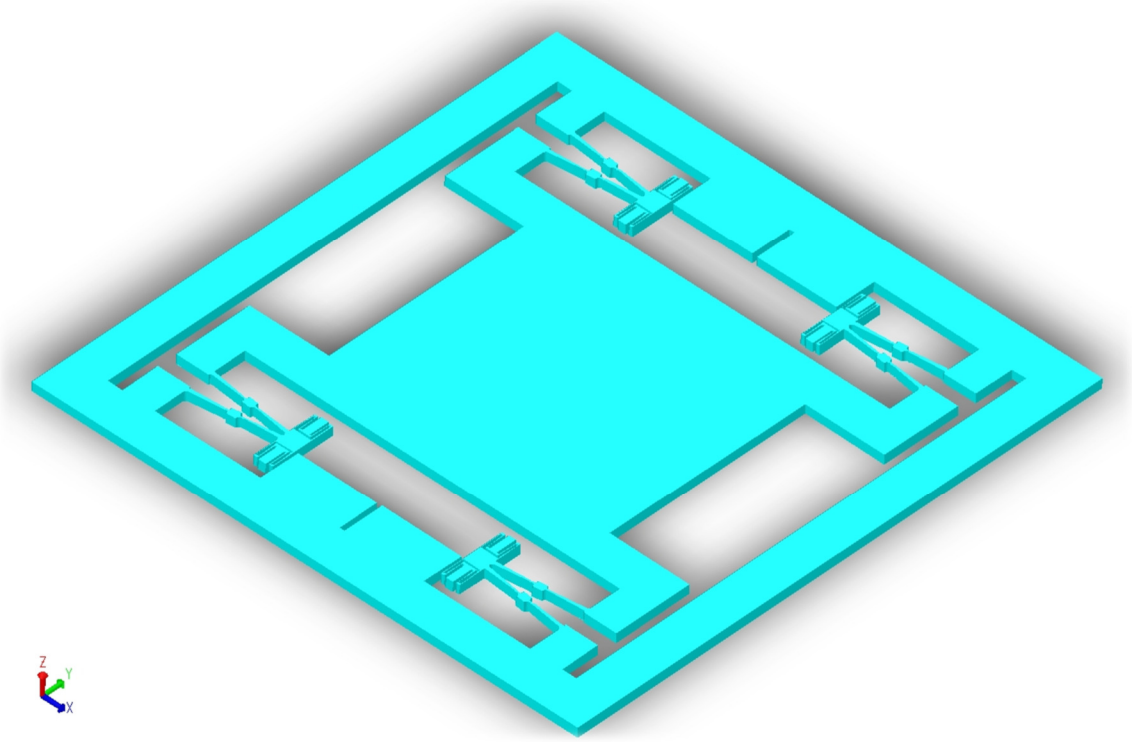

Figure 4.38 Tapered Flexure Revised UCI CMR Solid Model.

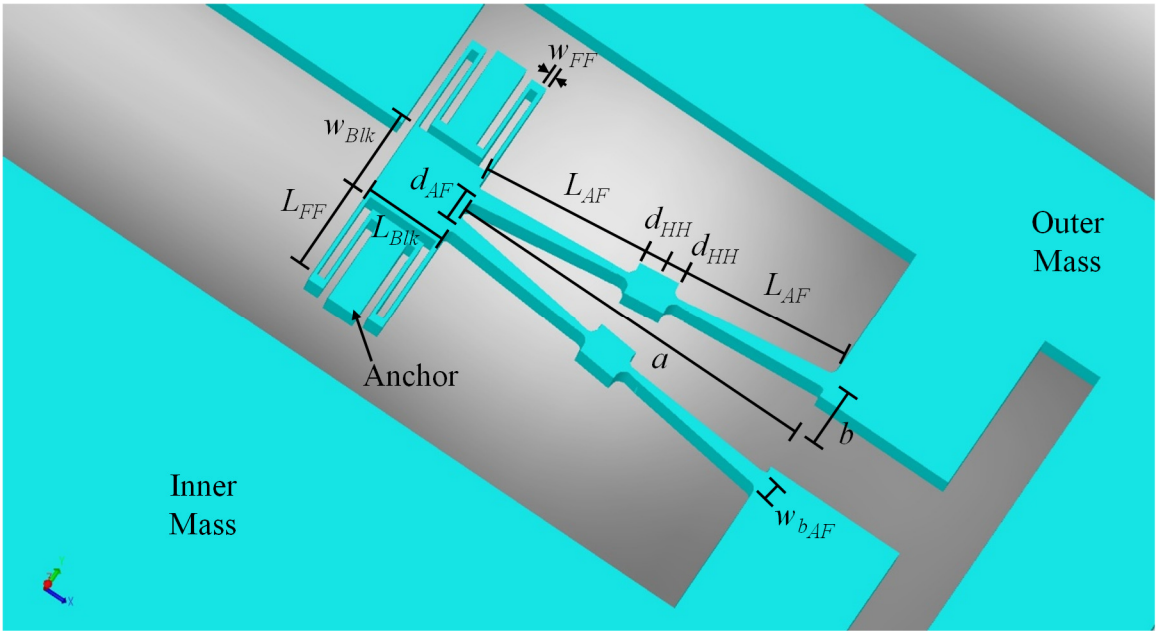

Figure 4.39 Tapered Flexure Revised UCI APLM Close-Up.

4.2.3 FEA Analyses and Results

As mentioned previously, a set of finite element analyses were performed on each of the APLM models in the concentric mass resonator configuration. These FEA analyses investigated (1) peak stress under symmetric loading conditions, (2) relative displacement of the inner and outer masses under asymmetric force loading conditions, (3) separation of anti-phase and in-phase resonant modes, and (4) thermoelastic damping of each design. This section provides a description of the analyses performed and presents the results of these analyses.

Before the finite element analyses were executed, a mesh sensitivity study was performed to determine the optimum mesher settings required to accurately estimate the desired parameters with a reasonable amount of computation time. The details of that mesh sensitivity study are provided in Section B.2 of Appendix B. The resulting mesher settings are provided in Figure 4.40. A couple of views of a representative concentric mass resonator mesh are shown in Figure 4.41 and Figure 4.42. In these figures it can be seen that these mesher settings resulted in denser meshes in and near the fillets and device edges, as well as a modest graduation of element size along the thickness of the model corresponding to the severity of typical stress gradients seen in Chapter 3.

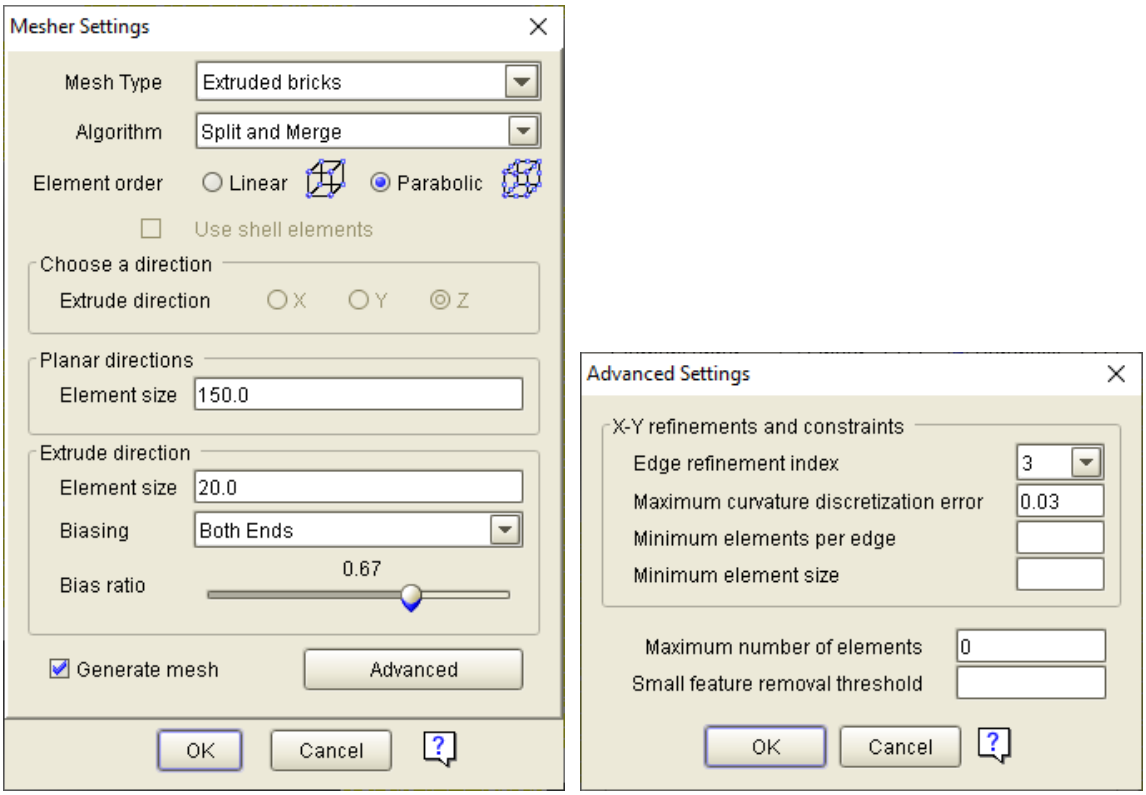

Figure 4.40 Concentric-Mass Resonator FEA Mesher Settings.

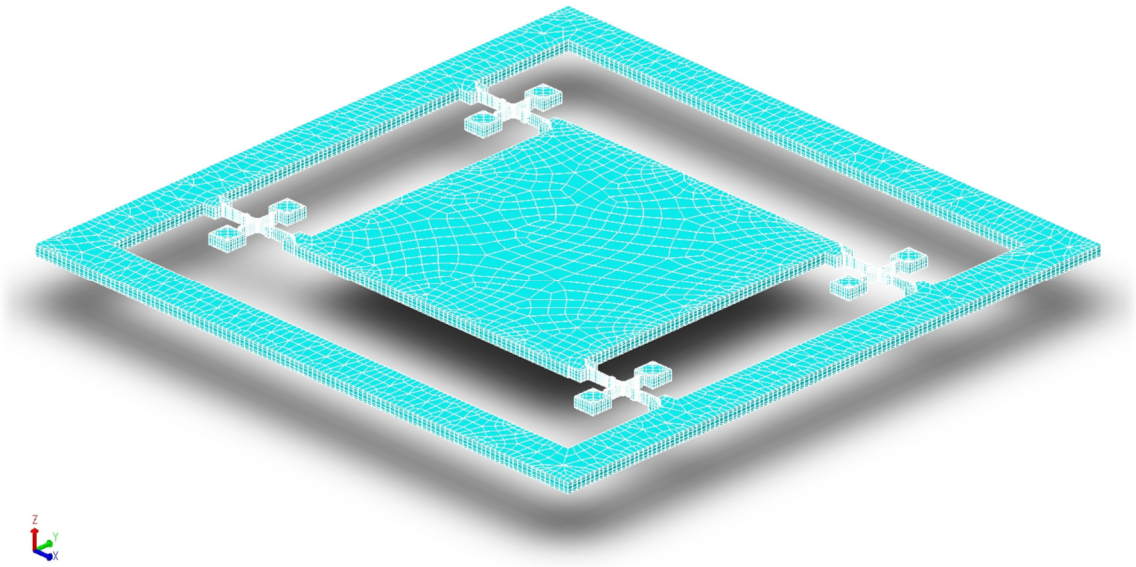

Figure 4.41 Concentric Mass Resonator Mesh for FEA, Oblique View.

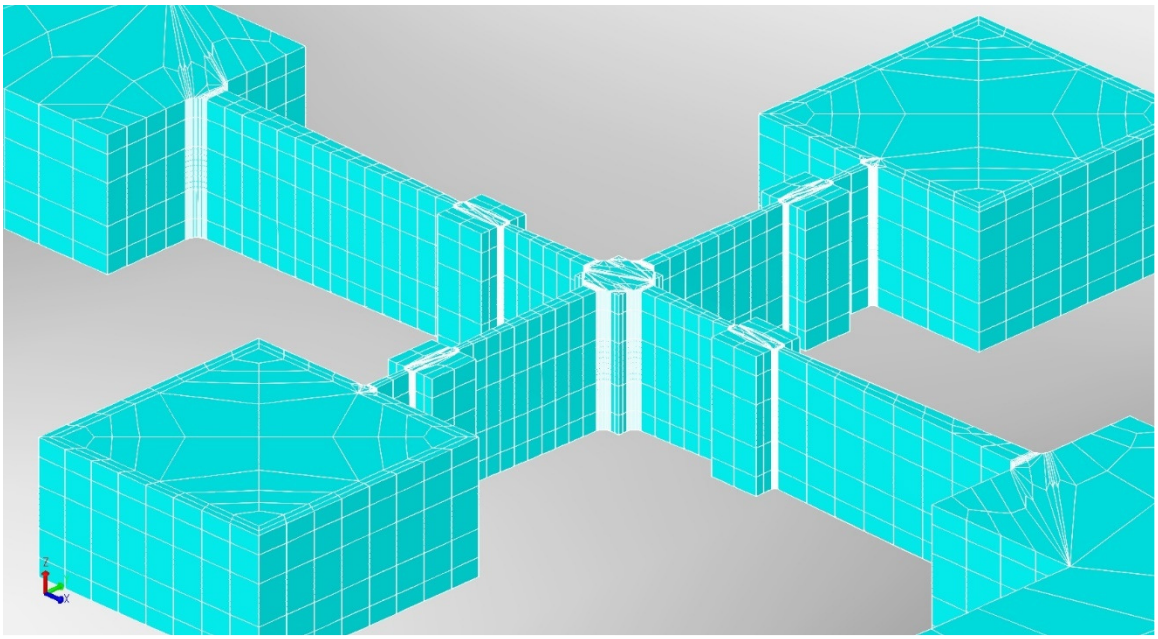

Figure 4.42 Concentric Mass Resonator Mesh for FEA, APLM View.

To compare the peak stresses under symmetric loading conditions for each of the designs, an FEA was designed to place the structures under similar loading conditions. For these analyses, the bottom of the oxide layer that attaches to the substrate, pictured in Figure 4.43 for the straight flexure pivot design, was given a *FixAll* boundary condition. Additionally, the edges of the inner and outer proof masses, pictured in Figure 4.44 for the straight flexure pivot design, were given *LoadPatch* conditions. For all designs, the outer proof mass edges were loaded with +1kPa and -1kPa. For the four-flexure pivot and six-flexure lever designs, the inner proof mass edges were loaded with +1.94365kPa and -1.94365kPa to keep the applied force the same as that applied to the outer mass. Similarly, for the UCI inner lever coupling design, the inner mass edges were loaded with +1.608538kPa and -1.608538kPa, and for the revised UCI inner lever coupling designs, the inner mass edges were loaded with +1.457738kPa and -1.457738kPa. This resulted in a net force of 600µN being applied to each proof mass for all designs.

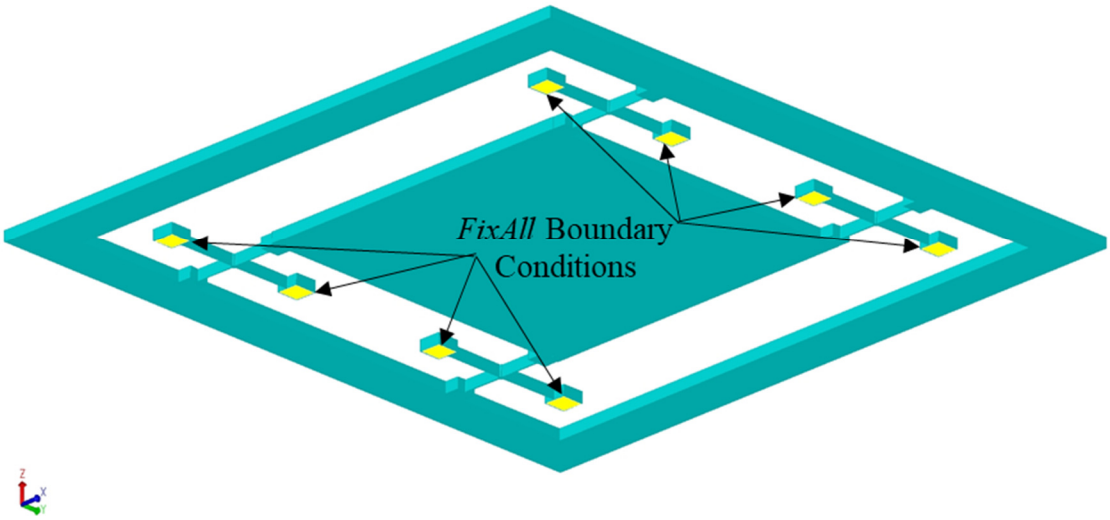

Figure 4.43 Four-Flexure Pivot *FixAll* Boundary Locations (Bottom View).

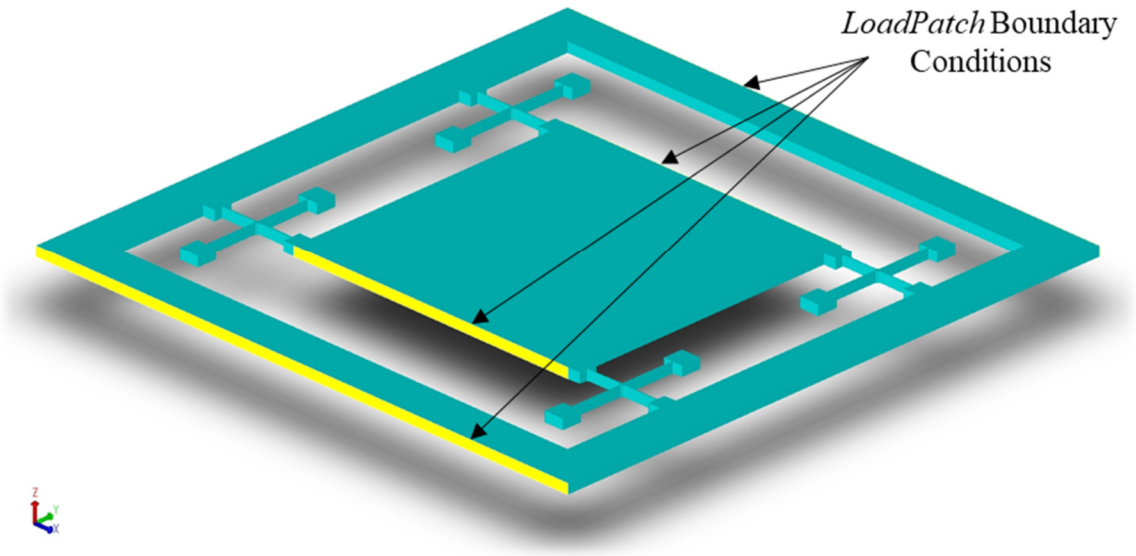

Figure 4.44 Four-Flexure Pivot *LoadPatch* Boundary Locations.

Inspection of the resulting data indicates that the stress was the highest in the center of the model along the Z-axis, as shown in Figure 4.45. Therefore, to capture the peak stress, a surface slice of data was extracted from the center of the model, as shown in Figure 4.46. The stress behavior was captured in two different ways. The first was simply a global search for the highest principal stress. This value is reported as "Peak Stress". The second, reported simply as "Stress", is a little more nuanced. As was noted in previous chapters, there is a stress peaking behavior that occurs at the location where the flexures attach to the anchor blocks or to the proof mass. It was also known that the straight flexures reach a natural maximum in stress at the attachment point independent of this stress peaking behavior. It was desirable to estimate the natural stress at the attachment point without the influence of the stress peaking behavior. This was accomplished by using data a small distance away from the attachment point (away from the stress peaking behavior) and calculating a linear fit of stress versus location. This fit was then extrapolated back to the attachment point. The exact range of locations used for each curve fit was unique for each case and determined by a visual inspection of the data using engineering judgement. Figure 4.47 shows a typical outline of the locations of the data points along the outer edge of the flexure structure around the point of interest. Figure 4.48 shows a typical set of data around the point of interest and highlights the range of data used for the curve fit calculation as well as the extrapolated line that provided the estimate of the stress at the attachment point. The geometry and dimensions of the tapered flexures were painstakingly designed to have constant stress on the outer edge of the flexure, which makes it unnecessary to apply this technique to the tapered flexures under symmetric loading conditions. However, under asymmetric loading

conditions, the stress on the outer edge of the tapered flexure was not necessarily constant. For this reason and to maintain consistency in the data analysis between flexure types and loading conditions, the extrapolated curve fit approach to estimate stress was applied to the tapered flexures under symmetric loading conditions as well.

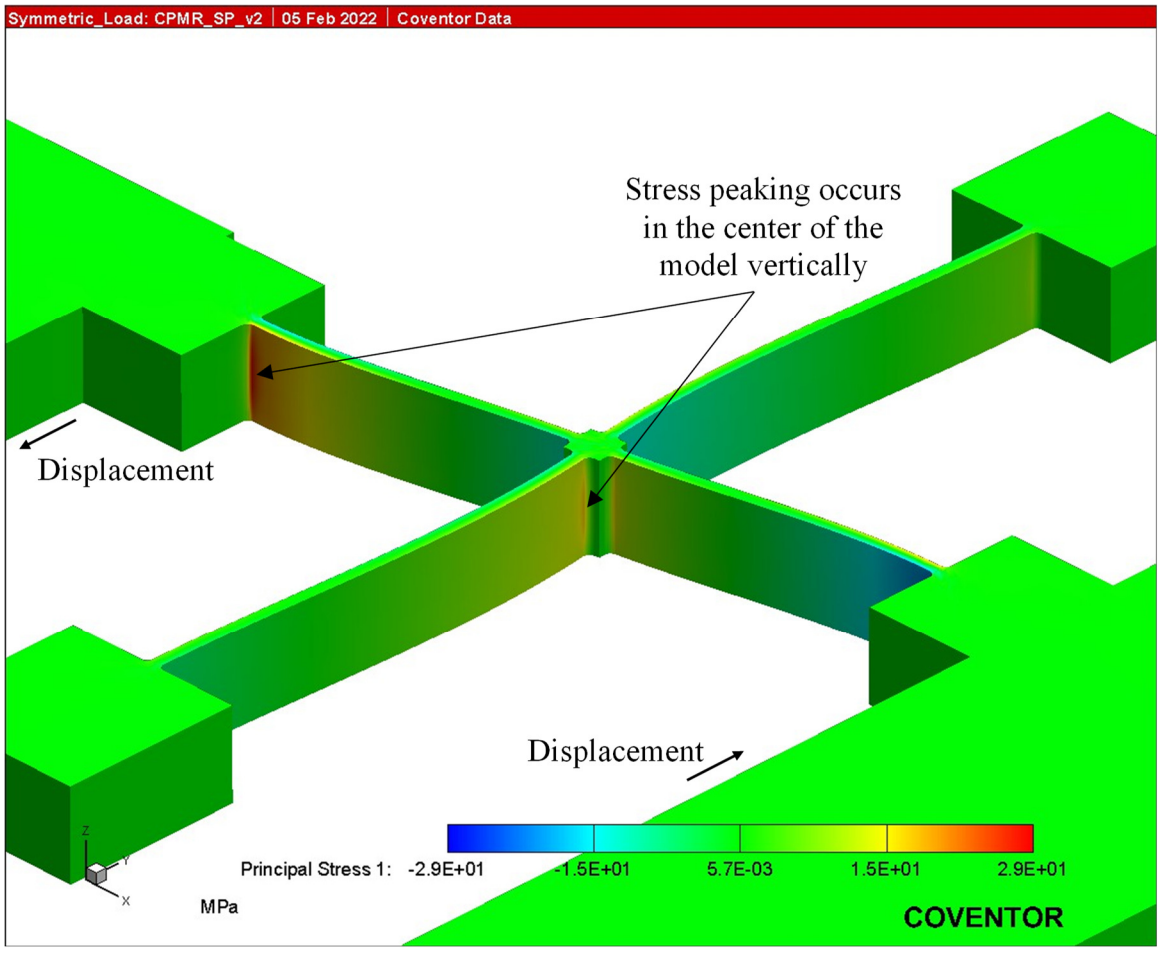

Figure 4.45 Stress Peaking in Center of Model Along the Z-axis.

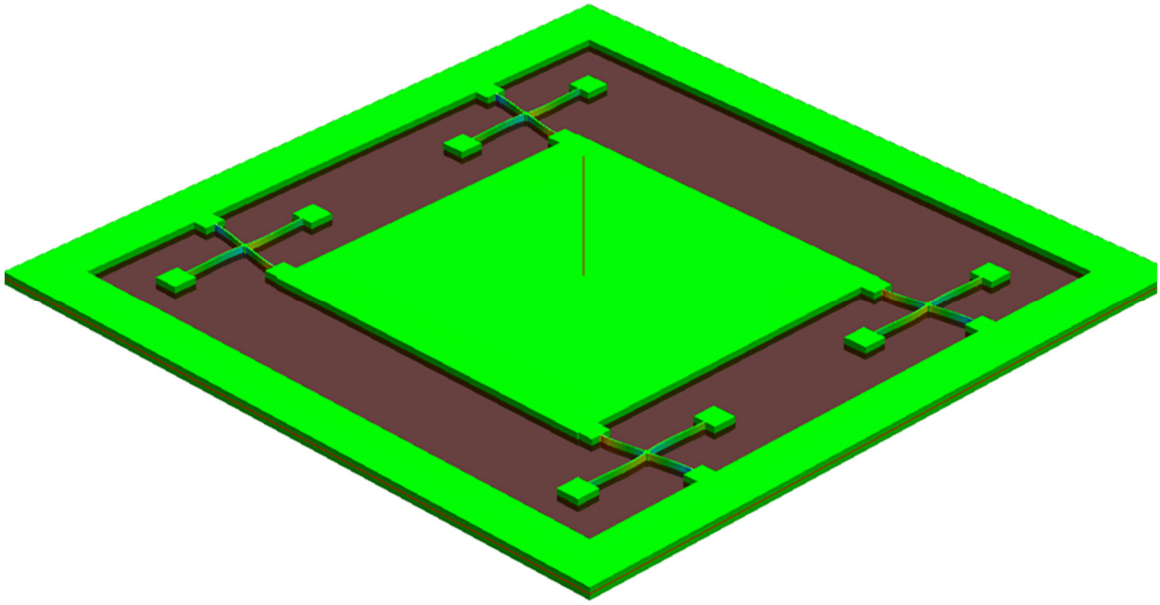

Figure 4.46 Data Slice Location to Capture Peak Stress.
The location of the planar surface data slice is pictured by the brown plane and is shown cutting through the center of the model vertically. Since the peak stress was known to occur in the vertical center of the model faces, this data slice made data processing less cumbersome than working with the global set of data.

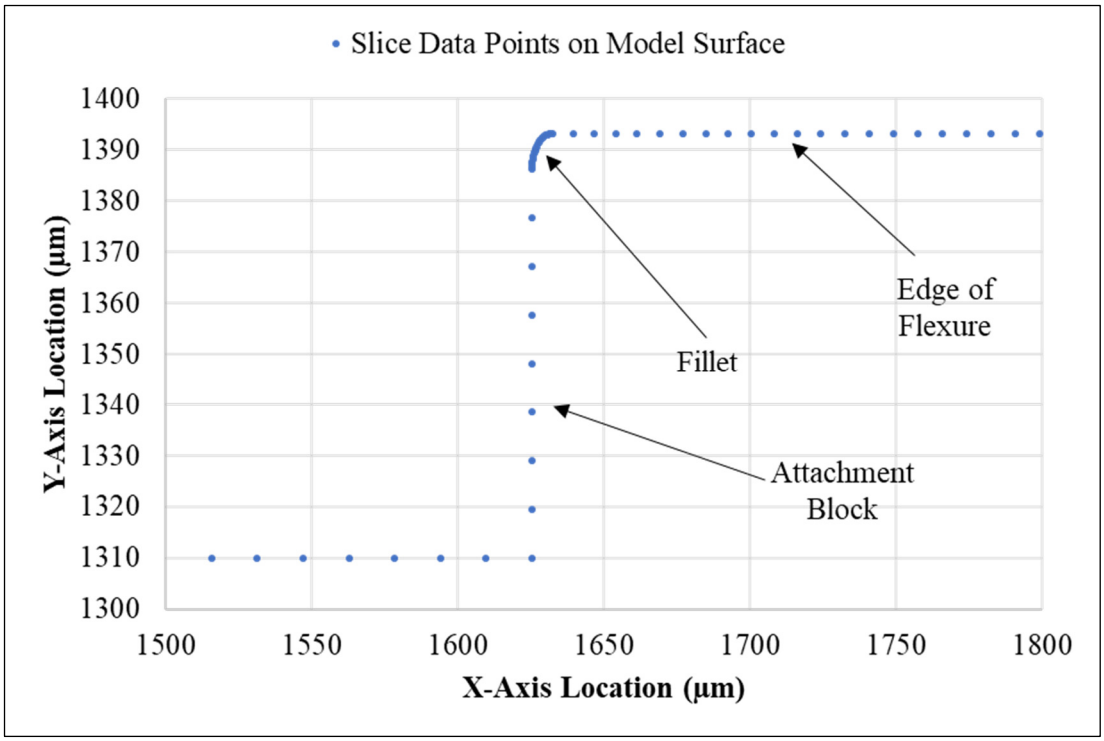

Figure 4.47 Typical Data Slice Point Locations Around Flexure Attachment Point.
This figure shows the locations of the individual data points in the planar surface data slice near one of the flexure attachment points. The figure shows the highest density of data points (corresponding to the finite elements) in the fillet with the flexure having the second highest density of data points. The attachment block had the lowest density of data points.

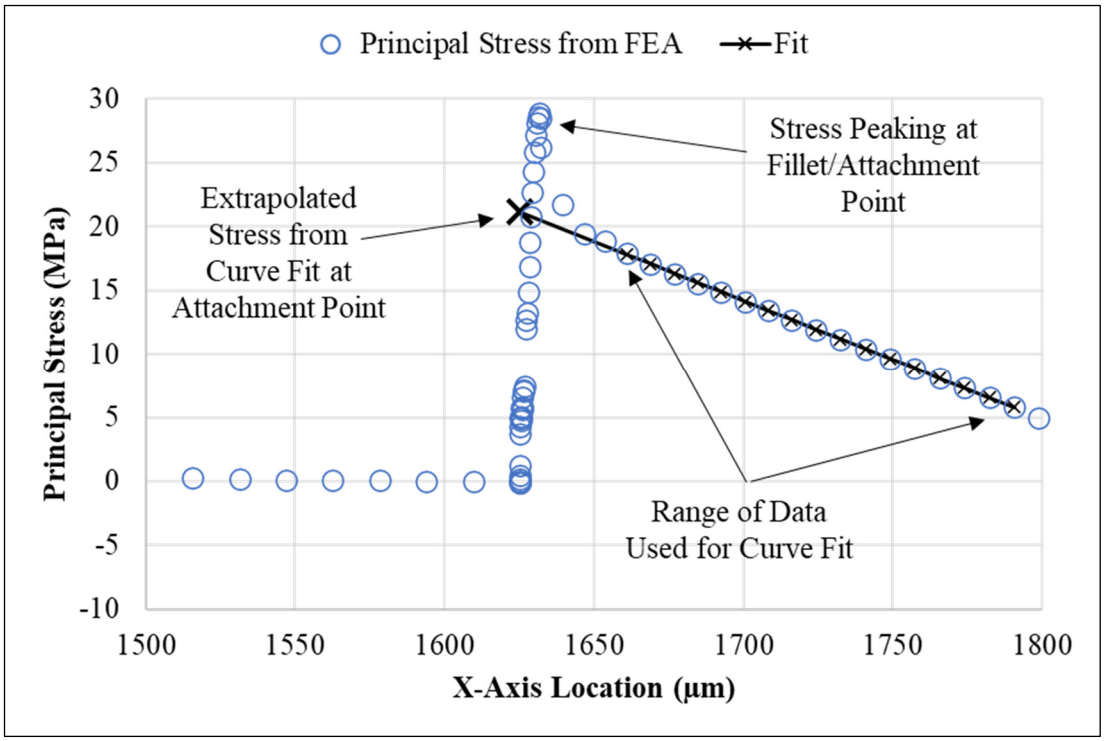

Figure 4.48 Principal Stress Data Points and Typical Curve Fit.
This figure highlights the distinction between what is being reported as "stress" and "peak stress". The "peak stress" is the absolute peak stress that includes the effects of stress peaking in the inner corner whereas "stress" is an estimate of the surface stress in the flexure at the base of the flexure without the effects of the stress peaking in the inner corner. This estimate is obtained through linear extrapolation of surface stress data in the flexure some distance away from the inner corner.

The primary results of the FEA analyses to determine peak stress under symmetric loading conditions are presented in Table 4.8. The data indicate that the tapered flexure designs have consistently lower stress than the equivalent straight flexure designs, reducing the Peak Stress by 30% and the Stress by 37% on average. The data also indicate that the six-flexure lever designs display the highest stress levels, and the revised UCI designs display the lowest stress levels. A slight variation in the displacements across the designs is noted stemming from the additional masses added to some designs to accommodate attachment points of the APLM geometries.

Table 4.8 Symmetric Loading Conditions FEA Results.

APLM Design	Displacement (μm)	Peak Stress (MPa)	Stress (MPa)
Straight Flexure Pivot	0.574	29.0	21.1
Tapered Flexure Pivot	0.557	21.1	12.7
Straight Flexure Lever	0.533	35.0	27.3
Tapered Flexure Lever	0.536	24.8	16.9
UCI Inner Lever Coupling	0.503	26.4	10.9
Straight Flexure Revised UCI	0.447	10.8	8.1
Tapered Flexure Revised UCI	0.449	7.3	5.3

For completeness, Figures 4.49 - 4.55 indicate the location of the measurement of the stress and the peak stress for each of the designs. For the UCI inner lever coupling design, the peak stress may be a little misrepresentative because it did not occur in the main clamped-clamped beam, but instead occurred in one of the tethers that connect one of the connector blocks to the proof mass. Additionally, the stress in the UCI inner lever coupling design was reported at the location where the clamped-clamped beam connects to an anchor as shown in Figure 4.55 but the peak stress in the clamped-clamped beam actually occurred in the center of the beam between the two tether connectors. It is important to recall here that no fillets were incorporated into the UCI inner lever coupling design and it is likely that the peak stress between the two tethers could have been significantly reduced using a combination of fillets and iterating the separation distance of the tether connectors. Therefore, it was decided that the location where the clamped-clamped beam attaches to the anchor block is the most representative location to use to characterize the typical stress for that design.

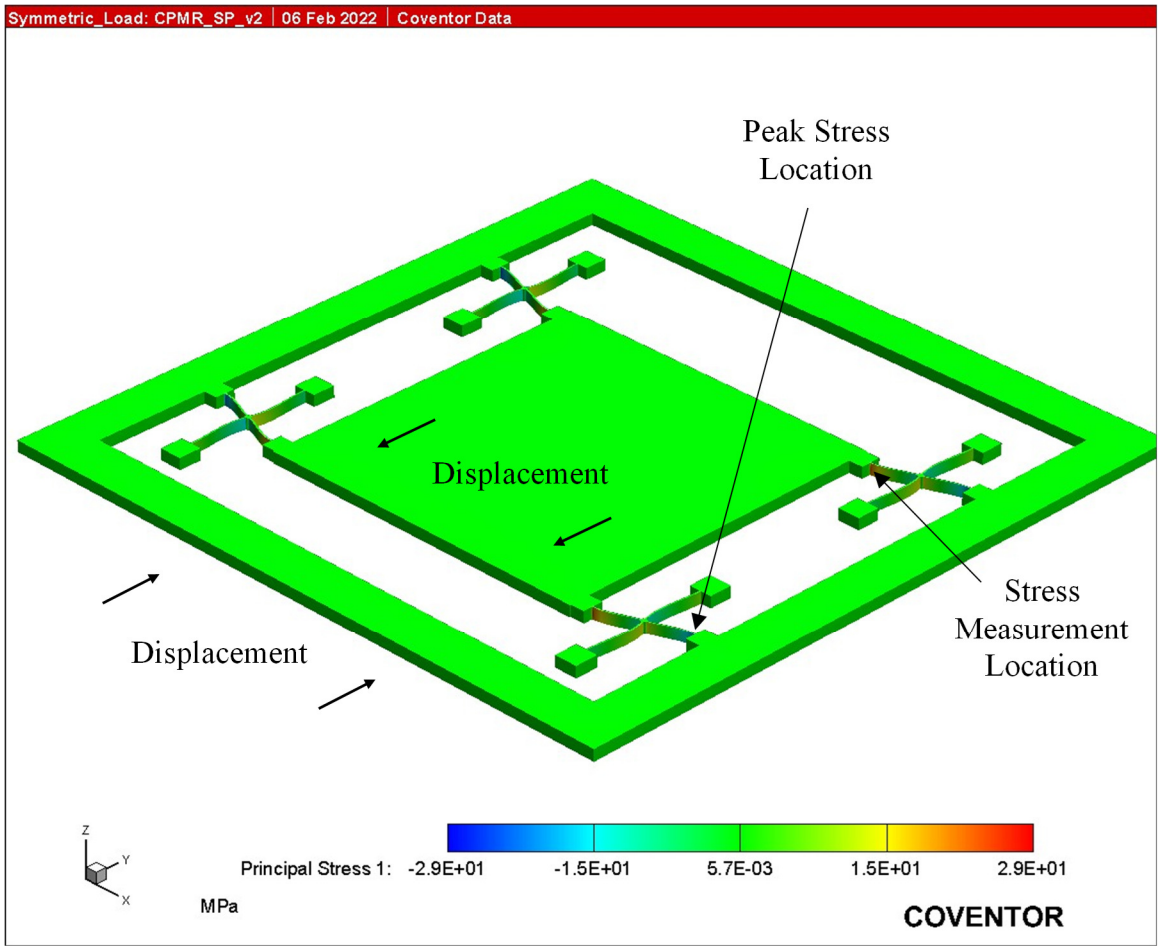

Figure 4.49 Straight Flexure Pivot Peak Stress Location Under Symmetric Load.

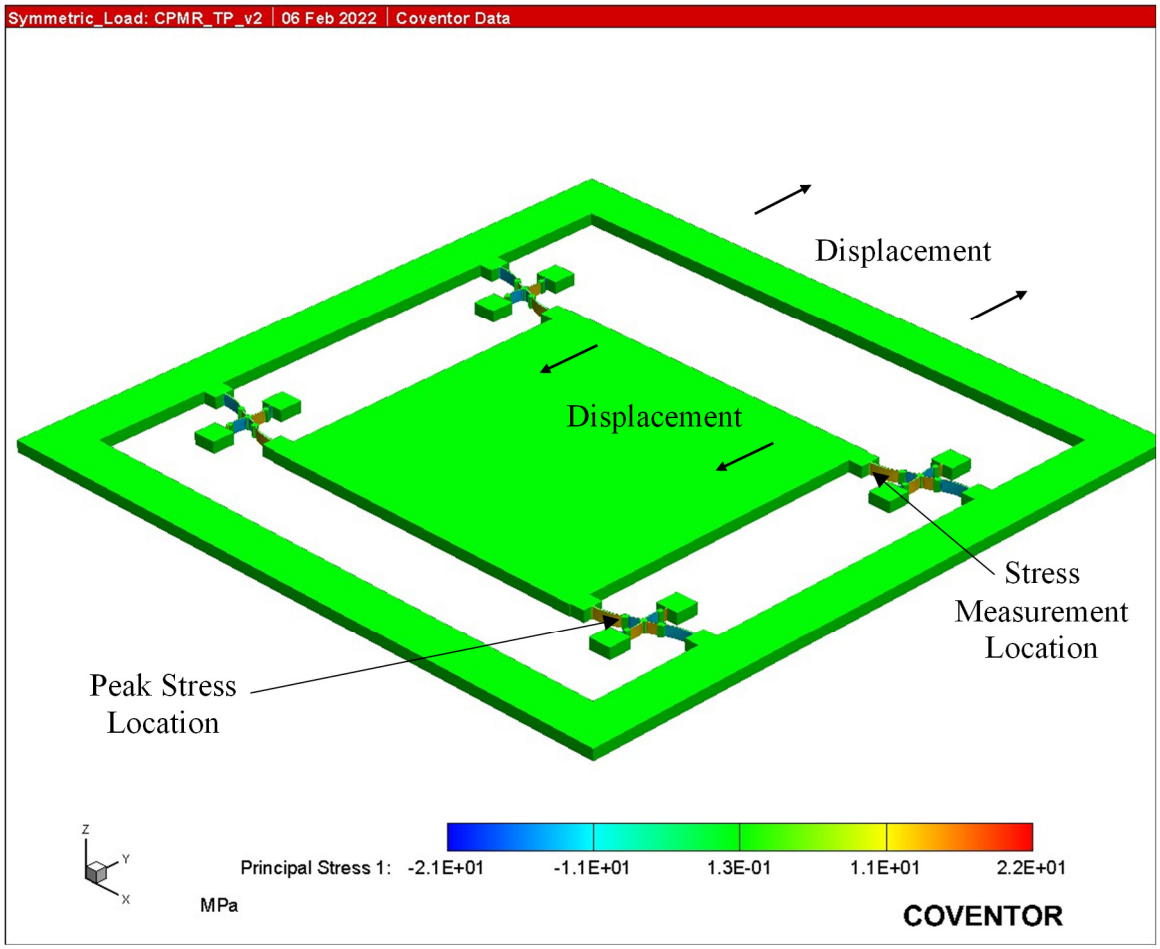

Figure 4.50 Tapered Flexure Pivot Peak Stress Location Under Symmetric Load.

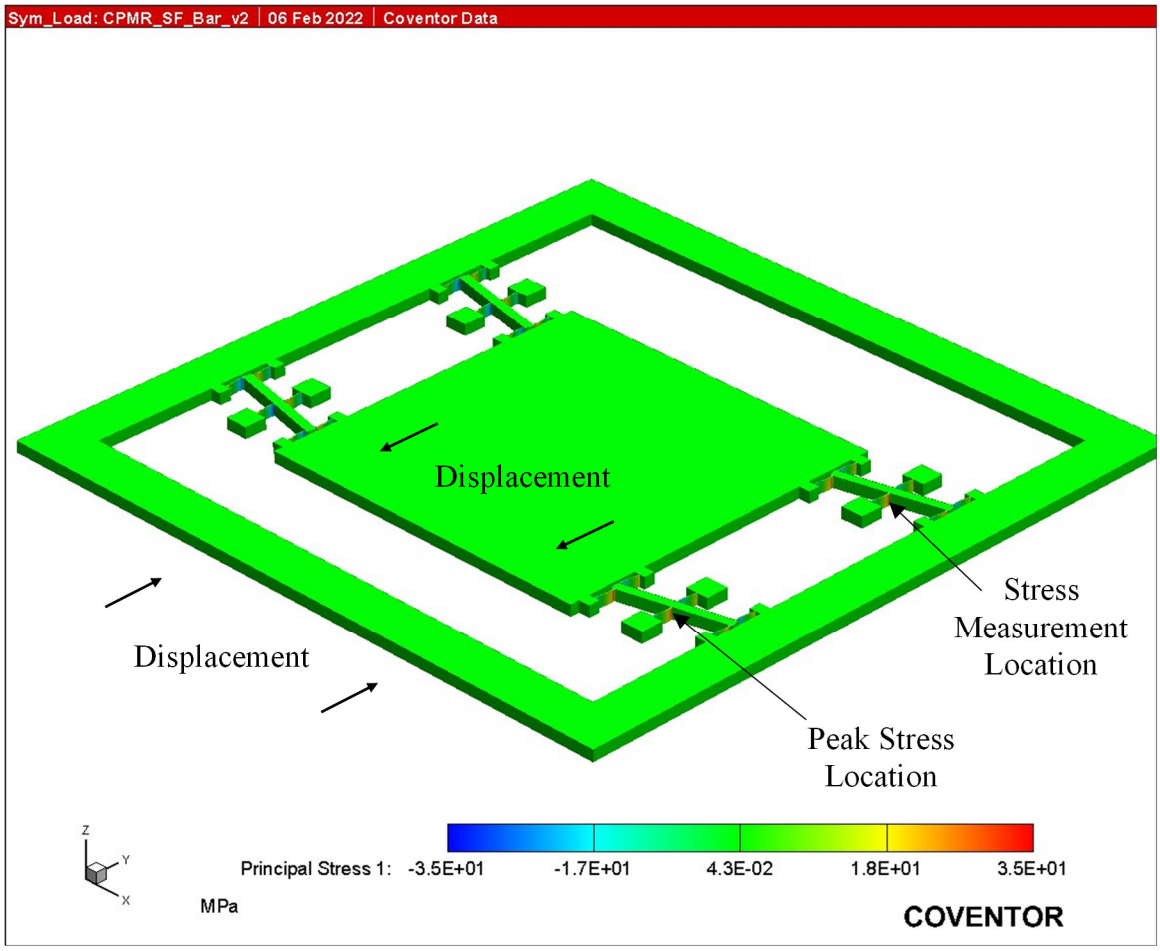

Figure 4.51 Straight Flexure Lever Peak Stress Location Under Symmetric Load.

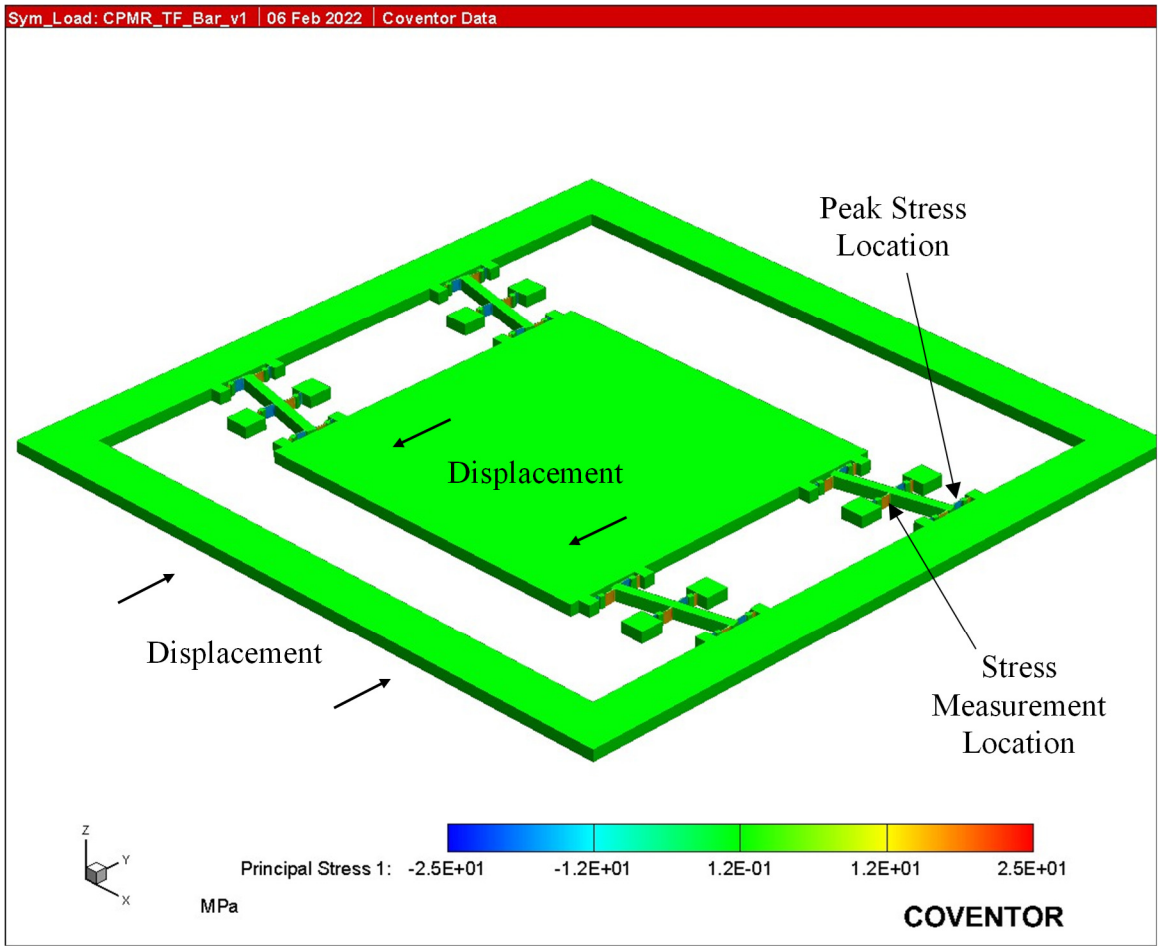

Figure 4.52 Tapered Flexure Lever Peak Stress Location Under Symmetric Load.

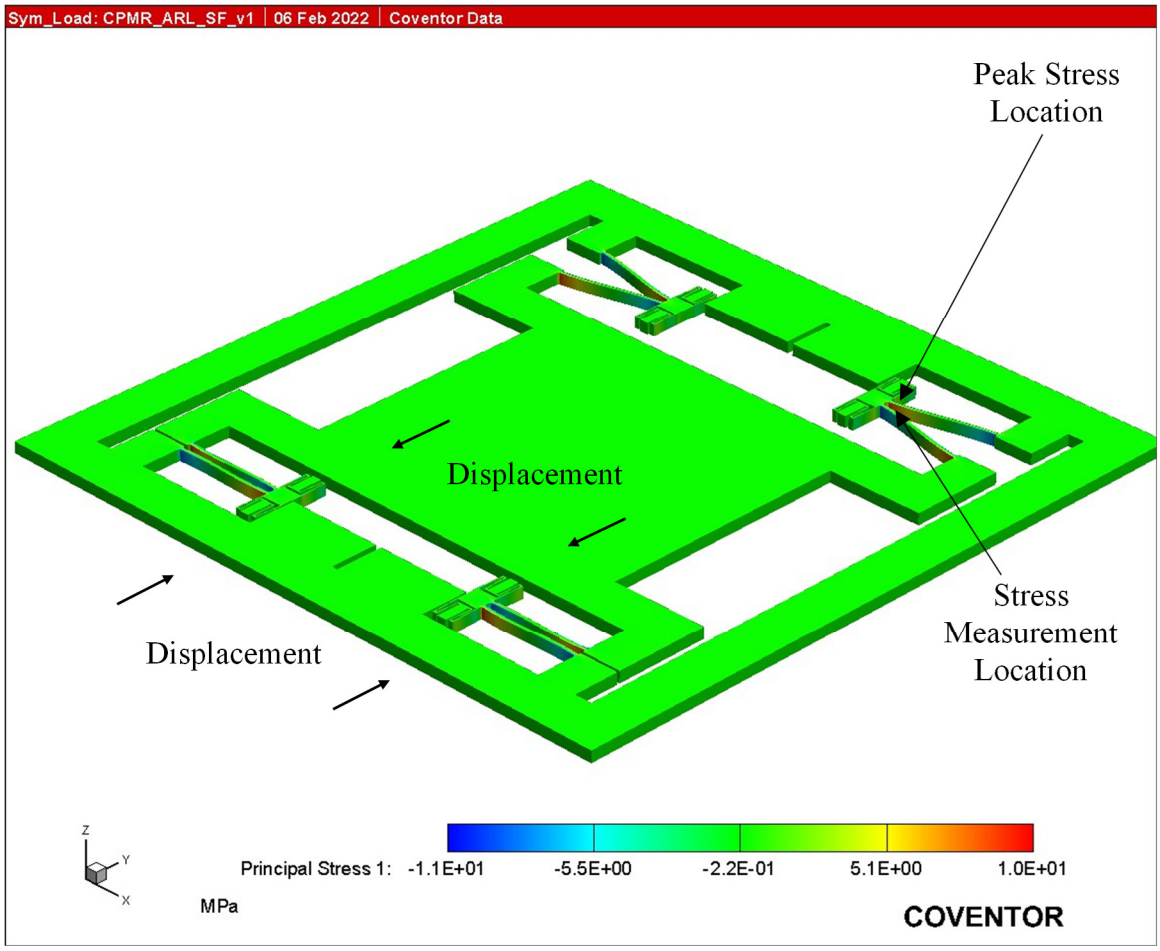

Figure 4.53 Straight Flexure Revised UCI Peak Stress Location Under Symmetric Load.

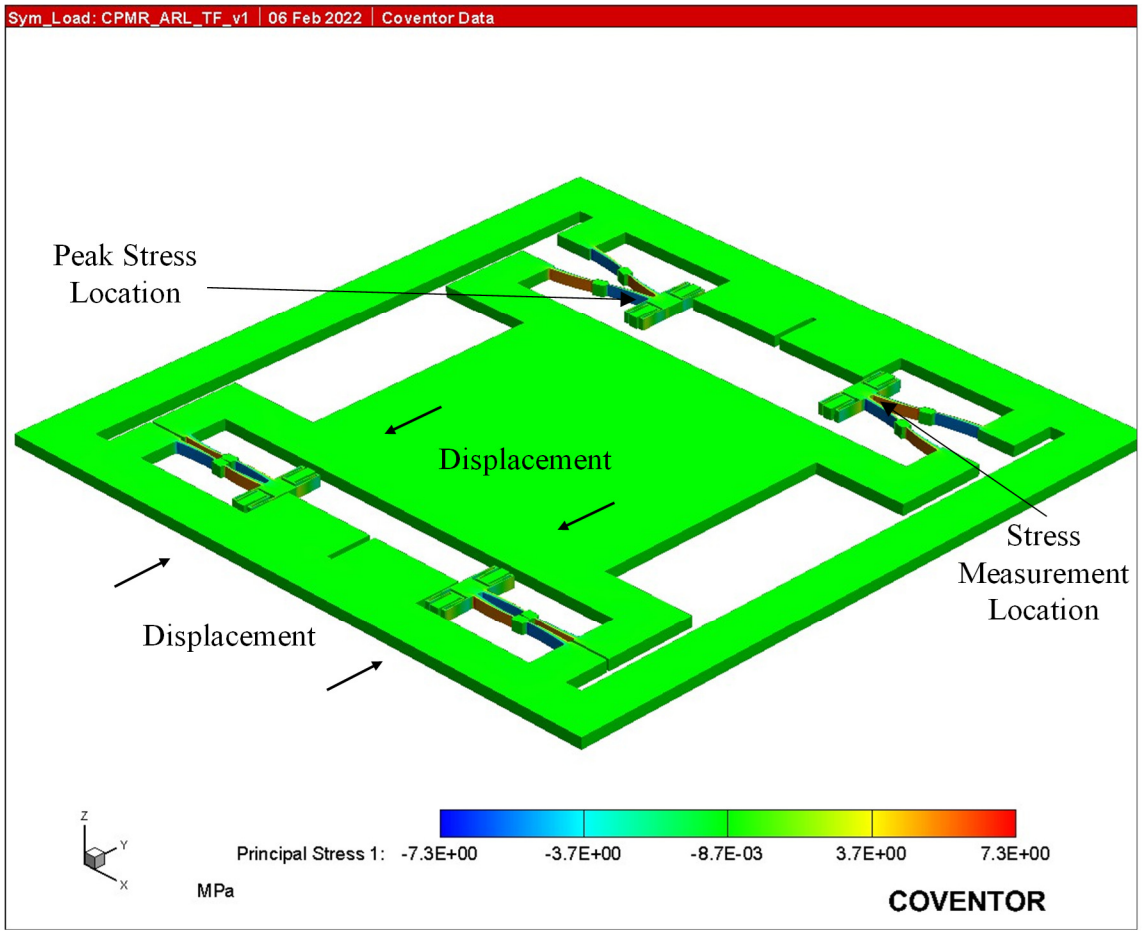

Figure 4.54 Tapered Flexure Revised UCI Peak Stress Location Under Symmetric Load.

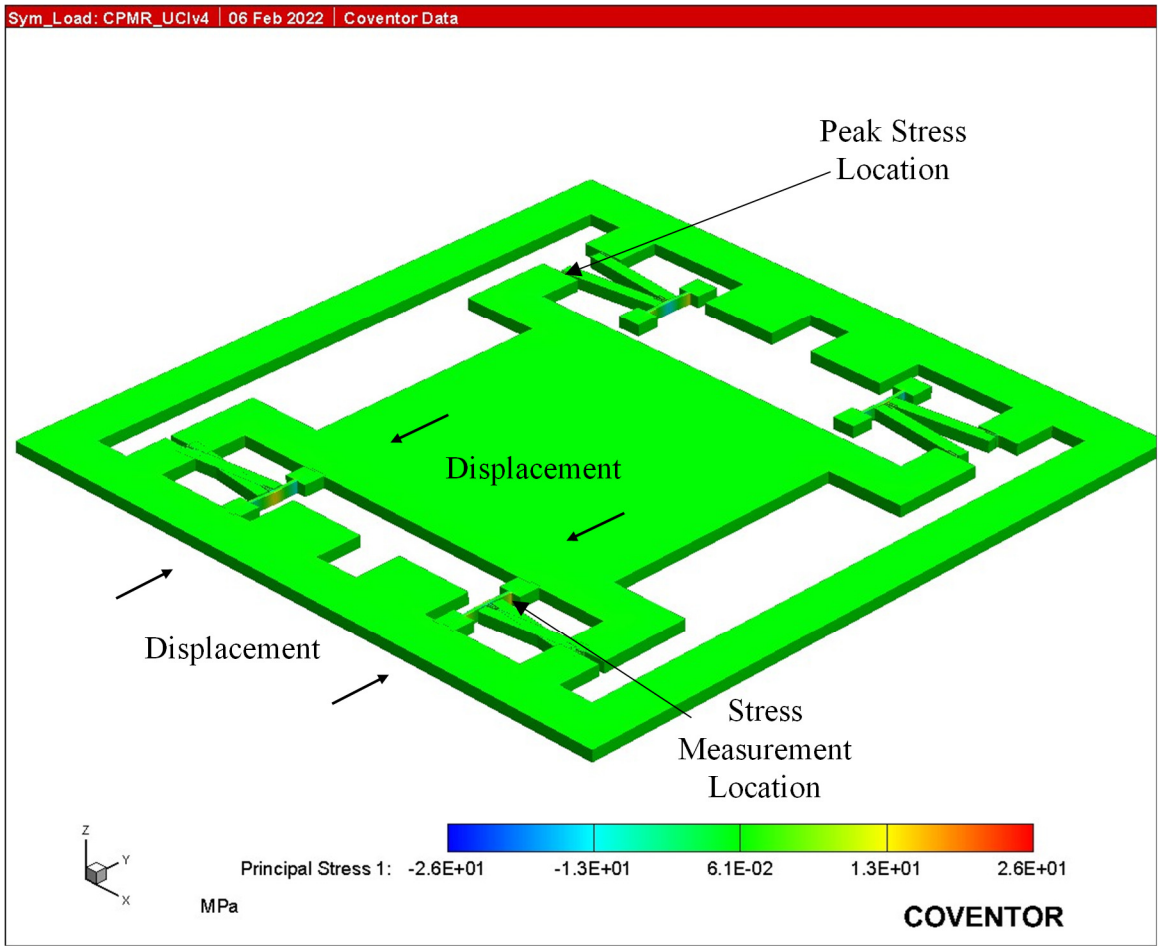

Figure 4.55 UCI Inner Lever Coupling Peak Stress Location Under Symmetric Load.

To compare the relative displacements under asymmetric loading conditions for each of the designs, an FEA was designed to place each of the structures under similar, asymmetric loading conditions. Similar to the symmetric loading FEAs, the bottom of the oxide layer that attaches to the substrate was given a *FixAll* boundary condition, as was pictured in Figure 4.43 for the straight flexure pivot design. For the asymmetric loading condition, however, only the edges of the outer proof mass were given *LoadPatch* conditions, similar to what was pictured in Figure 4.44. For all designs, the outer proof mass edges were loaded with +1kPa and -1kPa. This resulted in a net force of 600µN being applied to the outer proof mass for all designs.

The primary results of the FEA analyses are presented in Table 4.9. Here the definitions of peak stress and stress are the same as in the discussion for symmetric loading conditions. Once again, the data indicate that the tapered flexure designs have significantly lower stress than the equivalent straight flexure designs with the only exception being the peak stress for the tapered flexure pivot design. This design also demonstrated the worst coupling of the outer mass to the inner mass. The data also indicate that the four-flexure pivot designs generally demonstrate the highest stress levels with the lowest inter-mass coupling and the revised UCI designs demonstrate the lowest stress with a modest inter-mass coupling. The six-flexure lever designs consistently demonstrate the best inter-mass coupling (nearly one-for-one) with modest stress levels.

Table 4.9 Asymmetric Loading Condition FEA Results.

APLM Design	**Outer Mass Disp.** (μm)	**Inner Mass Disp.** (μm)	**Relative Disp.** (%)	**Peak Stress** (MPa)	**Stress** (MPa)
Straight Four-Flexure Pivot	0.436	-0.139	31.9	25.709	19.098
Tapered Four-Flexure Pivot	0.465	-0.092	19.8	28.198	15.669
Straight Six-Flexure Lever	0.274	-0.260	95.0	18.001	13.976
Tapered Six-Flexure Lever	0.275	-0.262	95.0	13.045	8.690
UCI Inner Lever Coupling	0.318	-0.183	57.4	23.077	12.653
Straight Flexure Revised UCI	0.282	-0.165	58.6	6.796	5.609
Tapered Flexure Revised UCI	0.284	-0.165	58.1	5.526	4.188

For completeness, Figures 4.56 - 4.62 indicate the location of the measurement of the peak stress for each of the designs. For this analysis the stress was estimated from the same flexure as the peak stress except for the UCI inner lever coupling design. For the

UCI inner lever coupling design, the peak stress again occurred in one of the tethers rather than in the clamped-clamped beam. Additionally, unlike the symmetric load case, the stress in the UCI inner lever coupling design for the asymmetric load case was expected to occur in the center of the clamped-clamped beam between the connection points of the two tethers. More specifically, it was expected that the highest stress location would be where the outer proof mass tether connected to the clamped-clamped beam as depicted in Figure 4.63, which is where the stress was estimated. Once again, no fillets were incorporated into the UCI inner lever coupling design and it is likely that the peak stress between the two tethers could have been significantly reduced using a combination of fillets and iterating the separation distance of the tether connectors.

A significant finding is that the tapered flexure lever design demonstrated nearly one-to-one displacement of the two proof masses and continued to exhibit uniform stress along the length of the flexure. Additionally, all tapered flexures in the tapered flexure lever design exhibited the same stress under the asymmetric load. This is shown in Figure 4.64. This was not the case for any other design except the straight flexure lever design. This is because the stiff lever equally distributes the load to all six flexures in the six-flexure lever designs which maintains their loading characteristics within the design intent, whereas asymmetric loading on the other APLM designs creates asymmetric loading on the flexures inconsistent with the design intent.

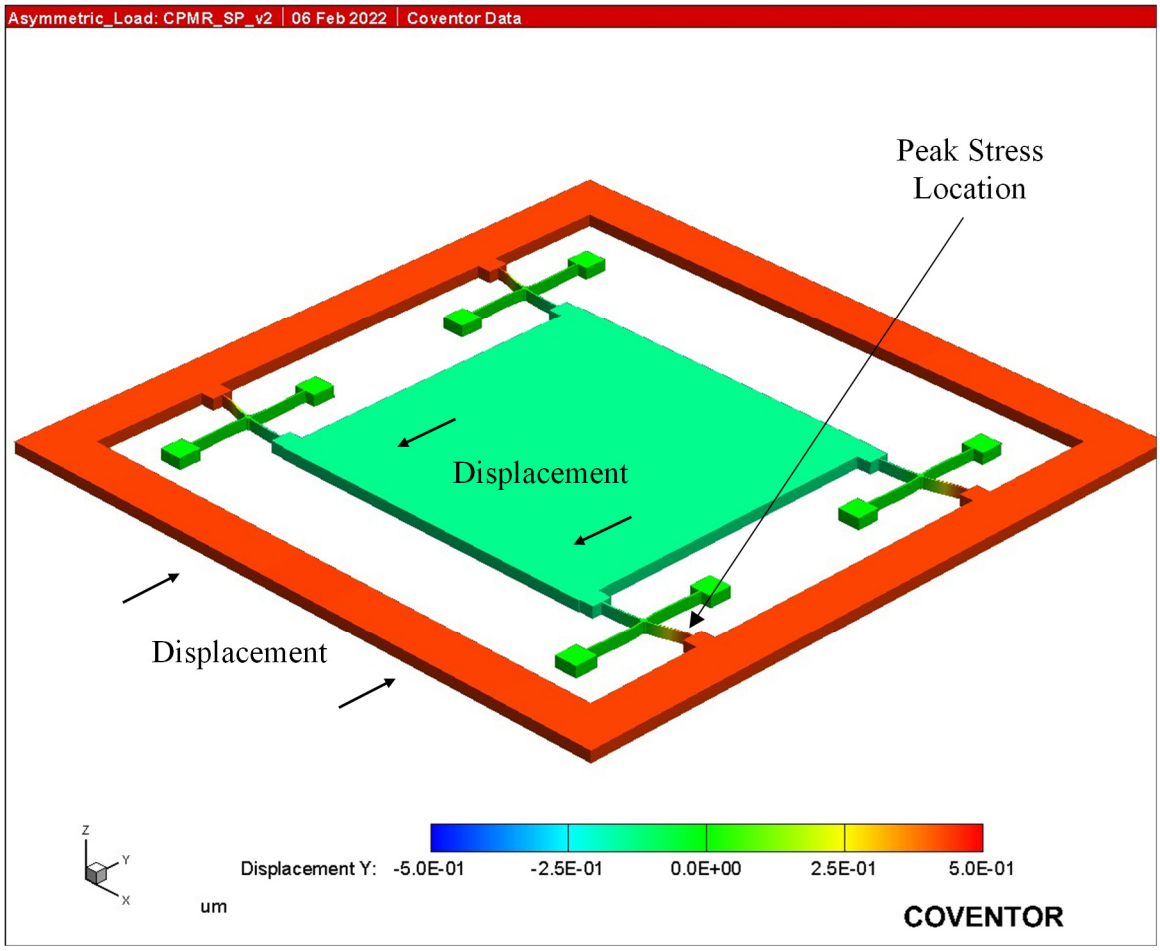

Figure 4.56 Straight Flexure Pivot Peak Stress Location Under Asymmetric Load.

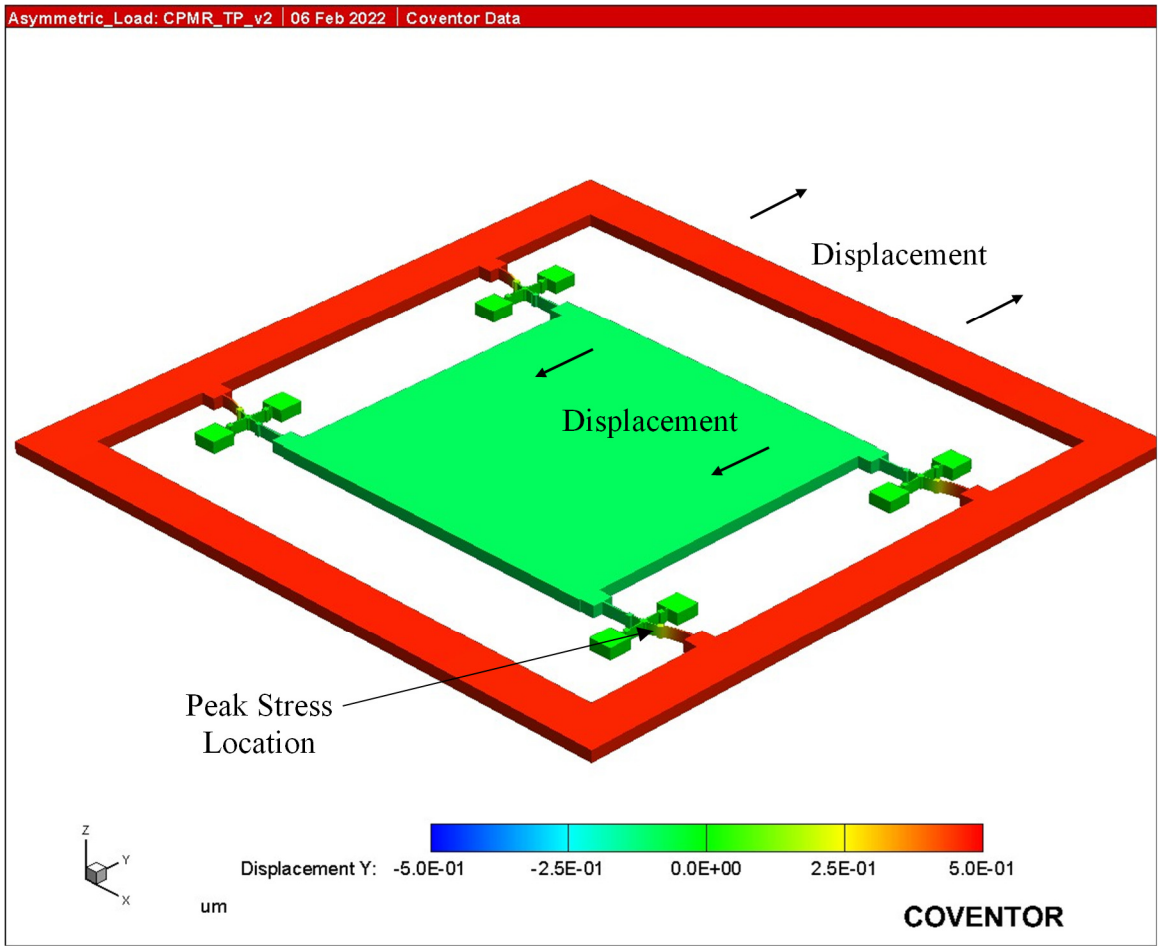

Figure 4.57 Tapered Flexure Pivot Peak Stress Location Under Asymmetric Load.

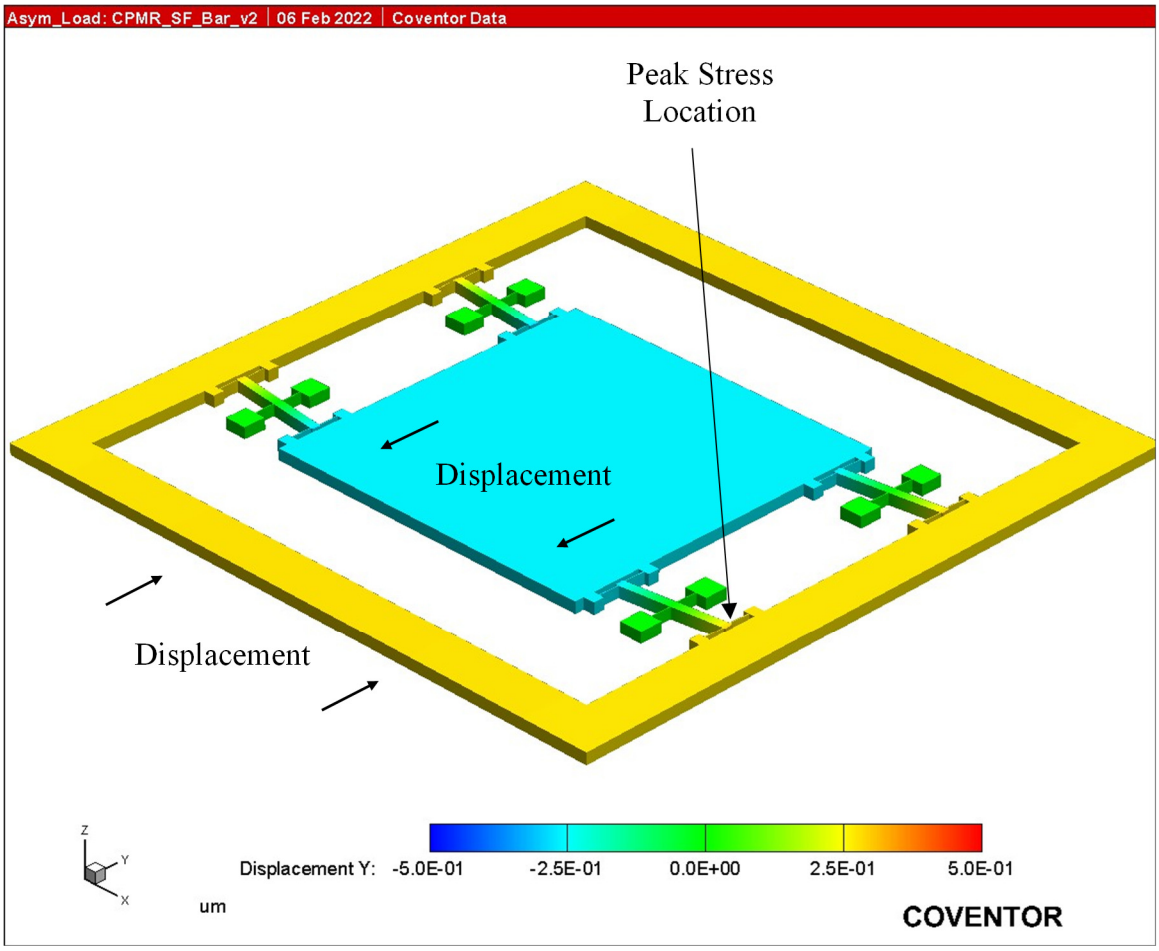

Figure 4.58 Straight Flexure Lever Peak Stress Location Under Asymmetric Load.

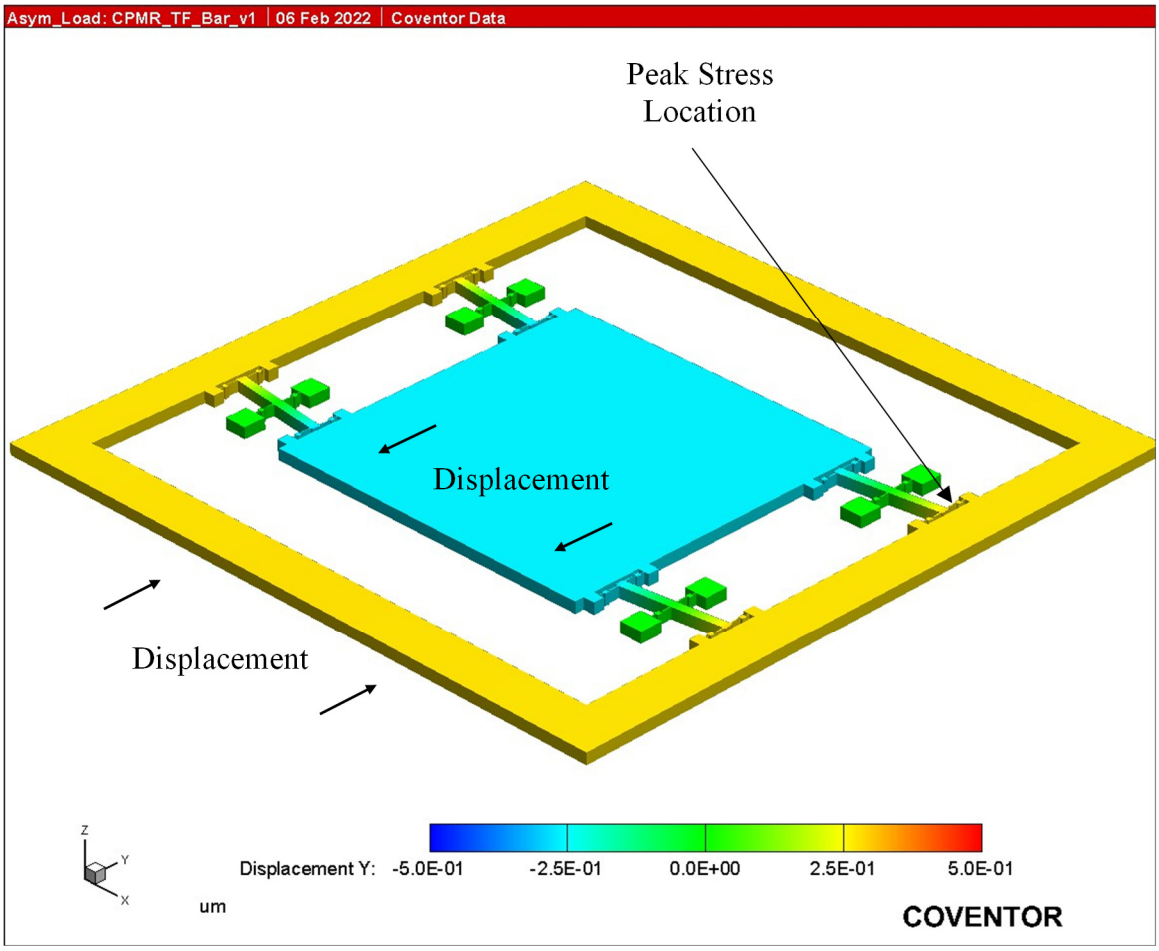

Figure 4.59 Tapered Flexure Lever Peak Stress Location Under Asymmetric Load.

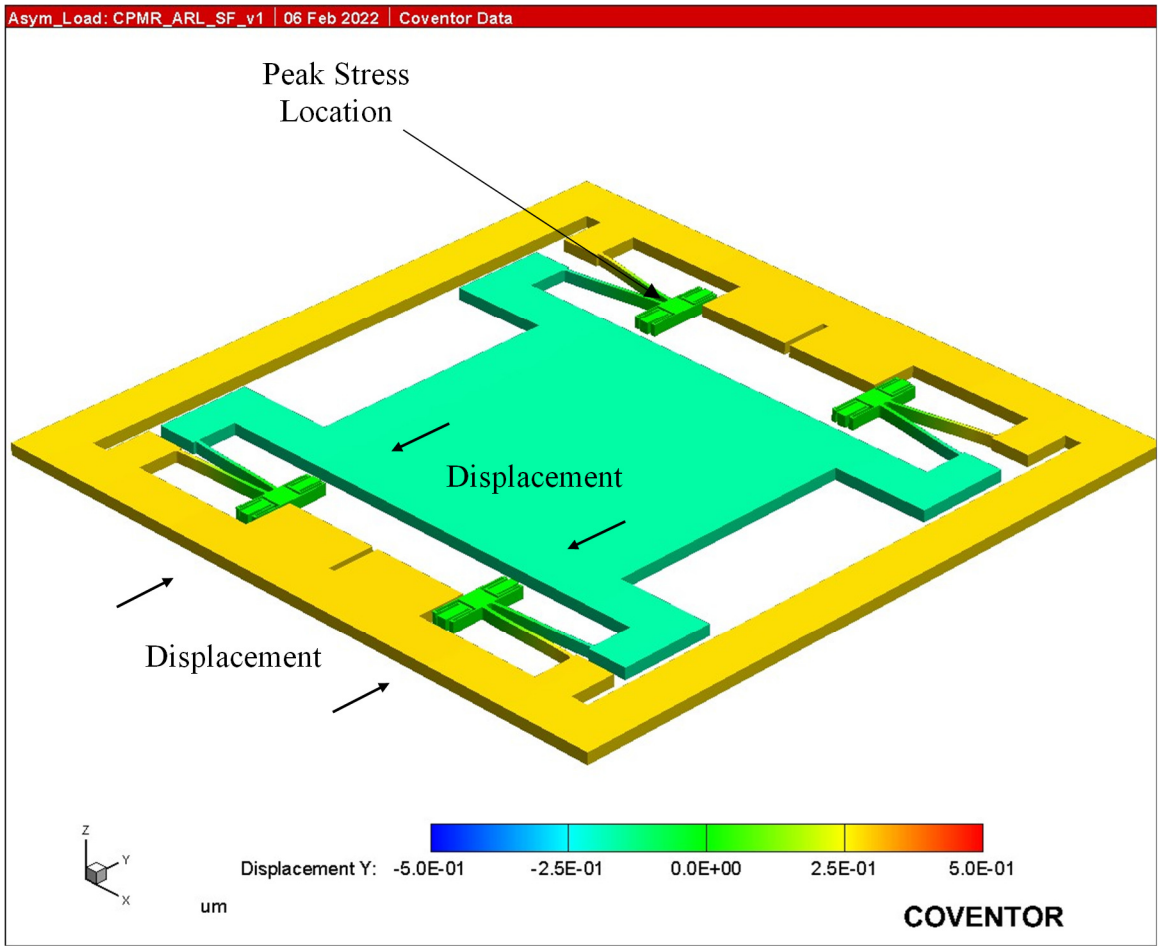

Figure 4.60 Straight Flexure Revised UCI Peak Stress Location Under Asymmetric Load.

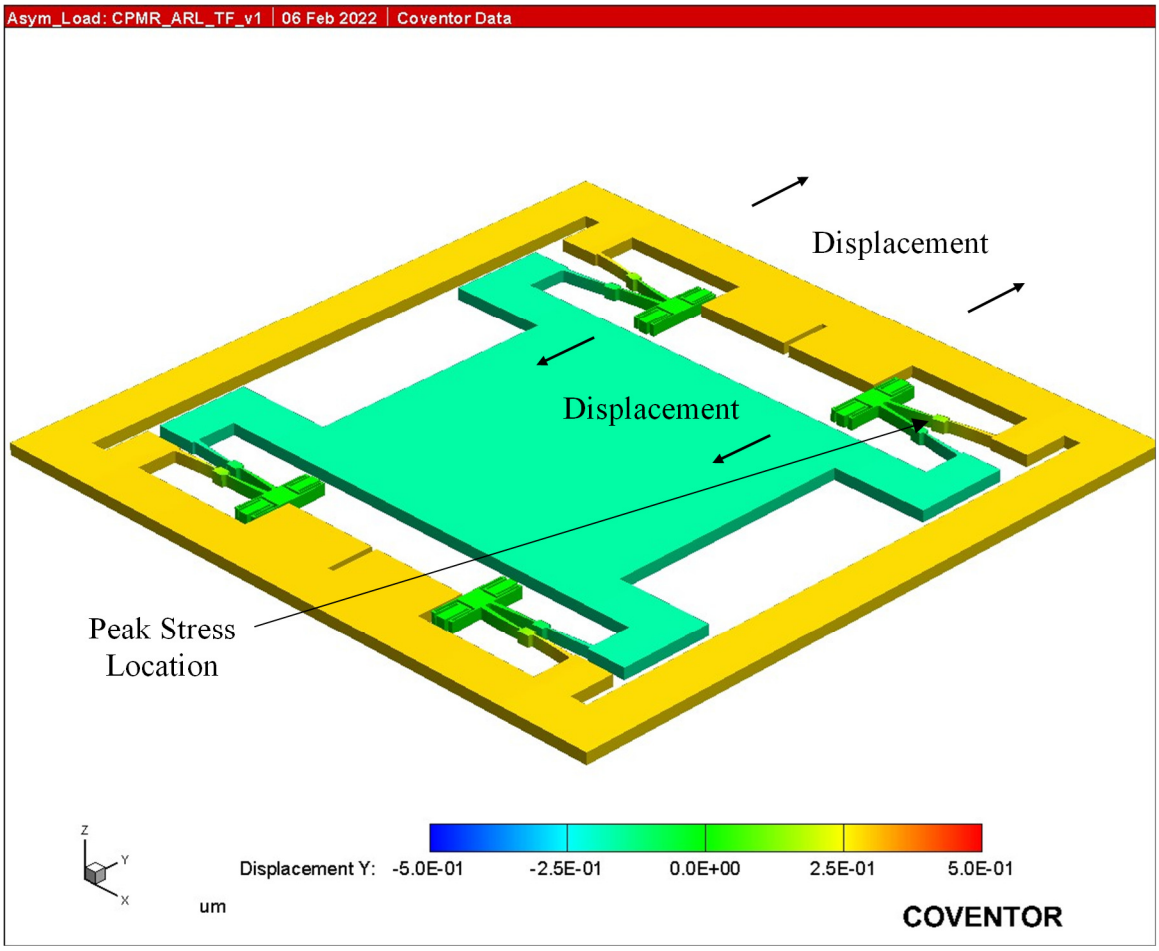

Figure 4.61 Tapered Flexure Revised UCI Peak Stress Location Under Asymmetric Load.

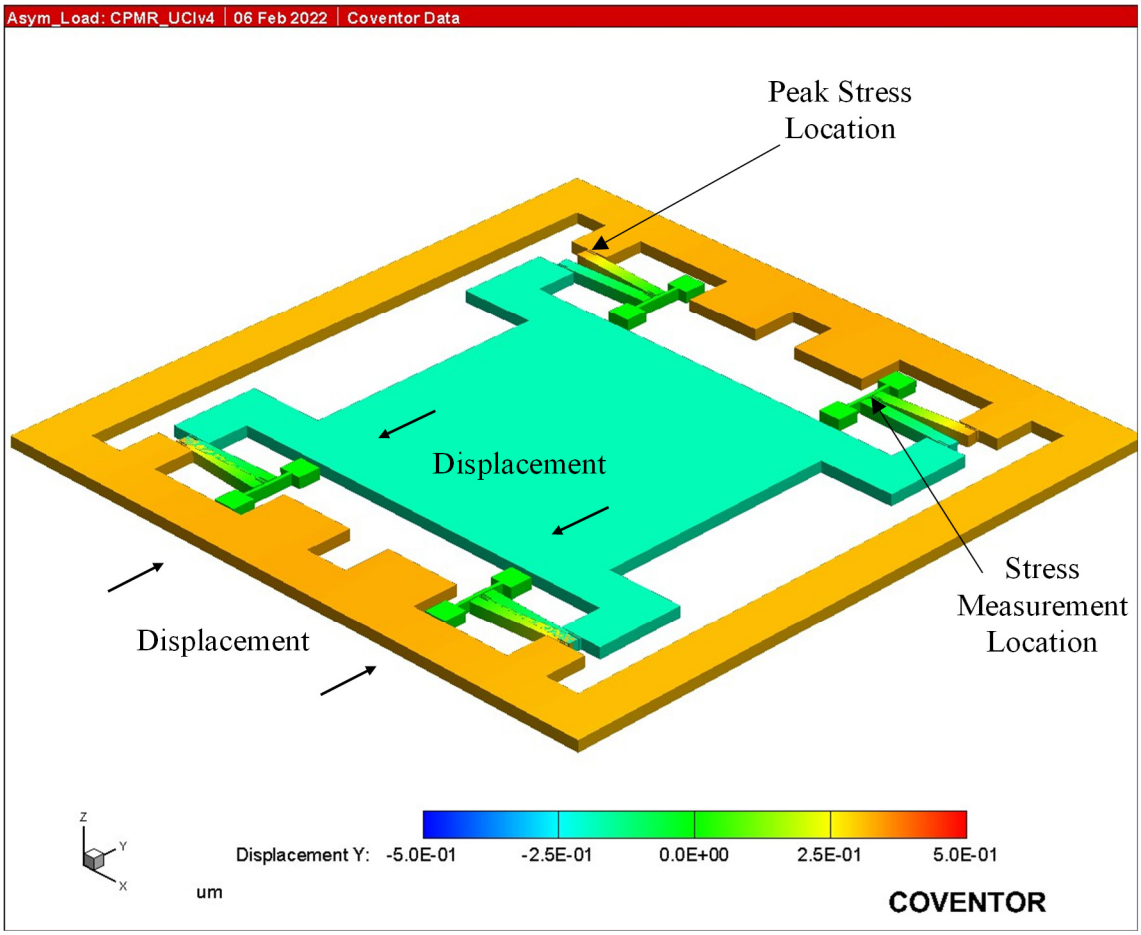

Figure 4.62 UCI Inner Lever Coupling Peak Stress Location Under Asymmetric Load.

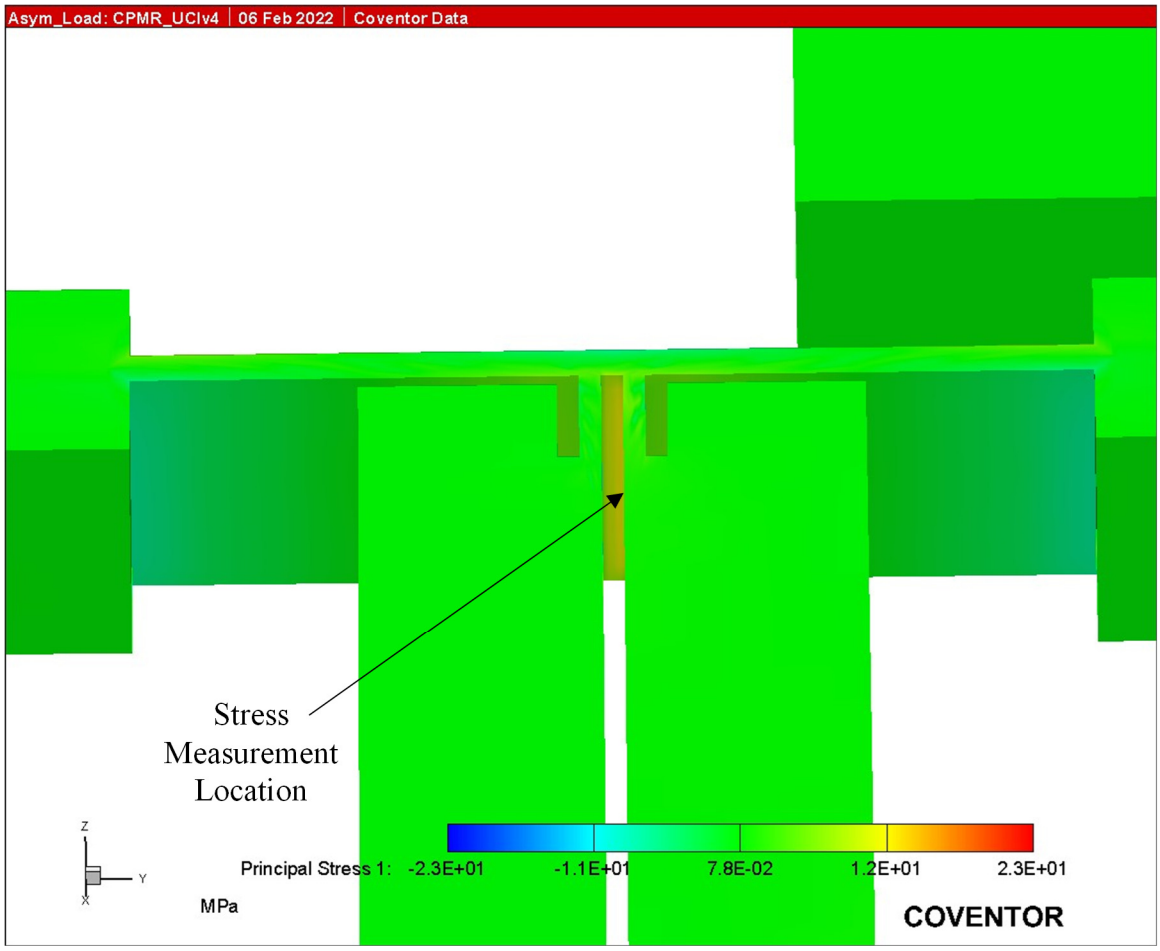

Figure 4.63 UCI Inner Lever Coupling Stress Location Under Asymmetric Load.

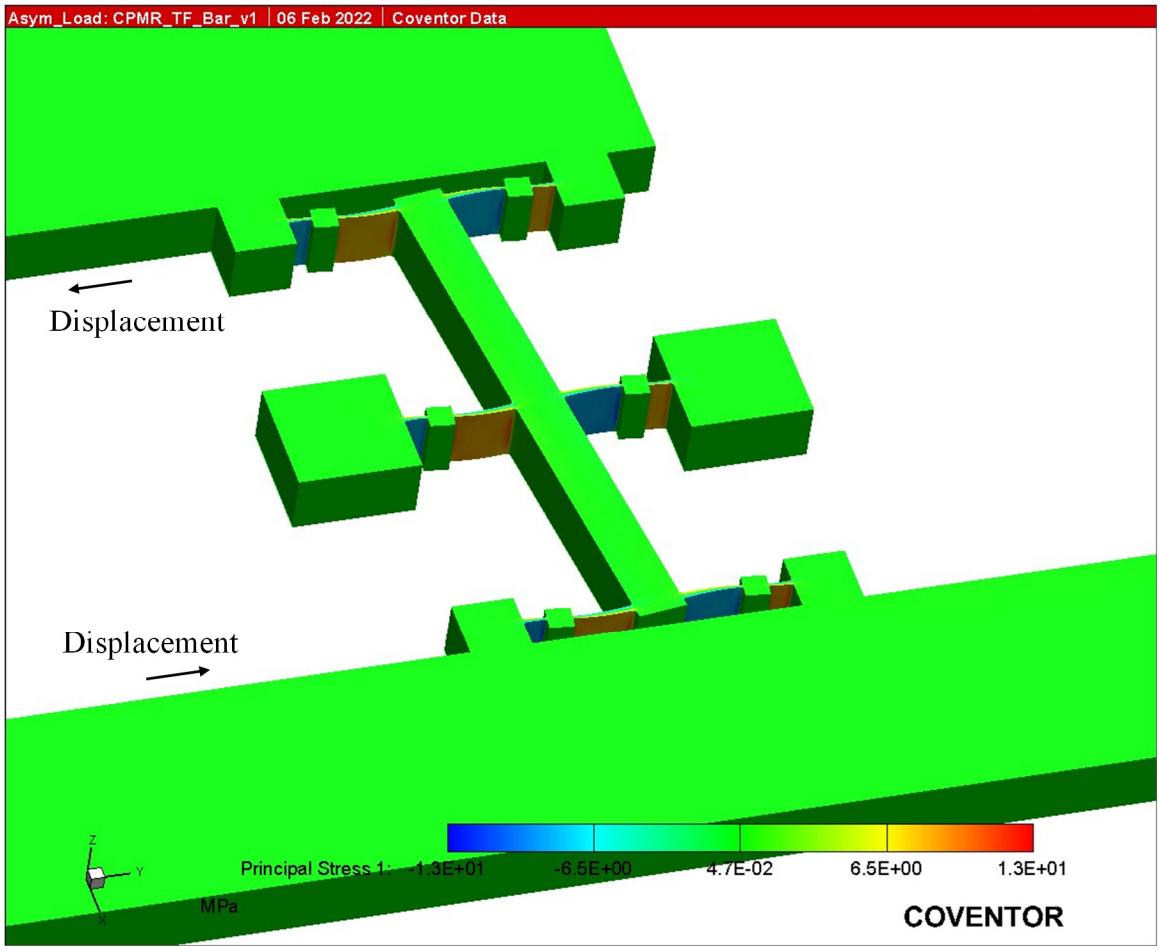

Figure 4.64 Tapered Flexure Lever Principal Stress Under Asymmetric Load.

To compare the modal separation effectiveness of the various APLM designs, a modal analysis was conducted on each design. Similar to the other analyses, the bottom of the oxide layer that attaches to the substrate, pictured in Figure 4.43 for the straight flexure pivot design, was given a *FixAll* boundary condition. The solver was configured to return the first 25 modes. For each design, the anti-phase mode and the in-phase mode resonant frequencies were identified and these are presented in Table 4.10. The table also presents the modal separation value which is calculated as follows:

$$Modal\ Separation = \frac{f_{IP} - f_{AP}}{f_{AP}} \cdot 100\%, \tag{4.55}$$

where f_{IP} is the in-phase resonant frequency and f_{AP} is the anti-phase resonant frequency.

Table 4.10 Modal Separation FEA Results.

APLM Design	**Anti-Phase Frequency (f_{AP})** (Hz)	**In-Phase Frequency (f_{IP})** (Hz)	**Modal Separation** (%)
Straight Four-Flexure Pivot	4924	6853	39.2
Tapered Four-Flexure Pivot	5002	6118	22.3
Straight Six-Flexure Lever	5097	32390	535.4
Tapered Six-Flexure Lever	5080	32411	538.0
UCI Inner Lever Coupling	4816	9181	90.6
Straight Flexure Revised UCI	5074	9923	95.6
Tapered Flexure Revised UCI	5059	9798	93.7

The data in the table indicate that all designs achieved anti-phase resonant frequencies very close to their design target of 5kHz. The four-flexure pivot designs demonstrated the poorest modal separation performance with the tapered flexure version of that design having the worst performance of all designs. The six-flexure lever designs demonstrated excellent performance with essentially no difference in modal separation performance between the straight and tapered flexures versions of that design. The lever to flexure stiffness ratio, *R*, for the six-flexure lever designs was designed to a value of 45. It was anticipated that this would result in a nominal modal separation on the order of $\sqrt{R} = \sqrt{45} \approx 6.7$ or 670% if the lever was the predominant compliant element for the in-phase mode. The values presented in Table 4.10 are not quite that high and indicate that other elements of the design are adding some compliance to the in-phase mode.

However, this level of modal separation is very impressive and this design essentially gives the designer the ability to place the in-phase resonant frequency at any reasonable, desired frequency. Finally, it is noted that the UCI inner lever coupling design and the revised UCI designs had very similar modal separation performance.

To compare the thermoelastic damping performance of the various APLM designs, a Direct Harmonic analysis was conducted on each design. Similar to the other analyses, the bottom of the oxide layer that attaches to the substrate, pictured in Figure 4.43 for the straight flexure pivot design, was given a *FixAll* boundary condition. Additionally, the edges of the inner and outer proof masses, pictured in Figure 4.44 for the straight flexure pivot design, were given *LoadPatch* Harmonic Surface Boundary Conditions at the anti-phase resonant frequency estimated by the modal analysis summarized in Table 4.10. For all designs, the outer proof mass edges were loaded with +10mPa and -10mPa. For the four-flexure pivot and six-flexure lever designs, the inner proof mass edges were loaded with -19.4365mPa and +19.4365mPa to keep the applied harmonic force the same as that for the outer mass. Similarly, for the UCI inner lever coupling design, the inner mass edges were loaded with -16.08538mPa and +16.08538mPa, and for the revised UCI inner lever coupling designs, the inner mass edges were loaded with -14.57738mPa and +14.57738mPa. This resulted in a net harmonic force of 6nN being applied to each proof mass for all designs.

To ensure a fair comparison across the designs it was necessary to account for the small variation in resonant frequencies across the designs. Therefore, in addition to the quality factor, the product of the resonant frequency and the quality factor, called the fQ product, is also presented in Table 4.11. The fQ product should provide a fair

comparison because the fQ product should be relatively constant for a particular design configuration as long as the device is operating in the isothermal mode.

Table 4.11 Thermoelastic Damping FEA Results.

APLM Design	**TED Quality Factor** Q_{TED} $(\times 10^3)$	**Frequency - Quality Factor Product** fQ (GHz)
Straight Flexure Pivot	608.8	2.998
Tapered Flexure Pivot	680.7	3.405
Straight Flexure Lever	861.8	4.393
Tapered Flexure Lever	915.7	4.652
UCI Inner Lever Coupling	79.9	0.385
Straight Flexure Revised UCI	148.1	0.751
Tapered Flexure Revised UCI	157.5	0.797

The data in the table indicate that the tapered flexure versions outperformed the straight flexure versions in all designs by a range of about 6-14%. The six-flexure lever design configuration significantly outperformed all other design configurations with an fQ product that is nearly 6 times that of the revised UCI design. It was noted in the analysis of the data from the UCI inner lever coupling design that the device was operating in the transition region between the isothermal regime and the Debye frequency. Therefore, it would not be entirely fair to compare the thermoelastic damping performance of this design to the other designs.

4.3 Discussion of APLM Study Results

Straight and tapered flexure versions of three different APLM designs were modeled in a concentric mass resonator configuration and compared against each other and to a reference design based on the UCI inner lever coupling mechanism. The performance of these designs was assessed for (1) stress and peak stress under symmetric loading conditions; (2) stress, peak stress, and relative mass displacement under asymmetric loading conditions; (3) modal separation of anti-phase and in-phase resonant modes; and (4) thermoelastic damping. A generalized comparison of the design configurations is fairly challenging. Therefore a "stoplight" chart is presented in Table 4.12 to provide a visual comparison of the designs.

One primary finding of this analysis is that the tapered flexure designs had consistently lower stress and peak stress than the equivalent design incorporating straight flexures, typically by about 35%. The only exception to this occurred in one location of the tapered flexure pivot design and was largely due to the asymmetric load configuration imparting a stress distribution that was significantly different from its intended design. The tapered flexure designs also demonstrated improved thermoelastic damping performance over the equivalent straight flexure designs, typically between 6-14%. With the exception of the tapered flexure pivot deign, there was generally no difference in the performance of the straight and tapered flexure designs for relative displacement under asymmetric loading conditions or for modal separation.

Table 4.12 Anti-Phase Lever Mechanism Stoplight Chart.

APLM Design	Symmetric Load		Asymmetric Load			Modal	Thermo-Elastic Damping
	Peak Stress	Stress	Relative Mass Displace-ment	Peak Stress	Stress	Modal Frequency Separation	$f \cdot Q$ Product
Straight Flexure Pivot							
Tapered Flexure Pivot							
Straight Flexure Lever							
Tapered Flexure Lever							
UCI Inner Lever Coupling							
Straight Flexure Revised UCI							
Tapered Flexure Revised UCI							

Legend

Worse  Better

The tapered flexure pivot design consistently demonstrated poor performance and was the most difficult to design. The root cause is a fundamental inconsistency in the characteristics of tapered flexures and the mode of operation of the four-flexure pivot APLM design. Tapered flexures have approximately twice as much rotational deflection as the equivalent straight flexure. The four-flexure pivot APLM design links the two masses in anti-phase mode through the rotation of the pivot point. The tapered flexures may be great candidates for the anchor flexures, but the guided flexures would

demonstrate better coupling performance if they had less rotational compliance. This suggests two alternate approaches to what was investigated in this work. The first is that it may be a fairer comparison if the proportionality constant that sets the ratio of displacements, *P*, of the tapered flexure design was set to twice that of the straight flexure design. The second is a hybrid four-flexure pivot design wherein the guided flexures are straight flexures and the anchor flexures are tapered flexures.

The four-flexure pivot designs demonstrated relatively high stress levels, poor inter-mass coupling, and poor modal separation, but did have the second highest thermoelastic damping performance. The revised UCI inner lever coupling design either matched or outperformed the original UCI inner lever coupling design in every category with the most significant finding being a significant reduction in stress while improving the thermoelastic damping performance. The tapered flexure version of the revised UCI design demonstrated very similar or significantly improved performance over the straight flexure version in every category. Finally, the six-flexure lever design exhibited some of the highest stress concentrations, but significantly outperformed all of the designs in every other category including near one-to-one inter-mass coupling, five times better modal separation than any other design, six times better thermoelastic damping performance than the revised UCI design, and maintained the same constant stress distribution under asymmetric loading conditions as it does under symmetric loading conditions. Comparing the straight and tapered flexure versions of the six-flexure lever design, the tapered flexure version again demonstrated very similar or significantly improved performance over the straight flexure version.

Therefore, if the designer is not pushing the flexures to the stress limits of the material, the tapered flexure lever design is the best design configuration. However, if the designer is expecting to stress the flexures near the limits of the material, then the tapered flexure revised UCI design will probably provide adequate performance in all categories while reducing the stress in the flexures.

It is important to note here that the "equivalence" of these designs was largely based on the lengths of key elements of the design. This effectively held all designs to a very similar footprint. It is recommended that future research investigate the sensitivity of each design to changes in this footprint to obtain a more complete comparative assessment of the designs.

Chapter 5. Dual-Mass Resonator Fabrication Experimental Results

This chapter presents the results of an extensive set of fabrication experiments conducted on a dual proof mass resonator configuration which experimentally measured the performance of quadratically tapered flexures, the inclusion of fillets, and the tapered flexure lever APLM. Specifically, the performance was estimated by statistical measurement of resonant frequency variability, and ringdown time performance and variability (presented as resonator quality factor, which is a measure of thermoelastic damping). The experimental results are compared with Finite Element Analysis (FEA) results for these experimental configurations.

There were six experiments consisting of a total of 20 distinct device designs. Some device designs contributed to more than one experiment. The six experiments are described below.

Experiment 1 - Characterize the impact of the inclusion of fillets on the performance of straight flexure resonators of three different flexure widths.

Experiment 2 - Characterize the impact of the inclusion of fillets on the performance of tapered flexure resonators of three different flexure base widths.

Experiment 3 - Using devices from Experiments 1 and 2, compare the performance of the straight and tapered flexure resonators with and without fillets for the three different flexure widths.

Experiment 4 - Characterize the trade-off between quality factor and sensitivity to manufacturing variations as a function of flexure length to hammerhead block size $\left(\frac{L}{d}\right)$ ratio in tapered flexures.

Experiment 5 - Characterize the performance of the tapered flexure lever APLM resonator and compared to that of the widest flexure width of the straight and tapered revised UCI APLMs of Experiments 1 and 2.

Experiment 6 - This is the Control in the experiment. Characterize the performance of legacy designs included on this wafer for comparison to that of other wafers.

We first describe the features and general operation of the dual-mass resonator configuration used for these experiments. We then describe the specific APLM and coupler spring design implementations that were evaluated, the performance predictions made through FEA modeling, and the experimental results arranged by experiment. Finally, we will present a short discussion of the overall findings which compare tapered flexures to straight flexures, the incorporation of fillets, and an overall comparison of the fabricated APLMs.

Fabrication data was collected for each experiment. However, issues with instrumentation prevented data collection from 10 of the 20 device designs. This was because the quality factor of these devices was so high that electrical contact with the probe card would cause the device to resonate with or without the presence of a drive signal, which made the estimation of ringdown time and quality factor impossible. Ultimately, data was collected from a total of 107 devices spanning 10 of the 20 designs,

including 64 devices from Experiments 1, 2 and 3, 35 devices from Experiment 4, 8 devices from Experiment 5, and 6 devices from Experiment 6 (Control).

5.1 Dual Mass Resonator Design Configuration

This section describes the features and general operation of the dual-mass resonator configuration used for the fabrication experiments. The work reported in this chapter was performed in partnership with researchers from the Army Research Laboratory who were experimenting with APLM and coupler spring configurations to improve the performance of the quad-mass gyroscope under development there. These researchers are the inventors of the straight flexure revised UCI APLM design described in the Chapter 4. These researchers had developed a dual-mass resonator configuration for their experiments including device layout, fabrication process, and a vacuum probe station experimental setup to interrogate the properties of these resonators. Their research goals aligned very closely with the present work. Therefore, their general layout, fabrication process, and experimental setup were leveraged in this work. A solid model rendering of the baseline dual-mass resonator configuration is shown in Figure 5.1 and an optical photograph of one of the fabricated devices is shown in Figure 5.2.

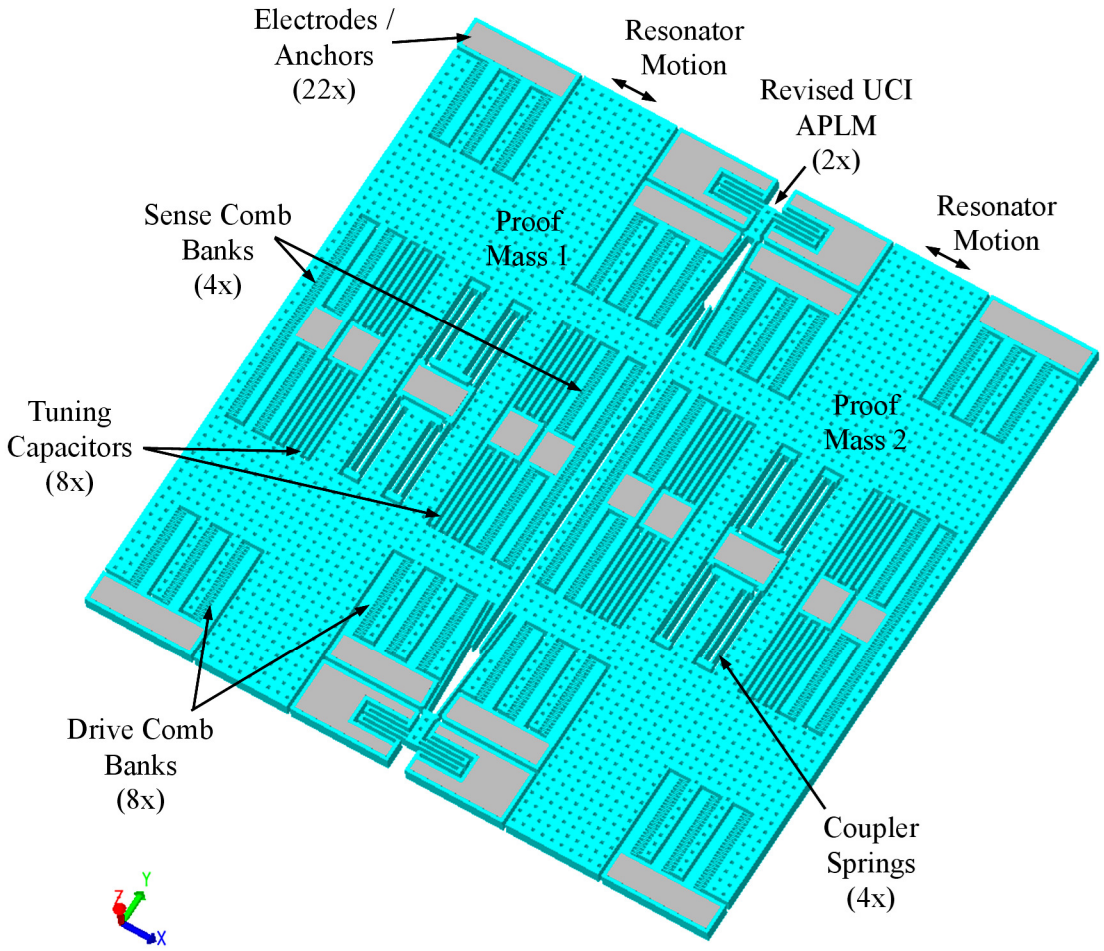

Figure 5.1 Dual-Mass Resonator Configuration for Fabrication Experiments.

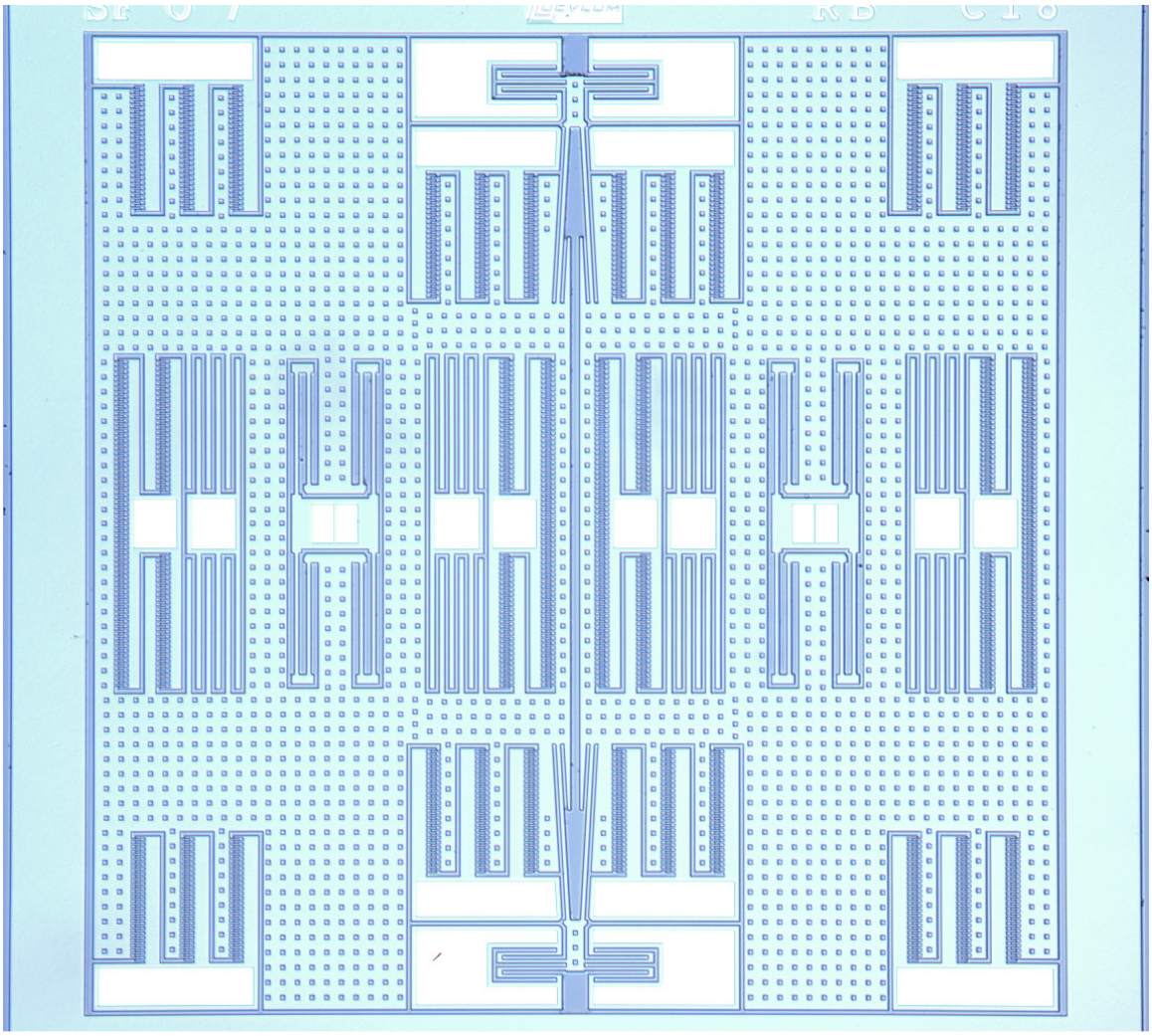

Figure 5.2 Dual-Mass Resonator Photo.

The dual mass resonator operates in anti-phase mode with the motion of the two masses being from left to right in Figure 5.2. The baseline device has two straight flexure revised UCI APLMs at the top and bottom of the center of the device which are the primary flexures in the quad mass gyroscope design. The baseline resonator design also has 4 pairs of coupler springs, two in the center of each proof mass. These coupler springs are folded flexures which are used in the quad mass gyroscope to transmit only a single axis of motion to the drive and sense longitudinal capacitors (comb banks). The

dual mass resonator device has 8 sets of drive longitudinal capacitors (comb banks) and 4 sets of sense longitudinal capacitors. Finally, the device has 4 banks of parallel plate capacitors for resonant frequency tuning. The device and electrode blocks are anchored to the substrate under each of the 22 metalized blocks. The overall dimensions of the device are 4mm by 4mm. The device is made in the 100µm thick <100> single crystal silicon device layer of a silicon on insulator wafer that has a 5µm silicon dioxide insulation layer on top of a 500µm substrate. The thicknesses of the device and substrate layers are common and readily available. The oxide layer thickness, however, is less common and required a special order. To fabricate an SOI wafer with an oxide layer of this thickness, oxide layers of 2.5µm each had to be grown on two different wafers which were subsequently bonded together. This additional thickness is preferable for this device design due to the relatively large extent of the design (4mm by 4mm), since a very small amount of wafer bowing could result in interference if a thinner oxide layer were used.

This dual-mass configuration was being used to investigate methods to reduce the sensitivity to DRIE manufacturing variations and improve the yield of the quad-mass gyroscopes. Specifically, improvements in resonant frequency matching, quality factors, and quality factor matching between the two axes of the quad mass gyroscope were being sought. These objectives align precisely with the goals of the research in this dissertation, with the only difference being that the intent herein was to apply these results to a concentric mass gyroscope configuration rather than a quad mass gyroscope configuration. Both of these gyroscope configurations are mode-matched gyroscopes and benefit from improvements to these common elements. Therefore, a wafer was laid out

which consisted of tapered flexure, filleted, and alternate APLM design experiments using their dual-mass resonator configuration. The wafer layout used the same electrode locations and fabrication processes as the previous dual mass resonator wafer, so that the existing vacuum probe card, experimental setup, and interrogation routines could be utilized.

The wafer layout included 638 resonators spanning 26 designs with 12 to 30 copies of each design distributed across the wafer to obtain performance statistics that capture manufacturing variations across the wafer. Six of the 26 designs were "hybrid" designs (180 devices) that incorporated both straight and tapered flexures and no information or analysis of those designs is included herein. Each of the resonators were interrogated for resonant frequency and quality factor, and an estimate of the average and standard deviation of these parameters was calculated for each design. Each of the 6 device designs in Experiments 1 and 2 had 21 devices oriented with the oscillatory motion along the x-axis of the wafer and 9 devices oriented with the oscillatory motion along the y-axis of the wafer. A higher number of devices were placed in the x-axis direction than the y-axis direction to mitigate against yield and fabrication issues thereby increasing the probability of obtaining a statistically significant number of similar devices for each design in the same orientation. For each y-axis device, an x-axis device was placed in an adjacent die location to provide the best possible comparison between the x and y axis devices. Average and standard deviation statistics for the resonant frequency and quality factor were calculated using these adjacent devices to characterize any directional sensitivity that may be present on the wafer.

5.2 Dual Mass Resonator Implementations, FEA Predictions, and Experimental Results

This section, arranged by experiment, describes the specific APLM and coupler spring design implementations that were evaluated, the performance predictions made through FEA modeling, and the experimental results.

Before the finite element analyses were executed, a mesh sensitivity study was performed to determine the optimum mesher settings required to accurately estimate the desired parameters in a reasonable amount of computation time. The details of that mesh sensitivity study are provided in Section B.2 of Appendix B. The resulting mesher settings are provided in Figure 5.3. Additionally, since the boundary conditions for all FEA analyses were applied as pressure-based surface boundary conditions, it was unnecessary to model the electrodes. Therefore, for the finite element analyses, the device and mesh were simplified significantly by removing the capacitive comb fingers and the release holes from the solid model. Since one of these modifications removed mass and the other modification increased mass, together they netted little change in the overall mass. A representative dual-mass resonator solid model with these features removed is provided in Figure 5.4 and several views of the resulting mesh for the same device are shown in Figures 5.5 - 5.8. It can be seen that these mesher settings resulted in denser meshes in and around the fillets and device edges, as well as a modest graduation of element size along the thickness of the model, each of which correspond to the severity of typical stress gradients seen in the FEA results presented in previous chapters.

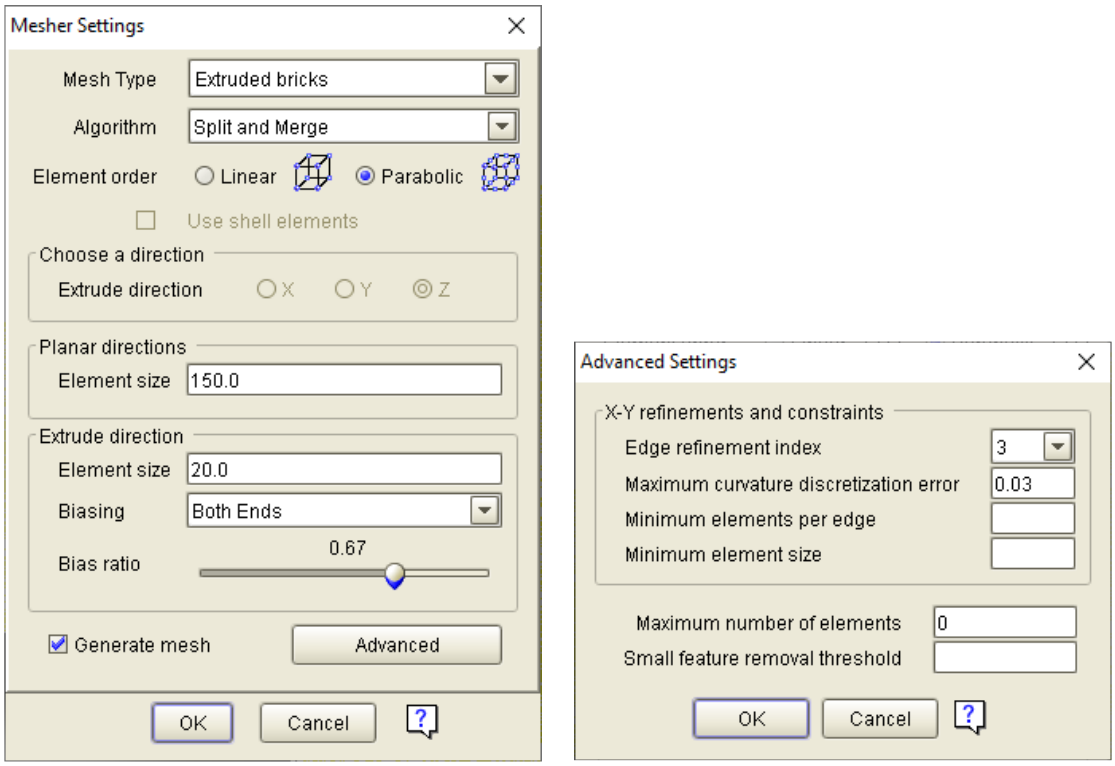

Figure 5.3 Dual-Mass Resonator FEA Mesher Settings.

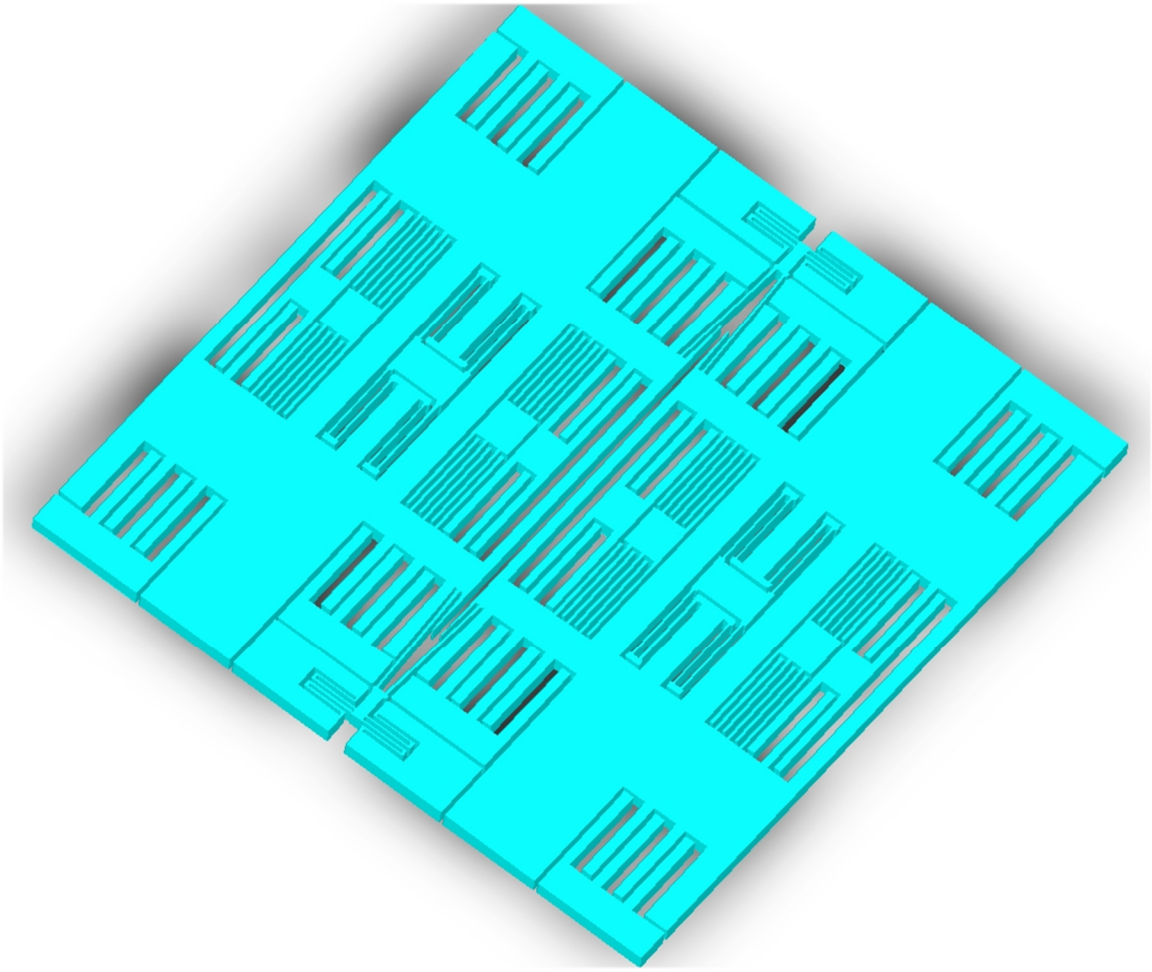

Figure 5.4 Simplified Dual-Mass Resonator Configuration for FEA.

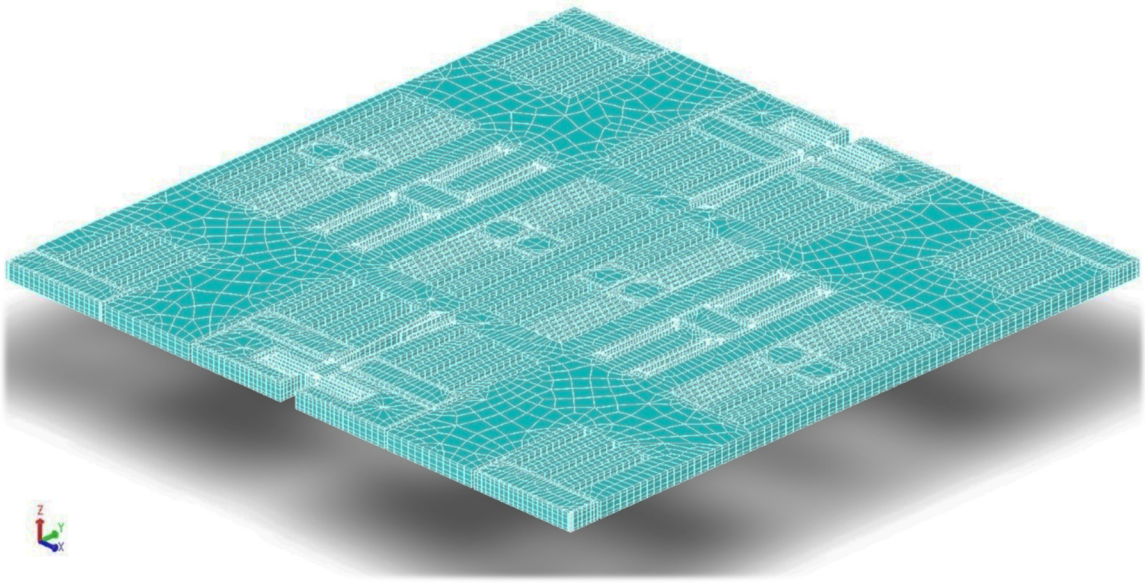

Figure 5.5 Simplified Dual-Mass Resonator Mesh for FEA, Oblique View.

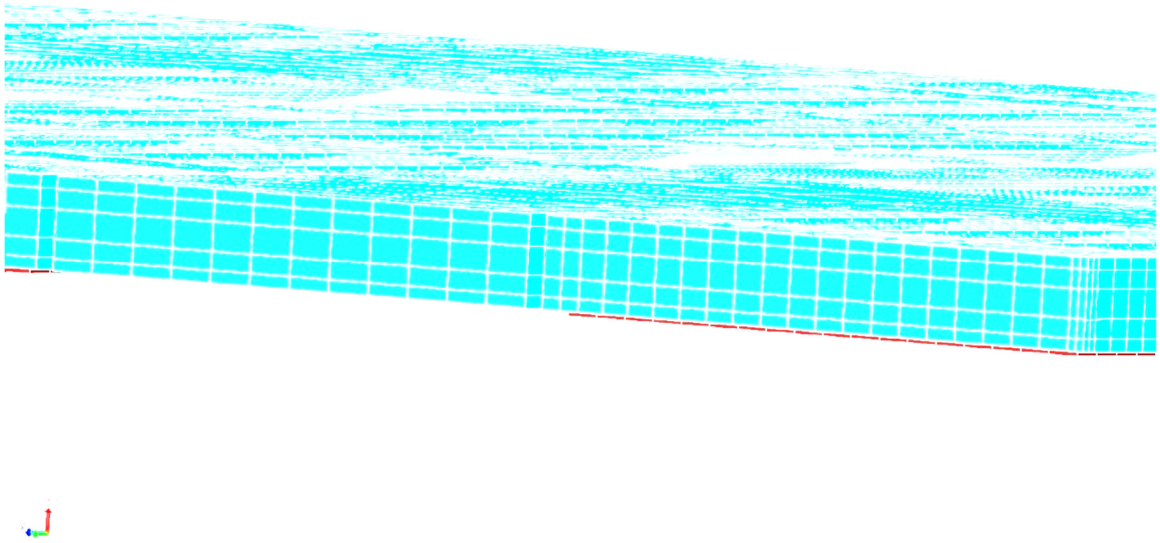

Figure 5.6 Simplified Dual-Mass Resonator Mesh for FEA, Edge View.

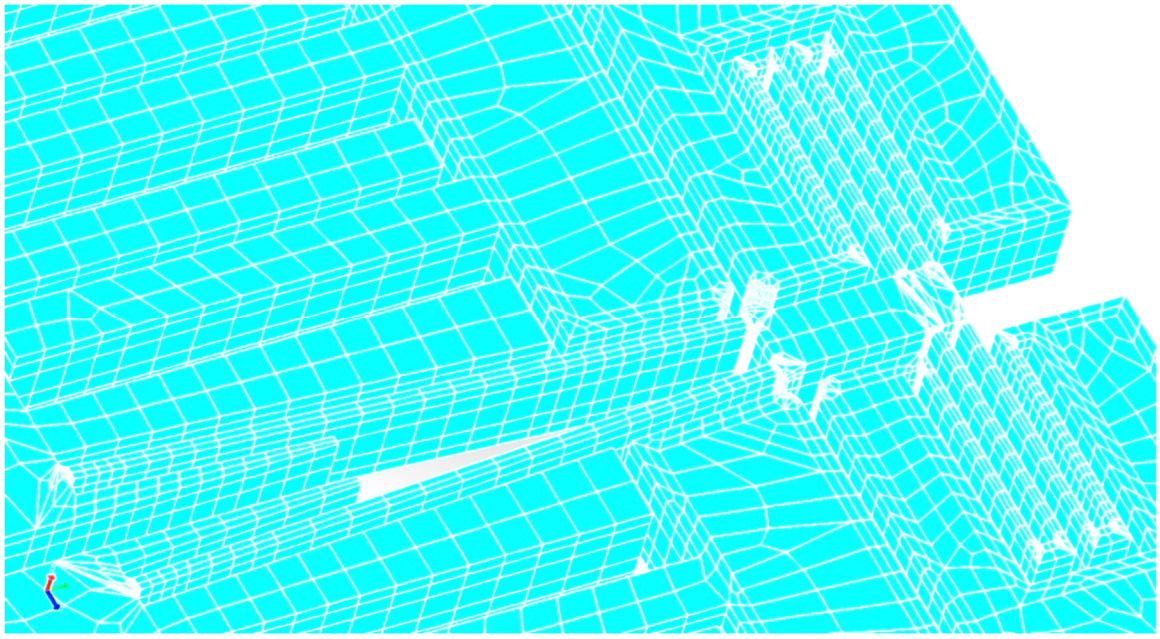

Figure 5.7 Simplified Dual-Mass Resonator Mesh for FEA, APLM View.

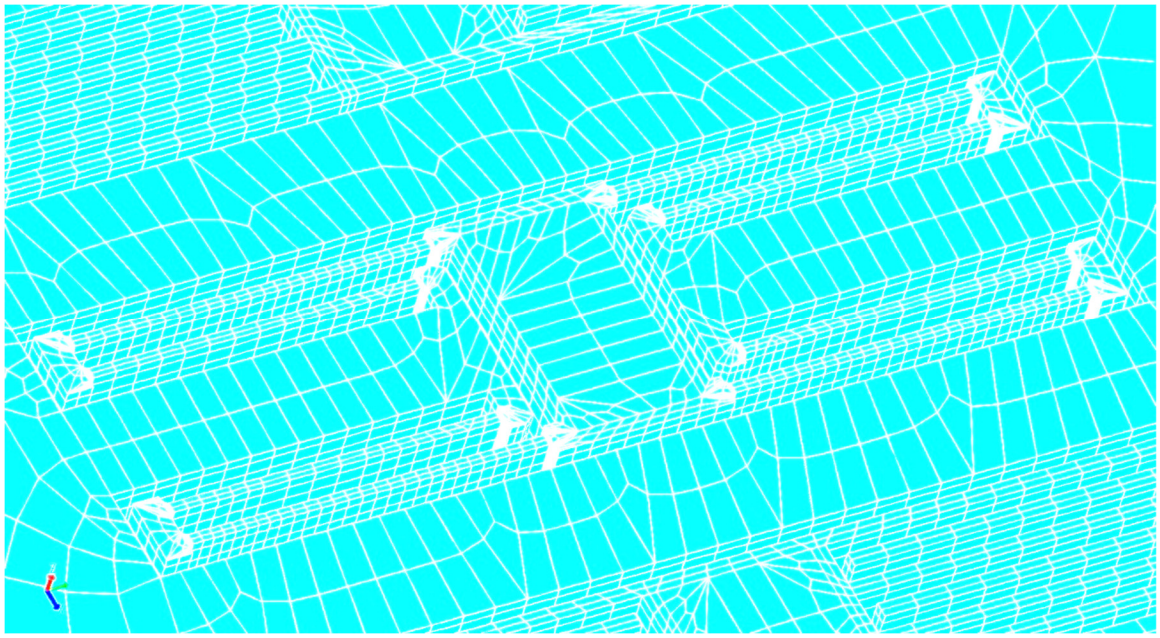

Figure 5.8 Simplified Dual-Mass Resonator Mesh for FEA, Coupler Spring View.

5.2.1 Experiment 1 - Straight Flexures with and without Fillets

The purpose of Experiment 1 was to assess the impact of the incorporation of fillets in straight flexure designs on resonant frequency and quality factor statistics. Experiment 1 consisted of 6 unique resonator designs incorporating 3 different straight flexure widths (7.5µm, 10µm, and 15µm) with and without fillets. Figure 5.9 shows a representative straight flexure revised UCI APLM layout with the flexure designators identified. Figure 5.10 shows a representative coupler spring layout with the flexure designators identified.

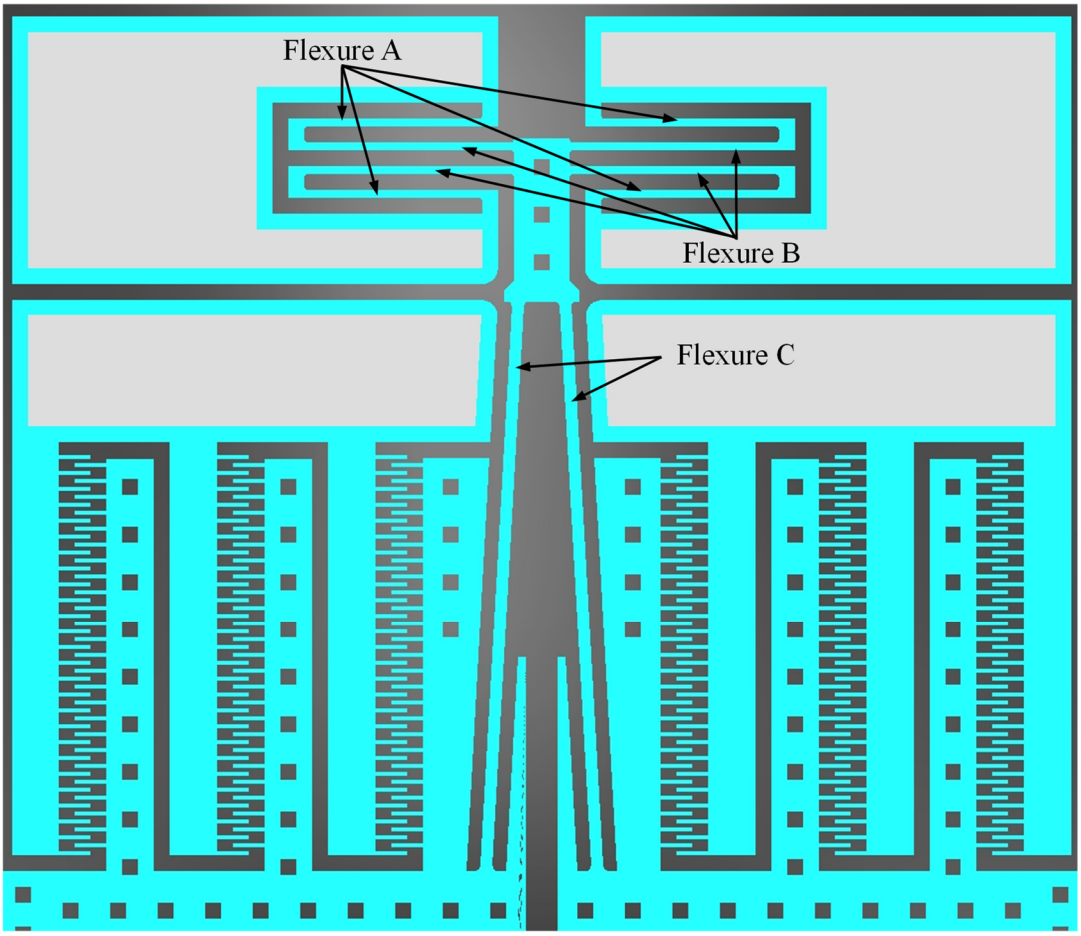

Figure 5.9 Experiment 1 Revised UCI APLM Flexure Element Designations.

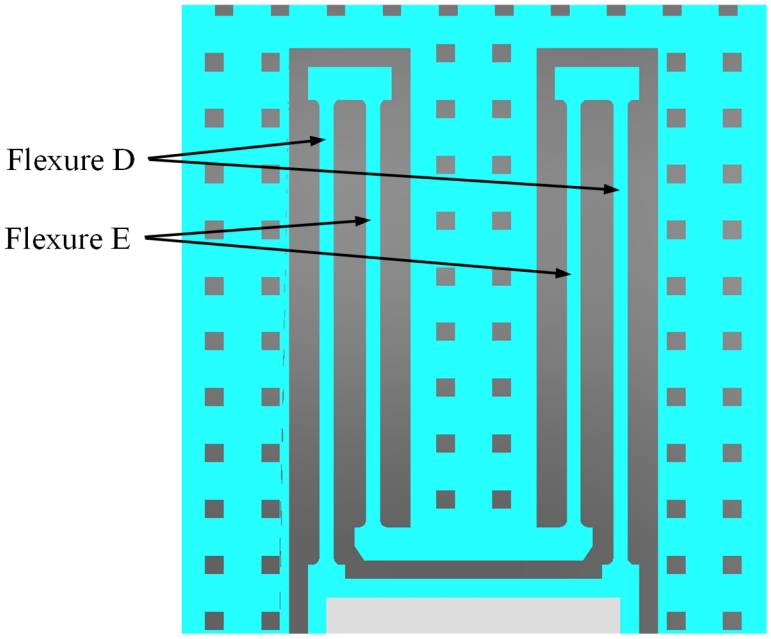

Figure 5.10 Experiment 1 Coupler Spring Flexure Element Designations.

Only the angled flexures in the revised UCI APLM were modified for the different flexure configurations as part of the design variations. The folded flexure and shuttle block portion of the revised UCI APLM design was held to a constant design consisting of 10µm width straight flexures with fillets, regardless of the flexure type, flexure width, or fillet configuration of the angled flexures. This was done to reduce fabrication risk and manufacturing variability on this portion of the design since it was not expected to have a significant impact on the overall performance of the device. Table 5.1 summarizes the design configuration for the folded flexure and shuttle block portion of the revised UCI APLM. The small shoulders on the sides of the shuttle protrude 13µm from the sides and are primarily there to accommodate the fillets of the angled flexures. Table 5.2 summarizes the angled flexure (Flexure C) design configurations of the revised UCI APLM for the various designs of Experiment 1. The variable names used in Table 5.1 and 5.2 were defined in Section 4.1.6 but are repeated graphically here in

Figure 5.11 for convenience. Table 5.3 summarizes the design configurations of the coupler springs for the various designs of Experiment 1. To enable visual comparison of the various designs in Experiment 1, optical photographs of the fabricated devices are provided zoomed into the APLMs in Figure 5.12 and zoomed into the coupler springs in Figure 5.13. Broader views of the solid model renderings of the APLMs are provided in Appendix C, Figures C.1 - C.6. Broader views of the solid model renderings of the coupler springs are provided in Appendix C, Figures C.7 - C.12.

Table 5.1 APLM Shuttle Block and Folded Flexure Design Configuration.

Parameter	Label	Units	Value
Shuttle Block Width	w_{Blk}	µm	70
Shuttle Block Length	L_{Blk}	µm	200
Flexure A Width	w_{FF_A}	µm	10
Flexure B Width	w_{FF_B}	µm	10
Flexure A Length	L_{FF_A}	µm	225
Flexure B Length	L_{FF_B}	µm	265
Angled Flexure Attachment Separation	d_{AF}	µm	60

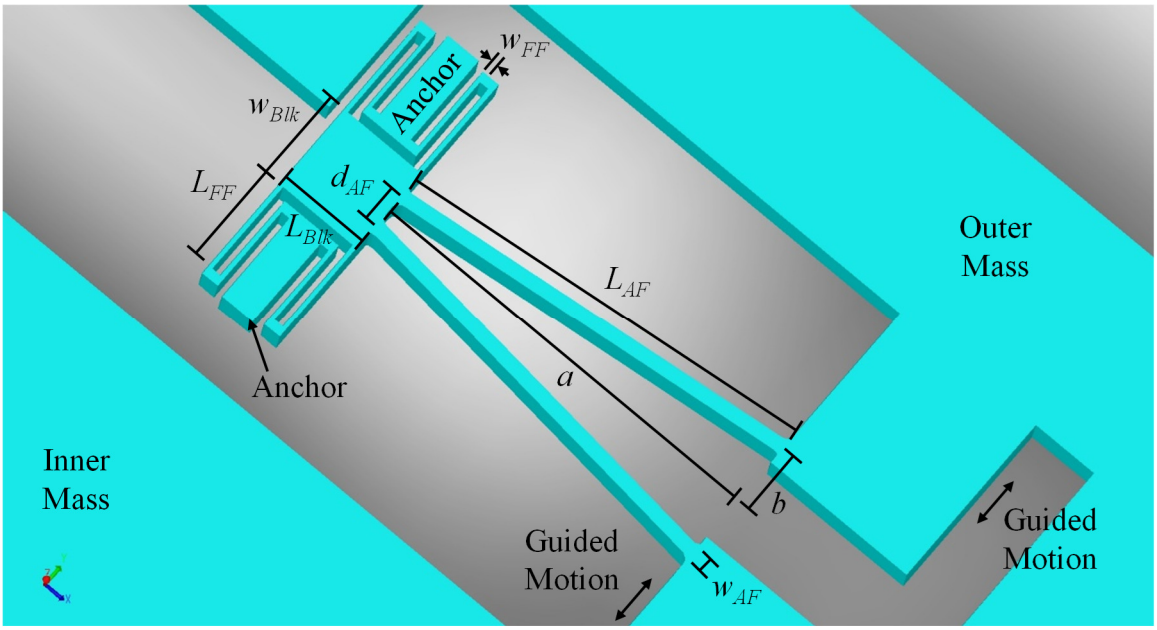

Figure 5.11 Straight Flexure Revised UCI APLM Variable Definitions.

Table 5.2 Experiment 1 Revised UCI APLM Flexure C Design Configurations.

Design	*a* (µm)	*b* (µm)	Flexure Width (µm)	Flexure Length (µm)	Fillets
1	720	40	7.5	721.110	No
2	720	40	7.5	721.110	Yes
3	720	40	10	721.110	No
4	720	40	10	721.110	Yes
5	720	40	15	721.110	No
6	720	40	15	721.110	Yes

Table 5.3 Experiment 1 Coupler Spring Design Configurations.

Design	Flexure D		Flexure E		Fillets
	Width (µm)	Length (µm)	Width (µm)	Length (µm)	
1	7.5	500	7.5	460	No
2	7.5	500	7.5	460	Yes
3	10	500	10	460	No
4	10	500	10	460	Yes
5	15	500	15	460	No
6	15	500	15	460	Yes

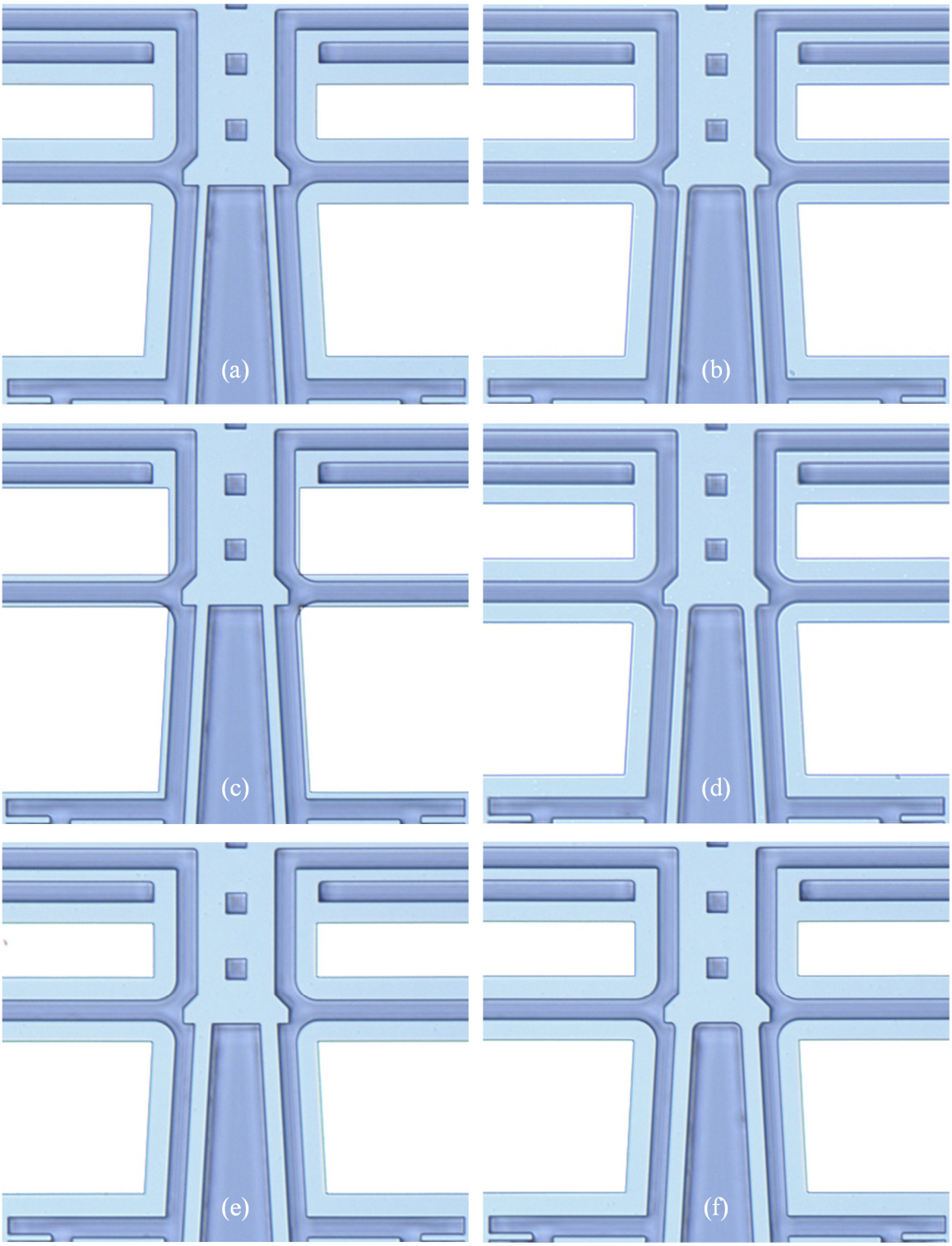

Figure 5.12 Experiment 1 Straight Flexure Revised UCI APLMs.
(a) Design 1, 7.5µm Width w/o Fillets; (b) Design 2, 7.5µm Width w/ Fillets; (c) Design 3, 10µm Width w/o Fillets; (d) Design 4, 10µm Width w/ Fillets; (e) Design 5, 15µm Width w/o Fillets; (f) Design 6, 15µm Width w/ Fillets.

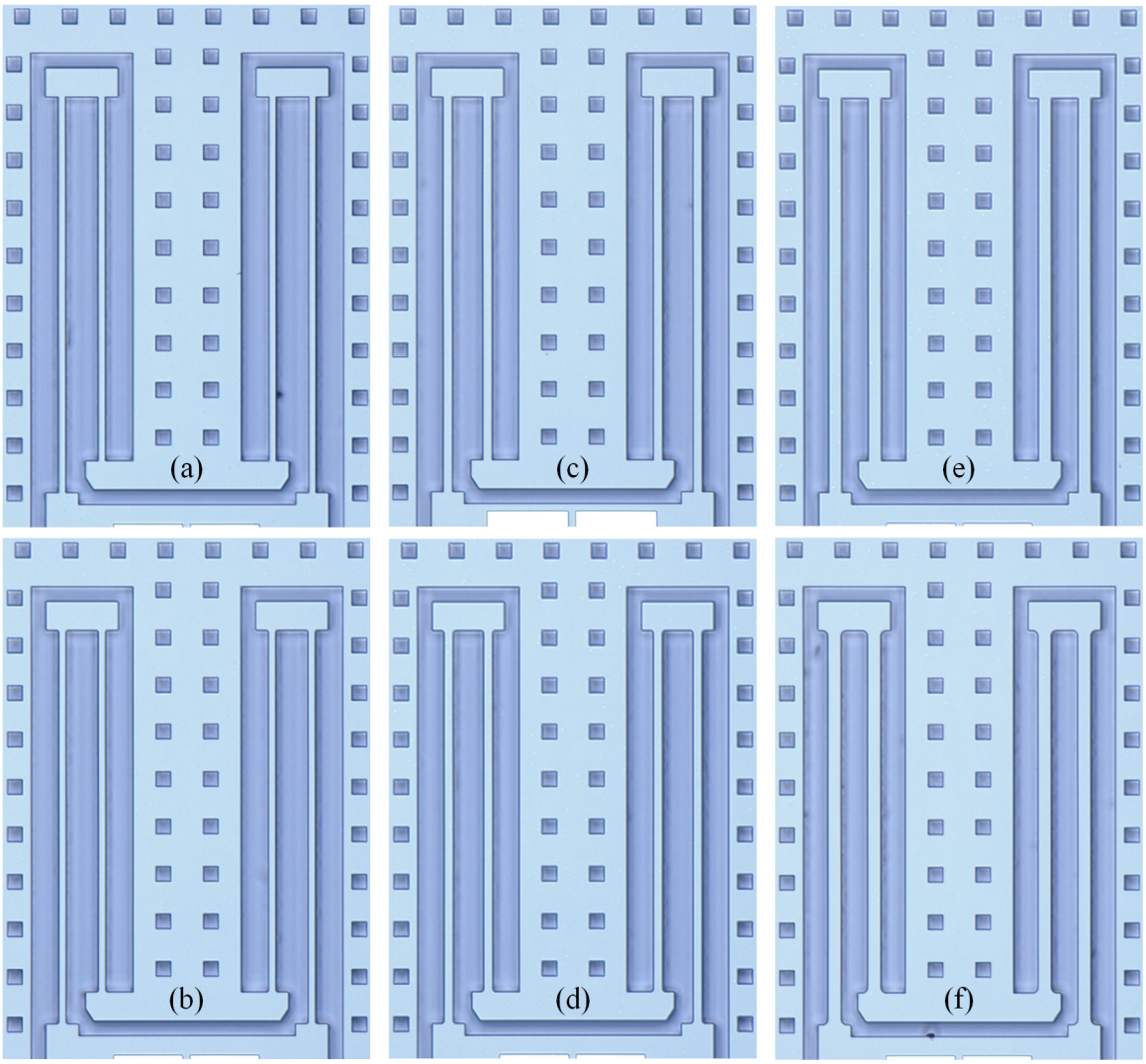

Figure 5.13 Experiment 1 Straight Flexure Coupler Springs.
(a) Design 1, 7.5µm Width w/o Fillets; (b) Design 2, 7.5µm Width w/ Fillets; (c) Design 3, 10µm Width w/o Fillets; (d) Design 4, 10µm Width w/ Fillets; (e) Design 5, 15µm Width w/o Fillets; (f) Design 6, 15µm Width w/ Fillets.

Two different finite element analyses were performed to predict the impact of the incorporation of fillets on the resonant frequency and quality factor statistics. These included modal analysis and thermoelastic damping analysis. To perform the modal analysis, the bottoms of all of the insulation layer pads, highlighted in yellow in Figure 5.14, were given a *FixAll* boundary condition and the solver was configured to return the first 10 structural modes. The anti-phase mode was identified from the results and is

reported as the resonant frequency. To perform the thermoelastic damping analysis, the anchor pads were once again given a *FixAll* boundary condition as shown in Figure 5.14, and two edges of the proof masses, shown in Figure 5.15, were given a *LoadPatch* harmonic boundary condition which applied a harmonic sinusoidal pressure of 0.1Pa peak at the resonant frequency indicated by the modal analysis. The dimensions of the edge of each proof mass were 3540µm long by 100µm thick. This resulted in each mass having a peak force load of 35.4nN applied to it.

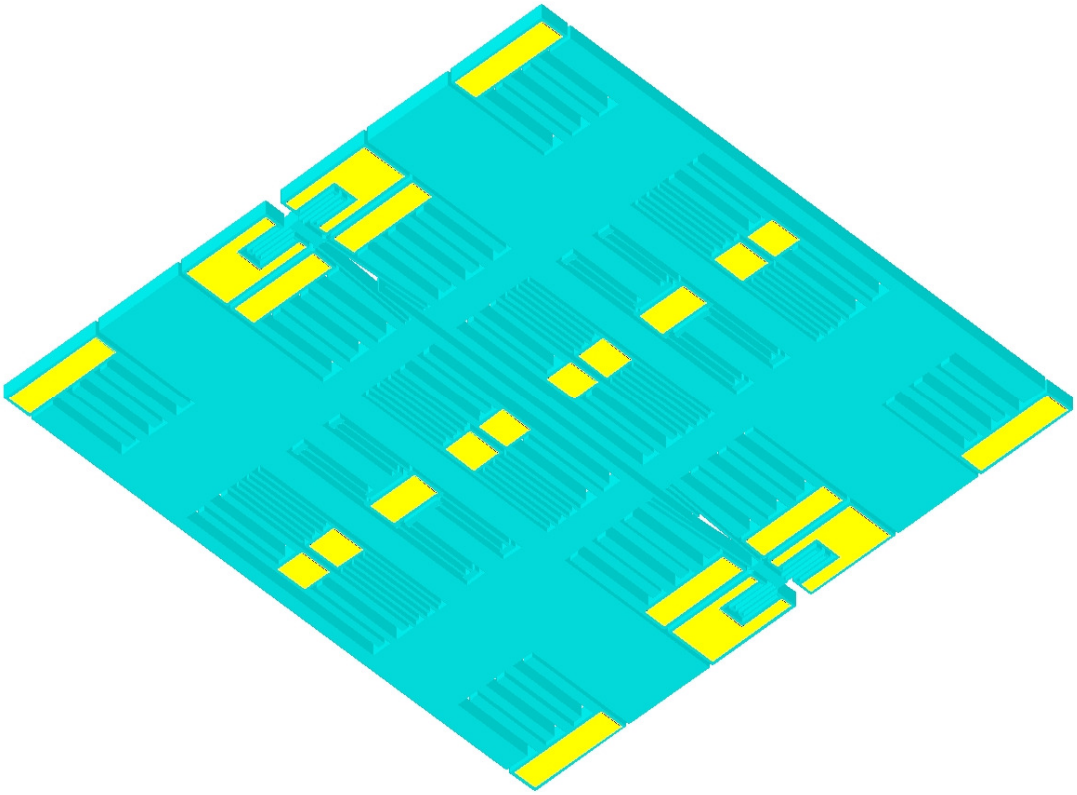

Figure 5.14 Anchor Pad Locations for Modal and TED Analyses (Bottom View).

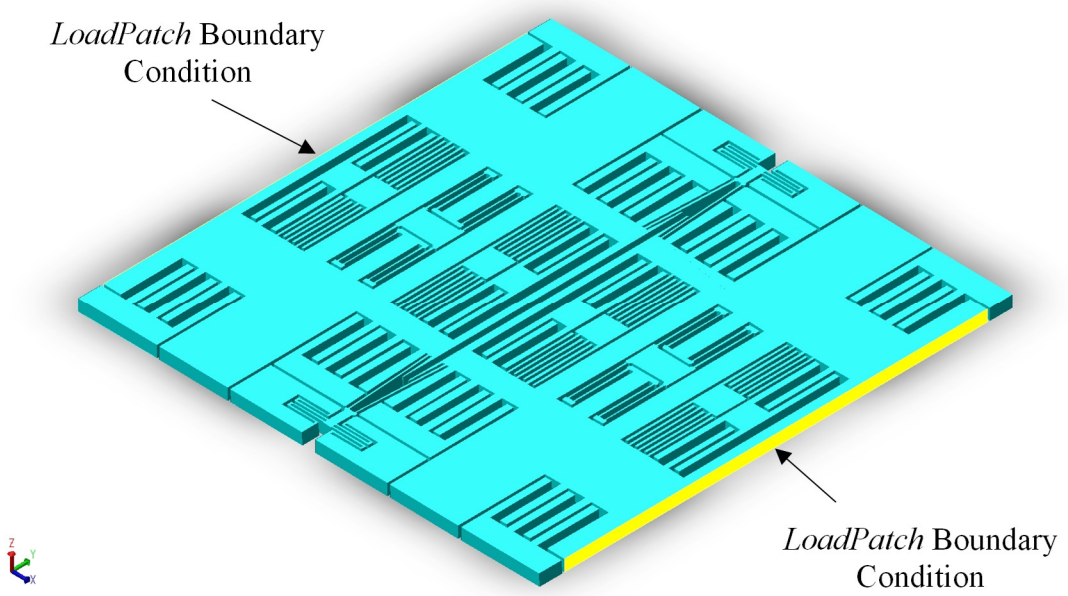

Figure 5.15 Harmonic Boundary Condition Surfaces for TED Analysis.

To estimate the sensitivity of the resonant frequency and thermoelastic damping to Critical Dimension Loss (CDLoss) of the flexure width, the flexures widths (including the fillets) of each of the six designs were varied by plus and minus 0.1μm and the modal analysis and thermoelastic damping analyses were conducted on each model. The modal analysis results are presented in Table 5.4 and the thermoelastic damping results are presented in Table 5.5. A linear least squares curve fit was applied to the three data points for each design and the slopes from those curve fits are provided in the tables as well. For the designs that included fillets, the fillets effectively shortened the length of the flexures thereby stiffening them and increasing their resonant frequencies by a small amount. The variation in the slopes between the designs with fillets and those without fillets was on the same order as the variation in the resonant frequencies. Therefore, it is a fairer comparison to normalize the slope by the nominal resonant frequency. These normalized slopes are also included in Table 5.4. Similarly, since the existence of the

fillets increased the resonant frequency, it also increased the thermoelastic damping (*i.e.*, reduced the quality factor). Therefore, the slopes in Table 5.5 were also normalized by their nominal quality factor and these normalized slopes are also included in Table 5.5. Table 5.6 presents the ratios of the normalized slopes for the designs with and without fillets. The data in this table shows how much fillets may mitigate resonant frequency and thermoelastic damping variations due to manufacturing variability in the flexure widths (*i.e.*, CDLoss). The results indicate that the simple incorporation of fillets alone does not significantly mitigate resonant frequency or thermoelastic damping variability due to CDLoss. The mitigation was negligible for the 7.5µm and 10µm flexure widths and was a modest 3-5% for the 15µm flexure width. However, it is important to recall here that this was not the purpose of including fillets. Fillets were included for two primary reasons which were to mitigate stress peaking at the ends of the flexures, and to reduce manufacturing variability in the inside corners. The latter effect could not be modeled and predicted using FEA because no statistical data was available for the manufacturing variability of the inside corners. However, representative optical photographs are provided in Figure 5.16 that show the over-etching that commonly occurs on inside corners (often referred to as "mouse bites") when fillets are not included, as compared with the smooth inside corners created when fillets are included.

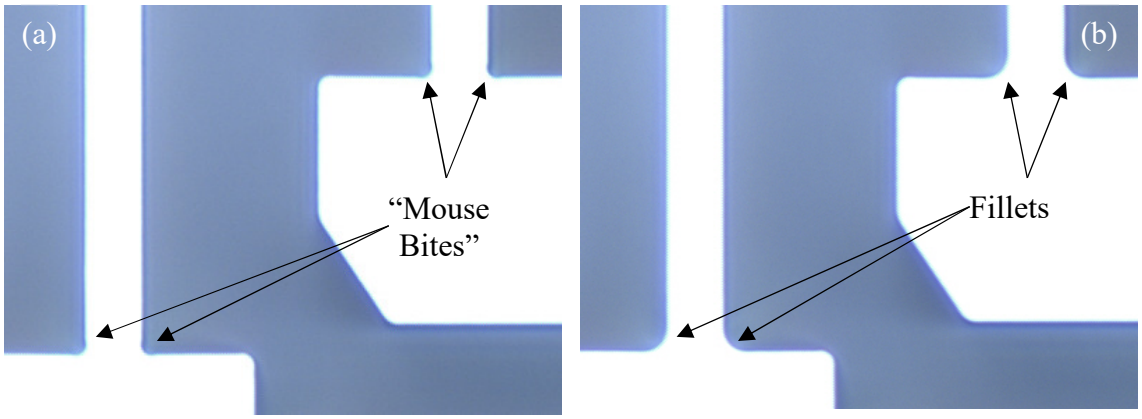

Figure 5.16 Photographs of Inside Corners, (a) without and (b) with Fillets.

Table 5.4 Experiment 1 FEA Resonant Frequency Results.

Design	Flexure Description	-0.1µm Flexure Width (Hz)	Nominal Flexure Width (Hz)	+0.1µm Flexure Width (Hz)	Slope (Hz/nm)	Normalized Slope ((ΔHz/Hz)/µm)
1	7.5µm w/o Fillets	2108.5	2148.6	2189.7	0.4061	0.1890
2	7.5µm w/ Fillets	2124.5	2165.4	2206.4	0.4097	0.1892
3	10µm w/o Fillets	3191.6	3237.7	3283.8	0.4609	0.1424
4	10µm w/ Fillets	3224.1	3271.0	3319.3	0.4762	0.1456
5	15µm w/o Fillets	5735.1	5786.9	5847.9	0.5640	0.0975
6	15µm w/ Fillets	5816.6	5872.4	5925.8	0.5460	0.0930

Table 5.5 Experiment 1 FEA Thermoelastic Damping (Q_{TED}) Results.

Design	Flexure Description	-0.1µm Flexure Width (unitless)	Nominal Flexure Width (unitless)	+0.1µm Flexure Width (unitless)	Slope (1/nm)	Normalized Slope (1/µm)
1	7.5µm w/o Fillets	4.295E+06	4.128E+06	3.966E+06	-1645.5	-0.3986
2	7.5µm w/ Fillets	4.217E+06	4.051E+06	3.892E+06	-1625.1	-0.4011
3	10µm w/o Fillets	1.685E+06	1.629E+06	1.576E+06	-547.4	-0.3360
4	10µm w/ Fillets	1.641E+06	1.587E+06	1.533E+06	-537.9	-0.3390
5	15µm w/o Fillets	4.245E+05	4.154E+05	4.058E+05	-93.4	-0.2250
6	15µm w/ Fillets	4.079E+05	3.988E+05	3.904E+05	-87.4	-0.2190

Table 5.6 Experiment 1 FEA with and without Fillets Slope Ratios.

Design	Flexure Width (µm)	Resonant Frequency Normalized Slope Ratio	Q_{TED} Normalized Slope Ratio
		(%)	(%)
1 & 2	7.5	0.1	0.6
3 & 4	10	2.3	0.9
5 & 6	15	-4.6	-2.6

As mentioned previously, the fabricated wafer included 30 copies of all 6 Experiment 1 resonator designs. For each of these designs, 9 copies were oriented with the resonator motion along the y-axis of the wafer and 21 were oriented with the resonator motion along the x-axis of the wafer. For each of the y-axis devices, an x-axis device was placed in an adjacent cell. The locations of the individual design

configurations on the wafer are shown for all designs in Appendix C, Figures C.25 - C.30, but a representative distribution is shown in Figure 5.17. The double block items are the locations where there was an x-axis device adjacent to a y-axis device. These figures demonstrate a relatively even distribution of the design instances across the wafer.

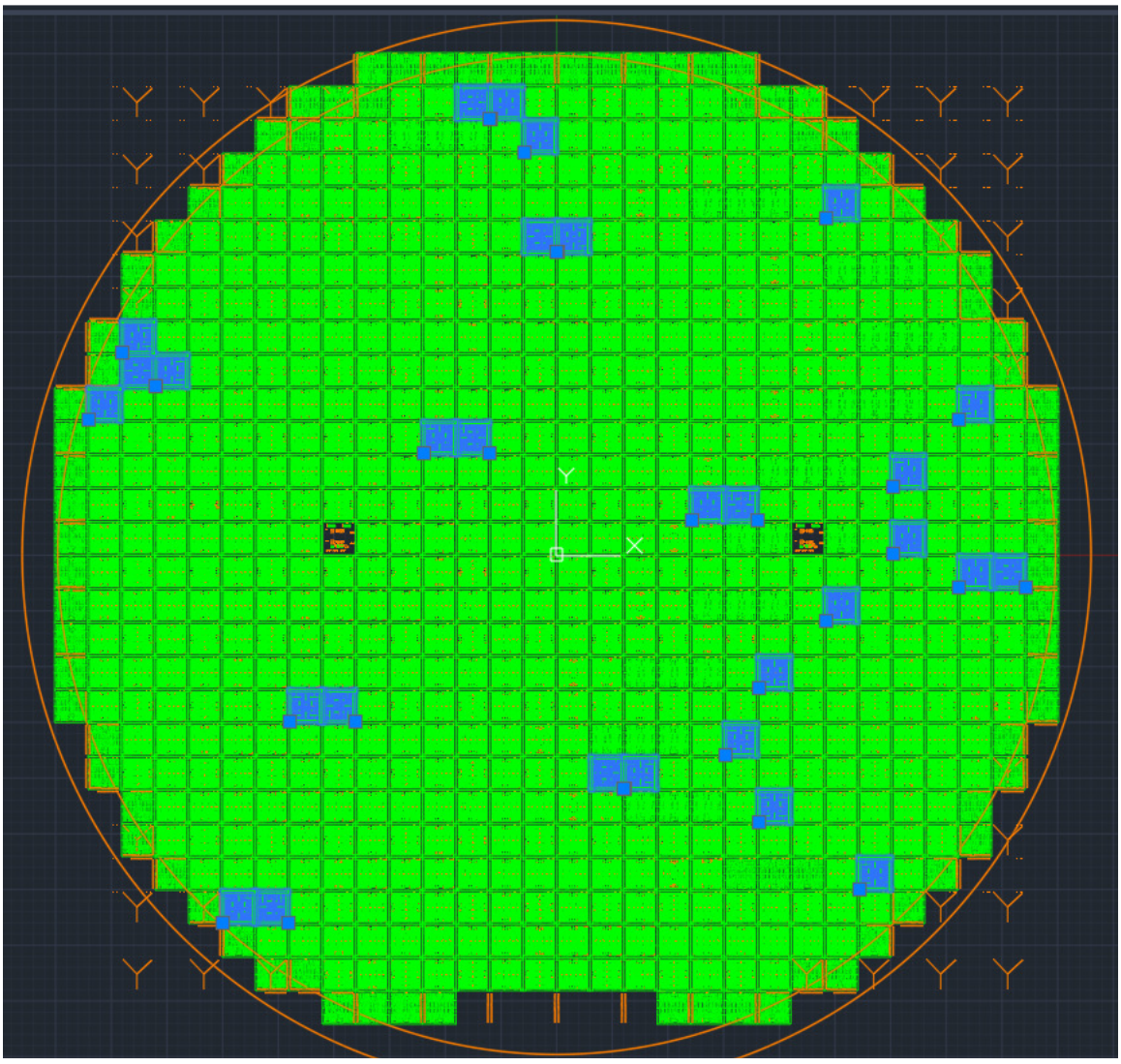

Figure 5.17 Experiment 1 Design 2 Locations on Wafer, 7.5µm Width w/ Fillet.

While it was anticipated that a search for the resonant frequency would be required to interrogate the devices, in practice the devices were very sensitive and the

vast majority of them exhibited some resonance as soon as the probe tips came into contact with the device. Therefore, the power spectral density of the sense signal was inspected immediately after probe tip contact and the approximate resonant frequency was readily identified. The lock-in amplifier was then set to output a 10mV peak sine wave at that frequency and the frequency was then adjusted by hand, typically in the tenths of hertz digit, until a significant response (>100mV sense signal) was obtained from the device at which time the drive signal was removed. This frequency value was recorded as the resonant frequency, f_R. The lock-in amplifier provided a demodulated amplitude output from the sense signal using this frequency which was recorded to a data file to estimate the ringdown time constant, τ_D. The ringdown time was estimated using a linear least squares curve fit of the natural logarithm of this demodulated amplitude signal as follows. The amplitude signal follows a traditional exponential decay equation given in Equation 5.1:

$$V_A = V_{A0} \cdot e^{-t/\tau_D} \quad , \tag{5.1}$$

where V_A is the amplitude signal, V_{A0} is the initial amplitude of the amplitude signal, t is time, and τ_D is the ringdown time constant. Taking the natural logarithm of both sides yields

$$\ln(V_A) = \ln\left(V_{A0} \cdot e^{-\frac{t}{\tau_D}}\right) = \ln(V_{A0}) \cdot \ln\left(e^{-\frac{t}{\tau_D}}\right) = \ln(V_{A0}) - \frac{t}{\tau_D} \quad , \tag{5.2}$$

which can easily be fitted with the standard line equation. Occasionally, due to a self-sustaining resonance, a device under test would not ring down to zero volts as is

suggested by Equation 5.1. In these cases, the final offset value was estimated and subtracted from the of the raw V_A data before computing the natural logarithm and performing the curve fit. This offset estimation was often iterated a few times to determine the offset that provided the best overall curve fit. The quality factor was then estimated using the following equation:

$$Q = \frac{\tau_D \cdot 2\pi f_R}{2} = \tau_D \cdot \pi \cdot f_R \,. \tag{5.3}$$

Typical vacuum levels in the vacuum probe station chamber were around 0.4μTorr, well below the pressure required to ensure that air damping did not limit the quality factor [86].

Much of the data collected from the first measurement set was suspect for many reasons including excessive noise on the sense channel and uncertainty about the quality of the contact between the probe pins and the device under test. Therefore, the data presented herein is largely from the second measurement set. As mentioned previously, data was only collected on the designs with 15μm width flexures because too many of the devices with 7.5μm and 10μm flexure widths would self-resonate which prevented ringdown data collection. Also, not all quality factor measurements were included in the quality factor results presented herein. There were two criteria that would cause a quality factor measurement to be excluded. The first criterion was if the quality factor was physically impossible. Thermoelastic damping is a fundamental material property that limits the quality factor of a resonator made of that material in a particular geometry. The second was if the quality factor was too low to be limited by thermoelastic damping. That is, if another source of damping was limiting the overall quality factor more than the

predicted thermoelastic damping, then that data point was excluded. Therefore, the measured quality factor had to fall between one-half and one of the predicted quality factor ($\frac{Q_{Predicted}}{2} \leq Q_{Measured} \leq Q_{Predicted}$) to be included in the statistics.

Table 5.7 presents the statistics of the acceptable resonant frequency and quality factor measurements taken from the second measurement set of the Experiment 1 x-axis devices. Unfortunately, there was significant across-wafer variation of both the resonant frequency and the quality factor which dominated the statistics in Table 5.7. Figure 5.18 and Figure 5.19 plot the measured resonant frequencies and quality factors, respectively, against the die location row on the wafer. The correlation between die location and both the resonant frequency and quality factor is very clear. Therefore, a linear least squares curve fit was applied to both the resonant frequency and the quality factor data as a function of wafer row and column number and this fit was subtracted from the raw measurements. Table 5.8 presents the statistics of the resonant frequency and quality factor measurements that were compensated for these across-wafer trends.

Table 5.7 Experiment 1 Probe Station Measurement Results, X-axis Devices.

Design	Flexure Description	Resonant Frequency (Hz)		Quality Factor (unitless)	
		Mean	St. Dev.	Mean	St. Dev.
5	15 µm w/o Fillets	4893.2	323.3	316315	44718.9
6	15 µm w/ Fillets	5000.7	328.8	318463	54407.7

The data indicate several things. First, the average resonant frequencies were significantly less that FEA predictions, which suggests a significant amount of CDLoss

(~1.6µm) in fabrication. Second, inclusion of fillets raised the average resonant frequency as predicted by the FEA. Third, fillets did reduce the variability of the resonant frequency and by quite a bit more than what was predicted by the FEA. This suggests that manufacturing variations of the inside corners contributes significantly to the overall resonant frequency variability and that the introduction of fillets can help mitigate that effect. Lastly, fillets do not appear to have a statistically significant effect on either the average quality factor or the quality factor variability.

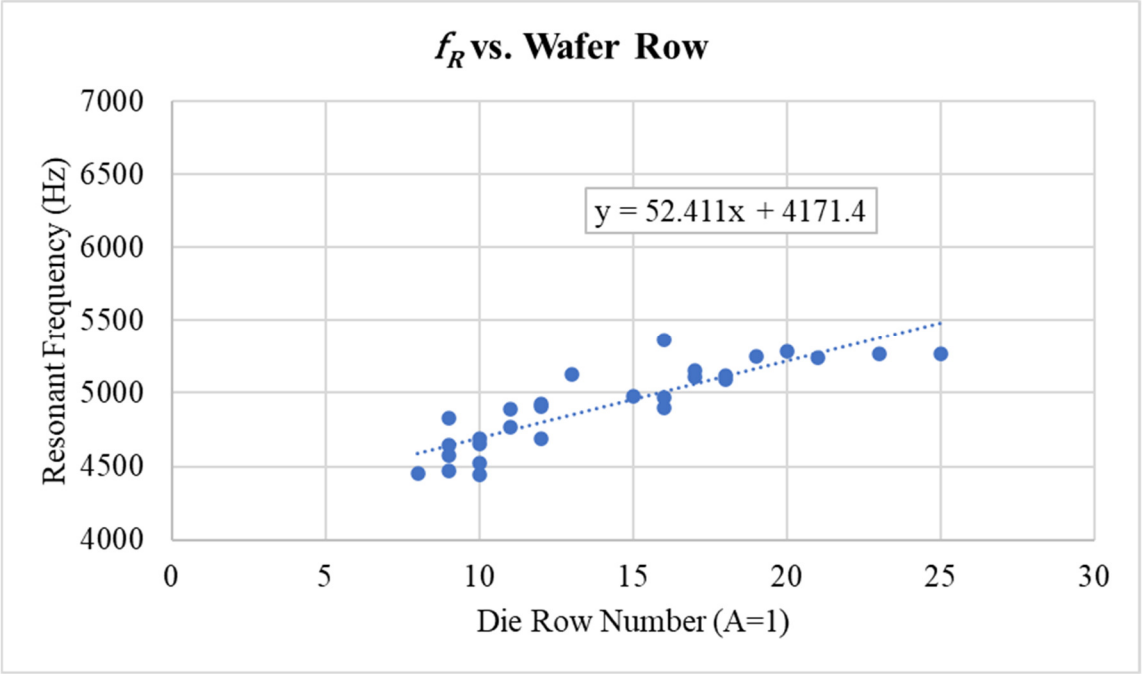

Figure 5.18 Experiment 1 Resonant Frequency Versus Wafer Row.

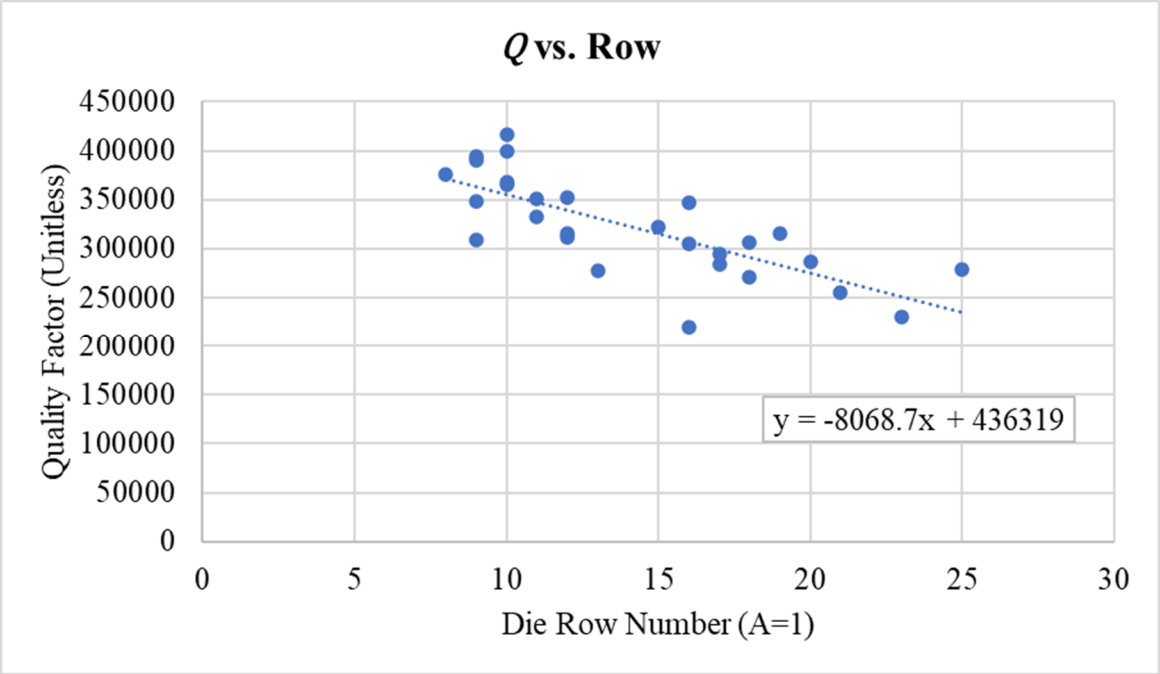

Figure 5.19 Experiment 1 Resonant Frequency Versus Wafer Row.

Table 5.8 Experiment 1 Results, X-axis Devices, Compensated for Across-Wafer Trends.

Design	Flexure Description	Resonant Frequency (Hz)		Quality Factor (unitless)	
		Mean	St. Dev.	Mean	St. Dev.
5	15 µm w/o Fillets	-23.9	139.8	-9421	32598.7
6	15 µm w/ Fillets	113.3	115.6	-8216	35337.4

Table 5.9 presents the statistics of the differences in resonant frequency and quality factor measurements taken from adjacent x-axis and y-axis devices. The differences were calculated by subtracting the y-axis measurement from the x-axis measurement. Since these differences were taken between devices that were adjacent to each other on the wafer, there was no need to compensate for across wafer variations.

The data indicate that adjacent x-axis and y-axis devices had resonant frequencies that were very closely matched but, even so, the introduction of fillets significantly reduced the variability of the resonant frequency deltas. The y-axis devices also appear to have a slightly higher resonant frequency on average than the x-axis devices. This could be due to a mask or lithography bias or some directionality in the fabrication process. The quality factor data, on the other hand, appears to be completely uncorrelated between the x-axis and y-axis devices except that the y-axis devices appear to have a higher quality factor on average than the x-axis devices. It is important to note here that, while there were nine pairs of each design on the wafer, due to yield issues, only 7 total pairs of devices were available for this analysis, 4 pairs for the 15µm wide design without fillets and only 3 pairs for the 15µm wide design with fillets. This limited data set should temper the over-interpretation of these findings as there is not enough data to support statistical confidence in the perceived correlation.

Table 5.9 Experiment 1 Measurement Results, X-axis and Y-axis Adjacent Devices.

Design	Flexure Description	Resonant Frequency Deltas (Hz)		Quality Factor Deltas (unitless)	
		Mean	St. Dev.	Mean	St. Dev.
5	15 µm w/o Fillets	-11.9	48.9	-54119	222393.1
6	15 µm w/ Fillets	-10.9	20.7	-120539	105577.5

5.2.2 Experiment 2 - Tapered Flexures with and without Fillets

The purpose of Experiment 2 was to assess the impact of the incorporation of fillets in tapered flexure designs on resonant frequency and quality factor statistics. Experiment 2 consisted of 6 unique resonator designs incorporating tapered flexure designs equivalent to the straight flexure designs in Experiment 1 that had widths of 7.5µm, 10µm, and 15µm, with and without fillets. Here again the "equivalent" tapered flexure is defined as one that has the same length as the straight flexure and a base width that gives the same linear spring constant.

For all of the tapered flexures designs in Experiment 2, given the length of the tapered flexure, *L*, the value of the half-length of the hammerhead feature, *d*, was selected to maintain an $\left(\frac{L}{d}\right)$ ratio of approximately 3 because previous analysis indicated this $\left(\frac{L}{d}\right)$ ratio would slightly improve the quality factor over that of the straight flexure while retaining similar performance for sensitivity to manufacturing variations. However, the value of the $\left(\frac{L}{d}\right)$ ratio was decreased in the 7.5µm equivalent flexure width designs to ensure that the minimum neck width of the tapered flexure was above the minimum feature size (5µm) allowed by the fabrication process design rules. This resulted in an $\left(\frac{L}{d}\right)$ ratio of approximately 2 for those designs.

Here we document the general procedure to replace a straight cantilever beam flexure with a tapered cantilever beam flexure. It is important to note that a guided flexure consists of two cantilever beams connected end to end. Similarly, a tapered guided flexure consists of two tapered cantilever beams connected end to end as was mentioned in Section 3.2.5. Therefore, the cantilever flexure lengths in the following

discussion correspond to half of the lengths of the straight flexures used in Experiment 1 designs.

Given a straight flexure of length, N, and width, w, to be replaced by a tapered flexure of length, L, with hammerhead half-length, d, and base width of w_b, first select a reasonable value for the hammerhead half-length, d. Noting that

$$L + d = N, \tag{5.4}$$

the value of d could alternatively be determined by first selecting a desired $\left(\frac{L}{d}\right)$ ratio and solving for d, which yields:

$$d = \frac{N}{\frac{L}{d} + 1}. \tag{5.5}$$

The length of the tapered flexure is then given by:

$$L = N - d. \tag{5.6}$$

Combining the equation for the linear spring constant of a tapered flexure given in Table 3.1 with the standard equivalent expression for the straight flexure [30], the base width of the equivalent tapered flexure, w_b, can then be determined using the following equation:

$$w_b = w \cdot \left\{ 2 \cdot \left[1 - \left(\frac{d}{N} \right)^{\frac{3}{2}} \right] \right\}^{1/3} \tag{5.7}$$

or alternatively, in terms of the $\left(\frac{L}{d}\right)$ ratio:

$$w_b = w \cdot \left\{ 2 \cdot \left[1 - \left(\frac{1}{\frac{L}{d} + 1} \right)^{\frac{3}{2}} \right] \right\}^{1/3} , \tag{5.8}$$

which asymptotically approaches $w\sqrt[3]{2}$ (approximately $1.26w$) as the $\left(\frac{L}{d}\right)$ ratio gets large and approaches zero as the $\left(\frac{L}{d}\right)$ ratio gets small. It is important to check the neck width of the tapered flexure at the hammerhead to ensure that it does not fall below the minimum allowable feature size of the fabrication process. The neck width (flexure width at the hammerhead) is given by:

$$w_{Neck} = w_b \cdot \sqrt{\frac{d}{N}} . \tag{5.9}$$

If the neck width falls below the minimum allowable feature size of the fabrication process, then *d* must be increased and the process must be iterated.

Figure 5.20 shows a representative tapered flexure revised UCI APLM layout with the flexure designators identified. Table 5.10 summarizes the Flexure C APLM design configurations for Experiment 2. The shuttle block and folded flexure portions of the APLM design were the same for all Experiment 2 design configurations and were identical to those described in Table 5.1 for the Experiment 1 configuration. The two flexures that constitute the coupler springs, Flexure D and Flexure E, are shown in Figure 5.21. Tables 5.11 and 5.12 summarize the Experiment 2 coupler spring design configurations for Flexure D and Flexure E, respectively. To enable visual comparison of the various designs in Experiment 2, optical photographs of the fabricated devices are

provided zoomed into the APLMs in Figure 5.22 and zoomed into the coupler springs in Figure 5.23. Broader views of the solid model renderings of the APLMs are provided in Appendix C, Figures C.13 - C.18. Broader views of the solid model renderings of the coupler springs are provided in Appendix C, Figures C.19 - C.24.

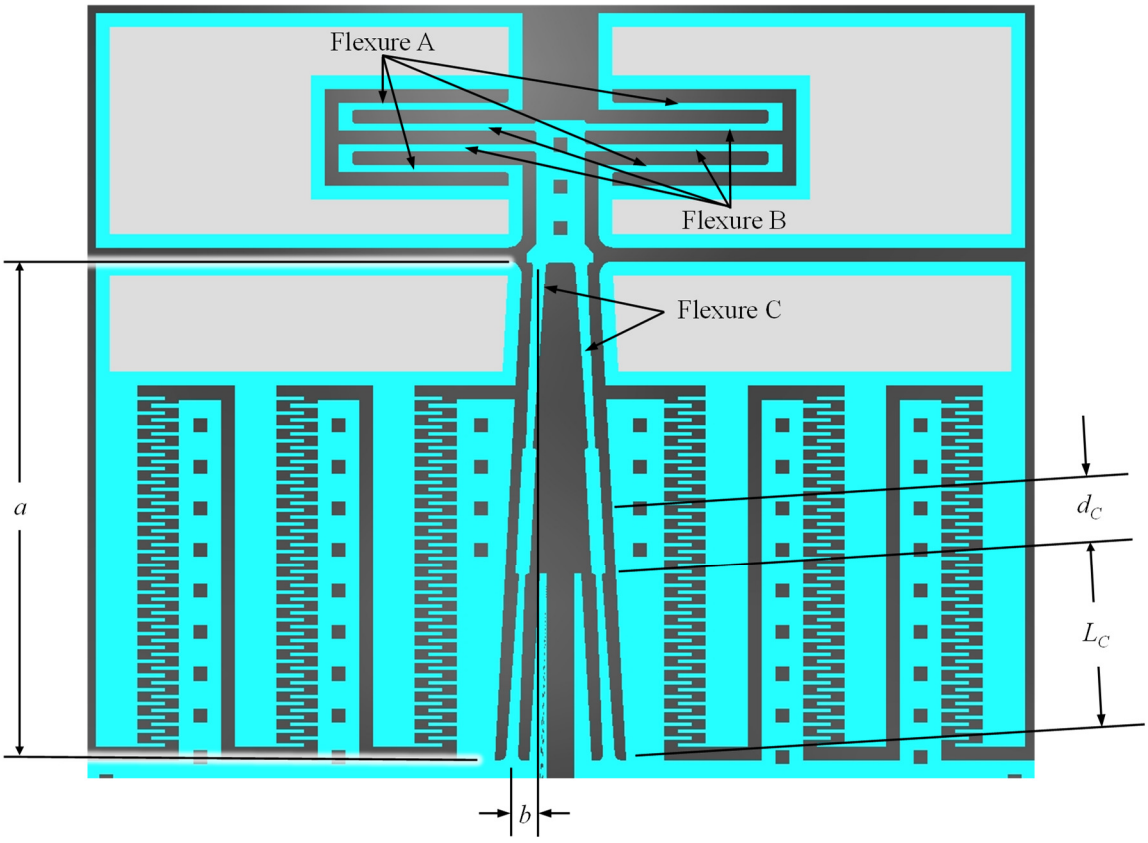

Figure 5.20 Experiment 2 Tapered Flexure Revised UCI APLM Element Designations.

Table 5.10 Experiment 2 Tapered Flexure Revised UCI APLM Design Configurations.

Design	*a* (µm)	*b* (µm)	Base Width w_{b_C} (µm)	Flexure Length L_C (µm)	Hammerhead Half-length d_C (µm)	*L/d* Ratio (unitless)	Fillets
1	720	40	8.801	240.555	120	2.005	No
2	720	40	8.801	240.555	120	2.005	Yes
3	720	40	12.052	270.555	90	3.006	No
4	720	40	12.052	270.555	90	3.006	Yes
5	720	40	18.078	270.555	90	3.006	No
6	720	40	18.078	270.555	90	3.006	Yes

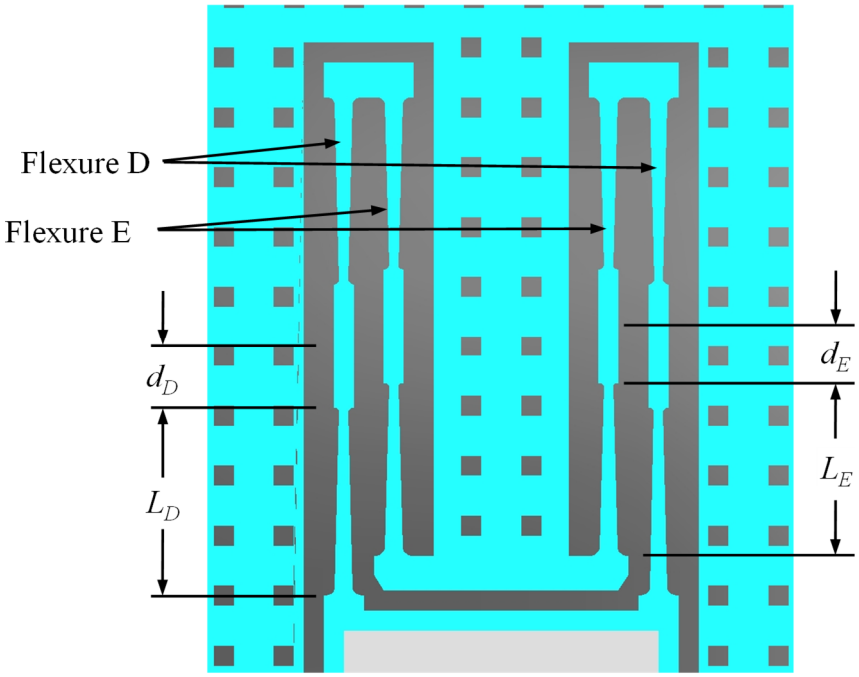

Figure 5.21 Experiment 2 Coupler Spring Element Designations.

Table 5.11 Experiment 2 Coupler Spring Flexure D Design Configurations.

Design	Base Width w_{b_D} (µm)	Flexure Length L_D (µm)	Hammerhead Half-length d_D (µm)	*L/d* Ratio (unitless)	Fillets
1	8.841	170	80	2.125	No
2	8.841	170	80	2.125	Yes
3	12.051	187.5	62.5	3.0	No
4	12.051	187.5	62.5	3.0	Yes
5	18.076	187.5	62.5	3.0	No
6	18.076	187.5	62.5	3.0	Yes

Table 5.12 Experiment 2 Coupler Spring Flexure E Design Configurations.

Design	Base Width w_{b_E} (µm)	Flexure Length L_E (µm)	Hammerhead Half-length d_E (µm)	*L/d* Ratio (unitless)	Fillets
1	8.822	155	75	2.067	No
2	8.822	155	75	2.067	Yes
3	12.051	172.5	57.5	3	No
4	12.051	172.5	57.5	3	Yes
5	18.076	172.5	57.5	3	No
6	18.076	172.5	57.5	3	Yes

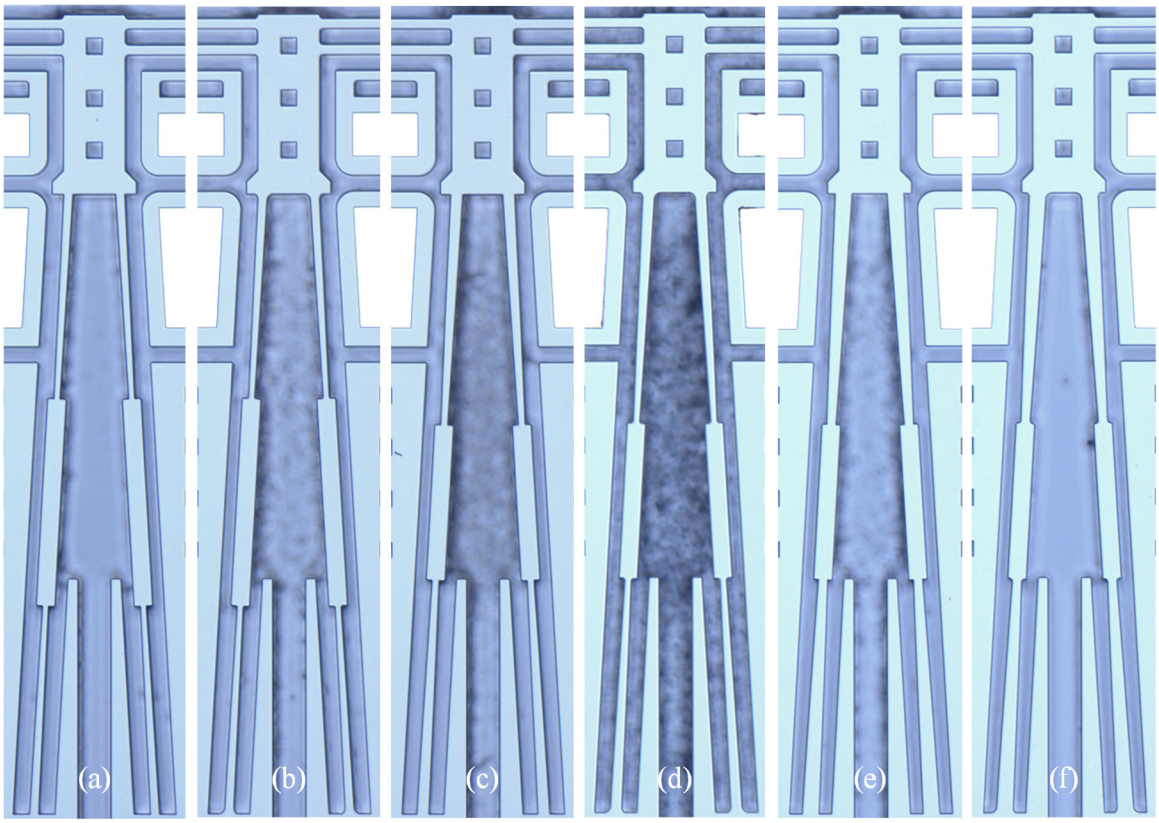

Figure 5.22 Experiment 2 Tapered Flexure Revised UCI APLMs.
(a) Design 1, 7.5µm Width w/o Fillets; (b) Design 2, 7.5µm Width w/ Fillets; (c) Design 3, 10µm Width w/o Fillets; (d) Design 4, 10µm Width w/ Fillets; (e) Design 5, 15µm Width w/o Fillets; (f) Design 6, 15µm Width w/ Fillets.

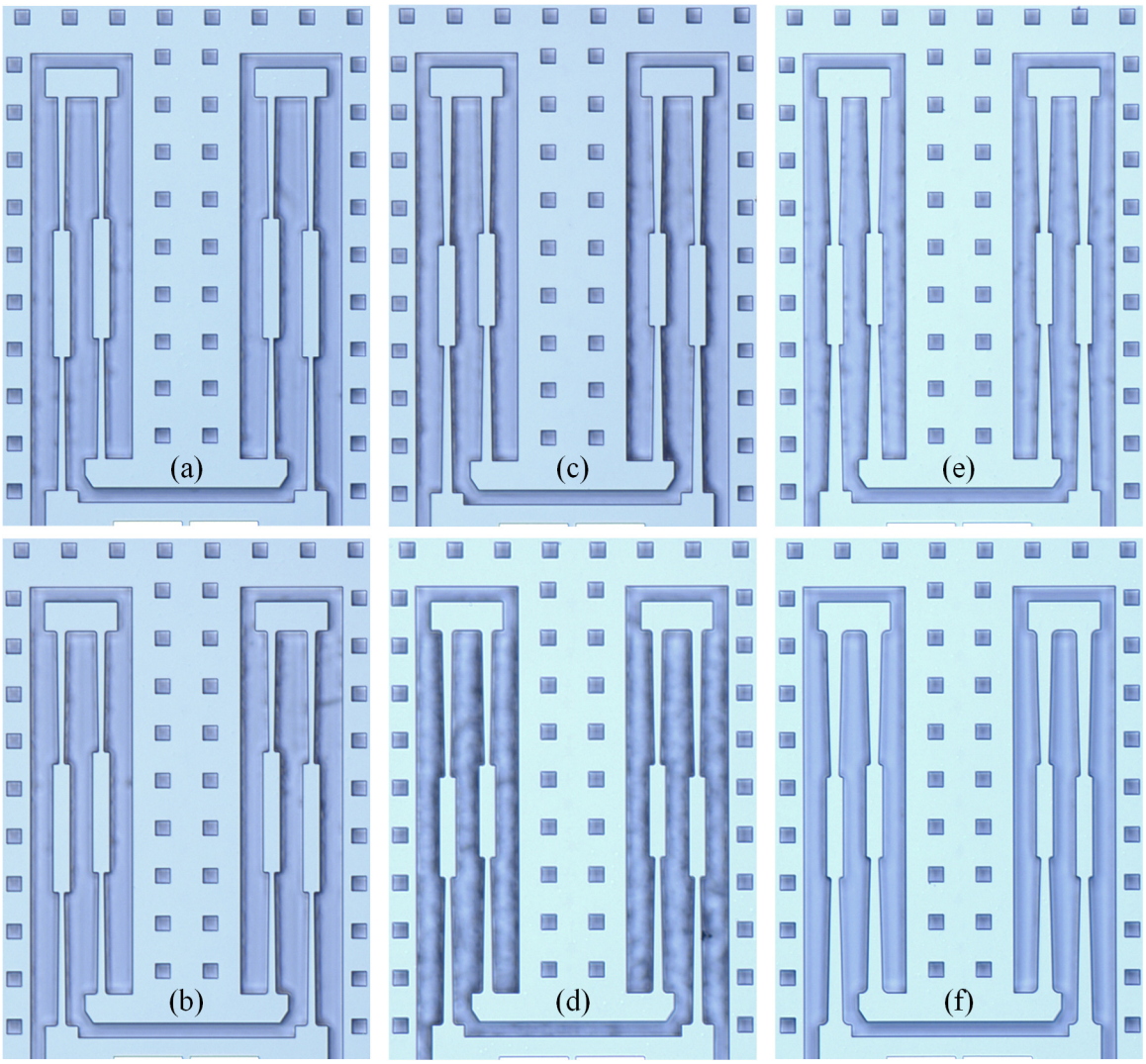

Figure 5.23 Experiment 2 Tapered Flexure Coupler Springs.
(a) Design 1, 7.5µm Width w/o Fillets; (b) Design 2, 7.5µm Width w/ Fillets; (c) Design 3, 10µm Width w/o Fillets; (d) Design 4, 10µm Width w/ Fillets; (e) Design 5, 15µm Width w/o Fillets; (f) Design 6, 15µm Width w/ Fillets.

Modal analysis and thermoelastic damping analysis were performed via finite element analysis on the device designs in Experiment 2 in a manner similar to that described in Section 5.2.1 for Experiment 1 to predict the impact of the incorporation of fillets on the resonant frequency and quality factor sensitivity to CDLoss. The modal analysis results are presented in Table 5.13 and the thermoelastic damping results are presented in Table 5.14. Similar to the results in Experiment 1, the fillets effectively

shortened the length of the flexures thereby increasing the resonant frequencies, and reducing the quality factor by a small amount. Table 5.15 presents the ratios of the normalized slopes for the designs with and without fillets. Similar to the results from Experiment 1 FEAs, the results indicate that the simple incorporation of fillets alone does not significantly mitigate resonant frequency and thermoelastic damping variability due to CDLoss, but the fillets do mitigate the stress peaking around the inside corner of the flexures and it was anticipated that the natural fillet radius variation in the manufacturing process would be significantly mitigated by the intentional inclusion of fillets in the design.

Table 5.13 Experiment 2 FEA Resonant Frequency Results.

Design	Flexure Description	-0.1µm Flexure Width (Hz)	Nominal Flexure Width (Hz)	+0.1µm Flexure Width (Hz)	Slope (Hz/nm)	Normalized Slope ((ΔHz/Hz)/µm)
1	7.5µm w/o Fillets	2107.1	2152.7	2196.0	0.4442	0.2063
2	7.5µm w/ Fillets	2122.7	2166.0	2209.4	0.4336	0.2002
3	10µm w/o Fillets	3194.0	3248.0	3287.1	0.4657	0.1434
4	10µm w/ Fillets	3216.2	3266.4	3316.7	0.5026	0.1539
5	15µm w/o Fillets	5708.2	5760.8	5818.8	0.5529	0.0960
6	15µm w/ Fillets	5783.9	5842.0	5902.4	0.5922	0.1014

Table 5.14 Experiment 2 FEA Thermoelastic Damping (Q_{TED}) Results.

Design	Flexure Description	-0.1µm Flexure Width (unitless)	Nominal Flexure Width (unitless)	+0.1µm Flexure Width (unitless)	Slope (1/nm)	Normalized Slope (1/µm)
1	7.5µm w/o Fillets	4.259E+06	4.074E+06	3.912E+06	-1735.3	-0.4259
2	7.5µm w/ Fillets	4.202E+06	4.031E+06	3.864E+06	-1689.8	-0.4192
3	10µm w/o Fillets	1.706E+06	1.642E+06	1.594E+06	-562.1	-0.3424
4	10µm w/ Fillets	1.684E+06	1.624E+06	1.566E+06	-590.8	-0.3638
5	15µm w/o Fillets	4.376E+05	4.280E+05	4.181E+05	-97.7	-0.2282
6	15µm w/ Fillets	4.258E+05	4.158E+05	4.063E+05	-97.7	-0.2349

Table 5.15 Experiment 2 FEA with and without Fillets Slope Ratios.

Design	Equivalent Flexure Width (µm)	Resonant Frequency Normalized Slope Ratio	Q_{TED} Normalized Slope Ratio
		(%)	(%)
1 & 2	7.5	-3.0	-1.6
3 & 4	10	7.3	6.3
5 & 6	15	5.6	3.0

Similar to Experiment 1, the fabricated wafer included 30 copies of all 6 Experiment 2 resonator designs with 9 copies oriented along the y-axis of the wafer and 21 oriented along the x-axis of the wafer. For each of the y-axis devices, an x-axis device was placed in an adjacent cell. The locations on the wafer for the individual design configurations are provided in Appendix C, Figures C.31 - C.36.

Resonant frequency and quality factor data was collected from the fabricated wafer and analyzed in a manner consistent with that described for Experiment 1. Table 5.16 presents the statistics of the acceptable resonant frequency and quality factor measurements for the Experiment 2 x-axis devices. Like Experiment 1, there was significant across-wafer variation of both the resonant frequency and the quality factor which dominated the statistics in Table 5.16. Table 5.17 presents the statistics of the resonant frequency and quality factor measurements that were compensated for these across-wafer trends.

Similar to the results of Experiment 1, the average resonant frequencies were significantly less than FEA predictions, which suggests a significant amount of CDLoss in fabrication. Fillets again raised the average resonant frequency as predicted by the FEA. Fillets also reduced the variability of the resonant frequency and by quite a bit more than what was predicted by the FEA, suggesting that manufacturing variations on the inside corners contributes significantly to the overall resonant frequency variability and that the introduction of fillets can help mitigate that effect. Only 4 of the Design 5 devices (without fillets) had quality factors that fell within the acceptable quality factor guidelines described in the previous section for Experiment 1, whereas 9 of the Design 6 devices (with fillets) had acceptable quality factors. Therefore, while it would not be wise to place too much value on the interpretation of the quality factor statistics presented in Tables 5.16 and 5.17, this dramatic difference in devices with acceptable quality factor suggests that the incorporation of fillets significantly increased the quality factor yield of the tapered flexure devices.

Table 5.16 Experiment 2 Probe Station Measurement Results, X-axis Devices.

Design	Flexure Description	Resonant Frequency (Hz)		Quality Factor (unitless)	
		Mean	St. Dev.	Mean	St. Dev.
5	15 µm w/o Fillets	4888.3	401.2	365762	49338.6
6	15 µm w/ Fillets	4917.1	324.4	310993	50568.2

Table 5.17 Experiment 2 Results, X-axis Devices, Compensated for Across-Wafer Trends.

Design	Flexure Description	Resonant Frequency (Hz)		Quality Factor (unitless)	
		Mean	St. Dev.	Mean	St. Dev.
5	15 µm w/o Fillets	-103.8	169.7	34403	23402.2
6	15 µm w/ Fillets	-0.4	122.7	-525	20720.3

Table 5.18 presents the statistics of the differences in resonant frequency and quality factor measurements taken from adjacent x-axis and y-axis devices. There was only one pair of devices for Design 5 (without fillets) that had acceptable frequency and quality factor measurements. Therefore, variability data is not available for that design and there is little confidence in the comparison of these results. However, these results are included for completeness. Once again, a significantly higher number of Design 6 devices (with fillets), four pairs, had acceptable frequency and quality factor measurements. This further supports the argument that the incorporation of fillets significantly increases the quality factor yield of the tapered flexure devices.

Table 5.18 Experiment 2 Measurement Results, X and Y-axis Adjacent Devices.

Design	Flexure Description	Resonant Frequency (Hz)		Quality Factor (unitless)	
		Mean	St. Dev.	Mean	St. Dev.
5	15 µm w/o Fillets	57.9	N/A	-291954	N/A
6	15 µm w/ Fillets	27.9	28.5	-76356	133419.8

5.2.3 Experiment 3 – Straight vs. Tapered Flexure Performance

The purpose of Experiment 3 was to use the devices from Experiments 1 and 2 to compare the performance of the straight and tapered flexure dual mass resonator configurations with and without fillets. There were no additional devices fabricated for this experiment as it is just a comparative analysis of the results from Experiments 1 and 2. Since no data is available for the 7.5µm and 10µm flexure width devices, this section focuses on the 15µm flexure width device results.

Tables 5.19 - 5.21 show the finite element predictions for normalized resonant frequency slopes, thermoelastic damping limited quality factor (Q_{TED}), and normalized Q_{TED} damping slopes, respectively, for the 15µm flexure width designs in Experiments 1 and 2. These analyses largely predict very comparable results between straight and tapered flexures. The most significant predictions were that tapered flexures were expected to increase the quality factor by 3-4% and that tapered flexures generally increased the slopes by a few percent. Additionally, while fillets reduced the slopes of the straight flexure designs by a few percent, they increased the slopes of both the resonant frequency and the quality factor in the tapered flexure designs by a few percent.

The experimental results for the x-axis devices from Experiment 1 and 2 are presented in Table 5.22 for the raw measurements and in Table 5.23 for the measurements that were compensated for across-wafer variations. The data supports the FEA prediction that tapered flexures increase the quality factor by a few percent and that tapered flexures increase the frequency variability by a few percent. However, the compensated data suggests that tapered flexures reduce the variability of the quality factor as compared with straight flexure designs. While there is a reduction in the quality factor variability of the tapered flexure design with fillets, the reduction is not statistically significant. However, this does suggest that the incorporation of fillets into the tapered flexure design did not significantly increase the quality factor variability as was suggested by the FEA predictions.

Table 5.19 FEA Normalized Resonant Frequency Slopes.

Design	Flexure Description	Experiment 1 Straight	Experiment 2 Tapered
		((ΔHz/Hz)/μm)	((ΔHz/Hz)/μm)
5	15μm w/o Fillets	0.097	0.096
6	15μm w/ Fillets	0.093	0.101

Table 5.20 FEA Q_{TED} Results.

Design	Flexure Description	Experiment 1 Straight	Experiment 2 Tapered
		Million	Million
5	15µm w/o Fillets	0.415	0.428
6	15µm w/ Fillets	0.399	0.416

Table 5.21 FEA Normalized Q_{TED} Damping Slopes.

Design	Flexure Description	Experiment 1 Straight	Experiment 2 Tapered
		μm^{-1}	μm^{-1}
5	15µm w/o Fillets	-0.225	-0.228
6	15µm w/ Fillets	-0.219	-0.235

Table 5.22 Experiment 1 and 2 Results, X-axis Devices.

Design	Flexure Description	Resonant Frequency		Quality Factor	
		(Hz)		(unitless)	
		Mean	St. Dev.	Mean	St. Dev.
Exp. 1, Straight Flexure	15 µm w/o Fillets	4893.2	323.3	316315	44718.9
	15 µm w/ Fillets	5000.7	328.8	318463	54407.7
Exp. 2, Tapered Flexure	15 µm w/o Fillets	4888.3	401.2	365762	49338.6
	15 µm w/ Fillets	4917.1	324.4	310993	50568.2

Table 5.23 Experiment 1 and 2 Results, X-axis Devices, Compensated for Across-Wafer Trends.

Design	Flexure Description	Resonant Frequency (Hz)		Quality Factor (unitless)	
		Mean	St. Dev.	Mean	St. Dev.
Exp. 1, Straight Flexure	15 µm w/o Fillets	-23.9	139.8	-9421	32598.7
	15 µm w/ Fillets	113.3	115.6	-8216	35337.4
Exp. 2, Tapered Flexure	15 µm w/o Fillets	-103.8	169.7	34403	23402.2
	15 µm w/ Fillets	-0.4	122.7	-525	20720.3

5.2.4 Experiment 4 - Quality Factor Versus Manufacturing Sensitivity Trade Off

The purpose of Experiment 4 was to characterize the trade-off between quality factor and sensitivity to manufacturing variations as a function of flexure length to hammerhead block size $\left(\frac{L}{d}\right)$ ratio in tapered flexures. Experiment 4 consisted of 4 resonator designs incorporating 4 different tapered flexures equivalent to the 10µm straight flexure design in Experiment 1. All designs in Experiment 4 included fillets. These four tapered flexure designs corresponded to $\left(\frac{L}{d}\right)$ ratios of 2, 3, 4, and 5. The design with the $\left(\frac{L}{d}\right)$ ratio of 3 was common to Design 4 of Experiment 2 while the other three designs were unique to Experiment 4. Unlike Experiments 1 and 2, only 12 copies of each of the Experiment 4 designs were included on the wafer and there were no devices placed in the y-axis orientation.

The procedure for direct flexure replacement documented in Section 5.2.2 was followed for the designs in Experiment 4. All of the feature labels are consistent with those defined in Figures 5.20 and 5.21 provided in Section 5.2.2. Table 5.24 summarizes the Flexure C APLM design configurations for Experiment 4. The shuttle block and folded flexure portions of the APLM design were the same for all Experiment 4 design configurations and were identical to those described in Table 5.1 for the Experiment 1 configuration. Tables 5.25 and 5.26 summarize the Experiment 4 coupler spring design configurations for Flexure D and Flexure E, respectively. Optical photographs of the fabricated device APLMs and coupler springs are provided in Figures 5.24 and 5.25, respectively.

Table 5.24 Experiment 4 Tapered Flexure Revised UCI APLM Design Configurations.

Design	*L/d* Ratio (unitless)	*a* (µm)	*b* (µm)	Base Width (µm)	Flexure Length L_C (µm)	Hammerhead Half-length d_C (µm)	Fillets
1	2.005	720	40	11.735	240.555	120	Yes
2	3.006	720	40	12.052	270.555	90	Yes
3	4.008	720	40	12.213	288.555	72	Yes
4	5.009	720	40	12.307	300.555	60	Yes

Table 5.25 Experiment 4 Coupler Spring Flexure D Design Configurations.

Design	*L/d* Ratio (unitless)	Base Width (µm)	Flexure Length L_D (µm)	Hammerhead Half-length d_D (µm)	Fillets
1	2.012	11.738	167.0	83.0	Yes
2	3.000	12.051	187.5	62.5	Yes
3	4.000	12.212	200.0	50.0	Yes
4	5.024	12.309	208.5	41.5	Yes

Table 5.26 Experiment 4 Coupler Spring Flexure E Design Configurations.

Design	*L/d* Ratio (unitless)	Base Width (µm)	Flexure Length L_E (µm)	Hammerhead Half-length d_E (µm)	Fillets
1	2.007	11.736	153.5	76.5	Yes
2	3.000	12.051	172.5	57.5	Yes
3	4.000	12.212	184.0	46.0	Yes
4	5.005	12.307	191.7	38.3	Yes

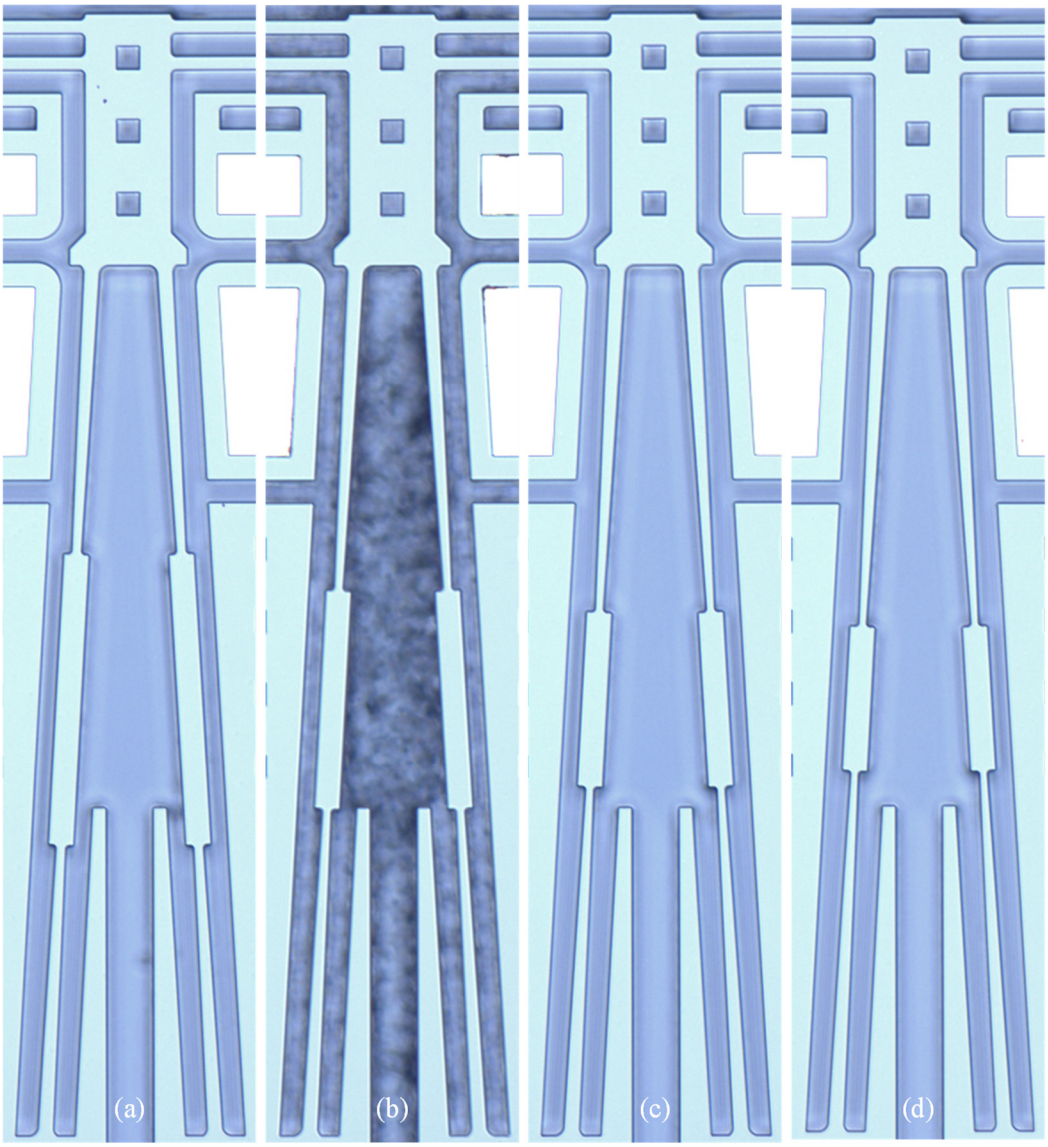

Figure 5.24 Experiment 4 Tapered Flexure Revised UCI APLM Designs.
(a) *L/d*=2, (b) *L/d*=3, (c) *L/d*=4, and (d) *L/d*=5.

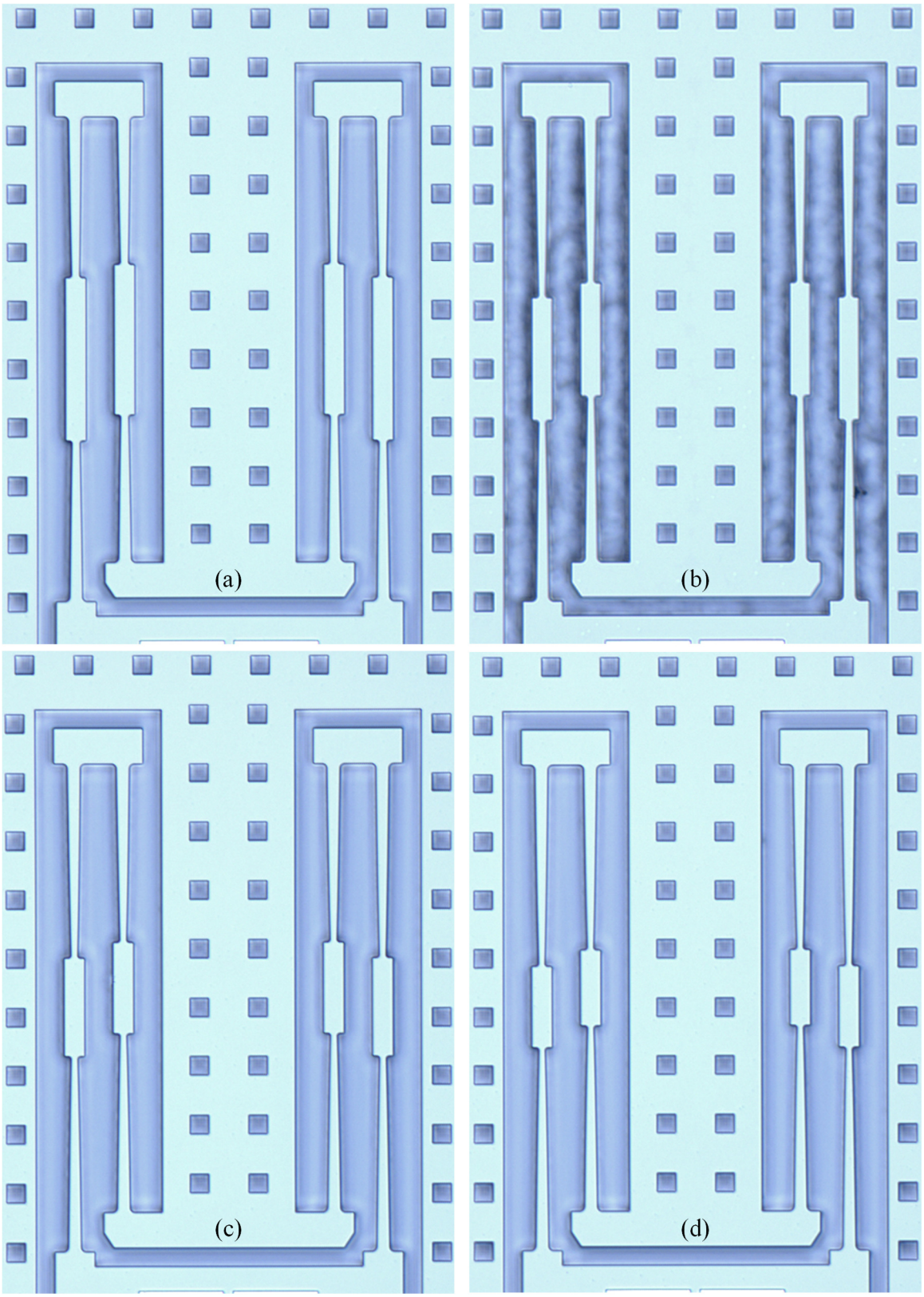

Figure 5.25 Experiment 4 Tapered Flexure Coupler Spring Designs.
(a) *L/d*=2, (b) *L/d*=3, (c) *L/d*=4, and (d) *L/d*=5.

Two finite element analyses, modal analysis and thermoelastic damping analysis, were performed on the device designs in Experiment 4 in a manner similar to that described in Section 5.2.1 to predict the impact of various $\left(\frac{L}{d}\right)$ ratios on the resonant frequency and quality factor statistics. The modal analysis results are presented in Table 5.27 and the thermoelastic damping results are presented in Table 5.28.

Figure 5.26 plots the resonant frequency normalized slope on the primary vertical axis against $\left(\frac{L}{d}\right)$ ratio. Figure 5.26 also plots the fQ_{TED} product on the secondary vertical axis. The data indicate that resonant frequency sensitivity to manufacturing variations is increasing with increasing $\left(\frac{L}{d}\right)$ ratio and the fQ_{TED} product is also increasing. This suggests that the $\left(\frac{L}{d}\right)$ ratio can be used by the designer to increase the fQ_{TED} product of the design but at the cost of increasing the resonant frequency sensitivity to manufacturing variations. Similarly, Figure 5.27 plots the Q_{TED} normalized slope on the primary vertical axis against $\left(\frac{L}{d}\right)$ ratio and plots the fQ_{TED} product on the secondary vertical axis. The data indicate that Q_{TED} sensitivity to manufacturing variations is increasing in magnitude with increasing $\left(\frac{L}{d}\right)$ ratio as is the fQ_{TED} product. This also suggests that the $\left(\frac{L}{d}\right)$ ratio could be used by the designer to increase the fQ_{TED} product of the design but this would also be at the cost of increasing the Q_{TED} sensitivity to manufacturing variations.

Table 5.27 Experiment 4 FEA Resonant Frequency Results.

Design	*L/d* Ratio	-0.1µm Flexure Width	Nominal Flexure Width	+0.1µm Flexure Width	Slope	Normalized Slope
		(Hz)	(Hz)	(Hz)	(Hz/nm)	((ΔHz/Hz)/µm)
1	2	3217.3	3266.9	3317.0	0.4985	0.1526
2	3	3216.2	3266.4	3316.7	0.5026	0.1539
3	4	3210.9	3261.9	3312.5	0.5079	0.1557
4	5	3208.6	3259.8	3311.6	0.5150	0.1580

Table 5.28 Experiment 4 FEA Thermoelastic Damping (Q_{TED}) Results.

Design	*L/d* Ratio	-0.1µm Flexure Width	Nominal Flexure Width	+0.1µm Flexure Width	Slope	Normalized Slope
		(unitless)	(unitless)	(unitless)	(1/nm)	(1/µm)
1	2	1.659E+06	1.601E+06	1.544E+06	-577.8	-0.3610
2	3	1.684E+06	1.624E+06	1.566E+06	-590.8	-0.3638
3	4	1.707E+06	1.645E+06	1.586E+06	-607.6	-0.3695
4	5	1.721E+06	1.658E+06	1.597E+06	-621.4	-0.3749

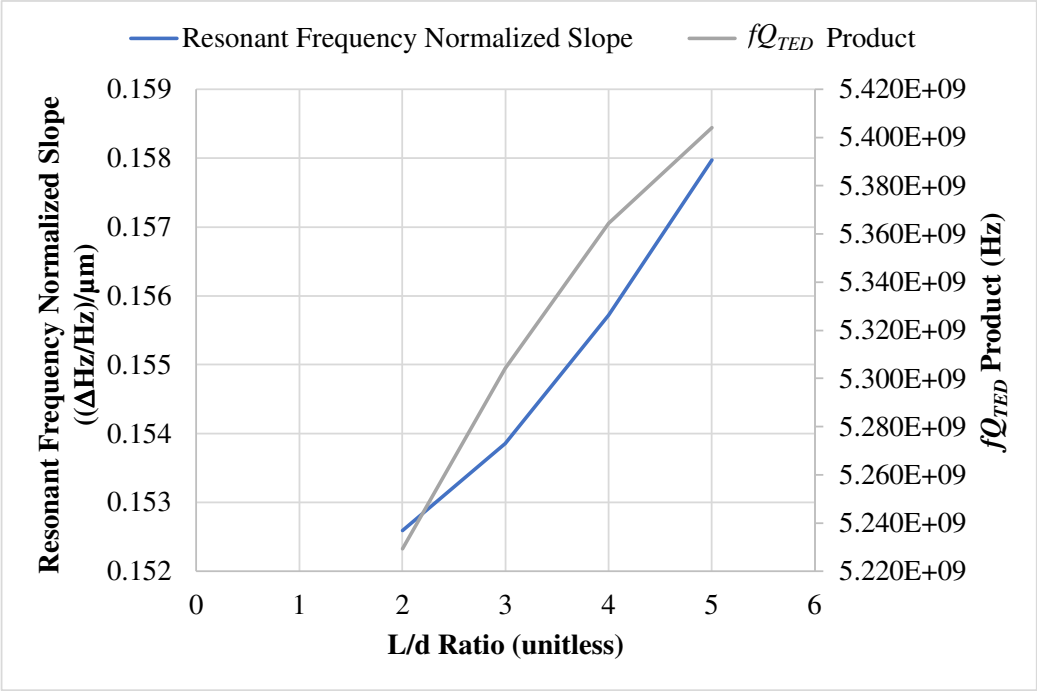

Figure 5.26 Experiment 4 Resonant Frequency Sensitivity vs. *fQ* Product Trade.

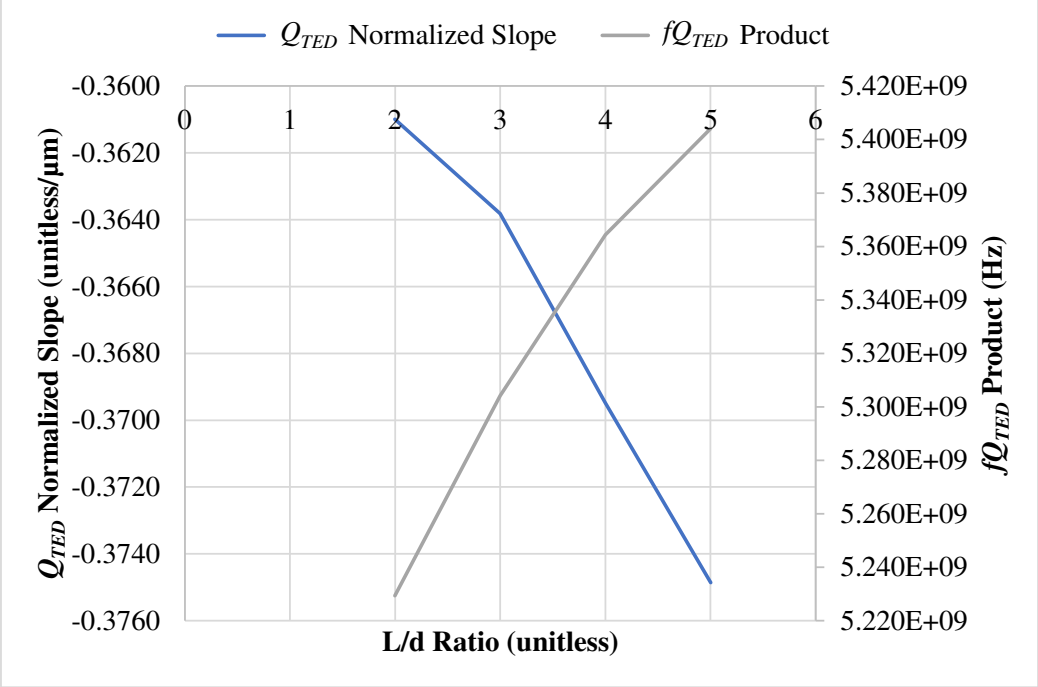

Figure 5.27 Experiment 4 Q_{TED} Sensitivity vs. *fQ* Product Trade.

The fabricated wafer included 12 copies of each of the resonator designs specific to Experiment 4 and 30 copies of the design common with Experiment 2, 9 of which were in the y-axis orientation. The locations on the wafer for the individual design configurations are provided in Appendix C, Figures C.37 - C.40.

Resonant frequency and quality factor measurements were taken from as many of the Experiment 4 devices as possible in the vacuum probe station in the same manner as described for Experiment 1 in Section 5.2.1. Many of the devices had quality factors that were so high that the devices self-resonated when they came into contact with the probe card electronics, which prevented ringdown estimates for these devices. Ringdown data was successfully collected from 35 distinct devices, but only 8 yielded acceptable quality factor measurements. However, acceptable resonant frequency measurements were obtained from 31 devices. Resonant frequency measurements were rejected if they were higher than FEA predictions.

Table 5.29 presents the statistics of the acceptable resonant frequency and quality factor measurements taken from the Experiment 4 devices. Due to the limited number of measurements available, the quality factor standard deviations presented in this table are calculated from only 2 or 3 data points. So, caution must be used when interpreting these quality factor results. The resonant frequency standard deviations were dominated by variations across the wafer. So, a linear curve fit against wafer row and column was applied to the data and the data was compensated for this linear variation. The resulting resonant frequency statistics are captured in Table 5.30. There was not enough ringdown sample data to perform a similar compensation on the quality factor data.

Once again, the resonant frequency measurements are well below the FEA predicted values, which suggests a significant amount of CDLoss (~1.8-2.0µm). While not many quality factors were within a factor of 2 of the FEA predicted values, there were 10 quality factor measurements that were in excess of one million and 12 of the rejected quality factor measurements were between five hundred thousand and one million measurements, which suggests that there was very little anchor loss and that the fabrication was generally fairly symmetric. However, fabrication asymmetry in the device or oxide layers, which leads to anchor loss, is one of the most likely causes of the poor quality factor performance from the other devices. Another likely source of poor quality factor performance is contamination either from the fabrication process or from residual chemicals in the probe chamber.

In general, the statistics for L/d=5 design were out of line with the other designs. One potential cause for this could be the width of the neck of the flexure compared to the amount of CDLoss. Based on the measured resonant frequency and assuming that the resonant frequency generally goes with width cubed, the CDLoss for this design was estimated to be about 2µm, whereas the expected neck width was only 5µm wide. Therefore, it is very likely that the strain distribution at the tip of this flexure was significantly different than it was designed to be. If the data from the L/d=5 design is disregarded, the resonant frequency standard deviation trend, quality factor trend, and quality factor standard deviation trend generally follow the FEA predicted resonant frequency slope trend, quality factor trend, and quality factor slope trend. Of significant note is the relationship between across-wafer compensated resonant frequency standard deviation and the average quality factor with respect to L/d ratio. This relationship is

plotted in Figure 5.28 and compares quite well to the FEA predicted relationship presented in Figure 5.26. This limited data notionally supports the ability of the L/d ratio to increase the quality factor at the expense of resonant frequency variability.

Table 5.29 Experiment 4 Measurement Results, X-axis Devices.

Design	*L/d* Ratio (unitless)	Resonant Frequency (Hz)		Quality Factor (unitless)	
		Mean	St. Dev.	Mean	St. Dev.
1	2	2450.6	312.3	1098371	35128
2	3	2435.8	334.8	1132059	N/A
3	4	2481.1	417.9	1214195	282995
4	5	2310.5	321.6	1046388	8338

Table 5.30 Experiment 4 Measurement Results Compensated for Across-Wafer Trends.

Design	*L/d* Ratio (unitless)	Resonant Frequency (Hz)	
		Mean	St. Dev.
1	2	5.1	62.8
2	3	18.4	172.7
3	4	51.4	348.5
4	5	-102.9	112.6

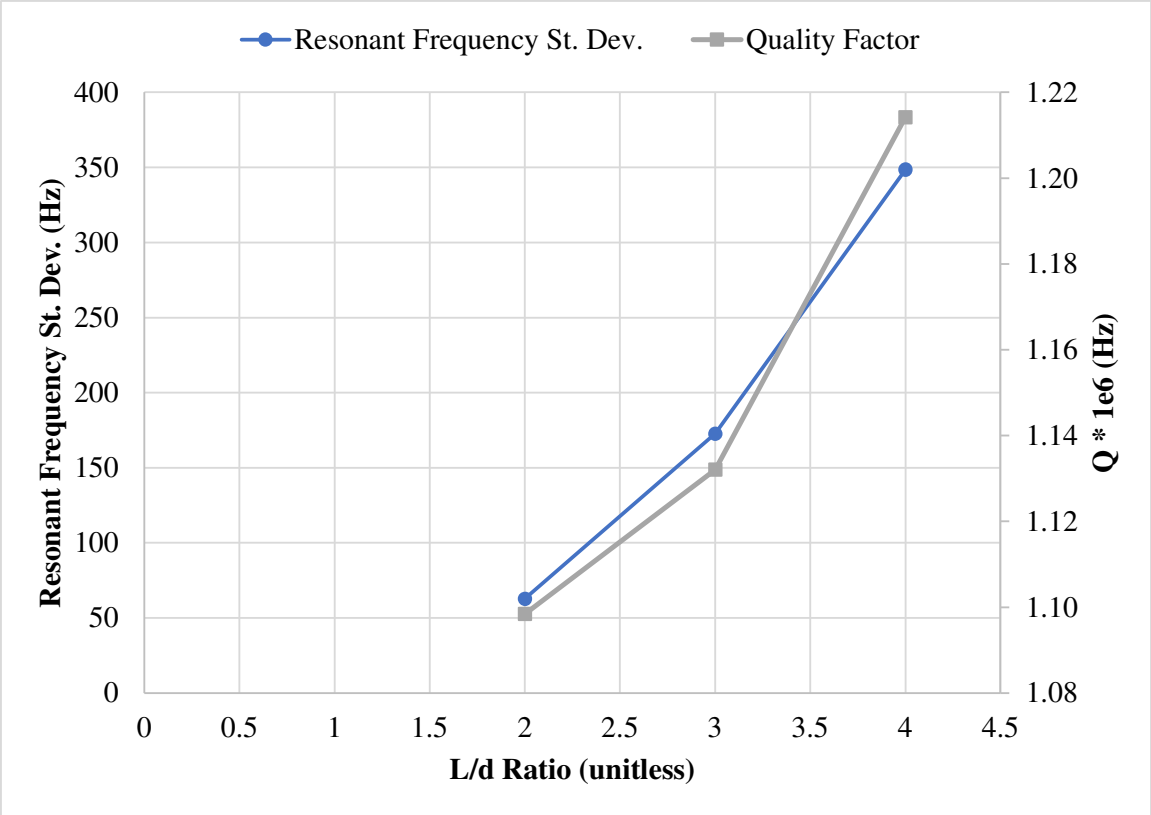

Figure 5.28 Experiment 4 Resonant Frequency St. Dev. vs. Quality Factor Measurements.

5.2.5 Experiment 5 - Tapered Flexure Lever APLM Performance

The purpose of Experiment 5 was to characterize the performance of the tapered flexure lever APLM and compare it to that of the straight and tapered flexure revised UCI APLMs of Experiments 1 and 2. Experiment 5 consisted of only 1 resonator design which replaced each of the revised UCI APLMs in the base configuration with a tapered flexure lever APLM with fillets. Figure 5.29 shows a solid model rendering of the Experiment 5 device and Figure 5.30 shows an optical photograph of the fabricated device. Incorporating the tapered flexure lever APLM into the dual mass resonator

configuration while maintaining all of the same electrical pad locations was a very difficult task and required significant rearrangement of all of the elements near the center of the design. Care was taken to ensure the same number of capacitive finger overlaps in each of the longitudinal capacitors as well as the same amount of capacitive area on the tuning capacitors, leading to some very uncommon and less than ideal geometries. The horseshoe-shaped electrode and anchor that formed the base of the revised UCI APLM designs was not used in the Experiment 5 design at all. This feature was retained, however, to provide a landing pad for the probe pin as well as a block for the electrode metalization since the same metalization mask was used for this design. A mixture of solid model renderings and optical photographs of these revised element configurations are provided in Figures 5.31 - 5.35. Twelve copies of the Experiment 5 design were included on the fabrication wafer.

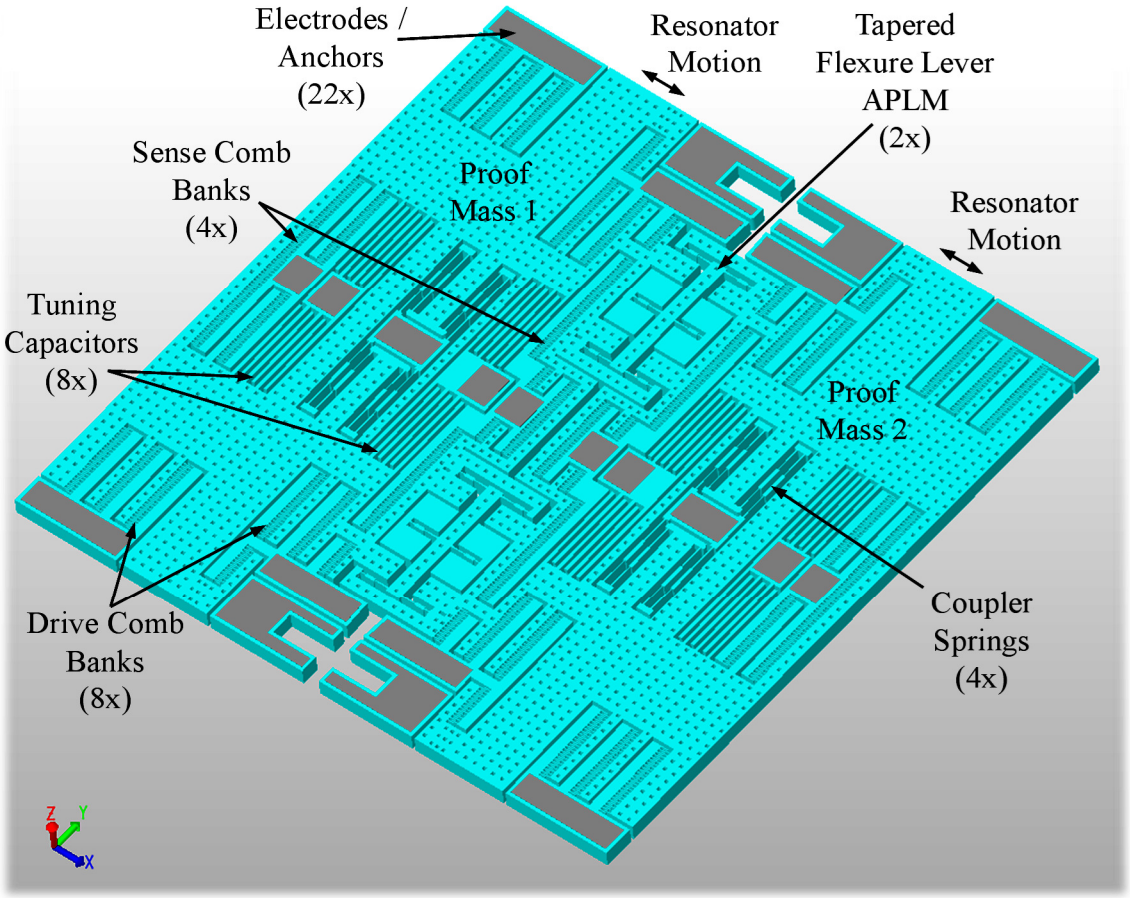

Figure 5.29 Experiment 5 Tapered Flexure Lever APLM DMR Solid Model.

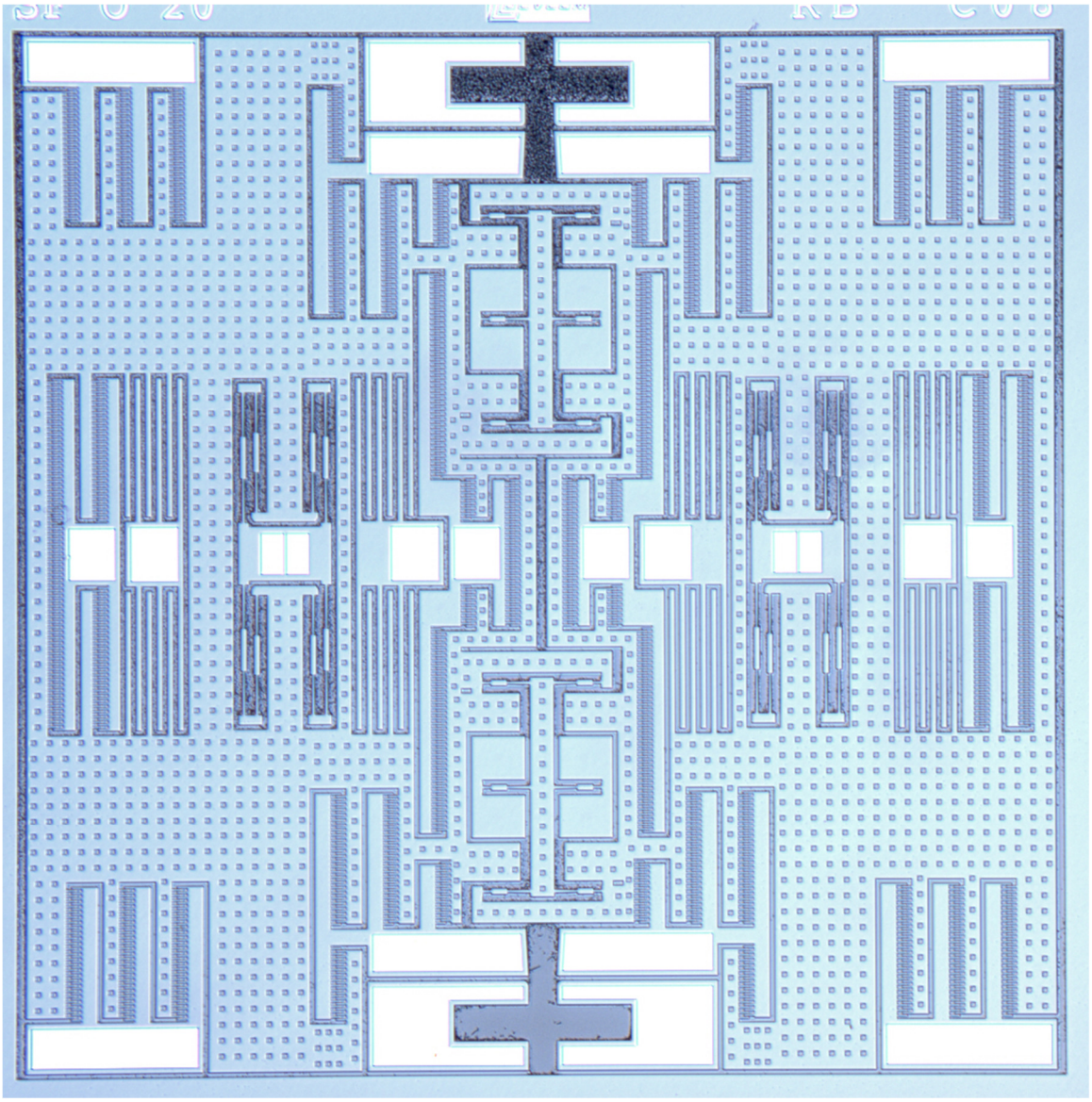

Figure 5.30 Experiment 5 Tapered Flexure Lever APLM DMR Photo.

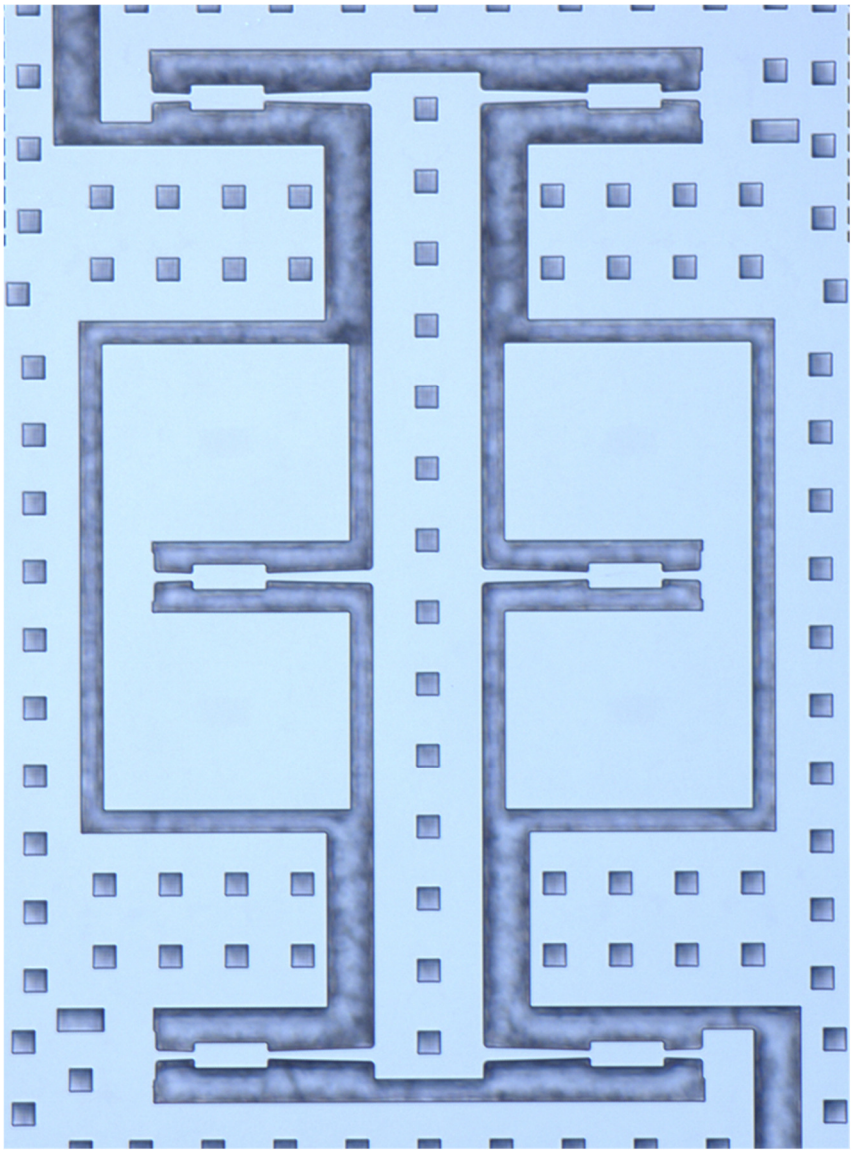

Figure 5.31 Experiment 5 Design, Tapered Flexure Lever APLM.

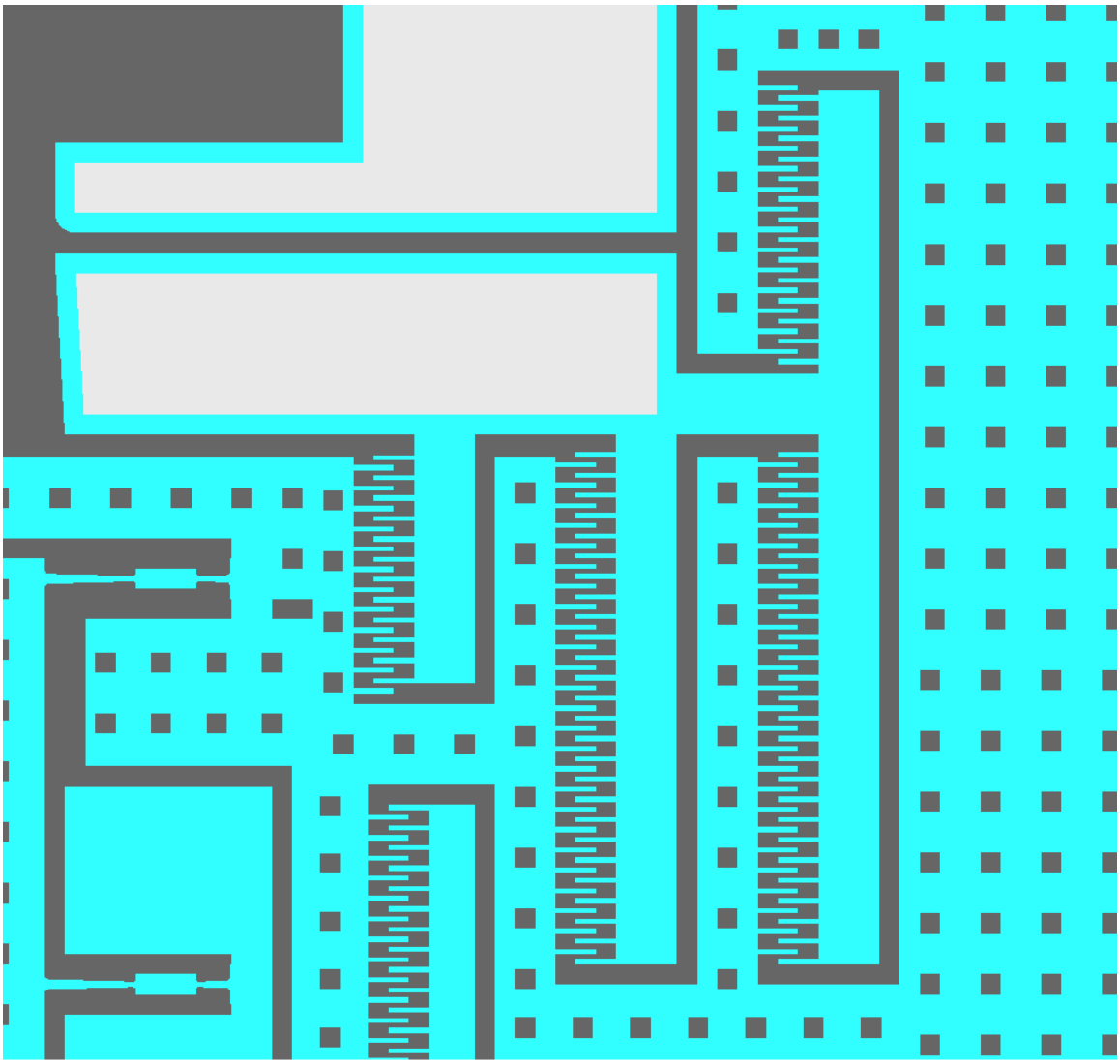

Figure 5.32 Experiment 5 Design, Revised Center Longitudinal Capacitive Drive.

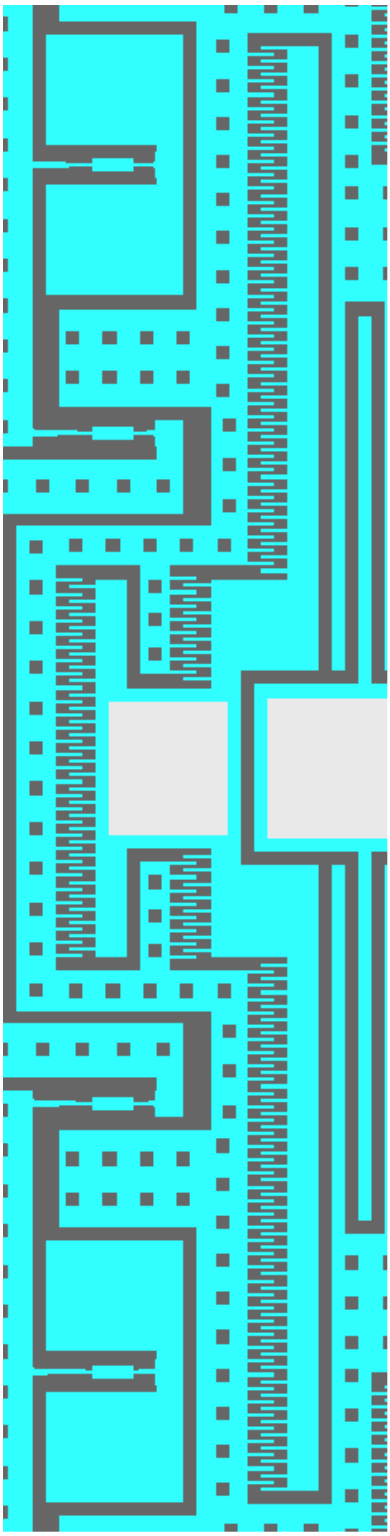

Figure 5.33 Experiment 5 Design, Revised Center Longitudinal Capacitive Sense Bank.

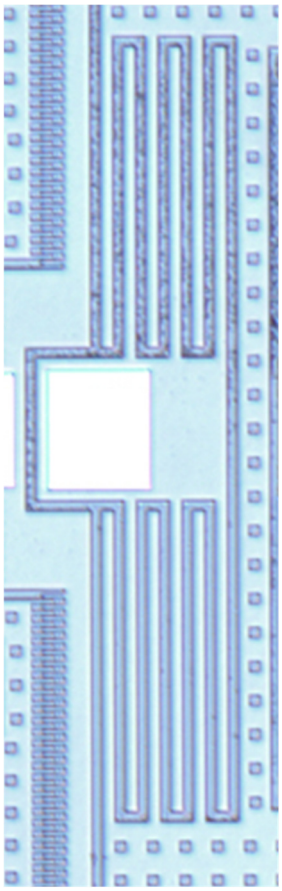

Figure 5.34 Experiment 5 Design, Revised Center Tuning Capacitors.

Figure 5.35 Experiment 5 Design, Revised Horseshoe-Shaped Electrodes/Anchors.

The geometry of the design led to a naturally stiff tapered flexure lever APLM design. Therefore, the Experiment 5 device was designed to match the spring constant of the 15µm wide straight flexure dual mass resonator design. An initial attempt to implement this design while keeping the 15µm wide coupler springs led to very thin flexures in the tapered flexure lever APLM. Therefore, the Experiment 5 coupler spring design utilizes the 7.5µm equivalent-width tapered flexure design with fillets from Experiment 2 Design 2. This approach led to more reasonable flexure widths in the tapered flexure lever APLM portion of the Experiment 5 design.

The procedure for tapered flexure lever APLM design documented in Section 4.1.4 was followed for this design. All of the feature labels are consistent with those defined in Figure 4.19 provided in Section 4.1.4 but that figure is repeated here as Figure 5.36 for convenience. Table 5.31 summarizes the tapered flexure lever APLM design for Experiment 5. Table 5.32 summarizes the Experiment 5 coupler spring design configuration which is identical to that of Experiment 2 Design 2 but is also repeated here for convenience. An optical photograph tapered flexure lever APLM of the fabricated device is provided in Figure 5.31 and an optical photograph of the coupler springs of the fabricated device is provided in Figure 5.37.

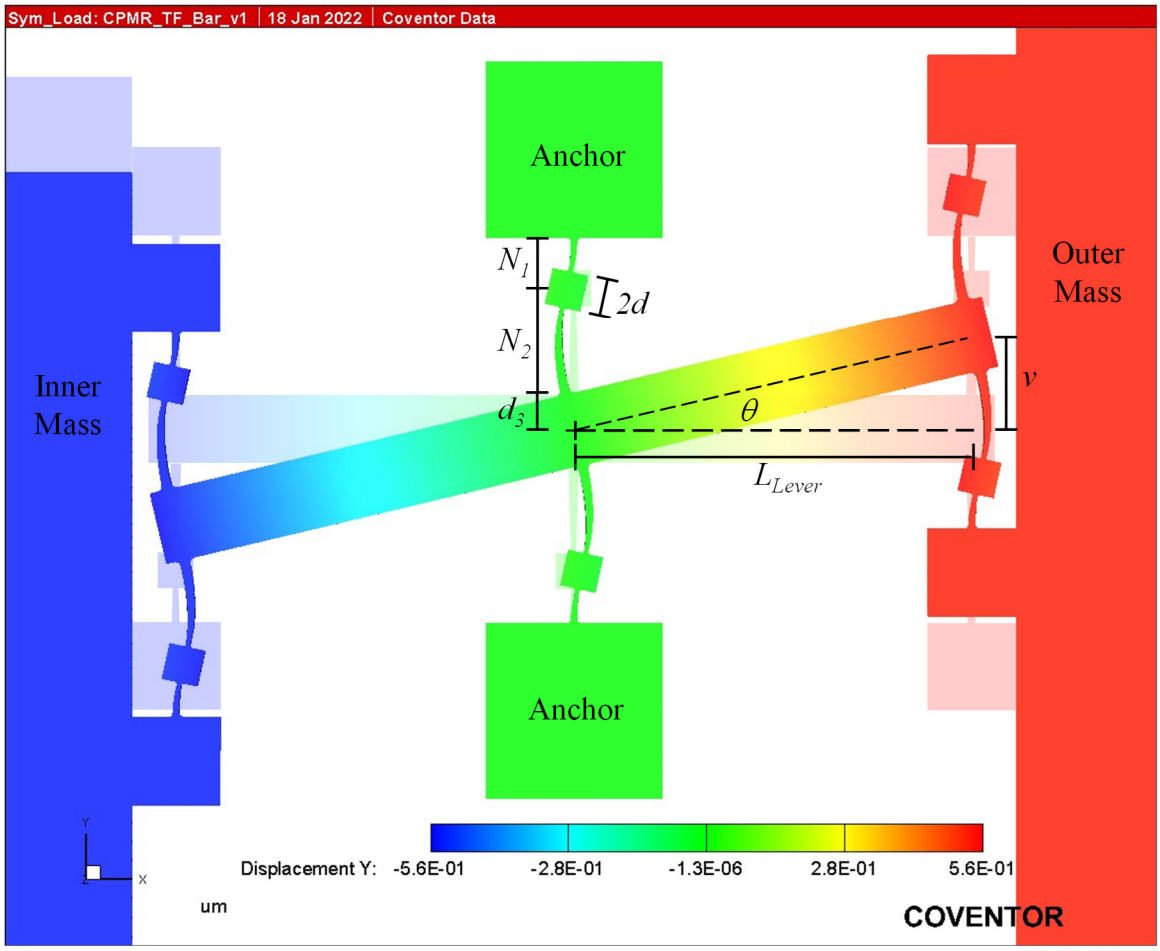

Figure 5.36 Tapered Flexure Lever APLM Dimension Labels.

Table 5.31 Experiment 5 Tapered Flexure Lever APLM Design.

Parameter	Label	Units	Value
Device Thickness	t	µm	100
Lever Length	L_{Lever}	µm	400
Lever to Flexure Stiffness Ratio	R	unitless	80
Lever Width	w_{Lever}	µm	90
Half Lever Width	d_3	µm	45
Flexure 1st Element Base Length	N_1	µm	63.176
Flexure 1st Element Base Width	w_{b1}	µm	7.468
Flexure 2nd Element Base Length	N_2	µm	120
Flexure 2nd Element Base Width	w_{b2}	µm	10.292
Tapered Flexure Half Hammerhead Size	d	µm	30
L to d Ratio for Flexure 1	$(L/d)_1$	unitless	1.106
L to d Ratio for Flexure 2	$(L/d)_2$	unitless	3.000

Table 5.32 Experiment 5 Coupler Spring Flexure Designs.

Flexure	L/d Ratio (unitless)	Base Width (µm)	Flexure Length L (µm)	Hammerhead Half-length d (µm)	Fillets
D	2.125	8.841	170	80	Yes
E	2.067	8.822	155	75	Yes

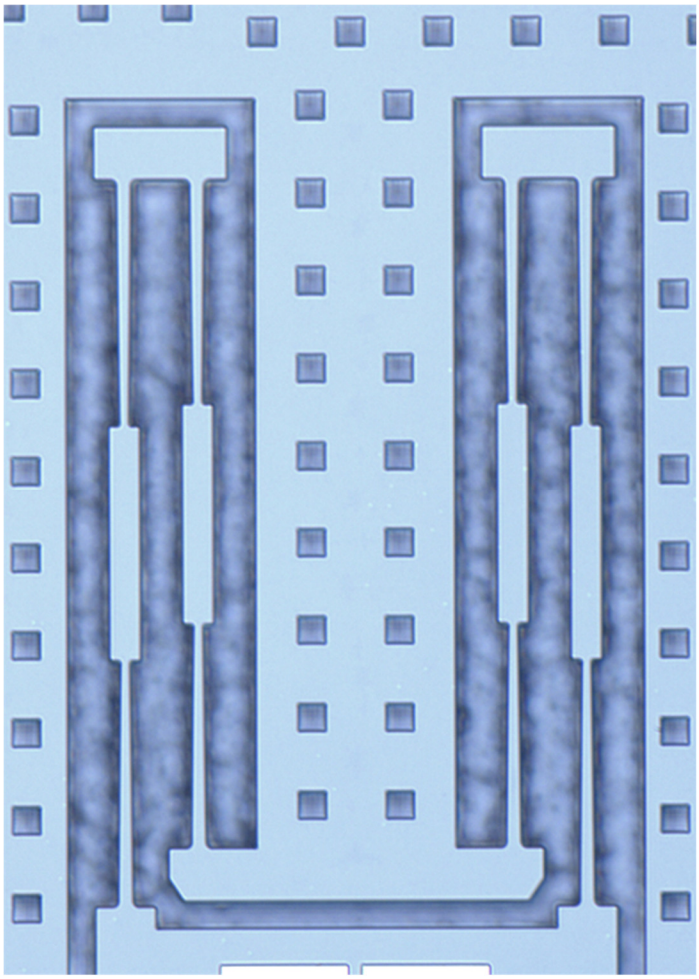

Figure 5.37 Experiment 5 Design, Coupler Springs.

Two finite element analyses, modal analysis and thermoelastic damping analysis, were performed on the Experiment 5 device design in a manner similar to that described in Section 5.2.1 to predict the performance of the tapered flexure lever APLM. Since the tapered flexure lever APLM resulted in different attachment points to the substrate, the *FixAll* boundary conditions that anchored the device in the FEAs are slightly different than the previous designs and are pictured in Figure 5.38. The outer edges of the resonator proof masses were not changed. So, there was no change to the *LoadPatch* conditions from the previous analyses.

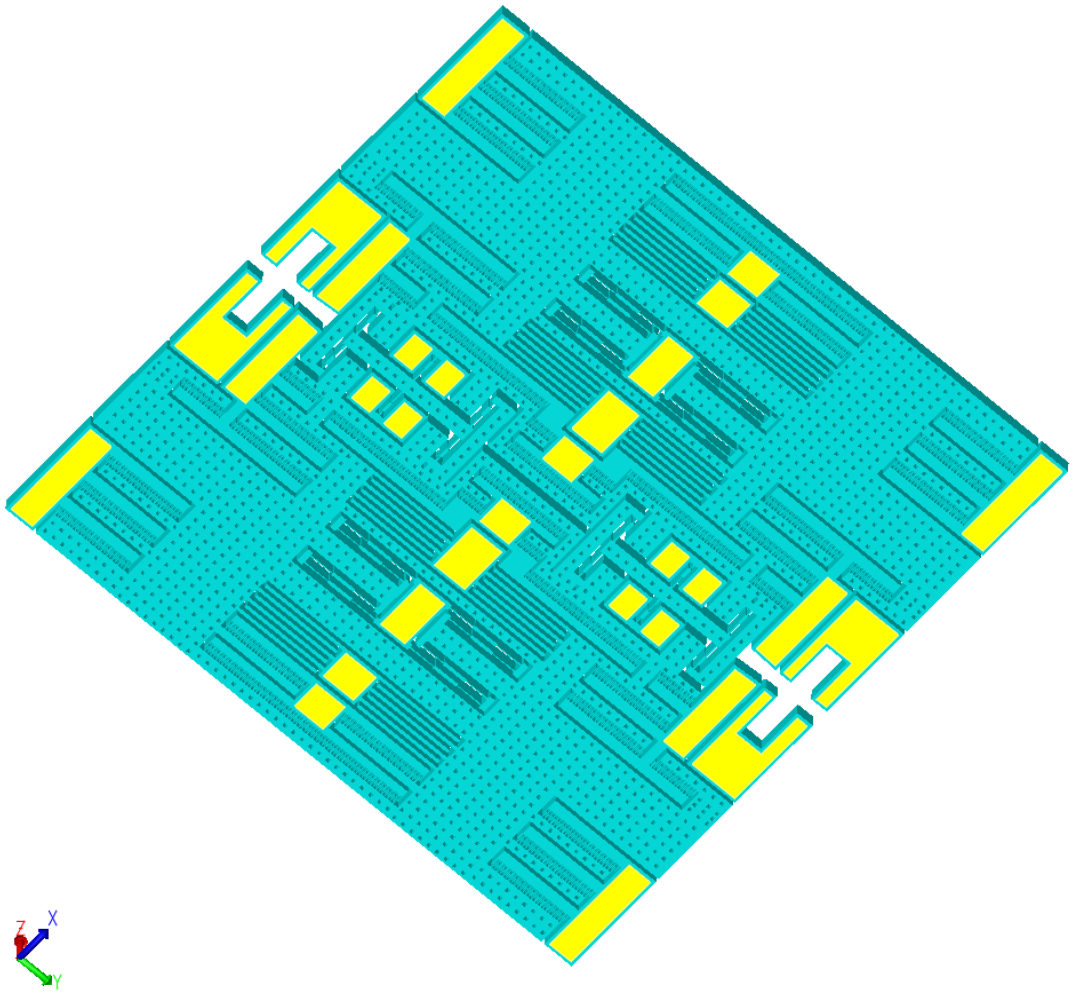

Figure 5.38 Experiment 5 Anchor FEA Boundary Condition Locations (Bottom View).

Once again, to estimate the sensitivity of the resonant frequency and thermoelastic damping to flexure width, the flexures widths (including the fillets) were varied by plus and minus 0.1µm and the modal analysis and thermoelastic damping analyses were conducted on each model. The modal analysis results are presented in Table 5.33 and the thermoelastic damping results are presented in Table 5.34. A linear least squares curve fit was applied to the three data points and the slopes from those curve fits are provided in the tables as well. Similar to what was done before, it is a fairer comparison to

normalize the slope by the nominal resonant frequency. These normalized slopes are also included in Tables 5.33 and 5.34.

The first thing to note about these results is that the resonant frequency was significantly higher than the resonant frequencies for the 15µm wide flexure designs from Experiments 1 and 2 found in Tables 5.4 and 5.13 respectively. While the Experiment 5 system was designed to have the same spring constant, the masses of the resonators were not able to be held constant due to layout constraints. Therefore, there was significantly less mass in the proof masses for the Experiment 5 design. The Generalized Mass parameter returned by the FEA for this mode of the modal analysis was 14.88% lower than that of Design 5 of Experiment 1 (15µm width straight flexures). This decrease in mass gives rise to the bulk of the increased resonant frequency. The second thing to note is that the Experiment 5 device exhibited higher Q_{TED} than the Experiment 1 and 2 devices with 15µm wide flexures summarized in Tables 5.5 and 5.14 respectively. Accounting for the significant differences in resonant frequencies by comparing the fQ_{TED} products of these designs indicates that the Experiment 5 design is 20-25% higher than that of the Experiment 1 and 2 designs, which is significantly less than the factor of nearly 6 that was seen in the APLM study. It also appears that this increase in thermoelastic damping performance comes at the cost of a significant increase in sensitivity to manufacturing variations, as the normalized slopes of both the resonant frequency and the Q_{TED} are about a factor of 2 larger than that of the Experiment 1 and 2 designs. The significant difference in predicted performance increase over that of the revised UCI design is likely due to overall geometric footprint constraints of the APLM. Tall and narrow footprints are likely to favor the revised UCI APLM designs while short

and wide footprints are likely to favor the lever APLM designs. This variability underscores the need for future research to develop a more thorough understanding of the impacts of geometric footprint on the performance of each of the APLM configurations.

Table 5.33 Experiment 5 FEA Resonant Frequency Results.

Description	-0.1µm Flexure Width	Nominal Flexure Width	+0.1µm Flexure Width	Slope	Normalized Slope
	(Hz)	(Hz)	(Hz)	(Hz/nm)	((ΔHz/Hz)/µm)
Tapered Flexure Lever APLM	6098.2	6214.7	6332.0	1.1692	0.1881

Table 5.34 Experiment 5 FEA Thermoelastic Damping (Q_{TED}) Results.

Description	-0.1µm Flexure Width	Nominal Flexure Width	+0.1µm Flexure Width	Slope	Normalized Slope
	(unitless)	(unitless)	(unitless)	(1/nm)	(1/µm)
Tapered Flexure Lever APLM	4.886E+05	4.669E+05	4.457E+05	-214.4	-0.4592

There was a significant challenge with obtaining ringdown measurements from the Experiment 5 devices on the fabricated wafer, which was that there was no bias voltage connected to the proof mass. In general, there were 6 locations where the proof mass was intended to be electrically connected to the bias voltage provided by the probe card. These can be seen in Figure 5.29 and include the four horseshoe anchors and the two coupler spring anchors. However, it was determined in initial testing of the

Experiment 1 devices that the probe pins contacting the coupler spring anchors were providing a mechanical energy loss path (anchor loss) and these pins were removed from the probe card, leaving only the horseshoe anchor pins to provide electrical contact to the proof mass. Since the horseshoe anchor is not electrically connected to the proof mass in the Experiment 5 device, there was no electrical connection to the proof mass for these devices in the experimental setup. Therefore, the experimental measurements (drive and sense signals) of the Experiment 5 devices were dependent on the existence of residual electrical charges on the proof mass which left drive and signal strength both uncertain and sometimes variable in amplitude.

Of the 12 Experiment 5 devices on the wafer, resonant frequency and quality factor data was collected from 8 devices, which is quite remarkable considering the lack of proof mass bias voltage. The raw measurement statistics are provided in Table 5.35 along with similar statistics from Experiments 1 and 2 for comparison. Once again, the average resonant frequency is significantly below (~27%) what was predicted by the FEA, which corresponds to a CDLoss of approximately 1.9μm, which is consistent with the CDLoss estimates from other experiments. The resonant frequency standard deviation is dominated by across-wafer variations and particularly dependent on the row location of the device. The locations of the Experiment 5 devices on the wafer are provided in Figure C.41 of Appendix C. The quality factors were significantly below the FEA predicted quality factors with only 2 of the 8 devices having quality factors within a factor of two of the FEA predicted value and none of the devices having an fQ product within a factor of two of the FEA predicted value. There are many potential causes for low quality factors in this Experiment. First and foremost, is the uncertainty in the signal

itself. Since there was no bias voltage on the proof mass, the fundamental source of the signal is not completely understood and could be a function of time or resonator displacement, which could corrupt the signal and the estimates of ringdown time and quality factor. The second is the potential for contamination. Repeated measurement of the Experiment 1 and 2 devices over time indicate that the quality factors of those devices were decreasing with time, which suggests that there is some contamination in the probe chamber that is depositing on the resonators over time and reducing the quality factor. Since the Experiment 5 devices were the last devices to be tested, this contamination would have impacted them the most. The significant amount of CDLoss could also be impacting the stress gradient in the tapered flexures which may have a detrimental impact on thermoelastic damping. The final potential reason for low quality factors could be anchor loss. The FEA was not able to provide an estimate for anchor loss and, as this is the first fabrication of this design, the design has not yet been proven to have low anchor loss. However, the general design was informed by sound principles reported in the literature and was not expected to have significant anchor loss. This is supported by the fact that two devices did have quality factors within a factor of two of the predicted quality factor. However, due to the geometrical layout constraints, this particular implementation contained some asymmetries and the FEA did predict a slight asymmetry in the proof mass displacements which could give rise to significant anchor loss.

The data also indicate that the standard deviation of the quality factor was higher than those from Experiments 1 and 2, but the quality factor was also strongly correlated to location on the wafer, particularly the row number. Therefore, the resonant frequency and quality factor data was compensated for across wafer variations as described

previously. The resulting statistics are provided in Table 5.36 along with similar statistics from Experiments 1 and 2 for comparison. The post-compensation average resonant frequency and quality factor were zero for the Experiment 5 devices because the curve fit was only applied to the Experiment 5 devices, whereas the curve fit for the Experiment 1 and 2 devices included all four designs within those Experiments. The standard deviations of the post-compensation resonant frequency and quality factor were 2 to 3 times lower than those of the Experiment 1 and 2 devices, which is in opposition to the FEA predictions based on the CDLoss sensitivity slopes. This may suggest that the primary cause of residual variability may be something other than CDLoss. It is important to keep in mind that comparing the post-compensation statistics may not be fair because only Experiment 5 devices were included in its curve fit whereas the curve fit for the Experiment 1 and 2 devices included all four designs.

Table 5.35 Experiment 5 Probe Station Measurement Results.

Design	Flexure Description	Resonant Frequency (Hz)		Quality Factor (unitless)	
		Mean	St. Dev.	Mean	St. Dev.
Exp. 5	Tapered Flexure Lever	4547.9	318.7	217212	41782.0
Exp. 1, Straight Flexure	15 µm w/o Fillets	4893.2	323.3	316315	44718.9
	15 µm w/ Fillets	5000.7	328.8	318463	54407.7
Exp. 2, Tapered Flexure	15 µm w/o Fillets	4888.3	401.2	365762	49338.6
	15 µm w/ Fillets	4917.1	324.4	310993	50568.2

Table 5.36 Experiment 5 Measurement Results Compensated for Across-Wafer Variations.

Design	Flexure Description	Resonant Frequency (Hz)		Quality Factor (unitless)	
		Mean	St. Dev.	Mean	St. Dev.
Exp. 5	Tapered Flexure Lever	0.0	64.6	0	9876.5
Exp. 1, Straight Flexure	15 µm w/o Fillets	-23.9	139.8	-9421	32598.7
	15 µm w/ Fillets	113.3	115.6	-8216	35337.4
Exp. 2, Tapered Flexure	15 µm w/o Fillets	-103.8	169.7	34403	23402.2
	15 µm w/ Fillets	-0.4	122.7	-525	20720.3

5.2.6 Experiment 6 - Control Experiment

Experiment 6 serves as the control for the broader set of dual mass resonator experiments. The primary purpose of Experiment 6 was to characterize the performance of legacy dual mass resonator designs on this wafer for comparison to other experimental wafers to monitor fabrication process consistency across wafers. There were 4 distinct designs included in Experiment 6. The first three designs were provided by researchers at the Army Research Lab (ARL) and are direct copies of designs included on other wafers. The fourth design was a mixture of a legacy design features and design features from this work. The mixed design incorporates a direct copy of a legacy revised UCI APLM design but also integrates the coupler spring structure used in this work that has been modified to accommodate fillets. Fillet accommodation required extended and

widened connectors in the coupler spring structure design but was not expected to impact device performance. Figure 5.39 shows a solid model rendering of the Design 4 device. Table 5.37 summarizes the design configurations for the folded flexure and shuttle block portion of the revised UCI APLM. The variable names used in Table 5.37 are defined in Section 4.1.6 and shown graphically in Figure 5.40. The separation distance of the center of the angled flexures on the shuttle block, d_{AF}, was 56 µm for Design 1, but was 60 µm for Designs 2, 3, and 4. Table 5.38 summarizes the Flexure C design configurations of the revised UCI APLM for the various designs of Experiment 5. The flexure width reported in Table 5.38 is the horizontal flexure width. The flexure in Design 4 was designed to have a transverse width of 10 µm which corresponds to a horizontal width of 10.015 µm as noted in Table 5.38. Table 5.39 summarizes the design configurations of the coupler springs for the various designs of Experiment 6. No fillets were included in any of the Experiment 6 designs. Since the first three designs were added directly to the wafer mask by ARL personnel, solid models of these designs were not available and no finite element analyses were conducted on these designs. However, optical photographs of the fabricated devices are provided in Figure 5.41 for the revised UCI APLMs and in Figure 5.42 for the coupler springs. Twelve copies of each of the Experiment 6 designs were included on the wafer. The locations on the wafer for the individual design configurations for Experiment 6 are provided in Appendix C, Figures C.42 - C.45. All Experiment 6 devices were x-axis devices.

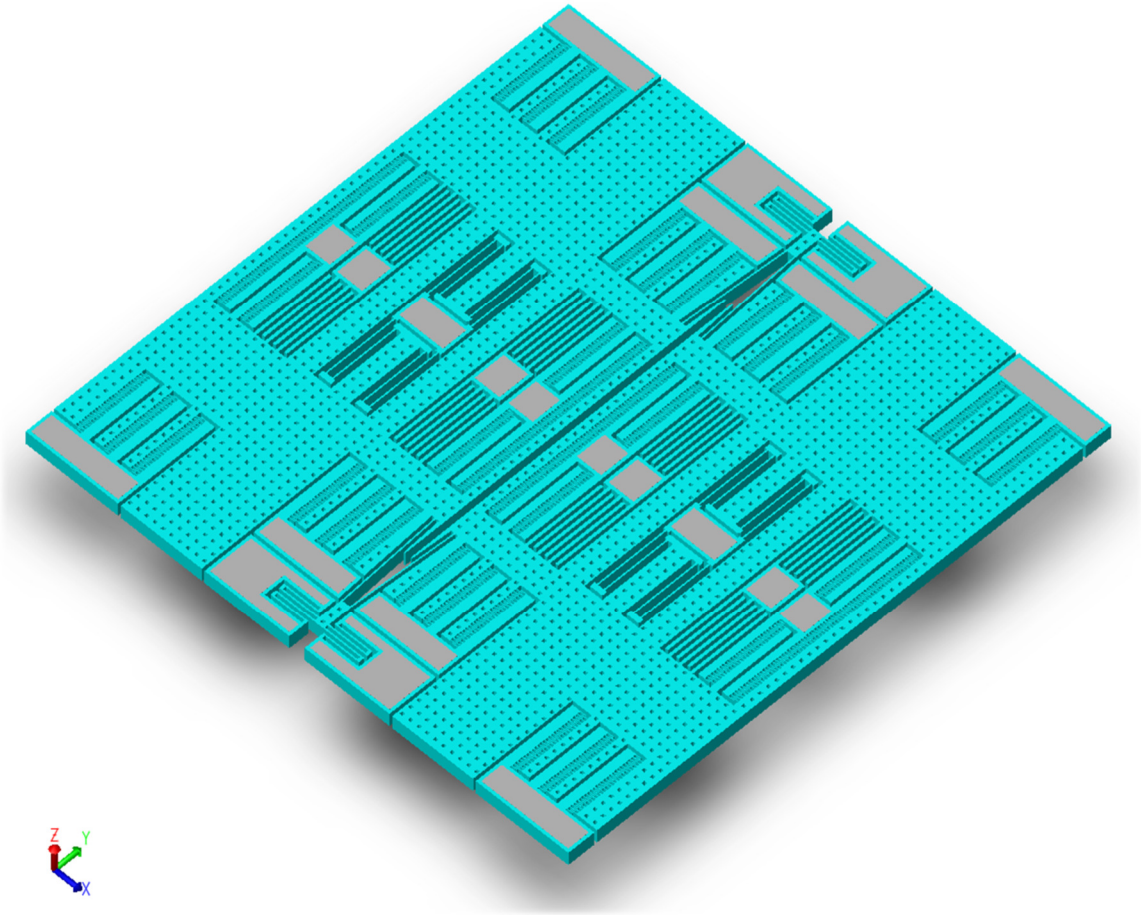

Figure 5.39 Experiment 6 Legacy DMR with Revised Coupler Springs.

Table 5.37 Experiment 6 APLM Shuttle Block and Folded Flexure Design Configurations.

Parameter	Label	Units	Value
Shuttle Block Width	w_{Blk}	µm	70
Shuttle Block Length	L_{Blk}	µm	200.5
Flexure A Width	w_{FF_A}	µm	10
Flexure B Width	w_{FF_B}	µm	10
Flexure A Length	L_{FF_A}	µm	225
Flexure B Length	L_{FF_B}	µm	265
Angled Flexure Separation Distance	d_{AF}	µm	60 (56 for Design 1)

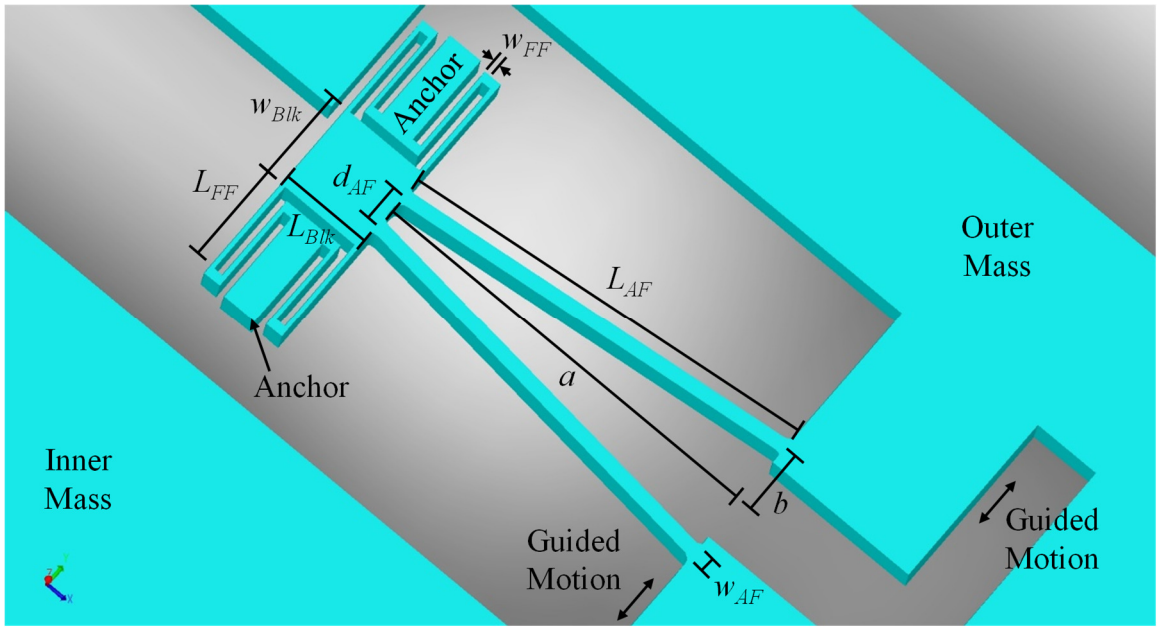

Figure 5.40 Straight Flexure Revised UCI APLM Variable Definitions.

Table 5.38 Experiment 6 Revised UCI APLM Flexure C Design Configurations.

Design	*a* (µm)	*b* (µm)	Flexure Width (µm)	Flexure Length (µm)	Fillets
1	720	40	14	721.110	No
2	720	40	10	721.110	No
3	720	40	10	721.110	No
4	720	40	10.015 (10)	721.110	No

Table 5.39 Experiment 6 Coupler Spring Design Configurations.

Design	Flexure D		Flexure E		Connector Width (µm)	Fillets
	Width (µm)	Length (µm)	Width (µm)	Length (µm)		
1	14	500	14	452	135	No
2	Split 5µm (2x) w/ 10µm gap	500	Split 5µm (2x) w/ 10µm gap	465	97	No
3	10	500	10	460	80	No
4	10	500	10	460	135	No

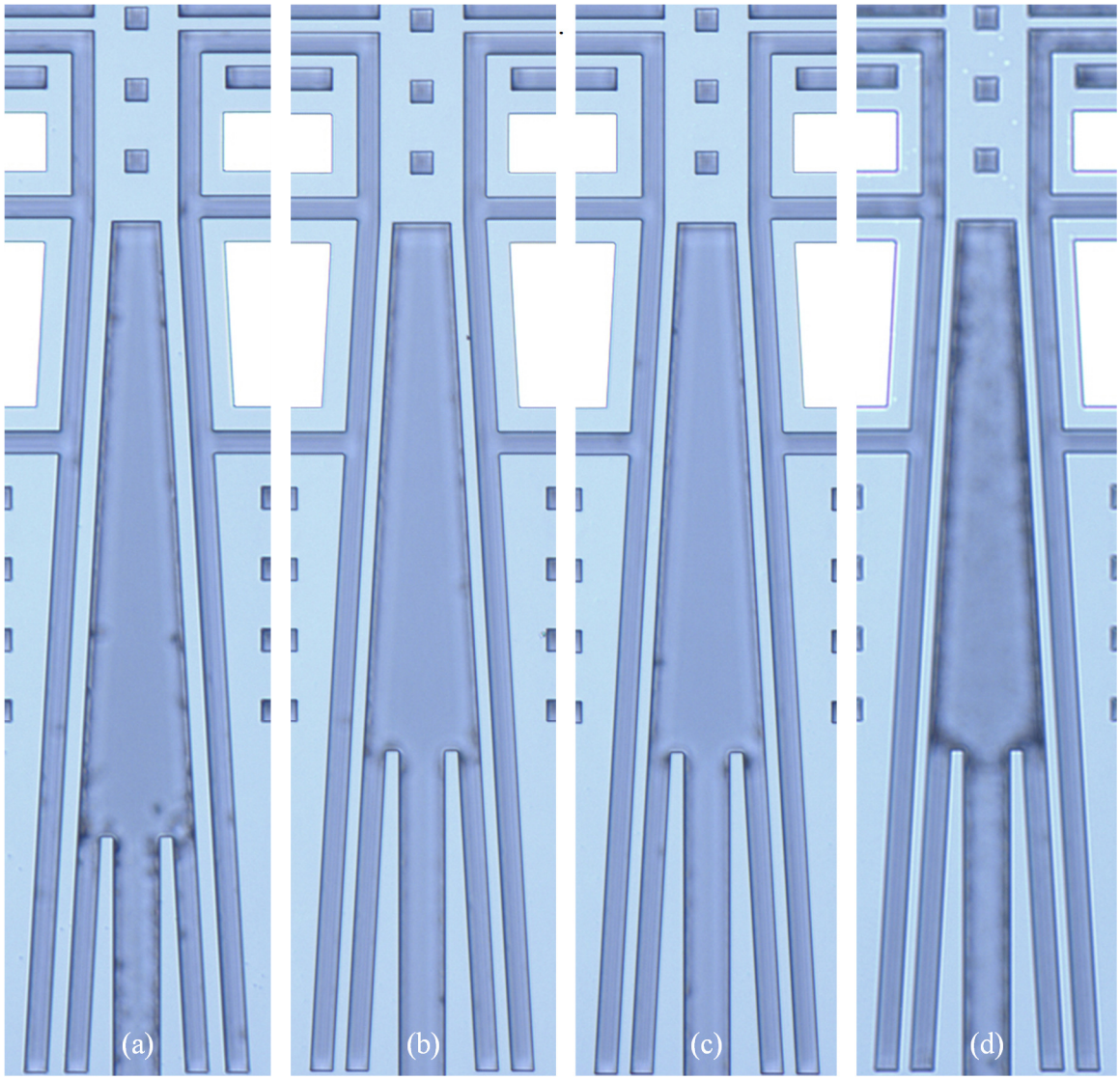

Figure 5.41 Experiment 6 Revised UCI APLM.
(a) Design 1 - Legacy 14µm Wide Flexures, (b) Design 2 - Legacy 10µm Flexures, (c) Design 3 - Legacy 10µm Flexures, (d) Design 4 - 10µm Flexures.

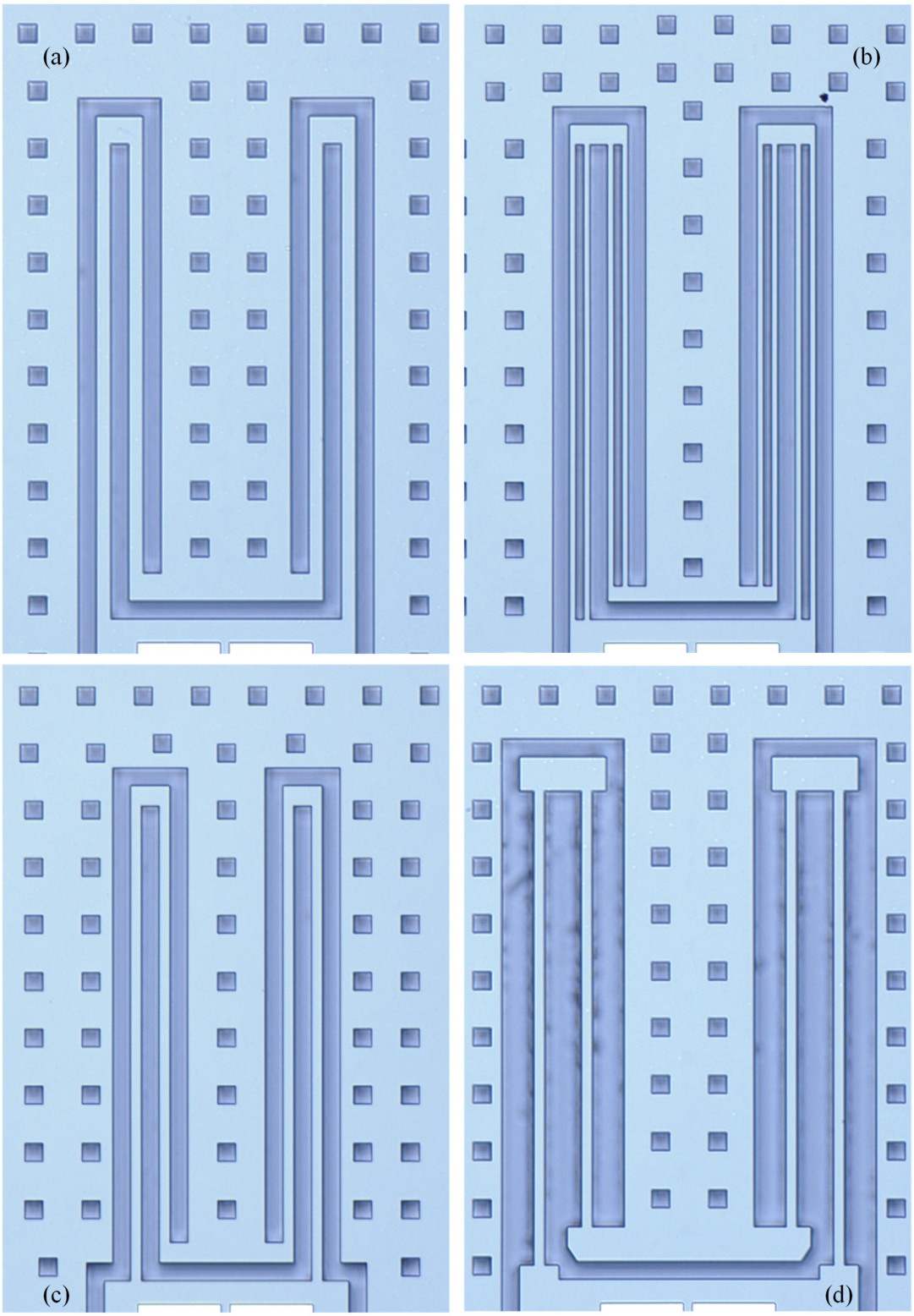

Figure 5.42 Experiment 6 Coupler Spring Designs.
(a) Design 1 - Legacy 14µm Wide Flexures, (b) Design 2 - Legacy Split Flexures, (c) Design 3 - Legacy 10µm Flexures, (b) Design 4 - 10µm Flexures w/ Fillet Accommodating Structure.

Two finite element analyses, modal analysis and thermoelastic damping analysis, were performed on the Experiment 6 Design 4 device in a manner similar to that described in Section 5.2.1 to predict the performance of the design. To estimate the sensitivity of the resonant frequency and thermoelastic damping to flexure width, the flexures widths (including the fillets) were varied by plus and minus 0.1µm and the modal analysis and thermoelastic damping analyses were conducted on each model. The modal analysis results are presented in Table 5.40 and the thermoelastic damping results are presented in Table 5.41. A linear least squares curve fit was applied to the three data points and the slopes from those curve fits are provided in the tables as well. Similar to the analyses in previous sections, the normalized slopes are also included in Table 5.40 and Table 5.41. These results should be most comparable to the results from Design 3 of Experiment 1 presented in Section 5.2.1, and comparison with the results presented in Table 5.4 and Table 5.5 confirm that assertion.

Table 5.40 Experiment 6 Design 4 FEA Resonant Frequency Results.

Design	-0.1µm Flexure Width	Nominal Flexure Width	+0.1µm Flexure Width	Slope	Normalized Slope
	(Hz)	(Hz)	(Hz)	(Hz/nm)	((ΔHz/Hz)/µm)
4	3199.7	3242.1	3287.3	0.4382	0.1352

Table 5.41 Experiment 6 Design 4 FEA Thermoelastic Damping (Q_{TED}) Results.

Design	-0.1µm Flexure Width	Nominal Flexure Width	+0.1µm Flexure Width	Slope	Normalized Slope
	(unitless)	(unitless)	(unitless)	(1/nm)	(1/µm)
4	1.680E+06	1.627E+06	1.573E+06	-533.4	-0.3279

Unfortunately, due to the stability issues associated with probing the devices with extremely high quality factors, data was only collected from 6 of the Design 3 devices. No data was collected from the other designs in this Control Experiment. Of those 6 devices, only 5 had acceptable resonant frequencies and only 4 had acceptable quality factors. An attempt was made to compensate this data for variations across the wafer, but with the limited data, caution must be used when interpreting those results. Table 5.42 presents the statistics for both the raw and compensated resonant frequency and quality factor measurements taken from the Experiment 6 devices. The majority of these statistics are similar to those for Experiment 4 with an L/d of 3, which is the most comparable design for which data is available. However, both the raw and compensated resonant frequency standard deviations are significantly better than that device or any other device reported herein. This is most likely because the majority of the acceptable Experiment 6 measurements were from devices that were relatively close on the wafer and therefore, not substantially impacted by the process variation across the wafer. Unfortunately, while this design was included on this wafer as a "control" for comparison to ensure similarity with other wafers, no data is currently available from other wafers to make such a comparison. So, the data is provided here for comparison to data from future wafers.

Table 5.42 Experiment 6 Probe Station Measurement Results.

Data Condition	Resonant Frequency (Hz)		Quality Factor (unitless)	
	Mean	St. Dev.	Mean	St. Dev.
Raw	2577.4	80.5	665965	53445
Compensated	0.0	22.0	0	44988

5.3 Overall Discussion of Dual Mass Resonator Experimental Results

For resonators and mode-matched gyroscopes, the primary factors that influence performance are the quality factor, quality factor variability (or quality factor mismatch), and frequency variability (or frequency mismatch). The purpose of the Dual Mass Resonator experiments was to determine experimentally if tapered flexures and fillets improved these parameters over constant cross-section flexures without fillets. Two additional purposes of the experiment were (1) to determine if the L/d ratio of the tapered flexure could be a useful tool for trading absolute quality factor against resonant frequency variability and quality factor variability, and (2) to assess the performance of the tapered flexure lever APLM.

The experimental wafer contained 456 devices from these 6 experiments with a total of 20 distinct designs. However, no data was able to be collected from the devices with significantly high quality factors due to noise and crosstalk on the probe card in the vacuum probe station causing system instability. Additionally, metalization layer issues prevented data collection from the devices on the top several rows of the wafer, and other, more common fabrication issues further limited wafer yield. Ultimately, data was

only collected from 107 total devices across 10 of the designs, but this included data from each of the 6 experiments. For completeness, there was one additional experiment on this wafer that contained 6 "hybrid" designs (180 devices) of the dual mass resonator that incorporated both straight and tapered flexures. However, very little data was collected on the devices from that experiment and no analysis of those results is included herein.

The following bullets summarize the findings of the dual mass resonator experiments:

- CDLoss estimates for the various experiments varied between 1.6µm and 2.0µm, which is significant relative to the flexure widths and the amount of taper in the flexures.
- There was a significant amount of resonant frequency and quality factor variation across the wafer that was consistently correlated to die location, particularly row location.
- There were several quality factor measurements that were in excess of one million, which suggests very little anchor loss and generally symmetric fabrication.
- After compensating for linear across-wafer variations, fillets reduced the resonant frequency variability in both the straight and tapered flexure designs by 20-30%.
- When comparing the resonant frequency differences of adjacent x-axis and y-axis devices, fillets reduced the resonant frequency variability by a factor of 2.36.

- These two findings about fillets suggest that fabrication variations in the inside corners may be a significant contributor to the resonant frequency variability.
- There was no clear indication that fillets had any impact on the variability of the quality factor.
- There was significantly higher yield (roughly a factor of 2) for tapered flexure devices with fillets than without fillets.
- The tapered flexure designs had quality factors that were a few percent higher than the equivalent straight flexure designs.
- After compensating for across wafer variations, tapered flexures increased the frequency variability by a few percent.
- After compensating for across wafer variations, tapered flexure designs reduced the quality factor variability by 30-40% over the equivalent straight flexure designs.
- After compensating for across wafer trends, the limited data collected from the L/d ratio experiments indicate that the L/d ratio of the tapered flexure could be used to trade quality factor against resonant frequency variability. The impact on quality factor variability was indeterminate.
- Most of the quality factor measurements from the tapered flexure lever APLMs were significantly below the values predicted by FEA. This could be due to any one of several reasons including the lack of a proof mass bias voltage, probe chamber contamination, CDLoss impact on thermoelastic damping, or anchor loss.

- After compensating for across wafer variations, the tapered flexure lever design had lower resonant frequency variability and lower quality factor variability than the equivalent straight and tapered flexure designs with or without fillets.

Chapter 7. Conclusions and Recommendations for Future Research

Since the introduction of the use of silicon as a mechanical material over 50 years ago, silicon sensors have been a constant topic of research for both academia and industry. The demonstrated potential to produce low-cost silicon sensors using wafer scale processing, often with co-fabricated electronics, has transformed the market of portable sensing to the point where they are included in nearly every mobile phone manufactured in the last decade. However, the relatively poor performance of these consumer-grade sensors, the demand for more ruggedized sensors for both the automotive and military markets, and the never-ending desire to reduce cost continue to fuel the demand for continued research.

This dissertation investigates the potential of tapered flexures and fillets to address all of those market pressures. It addresses performance improvements through the investigation of tapered flexures and new anti-phase lever mechanism architectures that could enable resonators and gyroscopes to achieve higher quality factors that improve sensitivity, bias, and noise performance. Both tapered flexures and fillets were investigated to reduce the stress in the flexures which produce more rugged devices. Finally, both tapered flexures and fillets were investigated to reduce the sensitivity to manufacturing variations which increases yield and reduces product cost. The specific contributions of this research and recommendations for future research are summarized below.

Contribution 1: It was demonstrated through Finite Element Analysis (FEA) that **quadratically tapered flexures exhibit approximately 40% less stress** than an equivalent non-tapered flexure of the same length. This reduction in stress could be exploited in gyroscopes, accelerometers, or resonators to increase the sensitivity, increase the range, reduce the noise floor, or increase the ruggedness of the device.

Contribution 2: It was demonstrated through FEA and confirmed through experiment that **quadratically tapered flexures exhibit approximately 10% lower thermoelastic damping** (*i.e.*, 10% higher quality factor) than an equivalent non-tapered flexure of the same length. This increase in quality factor could be exploited in gyroscopes or resonators to increase the sensitivity, reduce the noise floor, or reduce bias.

Contribution 3: It was experimentally observed that **quadratically tapered flexures reduced the variability of thermoelastic damping** (*i.e.*, quality factor variability) over that of an equivalent non-tapered flexure of the same length. This decrease in quality factor variability could be exploited to increase the yield of both gyroscopes and resonators, and to reduce bias error in gyroscopes.

Contribution 4: It was demonstrated through FEA that **stress peaking of flexure inside corners can be mitigated with radius fillets**

in both tapered and non-tapered flexures. This reduction in stress peaking is dependent on the ratio of the fillet radius to the local flexure width. This reduction in stress peaking could be exploited in gyroscopes, accelerometers, or resonators to increase the sensitivity, increase the operating range, reduce the noise floor, or increase the ruggedness of the device.

Contribution 5: It was discovered through FEA that the **stress peaking mitigation behavior of fillets follows a universal relationship** for both tapered and non-tapered flexures between the peak stress normalized to the local nominal stress and the fillet radius normalized to the local flexure width. This finding results in a single curve that can be used to size fillet radii for stress peaking mitigation for both tapered and non-tapered flexures.

Contribution 6: It was demonstrated through experiment that **fillets reduce the resonant frequency variability** by at least 20% and potentially as much as a factor of 2.36. This decrease in resonant frequency variability could be exploited to increase the yield of both gyroscopes and resonators, and to reduce quadrature error in gyroscopes.

Contribution 7: It was demonstrated through experiment that **fillets significantly increase the yield of resonators employing**

tapered flexures by a factor of roughly 2. This increase in yield could be exploited to reduce the cost of both gyroscopes and resonators.

Contribution 8: It was demonstrated through FEA and confirmed through experiment that **the ratio of the lengths of the tapered portion to the hammerhead portion of the tapered flexures (L/d ratio) could be used to trade quality factor against resonant frequency variability** in designs employing tapered flexures. This provides the design engineer a design variable to trade device performance against yield for both gyroscopes and resonators, and/or to trade bias, sensitivity, and noise performance against quadrature error in gyroscopes.

Contribution 9: **Five new anti-phase lever mechanism designs were formulated, analyzed through FEA, and two were demonstrated experimentally**. Complete design procedures were captured for each of these designs and their performance was assessed via FEA against two designs published in literature for several critical device parameters for gyroscopes and resonators. The strengths and weaknesses of each of these designs were captured and documented. Experimental data confirmed the benefits predicted by FEA of the tapered flexure revised UCI design, but did not

confirm the predicted reduction in thermoelastic damping predicted by FEA for the tapered flexure lever design. Several potential causes of this result were provided.

Contribution 10: It was demonstrated through experiment that **the tapered flexure lever anti-phase lever mechanism design reduced both the resonant frequency and quality factor variability** over equivalent straight and tapered flexure revised UCI designs. This reduction in variability could be exploited to increase in yield (reduce the cost) of both gyroscopes and resonators and/or to improve bias performance and reduce quadrature error in gyroscopes.

Recommendation 1: **Additional data should be collected from the existing experiment to validate these initial findings.** Many of the benefits of tapered flexures and fillets are either a fairly small percentage improvement or a statistical variability improvement, both of which require large data sets to validate. While a significant amount of data was collected and presented in this dissertation from several different designs, it was collected from a single wafer and no data was collected from several of the designs on the wafer. Additionally, no proof mass bias voltage could be applied to one of the designs which casts some doubt on the accuracy of

those findings. More wafers should be fabricated and interrogated both from the ARL facility used for the present research and from other third-party fabrication facilities to investigate the universality of these findings.

Recommendation 2: **Improvements should be made to the experimental setup to improve the confidence in the results.** Specifically, the loop instability of the devices with high quality factors needs to be addressed and corrected to enable accurate data collection from those devices. The probe chamber contamination problem which degrades the quality factors over time should also be investigated and addressed since several days or weeks are required to interrogate all of the 600+ devices on the wafer. Automating the interrogation process would be a significant help to gathering the large quantity of data required for this study. The fabrication process should be improved to reduce the variability across the wafer and/or every device should have an identical device adjacent to it on the wafer to enable side-by-side comparisons to be made in a manner similar to the y-axis device experiments in this research. Finally, the mask should be adjusted to account for the globally estimated CDLoss to enable closer comparison to the FEA predictions.

Recommendation 3: **Alternate resonator designs with larger thermoelastic damping (lower quality factors) should be used for experimentation** to ensure that the measured ringdown times and quality factors are limited only by thermoelastic damping. This would reduce the electronic instability problem, make the ringdown measurements easier and faster, and increase the confidence that the data collected is characterizing the thermoelastic damping performance.

Recommendation 4: **An investigation should be performed into the sensitivity of each APLM design to changes in the footprint** to obtain a more complete comparative assessment of the APLM designs. The "equivalence" of the APLM designs reported in this research was largely based on the lengths of key elements of the design which held all designs to a very similar footprint. Developing a more complete understanding of the sensitivity of these designs to changes in the footprint could lead to more insightful conclusions. A portion of that study should include the hybrid pivot configuration suggested in Chapter 4.

Recommendation 5: **A dedicated experiment should be contrived to investigate the tapered flexure lever anti-phase lever mechanism and compare it to the revised UCI design.** The experiment conducted in this research to investigate the tapered flexure

lever design required heavy modification of the base dual-mass resonator design and resulted in a device configuration that was significantly less than ideal. The potential thermoelastic damping performance gains of this design that were predicted by the FEA, coupled with the reduction in variability seen in the experimental data warrant further investigation and justify a dedicated experiment for this design where layout concessions for compatibility will not have to be made.

Recommendation 6: **Incorporate only fillets into the existing ARL Quadruple Mass Gyroscope (QMG) design and compare performance and yield to existing devices.** The findings in this dissertation indicate that incorporation of fillets should significantly improve yield and performance of the QMG, but this should be substantiated by experiment.

Recommendation 7: **Incorporate tapered flexures with fillets into the existing ARL Quadruple Mass Gyroscope (QMG) design and compare performance and yield to existing devices.** The findings in this dissertation indicate that incorporation of tapered flexures with fillets should significantly improve yield and performance of the QMG, but this should be substantiated by experiment.

Recommendation 8: **The benefits of tapered flexures and fillets should be investigated for other types of sensor and actuator designs.** Research at Carnegie Mellon University has investigated the use of tapered flexures to increase the range of high-g accelerometers, but this work suggests that tapered flexures with fillets may be able to decrease the variability and increase the yield of a broad class of in-plane silicon accelerometers and actuators.

Recommendation 9: **The benefits of tapered flexures and fillets should be investigated over various environmental factors such as thermal, vibration, and shock.** The reduction of stress and stress peaking, combined with the uniformity of the stress along the length of the flexure may make tapered flexures with fillets less sensitive to environmental changes. The impacts of these environmental stimuli are very difficult to model in FEA and the only reliable way to characterize them is through statistical experimental evaluation. An in-plane accelerometer design would be an excellent candidate sensor for an experiment to assess environmental sensitivities.

Recommendation 10: **An investigation should be performed into the potential benefits of quadratically tapered flexures for piezoelectric bimorph sensors and actuators.** The uniform strain field provided by the quadratically tapered flexure geometry

should be an excellent match for use in piezoelectric bimorph structures due to the need to have uniform strain across the length of the piezoelectric element. Similar to what was described by BEI in their Quartz rate sensor [71], the quadratically tapered flexure should increase the electromechanical coupling efficiency of piezoelectric bimorph elements commonly used in some silicon devices. This has the potential to lead to performance improvements in actuators, sensors, energy harvesting devices, power/voltage conversion devices, and other devices that employ piezoelectric bimorph structures.

References

[1] H. C. Nathanson, and R. A. Wickstrom, “A Resonant-Gate Silicon Surface Transistor with High-Q Bandpass Properties,” *Appl. Phys. Lett.*, Vol. 7, Iss. 4, p. 84-86, 1965.

[2] H. C. Nathanson, W. E. Newell, R. A. Wickstrom, and J. R. Davis, Jr., “The Resonant Gate Transistor,” *IEEE Trans. Electron Devices*, Vol. 14, Iss. 3, p. 117, 1967.

[3] K. Peterson, “Silicon as a Mechanical Material”, *Proceedings of the IEEE*, Vol. 70, pp. 420-457, 1982.

[4] B. Boxenhorn, and P. Greiff, “A Vibratory Micromechanical Gyroscope”, Paper 88-4177, https://doi-org.elib.uah.edu/10.2514/6.1988-4177, *AIAA Guidance and Controls Conference*, Minneapolis, MN, Aug. 15-17, 1988.

[5] P. Greiff, B. Boxenhorn, T. King, and L. Niles, "Silicon Monolithic Micromechanical Gyroscope", Transducers 91 Technical Digest, pp. 966-969, *1991 International Conference on Solid State Sensors and Actuators*, June 24,1991.

[6] J. Bernstein, S. Cho, A.T. King, A. Kourepenis, P. Maciel, M. Weinberg, “A micromachined comb-drive tuning fork rate gyroscope”, *Proc. IEEE MEMS*, 1993.

[7] https://www.dronezon.com/learn-about-drones-quadcopters/three-and-six-axis-gyro-stabilized-drones/, “Drone Gyro Stabilization, IMU And Flight Controllers Explained”, (Accessed on Nov. 11, 2019).

[8] https://www.youtube.com/watch?v=ORcu-c-qnjg, iPhone 4’s New Gyroscope, (Accessed on Nov. 11, 2019).

[9] https://en.wikipedia.org/wiki/Wii_Remote, Wii Remote, (Accessed on Nov. 11, 2019).

[10] https://aerospace.honeywell.com/en/learn/products/sensors/hg1930-inertial-measurement-unit, HG1930 Inertial Measurement Unit, (Accessed on Nov. 11, 2019).

[11] D. Senkal, A. Efimovskaya, A. M. Shkel, “Dual Foucault Pendulum Gyroscope”, Transducers 2015, 2015 IEEE.

[12] D. Senkal, A. Efimovskaya, A. M. Shkel, “Minimal Realization of Dynamically Balanced Lumped Mass WA Gyroscope: Dual Foucault Pendulum”, 2015 IEEE International Symposium on Inertial Sensors and Systems (ISISS) - ISISS 2015, 2015 IEEE.

[13] "IEEE Std 528™-2001", IEEE Standard for Inertial Sensor Terminology.

[14] N. Yazdi, F. Ayazi, K. Najafi,, “Micromachined Inertial Sensors,” Invited Paper, Proc. IEEE, Vol. 86, No. 8, Aug 1998.

[15] J. L. Meriam, L. G. Kraige, *Engineering Mechanics, Volume 2, Dynamics*, John Wiley and Sons, Inc., New York, 1986.

[16] A. M. Shkel, “Type I and Type II Micromachined Vibratory Gyroscopes”, Proc. IEEE/ION Position Location and Navigation Symp., San Diego, CA, Apr 24-26, 2006, pp. 586-593.

[17] A. M. Madni, L. E. Costlow, “A third generation, highly monitored, micromachined quartz rate sensor for safety-critical vehicle stability control”, 2001 IEEE Aerospace Conf. Proc., Vol. 5, IEEE, 2001.

[18] S. Kudo, S. Sugawara, N. Wakatuki, “Finite element analysis of single crystal tuning forks for gyroscopes”, Proc. 1996 IEEE Int. Frequency Control Symp., Conference Paper, IEEE, 1996.

[19] O. Bel, R. Bourquin, “Effect of geometrical electrode defects on the bias and sensitivity of tuning fork angular rate sensor”, Proc. 2001 IEEE Int. Frequency Control Symp. and PDA Exhibition, Conference Paper, IEEE, 2001

[20] Google Images, https://images.app.goo.gl/JrD5CrCDu9q62Mu8A, (Accessed on Sept. 24, 2019).

[21] J. S. Burdess, D. Wood, A. J. Harris, G. Cooper, J. Cruickshank, “Vibrating gyroscopes”, IEEE Colloquium on Measurement Using Resonant Sensing, Conference Paper, IET, 1993.

[22] F. Ayazi, K. Najafi, “A HARPSS polysilicon vibrating ring gyroscope”, *Journal of Microelectromechanical Systems*, Vol. 10, Issue 2, 2001, pp. 169-179.

[23] M. Kranz, S. Burgett, T. Hudson, M. Buncick, P. Ruffin, P. Ashley, J. McKee, “A wide dynamic range Silicon-on-Insulator MEMS gyroscope with digital force feedback”, Transducers 2003, 12th Int. Conf. on Solid-State Sensors, Actuators and Microsystems. Digest of Technical Papers, Vol. 1, IEEE, 2003.

[24] http://wikis.controltheorypro.com/File:Draper_Tuning_Fork_Gyrosope.png, (Accessed on Sept. 24, 2019).

[25] A. A. Trusov, I. P. Prikhodko, S. A. Zotov, A. R. Schofield, A. M. Shkel, "Ultra-high Q silicon gyroscopes with interchangeable rate and whole angle modes of operation", IEEE Sensors 2010, IEEE, 2010.

[26] S. An, Y. S. Oh, B. L. Lee, K. Y. Park, S. J. Kang, S. O. Choi, Y. I. Go, C. M. Song, "Dual-axis microgyroscope with closed-loop detection", *Proceedings of the Eleventh Annual International Workshop on MEMS 98*, 1998, pp. 328-333.

[27] https://www.memsjournal.com/2011/01/motion-sensing-in-the-iphone-4-mems-gyroscope.html, Figure 4, (Accessed on Sept. 24, 2019).

[28] B. R. Simon, *Mode Ordering in Anti-Phase Driven MEMS Gyroscopes and Accelerometers*, Dissertation, University of California at Irvine, 2014.

[29] IEEE Standard Specification Format Guide and Test Procedure for Coriolis Vibratory Gyros IEEE Std 1431-2004 Year: 2004 | Standard | Publisher: IEEE.

[30] V. Kaajakari, "Practical MEMS" Text book, Small Gear Publishing, ISBN: 978-0-9822991-0-4, p. 58, 2009.

[31] M. S. Weinberg, A. Kourepenis, "Error sources in in-plane silicon tuning-fork MEMS gyroscopes", Journal of Microelectromechanical Systems, Vol. 15, No. 3, pp. 479-491, IEEE, June 2006.

[32] W. A. Clark, R. T. Howe, and R. Horowitz, "Surface micromachined z-axis vibratory rate gyroscope," in Tech. Dig. Solid-State Sensor and Actuator Workshop, Hilton Head Island, SC, June 1996, pp. 283–287.

[33] J. A. Geen, and D. W. Carow, "Micromachined Gyros," US Patent 6,505,511 B1, Jan. 2003.

[34] A. A. Trusov, G. Atikyan, D. M. Rozelle, A. D. Meyer, S. A. Zotov, B. R. Simon, A. M. Shkel, "Force Rebalance, Whole Angle, and Self-Calibration Mechanization of Silicon MEMS Quad Mass Gyro," IEEE International Symposium on Inertial Sensors and Systems (ISISS 2014), Laguna Beach, CA, USA, February 25-26, 2014.

[35] A. A. Trusov, I. P. Prikhodko, D. M. Rozelle, A. D. Meyer, A. M. Shkel, "1 PPM precision self-calibration of scale factor in MEMS Coriolis vibratory gyroscopes", 2013 Transducers & Eurosensors XXVII: The 17th International Conference on Solid-State Sensors, Actuators and Microsystems (TRANSDUCERS & EUROSENSORS XXVII), 2013.

[36] A. A. Trusov, M. R. Phillips, G. H. McCammon, D. M. Rozelle, A. D. Meyer, “Continuously self-calibrating CVG system using hemispherical resonator gyroscopes,” 2015 IEEE International Symposium on Inertial Sensors and Systems (ISISS) Proceedings, 2015.

[37] A. A Trusov, A. D. Meyer, G. H. McCammon, A. Bettadapura, M. R. Philips, “Toward software defined coriolis vibratory gyroscopes with dynamic self-calibration,” 2016 DGON Inertial Sensors and Systems (ISS), 2016.

[38] J. Y. Cho, J-K. Woo, J. Yan, R. L. Peterson, K. Najafi, “Fused-Silica Micro Birdbath Resonator Gyroscope (μ -BRG)”, Journal of Microelectromechanical Systems, IEEE, Volume: 23, Issue: 1, 2014.

[39] D. Schwartz, D. Kim, R. M'Closkey, “A model-based approach to multi-modal mass tuning of a micro-scale resonator”, 2012 American Control Conference (ACC), IEEE, 2012.

[40] B. J. Gallacher, J. Hedley, J. S. Burdess, A. J. Harris, M. E. McNie, “Multimodal tuning of a vibrating ring using laser ablation”, Proceedings of the Institution of Mechanical Engineers, Part C: Journal of Mechanical Engineering Science, vol. 217, 5: pp. 557-576, May 1, 2003.

[41] C. H. Ahn, E. J. Ng, V. A. Hong, Y. Yang, B. J. Lee, M. W. Ward, and T. W. Kenny, “Geometric compensation of (100) single crystal silicon disk resonating gyroscope for mode-matching,” in Proc. 17th Int. Conf. Solid-State Sens., Actuators, Microsyst., Jun. 2013. pp. 1847–1850.

[42] C. H. Ahn, E. J. Ng, V. A. Hong, Y. Yang, B. J. Lee, I. Flader, T. W. Kenny, "Mode-Matching of Wineglass Mode Disk Resonator Gyroscope in (100) Single Crystal Silicon," in Journal of Microelectromechanical Systems, vol.24, no.2, pp.343-350, April 2015.

[43] I. P. Prikhodko, J. A. Gregory, W. A. Clark, J. A. Geen, M. W. Judy, C. H. Ahn, T. W. Kenny, “Mode-matched MEMS Coriolis vibratory gyroscopes: Myth or reality?”, 2016 IEEE/ION Position, Location and Navigation Symposium (PLANS 2016), IEEE, 2016.

[44] S. Sonmezoglu, S. E. Alper, T. Akin, "An Automatically Mode-Matched MEMS Gyroscope with Wide and Tunable Bandwidth," in Journal of Microelectromechanical Systems, vol.23, no.2, pp.284-297, April 2014.

[45] R. Antonello, R. Oboe, L. Prandi, F. Biganzoli, "Automatic Mode Matching in MEMS Vibrating Gyroscopes Using Extremum-Seeking Control," in IEEE Transactions on Industrial Electronics, vol.56, no.10, pp.3880-3891, Oct. 2009.

[46] G. H. Bryan, “On the Beats in the Vibrations of a Revolving Cylinder or Bell,” Cambridge Phil. Soc., vol. VII, pt. III, p. 101, Nov. 24, 1890.

[47] D. Lynch, "Coriolis Vibratory Gyros,” in Symposium Gyro Technology 1998, pp. 1.0-1.14. (Reproduced as Annex B. Coriolis Vibratory Gyros, pp. 56-66 of IEEE Std. 1431-2004).

[48] J. Zhang, C. He, Y. Liu, D. Liu, Q. Zhao, Z. Yang, G. Yan, “A novel scale factor calibration method for a MEMS gyroscope based on virtual coriolis force,” 10th IEEE International Conference on Nano/Micro Engineered and Molecular Systems, IEEE, 2015.

[49] A. A. Trusov, G. Atikyan, D. M. Rozelle, A. D. Meyer, S. A. Zotov, B. R. Simon, A. M. Shkel, “Flat Is Not Dead: Current and Future Performance of Si-MEMS Quad Mass Gyro (QMG) System,” 2014 IEEE/ION Position, Location and Navigation Symposium - PLANS 2014, IEEE/ION, 2014.

[50] A. D. Challoner, H. H. Ge, J. Y. Liu, “Boeing Disc Resonator Gyroscope ,” 2014 IEEE/ION Position, Location and Navigation Symposium - PLANS 2014, IEEE/ION, 2014.

[51] H. H. Ge, J. Y. Liu, B. Buchanan, “Bias self-calibration techniques using silicon disc resonator gyroscope,” 2015 IEEE International Symposium on Inertial Sensors and Systems (ISISS 2015) Proceedings, IEEE, 2015.

[52] M. Weinberg, R. Candler, S. Chandorkar, J. Varsanik, T. Kenny, and A. Duwel, “Energy loss in MEMS resonators and the impact on inertial and RF devices,” Proc. Int. Conf. Solid State Sens. Actuators Microsyst., Denver, CO, Jun. 21–25, 2009, pp. 688–695.

[53] K.Y. Yasumura, T.D. Stowe, E.M. Chow, T. Pfafman, T.W. Kenny, B.C. Stipe, D. Rugar, “Quality factors in micron- and submicron-thick cantilevers,” J. Microelectromech. Syst. 9 (1) (2000) 117–125.

[54] M.C. Cross, R. Lifshitz, “Elastic wave transmission at an abrupt junction in a thin plate with application to heat transport and vibrations in mesoscopic systems,” Phys. Rev. B 64 (2001) 1–22.

[55] Y.-H. Park and K. C. Park, “High-fidelity modeling of MEMS resonators – part I: anchor loss mechanisms through substrate,” J. Microelectromechanical Systems, vol. 13, no. 2, pp. 238–247, 2004.

[56] Y.-H. Park and K. C. Park, “High-fidelity modeling of MEMS resonators – part II: coupled beam-substrate dynamics and validation,” J. Microelectromechanical Systems, vol. 13, no. 2, pp. 248–257, 2004.

[57] Z. Hao, A. Erbil, and F. Ayazi, “An analytical model for support loss in micromachined beam resonators with in-plane flexural vibrations,” Sensors and Actuators, A: Physical, vol. 109, no. 1-2, pp. 156–164, 2003.

[58] A. A. Trusov, A. R. Schofield, A. M. Shkel, “Study of Substrate Energy Dissipation Mechanism in in-Phase and Anti-Phase Micromachined Vibratory Gyroscopes”, IEEE SENSORS 2008 Conference.

[59] Z. Hao, M. F. Zaman, A. Sharma, and F. Ayazi, “Energy loss mechanisms in a bulk-micromachined tuning fork gyroscope,” in Proc. IEEE Sensors Conference, 2006, pp. 1333–1336.

[60] S. Shahraini, M. Shahmohammadi, R. Abdolvand, “Support loss evasion in breathing-mode high-order silicon disc resonators,” 2017 IEEE International Ultrasonics Symposium (IUS), IEEE, 2017.

[61] C. Zener, “Internal Friction in Solids: I. Theory of Internal Friction in Reeds” Physical Review, Vol. 52, p. 230-235, Aug. 1, 1937.

[62] C. Zener, “Internal Friction in Solids: II. General Theory of Thermoelastic Internal Friction” Physical Review, Vol. 53, p. 90-99, Jan. 1, 1938.

[63] A. S. Nowick and B. S. Berry, Anelastic Relaxation in Crystalline Solids. New York: Academic, 1972.

[64] S. Prabhakar, S. Vengallatore, “Theory of Thermoelastic Damping in Micromechanical Resonators with Two-dimensional Heat Conduction,” IEEE/ASMA Journal of Microelectromechanical Systems, Vol. 17, No. 2, 2008.

[65] S. A. Chandorkar, H. Mehta, M. Agarwal, M. A. Hopcroft, C. M. Jha, R. N. Candler, G. Yama, G. Bahl, B. Kim, R. Melamud, K. E. Goodson, and T.W. Kenny, “Non-isothermal micromechanical resonators,” in Proc. MEMS, Kobe, Japan, 2007.

[66] A. Duwel, M. Weinstein, J. Gorman, J. Borenstein, P. Ward, “Quality factors of MEMS gyros and the role of thermoelastic damping”, Technical Digest. MEMS 2002 IEEE Int. Conf., IEEE, 2002.

[67] S. Ghaffari, S. A. Chandorkar, S. Wang, E. J. Ng, C. H. Ahn, V. Hong, Y. Yang, T. W. Kenny, “Quantum Limit of Quality Factor in Silicon Micro and Nano Mechanical Resonators”, Sci. Rep. 2013, 3, 3244.

[68] R. Lifshitz and M.L. Roukes, “Thermoelastic damping in micro-and nanomechanical systems,” Phys. Rev. B, vol. 61, no. 8, pp. 5600–5609, Feb 2000.

[69] R. N. Candler, M. Hopcroft, C. W. Low, S. Chandorkar, B. Kim, M. Varghese, A. Duwel, T. W. Kenny, “Impact of Slot Location on Thermoelastic Dissipation in Micromechanical Resonators”, The 13th International Conference on Solid-State Sensors, Actuators and Microsystems, Seoul, Korea, June 5-9, 2005.

[70] R. N. Candler, A. Duwel, M. Varghese, S. Chandorkar, M. Hopcroft, Woo-Tae Park, B. Kim, G. Yama, A. Partridge, M. Lutz, T. W. Kenny, “Impact of Geometry on Thermoelastic Dissipation in Micromechanical Resonant Beams”, Journal of Microelectromechanical Systems, Vol. 15, No. 4, p. 927-934, August 2006.

[71] A. M. Madni, L. E. Costlow, S. J. Knowles, “Common Design Techniques for BEI GyroChip Quartz Rate Sensors for Both Automotive and Aerospace/Defense Markets”, IEEE Sensors Journal, Vol. 3, NO. 5, Oct 2003.

[72] J. Y. Cho, J. Yan, J. A. Gregory, H. W. Eberhart, R. L. Peterson, K. Najafi, “3-Dimensional Blow Torch-Molding of Fused Silica Microstructures”, Journal of Microelectromechanical Systems, IEEE, Volume: 22, Issue: 6, 2013.

[73] J-K Woo, J. Y. Cho, C. Boyd, K. Najafi, “Whole-angle-mode micromachined fused-silica birdbath resonator gyroscope (WA-BRG)”, 2014 IEEE 27th International Conference on Micro Electro Mechanical Systems (MEMS).

[74] T. Nagourney, J. Y. Cho, B. Shiari, A. Darvishian, K. Najafi, “259 Second Ring-Down Time and 4.45 Million Quality Factor in 5.5 kHz Fused Silica Birdbath Shell Resonator”, 2017 19th International Conference on Solid-State Sensors, Actuators and Microsystems (TRANSDUCERS), IEEE, 2017.

[75] Y. Xie, H-C Hsieh, P. Pai, H. Kim, M. Tabib-Azar, C. H. Mastrangelo, “Precision curved micro hemispherical resonator shells fabricated by poached-egg micro-molding”, 2012 IEEE SENSORS.

[76] E. J. Eklund, A. M. Shkel, “Glass Blowing on a Wafer Level’, Journal of Microelectromechanical Systems, IEEE, Volume: 16, Issue: 2, 2007.

[77] S. A. Zotov, A. A. Trusov, A. M. Shkel, “Three-Dimensional Spherical Shell Resonator Gyroscope Fabricated Using Wafer-Scale Glassblowing”, Journal of Microelectromechanical Systems, IEEE, Volume: 21, Issue: 3, 2012.

[78] L. Sorenson, P. Shao, F. Ayazi, “Bulk and Surface Thermoelastic Dissipation in Micro-Hemispherical Shell Resonators”, Journal of Microelectromechanical Systems, IEEE, Volume: 24, Issue: 2, 2015.

[79] B. Sarac, G. Kumar, T. Hodges, S. Ding, A. Desai, J. Schroers, “Three-Dimensional Shell Fabrication Using Blow Molding of Bulk Metallic Glass”, Journal of Microelectromechanical Systems, IEEE, Volume: 20, Issue: 1, 2011.

[80] M. Kanik, P. Bordeenithikasem, J. Schroers, N. Selden, A. Desai, D. Kim, R. M'Closkey, “Microscale three-dimensional hemispherical shell resonators fabricated from metallic glass”, 2014 International Symposium on Inertial Sensors and Systems (ISISS), IEEE, 2014.

[81] M. Kanik, P. Bordeenithikasem, D. Kim, N. Selden, A. Desai, R. M’Closkey, J. Schroers, “Metallic Glass Hemispherical Shell Resonators”, Journal of Microelectromechanical Systems, IEEE, Volume: 24, Issue: 1, 2015.

[82] P. Li, H. Zhou, “Analysis of thermoelastic damping in linearly tapered microbeam resonators with rectangular cross-section”, 2018 4th International Conference on Control, Automation and Robotics (ICCAR), IEEE, 2018.

[83] P. Li, H. Zhou, L. Yang, “Thermoelastic damping analysis of double clamped microbeams with exponentially tapered thickness”, 2018 IEEE 3rd Advanced Information Technology, Electronic and Automation Control Conference (IAEAC), IEEE, 2018.

[84] https://www.siliconsensing.com/technology/evolution-of-vsg/, VSG3, (Accessed on Nov. 9, 2019).

[85] N. V. Lavrik, P. G. Datskos, “Optically Read Coriolis Vibratory Gyroscope Based On A Silicon Tuning Fork”, Nature Microsystems & Nanoengineering, 2019 Open Article, https://www.nature.com/articles/s41378-019-0087-9.pdf, https://doi.org/10.1038/s41378-019-0087-9, (Accessed on Nov. 9, 2019).

[86] B. Kim, M. Hopcroft, R. Candler, C. Jha, M. Agarwal, R. Melamud, S. Chandorkar, G. Yama, and T. Kenny, “Temperature dependence of quality factor in MEMS resonators,” J. Microelectromech. Syst., vol. 17, no. 3, pp. 755–766, Jun. 2008.

[87] M. Guney, V. Chung, X. Li, J. Paramesh, T. Mukherjee, G. Fedder, “Frequency Staggered Accelerometer Array for Improved Ringdown Behavior”, INERTIAL SENSORS 2019 IEEE.

[88] V. Chung, X. Li, M. Guney, J. Paramesh, T. Mukherjee, G. Fedder, “Hourglass-beam Nanogram-proof-mass Array: Toward a High Dynamic Range Accelerometer”, INERTIAL SENSORS 2019 IEEE.

[89] G. Gattere, F. Rizzini, L. Corso, A. Alessandri, F. Tripodi, S. Paleari, “Geometrical and Process Effects on MEMS Dimensional Loss: a Frequency Based Characterization”, International Symposium on Inertial Sensors and Systems (ISISS 2019) - Inertial 2019, IEEE, 2019.

[90] B. Simon, A. Trusov, A. Shkel, “Anti-Phase Mode Isolation in Tuning-Fork MEMS using a Lever Coupling Design”, SENSORS 2012 IEEE.

[91] C. Liu, *Foundations of MEMS*, Second Edition Text book, Pearson Publishing, ISBN: 978-0-132497367, p. 112, 2011.

[92] Nam-Ho Kim, B. V. Sankar, *Introduction to Finite Element Analysis and Design*, Text book, John Wiley & Sons, ISBN: 978-0-470-12539-7, p. 143, 2009.

[93] "CoventorWare 10.3: Using CoventorWare" Software Documentation, https://www.coventor.com/support/portal/mems-design-current/ (requires customer login), Link valid May 2019.

[94] A. Mazzoni, R. Rudy, R. Knight, J. Pulskamp, "Investigation of Thermoelastic Damping in Microelectromechanical System (MEMS) Quadruple-Mass Gyroscope (QMG) Designs" Defense Technical Information Center Technical Report, ARL-TR-9216 , Aug 2021, available at https://apps.dtic.mil/sti/pdfs/AD1144809.pdf accessed on 1/30/2022.

[95] T. Sauer, *Numerical Analysis*, Second Edition Text book, Pearson Education, Inc., ISBN: 978-0-321-78367-7, p. 131, 2012.

Appendix A. Relevant Mathematical Derivations

Appendix A presents mathematical derivations that were either too extensive for the main body or were ancillary to the primary arguments of this dissertation.

A.1 Euler-Bernoulli Beam Equation with Location-Dependent Moment of Inertia

This derivation picks up from Chapter III using Figure 3.4 and Equation 3.11 and proves that even if the moment of inertia is a function of the location along the length of the beam, it still remains outside of the second derivative in the standard Euler-Bernoulli beam equation.

First, we define the displacement field, $u(x, y)$, that describes the displacement of the material in the *x* direction as a function of both *x* and *y*: The differential equation for $u(x, y)$ can be written by inspection as:

$$u(x, y) = u_0(x) - y \cdot \frac{dv(x)}{dx}, \tag{A.1}$$

where $u_0(x)$ is the x axis displacement of the beam along the neutral axis of the beam at location x. In our analysis, we assume that the beam is in a pure bending mode and that there is no net axial force, P, along the x axis either in tension or compression acting on the beam over an individual cross section. Therefore, the first term of this equation will eventually be set to zero. That is, $u_0(x) = 0$. However, we will carry this term for now so that we will have a more generalized result for the displacement of the tapered flexure.

The normal strain, $\epsilon_{xx}(x,y)$, can then be written as the partial derivative with respect to x of the displacement field equation, Equation A.1:

$$\epsilon_{xx}(x,y) = \frac{\partial u(x,y)}{\partial x} = \frac{du_0(x)}{dx} - y \cdot \frac{d^2v(x)}{dx^2}. \tag{A.2}$$

Multiplying this equation by Young's Modulus, E, yields the equation for the stress, $\sigma_{xx}(x,y)$ as a function of x and y:

$$\sigma_{xx}(x,y) = E \cdot \epsilon_{xx}(x,y) = E \cdot \epsilon_0(x) - E \cdot y \cdot \frac{d^2v(x)}{dx^2}, \tag{A.3}$$

where the additional function, $\epsilon_0(x)$, has been defined to describe the strain of the beam along the neutral axis at location x, or:

$$\epsilon_0(x) = \frac{du_0(x)}{dx}. \tag{A.4}$$

The axial force, P_{A_x}, of any cross-sectional area, A_x, of the beam at location x, can then be found by integrating the stress over the entire cross-sectional area as follows:

$$P_{A_x} = \int_{A_x} \sigma_{xx}(x,y) dA_x. \tag{A.5}$$

Substituting Equation A.3 into Equation A.5 yields:

$$P_{A_x} = \int_{A_x} E \cdot \epsilon_0(x) dA_x - \int_{A_x} E \cdot y \cdot \frac{d^2v(x)}{dx^2} dA_x. \tag{A.6}$$

Since $\epsilon_0(x)$ and $v(x)$ are only functions of x, they can be pulled out of the area integration operation which is only integrating over y and z. This yields:

$$P_{A_x} = E \cdot \epsilon_0(x) \int_{A_x} dA_x - E \cdot \frac{d^2v(x)}{dx^2} \int_{A_x} y \cdot dA_x. \quad \text{(A.7)}$$

By inspection we know that:

$$\int_{A_x} dA_x = A_x. \quad \text{(A.8)}$$

Additionally, since the cross-sectional area of integration is symmetric in both axes and centered around the origin, then we also know that the first moment of inertia about y is zero, or:

$$\int_{A_x} y \cdot dA_x = 0. \quad \text{(A.9)}$$

Substituting Equation A.8 and Equation A.9 into Equation A.7 yields the following relation for the total axial force at location x:

$$P_{A_x} = E \cdot \epsilon_0(x) \cdot A_x - E \cdot \frac{d^2v(x)}{dx^2} \cdot 0 = E \cdot \epsilon_0(x) \cdot A_x. \quad \text{(A.10)}$$

Since there were no restrictions placed on the specific location, x, of this derivation, this result can be generalized to any location along the length of the flexure, or:

$$P(x) = E \cdot \epsilon_0(x) \cdot A(x). \quad \text{(A.11)}$$

This result is consistent with that of the non-tapered flexure with the exception that the cross-sectional area is now a function of x instead of a constant. For the specific problem at hand, deriving the linear and rotational spring constants of the tapered flexure

with a lumped mass on the end, we are assuming a pure bending mode for the flexure. That is, we are assuming no net axial extension or compression, *i.e.*, $\epsilon_0(x) = 0$ and, therefore, it follows that $P(x) = 0$.

The net bending moment, M_{A_x}, of any given cross-sectional area, A_x, of the beam at location x, can then be found by negative of the first moment of the stress about the axis of bending over the entire cross-sectional area as follows:

$$M_{A_x} = -\int_{A_x} y \cdot \sigma_{xx}(x, y) dA_x. \tag{A.12}$$

Substituting Equation A.3 into Equation A.12 yields:

$$M_{A_x} = -\int_{A_x} y \cdot E \cdot \epsilon_0(x) dA_x + \int_{A_x} E \cdot y^2 \cdot \frac{d^2 v(x)}{dx^2} dA_x. \tag{A.13}$$

Again, since $\epsilon_0(x)$ and $v(x)$ are only functions of x, they can be pulled out of the area integration operation which is only integrating over y and z. This yields:

$$M_{A_x} = -E \cdot \epsilon_0(x) \int_{A_x} y \cdot dA_x + E \cdot \frac{d^2 v(x)}{dx^2} \int_{A_x} y^2 \cdot dA_x. \tag{A.14}$$

From Equation A.9, it follows that the first term goes to zero. We also recognize that the second term is just the second moment of inertia of the cross-sectional area, I_{A_x}, or:

$$\int_{A_x} y^2 \cdot dA_x = I_{A_x}. \tag{A.15}$$

Substituting these results into Equation A.14 yields:

$$M_{A_x} = -E \cdot \epsilon_0(x) \cdot 0 + E \cdot \frac{d^2v(x)}{dx^2} \cdot I_{A_x} = E \cdot I_{A_x} \cdot \frac{d^2v(x)}{dx^2}. \quad \text{(A.16)}$$

Since there were no restrictions placed on the specific location, x, of this derivation, this result can be generalized to any location along the length of the flexure, or:

$$M(x) = E \cdot I(x) \cdot \frac{d^2v(x)}{dx^2}. \quad \text{(A.17)}$$

Comparing this result in Equation A.17 to the general Euler-Bernoulli Beam Equation found in Equation 3.11 answers the original question and constitutes the proof that, although it is a function of x, the second moment of inertia, $I(x)$, can remain outside of the second derivative with respect to x.

A.2 Tapered Beam Deflection Equation Derivations

This derivation picks up from Chapter III using Figure 3.4 and Equation 3.19 and derives the linear and angular deflection equations for quadratically tapered flexures with a point force load applied to the center of the hammerhead.

Equation 3.19 is repeated here for reference:

$$F \cdot (N - x) = E \cdot \frac{t \cdot w_b^3 \left(\frac{N-x}{N}\right)^{\frac{3}{2}}}{12} \cdot \frac{d^2v(x)}{dx^2}. \quad \text{(A.18)}$$

The solution to this equation is found using separation of variables as follows:

$$F \cdot (N - x)dx^2 = E \cdot \frac{t \cdot w_b^3 \left(\frac{N-x}{N}\right)^{\frac{3}{2}}}{12} \cdot d^2v \tag{A.19}$$

$$\frac{12 \cdot F \cdot (N-x)}{E \cdot t \cdot w_b^3 \cdot \left(\frac{N-x}{N}\right)^{\frac{3}{2}}} dx^2 = d^2v \tag{A.20}$$

$$d^2v = \frac{12 \cdot F \cdot (N-x)}{E \cdot t \cdot w_b^3 \cdot \left(\frac{N-x}{N}\right)^{\frac{3}{2}}} dx^2 \tag{A.21}$$

$$d^2v = \frac{12 \cdot F \cdot N^{\frac{3}{2}}}{E \cdot t \cdot w_b^3 \cdot (N-x)^{\frac{1}{2}}} dx^2 \tag{A.22}$$

$$\iint d^2v = \iint_0^x \frac{12 \cdot F \cdot N^{\frac{3}{2}}}{E \cdot t \cdot w_b^3 \cdot (N-x)^{\frac{1}{2}}} dx^2 \tag{A.23}$$

$$v(x) - x \cdot v'(0) - v(0) = \frac{12 \cdot F \cdot N^{\frac{3}{2}}}{E \cdot t \cdot w_b^3} \iint_0^x \frac{1}{(N-x)^{\frac{1}{2}}} dx^2. \tag{A.24}$$

Considering the left-hand side of Equation A.24, we assume that the boundary conditions of the displacement, v, and velocity, v', at location $x = 0$ are zero. This yields:

$$v(x) = \frac{12 \cdot F \cdot N^{\frac{3}{2}}}{E \cdot t \cdot w_b^3} \iint_0^x \frac{1}{(N-x)^{\frac{1}{2}}} dx^2. \tag{A.25}$$

We then evaluate the integral on the right-hand side as follows:

$$v(x) = \frac{12 \cdot F \cdot N^{\frac{3}{2}}}{E \cdot t \cdot w_b^3} \int_0^x \int_0^x (N - x)^{-\frac{1}{2}} dx\, dx \tag{A.26}$$

$$v(x) = \frac{12 \cdot F \cdot N^{\frac{3}{2}}}{E \cdot t \cdot w_b^3} \int_0^x \left\{ \left[\frac{(N-x)^{\frac{1}{2}}}{1/2} \cdot (-1) \right] \Bigg|_0^x \right\} dx \tag{A.27}$$

$$v(x) = \frac{12 \cdot F \cdot N^{\frac{3}{2}}}{E \cdot t \cdot w_b^3} \int_0^x \left\{ \left[-2 \cdot (N - x)^{\frac{1}{2}} + 2 \cdot N^{\frac{1}{2}} \right] \right\} dx \tag{A.28}$$

$$v(x) = \frac{12 \cdot F \cdot N^{\frac{3}{2}}}{E \cdot t \cdot w_b^3} \left\{ \int_0^x -2 \cdot (N - x)^{\frac{1}{2}}\, dx + \int_0^x 2 \cdot N^{\frac{1}{2}}\, dx \right\} \tag{A.29}$$

$$v(x) = \frac{12 \cdot F \cdot N^{\frac{3}{2}}}{E \cdot t \cdot w_b^3} \left\{ \left[\frac{-2 \cdot (N-x)^{\frac{3}{2}}}{3/2} \cdot (-1) \right] \Bigg|_0^x + \left[2 \cdot N^{\frac{1}{2}} \cdot x \right] \Bigg|_0^x \right\} \tag{A.30}$$

$$v(x) = \frac{12 \cdot F \cdot N^{\frac{3}{2}}}{E \cdot t \cdot w_b^3} \left\{ \left[\frac{4}{3} (N - x)^{\frac{3}{2}} - \frac{4}{3} N^{\frac{3}{2}} \right] + \left[2 \cdot N^{\frac{1}{2}} \cdot x \right] \right\} \tag{A.31}$$

$$v(x) = \frac{12 \cdot F \cdot N^{\frac{3}{2}}}{E \cdot t \cdot w_b^3} \left\{ \frac{4}{3} (N - x)^{\frac{3}{2}} + 2 \cdot N^{\frac{1}{2}} \cdot x - \frac{4}{3} N^{\frac{3}{2}} \right\}. \tag{A.32}$$

The angular deflection of the beam can then be found as the first derivative of the displacement equation with respect to x as follows:

$$\theta(x) = \frac{d}{dx} v(x) = \frac{12 \cdot F \cdot N^{\frac{3}{2}}}{E \cdot t \cdot w_b^3} \left\{ -2 \cdot (N - x)^{\frac{1}{2}} + 2 \cdot N^{\frac{1}{2}} \right\} \tag{A.33}$$

$$\theta(x) = \frac{24 \cdot F \cdot N^{\frac{3}{2}}}{E \cdot t \cdot w_b^3} \left\{ N^{\frac{1}{2}} - (N - x)^{\frac{1}{2}} \right\}. \quad \text{(A.34)}$$

Substituting Equation 3.14 back into Equation A.32 and Equation A.34, we arrive at the following two equations that describe the linear and angular deflections of the tapered beam:

$$v(x) = \frac{12 \cdot F \cdot (L+d)^{\frac{3}{2}}}{E \cdot t \cdot w_b^3} \left\{ \frac{4}{3}(L + d - x)^{\frac{3}{2}} + 2 \cdot (L + d)^{\frac{1}{2}} \cdot x - \frac{4}{3}(L + d)^{\frac{3}{2}} \right\} \quad \text{(A.35)}$$

and

$$\theta(x) = \frac{24 \cdot F \cdot (L+d)^{\frac{3}{2}}}{E \cdot t \cdot w_b^3} \left\{ (L + d)^{\frac{1}{2}} - (L + d - x)^{\frac{1}{2}} \right\}. \quad \text{(A.36)}$$

The linear deflection spring constant, k_e, for the end of the tapered beam (*i.e.*, at the location where the tapered beam meets the hammerhead, $x = L$) can be found as the ratio of the applied force, F, to the displacement, $v(x)$, as follows. First, we substitute $x = L$ into Equation A.35 to find the linear deflection of the beam at the end of the beam:

$$v(L) = \frac{12 \cdot F \cdot (L+d)^{\frac{3}{2}}}{E \cdot t \cdot w_b^3} \left\{ \frac{4}{3}(d)^{\frac{3}{2}} + 2 \cdot (L + d)^{\frac{1}{2}} \cdot L - \frac{4}{3}(L + d)^{\frac{3}{2}} \right\}. \quad \text{(A.37)}$$

Next, we evaluate the ratio of the force to the linear displacement to arrive at the desired linear spring constant:

$$k_e = \frac{F}{v(L)} = \frac{E \cdot t \cdot w_b^3}{12 \cdot (L+d)^{\frac{3}{2}}} \left\{ \frac{4}{3}(d)^{\frac{3}{2}} + 2 \cdot (L + d)^{\frac{1}{2}} \cdot L - \frac{4}{3}(L + d)^{\frac{3}{2}} \right\}. \quad \text{(A.38)}$$

The expression for the angular deflection at the end of the beam can be found by evaluating Equation A.36 at $x = L$. This yields:

$$\theta(L) = \frac{24 \cdot F \cdot (L+d)^{\frac{3}{2}}}{E \cdot t \cdot w_b^3} \left\{ (L+d)^{\frac{1}{2}} - (d)^{\frac{1}{2}} \right\}. \tag{A.39}$$

It is important to note here that the above equations were all derived for locations along the length of the beam, $0 \leq x \leq L$. For the purposes of the current research, it is desirable to obtain expressions for the linear and angular deflections of the hammer-head at the center of the hammer-head, that is at $x = L + d$. To extend the current results to this location, we will assume that the hammerhead is effectively infinitely stiff, which is justified because it is of relatively large width and of relatively short length. With this assumption, there is no additional angular deflection between the end of the beam, $x = L$, and the center of the hammerhead, $x = L + d$. Therefore, we have:

$$\theta(L+d) = \theta(L) = \frac{24 \cdot F \cdot (L+d)^{\frac{3}{2}}}{E \cdot t \cdot w_b^3} \left\{ (L+d)^{\frac{1}{2}} - (d)^{\frac{1}{2}} \right\}. \tag{A.40}$$

The linear deflection at locations within the hammerhead, $v_{HH}(x)$, can then be expressed as a combination of the linear deflection at the end of the beam, $v(L)$, plus a linear extension of the angular deflection at the end of the beam, $\theta(L)$, multiplied by the length of the extension, $(x - L)$, or:

$$v_{HH}(x) = v(L) + \theta(L) \cdot (x - L) \qquad L < x \leq L + d. \tag{A.41}$$

Substituting Equation A.37 and Equation A.40 into Equation A.41 gives the full expression for the linear deflection for locations within the hammerhead, or:

$$v_{HH}(x) = \frac{12 \cdot F \cdot (L+d)^{\frac{3}{2}}}{E \cdot t \cdot w_b^3}\left\{\frac{4}{3}(d)^{\frac{3}{2}} + 2 \cdot (L+d)^{\frac{1}{2}} \cdot L - \frac{4}{3}(L+d)^{\frac{3}{2}}\right\} +$$

$$\frac{24 \cdot F \cdot (L+d)^{\frac{3}{2}}}{E \cdot t \cdot w_b^3}\left\{(L+d)^{\frac{1}{2}} - (d)^{\frac{1}{2}}\right\} \cdot (x - L) \qquad L < x \leq L + d, \tag{A.42}$$

which simplifies to

$$v_{HH}(x) = \frac{12 \cdot F \cdot (L+d)^{\frac{3}{2}}}{E \cdot t \cdot w_b^3}\left\{\left[\frac{4}{3}(d)^{\frac{3}{2}} + 2 \cdot (L+d)^{\frac{1}{2}} \cdot L - \frac{4}{3}(L+d)^{\frac{3}{2}}\right] +\right.$$

$$\left.\left[2 \cdot (x - L) \cdot \left((L+d)^{\frac{1}{2}} - (d)^{\frac{1}{2}}\right)\right]\right\} \qquad L < x \leq L + d. \tag{A.43}$$

Evaluating this expression at the center of the hammerhead, $x = L + d$, yields the following:

$$v_{HH}(L+d) = \frac{12 \cdot F \cdot (L+d)^{\frac{3}{2}}}{E \cdot t \cdot w_b^3}\left\{\left[\frac{4}{3}(d)^{\frac{3}{2}} + 2 \cdot (L+d)^{\frac{1}{2}} \cdot L - \frac{4}{3}(L+d)^{\frac{3}{2}}\right] +\right.$$

$$\left.\left[2 \cdot (d) \cdot \left((L+d)^{\frac{1}{2}} - (d)^{\frac{1}{2}}\right)\right]\right\} \qquad L < x \leq L + d \tag{A.44}$$

$$v_{HH}(L+d) = \frac{12 \cdot F \cdot (L+d)^{\frac{3}{2}}}{E \cdot t \cdot w_b^3}\left\{2 \cdot L \cdot (L+d)^{\frac{1}{2}} + 2 \cdot d \cdot (L+d)^{\frac{1}{2}} - \frac{4}{3}(L+d)^{\frac{3}{2}} -\right.$$

$$\left.\frac{2}{3}(d)^{\frac{3}{2}}\right\} \qquad L < x \leq L + d \tag{A.45}$$

$$v_{HH}(L+d) = \frac{12 \cdot F \cdot (L+d)^{\frac{3}{2}}}{E \cdot t \cdot w_b^3}\left\{2 \cdot (L+d) \cdot (L+d)^{\frac{1}{2}} - \frac{4}{3}(L+d)^{\frac{3}{2}} - \frac{2}{3}(d)^{\frac{3}{2}}\right\}$$

$$L < x \leq L + d \tag{A.46}$$

$$v_{HH}(L+d) = \frac{12 \cdot F \cdot (L+d)^{\frac{3}{2}}}{E \cdot t \cdot w_b^3}\left\{2 \cdot (L+d)^{\frac{3}{2}} - \frac{4}{3}(L+d)^{\frac{3}{2}} - \frac{2}{3}(d)^{\frac{3}{2}}\right\}$$

$$L < x \leq L + d \qquad \text{(A.47)}$$

$$v_{HH}(L+d) = \frac{12 \cdot F \cdot (L+d)^{\frac{3}{2}}}{E \cdot t \cdot w_b^3}\left\{\frac{2}{3}(L+d)^{\frac{3}{2}} - \frac{2}{3}(d)^{\frac{3}{2}}\right\} \qquad L < x \leq L + d \qquad \text{(A.48)}$$

$$v_{HH}(L+d) = \frac{8 \cdot F}{E \cdot t \cdot w_b^3}\left\{(L+d)^3 - (L+d)^{\frac{3}{2}}(d)^{\frac{3}{2}}\right\} \quad L < x \leq L + d. \qquad \text{(A.49)}$$

Next, we evaluate the ratio of the force to the linear displacement to arrive at the linear spring constant at the center of the hammerhead, k_{HH} :

$$k_{HH} = \frac{E \cdot t \cdot w_b^3}{8 \cdot \left[(L+d)^3 - (L+d)^{\frac{3}{2}}(d)^{\frac{3}{2}}\right]}. \qquad \text{(A.50)}$$

Finally, we evaluate the ratio of the force to the angular displacement given in Equation A.40 to arrive at the angular spring constant at the center of the hammerhead, k_θ :

$$k_\theta = \frac{E \cdot t \cdot w_b^3}{24 \cdot \left[(L+d)^2 - (L+d)^{\frac{3}{2}}(d)^{\frac{1}{2}}\right]}. \qquad \text{(A.51)}$$

A.3 Straight Beam Deflection Equation Derivations

This section documents the derivation of the beam deflection and spring constant equations for a straight beam with a hammerhead feature in response to a force applied to the center of the hammerhead. This derivation picks up from Chapter III using Figure 3.4 and Equation 3.15, except that for the straight flexure, *I(x)* is a constant:

$$F \cdot (N - x) = E \cdot I \cdot \frac{d^2 v(x)}{dx^2}. \tag{A.52}$$

Separating variables yields:

$$\frac{F}{E \cdot I}(N - x)dx^2 = d^2 v \tag{A.53}$$

$$\frac{F}{E \cdot I}\left[N \iint_0^x dx\, dx - \iint_0^x x\, dx\, dx\right] = \iint_0^x d^2 v \tag{A.54}$$

$$\frac{F}{E \cdot I}\left[\frac{Nx^2}{2} - \frac{x^3}{6}\right] = v(x) - x\, v'(0) - v(0). \tag{A.55}$$

Since the beam is fixed-fixed at the origin and this is a static analysis, we know that $v(0) = 0$ and $v'(0) = 0$. So, we have:

$$v(x) = \frac{F}{E \cdot I}\left[\frac{Nx^2}{2} - \frac{x^3}{6}\right] \qquad 0 \le x \le L. \tag{A.56}$$

At x=L we have:

$$v(L) = \frac{F}{E \cdot I}\left[\frac{NL^2}{2} - \frac{L^3}{6}\right] \qquad x = L. \tag{A.57}$$

Substituting $N=L+d$ back in, we have:

$$v(L) = \frac{F}{E \cdot I}\left[\frac{(L+d)L^2}{2} - \frac{L^3}{6}\right] \qquad x = L \qquad \text{(A.58)}$$

$$v(L) = \frac{F}{E \cdot I}\left[\frac{3L^3+3dL^2-L^3}{6}\right] \qquad x = L \qquad \text{(A.59)}$$

$$v(L) = \frac{F}{E \cdot I}\left[\frac{2L^3+3dL^2}{6}\right] \qquad x = L \qquad \text{(A.60)}$$

$$v(L) = \frac{F}{E \cdot I}\left[\frac{L^3}{3} + \frac{dL^2}{2}\right] \qquad x = L. \qquad \text{(A.61)}$$

The angular deflection can be found by taking the first derivative of the linear deflection with respect to x. So, from Equation A.56, we have:

$$\theta(x) = \frac{d}{dx}v(x) = \frac{d}{dx}\left\{\frac{F}{E \cdot I}\left[\frac{Nx^2}{2} - \frac{x^3}{6}\right]\right\} \qquad 0 \le x \le L \qquad \text{(A.62)}$$

$$\theta(x) = \frac{F}{E \cdot I}\left[Nx - \frac{x^2}{2}\right] \qquad 0 \le x \le L. \qquad \text{(A.63)}$$

Evaluating this expression at the end of the flexure ($x=L$) leads to:

$$\theta(L) = \frac{F}{E \cdot I}\left[NL - \frac{L^2}{2}\right] \qquad x = L. \qquad \text{(A.64)}$$

Substituting $N=L+d$ back in, we have:

$$\theta(L) = \frac{F}{E \cdot I}\left[(L+d)L - \frac{L^2}{2}\right] \qquad x = L \qquad \text{(A.65)}$$

$$\theta(L) = \frac{F}{E \cdot I}\left[L^2 + dL - \frac{L^2}{2}\right] \qquad x = L \qquad \text{(A.66)}$$

$$\theta(L) = \frac{F}{E \cdot I}\left[\frac{L^2}{2} + dL\right] \qquad x = L. \qquad \text{(A.67)}$$

Here we assume that the hammerhead is essentially infinitely stiff so that the deflection equations can be projected across the length of the hammerhead by linear extension of the angular deflection at the end of the flexure, or:

$$v(x) = v(L) + (x - L) \cdot \theta(L) \qquad L \le x \le N \qquad \text{(A.68)}$$

$$v(x) = \frac{F}{E \cdot I}\left[\frac{L^3}{3} + \frac{dL^2}{2}\right] + (x - L) \cdot \frac{F}{E \cdot I}\left[\frac{L^2}{2} + dL\right] \qquad L \le x \le N \qquad \text{(A.69)}$$

$$v(x) = \frac{F}{E \cdot I}\left[\frac{L^3}{3} + \frac{dL^2}{2} + \frac{L^2 x}{2} + dLx - \frac{L^3}{2} - dL^2\right] \qquad L \le x \le N \qquad \text{(A.70)}$$

$$v(x) = \frac{F}{E \cdot I}\left[\frac{-L^3}{6} - \frac{dL^2}{2} + \frac{L^2 x}{2} + dLx\right] \qquad L \le x \le N \qquad \text{(A.71)}$$

$$v(x) = \frac{F}{E \cdot I}\left[\frac{L^2 x}{2} + dLx - \frac{L^3}{6} - \frac{dL^2}{2}\right] \qquad L \le x \le N. \qquad \text{(A.72)}$$

First, we evaluate this at the center of the hammerhead, $x=L+d$:

$$v(L + d) = \frac{F}{E \cdot I}\left[\frac{L^2(L+d)}{2} + dL(L + d) - \frac{L^3}{6} - \frac{dL^2}{2}\right] \qquad x = L + d \qquad \text{(A.73)}$$

$$v(L+d) = \frac{F}{E \cdot I}\left[\frac{L^3}{2} + \frac{dL^2}{2} + dL^2 + d^2L - \frac{L^3}{6} - \frac{dL^2}{2}\right] \qquad x = L + d \quad \text{(A.74)}$$

$$v(L+d) = \frac{F}{E \cdot I}\left[\frac{L^3}{3} + dL^2 + d^2L\right] \qquad x = L + d. \quad \text{(A.75)}$$

Solving Equation A.75 for the spring constant giving the deflection at the center of the hammerhead for a force applied at the center of the hammerhead yields:

$$k_{HHC\_S} = \frac{F}{v(L+d)} = \frac{F}{\frac{F}{E \cdot I}\left[\frac{L^3}{3} + dL^2 + d^2L\right]} \quad \text{(A.76)}$$

$$k_{HHC\_S} = \frac{E \cdot I}{\left[\frac{L^3}{3} + dL^2 + d^2L\right]} \quad \text{(A.77)}$$

$$k_{HHC\_S} = \frac{3 \cdot E \cdot I}{\left[L^3 + 3dL^2 + 3d^2L\right]}. \quad \text{(A.78)}$$

Recalling that:

$$I = \frac{t \cdot w^3}{12}, \quad \text{(A.79)}$$

and substituting yields:

$$k_{HHC\_S} = \frac{E \cdot t \cdot w^3}{4\left[L^3 + 3dL^2 + 3d^2L\right]}. \quad \text{(A.80)}$$

Evaluating Equation A.72 at the end of the hammerhead ($x=L+2d$), yields:

$$v(L+2d) = \frac{F}{E \cdot I}\left[\frac{L^2(L+2d)}{2} + dL(L+2d) - \frac{L^3}{6} - \frac{dL^2}{2}\right] \quad \text{(A.81)}$$

$$v(L+2d) = \frac{F}{E \cdot I}\left[\frac{L^3}{2} + dL^2 + dL^2 + 2d^2L - \frac{L^3}{6} - \frac{dL^2}{2}\right] \tag{A.82}$$

$$v(L+2d) = \frac{F}{E \cdot I}\left[\frac{L^3}{3} + \frac{3dL^2}{2} + 2d^2L\right]. \tag{A.83}$$

Solving Equation A.83 for the spring constant giving the deflection at the end of the hammerhead for a force applied at the center of the hammerhead yields:

$$k_{HHE\_S} = \frac{F}{v(L+2d)} = \frac{F}{\frac{F}{E \cdot I}\left[\frac{L^3}{3} + \frac{3dL^2}{2} + 2d^2L\right]} \tag{A.84}$$

$$k_{HHE\_S} = \frac{E \cdot I}{\left[\frac{L^3}{3} + \frac{3dL^2}{2} + 2d^2L\right]} \tag{A.85}$$

$$k_{HHE\_S} = \frac{6 \cdot E \cdot I}{\left[2L^3 + 9dL^2 + 12d^2L\right]}. \tag{A.86}$$

Substituting A.79 into this equation we have:

$$k_{HHE\_S} = \frac{E \cdot t \cdot w^3}{2\left[2L^3 + 9dL^2 + 12d^2L\right]} \tag{A.87}$$

$$k_{HHE\_S} = \frac{E \cdot t \cdot w^3}{4L^3 + 18dL^2 + 24d^2L}. \tag{A.88}$$

From Equation A.67 we find that the rotational spring constant is the same for all locations:

$$k_{\theta\_S} = k_{\theta HHC\_S} = k_{\theta HHE\_S} = \frac{F}{\theta(L)} = \frac{E \cdot I}{\frac{L^2}{2} + dL} \tag{A.89}$$

$$k_{\theta\_S} = k_{\theta HHC\_S} = k_{\theta HHE\_S} = \frac{F}{\theta(L)} = \frac{2 \cdot E \cdot I}{L^2 + 2dL}\,. \tag{A.90}$$

Substituting A.79 into this equation we have:

$$k_{\theta\_S} = k_{\theta HHC\_S} = k_{\theta HHE\_S} = \frac{F}{\theta(L)} = \frac{E \cdot t \cdot w^3}{6L^2 + 12dL}\,. \tag{A.91}$$

A.4 Tapered Flexure Deflection Sensitivity to CDLoss Derivations

This section provides the detailed derivation of the deflection equation of the tapered flexure for the CDLoss evaluation. Picking up from Equation 3.47, we have:

$$v(x) = \frac{12FN^{\frac{3}{2}}}{Etw_b^3} \iint_N^{N-x} \frac{1}{(y)^{\frac{1}{2}} + a} dydy\,. \tag{A.92}$$

Focusing on the first integral we first seek the solution for:

$$\int_N^{N-x} \frac{1}{(y)^{\frac{1}{2}} + a} dy. \tag{A.93}$$

Introducing a substitution of variables we let:

$$u = y^{\frac{1}{2}} + a \tag{A.94}$$

$$du = \frac{1}{2} y^{-\frac{1}{2}} dy \tag{A.95}$$

$$dy = 2y^{\frac{1}{2}}\, du, \tag{A.96}$$

which yields:

$$\int u^{-1} 2y^{\frac{1}{2}}\, du = \int u^{-1} 2(u-a)^{\frac{1}{2}}\, du \tag{A.97}$$

$$\int \frac{2u}{u}\, du - \int \frac{2a}{u}\, du = \int 2\, du - \int \frac{2a}{u}\, du \tag{A.98}$$

$$2u - 2a\ \ln(u) + C_0. \tag{A.99}$$

Substituting back in for *u* yields:

$$2\left(y^{\frac{1}{2}} + a\right) - 2a\ \ln\left(y^{\frac{1}{2}} + a\right) + C_0 \tag{A.100}$$

$$2\sqrt{y} - 2a\ \ln\left(a + \sqrt{y}\right) + 2a + \ C_0. \tag{A.101}$$

Combining the constants of integration as:

$$C_1 = 2a + C_0, \tag{A.102}$$

we have:

$$2\sqrt{y} - 2a\ \ln\left(a + \sqrt{y}\right) + C_1. \tag{A.103}$$

Here we note that the physical interpretation of this equation is the slope of the flexure. To solve for the constant of integration, we evaluate this expression at a location where we know the slope. We are assuming that the flexure in its original condition is nominally aligned with the coordinate frame. Therefore, this slope will be zero at *x=0*,

which corresponds to $y=N$. Substituting $y=N$ and setting this expression equal to zero yields:

$$2\sqrt{N} - 2a\ \ln\left(a+\sqrt{N}\right) + C_1 = 0 \tag{A.104}$$

$$C_1 = -2\sqrt{N} + 2a\ \ln\left(a+\sqrt{N}\right). \tag{A.105}$$

This leaves us with the final expression for the first integral as:

$$2\sqrt{y} - 2a\ \ln\left(a+\sqrt{y}\right) - 2\sqrt{N} + 2a\ \ln\left(a+\sqrt{N}\right). \tag{A.106}$$

Substituting this back into Equation A.92, we have:

$$v(x) = \frac{12FN^{\frac{3}{2}}}{Etw_b^3}\int_N^{N-x}\left\{2\sqrt{y} - 2a\ \ln\left(a+\sqrt{y}\right) - 2\sqrt{N} + 2a\ \ln\left(a+\sqrt{N}\right)\right\}dy, \tag{A.107}$$

which was the integrand shown in Equation 3.48 of Chapter 3. We will now turn our attention to this second integration. The integration of the first and third terms are trivial, but the second term requires some effort. Focusing on this term alone we need to find:

$$\int \ln\left(a+\sqrt{y}\right)dy. \tag{A.108}$$

The following is commonly found in tables of integrals:

$$\int \ln(u)\,du = u\ln(u) - u + C\ . \tag{A.109}$$

So here we let

$$u = a + \sqrt{y} \tag{A.110}$$

$$du = \frac{1}{2} y^{-\frac{1}{2}} dy \tag{A.111}$$

$$dy = 2y^{\frac{1}{2}} du \tag{A.112}$$

$$dy = 2(u-a)^{\frac{1}{2}} du\,. \tag{A.113}$$

Plugging these into Equation A.108 gives:

$$\int \ln(u)\, 2(u-a) du \tag{A.114}$$

$$2\int u \ln(u)\, du - 2a \int \ln(u)\, du. \tag{A.115}$$

Looking at the first term, the solution is commonly found in many tables of integrals as:

$$\int u \ln(u)\, du = \frac{u^2}{2}\left[\ln(u) - \frac{1}{2}\right] + C, \tag{A.116}$$

and the solution of the second term was provided earlier. Putting these together we find the total integral of Equation A.108 to be:

$$2\left\{\frac{u^2}{2}\left[\ln(u) - \frac{1}{2}\right]\right\} - 2a[u \ln(u) - u] \tag{A.117}$$

$$(u^2 - 2au)\ln(u) - \frac{u^2}{2} + 2au. \tag{A.118}$$

Here the constants of integration have been omitted because we know that we are going evaluate this integral over a definite interval and that these constants will eventually cancel out. Now substituting back in $u = a + \sqrt{y}$ we have the following:

$$\left(\left(a+\sqrt{y}\right)^2 - 2a\left(a+\sqrt{y}\right)\right)\ln\left(a+\sqrt{y}\right) - \frac{(a+\sqrt{y})^2}{2} + 2a\left(a+\sqrt{y}\right) \quad \text{(A.119)}$$

$$\left(a^2 + 2a\sqrt{y} + y - 2a^2 - 2a\sqrt{y}\right)\ln\left(a+\sqrt{y}\right) - \frac{a^2}{2} - a\sqrt{y} - \frac{y}{2} + 2a^2 + 2a\sqrt{y} \quad \text{(A.120)}$$

$$(y-a^2)\ln\left(a+\sqrt{y}\right) + a\sqrt{y} - \frac{y}{2} + C. \quad \text{(A.121)}$$

Here all of the constants have been grouped into a single constant which will now be discarded because the integration will be over a definite interval where this constant term will cancel out. Going back to Equation A.107 and solving the integral using the above expression for the second term we have:

$$v(x) = \frac{12FN^{\frac{3}{2}}}{Etw_b^3}\left\{\frac{4}{3}y^{\frac{3}{2}} - 2a\left[(y-a^2)\ln\left(a+\sqrt{y}\right) + a\sqrt{y} - \frac{y}{2}\right] + C_1 y\right\}\Big|_{N}^{N-x} \quad \text{(A.122)}$$

$$v(x) = \frac{12FN^{\frac{3}{2}}}{Etw_b^3}\left\{\frac{4}{3}(N-x)^{\frac{3}{2}} - 2a\left[(N-x-a^2)\ln\left(a+\sqrt{N-x}\right) + a\sqrt{N-x} - \frac{N-x}{2}\right] + C_1(N-x) - \frac{4}{3}N^{\frac{3}{2}} + 2a\left[(N-a^2)\ln\left(a+\sqrt{N}\right) + a\sqrt{N} - \frac{N}{2}\right] - C_1 N\right\} \quad \text{(A.123)}$$

$$v(x) = \frac{12FN^{\frac{3}{2}}}{Etw_b^3}\left\{\frac{4}{3}(N-x)^{\frac{3}{2}} - \frac{4}{3}N^{\frac{3}{2}} - C_1 x + 2a\left[(N-a^2)\ln\left(a+\sqrt{N}\right) - (N-x-a^2)\ln\left(a+\sqrt{N-x}\right) + a\sqrt{N} - a\sqrt{N-x} - \frac{x}{2}\right]\right\}. \quad \text{(A.124)}$$

Substituting back in for C_1 yields:

$$v(x) = \frac{12FN^{\frac{3}{2}}}{Etw_b^3}\left\{\frac{4}{3}(N-x)^{\frac{3}{2}} - \frac{4}{3}N^{\frac{3}{2}} - [-2\sqrt{N} + 2a\ln(a+\sqrt{N})]x + 2a\left[(N - a^2)\ln(a+\sqrt{N}) - (N-x-a^2)\ln(a+\sqrt{N-x}) + a\sqrt{N} - a\sqrt{N-x} - \frac{x}{2}\right]\right\} \quad \text{(A.125)}$$

$$v(x) = \frac{12FN^{\frac{3}{2}}}{Etw_b^3}\left\{\frac{4}{3}(N-x)^{\frac{3}{2}} - \frac{4}{3}N^{\frac{3}{2}} + 2x\sqrt{N} - 2ax\ln(a+\sqrt{N}) + 2a\left[(N-a^2)\ln(a+\sqrt{N}) - (N-x-a^2)\ln(a+\sqrt{N-x}) + a(\sqrt{N}-\sqrt{N-x}) - \frac{x}{2}\right]\right\} \quad \text{(A.126)}$$

$$v(x) = \frac{12FN^{\frac{3}{2}}}{Etw_b^3}\left\{\frac{4}{3}(N-x)^{\frac{3}{2}} - \frac{4}{3}N^{\frac{3}{2}} + 2x\sqrt{N} + 2a\left[(N-x-a^2)\ln(a+\sqrt{N}) - (N-x-a^2)\ln(a+\sqrt{N-x}) + a(\sqrt{N}-\sqrt{N-x}) - \frac{x}{2}\right]\right\} \quad \text{(A.127)}$$

$$v(x) = \frac{12FN^{\frac{3}{2}}}{Etw_b^3}\left\{\frac{4}{3}(N-x)^{\frac{3}{2}} + 2x\sqrt{N} - \frac{4}{3}N^{\frac{3}{2}} + 2a\left[(N-x-a^2)[\ln(a+\sqrt{N}) - \ln(a+\sqrt{N-x})] + a(\sqrt{N}-\sqrt{N-x}) - \frac{x}{2}\right]\right\}, \quad \text{(A.128)}$$

which is the result referenced in Chapter 3 as Equation 3.51. Using the definition of the derivative we have:

$$S\{v_t(L)\}_w = \lim_{\Delta_b \to 0} \frac{v(L)_{\Delta_b=\Delta_b} - v(L)_{\Delta_b=0}}{\Delta_b}, \quad \text{(A.129)}$$

where the subscript t has been introduced to indicate that this is for the tapered flexure. Letting x=L in Equation A.128 we have:

$$v_t(L) = \frac{12FN^{\frac{3}{2}}}{Etw_b^3}\left\{\frac{4}{3}(d)^{\frac{3}{2}} + 2L\sqrt{N} - \frac{4}{3}N^{\frac{3}{2}} + 2a\left[(d-a^2)[\ln(a+\sqrt{N}) - \ln(a+\sqrt{d})] + a(\sqrt{N}-\sqrt{d}) - \frac{L}{2}\right]\right\}. \quad \text{(A.130)}$$

Now substituting back in for a we get:

$$v_t(L) = \frac{12FN^{\frac{3}{2}}}{Etw_b^3}\left\{\frac{4}{3}d^{\frac{3}{2}} + 2L\sqrt{N} - \frac{4}{3}N^{\frac{3}{2}} + 6N^{\frac{1}{2}}\frac{\Delta_b}{w_b}\left[\left(d - \left(3N^{\frac{1}{2}}\frac{\Delta_b}{w_b}\right)^2\right)\left[\ln\left(3N^{\frac{1}{2}}\frac{\Delta_b}{w_b} + \sqrt{N}\right) - \ln\left(3N^{\frac{1}{2}}\frac{\Delta_b}{w_b} + \sqrt{d}\right)\right] + \left(3N^{\frac{1}{2}}\frac{\Delta_b}{w_b}\right)\left(\sqrt{N} - \sqrt{d}\right) - \frac{L}{2}\right]\right\} \quad \text{(A.131)}$$

$$v_t(L) = \frac{12FN^{\frac{3}{2}}}{Etw_b^3}\left\{\frac{4}{3}d^{\frac{3}{2}} + 2L\sqrt{N} - \frac{4}{3}N^{\frac{3}{2}} - 3LN^{\frac{1}{2}}\frac{\Delta_b}{w_b} + 6dN^{\frac{1}{2}}\frac{\Delta_b}{w_b}\left[\ln\left(3N^{\frac{1}{2}}\frac{\Delta_b}{w_b} + \sqrt{N}\right) - \ln\left(3N^{\frac{1}{2}}\frac{\Delta_b}{w_b} + \sqrt{d}\right)\right] + 18N\left(\frac{\Delta_b}{w_b}\right)^2\left(\sqrt{N} - \sqrt{d}\right) - 54N^{\frac{3}{2}}\left(\frac{\Delta_b}{w_b}\right)^3\left[\ln\left(3N^{\frac{1}{2}}\frac{\Delta_b}{w_b} + \sqrt{N}\right) - \ln\left(3N^{\frac{1}{2}}\frac{\Delta_b}{w_b} + \sqrt{d}\right)\right]\right\}. \quad \text{(A.132)}$$

Substituting this back into Equation A.129 yields:

$$S\{v_t(L)\}_w = \lim_{\Delta_b \to 0} \frac{\frac{12FN^{\frac{3}{2}}}{Etw_b^3}\left\{\begin{array}{c}\frac{4}{3}d^{\frac{3}{2}} + 2L\sqrt{N} - \frac{4}{3}N^{\frac{3}{2}} - 3LN^{\frac{1}{2}}\frac{\Delta_b}{w_b} + 6dN^{\frac{1}{2}}\frac{\Delta_b}{w_b}\left[\ln\left(3N^{\frac{1}{2}}\frac{\Delta_b}{w_b} + \sqrt{N}\right) - \ln\left(3N^{\frac{1}{2}}\frac{\Delta_b}{w_b} + \sqrt{d}\right)\right] \\ + 18N\left(\frac{\Delta_b}{w_b}\right)^2\left(\sqrt{N} - \sqrt{d}\right) - 54N^{\frac{3}{2}}\left(\frac{\Delta_b}{w_b}\right)^3\left[\ln\left(3N^{\frac{1}{2}}\frac{\Delta_b}{w_b} + \sqrt{N}\right) - \ln\left(3N^{\frac{1}{2}}\frac{\Delta_b}{w_b} + \sqrt{d}\right)\right]\end{array}\right\} - \frac{12FN^{\frac{3}{2}}}{Etw_b^3}\left\{\frac{4}{3}d^{\frac{3}{2}} + 2L\sqrt{N} - \frac{4}{3}N^{\frac{3}{2}}\right\}}{\Delta_b} \quad \text{(A.133)}$$

$$S\{v_t(L)\}_w = \lim_{\Delta_b \to 0} \frac{\frac{12FN^{\frac{3}{2}}}{Etw_b^3}\left\{\begin{array}{c} - 3LN^{\frac{1}{2}}\frac{\Delta_b}{w_b} + 6dN^{\frac{1}{2}}\frac{\Delta_b}{w_b}\left[\ln\left(3N^{\frac{1}{2}}\frac{\Delta_b}{w_b} + \sqrt{N}\right) - \ln\left(3N^{\frac{1}{2}}\frac{\Delta_b}{w_b} + \sqrt{d}\right)\right] \\ + 18N\left(\frac{\Delta_b}{w_b}\right)^2\left(\sqrt{N} - \sqrt{d}\right) - 54N^{\frac{3}{2}}\left(\frac{\Delta_b}{w_b}\right)^3\left[\ln\left(3N^{\frac{1}{2}}\frac{\Delta_b}{w_b} + \sqrt{N}\right) - \ln\left(3N^{\frac{1}{2}}\frac{\Delta_b}{w_b} + \sqrt{d}\right)\right]\end{array}\right\}}{\Delta_b}. \quad \text{(A.134)}$$

Dividing through by the Δ_b in the denominator and evaluating in the limit yields:

$$S\{v_t(L)\}_w = \frac{12FN^{\frac{3}{2}}}{Etw_b^3}\left\{-\frac{3LN^{\frac{1}{2}}}{w_b} + \frac{6dN^{\frac{1}{2}}}{w_b}\left[\ln\sqrt{N} - \ln\sqrt{d}\right]\right\} \quad \text{(A.135)}$$

$$S\{v_t(L)\}_w = \frac{12FN^{\frac{3}{2}}}{Etw_b^3}\left\{-\frac{3LN^{\frac{1}{2}}}{w_b} + \frac{3dN^{\frac{1}{2}}}{w_b}\left[\ln\left(\frac{N}{d}\right)\right]\right\} \tag{A.136}$$

$$S\{v_t(L)\}_w = \frac{36N^2F}{Etw_b^4}\left\{-L + d\ln\left(\frac{N}{d}\right)\right\}, \tag{A.137}$$

which is the equation provided as Equation 3.53 in Chapter 3.

A.5 Straight Flexure Pivot APLM Design Equation Derivations

This section documents the derivation of the design equations for the straight flexure pivot APLM design. This derivation is based on the device layout pictured in Figure 4.8(a) and uses the deflections defined in Figure 4.15. This derivation will also use the variables defined in Section 4.1.1. It is assumed that the designer is provided with the desired spring constant that needs to be applied to a single proof mass. It is also assumed that the designer is either given or will use engineering judgement to select the proportionality constant, P, and the length of the guided flexure, L_G. This derivation focuses on the evaluation of one proof mass, one guided flexure, and one anchor flexure under the assumption of symmetry with the other two elements.

The linear deflection of a straight flexure force-loaded at the tip is given by:

$$d_{F\_Str} = \frac{L^3}{3EI}F = \frac{4L^3}{Etw^3}F, \tag{A.138}$$

where E is the Young's Modulus of the flexure material, and F is the force applied to the tip. The angular deflection at the tip of a straight flexure force-loaded at the tip is given by:

$$\theta_{F\_Str} = \frac{L^2}{2EI} F = \frac{6L^2}{Etw^3} F. \tag{A.139}$$

The linear deflection of a straight flexure moment-loaded at the tip is given by:

$$d_{M\_Str} = \frac{L^2}{2EI} M = \frac{6L^2}{Etw^3} M, \tag{A.140}$$

where M is the moment applied to the tip. The angular deflection at the tip of a straight flexure moment-loaded at the tip is given by:

$$\theta_{M\_Str} = \frac{L}{EI} M = \frac{12L}{Etw^3} M. \tag{A.141}$$

For this derivation, we need to define two additional virtual displacements. These are the projected displacement of the rotation of the tip due to an applied force, $d_{F\theta\_Str}$, and the projected displacement of the rotation of the tip due to an applied moment, $d_{M\theta\_Str}$. These quantities are pictured in Figure A.1 and Figure A.2 for the applied force and moment, respectively. Mathematically these two quantities are given by the following expressions:

$$d_{F\theta\_Str} = L \cdot \theta_{F\_Str} = \frac{L^3}{2EI} F = \frac{6L^3}{Etw^3} F \tag{A.142}$$

$$d_{M\theta\_Str} = L \cdot \theta_{M\_Str} = \frac{L^2}{EI} M = \frac{12L^2}{Etw^3} M. \tag{A.143}$$

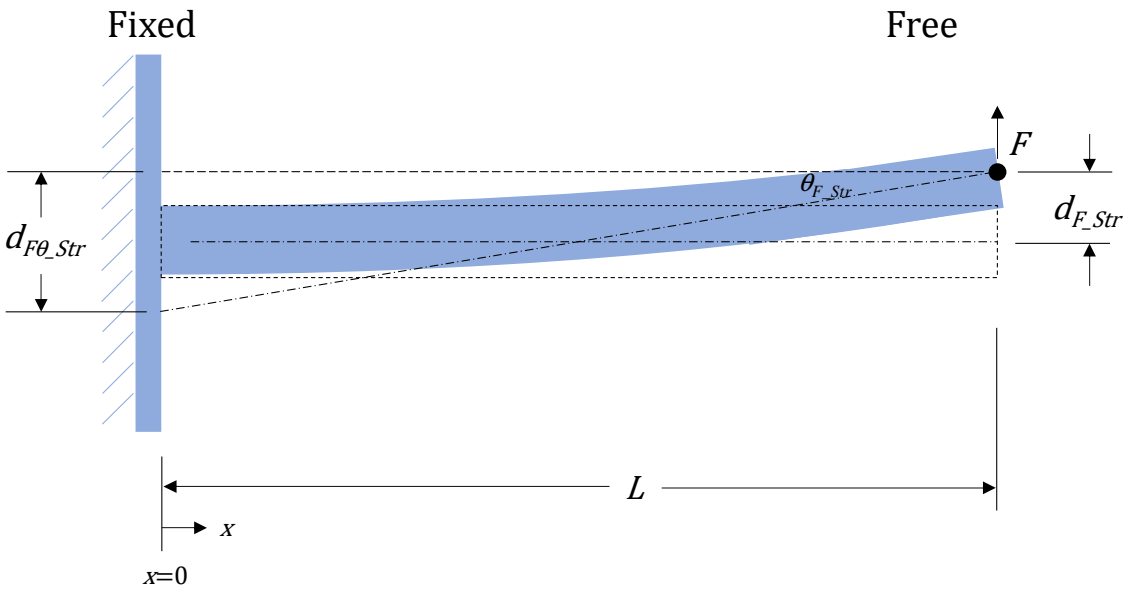

Figure A.1 Diagram of Force Deflections of a Straight Flexure.

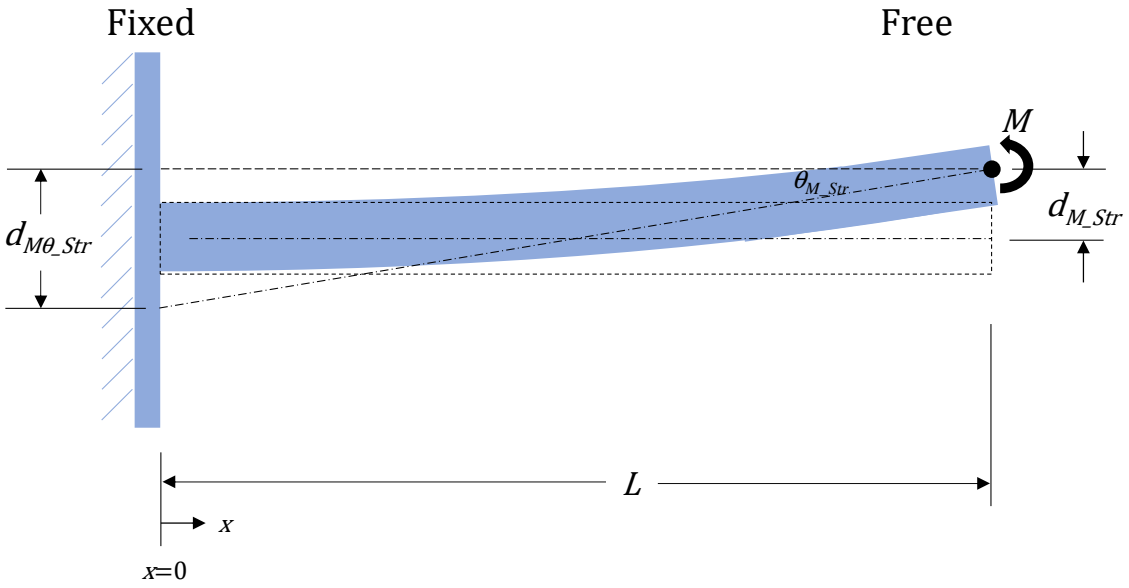

Figure A.2 Diagram of Moment Deflections of a Straight Flexure.

Inspection of Figure 4.15 indicates that both a force and a moment are being applied to the guided flexure at the pivot point. The moment is being applied to the

guided flexure at the pivot point such that it would cause a deflection in the opposite direction of the deflection from the force. Therefore, we write the following equations:

$$d_{TotG} = c = d_{FG_{Str}} - d_{MG_{Str}} = \frac{L_G^3}{3EI_G}F - \frac{L_G^2}{2EI_G}M \tag{A.144}$$

and

$$\theta_{Tot} = \theta_{FG_{Str}} - \theta_{MG_{Str}} = \frac{L_G^2}{2EI_G}F - \frac{L_G}{EI_G}M. \tag{A.145}$$

Applying the virtual displacement defined in Equations A.142 and A.143, we have:

$$d_{\theta TotG_{Str}} \equiv d_{F\theta G_{Str}} - d_{M\theta G_{Str}} = L_G \cdot \theta_{FG_{Str}} - L_G \cdot \theta_{MG_{Str}} \tag{A.146}$$

$$d_{\theta TotG_{Str}} = L_G \cdot \theta_{Tot} = \frac{L_G^3}{2EI_G}F - \frac{L_G^2}{EI_G}M = a. \tag{A.147}$$

Referring back to Equation 4.2, we want to set:

$$d_{\theta TotG_{Str}} = P \cdot d_{TotG}. \tag{A.148}$$

Substituting Equation A.144 and Equation A.147 into Equation A.148 yields:

$$\frac{L_G^3}{2EI_G}F - \frac{L_G^2}{EI_G}M = P \cdot \left[\frac{L_G^3}{3EI_G}F - \frac{L_G^2}{2EI_G}M\right], \tag{A.149}$$

which can be reduced through the following steps:

$$\frac{L_G}{2}F - M = P \cdot \left[\frac{L_G}{3}F - \frac{1}{2}M\right] \tag{A.150}$$

$$\frac{L_G}{2}F - P \cdot \frac{L_G}{3}F = M - P \cdot \frac{1}{2}M \tag{A.151}$$

$$(3L_G - 2L_G P)F = (6 - 3P)M, \tag{A.152}$$

which gives us the moment to force ratio required to satisfy the *P* constraint:

$$\frac{M}{F} = \frac{L_G(3-2P)}{3(2-P)} \tag{A.153}$$

or

$$M = \frac{(3-2P)}{3(2-P)} \cdot (F \cdot L_G) \tag{A.154}$$

and

$$F = \frac{3(2-P)}{(3-2P)} \cdot \frac{M}{L_G}. \tag{A.155}$$

It is important to note here that the total moment applied to the guided flexure is not simply the product of the force, *F*, and the guided flexure length, L_G, as one may be inclined to postulate. While that is certainly one part of the moment applied to the guided flexure, the anchor flexure will also be exerting a moment on the tip of the guided flexure as well and that moment depends entirely on the selection of *P*.

It is also important to note here the bounds on the selection of the proportionality constant, *P*. Here we investigate two cases. The first is the case where the anchor flexures are essentially infinitely stiff and there is no rotation of the pivot point. In this case, θ_{Tot} is zero and therefore *a* will also be zero. Since *a* is zero then *P* also has to be

zero and this sets the lower bound for *P*. With P set to zero, investigation of Equation A.154 indicates that the moment that must be exerted by the pivot point is given by:

$$M = \frac{1}{2} \cdot (F \cdot L_G). \tag{A.156}$$

The second case is where the anchor flexures are infinitely compliant and exert no moment on the guided flexure. In this case, the moment must be equal to zero. Setting Equation A.154 to zero yields the following relation:

$$0 = \frac{(3-2P)}{3(2-P)} \cdot (F \cdot L_G) \tag{A.157}$$

$$0 = (3 - 2P) \tag{A.158}$$

$$P = \frac{3}{2}, \tag{A.159}$$

which sets the upper bound on obtainable values of *P*. Therefore, *P* is limited to the following range:

$$0 \leq P \leq \frac{3}{2}. \tag{A.160}$$

Proceeding with the derivation of the governing equations, we substitute Equation A.154 into Equation A.144 yielding:

$$d_{TotG} = \frac{L_G^3}{3EI_G} F - \frac{L_G^2}{2EI_G} \left[\frac{(3-2P)}{3(2-P)} \cdot (F \cdot L_G) \right], \tag{A.161}$$

which can be simplified through the following steps:

$$d_{TotG} = \left[\frac{1}{3} - \frac{3-2P}{6(2-P)}\right]\frac{L_G^3}{EI_G}F \tag{A.162}$$

$$d_{TotG} = \left[\frac{2(2-P)-3+2P}{6(2-P)}\right]\frac{L_G^3}{EI_G}F \tag{A.163}$$

$$d_{TotG} = \left[\frac{4-2P-3+2P}{6(2-P)}\right]\frac{L_G^3}{EI_G}F \tag{A.164}$$

$$d_{TotG} = \left[\frac{1}{6(2-P)}\right]\frac{L_G^3}{EI_G}F. \tag{A.165}$$

Therefore, the total spring constant of the straight flexure pivot APLM is given by:

$$k_{SP_{Str}} = \frac{F}{d_{TotG}} = \frac{6(2-P)EI_G}{L_G^3}. \tag{A.166}$$

Substituting in:

$$I_G = \frac{tw_G^3}{12} \tag{A.167}$$

yields:

$$k_{SP_{Str}} = \frac{(2-P)Etw_G^3}{2L_G^3}. \tag{A.168}$$

Solving this equation for the width of the guided flexure, w_G, yields one of the key equations used in the straight flexure pivot APLM design procedure:

$$w_G = L_G\left[\frac{2}{2-P}\frac{k_{SP_{Str}}}{Et}\right]^{\frac{1}{3}}. \tag{A.169}$$

With the guided flexure designed, we turn our attention to the design of the anchor flexure, but first we must derive the spring constant that relates the angular deflection of the guided flexure to the applied moment. Substituting Equation A.155 into Equation A.145 gives:

$$\theta_{Tot} = \frac{L_G^2}{2EI_G}\frac{3(2-P)}{(3-2P)} \cdot \frac{M}{L_G} - \frac{L_G}{EI_G}M, \tag{A.170}$$

which can be simplified through the following procedure:

$$\theta_{Tot} = \left[\frac{3}{2}\frac{(2-P)}{(3-2P)} - 1\right]\frac{L_G}{EI_G}M \tag{A.171}$$

$$\theta_{Tot} = \left[\frac{6-3P-6+4P}{2(3-2P)}\right]\frac{L_G}{EI_G}M \tag{A.172}$$

$$\theta_{Tot} = \left[\frac{P}{2(3-2P)}\right]\frac{L_G}{EI_G}M. \tag{A.173}$$

This can be further rearranged to provide the rotational spring constant due to the moment as follows:

$$k_{\theta TotMG\_Str} = \frac{M}{\theta_{Tot}} = \left[\frac{2(3-2P)}{P}\right]\frac{EI_G}{L_G}. \tag{A.174}$$

Now we turn our attention to the anchor flexures to find an expression for the equivalent spring constant. Since there is no net displacement of the anchor flexures at the pivot point, we have:

$$d_{TotA} = 0 = d_{MA_{Str}} - d_{FA_{Str}} \tag{A.175}$$

$$d_{FA_{Str}} = d_{MA_{Str}}. \tag{A.176}$$

Substituting Equation A.138 and Equation A.140 into Equation A.176 yields:

$$\frac{F_A L_A^3}{3EI_A} = \frac{ML_A^2}{2EI_A}, \tag{A.177}$$

which readily simplifies to:

$$F_A = \frac{3}{2}\frac{M}{L_A}. \tag{A.178}$$

The rotational deflection must be the same as that of the guided flexure. So:

$$\theta_{Tot} = \theta_{MA_{Str}} - \theta_{FA_{Str}}. \tag{A.179}$$

Substituting Equation A.139 and Equation A.141 into Equation A.179 yields:

$$\theta_{Tot} = \frac{L_A}{EI_A}M - \frac{L_A^2}{2EI_A}F_A. \tag{A.180}$$

Substituting Equation A.178 into Equation A.180 yields:

$$\theta_{Tot} = \frac{L_A}{EI_A}M - \frac{L_A^2}{2EI_A}\left[\frac{3}{2}\frac{M}{L_A}\right], \tag{A.181}$$

which simplifies as follows:

$$\theta_{Tot} = \left[\frac{L_A}{EI_A} - \frac{3L_A}{4EI_A}\right]M \tag{A.182}$$

$$\theta_{Tot} = \frac{L_A}{4EI_A}M. \tag{A.183}$$

This provides the relationship to find the desired rotational spring constant for a moment applied to the anchor flexure:

$$k_{\theta TotMA\_Str} = \frac{M}{\theta_{Tot}} = \frac{4EI_A}{L_A}. \tag{A.184}$$

For the APLM system to be in equilibrium, these two spring constants in Equation A.174 and Equation A.184 have to be equal to one another. Setting these two spring constants equal to one another yields the following:

$$k_{\theta TotMA\_Str} = \frac{4EI_A}{L_A} = k_{\theta TotMG\_Str} = \left[\frac{2(3-2P)}{P}\right]\frac{EI_G}{L_G}. \tag{A.185}$$

We will now assume that we want the peak stress of each flexure to be the same at the pivot point. Since the moments are the same at the pivot point in both flexures, this can easily be accomplished by setting the widths of the two flexures equal to one another, or:

$$w_A = w_G. \tag{A.186}$$

Since the thicknesses of the two flexures are the same, this also sets their moments of inertia to be the same, or:

$$I_A = I_G. \tag{A.187}$$

Substituting Equation A.187 into Equation A.185 yields:

$$\frac{4EI_A}{L_A} = \left[\frac{2(3-2P)}{P}\right]\frac{EI_A}{L_G}, \tag{A.188}$$

which simplifies to:

$$\frac{4}{L_A} = \left[\frac{2(3-2P)}{P}\right]\frac{1}{L_G}. \tag{A.189}$$

This provides us with the final design equation for the straight flexure pivot APLM which is to solve for the length of the anchor flexure:

$$L_A = \left[\frac{4P}{2(3-2P)}\right]L_G = \frac{2P}{(3-2P)}L_G. \tag{A.190}$$

One final note is that the four-flexure pivot APLMs pictured in Figure 4.8 and Figure 4.15 have a small square block at the center of the pivot point which was neglected in this derivation. There are three factors that enable this to be neglected. The first is that the moment in this region due to the force applied at the pivot point should be small due to the close proximity (short lever arm) to the force which results in negligible additional bending of the flexure. The second is that the moment applied from the anchor flexure is expected to be small to allow for strong coupling between the two masses, again resulting in negligible additional bending of the flexure. Finally, the size of the block is small compared to the overall lengths of the guided and anchor flexures, resulting in negligible additional deflection.

A.6 Tapered Flexure Pivot APLM Design Equation Derivations

This section documents the derivation of the design equations for the tapered flexure pivot APLM design. This derivation is based on the device layout pictured in Figure 4.8(b) and uses the deflections defined in Figure 4.16 as well as tapered flexure equivalents to Figure A.1 and Figure A.2. This derivation will also use the variables defined in Section 4.1.2. It is assumed that the designer is provided with the desired

spring constant that needs to be applied to the proof mass. It is also assumed that the designer is either given or will use engineering judgement to select the proportionality constant, P, and the total length of the second element of the guided flexure, N_{2G}. This derivation focuses on the evaluation of one proof mass, one guided flexure, and one anchor flexure under the assumption of symmetry with the other two elements. For this derivation, it is assumed that the length of the block at the center of the pivot point is negligible.

From Table 3.1, the linear deflection at the center of the hammerhead of a tapered flexure force-loaded at the center of the hammerhead is given by:

$$d_{F\_Tap} = \frac{8}{E \cdot t \cdot w_b^3}\left\{(L+d)^3 - (L+d)^{\frac{3}{2}}(d)^{\frac{3}{2}}\right\}F, \tag{A.191}$$

where E is the Young's Modulus of the flexure material, and F is the force applied to the center of the hammerhead. The angular deflection at the center of the hammerhead of a tapered flexure force-loaded at the center of the hammerhead is given by:

$$\theta_{F\_Tap} = \frac{24 \cdot (L+d)^{\frac{3}{2}}}{E \cdot t \cdot w_b^3}\left\{(L+d)^{\frac{1}{2}} - (d)^{\frac{1}{2}}\right\}F. \tag{A.192}$$

It is now necessary to derive the linear deflection at the center of the hammerhead of a tapered flexure moment-loaded at the center of the hammerhead. Similar to the force loaded system previously shown in Figure 3.4, Figure A.3 shows a diagram of the mechanical system under an applied moment, M.

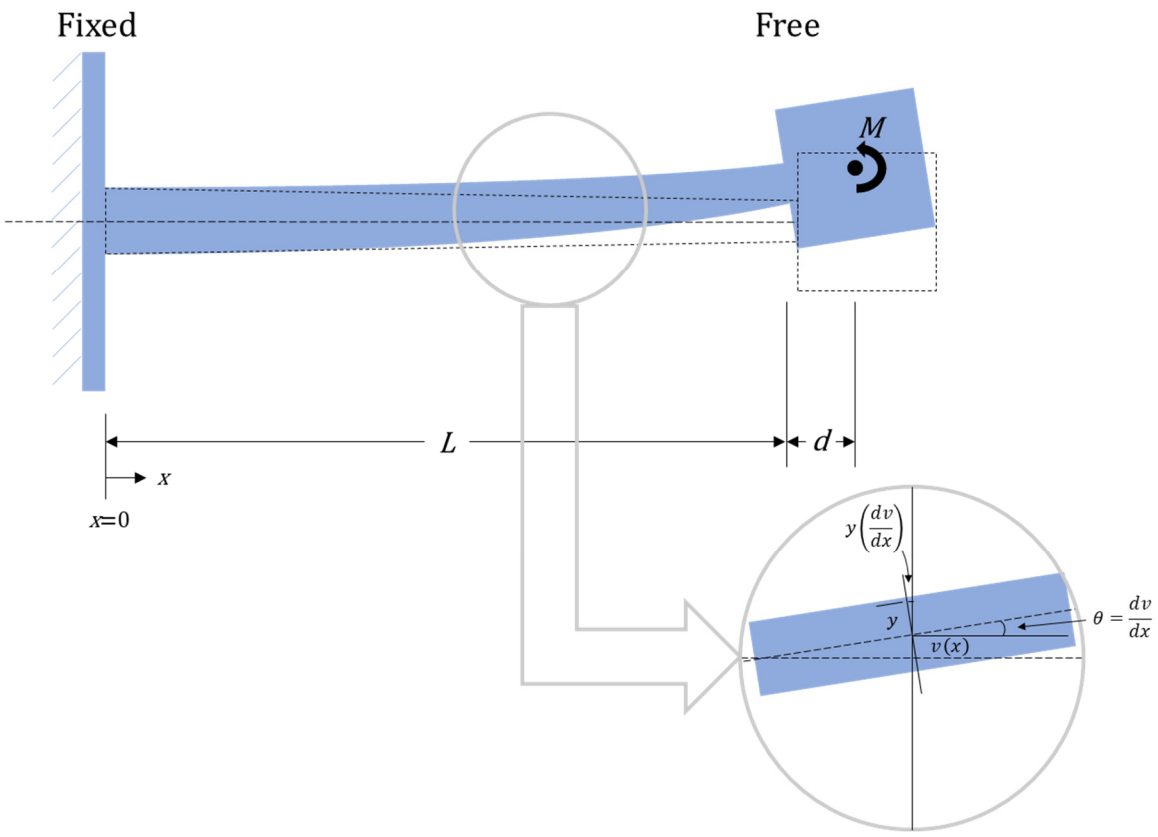

Figure A.3 Mechanical Diagram of Tapered Flexure for Moment Deflection Derivation.

Applying the Euler-Bernoulli Beam equation presented in Equation 3.11 combined with Equation 3.18 which describes the moment of inertia of the tapered beam, we begin our derivation with the following expression:

$$M = E \cdot \frac{t \cdot w_b^3 \left(\frac{N-x}{N}\right)^{\frac{3}{2}}}{12} \cdot \frac{d^2 v(x)}{dx^2}. \tag{A.193}$$

Separating variables we have:

$$\frac{M}{E \cdot \frac{t \cdot w_b^3 \left(\frac{N-x}{N}\right)^{\frac{3}{2}}}{12}} dx^2 = d^2 v. \tag{A.194}$$

Double integrating gives us:

$$v_{M_T}(x) = \frac{12 \cdot M}{E \cdot t \cdot w_b^3} \iint_0^x \left(\frac{N-x}{N}\right)^{-\frac{3}{2}} dxdx, \tag{A.195}$$

where $v_{M_T}(x)$ is the deflection of the tapered flexure at location *x* due to an applied moment. Solving the first integral leads to:

$$v_{M_T}(x) = \frac{12 \cdot M \cdot N^{\frac{3}{2}}}{E \cdot t \cdot w_b^3} \int_0^x \left[\frac{(N-x)^{-\frac{1}{2}}}{-\frac{1}{2}}(-1) + C\right] dx \tag{A.196}$$

$$v_{M_T}(x) = \frac{24 \cdot M \cdot N^{\frac{3}{2}}}{E \cdot t \cdot w_b^3} \int_0^x \left[(N-x)^{-\frac{1}{2}} + C\right] dx. \tag{A.197}$$

We find the constant of integration by noting that this first integrand represents the angular deflection of the flexure which we assume to be zero at *x=0*. So, we let:

$$(N-0)^{-\frac{1}{2}} + C = 0 \tag{A.198}$$

$$C = -N^{-\frac{1}{2}}. \tag{A.199}$$

Substituting this back into Equation A.197 we have:

$$v_{M_T}(x) = \frac{24 \cdot M \cdot N^{\frac{3}{2}}}{E \cdot t \cdot w_b^3} \int_0^x \left[(N-x)^{-\frac{1}{2}} - N^{-\frac{1}{2}}\right] dx. \tag{A.200}$$

Solving the second integral yields:

$$v_{M_T}(x) = \frac{24 \cdot M \cdot N^{\frac{3}{2}}}{E \cdot t \cdot w_b^3} \left[\frac{(N-x)^{\frac{1}{2}}}{\frac{1}{2}}(-1) - xN^{-\frac{1}{2}} + C_2\right]\Big|_0^x \tag{A.201}$$

$$v_{M_T}(x) = \frac{24 \cdot M \cdot N^{\frac{3}{2}}}{E \cdot t \cdot w_b^3}\left[-2 \cdot (N-x)^{\frac{1}{2}} - x \cdot N^{-\frac{1}{2}} + C_2\right]\Big|_0^x \tag{A.202}$$

$$v_{M_T}(x) = \frac{24 \cdot M \cdot N^{\frac{3}{2}}}{E \cdot t \cdot w_b^3}\left[-2 \cdot (N-x)^{\frac{1}{2}} - x \cdot N^{-\frac{1}{2}} + 2 \cdot N^{\frac{1}{2}}\right]. \tag{A.203}$$

which is valid over the range of $0 \leq x \leq L$. Taking the first derivative of this expression to find the angular deflection of the tapered flexure due to an applied moment, we have:

$$\theta_{M_T}(x) = \frac{d}{dx}\left\{\frac{24 \cdot M \cdot N^{\frac{3}{2}}}{E \cdot t \cdot w_b^3}\left[-2 \cdot (N-x)^{\frac{1}{2}} - x \cdot N^{-\frac{1}{2}} + 2 \cdot N^{\frac{1}{2}}\right]\right\} \tag{A.204}$$

$$\theta_{M_T}(x) = \frac{24 \cdot M \cdot N^{\frac{3}{2}}}{E \cdot t \cdot w_b^3}\left[\left(\frac{1}{2}\right) \cdot (-2) \cdot (N-x)^{-\frac{1}{2}}(-1) - N^{-\frac{1}{2}}\right] \tag{A.205}$$

$$\theta_{M_T}(x) = \frac{24 \cdot M \cdot N^{\frac{3}{2}}}{E \cdot t \cdot w_b^3}\left[(N-x)^{-\frac{1}{2}} - N^{-\frac{1}{2}}\right], \tag{A.206}$$

which is also valid over the range of $0 \leq x \leq L$. Here we assume that the hammerhead feature is essentially infinitely stiff and we extend Equation A.206 through the hammerhead by assuming that θ takes on the value at the end of the flexure where $x = L$:

$$\theta_{M_T}(x) = \frac{24 \cdot M \cdot N^{\frac{3}{2}}}{E \cdot t \cdot w_b^3}\left[(N-L)^{-\frac{1}{2}} - N^{-\frac{1}{2}}\right] \qquad L \leq x \leq L + 2d \tag{A.207}$$

$$\theta_{M_T}(x) = \frac{24 \cdot M \cdot N^{\frac{3}{2}}}{E \cdot t \cdot w_b^3}\left[d^{-\frac{1}{2}} - N^{-\frac{1}{2}}\right] \qquad L \leq x \leq L + 2d \tag{A.208}$$

$$\theta_{M_T}(x) = \theta_{M_T HHC} = \frac{24 \cdot M}{E \cdot t \cdot w_b^3}\left[N^{\frac{3}{2}} d^{-\frac{1}{2}} - N\right] \qquad L \leq x \leq L + 2d. \tag{A.209}$$

Now, we extend the range of the deflection equation given in Equation A.203 through the hammerhead by linear extension of the rotation of the hammerhead given in Equation A.209 by:

$$v_{M_T}(x) = v_{M_T}(L) + (x - L) \cdot \theta_{M_T}(L) \qquad L \le x \le L + 2d \qquad \text{(A.210)}$$

$$v_{M_T}(x) = \frac{24 \cdot M \cdot N^{\frac{3}{2}}}{E \cdot t \cdot w_b^3} \left\{ \left[-2 \cdot (N - L)^{\frac{1}{2}} - L \cdot N^{-\frac{1}{2}} + 2 \cdot N^{\frac{1}{2}} \right] + (x - L) \left[d^{-\frac{1}{2}} - N^{-\frac{1}{2}} \right] \right\} \quad \text{(A.211)}$$

$$v_{M_T}(x) = \frac{24 \cdot M \cdot N^{\frac{3}{2}}}{E \cdot t \cdot w_b^3} \left\{ \left[-2 \cdot d^{\frac{1}{2}} - L \cdot N^{-\frac{1}{2}} + 2 \cdot N^{\frac{1}{2}} \right] + (x - L) \left[d^{-\frac{1}{2}} - N^{-\frac{1}{2}} \right] \right\}, \qquad \text{(A.212)}$$

which is valid over the range of $L \le x \le L + 2d$. Evaluating this expression at $x=N$ to find the deflection at the center of the hammerhead we have:

$$v_{M_T}(N) = \frac{24 \cdot M \cdot N^{\frac{3}{2}}}{E \cdot t \cdot w_b^3} \left\{ \left[-2 \cdot d^{\frac{1}{2}} - L \cdot N^{-\frac{1}{2}} + 2 \cdot N^{\frac{1}{2}} \right] + (N - L) \left[d^{-\frac{1}{2}} - N^{-\frac{1}{2}} \right] \right\}. \qquad \text{(A.213)}$$

Using $L = N - d$ and $N - L = d$ we get:

$$v_{M_T HHC} = \frac{24 \cdot M \cdot N^{\frac{3}{2}}}{E \cdot t \cdot w_b^3} \left\{ \left[-2 \cdot d^{\frac{1}{2}} - (N - d) \cdot N^{-\frac{1}{2}} + 2 \cdot N^{\frac{1}{2}} \right] + d \left[d^{-\frac{1}{2}} - N^{-\frac{1}{2}} \right] \right\} \qquad \text{(A.214)}$$

$$v_{M_T HHC} = \frac{24 \cdot M \cdot N^{\frac{3}{2}}}{E \cdot t \cdot w_b^3} \left\{ -2 \cdot d^{\frac{1}{2}} - N^{\frac{1}{2}} + dN^{-\frac{1}{2}} + 2 \cdot N^{\frac{1}{2}} + d^{\frac{1}{2}} - dN^{-\frac{1}{2}} \right\} \qquad \text{(A.215)}$$

$$v_{M_T HHC} = \frac{24 \cdot M \cdot N^{\frac{3}{2}}}{E \cdot t \cdot w_b^3} \left\{ N^{\frac{1}{2}} - d^{\frac{1}{2}} \right\} \qquad \text{(A.216)}$$

$$v_{M_T HHC} = \frac{24 \cdot M}{E \cdot t \cdot w_b^3}\left\{N^2 - N^{\frac{3}{2}} d^{\frac{1}{2}}\right\}. \tag{A.217}$$

With the basic equations derived, we turn our attention back to the composite guided flexure in Figure 4.16. We see by inspection that the pivot point is applying both a force, F_G, and a moment, M_G, to the end of the composite guided flexure and that the moment is applied in the direction to offset the deflection from the applied force. Since we will place the block in the guided flexure in the location of zero net moment, we can write by inspection that:

$$M_G = F_G N_{1G}. \tag{A.218}$$

Evaluating the deflections at the center of the hammerhead, we express the total deflection of the composite guided flexure as a function of the deflections of each of the flexures in the composite guided flexure by writing:

$$c = v_{Tot} = v_{FN2G} + v_{FN1G} + \theta_{Tot} \cdot N_{1G}. \tag{A.219}$$

Similar to what was done with the straight flexure pivot APLM, we define a proportionality constant, P, that relates how much of the total deflection is related to the rotation of the pivot point as:

$$a = P \cdot c \tag{A.220}$$

$$P = \frac{a}{c} = \frac{(N_{1G} + N_{2G}) \cdot \theta_{Tot}}{v_{Tot}}. \tag{A.221}$$

Due to the natural relationship between the linear and angular deflection spring constants of tapered flexures, it will be shown that the value of P is limited between 0

(zero) when the anchor flexures are infinitely stiff, and 3 when the anchor flexures have infinite compliance. Lower values of P reduce the coupling across the APLM that occurs through the angular deflection of the pivot point. While higher values of P increase this coupling, they result in long thin anchor flexures that may be difficult to realize in practice.

To establish the bounds on the selection of the proportionality constant, P, we investigate two cases. The first is the case where the anchor flexures are essentially infinitely stiff and there is no rotation of the pivot point. In this case, θ_{Tot} is zero and therefore a will also be zero. Since a is zero then P also has to be zero and this sets the lower bound for P. The second case is where the anchor flexures are infinitely compliant and exert no moment on the guided flexure. In this case, the moment at the pivot point must be equal to zero. Setting Equation A.218 to zero yields the following relation:

$$M_G = F_G N_{1G} = 0 \qquad P = 0. \qquad \text{(A.222)}$$

Since the force, F_G, is non-zero, this implies that the length of the first element of the guided flexure, N_{1G}, must be zero:

$$N_{1G} = 0 \qquad P = 0. \qquad \text{(A.223)}$$

which means that the guided flexure becomes just a single, tapered flexure, N_{2G}. This sets the upper bound on obtainable values of P as the ratio of the angular and linear deflections of a tapered flexure multiplied by the length of the flexure. Therefore, P is limited to the following maximum range:

$$P_{max} = \frac{\theta_{HHC} \cdot N}{v_{HHC}} = \frac{\frac{24 \cdot F \cdot (N)^{\frac{3}{2}}}{E \cdot t \cdot w_b^3}\left\{(N)^{\frac{1}{2}} - (d)^{\frac{1}{2}}\right\} \cdot N}{\frac{8 \cdot F}{E \cdot t \cdot w_b^3}\left\{(N)^3 - (N)^{\frac{3}{2}}(d)^{\frac{3}{2}}\right\}} \tag{A.224}$$

$$P_{max} = \frac{3 \cdot N^{\frac{5}{2}} \cdot \left\{(N)^{\frac{1}{2}} - (d)^{\frac{1}{2}}\right\}}{(N)^3 - (N)^{\frac{3}{2}}(d)^{\frac{3}{2}}} . \tag{A.225}$$

Here we see that the maximum value of *P* is dependent on the size of the hammerhead, *d*, with *P* reaching its absolute maximum when there is no hammerhead or *d=0*. So, letting *d=0* we have:

$$P_{max} = \frac{3 \cdot N^{\frac{5}{2}} \cdot \left\{(N)^{\frac{1}{2}}\right\}}{(N)^3} = 3 . \tag{A.226}$$

So, for the tapered flexure pivot APLM design, the maximum value of *P* is 3 and the final range of *P* is:

$$0 \leq P \leq 3 . \tag{A.227}$$

Comparison of this with that of the straight flexure indicates that an equivalent tapered flexure with no hammerhead has twice as much angular rotation as that of the straight flexure. As an aside note, analysis of the above relationships reveals that the *L/d* ratio required to make the tapered flexure have the same rotational spring constant as the straight flexure is 1.618034, also known as The Golden Ratio.

Inspection of Figure 4.16 indicates that the total angular deflection of the pivot point is:

$$\theta_{Tot} = \theta_{FN2G} - \theta_{FN1G} . \tag{A.228}$$

Combining Equation A.219 and Equation A.221, we have:

$$P = \frac{(N_{1G}+N_{2G})\cdot\theta_{Tot}}{v_{FN2G}+v_{FN1G}+\theta_{Tot}\cdot N_1}\,. \tag{A.229}$$

Now substituting in Equation A.228 yields:

$$P = \frac{(\theta_{FN2G}-\theta_{FN1G})\cdot(N_{1G}+N_{2G})}{v_{FN2G}+v_{FN1G}+(\theta_{FN2G}-\theta_{FN1G})\cdot N_1} \tag{A.230}$$

$$(\theta_{FN2G}-\theta_{FN1G})\cdot(N_{1G}+N_{2G}) = P\cdot[v_{FN2G}+v_{FN1G}+(\theta_{FN2G}-\theta_{FN1G})\cdot N_1]\,. \tag{A.231}$$

Before proceeding, we note that we would like to set the stresses in each element of the guided flexure to be the same. To do this, we note that the force, F, acting on N_{1G} and N_{2G} is the same. Referring back to Equation 3.8 we have:

$$T_{maxN1G} = \frac{6\cdot F\cdot N_{1G}}{t\cdot {w_{b1}}^2} \tag{A.232}$$

and

$$T_{maxN2G} = \frac{6\cdot F\cdot N_{2G}}{t\cdot {w_{b2}}^2}\,. \tag{A.233}$$

Setting these equal yields:

$$T_{maxN1G} = T_{maxN2G} \tag{A.234}$$

$$\frac{6\cdot F\cdot N_{1G}}{t\cdot {w_{b1}}^2} = \frac{6\cdot F\cdot N_{2G}}{t\cdot {w_{b2}}^2} \tag{A.235}$$

$$\frac{N_{1G}}{{w_{b1}}^2} = \frac{N_{2G}}{{w_{b2}}^2}\,. \tag{A.236}$$

This enables us to express w_{b2} in terms of w_{b1} as:

$$w_{b2} = w_{b1}\sqrt{\frac{N_{2G}}{N_{1G}}}\,. \tag{A.237}$$

Now finding the linear and angular deflection equations from Table 3.1, we have:

$$v_{FN1G} = \frac{8 \cdot F}{E \cdot t \cdot w_{b1}^3}\left\{N_{1G}^3 - N_{1G}^{\frac{3}{2}} \cdot d^{\frac{3}{2}}\right\} \tag{A.238}$$

$$\theta_{FN1G} = \frac{24 \cdot F \cdot N_{1G}^{\frac{3}{2}}}{E \cdot t \cdot w_{b1}^3}\left\{N_{1G}^{\frac{1}{2}} - d^{\frac{1}{2}}\right\} \tag{A.239}$$

$$v_{FN2G} = \frac{8 \cdot F}{E \cdot t \cdot w_{b2}^3}\left\{N_{2G}^3 - N_{2G}^{\frac{3}{2}} \cdot d^{\frac{3}{2}}\right\} \tag{A.240}$$

$$\theta_{FN2G} = \frac{24 \cdot F \cdot N_{2G}^{\frac{3}{2}}}{E \cdot t \cdot w_{b2}^3}\left\{N_{2G}^{\frac{1}{2}} - d^{\frac{1}{2}}\right\}. \tag{A.241}$$

It will be beneficial to express this set of equations in terms of just one of the flexure widths. So, here we substitute Equation A.237 into Equation A.240:

$$v_{FN2G} = \frac{8 \cdot F \cdot N_{1G}^{\frac{3}{2}}}{E \cdot t \cdot w_{b1}^3 \cdot N_{2G}^{\frac{3}{2}}}\left\{N_{2G}^3 - N_{2G}^{\frac{3}{2}} \cdot d^{\frac{3}{2}}\right\} \tag{A.242}$$

$$v_{FN2G} = \frac{8 \cdot F}{E \cdot t \cdot w_{b1}^3}\left\{N_{1G}^{\frac{3}{2}} \cdot N_{2G}^{\frac{3}{2}} - N_{1G}^{\frac{3}{2}} \cdot d^{\frac{3}{2}}\right\}. \tag{A.243}$$

We also substitute Equation A.237 into Equation A.241:

$$\theta_{FN2G} = \frac{24 \cdot F \cdot N_{2G}^{\frac{3}{2}} \cdot N_{1G}^{\frac{3}{2}}}{E \cdot t \cdot w_{b1}^3 \cdot N_{2G}^{\frac{3}{2}}} \left\{ N_{2G}^{\frac{1}{2}} - d^{\frac{1}{2}} \right\} \tag{A.244}$$

$$\theta_{FN2G} = \frac{24 \cdot F}{E \cdot t \cdot w_{b1}^3} \left\{ N_{1G}^{\frac{3}{2}} \cdot N_{2G}^{\frac{1}{2}} - N_{1G}^{\frac{3}{2}} \cdot d^{\frac{1}{2}} \right\}. \tag{A.245}$$

Substituting Equations A.238, A.239, A.243 and A.245 into Equation A.231 yields:

$$\frac{24 \cdot F}{E \cdot t \cdot w_{b1}^3} \left(\left\{ N_{1G}^{\frac{3}{2}} \cdot N_{2G}^{\frac{1}{2}} - N_{1G}^{\frac{3}{2}} \cdot d^{\frac{1}{2}} \right\} - \left\{ N_{1G}^2 - N_{1G}^{\frac{3}{2}} \cdot d^{\frac{1}{2}} \right\} \right) \cdot (N_{1G} + N_{2G}) = P \cdot \left[\frac{8 \cdot F}{E \cdot t \cdot w_{b1}^3} \left\{ N_{1G}^{\frac{3}{2}} \cdot N_{2G}^{\frac{3}{2}} - N_{1G}^{\frac{3}{2}} \cdot d^{\frac{3}{2}} \right\} + \frac{8 \cdot F}{E \cdot t \cdot w_{b1}^3} \left\{ N_{1G}^3 - N_{1G}^{\frac{3}{2}} \cdot d^{\frac{3}{2}} \right\} + \frac{24 \cdot F}{E \cdot t \cdot w_{b1}^3} \left(\left\{ N_{1G}^{\frac{3}{2}} \cdot N_{2G}^{\frac{1}{2}} - N_{1G}^{\frac{3}{2}} \cdot d^{\frac{1}{2}} \right\} - \left\{ N_{1G}^2 - N_{1G}^{\frac{3}{2}} \cdot d^{\frac{1}{2}} \right\} \right) \cdot N_1 \right]. \tag{A.246}$$

Noting that there is a factor of $\frac{8 \cdot F}{E \cdot t \cdot w_{b1}^3}$ in every term, we divide both sides by this factor:

$$3 \left(\left\{ N_{1G}^{\frac{3}{2}} \cdot N_{2G}^{\frac{1}{2}} - N_{1G}^{\frac{3}{2}} \cdot d^{\frac{1}{2}} \right\} - \left\{ N_{1G}^2 - N_{1G}^{\frac{3}{2}} \cdot d^{\frac{1}{2}} \right\} \right) \cdot (N_{1G} + N_{2G}) = P \cdot \left[\left\{ N_{1G}^{\frac{3}{2}} \cdot N_{2G}^{\frac{3}{2}} - N_{1G}^{\frac{3}{2}} \cdot d^{\frac{3}{2}} \right\} + \left\{ N_{1G}^3 - N_{1G}^{\frac{3}{2}} \cdot d^{\frac{3}{2}} \right\} + 3 \left(\left\{ N_{1G}^{\frac{3}{2}} \cdot N_{2G}^{\frac{1}{2}} - N_{1G}^{\frac{3}{2}} \cdot d^{\frac{1}{2}} \right\} - \left\{ N_{1G}^2 - N_{1G}^{\frac{3}{2}} \cdot d^{\frac{1}{2}} \right\} \right) \cdot N_1 \right] \tag{A.247}$$

$$3 \left(N_{1G}^{\frac{3}{2}} \cdot N_{2G}^{\frac{1}{2}} - N_{1G}^2 \right) (N_{1G} + N_{2G}) = P \cdot \left[N_{1G}^{\frac{3}{2}} \cdot N_{2G}^{\frac{3}{2}} - 2 \cdot N_{1G}^{\frac{3}{2}} \cdot d^{\frac{3}{2}} + N_{1G}^3 + 3 \cdot N_1 \cdot \left(N_{1G}^{\frac{3}{2}} \cdot N_{2G}^{\frac{1}{2}} - N_{1G}^2 \right) \right]. \tag{A.248}$$

Dividing all terms by $N_{1G}^{\frac{3}{2}}$ we get:

$$3\left(N_{2G}^{\frac{1}{2}}-N_{1G}^{\frac{1}{2}}\right)(N_{1G}+N_{2G})=P\cdot\left[N_{2G}^{\frac{3}{2}}-2\cdot d^{\frac{3}{2}}+N_{1G}^{\frac{3}{2}}+3\cdot N_1\cdot\left(N_{2G}^{\frac{1}{2}}-N_{1G}^{\frac{1}{2}}\right)\right] \tag{A.249}$$

$$3N_{1G}N_{2G}^{\frac{1}{2}}-3N_{1G}^{\frac{3}{2}}+3N_{2G}^{\frac{3}{2}}-3N_{1G}^{\frac{1}{2}}N_{2G}=PN_{2G}^{\frac{3}{2}}-2Pd^{\frac{3}{2}}-2PN_{1G}^{\frac{3}{2}}+3PN_1N_{2G}^{\frac{1}{2}} \tag{A.250}$$

$$(2P-3)N_{1G}^{\frac{3}{2}}+(3-3P)N_{1G}N_{2G}^{\frac{1}{2}}-3N_{1G}^{\frac{1}{2}}N_{2G}+(3-P)N_{2G}^{\frac{3}{2}}+2Pd^{\frac{3}{2}}=0\,. \tag{A.251}$$

Here we will assume that the designer will either choose or be given N_{2G} and P. So, we must solve the nonlinear equation in Equation A.251 for N_{1G}. We will accomplish this using Newton's Method. So, we define the function $f(N_{1G})$, which we want to go to zero, to be:

$$f(N_{1G})=(2P-3)N_{1G}^{\frac{3}{2}}+(3-3P)N_{1G}N_{2G}^{\frac{1}{2}}-3N_{1G}^{\frac{1}{2}}N_{2G}+(3-P)N_{2G}^{\frac{3}{2}}+2Pd^{\frac{3}{2}}\,. \tag{A.252}$$

Finding the derivative of $f(N_{1G})$ we have:

$$f'(N_{1G})=\frac{3(2P-3)}{2}N_{1G}^{\frac{1}{2}}+(3-3P)N_{2G}^{\frac{1}{2}}-\frac{3}{2}N_{1G}^{-\frac{1}{2}}N_{2G}\,. \tag{A.253}$$

The value of N_{1G} will be found by first taking a guess and iterating as follows until the value has adequately converged:

$$N_{1G_{New}}=N_{1G_{Old}}-\frac{f\left(N_{1G_{Old}}\right)}{f'\left(N_{1G_{Old}}\right)}. \tag{A.254}$$

Now that we have N_{1G} and N_{2G}, we turn our attention back to Equation A.219 to find the overall linear spring constant, $k_{Fv_{Tot}}$, for the tapered flexure pivot APLM using:

$$v_{Tot}=v_{FN2G}+v_{FN1G}+\theta_{Tot}\cdot N_1=v_{FN2G}+v_{FN1G}+(\theta_{FN2G}-\theta_{FN1G})\cdot N_1\,. \tag{A.255}$$

Substituting Equations A.238, A.239, A.243 and A.245 into this expression we have:

$$v_{Tot} = \frac{8 \cdot F}{E \cdot t \cdot w_{b1}^3}\left\{N_{1G}^{\frac{3}{2}} \cdot N_{2G}^{\frac{3}{2}} - N_{1G}^{\frac{3}{2}} \cdot d^{\frac{3}{2}}\right\} + \frac{8 \cdot F}{E \cdot t \cdot w_{b1}^3}\left\{N_{1G}^3 - N_{1G}^{\frac{3}{2}} \cdot d^{\frac{3}{2}}\right\} + \left(\frac{24 \cdot F}{E \cdot t \cdot w_{b1}^3}\left\{N_{1G}^{\frac{3}{2}} \cdot N_{2G}^{\frac{1}{2}} - N_{1G}^{\frac{3}{2}} \cdot d^{\frac{1}{2}}\right\} - \frac{24 \cdot F \cdot N_{1G}^{\frac{3}{2}}}{E \cdot t \cdot w_{b1}^3}\left\{N_{1G}^{\frac{1}{2}} - d^{\frac{1}{2}}\right\}\right) \cdot N_1 \tag{A.256}$$

$$v_{Tot} = \frac{8 \cdot F}{E \cdot t \cdot w_{b1}^3}\left\{N_{1G}^{\frac{3}{2}} \cdot N_{2G}^{\frac{3}{2}} - N_{1G}^{\frac{3}{2}} \cdot d^{\frac{3}{2}} + N_{1G}^3 - N_{1G}^{\frac{3}{2}} \cdot d^{\frac{3}{2}} + 3N_{1G}^{\frac{5}{2}} \cdot N_{2G}^{\frac{1}{2}} - 3N_{1G}^3\right\} \tag{A.257}$$

$$v_{Tot} = \frac{8 \cdot F}{E \cdot t \cdot w_{b1}^3}\left\{N_{1G}^{\frac{3}{2}} N_{2G}^{\frac{3}{2}} - 2N_{1G}^{\frac{3}{2}} d^{\frac{3}{2}} - 2N_{1G}^3 + 3N_{1G}^{\frac{5}{2}} N_{2G}^{\frac{1}{2}}\right\}. \tag{A.258}$$

Plugging this into the equation for the spring constant, we have:

$$k_{Fv_{Tot}} = \frac{F}{v_{Tot}} \tag{A.259}$$

$$k_{Fv_{Tot}} = \frac{F}{\frac{8F}{E \cdot t \cdot w_{b1}^3}\left[N_{1G}^{\frac{3}{2}} N_{2G}^{\frac{3}{2}} - 2d^{\frac{3}{2}} N_{1G}^{\frac{3}{2}} - 2N_{1G}^3 + 3N_{1G}^{\frac{5}{2}} N_{2G}^{\frac{1}{2}}\right]} \tag{A.260}$$

$$k_{Fv_{Tot}} = \frac{E \cdot t \cdot w_{b1}^3}{8\left[N_{1G}^{\frac{3}{2}} N_{2G}^{\frac{3}{2}} - 2d^{\frac{3}{2}} N_{1G}^{\frac{3}{2}} - 2N_{1G}^3 + 3N_{1G}^{\frac{5}{2}} N_{2G}^{\frac{1}{2}}\right]} \tag{A.261}$$

$$k_{Fv_{Tot}} = \frac{E \cdot t \cdot w_{b1}^3}{8N_{1G}^{\frac{3}{2}}\left[N_{2G}^{\frac{3}{2}} - 2d^{\frac{3}{2}} - 2N_{1G}^{\frac{3}{2}} + 3N_{1G} N_{2G}^{\frac{1}{2}}\right]}. \tag{A.262}$$

Assuming that the designer is given a value for $k_{Fv_{Tot}}$, and after having solved for N_{1G} and N_{2G}, the designer will need to solve for w_{b1}. So, solving Equation A.262 for w_{b1} we have:

$$w_{b1} = \left\{ \frac{k_{Fv_{Tot}} \cdot 8 \cdot N_{1G}^{\frac{3}{2}} \left[N_{2G}^{\frac{3}{2}} - 2d^{\frac{3}{2}} - 2N_{1G}^{\frac{3}{2}} + 3N_{1G} N_{2G}^{\frac{1}{2}} \right]}{E \cdot t} \right\}^{\frac{1}{3}}. \tag{A.263}$$

The designer would then use Equation A.237 to solve for w_{b2}, which completes the design of the guided flexure. However, we will need the angular displacement spring constant due to an applied moment $k_{M\theta_{Tot}}$ for the design of the anchor flexure. So, by definition we have:

$$k_{M\theta_{Tot}} = \frac{M}{\theta_{Tot}}. \tag{A.264}$$

Substituting in Equations A.218 and A.228 we have:

$$k_{M\theta_{Tot}} = \frac{F_G N_{1G}}{\theta_{FN2G} - \theta_{FN1G}}. \tag{A.265}$$

Substituting in Equations A.239 and A.245 we have:

$$k_{M\theta_{Tot}} = \frac{F_G N_{1G}}{\frac{24 \cdot F_G}{E \cdot t \cdot w_{b1}^3} \left\{ N_{1G}^{\frac{3}{2}} \cdot N_{2G}^{\frac{1}{2}} - N_{1G}^{\frac{3}{2}} \cdot d^{\frac{1}{2}} \right\} - \frac{24 \cdot F_G \cdot N_{1G}^{\frac{3}{2}}}{E \cdot t \cdot w_{b1}^3} \left\{ N_{1G}^{\frac{1}{2}} - d^{\frac{1}{2}} \right\}} \tag{A.266}$$

$$k_{M\theta_{Tot}} = \frac{E \cdot t \cdot w_{b1}^3}{24 N_{1G}^{\frac{1}{2}} \left[N_{2G}^{\frac{1}{2}} - N_{1G}^{\frac{1}{2}} \right]}. \tag{A.267}$$

Having the guided flexure now fully designed, we turn our attention to the anchor flexure. The primary difference between the anchor flexure and the guided flexure is that the anchor flexure has no net linear displacement. So, inspection of the Anchor flexure enables us to write the following equation:

$$M_A = M_G = F_A N_{2A}. \tag{A.268}$$

By investigating the deflections at the center of the hammerhead we express the total deflection of the composite anchor flexure as a function of the deflections of each of the flexures in the composite anchor flexure by writing:

$$v_{TotA} = v_{FN2A} + v_{FN1A} - \theta_{Tot} \cdot N_{2A}, \tag{A.269}$$

where

$$\theta_{Tot} = \theta_{FN2A} - \theta_{FN1A}. \tag{A.270}$$

We also note that since the moments of the anchor and guided flexures are the same at the pivot point, and we want to have the same peak stress in all flexure elements, this requires that the base width of the N_{2A} flexure be the same as the base width of the N_{1G} flexure. That is:

$$w_{b_{N2A}} = w_{b_{N1G}}. \tag{A.271}$$

The requirement to maintain the same peak stress imposes the same ratio on the anchor flexures as it did for the guided flexures. Therefore, from Equation A.237 we can write:

$$w_{b2A} = w_{b1A}\sqrt{\frac{N_{2A}}{N_{1A}}} \tag{A.272}$$

or

$$w_{b1A} = w_{b2A}\sqrt{\frac{N_{1A}}{N_{2A}}}\,. \tag{A.273}$$

Also, by similarity to Equations A.238, A.239, A.240 and A.241, we can write the equations for the linear and angular deflections of the anchor flexure as:

$$v_{FN1A} = \frac{8 \cdot F_A}{E \cdot t \cdot w_{b1A}^3}\left\{N_{1A}^3 - N_{1A}^{\frac{3}{2}} \cdot d^{\frac{3}{2}}\right\} \tag{A.274}$$

$$\theta_{FN1A} = \frac{24 \cdot F_A}{E \cdot t \cdot w_{b1A}^3}\left\{N_{1A}^2 - N_{1A}^{\frac{3}{2}} \cdot d^{\frac{1}{2}}\right\} \tag{A.275}$$

$$v_{FN2A} = \frac{8 \cdot F_A}{E \cdot t \cdot w_{b2A}^3}\left\{N_{2A}^3 - N_{2A}^{\frac{3}{2}} \cdot d^{\frac{3}{2}}\right\} \tag{A.276}$$

$$\theta_{FN2A} = \frac{24 \cdot F_A}{E \cdot t \cdot w_{b2A}^3}\left\{N_{2A}^2 - N_{2A}^{\frac{3}{2}} \cdot d^{\frac{1}{2}}\right\}. \tag{A.277}$$

Once again it will be beneficial to express this set of equations in terms of just one of the flexure widths, but in the case of the anchor flexures, since we will know w_{b2A} from the design of the guided flexure, we wish to express these in terms of w_{b2A}. So, here we substitute Equation A.273 into Equation A.274:

$$v_{FN1A} = \frac{8 \cdot F_A \cdot N_{2A}^{\frac{3}{2}}}{E \cdot t \cdot w_{b2A}^3 \cdot N_{1A}^{\frac{3}{2}}} \left\{ N_{1A}^3 - N_{1A}^{\frac{3}{2}} \cdot d^{\frac{3}{2}} \right\} \tag{A.278}$$

$$v_{FN1A} = \frac{8 \cdot F_A}{E \cdot t \cdot w_{b2A}^3} \left\{ N_{1A}^{\frac{3}{2}} \cdot N_{2A}^{\frac{3}{2}} - N_{2A}^{\frac{3}{2}} \cdot d^{\frac{3}{2}} \right\}. \tag{A.279}$$

We also substitute Equation A.273 into Equation A.275:

$$\theta_{FN1A} = \frac{24 \cdot F_A \cdot N_{2A}^{\frac{3}{2}}}{E \cdot t \cdot w_{b2A}^3 \cdot N_{1A}^{\frac{3}{2}}} \left\{ N_{1A}^2 - N_{1A}^{\frac{3}{2}} \cdot d^{\frac{1}{2}} \right\} \tag{A.280}$$

$$\theta_{FN1A} = \frac{24 \cdot F_A}{E \cdot t \cdot w_{b2A}^3} \left\{ N_{1A}^{\frac{1}{2}} \cdot N_{2A}^{\frac{3}{2}} - N_{2A}^{\frac{3}{2}} \cdot d^{\frac{1}{2}} \right\}. \tag{A.281}$$

Substituting A.277 and A.281 into A.270, we have:

$$\theta_{Tot} = \frac{24 \cdot F_A}{E \cdot t \cdot w_{b2A}^3} \left\{ N_{2A}^2 - N_{2A}^{\frac{3}{2}} \cdot d^{\frac{1}{2}} \right\} - \frac{24 \cdot F_A}{E \cdot t \cdot w_{b2A}^3} \left\{ N_{1A}^{\frac{1}{2}} \cdot N_{2A}^{\frac{3}{2}} - N_{2A}^{\frac{3}{2}} \cdot d^{\frac{1}{2}} \right\} \tag{A.282}$$

$$\theta_{Tot} = \frac{24 \cdot F_A}{E \cdot t \cdot w_{b2A}^3} \left\{ N_{2A}^2 - N_{1A}^{\frac{1}{2}} \cdot N_{2A}^{\frac{3}{2}} \right\}. \tag{A.283}$$

Here we return to the rotational spring constant due to the moment around the pivot point which by definition would be:

$$k_{M\theta_{Tot}} = \frac{M}{\theta_{Tot}}. \tag{A.284}$$

Substituting Equations A.268 and A.270 we have:

$$k_{M\theta_{Tot}} = \frac{F_A N_{2A}}{\theta_{FN2A} - \theta_{FN1A}} . \tag{A.285}$$

Substituting Equation A.283 we have:

$$k_{M\theta_{Tot}} = \frac{F_A N_{2A}}{\frac{24 \cdot F_A}{E \cdot t \cdot w_{b2A}^3}\left\{N_{2A}^2 - N_{1A}^{\frac{1}{2}} \cdot N_{2A}^{\frac{3}{2}}\right\}} \tag{A.286}$$

$$k_{M\theta_{Tot}} = \frac{E \cdot t \cdot w_{b2A}^3}{24 \cdot \left\{N_{2A} - N_{1A}^{\frac{1}{2}} \cdot N_{2A}^{\frac{1}{2}}\right\}} . \tag{A.287}$$

This gives us one critical relationship that we will use to solve for N_{1A} and N_{2A}. The second critical relationship is derived from Equation A.269. So, setting that equation equal to zero because we want no net linear displacement of the pivot point, and substituting in Equations A.279, A.276, and A.283, we have:

$$v_{TotA} = 0 = \frac{8 \cdot F_A}{E \cdot t \cdot w_{b2A}^3}\left\{N_{2A}^3 - N_{2A}^{\frac{3}{2}} \cdot d^{\frac{3}{2}}\right\} + \frac{8 \cdot F_A}{E \cdot t \cdot w_{b2A}^3}\left\{N_{1A}^{\frac{3}{2}} \cdot N_{2A}^{\frac{3}{2}} - N_{2A}^{\frac{3}{2}} \cdot d^{\frac{3}{2}}\right\} -$$

$$\frac{24 \cdot F_A}{E \cdot t \cdot w_{b2A}^3}\left\{N_{2A}^2 - N_{1A}^{\frac{1}{2}} \cdot N_{2A}^{\frac{3}{2}}\right\} \cdot N_{2A} \tag{A.288}$$

$$0 = \frac{8 \cdot F_A}{E \cdot t \cdot w_{b2A}^3}\left\{N_{2A}^3 - N_{2A}^{\frac{3}{2}} d^{\frac{3}{2}} + N_{1A}^{\frac{3}{2}} N_{2A}^{\frac{3}{2}} - N_{2A}^{\frac{3}{2}} d^{\frac{3}{2}} - 3N_{2A}^3 + 3N_{1A}^{\frac{1}{2}} N_{2A}^{\frac{5}{2}}\right\} \tag{A.289}$$

$$0 = \frac{8 \cdot F_A \cdot N_{2A}^{\frac{3}{2}}}{E \cdot t \cdot w_{b2A}^3}\left\{N_{1A}^{\frac{3}{2}} + 3N_{1A}^{\frac{1}{2}} N_{2A} - 2N_{2A}^{\frac{3}{2}} - 2d^{\frac{3}{2}}\right\} \tag{A.290}$$

$$\left[N_{1A}^{\frac{3}{2}} + 3N_{1A}^{\frac{1}{2}} N_{2A} - 2N_{2A}^{\frac{3}{2}} - 2d^{\frac{3}{2}}\right] = 0 . \tag{A.291}$$

Here we must employ the Multivariate Newton's Method for simultaneously solving multiple nonlinear equations. The first nonlinear equation, f_A, is derived from Equation A.291 above:

$$f_A(N_{1A}, N_{2A}) = \left[N_{1A}^{\frac{3}{2}} + 3N_{1A}^{\frac{1}{2}}N_{2A} - 2N_{2A}^{\frac{3}{2}} - 2d^{\frac{3}{2}}\right] = 0 \ . \tag{A.292}$$

The second nonlinear equation, g_A, comes from Equation A.287 which we rearrange to get into a form that we want to equal zero:

$$g_A(N_{1A}, N_{2A}) = k_{M\theta_{Tot}} - \frac{E \cdot t \cdot w_{b2A}^3}{24 \cdot \left\{N_{2A} - N_{1A}^{\frac{1}{2}} \cdot N_{2A}^{\frac{1}{2}}\right\}} = 0 \ . \tag{A.293}$$

We then define the function vector, $\boldsymbol{F}$, as:

$$\boldsymbol{F} = \begin{bmatrix} f_A(N_{1A}, N_{2A}) \\ g_A(N_{1A}, N_{2A}) \end{bmatrix} . \tag{A.294}$$

We also define the Jacobian matrix, $\boldsymbol{DF}$, as:

$$\boldsymbol{DF} = \begin{bmatrix} \frac{\partial f}{\partial N_{1A}} & \frac{\partial f}{\partial N_{2A}} \\ \frac{\partial g}{\partial N_{1A}} & \frac{\partial g}{\partial N_{2A}} \end{bmatrix} = \begin{bmatrix} a_{DF} & b_{DF} \\ c_{DF} & d_{DF} \end{bmatrix} . \tag{A.295}$$

Here the designer will have to make an initial guess for the vector, $\boldsymbol{x}$, of flexure lengths:

$$\boldsymbol{x_0} = \begin{bmatrix} N_{1A_0} \\ N_{2A_0} \end{bmatrix} . \tag{A.296}$$

Iterations of the vector, $\boldsymbol{x}$, will follow the following equation:

$$\boldsymbol{x_{n+1}} = \boldsymbol{x_n} - [\boldsymbol{DF}(\boldsymbol{x_n})]^{-1}\boldsymbol{F}(\boldsymbol{x_n})\ . \tag{A.297}$$

The partial derivatives that populate the Jacobian are derived below. From Equation A.292 we find:

$$a_{DF} = \frac{\partial f}{\partial N_{1A}} = \frac{\partial}{\partial N_{1A}}\left[N_{1A}^{\frac{3}{2}} + 3N_{1A}^{\frac{1}{2}}N_{2A} - 2N_{2A}^{\frac{3}{2}} - 2d^{\frac{3}{2}}\right] \tag{A.298}$$

$$a_{DF} = \frac{\partial f}{\partial N_{1A}} = \left[\frac{3}{2}N_{1A}^{\frac{1}{2}} + \frac{3}{2}N_{1A}^{-\frac{1}{2}}N_{2A}\right] \tag{A.299}$$

$$b_{DF} = \frac{\partial f}{\partial N_{2A}} = \frac{\partial}{\partial N_{2A}}\left[N_{1A}^{\frac{3}{2}} + 3N_{1A}^{\frac{1}{2}}N_{2A} - 2N_{2A}^{\frac{3}{2}} - 2d^{\frac{3}{2}}\right] \tag{A.300}$$

$$b_{DF} = \frac{\partial f}{\partial N_{2A}} = \left[3N_{1A}^{\frac{1}{2}} - 3N_{2A}^{\frac{1}{2}}\right]. \tag{A.301}$$

From Equation A.293 we find:

$$c_{DF} = \frac{\partial g}{\partial N_{1A}} = \frac{\partial}{\partial N_{1A}}\left[k_{M\theta_{Tot}} - \frac{E\cdot t\cdot w_{b2A}^3}{24}\left\{N_{2A} - N_{1A}^{\frac{1}{2}}\cdot N_{2A}^{\frac{1}{2}}\right\}^{-1}\right] \tag{A.302}$$

$$c_{DF} = \frac{\partial g}{\partial N_{1A}} = \left[\frac{E\cdot t\cdot w_{b2A}^3}{24}\left\{N_{2A} - N_{1A}^{\frac{1}{2}}\cdot N_{2A}^{\frac{1}{2}}\right\}^{-2}\left(-\frac{1}{2}N_{1A}^{-\frac{1}{2}}\cdot N_{2A}^{\frac{1}{2}}\right)\right] \tag{A.303}$$

$$c_{DF} = \frac{\partial g}{\partial N_{1A}} = -\frac{E\cdot t\cdot w_{b2A}^3}{48}\frac{N_{1A}^{-\frac{1}{2}}\cdot N_{2A}^{\frac{1}{2}}}{\left(N_{2A} - N_{1A}^{\frac{1}{2}}\cdot N_{2A}^{\frac{1}{2}}\right)^2} \tag{A.304}$$

$$d_{DF} = \frac{\partial g}{\partial N_{2A}} = \frac{\partial}{\partial N_{2A}}\left[k_{M\theta_{Tot}} - \frac{E \cdot t \cdot w_{b2A}^3}{24}\left\{N_{2A} - N_{1A}^{\frac{1}{2}} \cdot N_{2A}^{\frac{1}{2}}\right\}^{-1}\right] \tag{A.305}$$

$$d_{DF} = \frac{\partial g}{\partial N_{2A}} = \left[\frac{E \cdot t \cdot w_{b2A}^3}{24}\left\{N_{2A} - N_{1A}^{\frac{1}{2}} \cdot N_{2A}^{\frac{1}{2}}\right\}^{-2}\left(1 - \frac{1}{2}N_{1A}^{\frac{1}{2}} \cdot N_{2A}^{-\frac{1}{2}}\right)\right] \tag{A.306}$$

$$d_{DF} = \frac{\partial g}{\partial N_{2A}} = \frac{E \cdot t \cdot w_{b2A}^3}{24}\frac{\left(1 - \frac{1}{2} \cdot N_{1A}^{\frac{1}{2}} \cdot N_{2A}^{-\frac{1}{2}}\right)}{\left(N_{2A} - N_{1A}^{\frac{1}{2}} \cdot N_{2A}^{\frac{1}{2}}\right)^2}. \tag{A.307}$$

The determinant of $\boldsymbol{DF}$ can then be calculated using the following equation:

$$|\boldsymbol{DF}| = a_{DF}d_{DF} - b_{DF}c_{DF}\ . \tag{A.308}$$

Finally, the updated estimates for N_{1A} and N_{2A} in each iteration can be found using the following equations:

$$N_{1A_{n+1}} = N_{1A_n} - \frac{d_{DF} \cdot f(N_{1A_n}, N_{2A_n}) - b_{DF} \cdot g(N_{1A_n}, N_{2A_n})}{|\boldsymbol{DF}(N_{1A_n}, N_{2A_n})|} \tag{A.309}$$

$$N_{2A_{n+1}} = N_{2A_n} - \frac{c_{DF} \cdot f(N_{1A_n}, N_{2A_n}) - a_{DF} \cdot g(N_{1A_n}, N_{2A_n})}{|\boldsymbol{DF}(N_{1A_n}, N_{2A_n})|}\ . \tag{A.310}$$

The final step in the design of the tapered flexure pivot APLM is the calculation of the width of the first element of the anchor flexure which is accomplished through Equation A.273.

A.7 Straight Flexure Lever APLM Design Equation Derivations

This section documents the derivation of the design equations for the straight flexure lever APLM design. This derivation is based on the device layout pictured in Figure 4.10(a) and uses the dimensions defined in Figure 4.18. It is assumed that the designer is provided with the desired spring constant that needs to be applied to the proof mass. It is also assumed that the designer is either given or will use engineering judgement to select the length of the lever, L_{Lever}. This derivation focuses on the evaluation of one proof mass and one set of three flexures under the assumption of symmetry with the other proof mass and three flexures. Unlike the derivations for the four-flexure pivot design which neglected the width of the block at the pivot point, this derivation will account for the width of the lever arm, $2d_3$.

Assuming that the desired spring constant, k_{v_Tot}, has been provided or derived from a resonant frequency requirement, and that the length of the lever arm, L_{Lever}, has either been given or selected from engineering judgment, we desire that the stiffness of the lever arm, k_{Lever}, be some factor, R, stiffer than the required spring constant. That is:

$$k_{Lever} = R \cdot k_{v\_Tot} \,. \tag{A.311}$$

Substituting in the standard equation for the stiffness of a cantilever beam for k_{Lever}, we have:

$$k_{Lever} = \frac{E \cdot t \cdot w_{Lever}^3}{4 \cdot L_{Lever}^3} = R \cdot k_{v\_Tot} \,. \tag{A.312}$$

where w_{Lever} is the width of the lever. This equation provides a minimum bound for the acceptable value of w_{Lever}, which is:

$$w_{Lever} \geq L_{Lever}\left(\frac{4 \cdot R \cdot k_{v_{Tot}}}{E \cdot t}\right)^{\frac{1}{3}}. \tag{A.313}$$

Since the constant d_3 is only half the width of the lever arm, it must be chosen to be more than half of this result:

$$d_3 \geq \frac{L_{Lever}}{2}\left(\frac{4 \cdot R \cdot k_{v_{Tot}}}{E \cdot t}\right)^{\frac{1}{3}}. \tag{A.314}$$

The operation of the lever APLM is essentially converting the force applied to the proof mass into a moment through the lever arm, L_{Lever}. Therefore, we can also calculate the desired spring constant that relates the angular displacement to the applied moment, $k_{M\theta Tot}$:

$$k_{M\theta Tot} = \frac{M}{\theta} = \frac{F \cdot L_{Lever}}{v/L_{Lever}} = \frac{F}{v} \cdot L_{Lever}^2 = k_{v_{Tot}} \cdot L_{Lever}^2 \,. \tag{A.315}$$

Since we know that each proof mass effectively has three flexures supplying this moment, we can calculate the net rotational spring constant for each flexure as follows:

$$k_{M\theta Flex} = \frac{k_{M\theta Tot}}{3} = \frac{k_{v_{Tot}} \cdot L_{Lever}^2}{3} \,. \tag{A.316}$$

Here we define a variable, N, that will represent the total flexure length:

$$N = L_{Flex} + d_3. \tag{A.317}$$

Here we also note that the flexure has both a force and a moment applied to it at the center of the pivot point which is beyond the end of the flexure. The linear deflection of a cantilever beam due to an applied force is given by:

$$v_F(x) = \frac{F}{EI}\left(\frac{Nx^2}{2} - \frac{x^3}{6}\right) \qquad 0 \le x \le L_{Flex}, \tag{A.318}$$

which is only valid out to L_{Flex} since the lever is extremely stiff. Therefore, if we want the displacement at $x = N$, we must extend the displacement through the lever arm using the rotation, θ_F, which is given by:

$$\theta_F(x) = \frac{F}{EI}\left(Nx\ - \frac{x^2}{2}\right) \qquad 0 \le x \le L_{Flex}. \tag{A.319}$$

Therefore, we can find the displacement at $x = N$ due to an applied force at $x = N$ using the following relationship:

$$v_F(N) = v_F(L_{Flex}) + d_3 \cdot \theta_F(L_{Flex}). \tag{A.320}$$

Performing the proper substitutions yields:

$$v_F(N) = \frac{F}{EI}\left(\frac{N \cdot L_{Flex}^2}{2} - \frac{L_{Flex}^3}{6}\right) + d_3 \cdot \frac{F}{EI}\left(N \cdot L_{Flex}\ - \frac{L_{Flex}^2}{2}\right) \tag{A.321}$$

$$v_F(N) = \frac{F}{EI}\left(\frac{N \cdot L_{Flex}^2}{2} - \frac{L_{Flex}^3}{6} + d_3 \cdot N \cdot L_{Flex} - d_3 \cdot \frac{L_{Flex}^2}{2}\right) \tag{A.322}$$

$$v_F(N) = \frac{F \cdot L_{Flex}}{6EI}(3NL_{Flex} - L_{Flex}^2 + 6d_3N - 3d_3L_{Flex}). \tag{A.323}$$

Similarly, linear deflection of a cantilever beam due to an applied moment is given by:

$$v_M(x) = \frac{Mx^2}{2EI} \qquad 0 \le x \le L_{Flex}, \qquad \text{(A.324)}$$

and the angular displacement of the cantilever beam due to an applied moment is given by:

$$\theta_M(x) = \frac{Mx}{EI} \qquad 0 \le x \le L_{Flex}, \qquad \text{(A.325)}$$

which is again only valid to the point where the flexure connects to the lever arm. We extend this displacement through the lever arm using the following relation:

$$v_M(N) = v_M(L_{Flex}) + d_3 \cdot \theta_M(L_{Flex}). \qquad \text{(A.326)}$$

Performing the appropriate substitutions, we find:

$$v_M(N) = \frac{ML_{Flex}^2}{2EI} + d_3 \cdot \frac{ML_{Flex}}{EI} \qquad \text{(A.327)}$$

$$v_M(N) = \frac{ML_{Flex}}{2EI}(L_{Flex} + 2d_3). \qquad \text{(A.328)}$$

Since we know that there will be no net displacement at the pivot point, then the displacement due to the force must be equal to the displacement due to the moment, or:

$$v_M(N) = v_F(N). \qquad \text{(A.329)}$$

Since we will ultimately be looking for a spring constant that relates rotational displacement to the applied moment, $k_{M\theta Flex}$ ·, we now substitute Equations A.323 and A.328 into Equation A.329 and solve for F in terms of M:

$$\frac{ML_{Flex}}{2EI}(L_{Flex} + 2d_3) = \frac{F \cdot L_{Flex}}{6EI}(3NL_{Flex} - L_{Flex}^2 + 6d_3N - 3d_3L_{Flex}) \qquad \text{(A.330)}$$

$$F = \frac{3M(L_{Flex}+2d_3)}{(3NL_{Flex}-L_{Flex}^2+6d_3N-3d_3L_{Flex})} . \quad \text{(A.331)}$$

Noting here that $L_{Flex} + d_3 = N$, we find:

$$F = \frac{3M(N+d_3)}{(3L_{Flex}(N-d_3)-L_{Flex}^2+6d_3N)} \quad \text{(A.332)}$$

$$F = \frac{3M(N+d_3)}{(2L_{Flex}^2+6d_3N)} . \quad \text{(A.333)}$$

Now that we have derived one constraint based on the requirement to have no net linear displacement, we can derive an expression for the net rotation. By inspection we see that:

$$\theta = \theta_M(N) - \theta_F(N) . \quad \text{(A.334)}$$

Since the lever is significantly stiffer than the flexure, we note that:

$$\theta_M(N) = \theta_M(L_{Flex}) \quad \text{(A.335)}$$

and

$$\theta_F(N) = \theta_F(L_{Flex}) . \quad \text{(A.336)}$$

Therefore, performing the proper substitutions, we have:

$$\theta = \theta_M(L_{Flex}) - \theta_F(L_{Flex}) = \frac{ML_{Flex}}{EI} - \frac{F}{EI}\left(N \cdot L_{Flex} - \frac{L_{Flex}^2}{2}\right) \quad \text{(A.337)}$$

$$\theta = \frac{L_{Flex}}{EI}\left[M - \frac{F}{2}(2N - L_{Flex})\right] . \quad \text{(A.338)}$$

Noting here that $N - L_{Flex} = d_3$, we find:

$$\theta = \frac{L_{Flex}}{EI}\left[M - \frac{F}{2}(N + d_3)\right]. \tag{A.339}$$

Substituting F from Equation A.333 into this expression yields:

$$\theta = \frac{L_{Flex}}{EI}\left[M - \frac{\frac{3M(N+d_3)}{\left(2L_{Flex}^2+6d_3N\right)}}{2}(N + d_3)\right] \tag{A.340}$$

$$\theta = \frac{L_{Flex}}{EI}\left[M - \frac{3}{2}\frac{M(N+d_3)^2}{\left(2L_{Flex}^2+6d_3N\right)}\right] \tag{A.341}$$

$$\theta = M \cdot \frac{L_{Flex}}{EI}\left[1 - \frac{3}{2}\frac{(N+d_3)^2}{\left(2L_{Flex}^2+6d_3N\right)}\right]. \tag{A.342}$$

By definition we find:

$$k_{M\theta Flex} = \frac{M}{\theta} = \frac{EI}{L_{Flex}}\left[1 - \frac{3}{2}\frac{(N+d_3)^2}{\left(2L_{Flex}^2+6d_3N\right)}\right]^{-1}. \tag{A.343}$$

Substituting in for the moment of inertia:

$$k_{M\theta Flex} = \frac{E \cdot t \cdot w_{Flex}^3}{12 \cdot L_{Flex}}\left[1 - \frac{3}{2}\frac{(N+d_3)^2}{\left(2L_{Flex}^2+6d_3N\right)}\right]^{-1}. \tag{A.344}$$

Solving this for w_{Flex} we have:

$$w_{Flex} = \left\{k_{M\theta Flex}\frac{12 \cdot L_{Flex}}{E \cdot t}\left[1 - \frac{3}{2}\frac{(N+d_3)^2}{\left(2L_{Flex}^2+6d_3N\right)}\right]\right\}^{\frac{1}{3}}. \tag{A.345}$$

which completes the design of the straight flexure lever APLM.

A.8 Tapered Flexure Lever APLM Design Equation Derivations

This section documents the derivation of the design equations for the tapered flexure lever APLM design. This derivation is based on the device layout pictured in Figure 4.10(b) and uses the dimensions defined in Figure 4.19. It is assumed that the designer is provided with the desired spring constant that needs to be applied to the proof mass. It is also assumed that the designer is either given or will use engineering judgement to select the length of the lever, L_{Lever}. This derivation focuses on the evaluation of one proof mass and one set of three flexures under the assumption of symmetry with the other proof mass and three flexures. Similar to the derivation for the straight flexure lever design, this derivation will account for the width of the lever arm, $2d_3$. The first part of this derivation is identical to that documented in the previous section, but is repeated here for continuity.

Assuming that the desired spring constant, k_{v_Tot}, has been provided or derived from a resonant frequency requirement, and that the length of the lever arm, L_{Lever}, has either been given or selected from engineering judgment, we desire that the stiffness of the lever arm, k_{Lever}, be some factor, R, stiffer than the required spring constant. That is:

$$k_{Lever} = R \cdot k_{v\_Tot} \ . \tag{A.346}$$

Substituting in the standard equation for the stiffness of a cantilever beam for k_{Lever}, we have:

$$k_{Lever} = \frac{E \cdot t \cdot w_{Lever}^3}{4 \cdot L_{Lever}^3} = R \cdot k_{v\_Tot}, \tag{A.347}$$

where w_{Lever} is the width of the lever. This equation provides a minimum bound for the acceptable value of w_{Lever}, which is:

$$w_{Lever} \geq L_{Lever}\left(\frac{4 \cdot R \cdot k_{v_{Tot}}}{E \cdot t}\right)^{\frac{1}{3}}. \tag{A.348}$$

Since the constant d_3 is only half the width of the lever arm, it must be chosen to be more than half of this result:

$$d_3 \geq \frac{L_{Lever}}{2}\left(\frac{4 \cdot R \cdot k_{v_{Tot}}}{E \cdot t}\right)^{\frac{1}{3}}. \tag{A.349}$$

Since this lever arm is essentially converting the force applied to the proof mass into a moment through the lever arm, L_{Lever}, we can also calculate the desired spring constant that relates the angular displacement to the applied moment, $k_{M\theta}$:

$$k_{M\theta Tot} = \frac{M}{\theta} = \frac{F_{Lever} \cdot L_{Lever}}{v/L_{Lever}} = \frac{F}{v} \cdot L_{Lever}^2 = k_{v_{Tot}} \cdot L_{Lever}^2 \,. \tag{A.350}$$

Since we know that each proof mass effectively has three flexures supplying the moment, we can calculate the net rotational spring constant for each flexure as follows:

$$k_{M\theta Flex} = \frac{k_{M\theta Tot}}{3} = \frac{k_{v_{Tot}} \cdot L_{Lever}^2}{3} \,. \tag{A.351}$$

Here we will revisit Figure 4.19 and write a few equations by inspection. We know that we will design the lengths of flexures N_1 and N_2 such that the hammerhead feature will be placed at the location where there is no net moment acting on either flexure. Therefore, we should be able to write all of our equations based on only the

equivalent force that is acting on these flexures in this location. First, we note that the total rotational displacement can be calculated by:

$$\theta = \theta_{FN2} - \theta_{FN1}. \tag{A.352}$$

where θ_{FN2} is the rotational displacement of flexure number 2 due to the net force being applied at the center of the hammerhead, and θ_{FN1} is the rotational displacement of flexure number 1 due to the net force being applied at the center of the hammerhead. Next, by inspection of the displacements at the center of the hammerhead we note that the total displacement can be given by:

$$v_{F_{Tot}} = v_{FN1} + v_{FN2} - (N_2 + d_3) \cdot \theta. \tag{A.353}$$

Here we note that we want the total displacement of the flexure to be zero. So, we set this last expression equal to zero:

$$v_{F_{Tot}} = v_{FN1} + v_{FN2} - (N_2 + d_3) \cdot \theta = 0\ . \tag{A.354}$$

Substituting Equation A.352 into A.354 we have:

$$v_{FN1} + v_{FN2} - (N_2 + d_3) \cdot (\theta_{FN2} - \theta_{FN1}) = 0\ . \tag{A.355}$$

Similar to what was done for the Tapered Flexure Pivot APLM design, we would like to set the maximum stresses in every element of the tapered flexures to be the same. To do this, we note that the force, *F*, acting on N_1 and N_2 is the same. Referring back to Equation 3.8 we have:

$$T_{maxN1} = \frac{6 \cdot F \cdot N_1}{t \cdot {w_{b1}}^2} \tag{A.356}$$

and

$$T_{maxN2} = \frac{6 \cdot F \cdot N_2}{t \cdot {w_{b2}}^2} . \tag{A.357}$$

Setting these equal yields:

$$T_{maxN1} = T_{maxN2} \tag{A.358}$$

$$\frac{6 \cdot F \cdot N_1}{t \cdot {w_{b1}}^2} = \frac{6 \cdot F \cdot N_2}{t \cdot {w_{b2}}^2} \tag{A.359}$$

$$\frac{N_1}{{w_{b1}}^2} = \frac{N_2}{{w_{b2}}^2} . \tag{A.360}$$

This enables us to express w_{b2} in terms of w_{b1} as:

$$w_{b2} = w_{b1} \sqrt{\frac{N_2}{N_1}} . \tag{A.361}$$

Now finding the linear and angular deflection equations from Table 3.1:

$$v_{FN1} = \frac{8 \cdot F}{E \cdot t \cdot w_{b1}^3} \left\{ N_1^3 - N_1^{\frac{3}{2}} \cdot d^{\frac{3}{2}} \right\} \tag{A.362}$$

$$\theta_{FN1} = \frac{24 \cdot F \cdot N_1^{\frac{3}{2}}}{E \cdot t \cdot w_{b1}^3} \left\{ N_1^{\frac{1}{2}} - d^{\frac{1}{2}} \right\} \tag{A.363}$$

$$v_{FN2} = \frac{8 \cdot F}{E \cdot t \cdot w_{b2}^3} \left\{ N_2^3 - N_2^{\frac{3}{2}} \cdot d^{\frac{3}{2}} \right\} \tag{A.364}$$

$$\theta_{FN2} = \frac{24 \cdot F \cdot N_2^{\frac{3}{2}}}{E \cdot t \cdot w_{b2}^3} \left\{ N_2^{\frac{1}{2}} - d^{\frac{1}{2}} \right\}. \tag{A.365}$$

It will be beneficial to express this set of equations in terms of just one of the flexure widths. So, here we substitute Equation A.361 into Equation A.364:

$$v_{FN2} = \frac{8 \cdot F \cdot N_1^{\frac{3}{2}}}{E \cdot t \cdot w_{b1}^3 \cdot N_2^{\frac{3}{2}}} \left\{ N_2^3 - N_2^{\frac{3}{2}} \cdot d^{\frac{3}{2}} \right\} \tag{A.366}$$

$$v_{FN2} = \frac{8 \cdot F}{E \cdot t \cdot w_{b1}^3} \left\{ N_1^{\frac{3}{2}} \cdot N_2^{\frac{3}{2}} - N_1^{\frac{3}{2}} \cdot d^{\frac{3}{2}} \right\}. \tag{A.367}$$

We also substitute Equation A.361 into Equation A.365:

$$\theta_{FN2} = \frac{24 \cdot F \cdot N_2^{\frac{3}{2}} \cdot N_1^{\frac{3}{2}}}{E \cdot t \cdot w_{b1}^3 \cdot N_2^{\frac{3}{2}}} \left\{ N_2^{\frac{1}{2}} - d^{\frac{1}{2}} \right\} \tag{A.368}$$

$$\theta_{FN2} = \frac{24 \cdot F}{E \cdot t \cdot w_{b1}^3} \left\{ N_1^{\frac{3}{2}} \cdot N_2^{\frac{1}{2}} - N_1^{\frac{3}{2}} \cdot d^{\frac{1}{2}} \right\}. \tag{A.369}$$

Combining Equation A.352 with Equations A.363 and A.369 yields:

$$\theta = \frac{24 \cdot F}{E \cdot t \cdot w_{b1}^3} \left\{ N_1^{\frac{3}{2}} \cdot N_2^{\frac{1}{2}} - N_1^{\frac{3}{2}} \cdot d^{\frac{1}{2}} \right\} - \frac{24 \cdot F \cdot N_1^{\frac{3}{2}}}{E \cdot t \cdot w_{b1}^3} \left\{ N_1^{\frac{1}{2}} - d^{\frac{1}{2}} \right\} \tag{A.370}$$

$$\theta = \frac{24 \cdot F}{E \cdot t \cdot w_{b1}^3} \left\{ N_1^{\frac{3}{2}} \cdot N_2^{\frac{1}{2}} - N_1^{\frac{3}{2}} \cdot d^{\frac{1}{2}} - N_1^2 + N_1^{\frac{3}{2}} \cdot d^{\frac{1}{2}} \right\} \tag{A.371}$$

$$\theta = \frac{24 \cdot F}{E \cdot t \cdot w_{b1}^3} \left\{ N_1^{\frac{3}{2}} \cdot N_2^{\frac{1}{2}} - N_1^2 \right\}. \quad \text{(A.372)}$$

Here we note that the moment acting on the flexure at the center of the lever, M_{Flex}, is the product of the force acting on the center of the hammerhead, F, and the distance from the center of the hammerhead to the center of the lever arm, $(N_2 + d_3)$, or:

$$M_{Flex} = F \cdot (N_2 + d_3). \quad \text{(A.373)}$$

We can now write an expression for the rotational spring constant of a single flexure by combining Equation A.372 and Equation A.373 as follows:

$$k_{M\theta Flex} = \frac{M_{Flex}}{\theta} = \frac{F \cdot (N_2 + d_3)}{\frac{24 \cdot F}{E \cdot t \cdot w_{b1}^3} \left\{ N_1^{\frac{3}{2}} \cdot N_2^{\frac{1}{2}} - N_1^2 \right\}} \quad \text{(A.374)}$$

$$k_{M\theta Flex} = \frac{E \cdot t \cdot w_{b1}^3 \cdot (N_2 + d_3)}{24 \left\{ N_1^{\frac{3}{2}} \cdot N_2^{\frac{1}{2}} - N_1^2 \right\}}. \quad \text{(A.375)}$$

Now combining Equations A.362, A.367, A.372, and A.354 we have:

$$v_{F_{Tot}} = \frac{8 \cdot F}{E \cdot t \cdot w_{b1}^3} \left\{ N_1^3 - N_1^{\frac{3}{2}} \cdot d^{\frac{3}{2}} \right\} + \frac{8 \cdot F}{E \cdot t \cdot w_{b1}^3} \left\{ N_1^{\frac{3}{2}} \cdot N_2^{\frac{3}{2}} - N_1^{\frac{3}{2}} \cdot d^{\frac{3}{2}} \right\} -$$

$$(N_2 + d_3) \cdot \frac{24 \cdot F}{E \cdot t \cdot w_{b1}^3} \left\{ N_1^{\frac{3}{2}} \cdot N_2^{\frac{1}{2}} - N_1^2 \right\} = 0 \quad \text{(A.376)}$$

$$N_1^3 - N_1^{\frac{3}{2}} \cdot d^{\frac{3}{2}} + N_1^{\frac{3}{2}} \cdot N_2^{\frac{3}{2}} - N_1^{\frac{3}{2}} \cdot d^{\frac{3}{2}} - (N_2 + d_3) \cdot 3 \cdot \left[N_1^{\frac{3}{2}} \cdot N_2^{\frac{1}{2}} - N_1^2 \right] = 0 \quad \text{(A.377)}$$

$$N_1^3 - 2N_1^{\frac{3}{2}}d^{\frac{3}{2}} + N_1^{\frac{3}{2}}N_2^{\frac{3}{2}} - 3N_1^{\frac{3}{2}}N_2^{\frac{3}{2}} + 3N_1^2N_2 - 3d_3N_1^{\frac{3}{2}}N_2^{\frac{1}{2}} + 3d_3N_1^2 = 0 \qquad \text{(A.378)}$$

$$N_1^3 - 2N_1^{\frac{3}{2}}d^{\frac{3}{2}} - 2N_1^{\frac{3}{2}}N_2^{\frac{3}{2}} + 3N_1^2N_2 - 3d_3N_1^{\frac{3}{2}}N_2^{\frac{1}{2}} + 3d_3N_1^2 = 0\ . \qquad \text{(A.379)}$$

Dividing both sides by $N_1^{\frac{3}{2}}$ yields:

$$N_1^{\frac{3}{2}} - 2d^{\frac{3}{2}} - 2N_2^{\frac{3}{2}} + 3N_1^{\frac{1}{2}}N_2 - 3d_3N_2^{\frac{1}{2}} + 3d_3N_1^{\frac{1}{2}} = 0\ . \qquad \text{(A.380)}$$

Here we will once again employ Newton's Method to solve this nonlinear equation numerically. So, we define this equation as the function, $f(N_1)$, as follows:

$$f(N_1) = N_1^{\frac{3}{2}} - 2d^{\frac{3}{2}} - 2N_2^{\frac{3}{2}} + 3N_1^{\frac{1}{2}}N_2 - 3d_3N_2^{\frac{1}{2}} + 3d_3N_1^{\frac{1}{2}}\ . \qquad \text{(A.381)}$$

Now taking the first derivative of this function with respect to N_1:

$$f'(N_1) = \frac{3}{2}N_1^{\frac{1}{2}} + \frac{3}{2}N_1^{-\frac{1}{2}}N_2 + \frac{3}{2}d_3N_1^{-\frac{1}{2}}\ . \qquad \text{(A.382)}$$

The value of N_1 will be found by selecting values for N_2, d, and, d_3 and taking a guess for the value of N_1. Then the designer will iterate N_1 as follows until the value has adequately converged:

$$N_{1_{New}} = N_{1_{Old}} - \frac{f\left(N_{1_{Old}}\right)}{f'\left(N_{1_{Old}}\right)}\ . \qquad \text{(A.383)}$$

Now that we have N_1, N_2, d, and d_3, we turn our attention back to Equation A.375 and solve for the width of the N_1 flexure, w_{b1}, as follows:

$$w_{b1} = \left[\frac{24 \cdot k_{M\theta Flex} \cdot \left(N_1^{\frac{3}{2}} \cdot N_2^{\frac{1}{2}} - N_1^2\right)}{E \cdot t \cdot (N_2 + d_3)}\right]^{\frac{1}{3}}. \quad \text{(A.384)}$$

Finally, we use Equation A.361 to find w_{b2} and complete the design of the Tapered Flexure Lever APLM.

Appendix B. Mesh Sensitivity Studies

Appendix B presents the results of the mesh sensitivity studies. The first section provides the mesh sensitivity study that was performed for the fillet investigation documented in Chapter III and the second section provides the mesh sensitivity study that was performed for the concentric mass FEAs documented in Chapter IV and the dual-mass resonator FEAs documented in Chapter V.

B.1 Mesh Sensitivity Study for the Fillet Investigation

To determine the mesh settings to use for the fillet study documented in Section 3.3, several mesh parameters were investigated. These included:

Mesh Type – *Extruded Bricks*, and *Tetrahedrons*,

Algorithm – *Hex-Dominant*, *Pave and QMorph*, and *Split and Merge*,

Element Order – *Parabolic*,

Element Size – in both the *Planar* and *Extrude* directions,

Edge Refinement Index – *0*, *1*, *2*, and *3*,

Maximum Curvature Discretization Error – *0.01*, *0.05*,

Minimum Elements Per Edge – *unspecified* up to *4*,

Minimum Element Size – *0.1*, and

Small Feature Removal Threshold – *0.1*.

The *Extruded Bricks* mesh operates by first creating a surface mesh of quadrilaterals and then extruding them through the thickness of the device to create a

volume mesh of hexahedrals. The *Tetrahedrons* mesh type directly creates a volume mesh of tetrahedrons. While it is generally recommended to use the *Tetrahedrons* mesh type for complex geometries that do not lend themselves to the *Extruded Bricks* approach, it was also known that the *Tetrahedrons* meshing algorithm has historically had difficulties generating meshes for curved geometries. Therefore, the *Tetrahedrons* mesh type was briefly investigated and showed similar results to the *Extruded Bricks* mesh type with a similar number of volume elements for the straight tuning fork configuration. So, the *Extruded Bricks* mesh type was selected for the fillet study.

There were three surface meshing algorithms investigated to generate the surface mesh to be extruded with the *Extruded Bricks* mesher. The *Hex-Dominant* algorithm uses predominantly hexahedral elements but will employ wedges when hexahedral elements are not possible or create poor geometries. The *Pave and QMorph* algorithm starts from the boundary of an extrude face and paves the surface with an unstructured, quadrilateral mesh moving inward. The *Split and Merge* algorithm uses Delaunay triangulation on the extrude face to generate a 2-D mesh from which quadrilaterals are formed using a series of merge, splits, edge swaps, and similar operations. While the *Hex-Dominant* algorithm generally creates the highest quality meshes, the *Split and Merge* algorithm has a much higher probability of producing a mesh for curved models and was desired for the tapered flexure models.

The mesher supports both *Linear* and *Parabolic* order elements. *Linear* elements have nodes only on the vertexes of the elements creating 8-node bricks, while *Parabolic* elements have nodes on each of the vertexes, but adds one node in the center of each element edge, one node in the center of each element face, and a node at the element

center to give a 27-node brick. *Parabolic* elements are also known as *Quadratic* elements. All meshes used for the fillet study employed *Parabolic* elements.

The *Element Size* in both the *Planar* and *Extrude* directions sets a soft upper bound on the length of the elements in that direction. It is possible that some elements could be up to twice the specified size, especially with the *Split and Merge* algorithm. *Planar* element sizes from *unspecified* down to 5 µm and *Extrude* element sizes from 15 to 20 µm were evaluated in this mesh sensitivity analysis for the fillet study.

The *Edge Refinement Index* creates a refined mesh towards the boundaries of the model. This option forces the lengths of the element edges to be proportional to the total length of that model edge. The range of values is from *0* to *3*, with *0* being no refinement and *3* being the maximum refinement. All possible settings of the *Edge Refinement Index* were evaluated as a part of this mesh sensitivity analysis.

The *Maximum Curvature Discretization Error* setting controls the accuracy of the mesh in curved portions of the model faces. Figure B.1 shows a graphical representation of the curvature discretization error. If a is the maximum distance between the model face and the element face, and b is the length of the element face, then the curvature discretization error is defined by the ratio of a/b. For parabolic elements, the parabolic vertices (*i.e.*, the midpoint of the element edges) are snapped to the true geometry of the model. Therefore, the dimension a may not occur in the center of an element edge. A range of values from *0.01* up to *0.05* was investigated for the mesh sensitivity analysis.

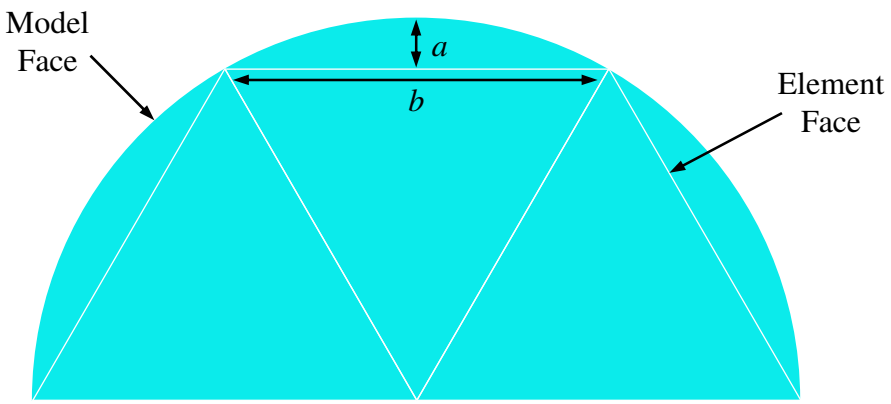

Figure B.1 Maximum Curvature Discretization Error Dimensions.

The *Minimum Elements Per Edge* option allows the user to specify the minimum number of elements required along the length of each of the model edges. The default value for this parameter is *2*, and the ranges of values explored for this mesh sensitivity study varied from *unspecified* up to *4*.

The *Minimum Element Size* option allows the user to specify the minimum allowable mesh size to prevent over refinement of the mesh especially when mesh refinement has been specified for curved surfaces. This value was set to 0.1µm for all meshes investigated in this mesh sensitivity study.

The *Small Feature Removal Threshold* option removes the mesh edges on model edges that are below the threshold. The smallest model feature in the fillet study was the fillet of 1µm radius. There should be no model edges smaller than what would be required to represent that 1µm radius. Therefore, this value was set to one-tenth of that value, 0.1µm, for all meshes investigated in this mesh sensitivity study.

The mesh sensitivity study involved investigating these mesh parameters on two models including one straight flexure tuning fork and one tapered flexure tuning fork. All models used flexure lengths of 300µm and equivalent flexure widths of 10µm. Both

tuning forks employed fillets with 8µm radius. Solid model renderings of these structures are provided in Figure B.2 and Figure B.3, for the straight and tapered flexure tuning fork models, respectively.

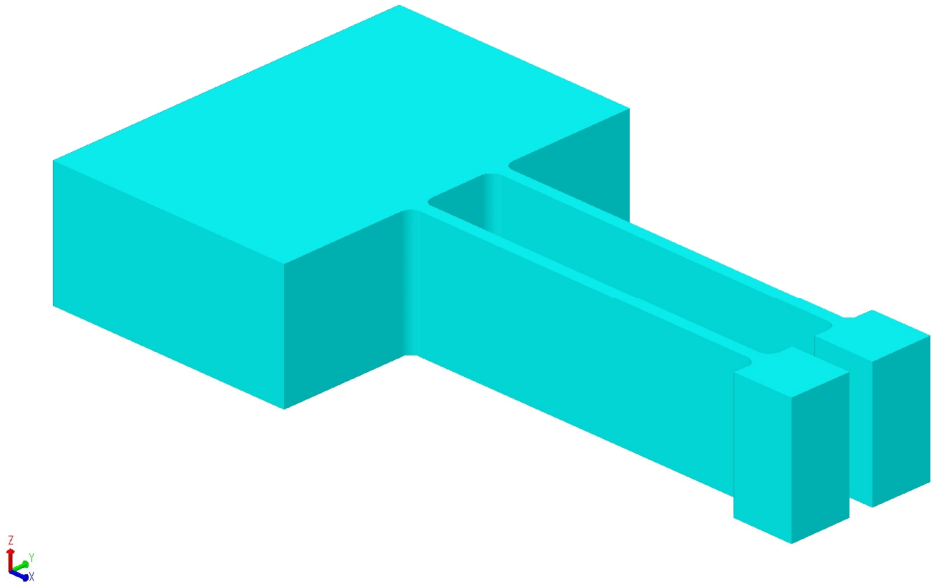

Figure B.2 Straight Tuning Fork Model for Mesh Study.

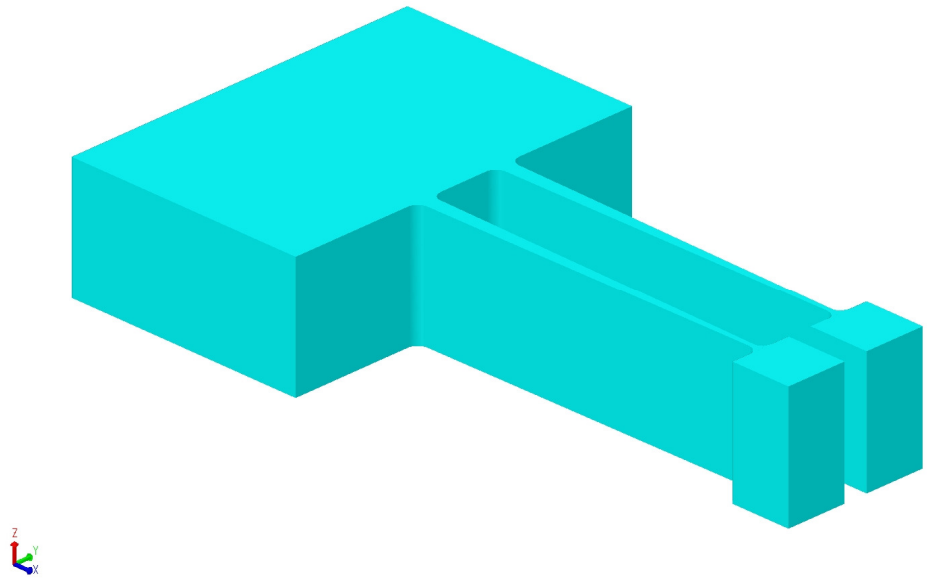

Figure B.3 Tapered Tuning Fork Model for Mesh Study.

For the purposes of this mesh sensitivity study, the outer hammerhead faces were pressure loaded using a *LoadPatch* boundary condition and the deflection of the tuning fork in the y-axis direction was used as the primary mesh sensitivity metric. The surfaces that were given the *LoadPatch* boundary conditions are highlighted in Figure B.4 and Figure B.5. These surfaces were loaded with a 1kPa pressure load for all analyses in this mesh sensitivity study. The model was anchored at the bottom of the insulation layer by giving that surface a *FixAll* boundary condition as shown in Figure B.6. Other metrics used in this mesh sensitivity study included the number of volume elements in the mesh and the time required for the solver to converge on a solution.

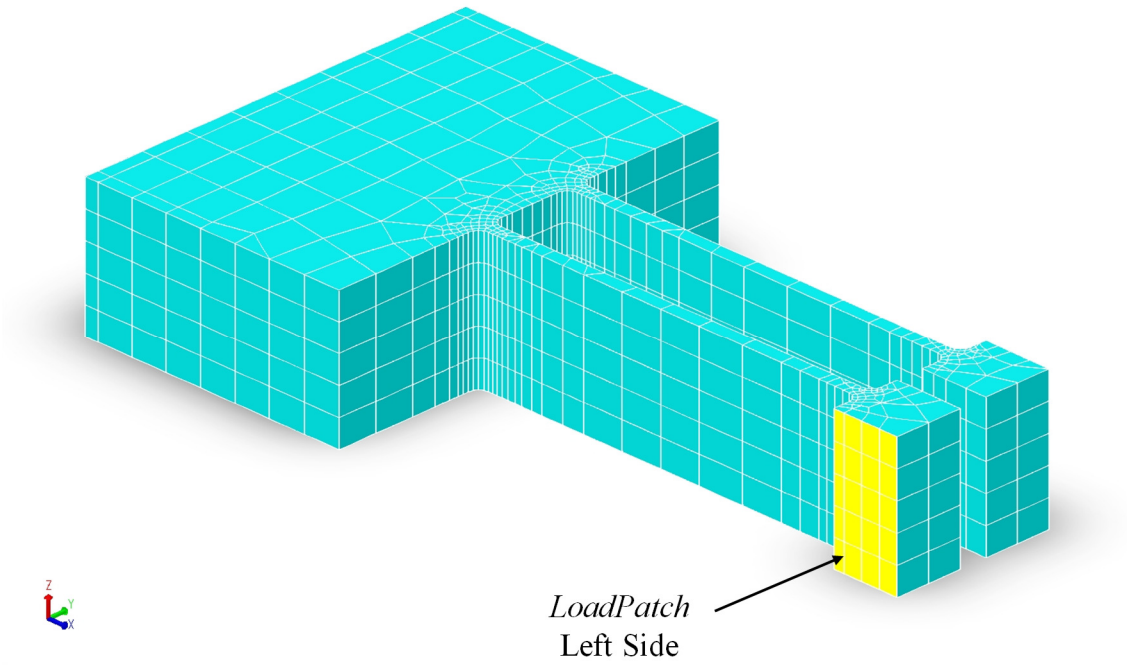

Figure B.4 Left Side *LoadPatch* Surface for Fillet Mesh Sensitivity Study.

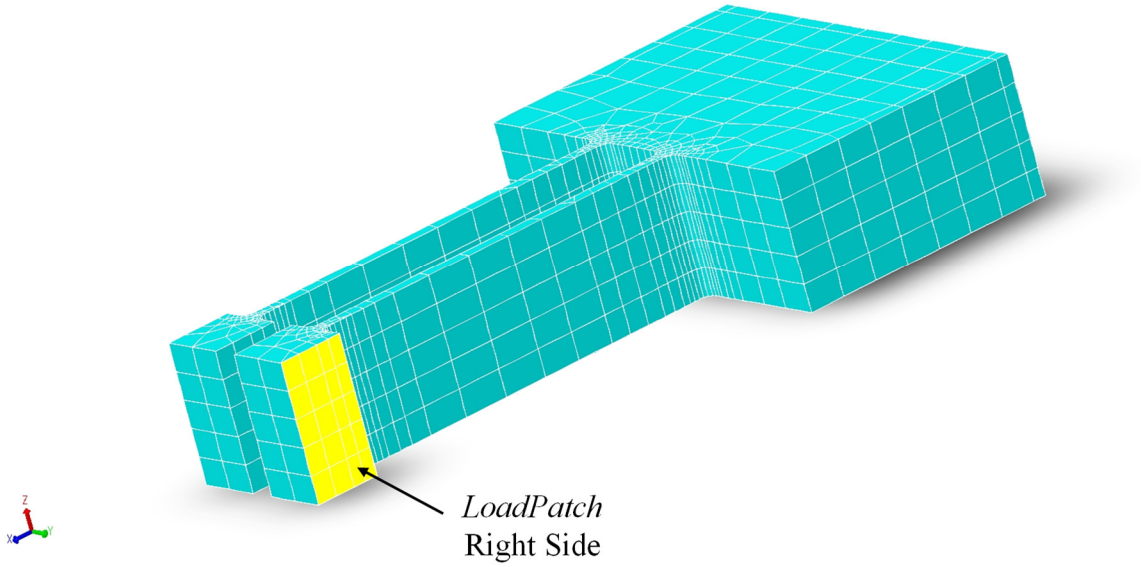

Figure B.5 Right Side *LoadPatch* Surface for Fillet Mesh Sensitivity Study.

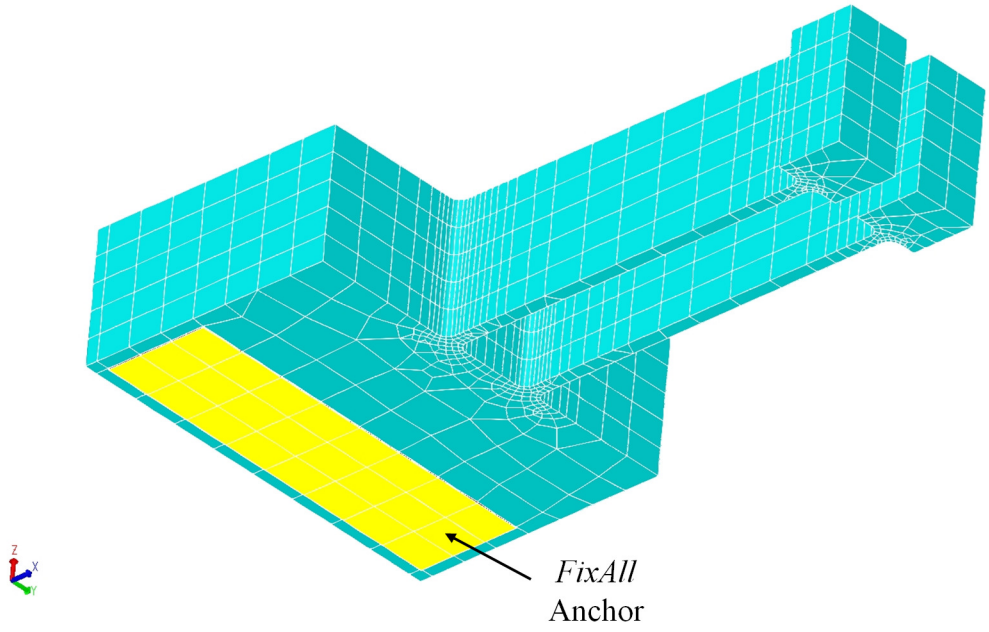

Figure B.6 *FixAll* Anchor Surface for Fillet Mesh Sensitivity Study.

The results of the mesh sensitivity study are summarized in Table B.1 and Table B.2 for the straight flexure tuning fork and the tapered flexure tuning fork models, respectively. The majority of the mesh study was performed on the straight flexure tuning fork using the *Hex-Dominant* paving algorithm because that algorithm generally provides the highest quality meshes using predominantly hexahedral elements. An initial value of 5µm was chosen for the *Planar Element Size* because that was the best method to ensure that there were two elements across the width of the flexure. An initial *Extrude Element Size* of 20µm was chosen based on prior experience which indicated that 5 elements in the extrude direction gave better results than 4 elements in the extrude direction. An initial *Edge Refinement Index* of *0* was chosen because it was known that the mesh study would explore all possible values for this parameter. An initial value of *0.05* (*5%*) was chosen for the *Maximum Curvature Discretization Error* based on the

somewhat arbitrary assessment that it was desired for this criterion to be a little better than one order of magnitude (*i.e.*, lower that *0.1* or *10%*). An initial value of *4* was chosen for the *Minimum Elements Per Edge* to ensure that every edge had at least *4* elements, which was largely driven by the desire to accurately capture the stress gradients on either side of the fillets. The progression of mesh refinement is discussed in the following paragraphs.

Table B.1 Straight Flexure Tuning Fork Mesh Study Settings and Results.

Mesh #	Algorithm	Planar Element Size (μm)	Extrude Element Size (μm)	Edge Refinement Index	Maximum Curvature Discretization Error	Minimum Elements per Edge	# of Volume Elements	Y-displacement (μm)	Solution Time (hh:mm:ss)
1	Hex-Dominant	5	20	0	0.05	4	15621	0.04358	0:01:25
2	Hex-Dominant	5	20	0	0.05	Unspec.	15496	0.04358	0:01:32
3	Hex-Dominant	5	20	1	0.05	Unspec.	15496	0.04358	0:01:36
4	Hex-Dominant	5	20	2	0.05	Unspec.	31067	0.04358	0:03:05
5	Hex-Dominant	5	20	3	0.05	Unspec.	46625	0.04359	0:04:45
6	Hex-Dominant	Unspec.	20	3	0.05	Unspec.	1759	0.04355	0:00:09
7	Hex-Dominant	5	20	3	0.01	Unspec.	50110	0.04359	0:05:17
8	Split and Merge	5	20	3	0.01	Unspec.	45390	0.04358	0:04:27
9	Split and Merge	5	15	3	0.01	Unspec.	62642	0.04360	0:07:00
10	Split and Merge	10	20	3	0.01	Unspec.	16756	0.04356	0:01:34

Table B.2 Tapered Flexure Tuning Fork Mesh Study Settings and Results.

Mesh #	Algorithm	# of Volume Elements	Y-displacement	Solution Time (hh:mm:ss)
1	Hex-Dominant	49635	0.04652	0:05:31
2	Pave, Q-Morph	63559	0.04652	0:06:27
3	Split and Merge	44930	0.04651	0:04:19

The first mesh refinement began with dropping the constraint of 4 for the *Minimum Elements Per Edge*. A comparison of the meshes with and without this constraint is shown in Figure B.7 (a) and (b), respectively, where the flexure meets the hammerhead. While this constraint did provide additional refinement in the fillet and in the area of the hammerhead near the fillet, the y-axis displacement results in Table B.1 indicate that this refinement did not significantly impact the analysis results. So, this constraint was not retained.

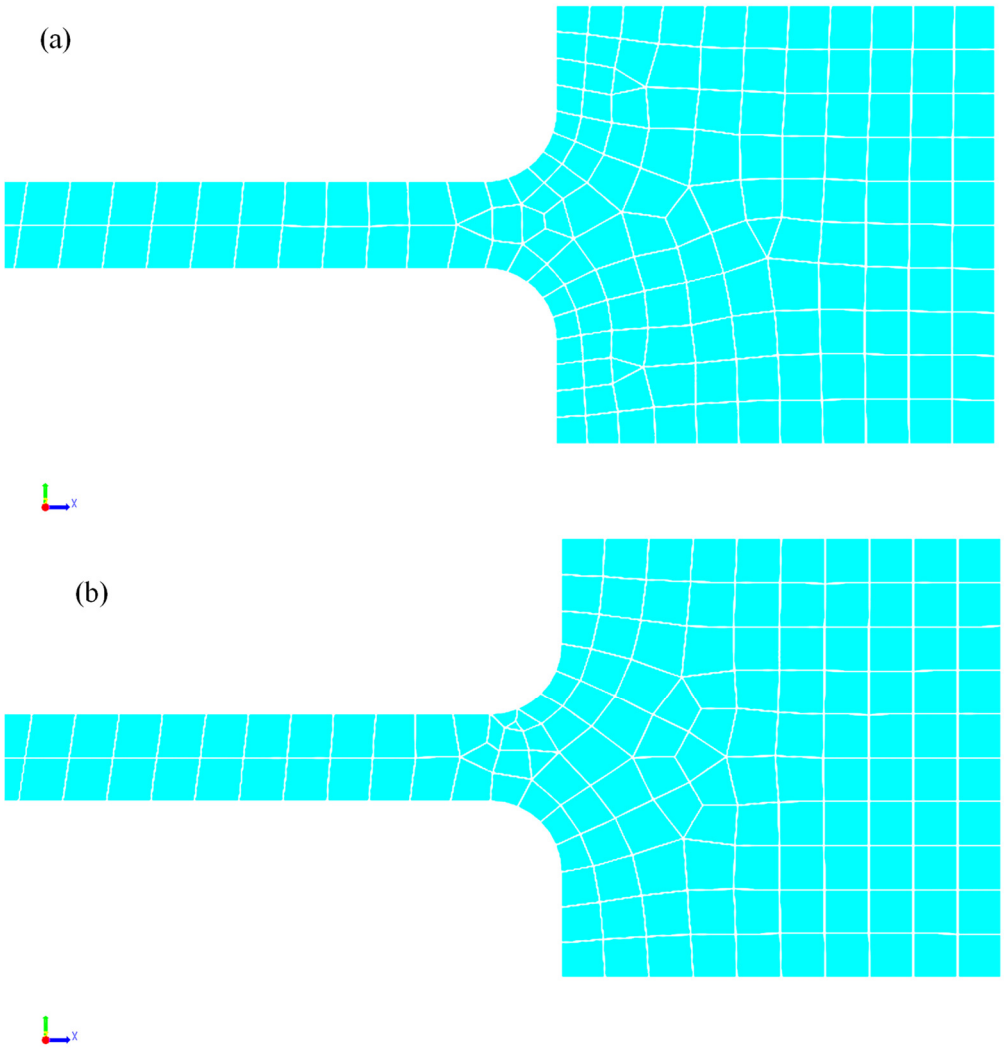

Figure B.7 Mesh with (a) and without (b) the *Minimum Elements Per Edge* Constraint.

The next mesh refinement investigated was the *Edge Refinement Index*. All four values of the *Edge Refinement Index* were explored and the resulting meshes near the hammerhead are pictured in Figure B.8. The data in Table B.1 and the images in Figure B.8 (a) and (b) indicate that there was no difference in the mesh for *Edge Refinement Index* values of *0* or *1*. There were, however, significantly increasing numbers of elements for *Edge Refinement Index* values of *2* and *3*, and Figure B.8 (c) and (d) shows significantly refined mesh around the fillets for the *Edge Refinement Index* values of *2* and *3*. Although there was no significant difference reported in the y-axis displacement between these meshes, it was decided to retain the *Edge Refinement Index* value of *3* to ensure adequate meshes for the smaller fillet sizes.

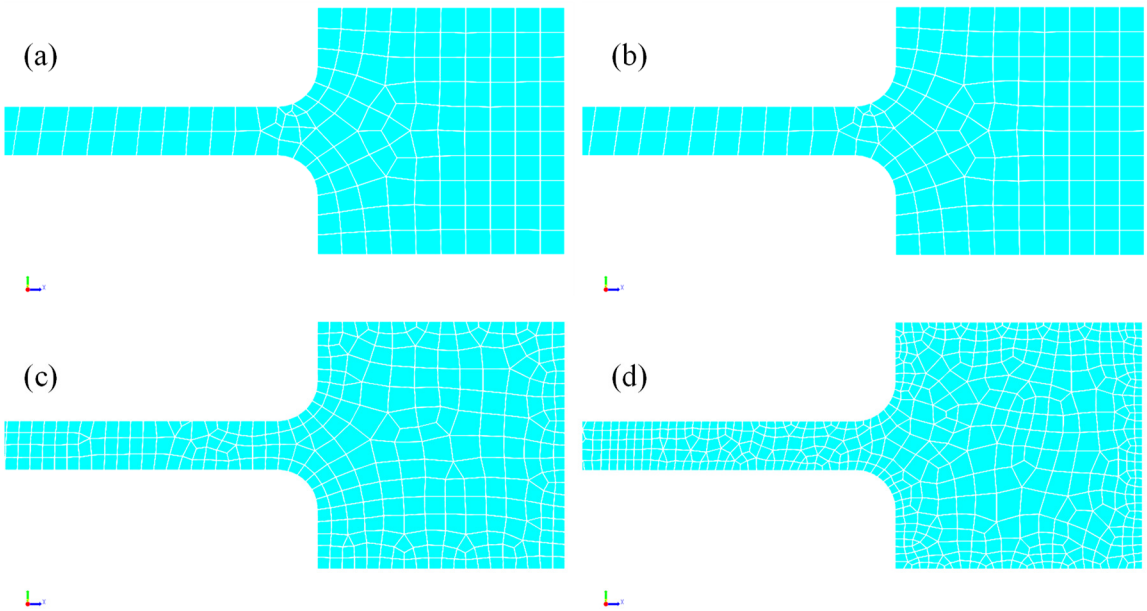

Figure B.8 Meshes with *Edge Refinement Index* Values of (a) *0*, (b) *1*, (c) *2*, and (d) *3*.

The next mesh adjustment investigated the quality of the mesh that resulted from removing the constraint on the *Element Size* in the *Planar* direction. A visual comparison

of the meshes where the flexures meet the hammerheads is provided in Figure B.9. The images in Figure B.9 indicate that there was a significant difference in mesh refinement in areas far away from the fillets, but these settings maintained a reasonable mesh density near the fillets. The FEA results in Table B.1 indicate that, although eliminating the *Minimum Element Size* specification in the *Planar* direction resulted in a mesh with 30 times fewer volume elements, the y-axis displacement only differed by 0.1% from the mesh with a specified value of 5µm. Even so, it seemed prudent to ensure there were at least two elements across the width of the flexure.

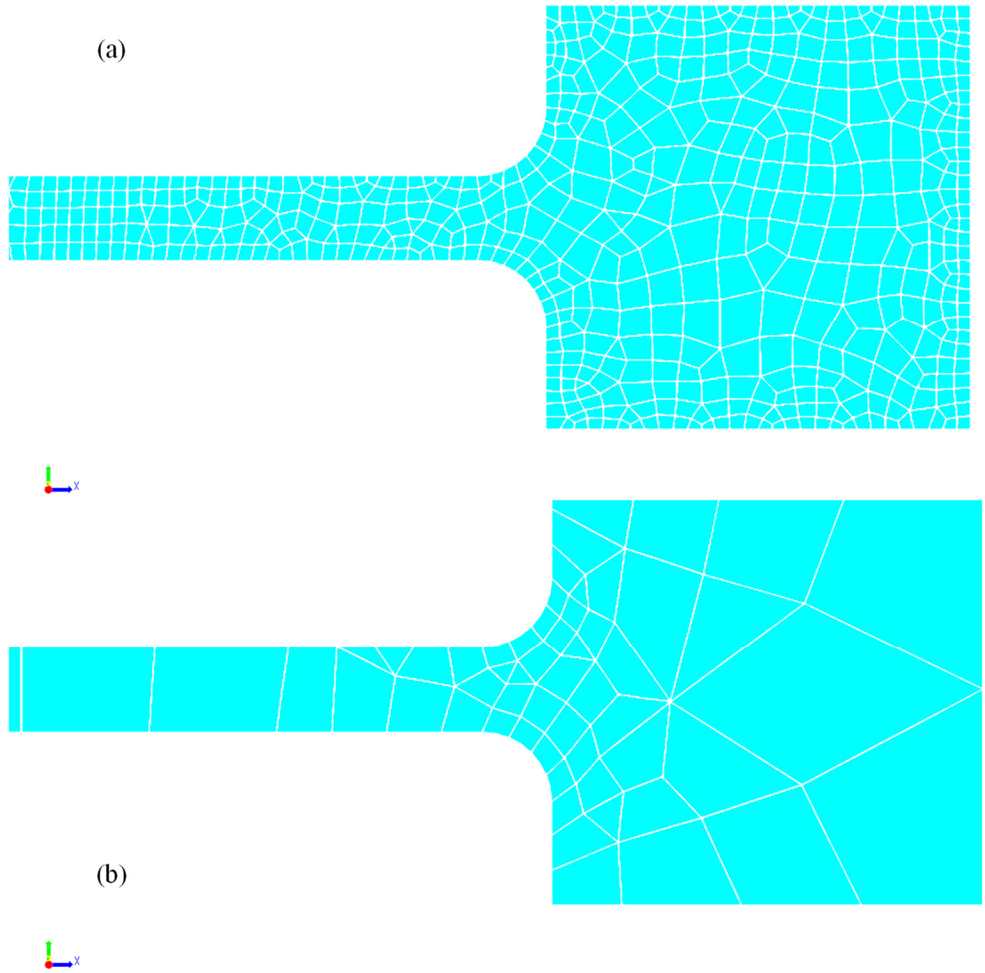

Figure B.9 Meshes with *Minimum Element Size* Values of (a) 5µm and (b) *Unspecified.*

The next mesh adjustment investigated a reduction in the *Maximum Curvature Discretization Error* to 0.01. A visual comparison of meshes 5 and 7 where the flexures meet the hammerheads is provided in Figure B.10. The images in Figure B.10 indicate that there was a significant increase in mesh refinement in areas near the fillets, but the FEA results in Table B.1 indicate that there was no change in the resulting y-axis displacement. So, with only roughly 10% increase in mesh elements, either setting would be acceptable, and the value of 0.01 was chosen.

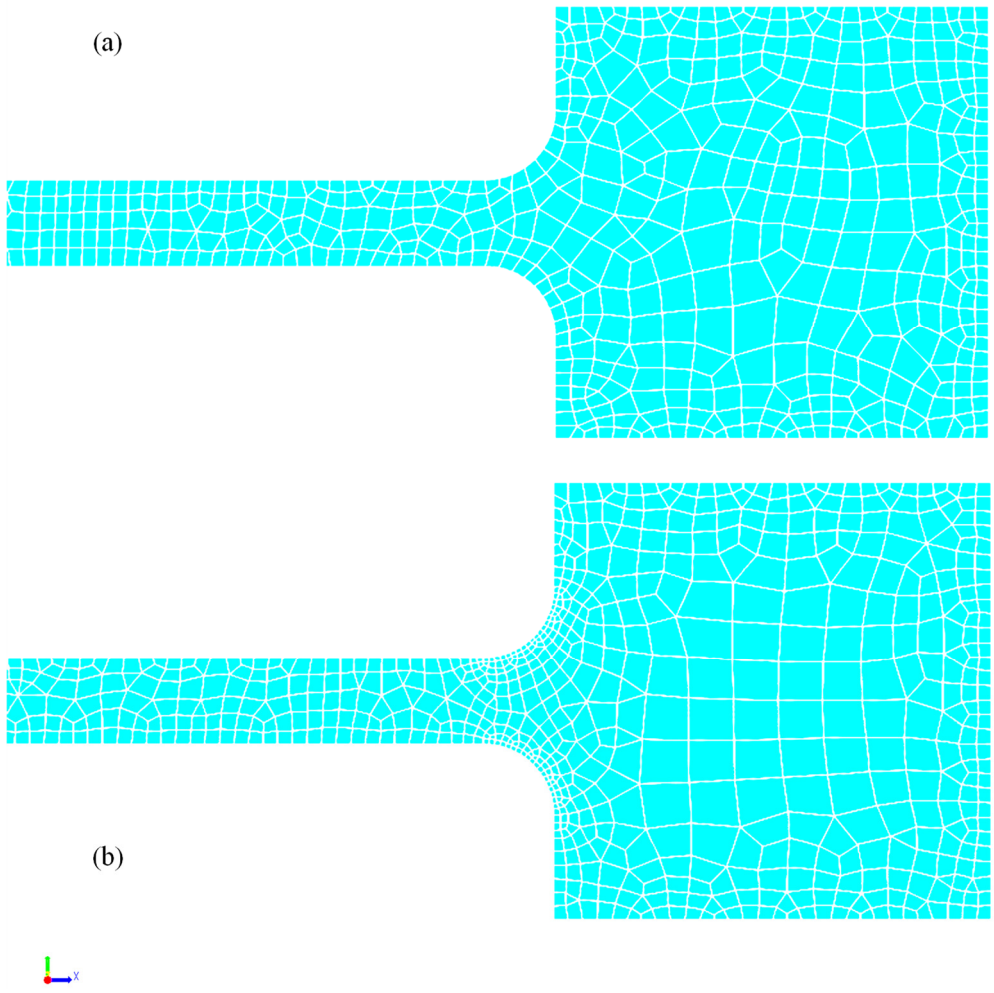

Figure B.10 Meshes with *Maximum Curvature Discretization Error* Values of (a) 0.05 and (b) 0.01.

The next investigation involved changing the paving algorithm to *Split and Merge*. A visual comparison of meshes 7 and 8 where the flexures meet the hammerheads is provided in Figure B.11. The images in Figure B.11 indicate that there was a significant increase in mesh refinement in the model edges in the fillets, but the FEA results in Table B.1 again indicate that there was no appreciable change in the resulting y-axis displacement. The *Split and Merge* paving algorithm also resulted in roughly 10% fewer mesh elements, and because this algorithm is more likely to return meshes for complicated (curved) geometries, this algorithm was selected.

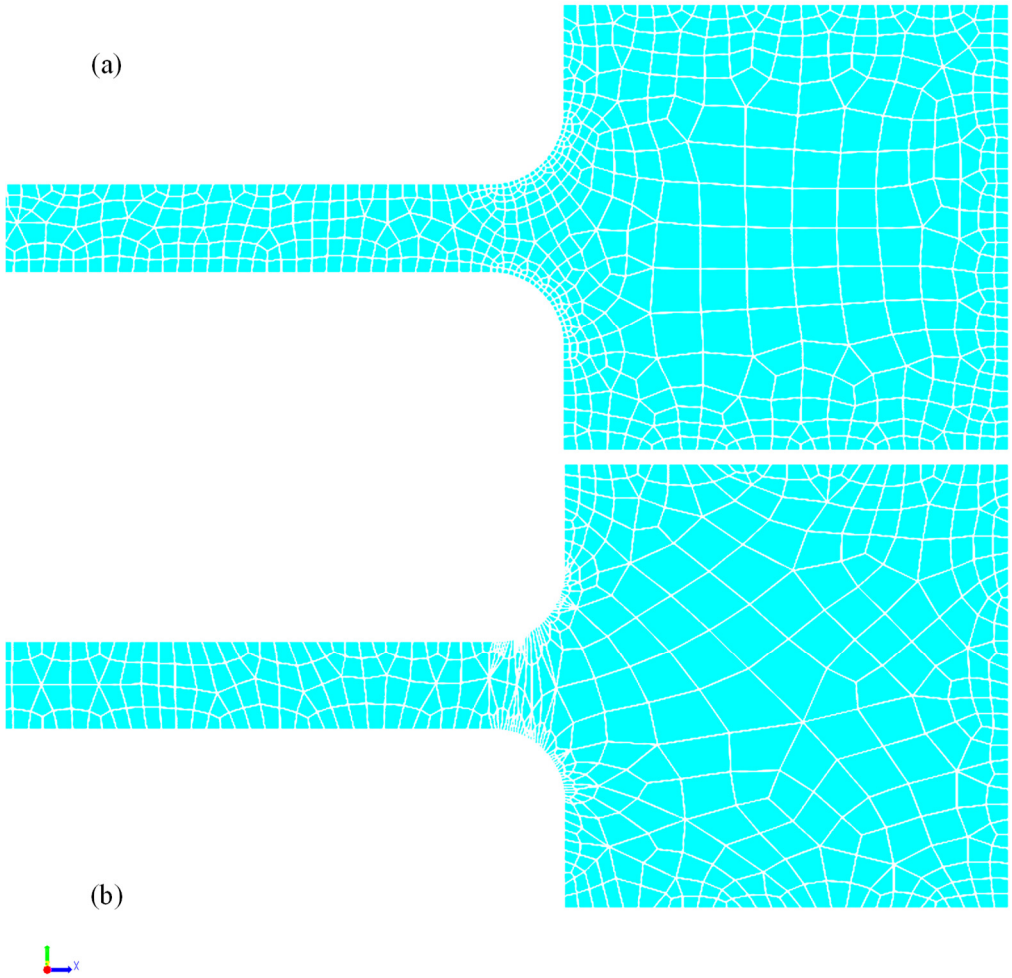

Figure B.11 Meshes from (a) *Hex-Dominant* and (b) *Split and Merge.*

While it was already decided that the *Edge Refinement Index* setting of *3* and the *Maximum Curvature Discretization Error* setting of *0.01* were going to be retained, it was desired to double-check the sensitivity to the *Minimum Element Size* settings while using the *Split and Merge* algorithm. So, mesh 9 set the *Minimum Element Size* in the *Extrude* direction to 15µm and mesh 10 set the *Minimum Element Size* in the *Planar* direction to 10µm. Figure B.12 and Figure B.13 provide a visual comparison of these three meshes, from the side view and the tope view of the hammerhead, respectively. Once again, the data in Table B.1 indicate that there was no appreciable difference in the y-axis displacement from any of these meshes. In fact, the results presented in Table B.1 indicate that, although the number of volume elements in the various meshes varied from 1,759 up to 62,642, there was no appreciable difference in the y-axis displacements and that any of these mesh settings would likely be adequate. Therefore, the mesher settings of mesh 8 were selected for the fillet study because they included (1) an algorithm that was the most likely to return a mesh for complex or curved geometries, (2) *Minimum Element Size* in the *Planar* direction that would ensure a minimum of two elements across the flexures, (3) the maximum *Edge Refinement Index* value to ensure stress gradients along the edges are adequately captured, and (4) an aggressive value for the *Maximum Curvature Discretization Error* of 0.01 (or 1%) to ensure accurate representation of the tapered flexures and fillets.

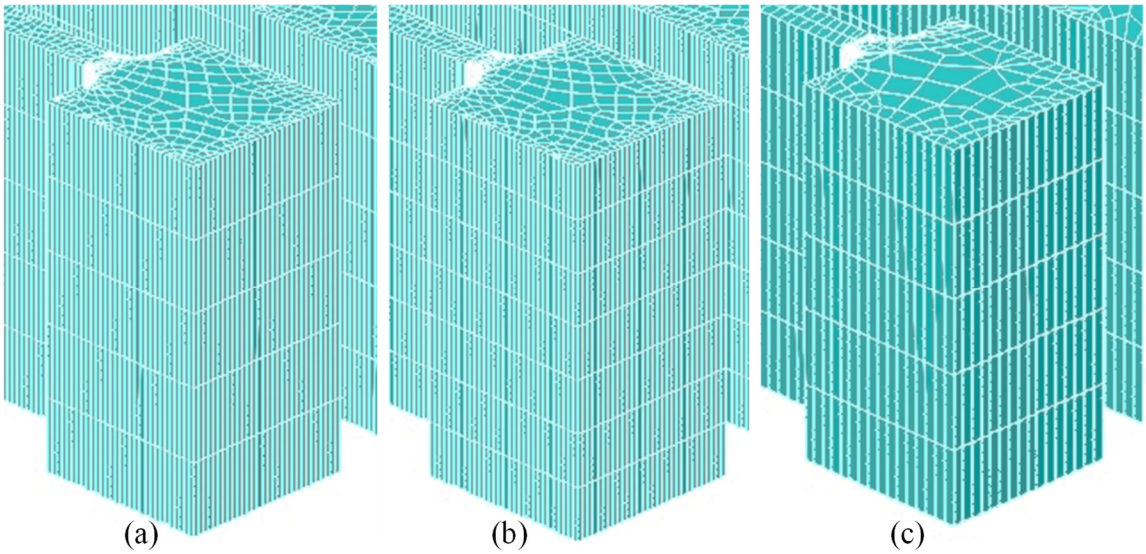

Figure B.12 Hammerhead Side View for Meshes with (a) Final Mesher Settings, (b) 15µm *Extrude Element Size*, and (c) 10µm *Planar Element Size.*

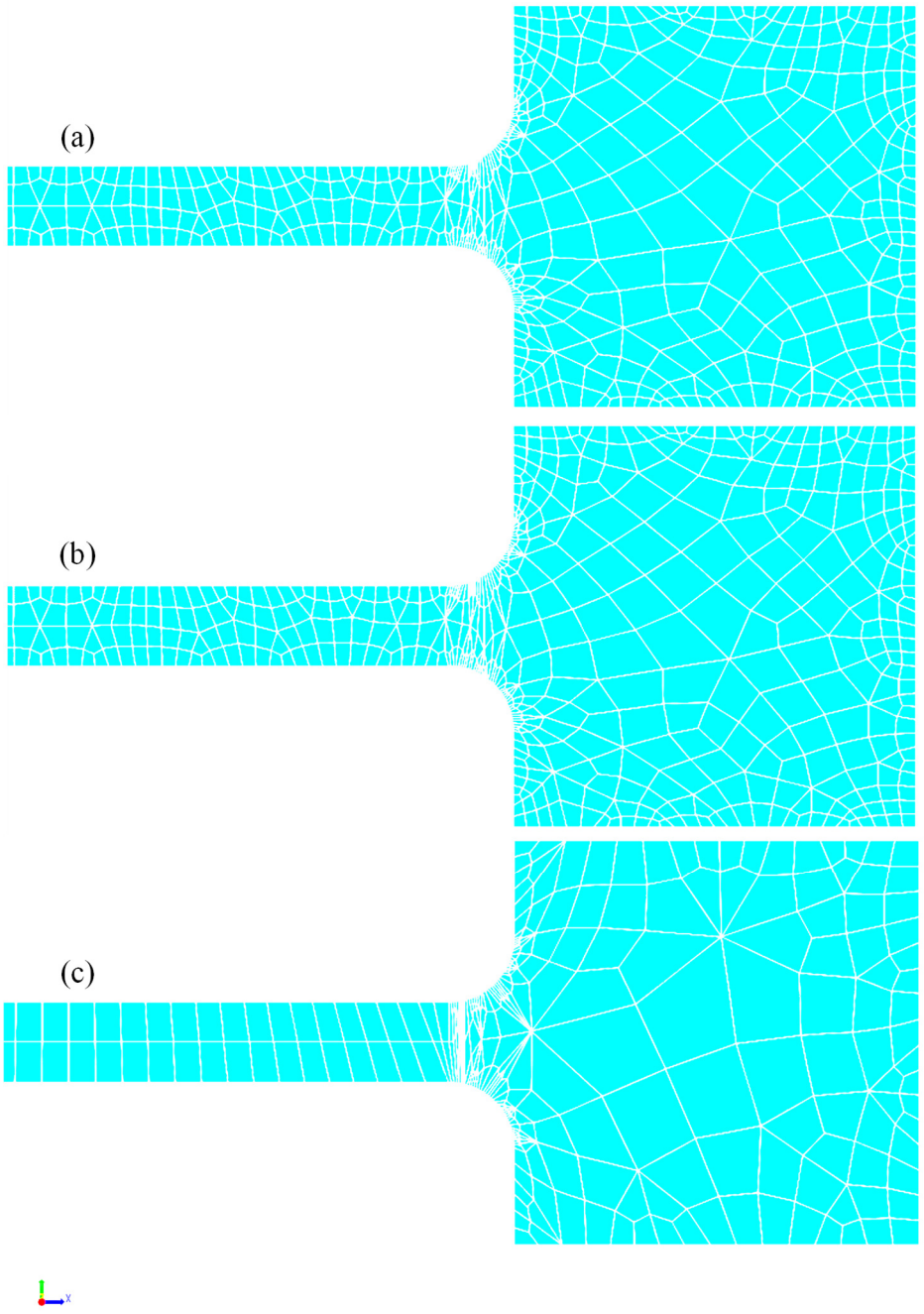

Figure B.13 Hammerhead Top View for Meshes with (a) Final Mesher Settings, (b) 15µm *Extrude Element Size*, and (c) 10µm *Planar Element Size*.

The final investigation performed in this mesh sensitivity study was to compare the three paving algorithms on the tapered flexure tuning fork using the final mesh refinement parameters from mesh 8 of the straight flexure tuning fork. The three paving

algorithms were *Hex-Dominant*, *Pave and QMorph*, *and Split and Merge*. The results of these FEAs were presented in Table B.2 and indicated very similar results from all three meshes. The number of volume elements varied from about 45,000 to about 64,000 and Solution times varied from a little over 4 minutes to about 6.5 minutes. Figure B.14 shows a visual comparison of the three meshes where the flexure meets the hammerhead. All three have high mesh density in the fillet area and adequate number of elements across the flexure. Any of these mesh algorithms would be acceptable but the *Split and Merge* algorithm was chosen because it has the most likely to return a mesh for complex or curved geometries such as those investigated in this fillet study.

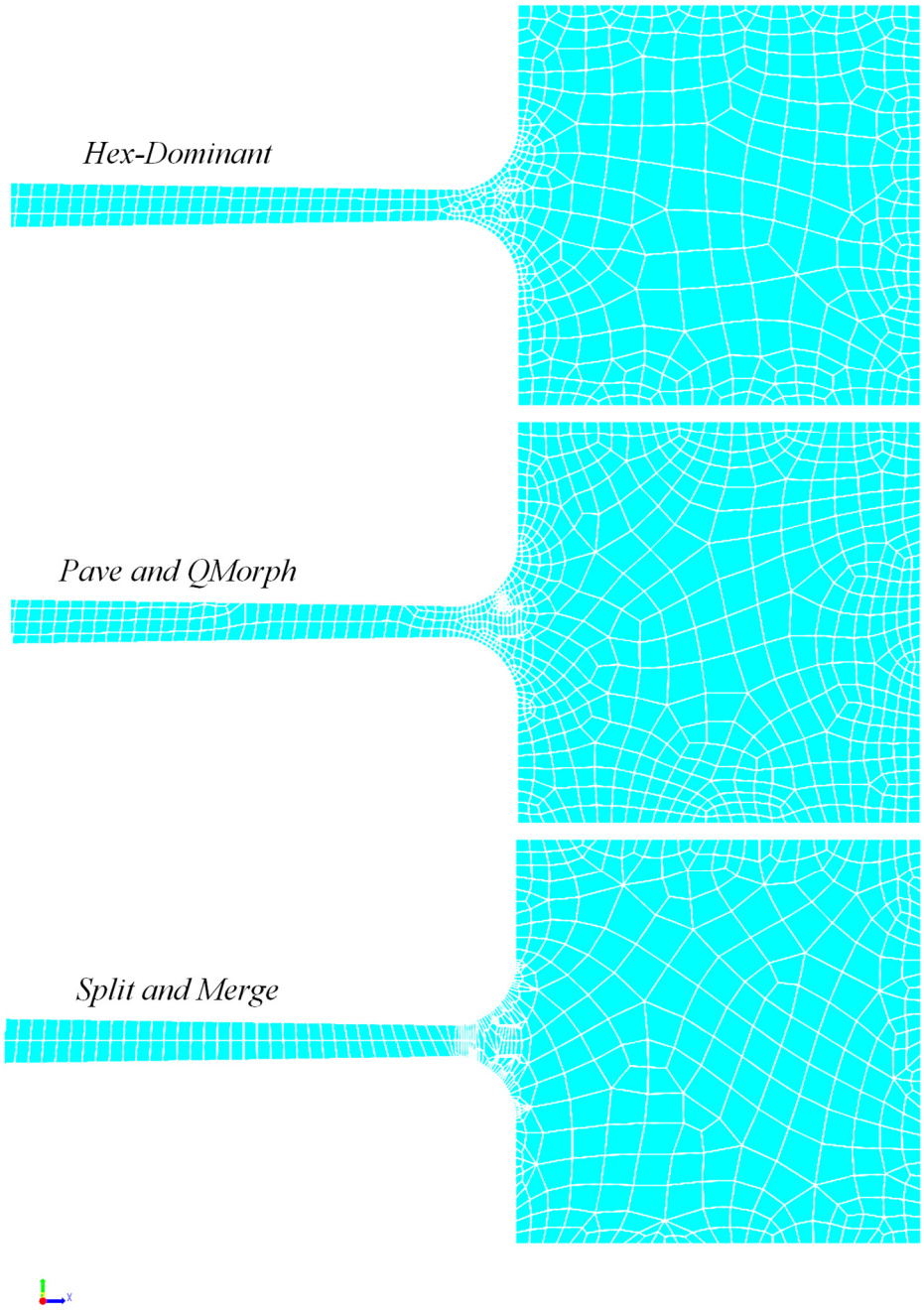

Figure B.14 Tapered Flexure Tuning Fork Meshes Using Various Paving Algorithms.

B.2 Dual Mass Resonator FEA Mesh Sensitivity Study

This section documents the mesh sensitivity study that was performed for the Anti-Phase Lever Mechanism (APLM) and dual mass resonator analyses that were documented in Section 4.2 and Section 5.2, respectively. This mesh sensitivity study was performed on one straight flexure version and one tapered flexure version of the dual mass resonator configuration and the resulting mesher settings were used in both sets of analyses.

The models used for this mesh study were based on the dual mass resonator configuration covered in Chapter V and a solid model rendering is provided in Figure B.15. For the purposes of the mesh study, no voltages would be applied to the electrodes. Therefore, simplified versions of the dual mass resonator solid models were used for the mesh study that eliminated the capacitive comb fingers. This resulted in the simplified solid model as shown in Figure B.16. The APLMs used in the models included one straight flexure and one tapered flexure version of the revised University of California at Irvine (UCI) inner lever coupling design each with an equivalent flexure width of 10µm. Solid model renderings of these APLMs are provided in Figure B.17 and Figure B.18 for the straight and tapered flexures, respectively. The coupler springs also included straight flexure and tapered flexure versions with equivalent flexure widths of 10µm. Solid model renderings of these coupler springs are provided in Figure B.19 and Figure B.20 for the straight and tapered flexures, respectively.

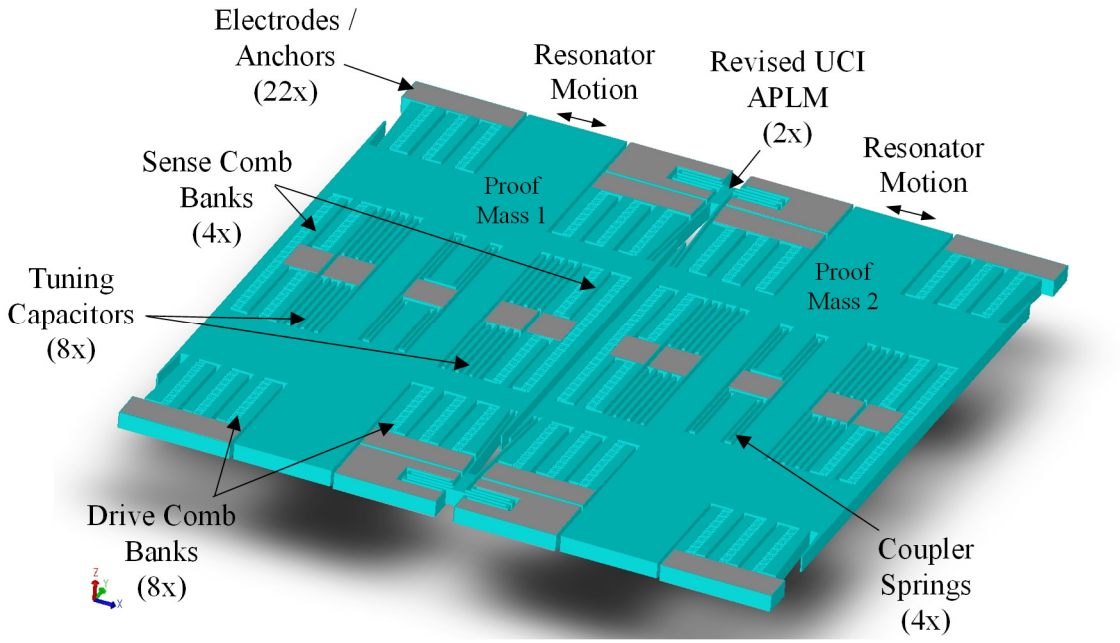

Figure B.15 Dual Mass Resonator Solid Model for Mesh Sensitivity Study.

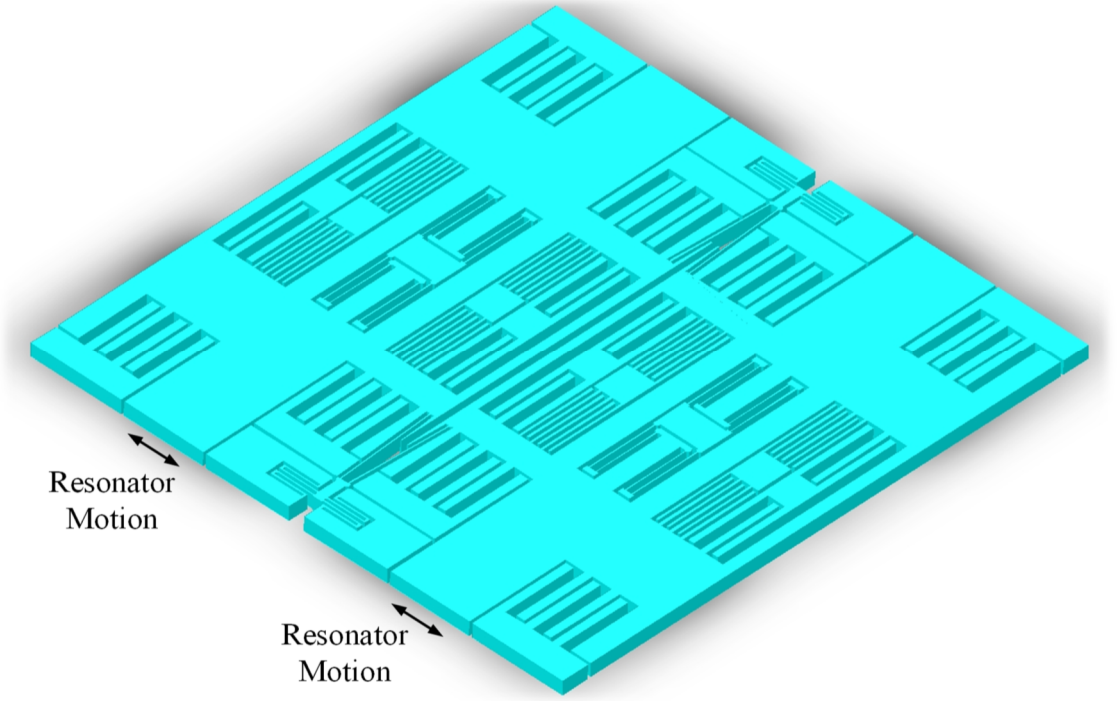

Figure B.16 Simplified Dual Mass Resonator Solid Model for Mesh Sensitivity Study.

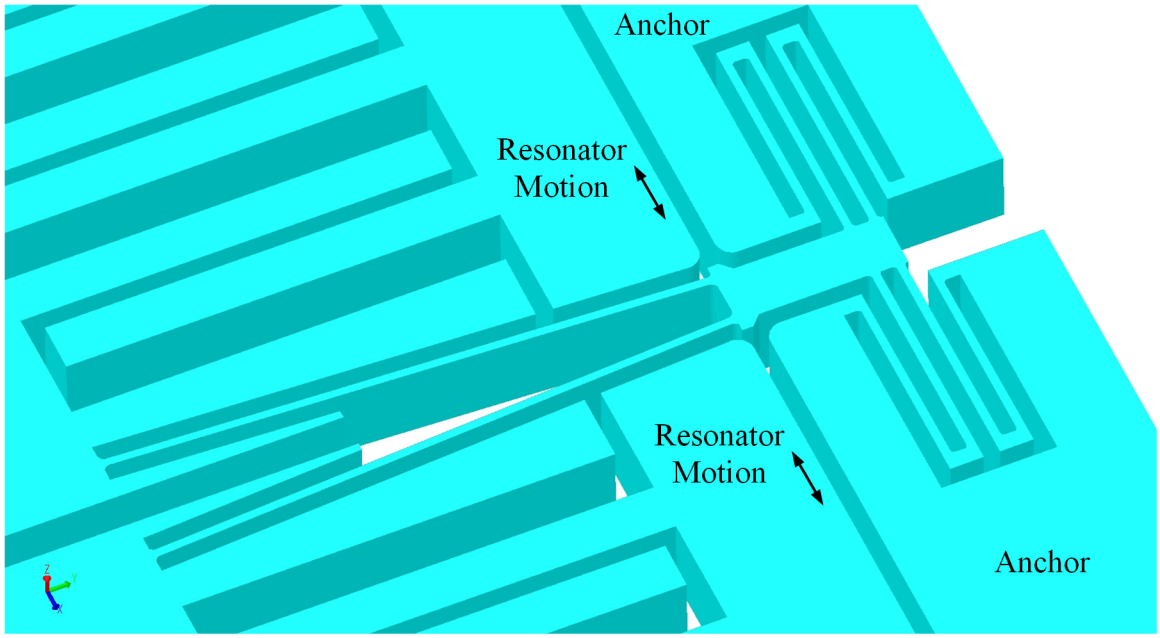

Figure B.17 Straight Flexure Revised UCI APLM Solid Model.

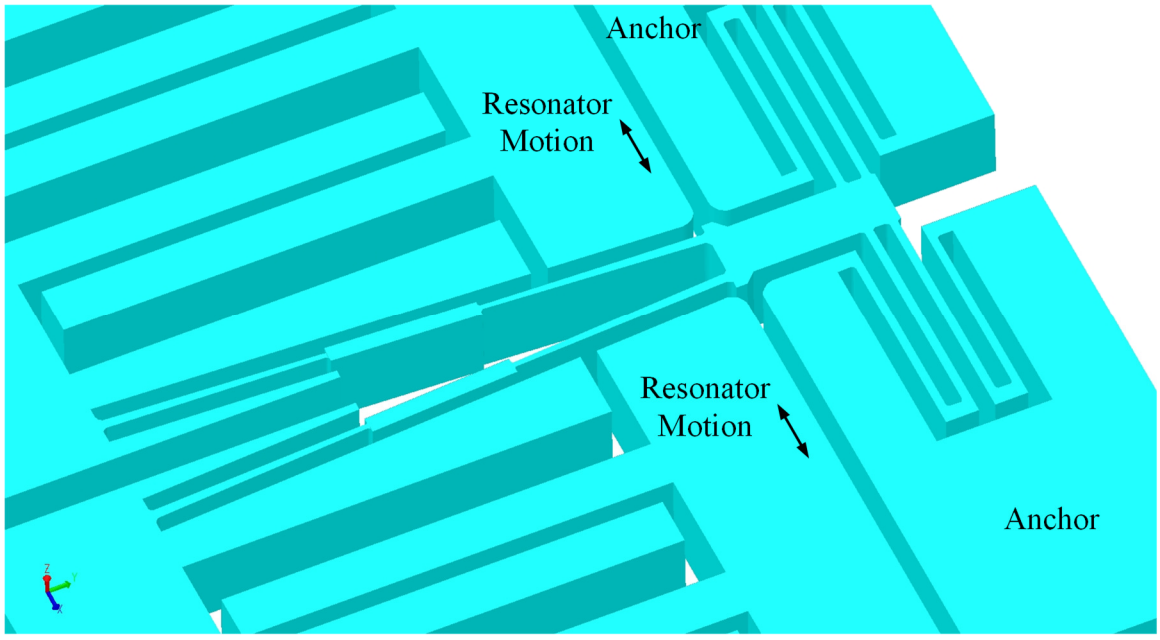

Figure B.18 Tapered Flexure Revised UCI APLM Solid Model.

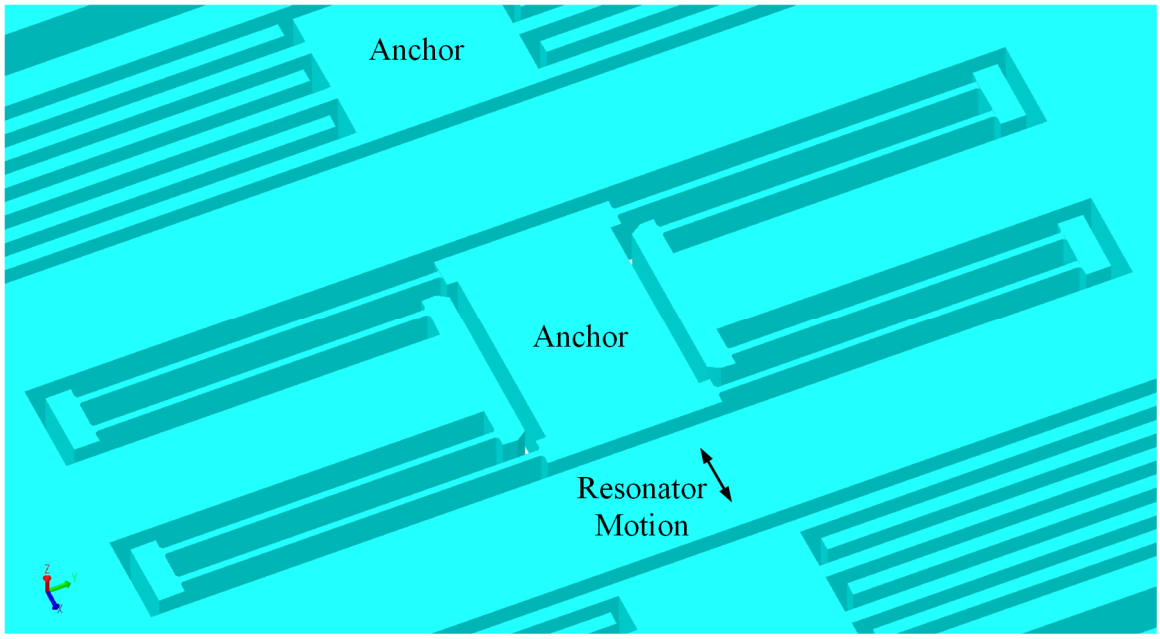

Figure B.19 Straight Flexure Coupler Springs Solid Model.

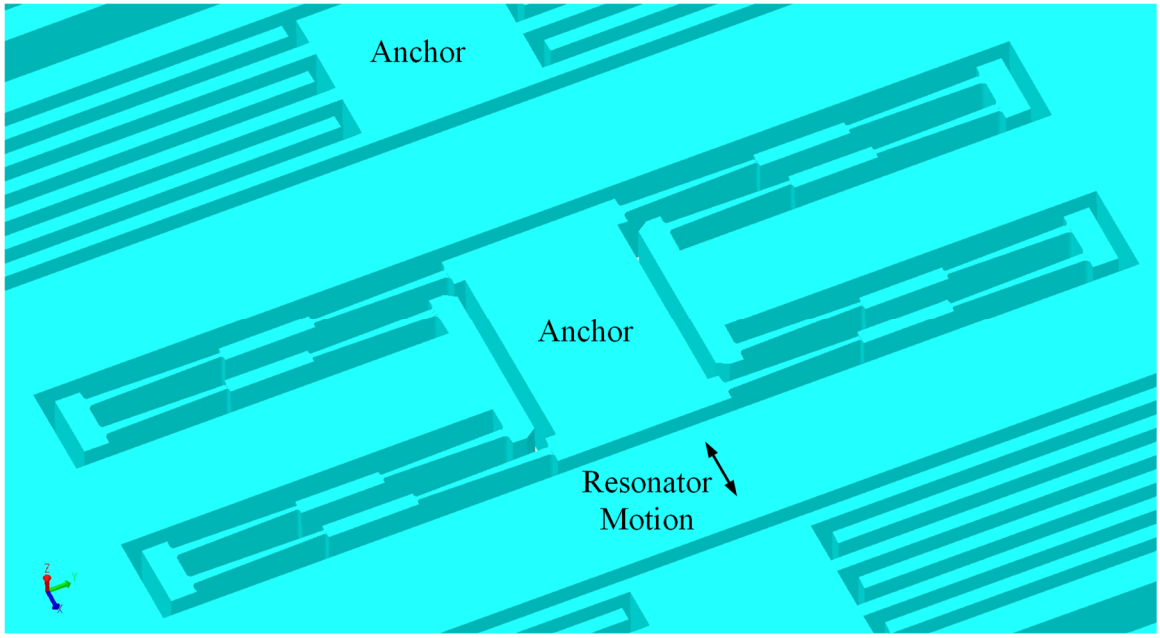

Figure B.20 Tapered Flexure Coupler Springs Solid Model.

There were two FEAs conducted on each model for each mesh. These included a modal analysis and a thermoelastic damping analysis. For the modal analysis the anti-phase resonant mode was tracked for convergence and for the thermoelastic damping analysis, the quality factor due to thermoelastic damping at the anti-phase resonant frequency was tracked for convergence. For the modal analysis and the thermoelastic damping analysis, the locations where the oxide layer contacted the substrate were given a *FixAll* boundary condition as shown in Figure B.21 and the solver was set to return the first 10 modes. The anti-phase mode was always the first mode returned by the solver. For the thermoelastic damping analysis, the solver was configured to estimate the thermoelastic damping losses at the anti-phase resonant frequency returned by the modal analysis as well as at one frequency just below and above that resonant frequency. The harmonic motion was set up by placing a pressure load of 0.1 Pa on one face of each of the masses in the dual mass resonator using a *LoadPatch* harmonic surface boundary condition. The two surfaces that were given this harmonic surface boundary condition are pictured in Figure B.22. This low of a pressure was necessary because quality factors in excess of one million were expected and the resulting displacements could easily be large enough to excite non-linearities in the materials if larger values of pressures were chosen.

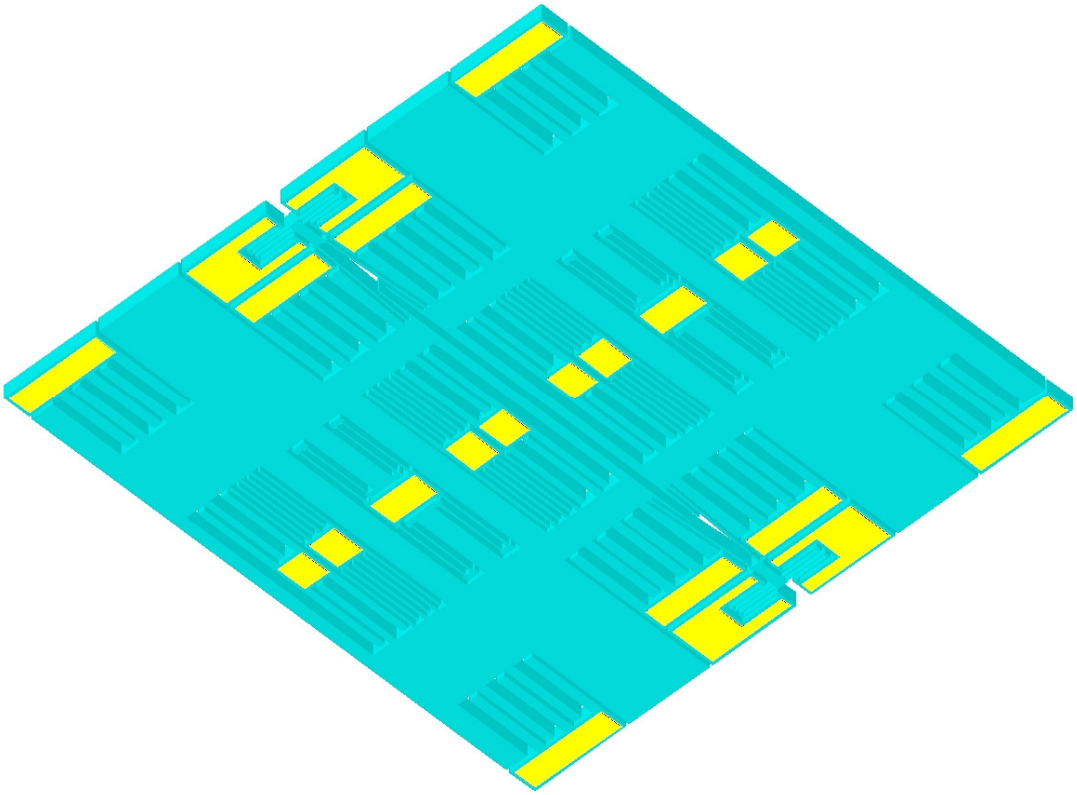

Figure B.21 Anchor Pad Locations for Modal and TED Analyses (Bottom View).

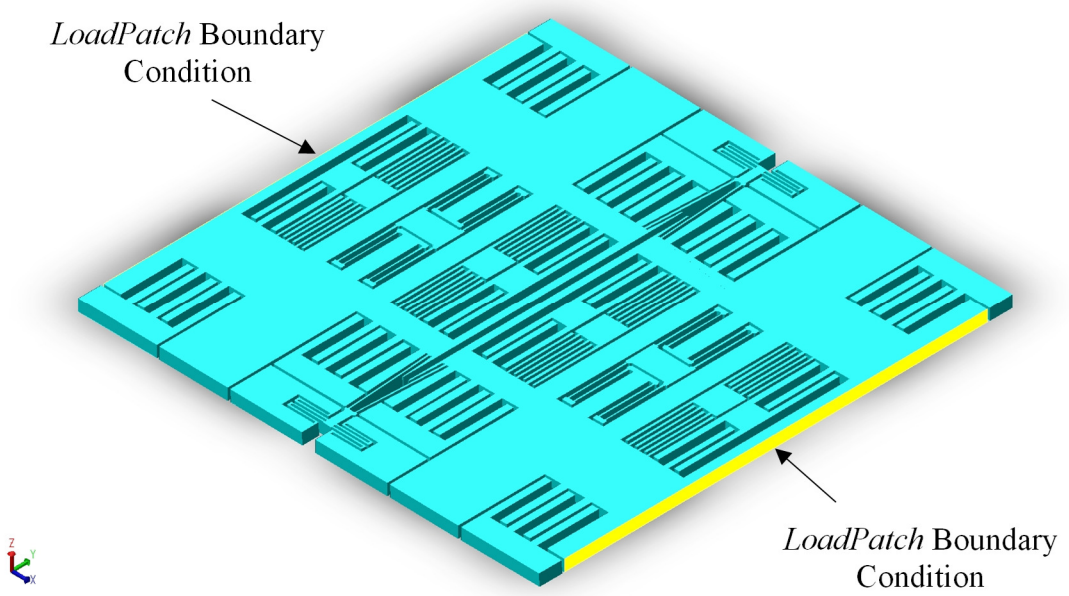

Figure B.22 Harmonic Boundary Condition Surfaces for TED Analysis.

There were two additional mesher settings employed for this analysis that were not employed in previous analyses. These are the extrude direction *Biasing* and *Bias Ratio*. These were employed because the stress gradients along the z-axis (the extrude direction) in previous analyses were noted to be higher toward the top and bottom of the device layer and were relatively constant toward the center, as shown in Figure B.23. The *Biasing* mesher option allows the user to specify where the user would like smaller elements and where the user would like larger elements along the extrude direction. The choices for this option are *None*, *Both Ends*, *Positive End*, *Negative End*, and *Center*. Based on the stress distribution in the flexures near the attachment blocks shown in Figure B.23, a *Biasing* option of *Both Ends* was chosen for all meshes in this analysis. The *Bias Ratio* specifies the ratio of the element sizes in the bias direction. The range of values for this option is 0.0 to 1.0. A value of 1.0 implies that the ratio of element sizes is one and therefore creates elements that are all the same size, which is the same as no

biasing. A *Bias Ratio* of 0.5 means that each element is half as big as the adjacent element. For the analyses performed herein, a *Bias Ratio* of 0.67 was chosen for all meshes and resulted in the type of vertical mesh size graduation shown in Figure B.24.

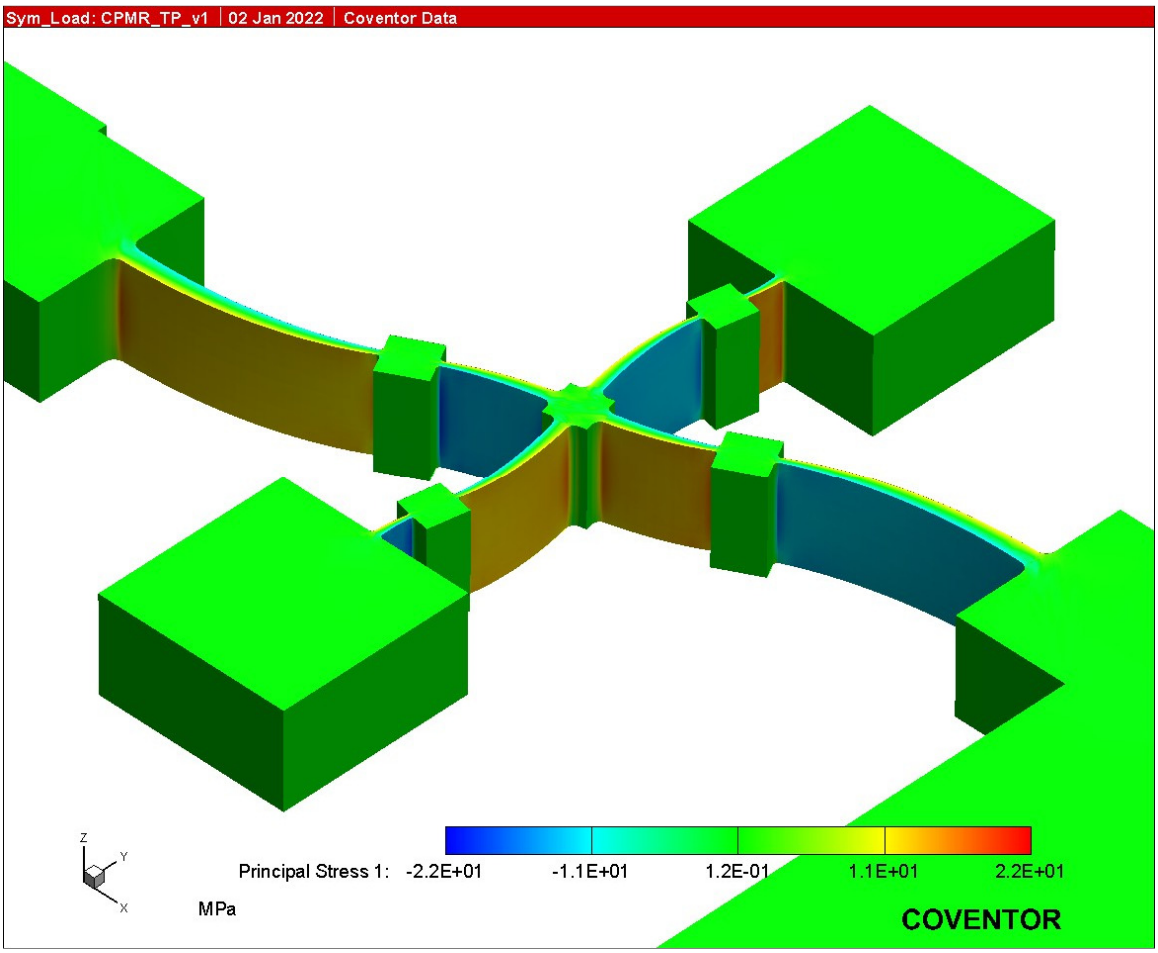

Figure B.23 Equivalent Principle Stress in the Tapered Flexure Pivot APLM.

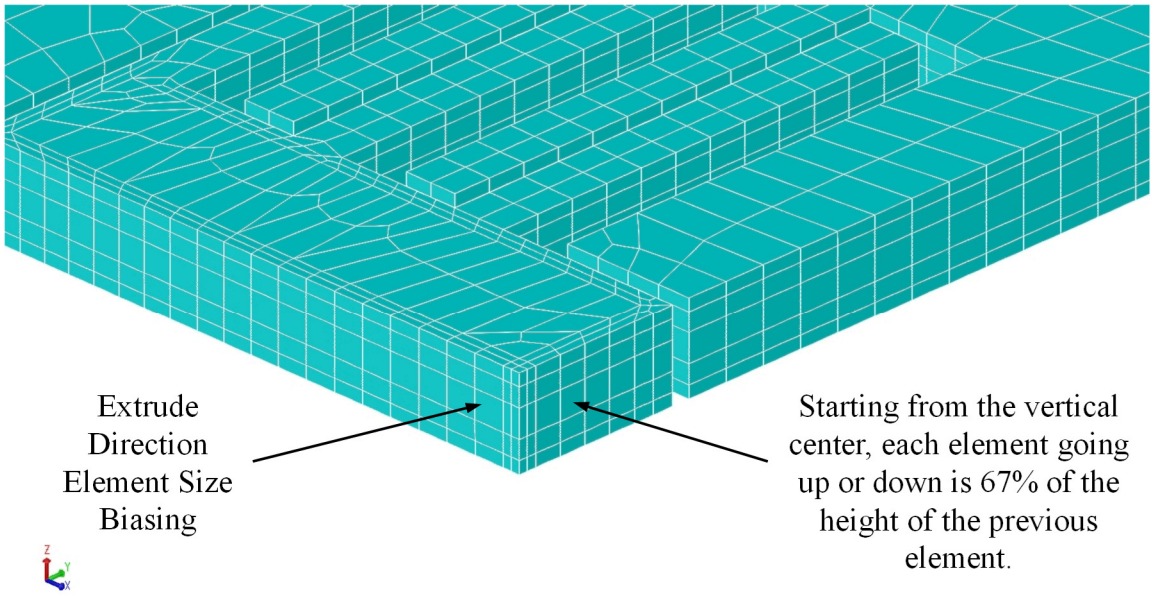

Figure B.24 Extrude Direction Element *Biasing*.

Only four mesher options were investigated as a part of this mesh sensitivity study. These included *Planar Element Size*, *Extrude Element Size*, *Edge Refinement Index*, and *Maximum Curvature Discretization Error*. In addition to setting the *Bias* to *Both Ends*, and the *Bias Ratio*, to 0.67, the other fixed mesher parameters included a mesh type of *Extruded Bricks* with *Parabolic* elements, the use of the *Split and Merge* paving algorithm, and nothing would be specified for the *Minimum Elements Per Edge*, *Minimum Element Size*, or the *Small Feature Removal Threshold* settings.

The overall process for this mesh sensitivity study was to begin with a baseline set of mesher settings for the four mesher options being investigated. Then each one of these setting would be refined one at a time until the resonant frequency and thermoelastic damping values converged for both the straight flexure resonator and the tapered flexure resonator. Generally, a change of no more than 0.25% from the previous setting was considered converged. The baseline settings for these four mesher options were a *Planar*

Element Size of 200µm, an *Extrude Element Size* of 50µm, an *Edge Refinement Index* of *0*, and a *Maximum Curvature Discretization Error* of 0.05.

The first mesher parameter investigated was the *Planar Element Size*. Table B.3 shows the FEA results as the *Planar Element Size* parameter was varied from 200µm down to 100µm. Figure B.25 through Figure B.27 show the resulting meshes for the tapered flexure based dual mass resonator. The data in Table B.3 indicate that all FEA metrics changed significantly when the *Planar Element Size* was changed from 200µm down to 150µm, but none changed significantly when that parameter was further refined to 100µm. Therefore, the solution was considered to be converged at a *Planar Element Size* setting of 150µm.

Table B.3 Planar Element Size Mesh Sensitivity Results.

Planar Element Size (µm)	Tapered Flexure # of Vol. Elements	Tapered Flexure Modal Frequency (Hz)	Tapered Flexure Q ($\times 10^6$)	Straight Flexure # of Vol. Elements	Straight Flexure Modal Frequency (Hz)	Straight Flexure Q ($\times 10^6$)
200	13673	3290.0	1.5500	12225	3367.6	1.5091
150	16008	3283.1	1.5768	14306	3294.1	1.5406
100	19808	3279.1	1.5747	17848	3286.4	1.5387

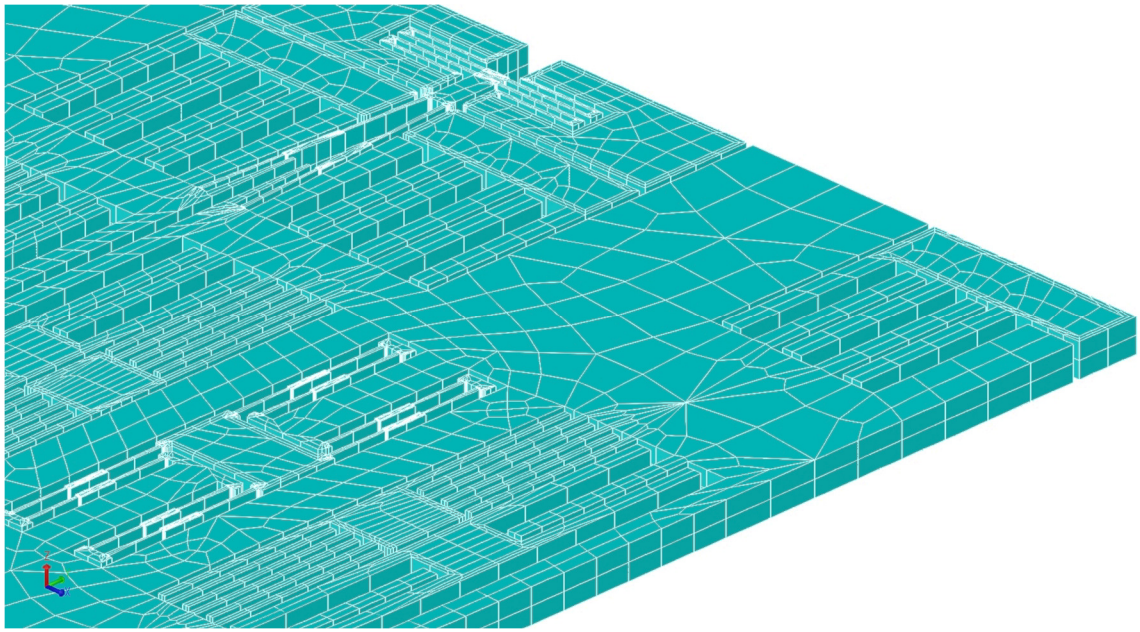

Figure B.25 200µm Planar Element Size Mesh.

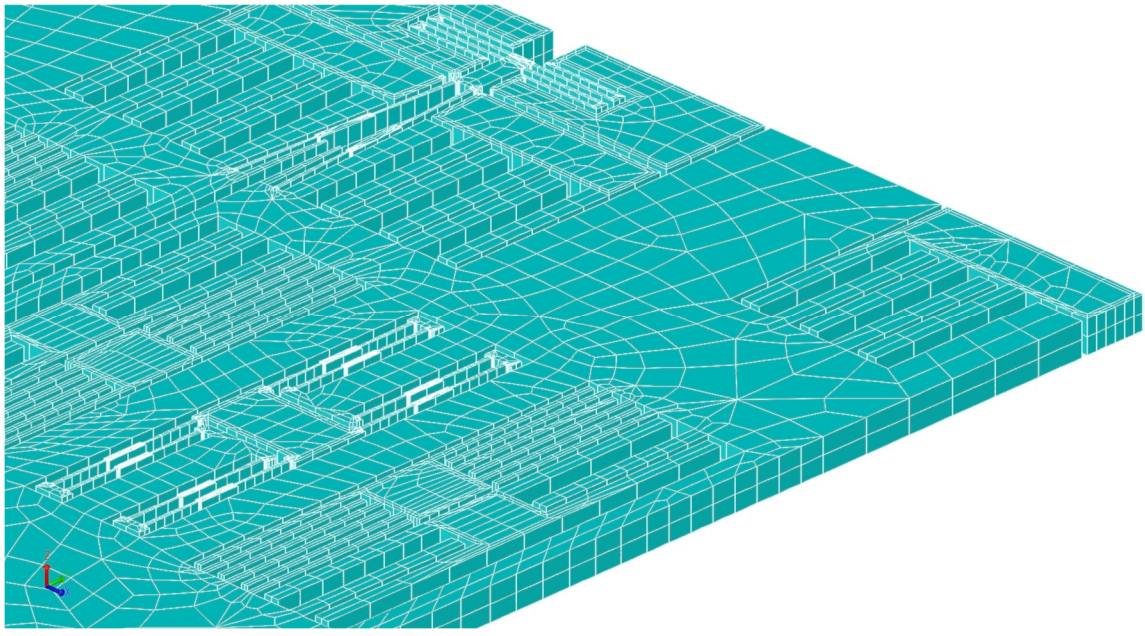

Figure B.26 150µm Planar Element Size Mesh.

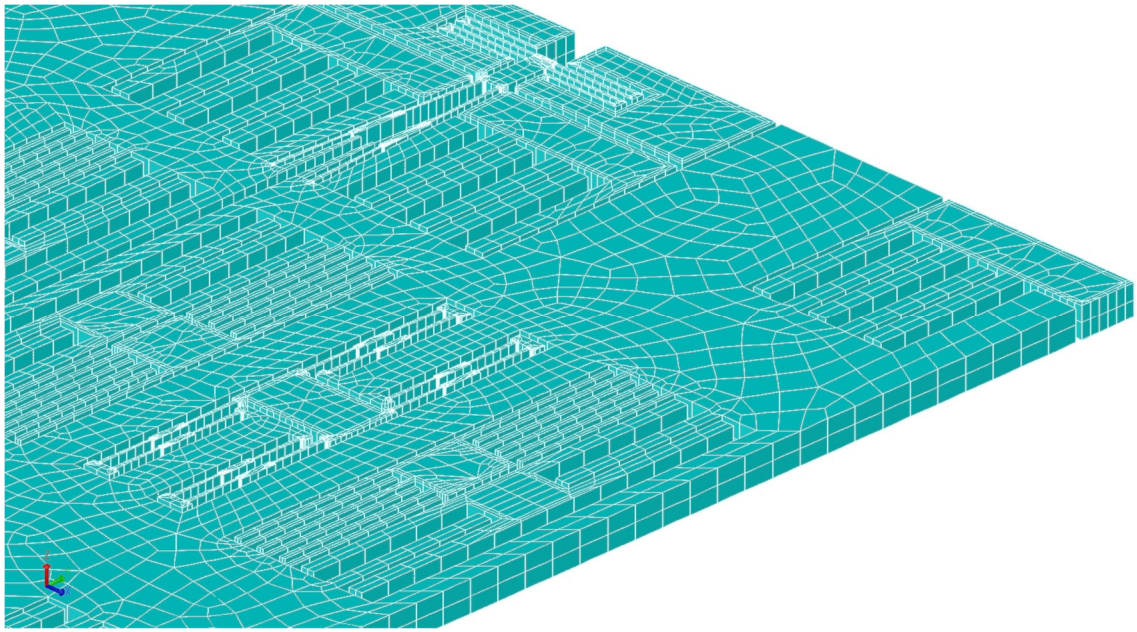

Figure B.27 100µm Planar Element Size Mesh.

The next mesher parameter investigated was the *Extrude Element Size*. Table B.4 shows the FEA results as the *Extrude Element Size* parameter was varied from 50µm down to 20µm. Figure B.28 through Figure B.31 show the resulting meshes for the tapered flexure based dual mass resonator. The data in Table B.4 indicate that, while the *Extrude Element Size* did not have a significant impact on the resonant frequency estimate, it did significantly alter the estimate of the thermoelastic damping. In fact, the final refinement from 25µm down to 20µm led to a change in the quality factor due thermoelastic damping that was just below the defined convergence threshold. Therefore, the *Extrude Element Size* of 25µm meets the criteria for convergence.

Table B.4 Extrude Element Size Mesh Sensitivity Results.

Extrude Element Size (μm)	Tapered Flexure # of Vol. Elements	Tapered Flexure Modal Frequency (Hz)	Tapered Flexure Q ($\times 10^6$)	Straight Flexure # of Vol. Elements	Straight Flexure Modal Frequency (Hz)	Straight Flexure Q ($\times 10^6$)
50	13673	3290.0	1.5500	12225	3367.6	1.5091
34	20265	3283.9	1.5806	18093	3361.7	1.5387
25	26857	3282.4	1.5871	23961	3360.2	1.5450
20	33449	3281.5	1.5907	29829	3359.4	1.5484

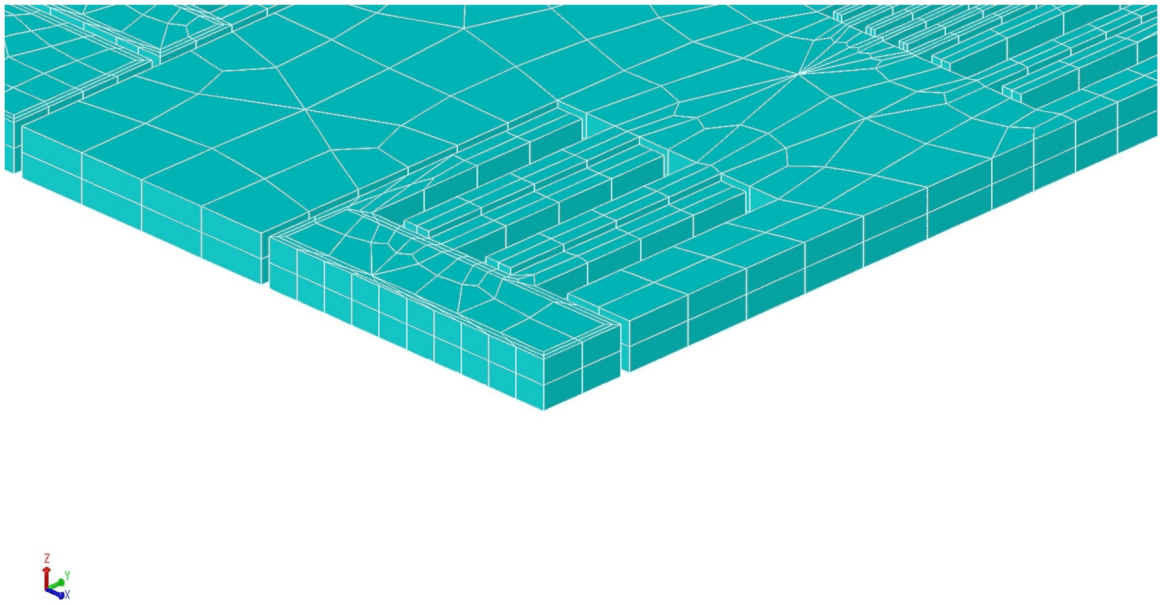

Figure B.28 50μm Extrude Element Size Mesh Edge.

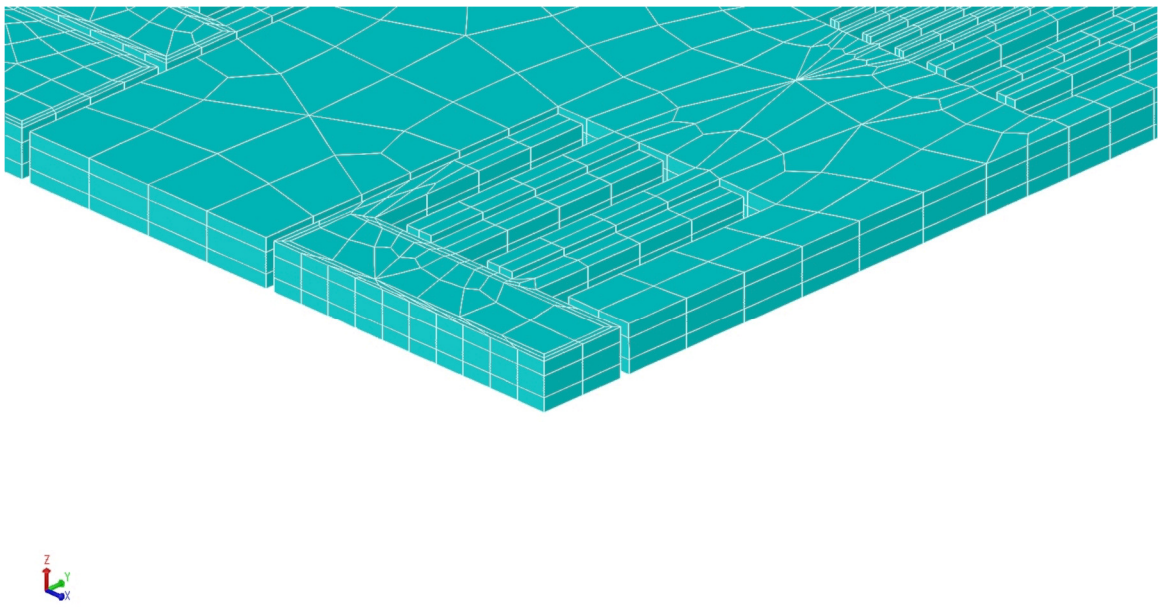

Figure B.29 34µm Extrude Element Size Mesh Edge.

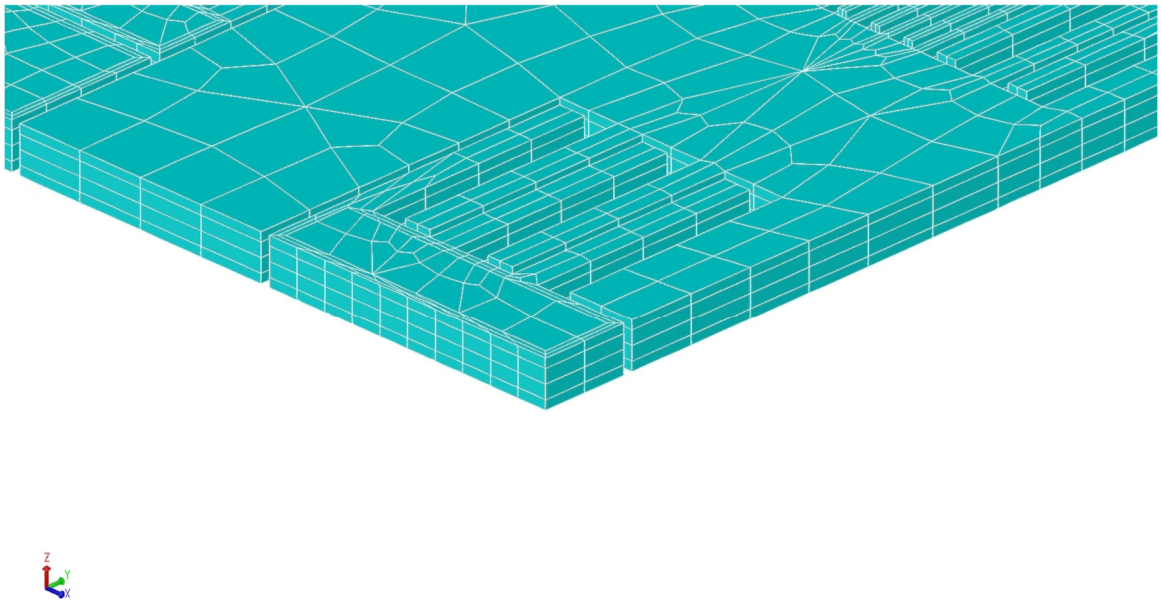

Figure B.30 25µm Extrude Element Size Mesh Edge.

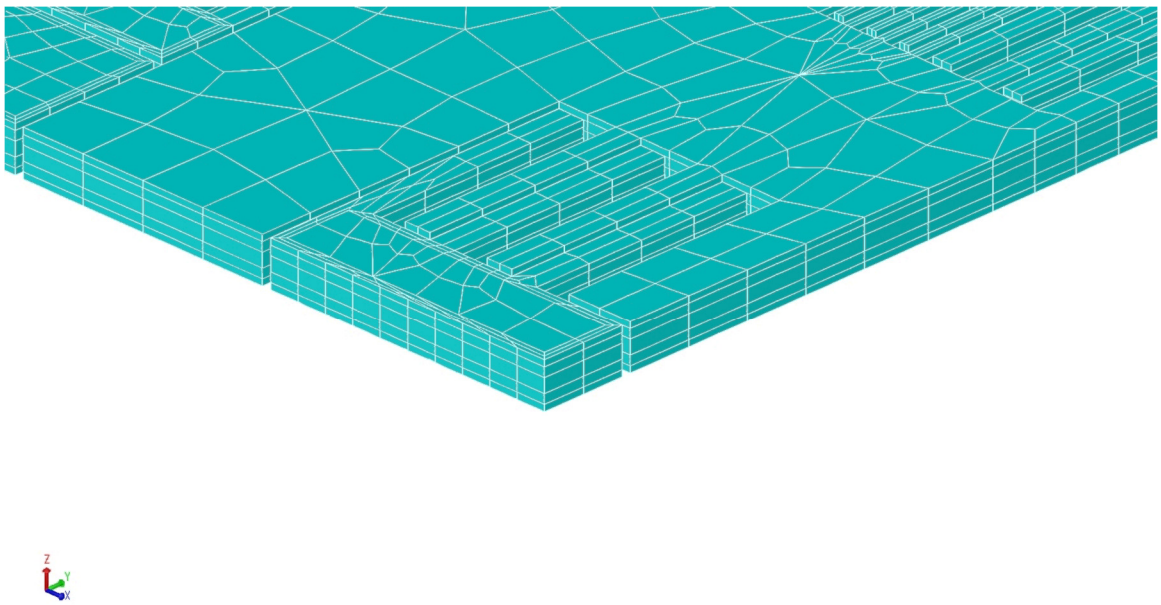

Figure B.31 20µm Extrude Element Size Mesh Edge.

The third mesher parameter investigated was the *Edge Refinement Index*. Table B.5 shows the FEA results as the *Edge Refinement Index* parameter was varied from *0* to *3*, which spans the full allowable range of this parameter. Figure B.32 through Figure B.35 show the resulting meshes for the tapered flexure based dual mass resonator zoomed in on the revised UCI APLM to highlight the differences between the meshes. The primary difference in the meshes seems to be a significant increase in the number of elements along the length of the flexures for *Edge Refinement Indices* of *2* and *3*. The data in Table B.5 indicate that there was no difference at all in the meshes returned when using *Edge Refinement Index* values of *0* or *1*. All of the metric parameters changed significantly when the *Edge Refinement Index* was changed to a value of *2* and the quality factors due to thermoelastic damping were further refined significantly when the value was changed to *3*. Therefore, an *Edge Refinement Index* value of *3* is required to meet the criteria for convergence.

Table B.5 Edge Refinement Index Mesh Sensitivity Results.

Edge Refinement Index	Tapered Flexure # of Vol. Elements	Tapered Flexure Modal Frequency (Hz)	Tapered Flexure Q ($\times 10^6$)	Straight Flexure # of Vol. Elements	Straight Flexure Modal Frequency (Hz)	Straight Flexure Q ($\times 10^6$)
0	13673	3290.0	1.5500	12225	3367.6	1.5091
1	13673	3290.0	1.5500	12225	3367.6	1.5091
2	18429	3279.1	1.5776	16675	3286.5	1.5411
3	21897	3275.3	1.5817	20114	3279.2	1.5466

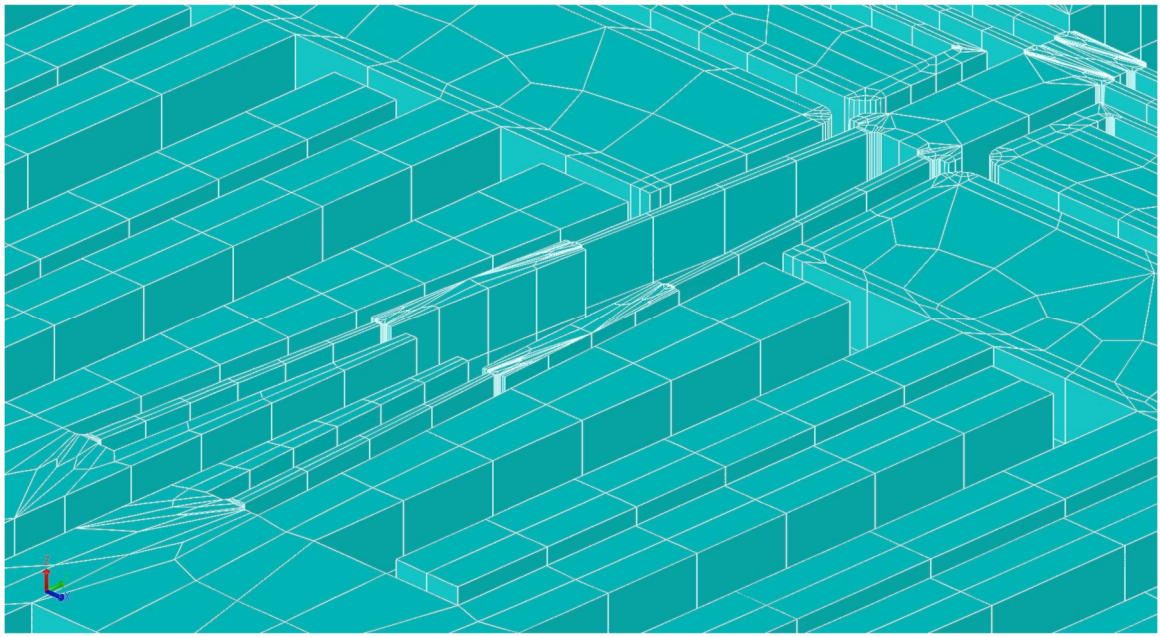

Figure B.32 Mesh with Edge Refinement Index of 0.

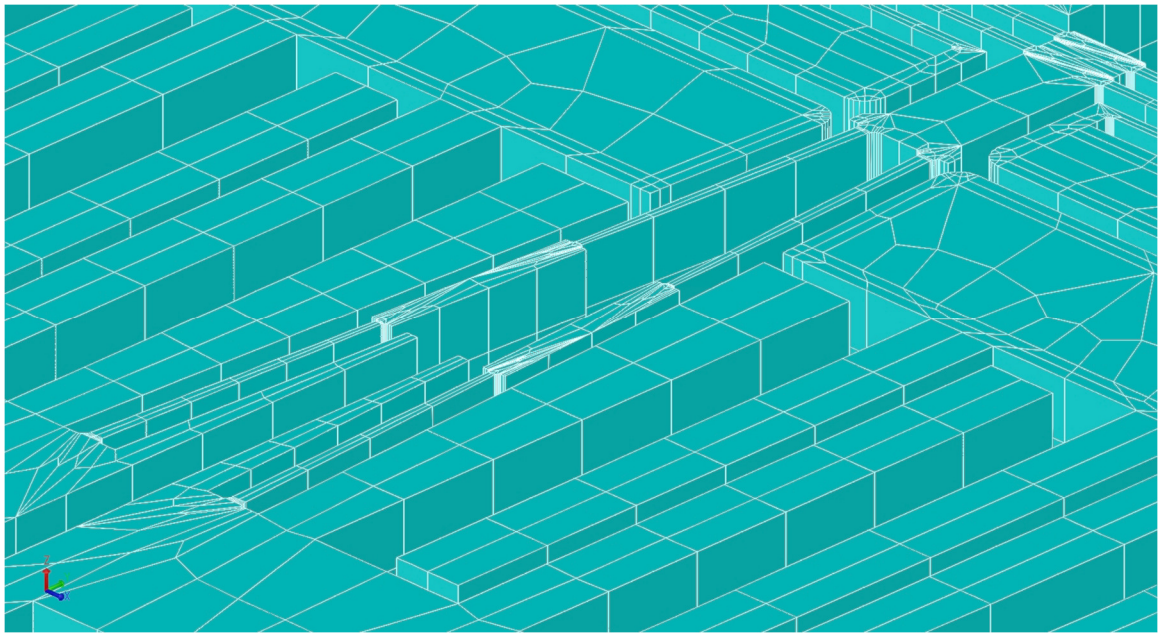

Figure B.33 Mesh with Edge Refinement Index of 1.

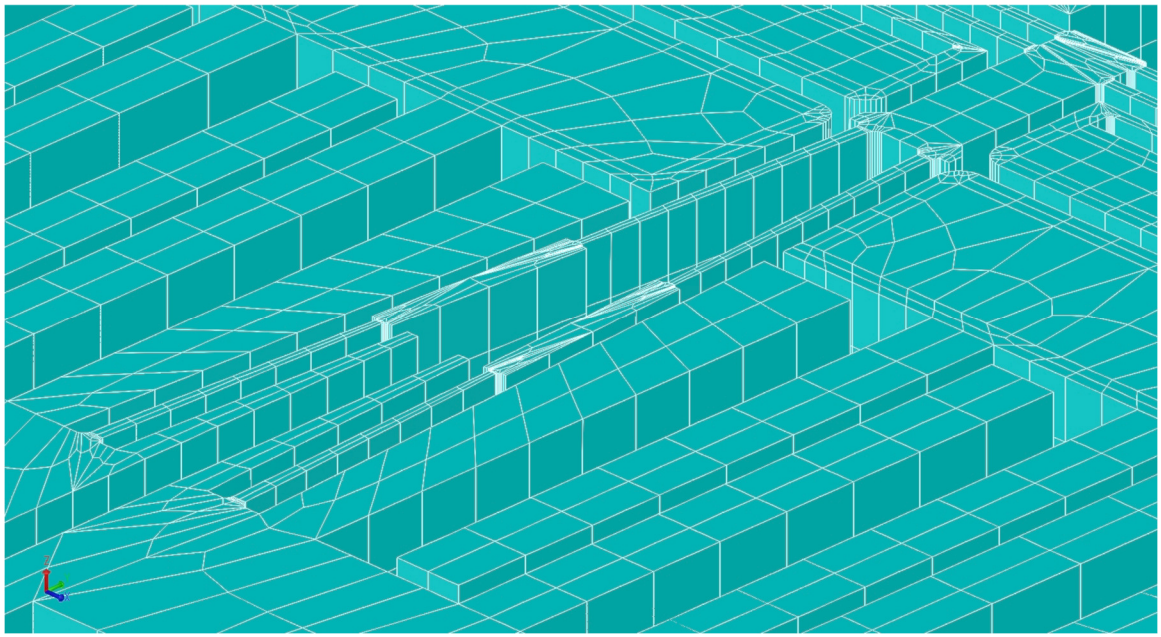

Figure B.34 Mesh with Edge Refinement Index of 2.

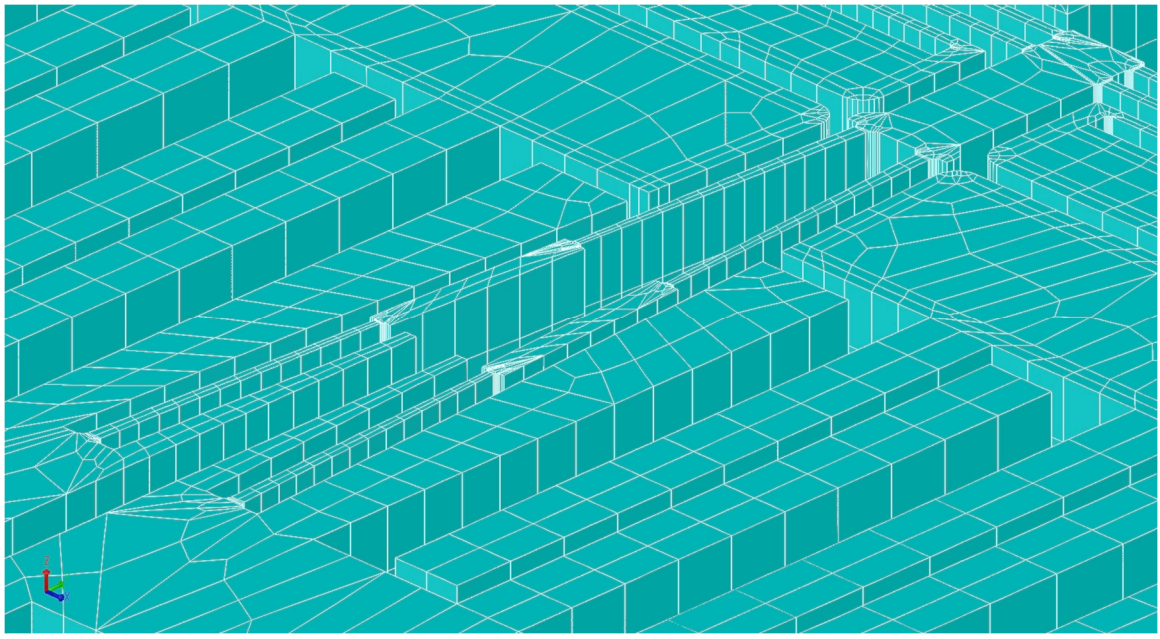

Figure B.35 Mesh with Edge Refinement Index of 3.

The final mesher parameter investigated was the *Maximum Curvature Discretization Error*. Table B.6 shows the FEA results as the *Maximum Curvature Discretization Error* parameter was varied from 0.05 down to 0.01. Figure B.36 through Figure B.38 show the resulting meshes for the tapered flexure based dual mass resonator zoomed in on the revised UCI APLM shuttle to highlight the differences between the meshes. The primary difference in the meshes is a significant increase in the number of elements in the fillets and in the rounded corners for smaller values of the *Maximum Curvature Discretization Error*. The data in Table B.6 indicate some relatively strange behavior. All of the data for the tapered flexure based dual mass resonator is well behaved and did not change significantly with changing values of the *Maximum Curvature Discretization Error*. The data from the straight flexure based dual mass resonator did change significantly for a *Maximum Curvature Discretization Error* value of 0.03, but the data from the mesh with a *Maximum Curvature Discretization Error*

value of 0.01 was very close to that of the mesh with a value of 0.05. It is also noted that the quality factor from the thermoelastic damping is expected to be inversely proportional to the resonant frequency and the quality factor data for the straight flexure based dual mass resonator tracks the inverse of the resonant frequency very closely. So, it appears that the resonant frequency estimate for the straight flexure based dual mass resonator with a *Maximum Curvature Discretization Error* of 0.03 is just out of family with the rest of the data. Therefore, any *Maximum Curvature Discretization Error* value of 0.05 or better meets the criteria for convergence.

Table B.6 Maximum Curvature Discretization Error Mesh Sensitivity Results.

Maximum Curvature Dicretization Error	Tapered Flexure # of Vol. Elements	Tapered Flexure Modal Frequency (Hz)	Tapered Flexure Q ($\times 10^6$)	Straight Flexure # of Vol. Elements	Straight Flexure Modal Frequency (Hz)	Straight Flexure Q ($\times 10^6$)
0.05	13673	3290.0	1.5500	12225	3367.6	1.5091
0.03	15779	3288.9	1.5514	13513	3351.2	1.5193
0.01	25479	3290.3	1.5508	20011	3366.9	1.5123

Figure B.36 Mesh with Maximum Curvature Discretization Error of 0.05.

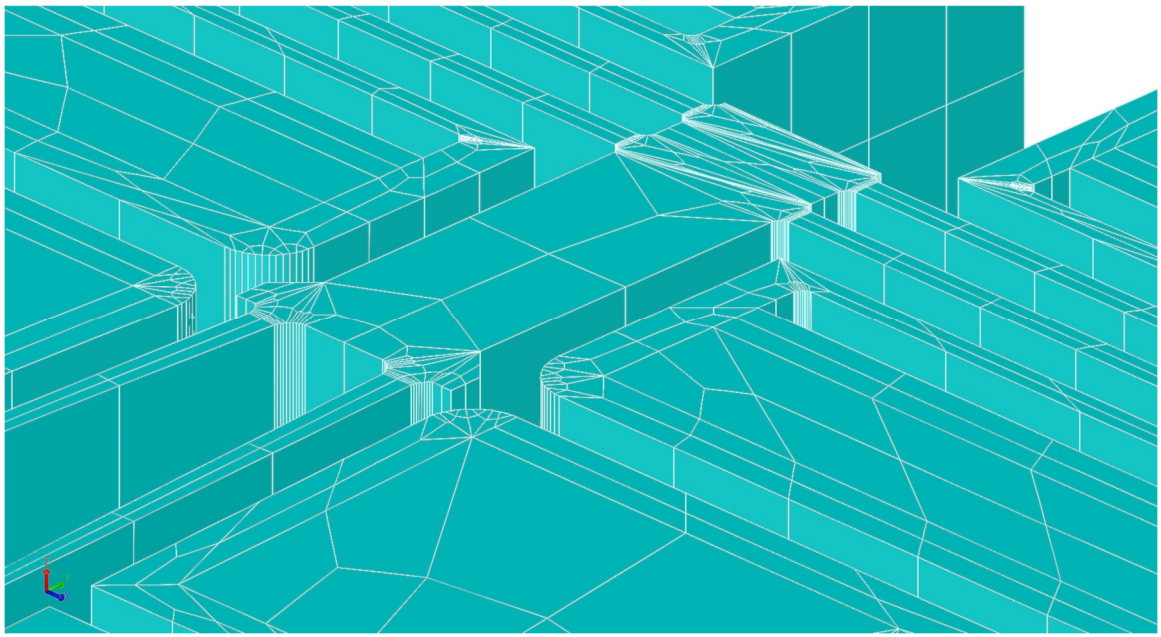

Figure B.37 Mesh with Maximum Curvature Discretization Error of 0.03.

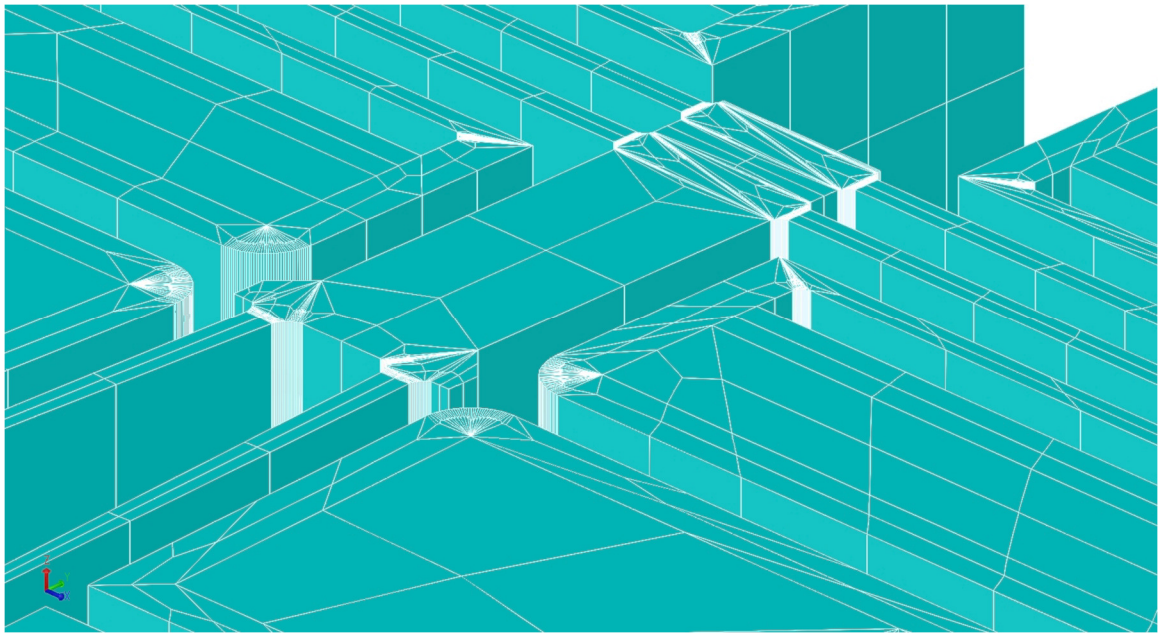

Figure B.38 Mesh with Maximum Curvature Discretization Error of 0.01.

Aggregating all of the converged values for the mesher parameters we have a *Planar Element Size* of 150µm, an *Extrude Element Size* of 25µm, an *Edge Refinement Index* of *3*, and a *Maximum Curvature Discretization Error* of 0.03. Placing all of these parameters into the same mesh yielded resonant frequencies and quality factors for both the straight and tapered flexure versions of the dual mass resonator that were significantly different from any of the values seen in the individual trade studies. This warranted a little further mesh sensitivity investigation. Table B.7 presents the results of the mesh sensitivity study on the aggregated parameters. The first row in Table B.7 is the original Baseline mesh parameters and the second row is the individually converged mesh parameters. Since the *Edge Refinement Index* was already set as high as allowed, an attempt was made to set all of the other parameters up one level of refinement and those results are shown in the third row of Table B.7. While these changes in parameter values marked a significant increase in mesh refinement, the estimated resonant frequencies did

not change significantly. Unfortunately, the refined mesh resulted in so many elements that the thermoelastic damping module in Coventor could not converge to a solution. Since the thermoelastic damping analysis is critical to the current research, this set of mesh parameters would not be possible to carry forward for the intended analyses. Reviewing the individual parameter sensitivity study findings it was the *Extrude Element Size* that just barely met the convergence criteria for the 25µm value. Therefore, the *Planar Element Size* and the *Maximum Curvature Discretization Error* values were set back to their original aggregate values and the *Extrude Element Size* was refined to 20µm. The FEA results using this mesh are presented in row 4 of Table B.7. Comparing these results to the available results in rows 2 and 3 of Table B.7 indicates that the data has met the convergence criteria but the quality factor from thermoelastic damping just barely met the criteria with a change of 0.22% for both the straight and tapered flexure versions of the dual mass resonator. Since this just barely met the convergence criteria, one more set of mesh parameters was attempted by further refining the *Extrude Element Size* to 16.67µm and leaving all other parameters unchanged. The FEA results from this mesh are presented in row 5 of Table B.7. Once again, the refined mesh resulted in so many elements for the tapered flexure based dual mass resonator that the thermoelastic damping module in Coventor could not converge to a solution, but the other metrics all indicated no significant shift in results. Therefore, the mesh parameters in row 4 of Table B.7, which are highlighted in green, were selected as the final mesh parameter settings for the APLM and dual mass resonator finite element analyses. Figure B.39 through Figure B.43 show the resulting meshes for the tapered flexure based dual mass resonator zoomed in on the revised UCI APLM to highlight the differences in the meshes.

Table B.7 Aggregate Parameters Mesh Sensitivity Results.

Planar Element Size (μm)	Extrude Element Size (μm)	Edge Refinement Index	Maximum Curvature Dicretization Error	Tapered Flexure # of Vol. Elements	Tapered Flexure Modal Frequency (Hz)	Tapered Flexure Q ($\times 10^6$)	Straight Flexure # of Vol. Elements	Straight Flexure Modal Frequency (Hz)	Straight Flexure Q ($\times 10^6$)
200	50	0	0.05	13673	3290.0	1.5500	12225	3367.6	1.5091
150	25	3	0.03	56564	3267.3	1.6204	49684	3271.8	1.5832
100	20	3	0.01	118272	3266.2	DNC	100885	3270.9	DNC
150	20	3	0.03	70410	3266.4	1.6240	61816	3271.0	1.5866
150	16.67	3	0.03	84256	3266.1	DNC	73948	3270.7	1.5877

"DNC" indicates that the solution Did Not Converge.

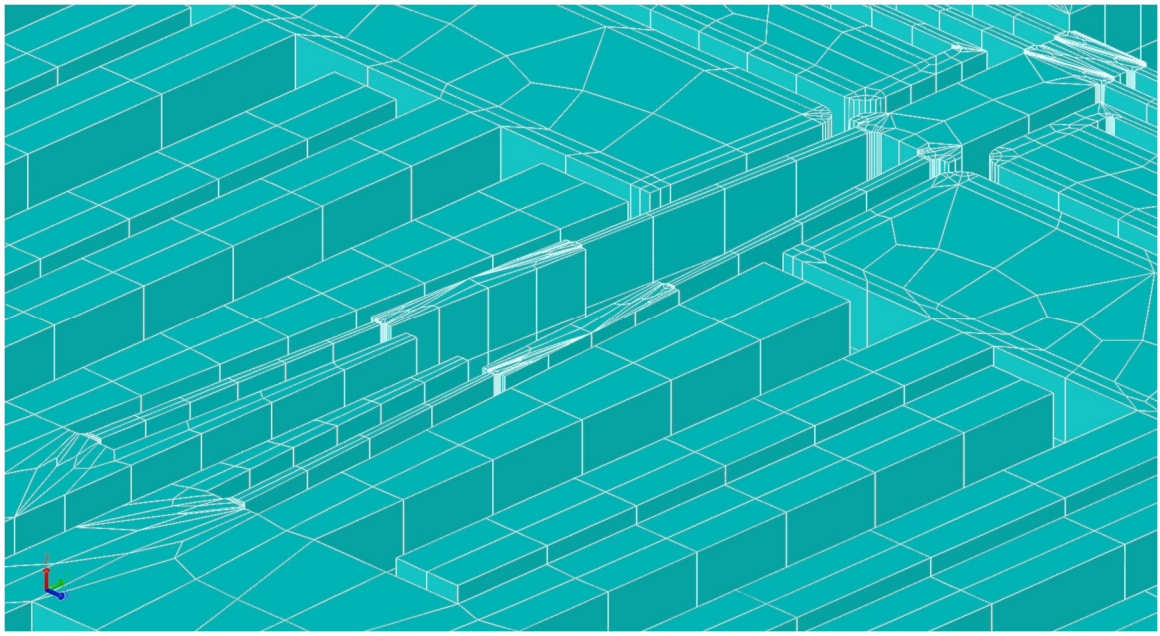

Figure B.39 Mesh from Baseline Aggregate Mesh Settings.

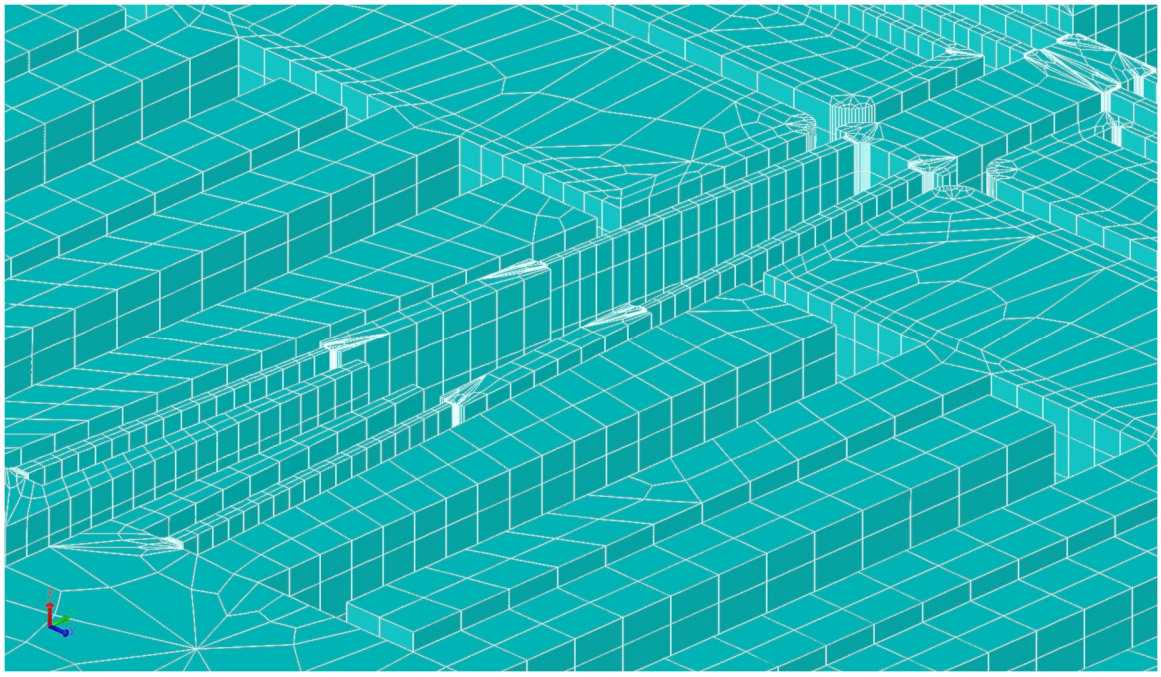

Figure B.40 Mesh from Aggregate Mesh Settings from Individual Sensitivity Studies.

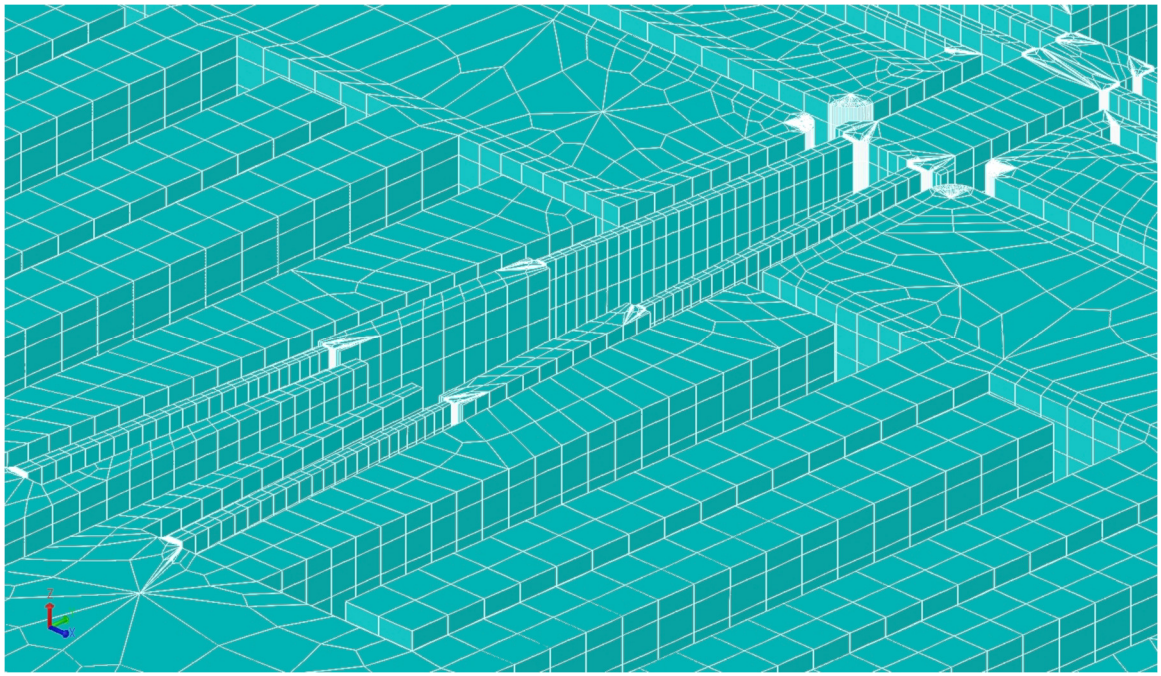

Figure B.41 Mesh from Aggregate Mesh Settings with All Parameters Refined.

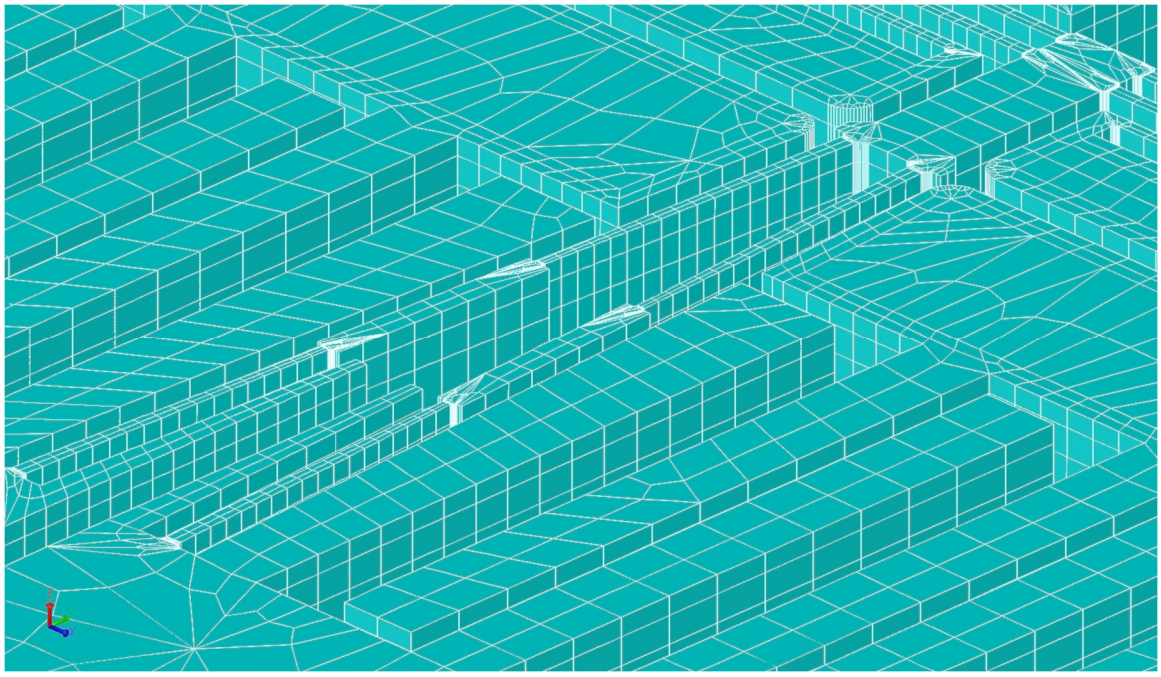

Figure B.42 Mesh from Final Mesh Settings (20µm Extrude Element Size).

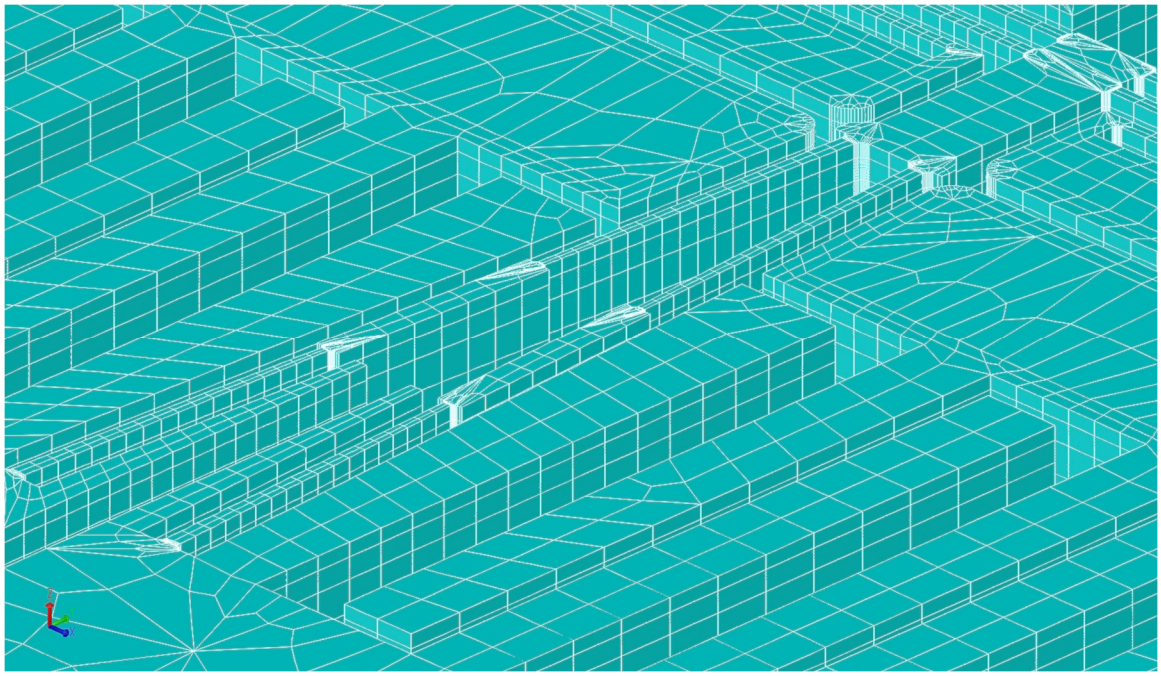

Figure B.43 Mesh from Aggregate Mesh Settings with 16.67µm Extrude Element Size.

Appendix C. Additional Figures for Dual Mass Resonator Fabrication

Appendix C provides additional figures of the dual mass resonator fabrication experiments for completeness. These include additional close-up views of the various revised UCI APLM designs and coupler spring designs as well as specific design locations on the fabrication wafer.

C.1 Dual-Mass Resonator Experiment APLM and Coupler Spring Close-up Views

Broad views of the solid model renderings of the straight flexure revised UCI APLM designs from dual-mass resonator Experiment 1 are provided in Figure C.1 through Figure C.6. Broad views of the solid model renderings of the straight flexure coupler spring designs from dual-mass resonator Experiment 1 are provided in Figure C.7 through Figure C.12.

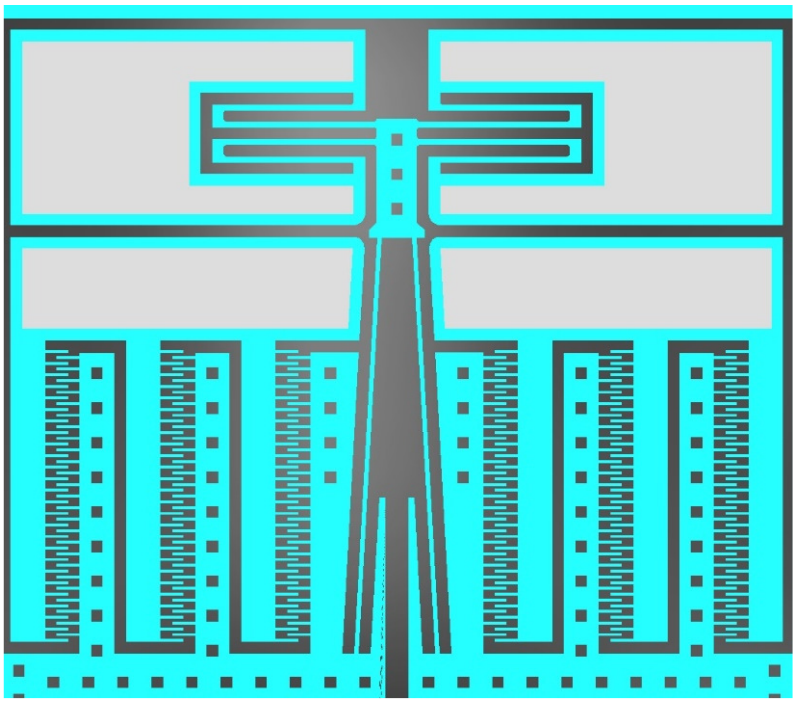

Figure C.1 Experiment 1 Design 1 Revised UCI APLM, 7.5µm Width w/o Fillets.

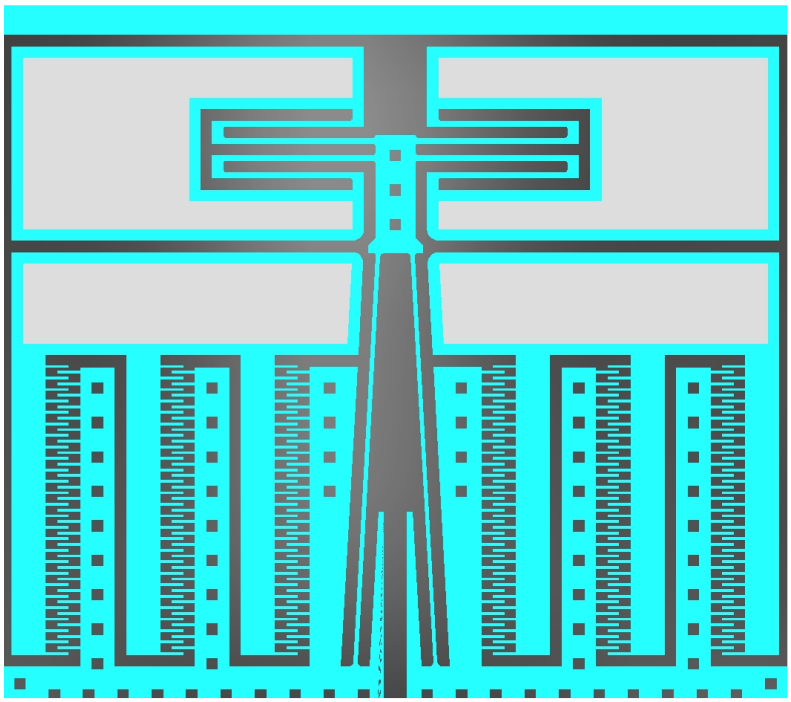

Figure C.2 Experiment 1 Design 2 Revised UCI APLM, 7.5µm Width w/ Fillets.

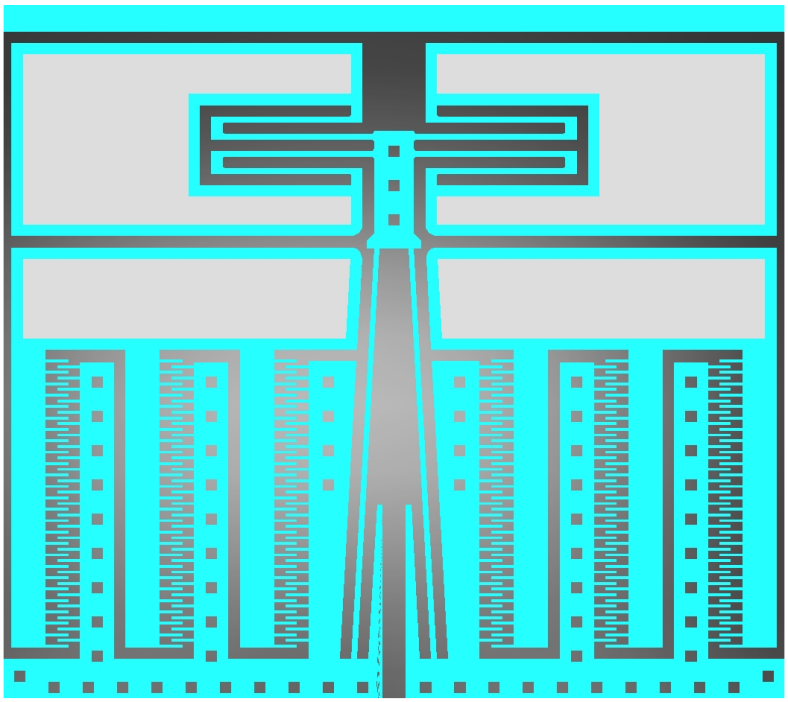

Figure C.3 Experiment 1 Design 3 Revised UCI APLM, 10µm Width w/o Fillets.

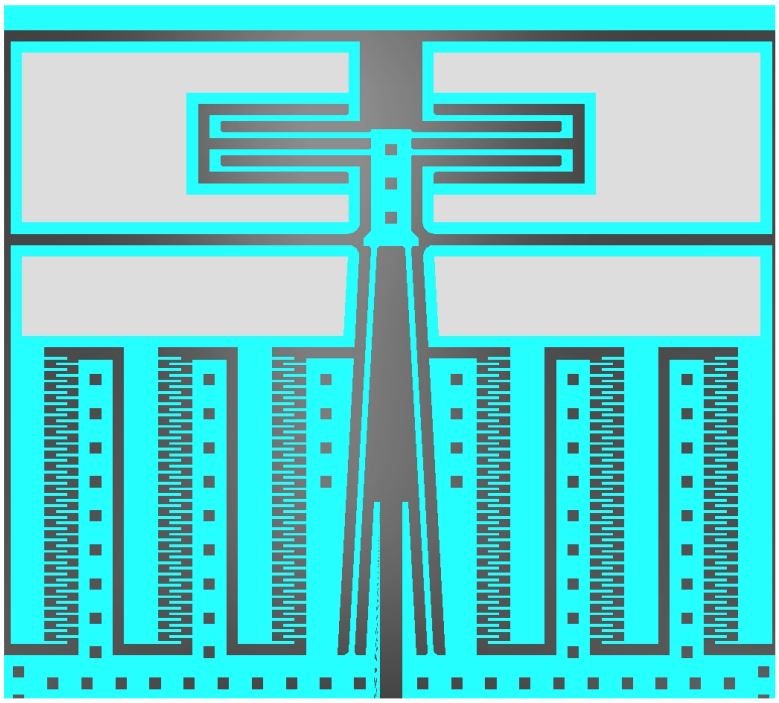

Figure C.4 Experiment 1 Design 4 Revised UCI APLM, 10µm Width w/ Fillets.

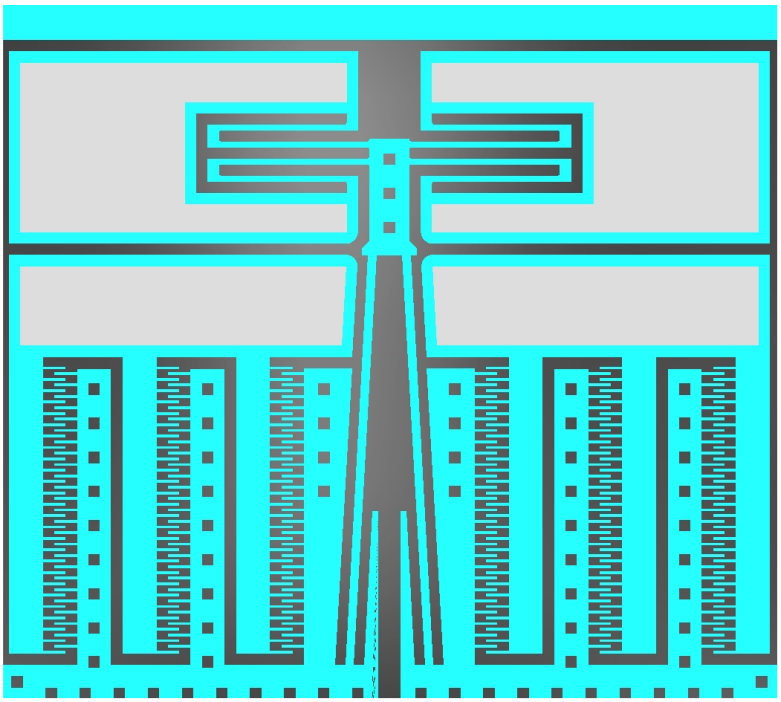

Figure C.5 Experiment 1 Design 5 Revised UCI APLM, 15µm Width w/o Fillets.

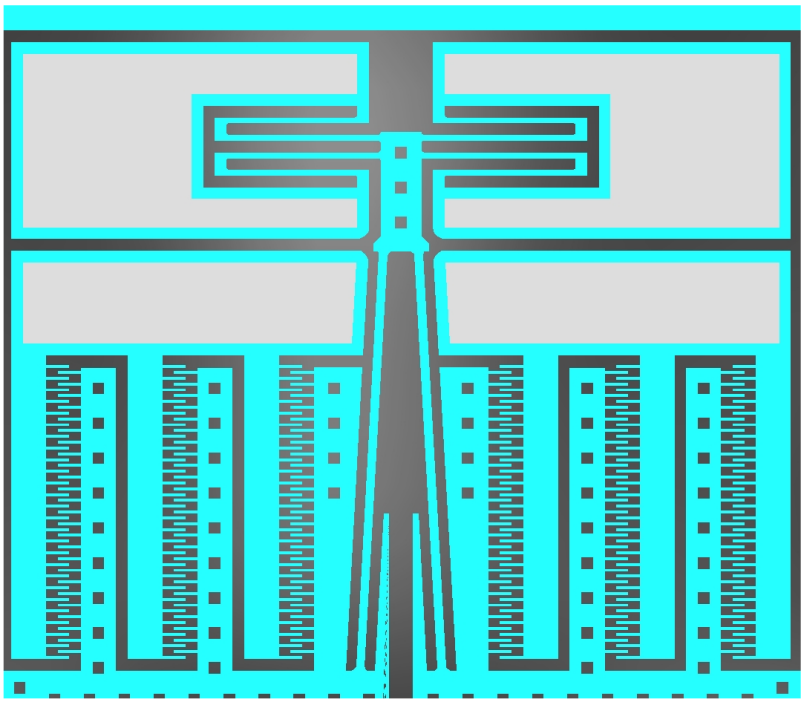

Figure C.6 Experiment 1 Design 6 Revised UCI APLM, 15µm Width w/ Fillets.

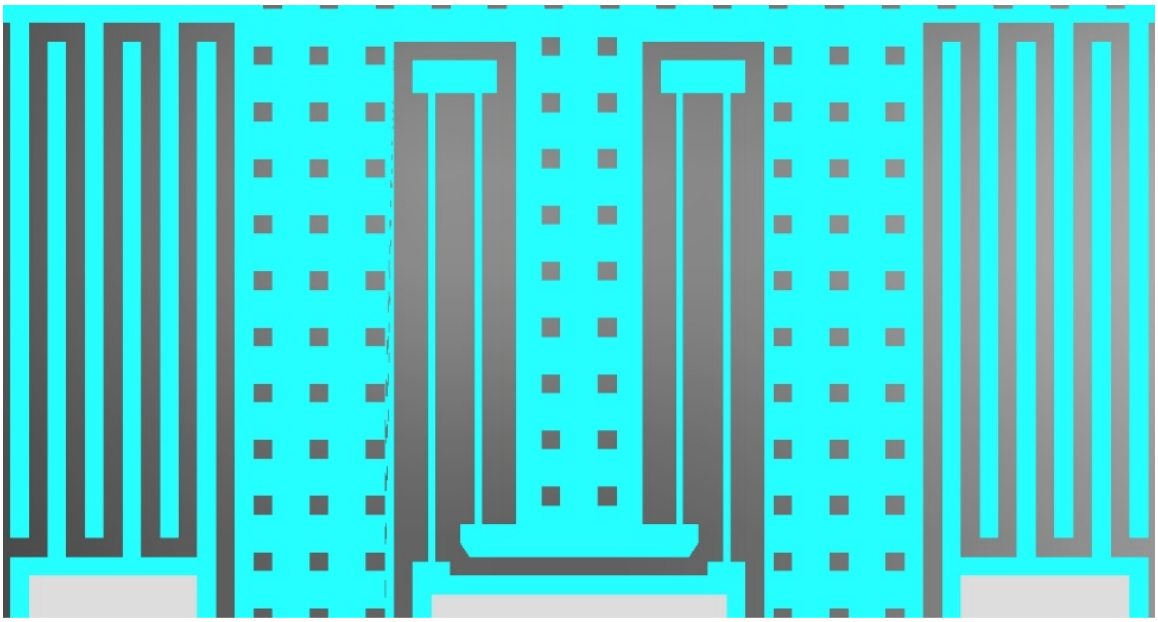

Figure C.7 Experiment 1 Design 1 Coupler Spring, 7.5µm Width w/o Fillets.

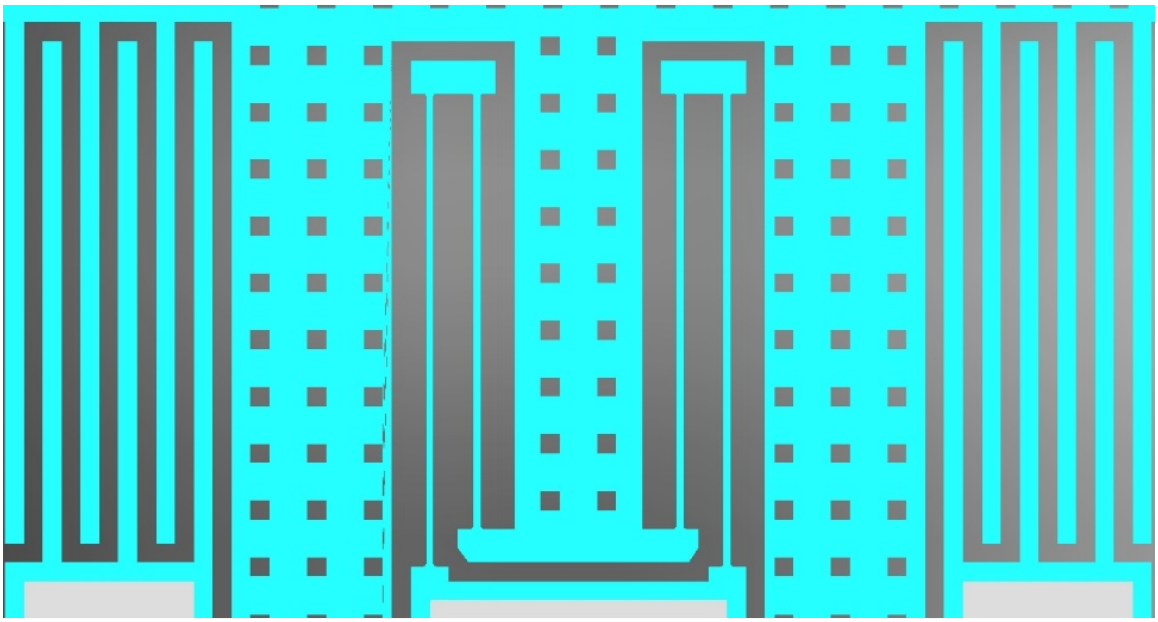

Figure C.8 Experiment 1 Design 2 Coupler Spring, 7.5µm Width w/ Fillets.

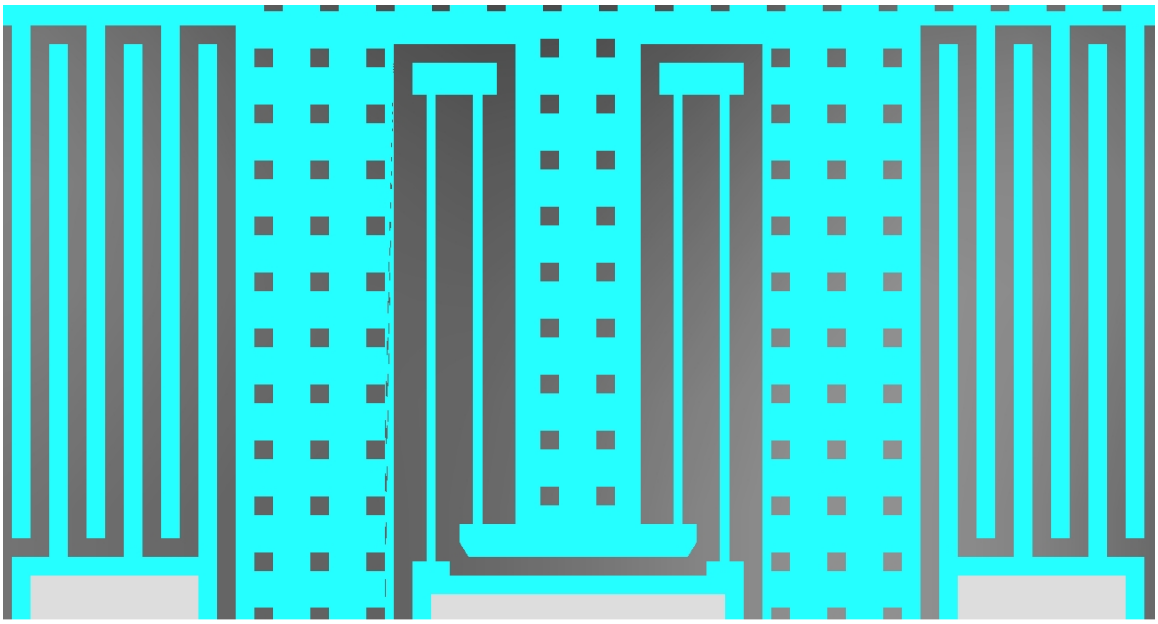

Figure C.9 Experiment 1 Design 3 Coupler Spring, 10µm Width w/o Fillets.

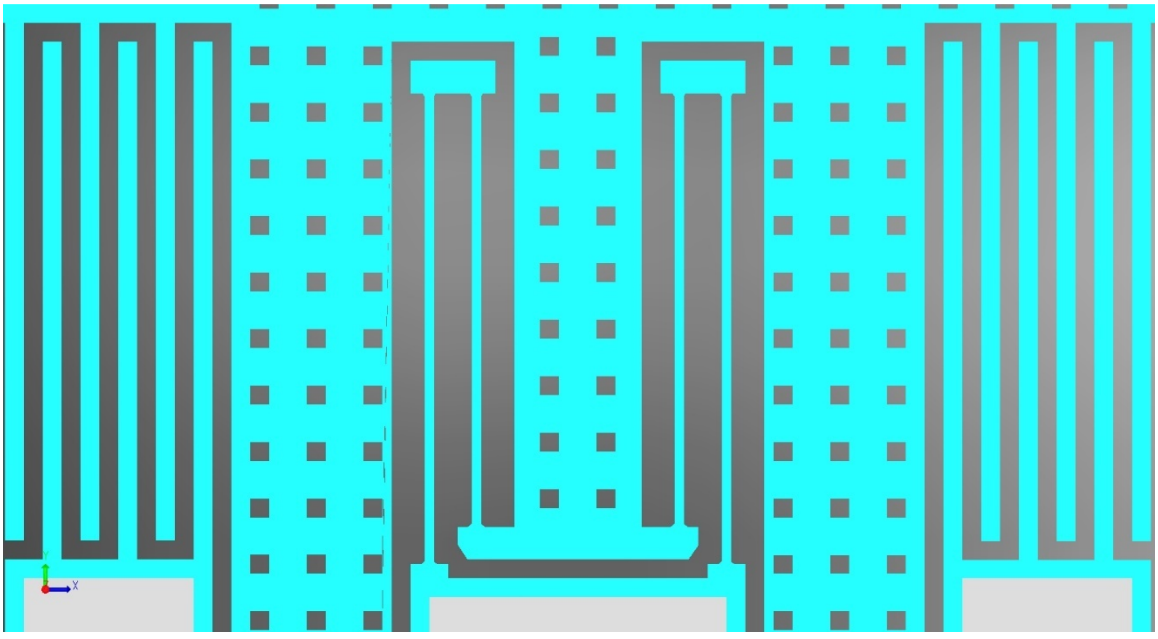

Figure C.10 Experiment 1 Design 4 Coupler Spring, 10µm Width w/ Fillets.

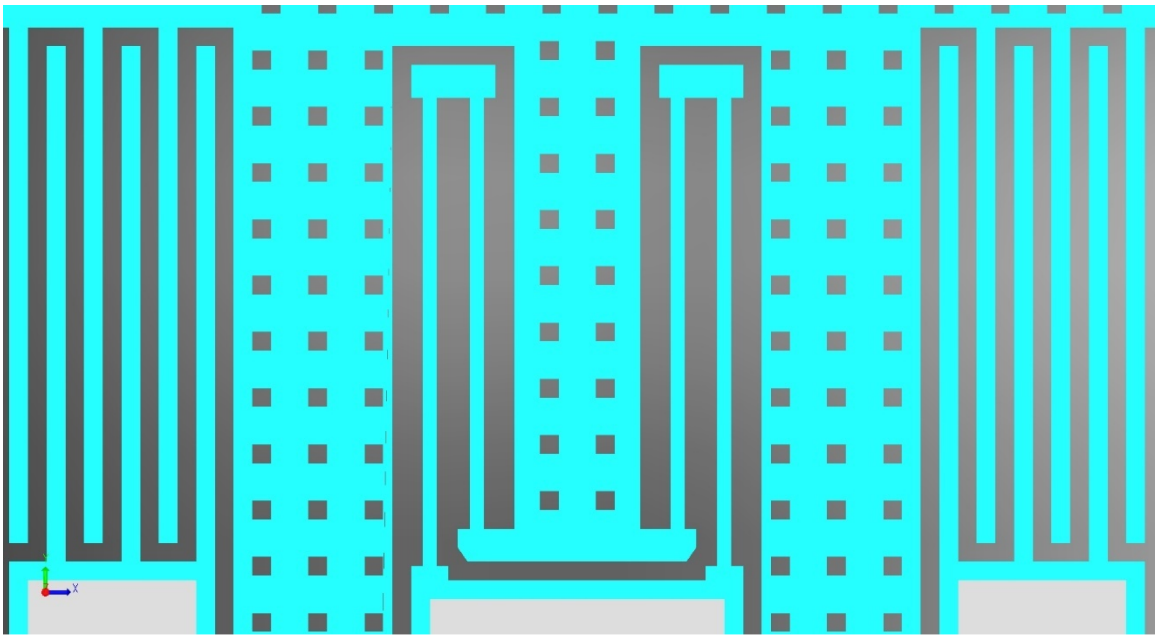

Figure C.11 Experiment 1 Design 5 Coupler Spring, 15µm Width w/o Fillets.

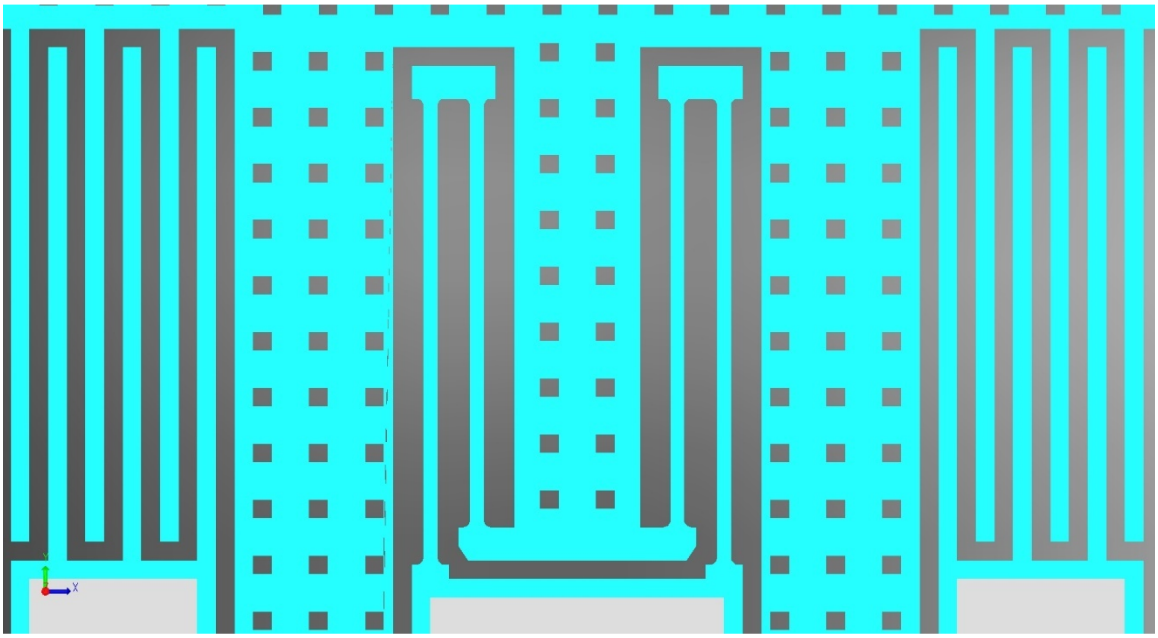

Figure C.12 Experiment 1 Design 6 Coupler Spring, 15µm Width w/ Fillets.

Broad views of the solid model renderings of the tapered flexure revised UCI APLM designs from dual-mass resonator Experiment 2 are provided in Figure C.13 through Figure C.18. Broad views of the solid model renderings of the straight flexure coupler spring designs from dual-mass resonator Experiment 1 are provided in Figure C.19 through Figure C.24.

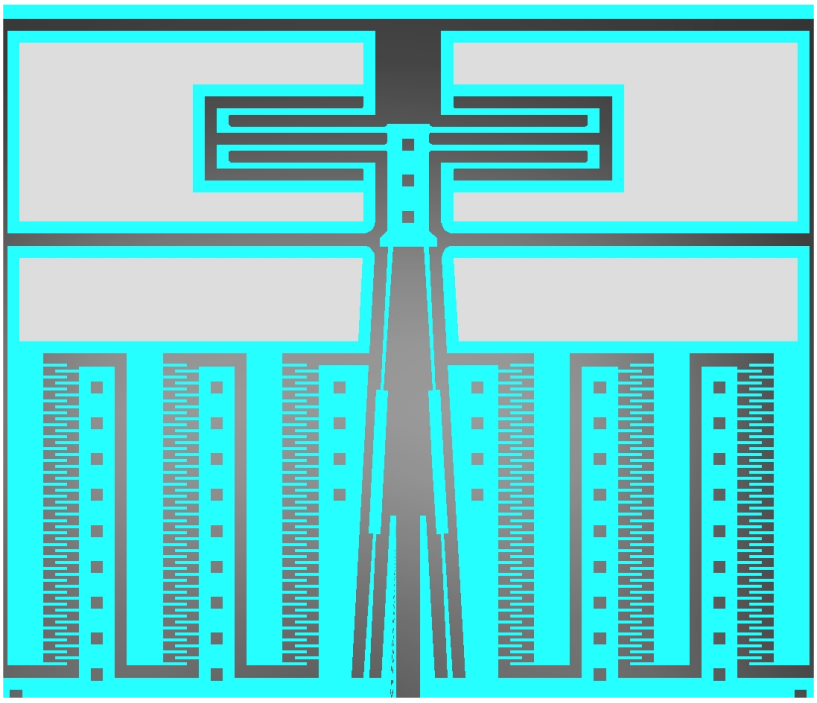

Figure C.13 Experiment 2 Design 1 Revised UCI APLM, 7.5µm Width w/o Fillets.

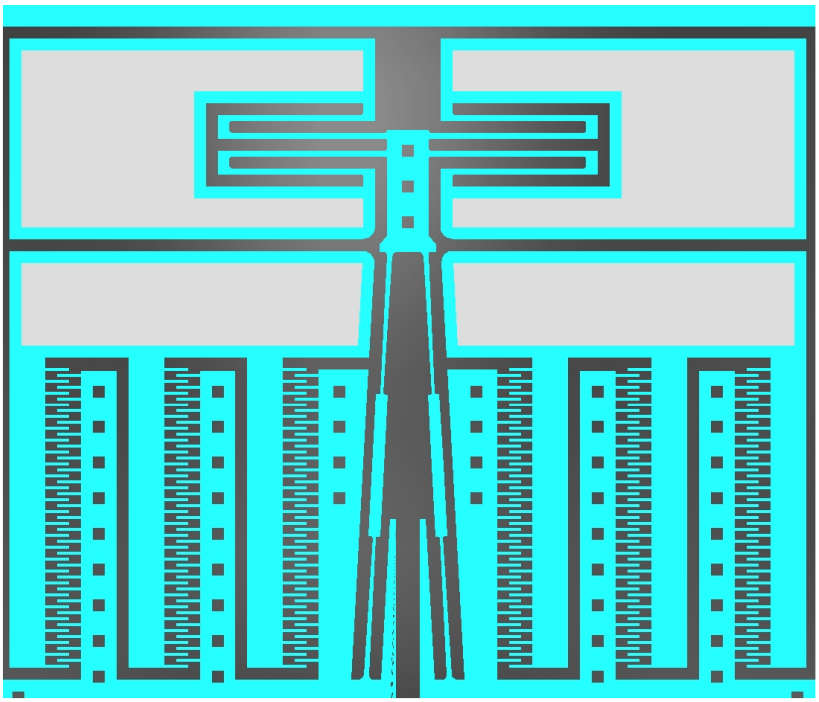

Figure C.14 Experiment 2 Design 2 Revised UCI APLM, 7.5µm Width w/ Fillets.

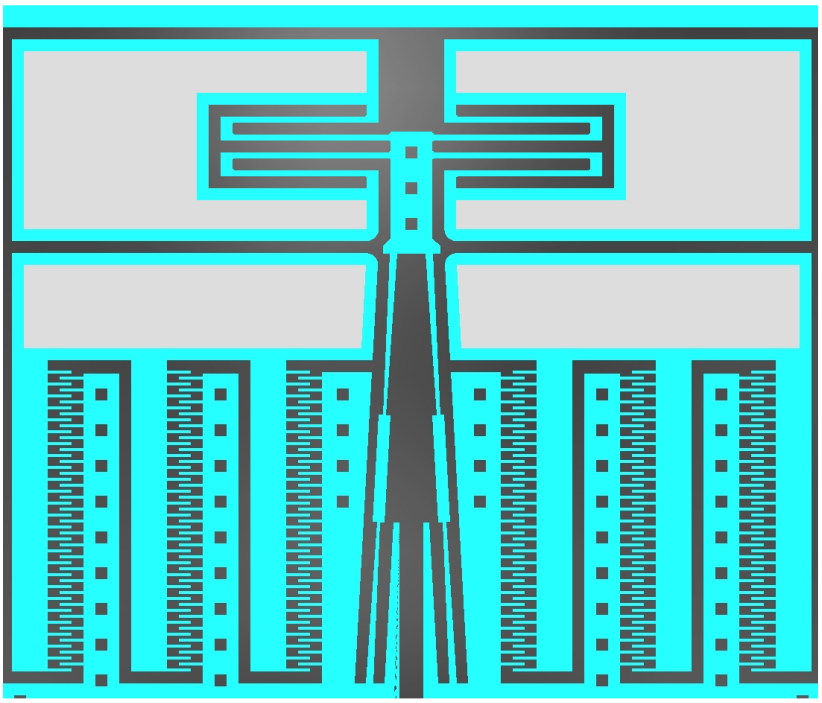

Figure C.15 Experiment 2 Design 3 Revised UCI APLM, 10µm Width w/o Fillets.

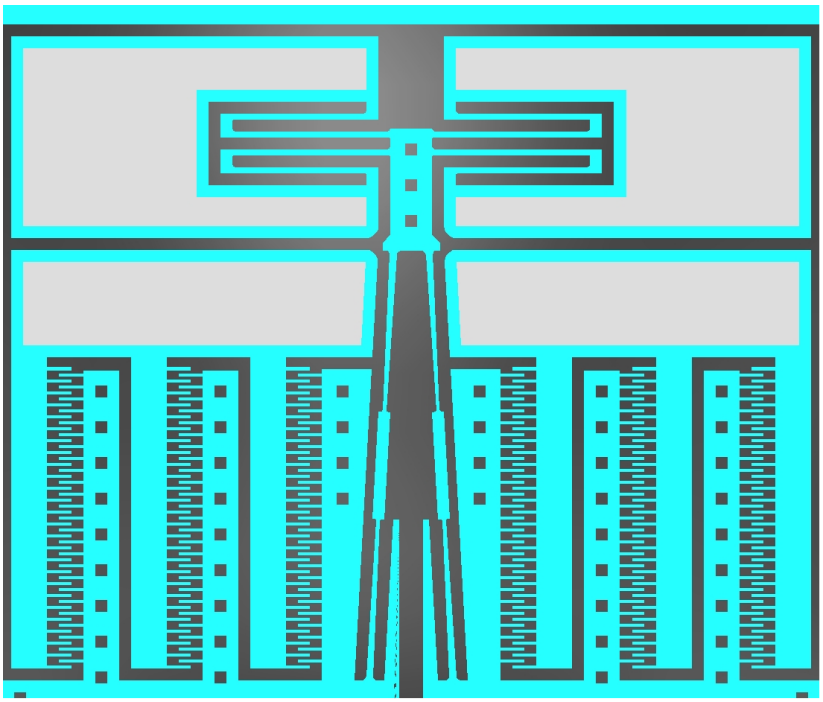

Figure C.16 Experiment 2 Design 4 Revised UCI APLM, 10µm Width w/ Fillets.

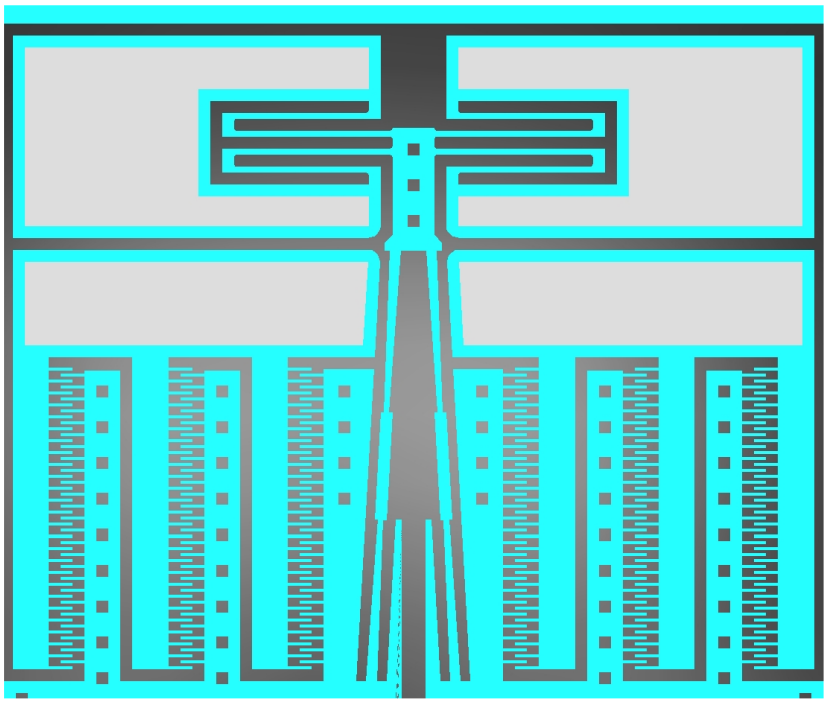

Figure C.17 Experiment 2 Design 5 Revised UCI APLM, 15µm Width w/o Fillets.

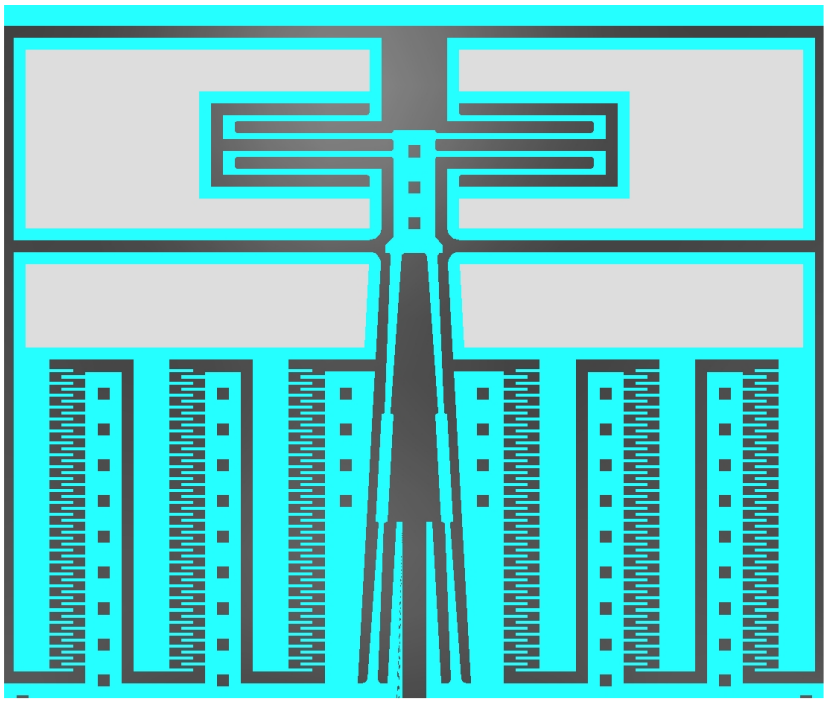

Figure C.18 Experiment 2 Design 6 Revised UCI APLM, 15µm Width w/ Fillets.

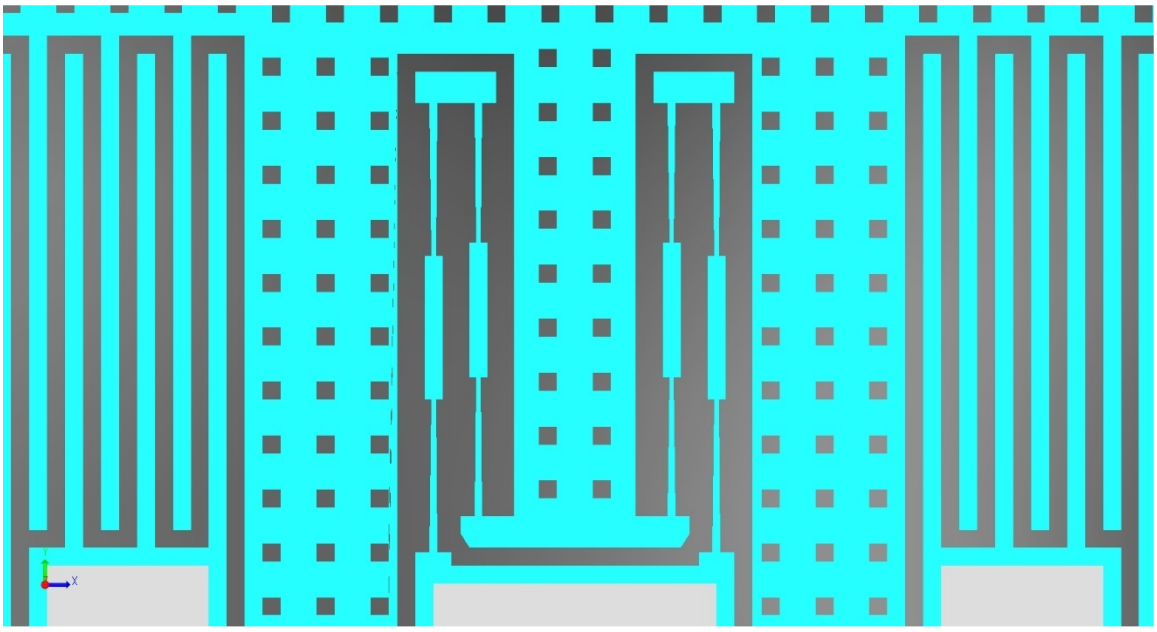

Figure C.19 Experiment 2 Design 1 Coupler Springs, 7.5µm Width w/o Fillets.

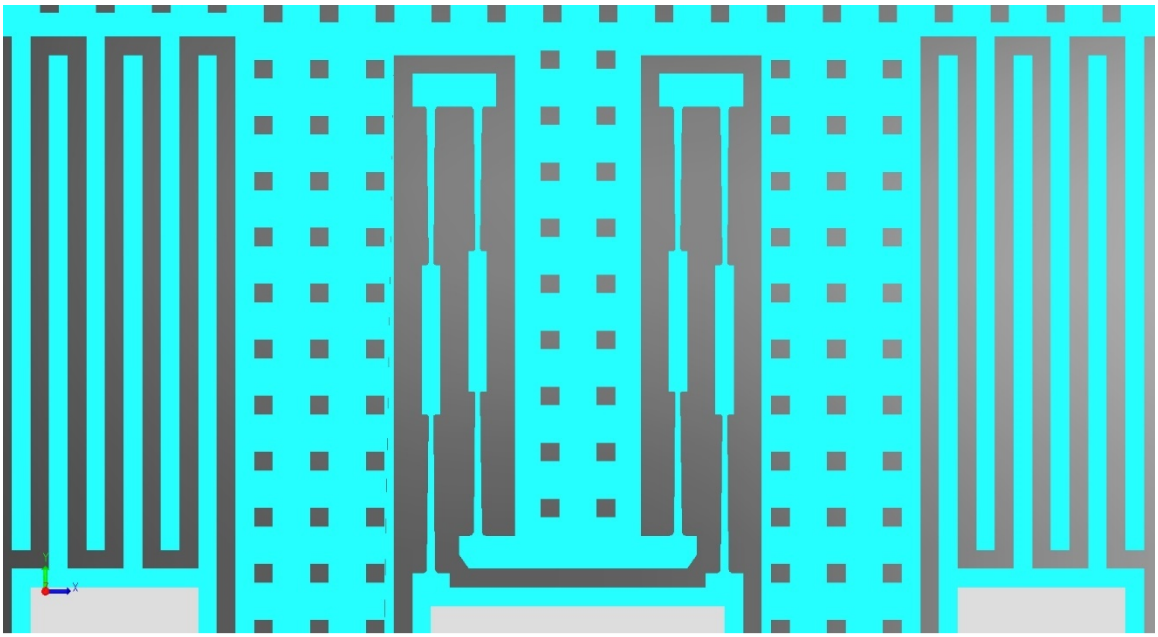

Figure C.20 Experiment 2 Design 2 Coupler Springs, 7.5µm Width w/ Fillets.

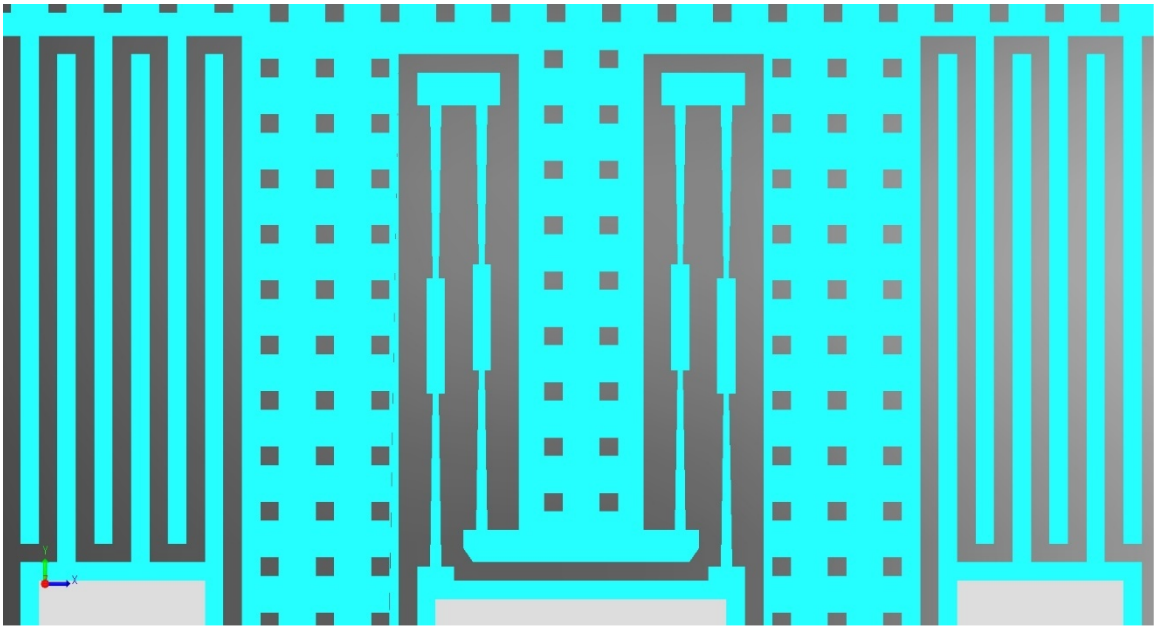

Figure C.21 Experiment 2 Design 3 Coupler Springs, 10µm Width w/o Fillets.

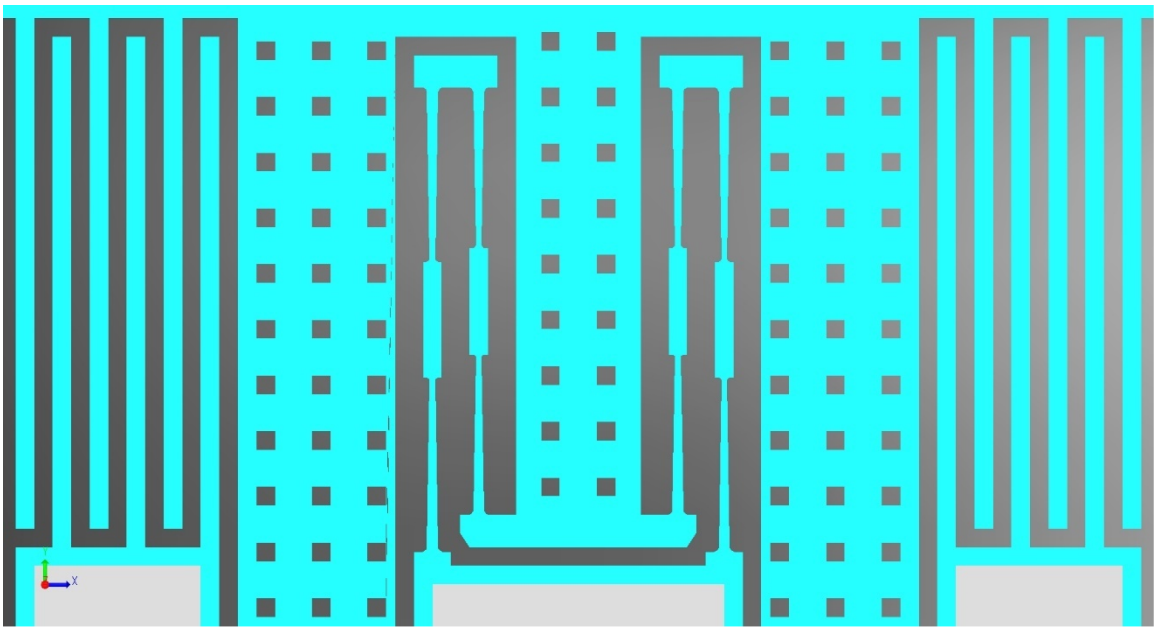

Figure C.22 Experiment 2 Design 4 Coupler Springs, 10µm Width w/ Fillets.

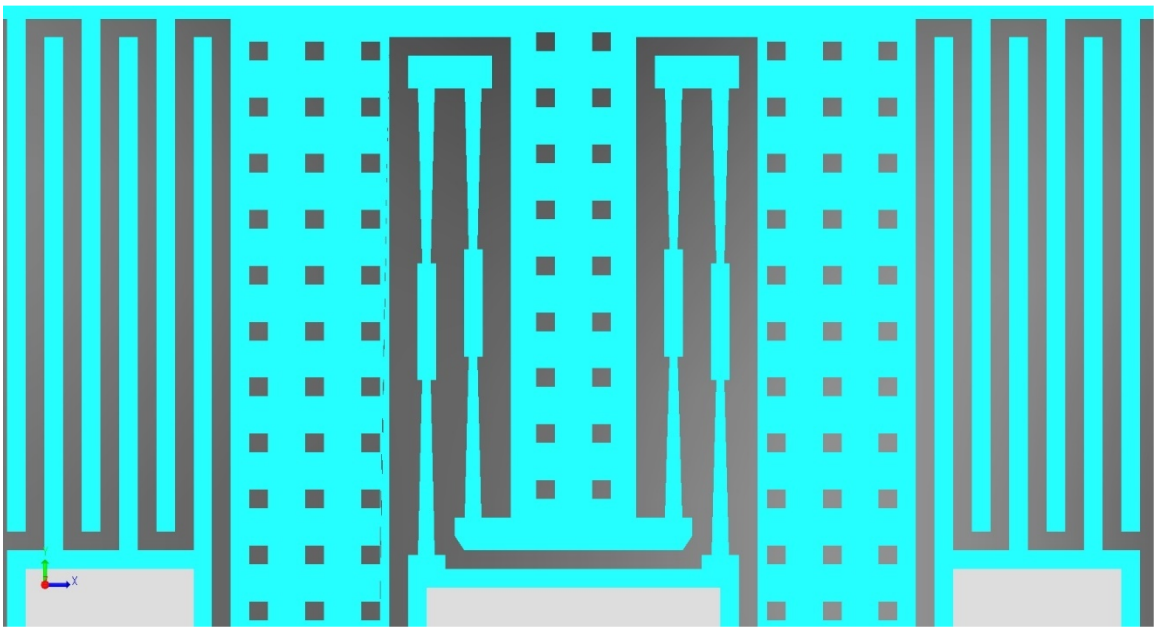

Figure C.23 Experiment 2 Design 5 Coupler Springs, 15µm Width w/o Fillets.

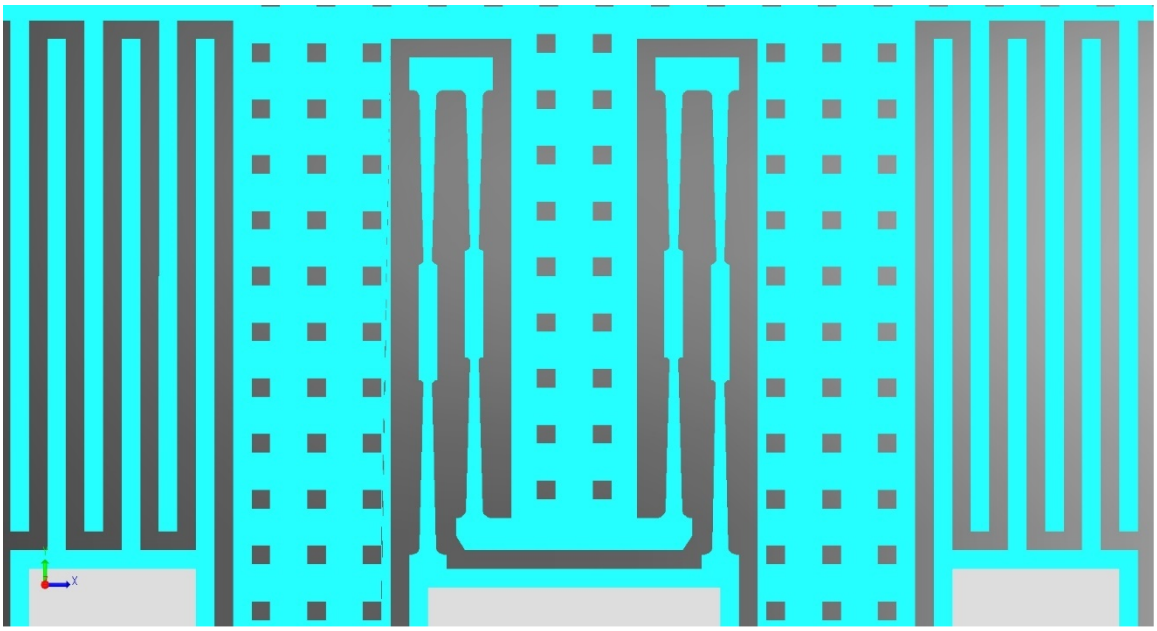

Figure C.24 Experiment 2 Design 6 Coupler Springs, 15µm Width w/ Fillets.

C.2 Experimental Design Wafer Locations and Distributions

The locations on the wafer of the individual design configurations for straight flexure dual-mass resonator Experiment 1 are shown for all designs in Figure C.25 through Figure C.30. The double block items are the locations where there was an x-axis device adjacent to a y-axis device. These figures demonstrate a relatively even distribution of the design instances across the wafer.

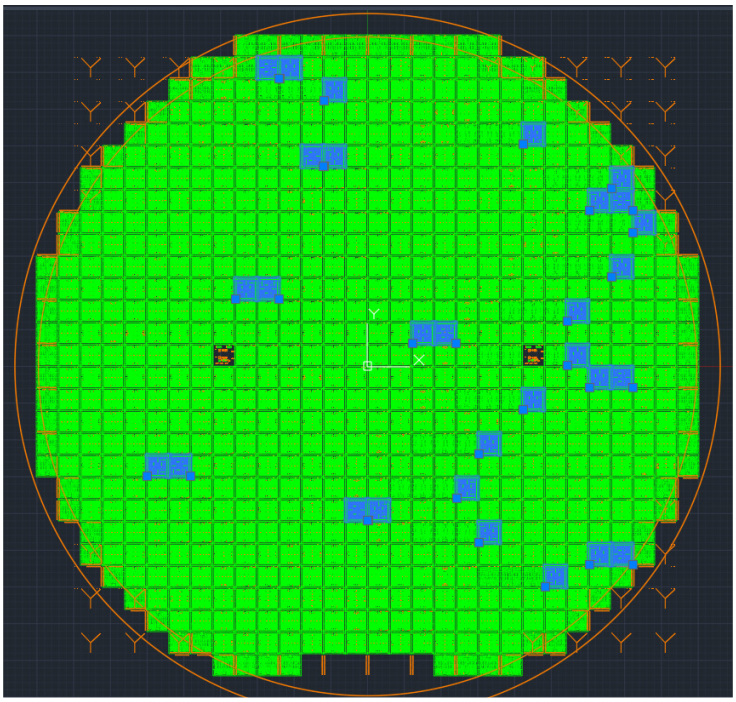

Figure C.25 Experiment 1 Design 1 Locations on Wafer, 7.5µm Width w/o Fillet.

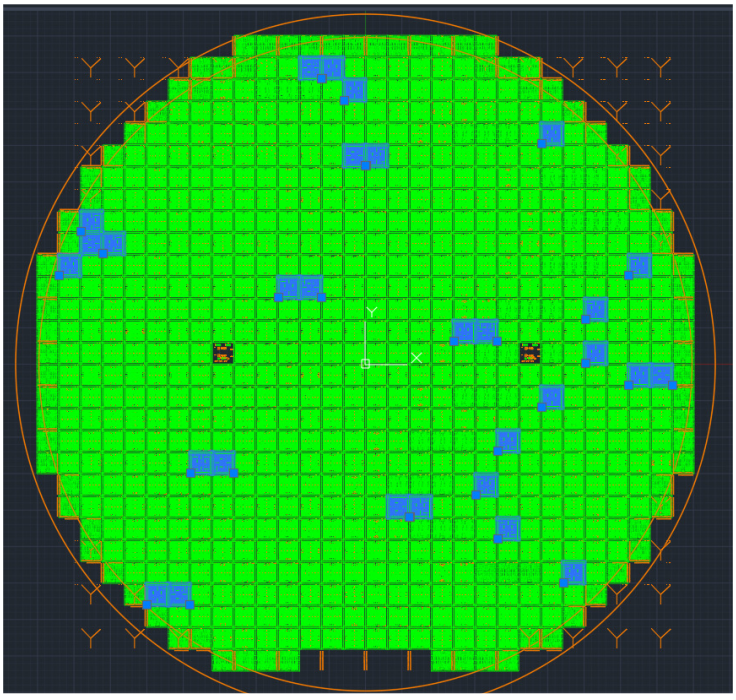

Figure C.26 Experiment 1 Design 2 Locations on Wafer, 7.5µm Width w/ Fillet.

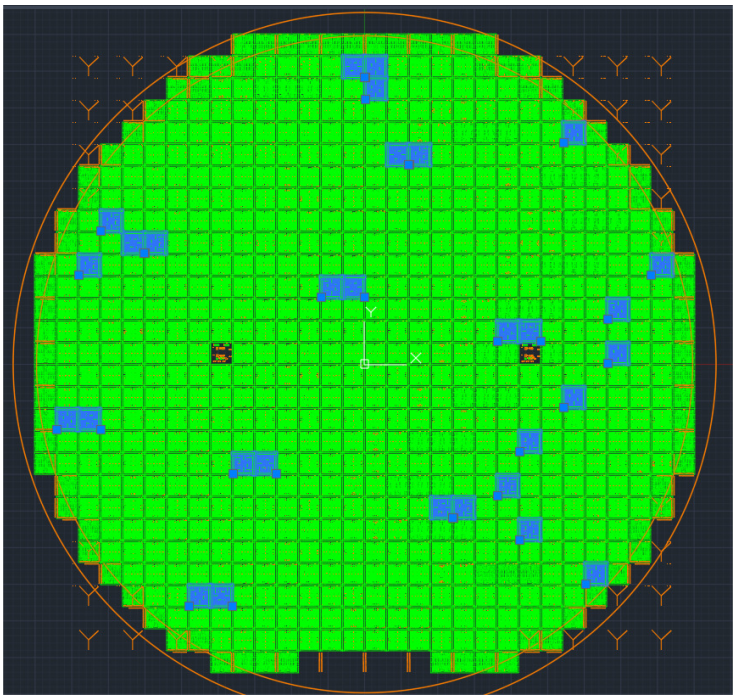

Figure C.27 Experiment 1 Design 3 Locations on Wafer, 10µm Width w/o Fillet.

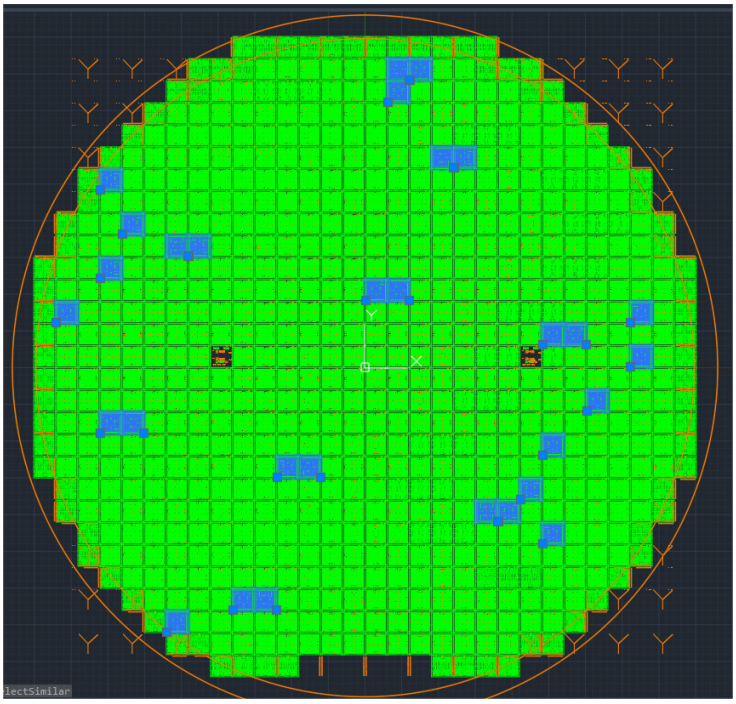

Figure C.28 Experiment 1 Design 4 Locations on Wafer, 10µm Width w/ Fillet.

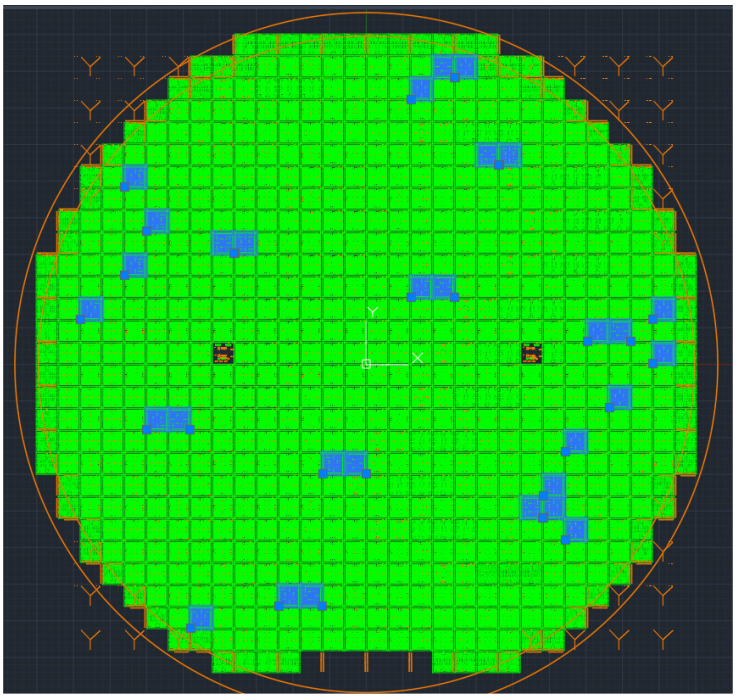

Figure C.29 Experiment 1 Design 5 Locations on Wafer, 15µm Width w/o Fillet.

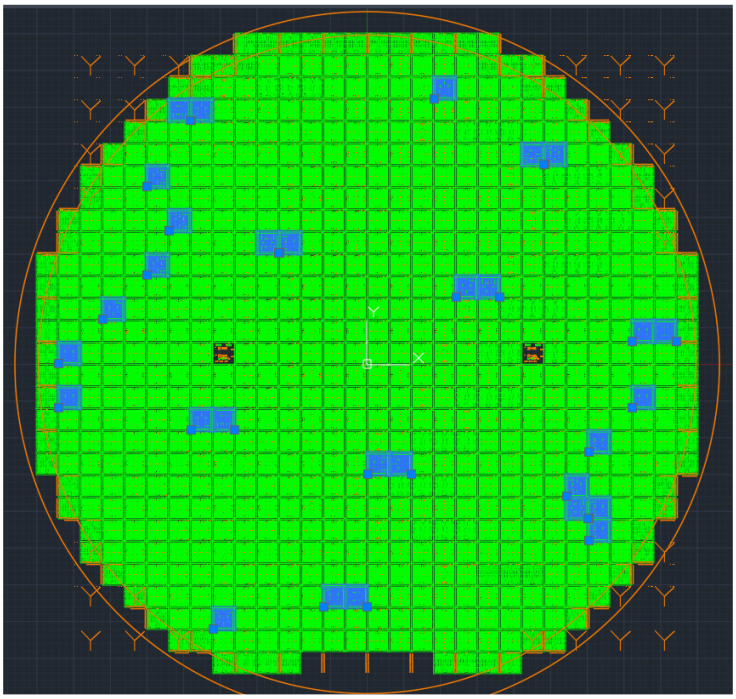

Figure C.30 Experiment 1 Design 6 Locations on Wafer, 15µm Width w/ Fillet.

The locations on the wafer of the individual design configurations for tapered flexure dual-mass resonator Experiment 2 are shown for all designs in Figure C.31 through Figure C.36. The double block items are the locations where there was an x-axis device adjacent to a y-axis device. These figures demonstrate a relatively even distribution of the design instances across the wafer.

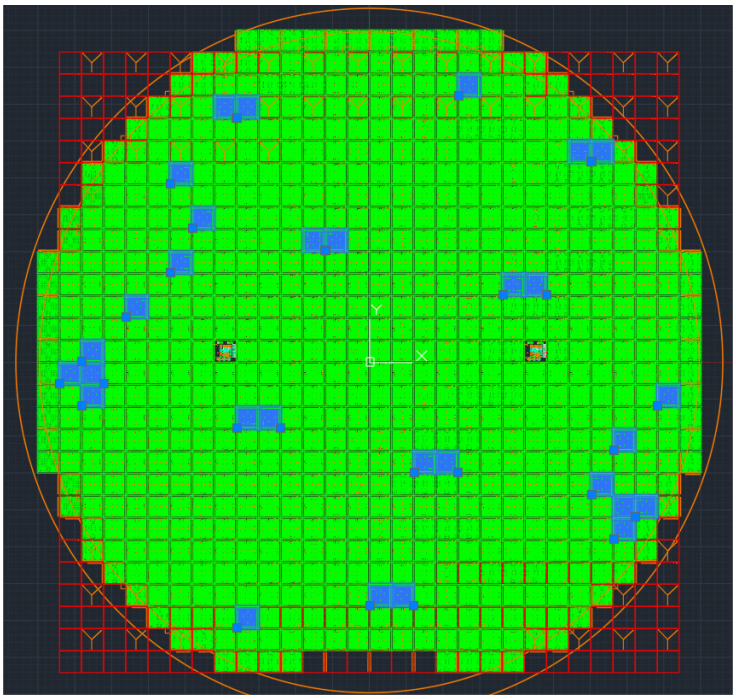

Figure C.31 Experiment 2 Design 1 Locations on Wafer, 7.5µm Width No Fillet.

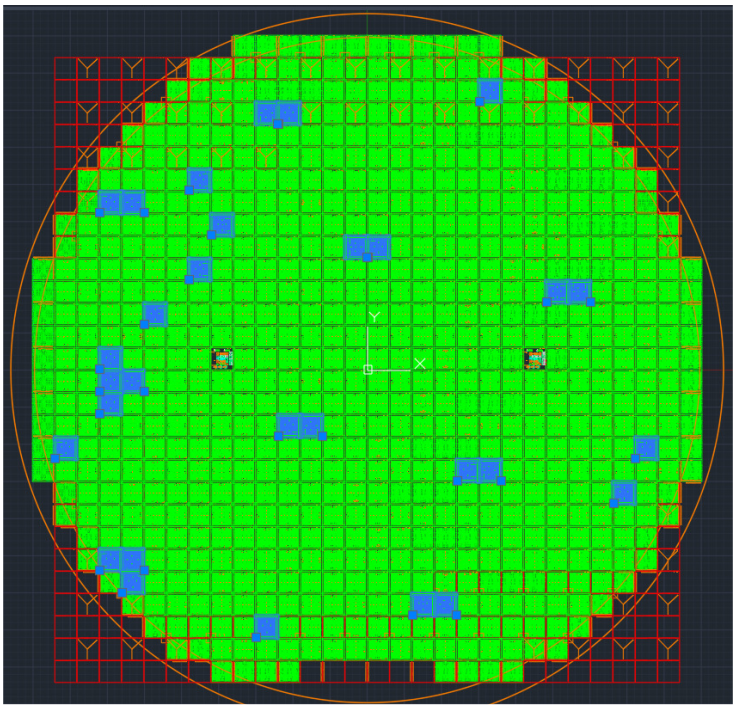

Figure C.32 Experiment 2 Design 2 Locations on Wafer, 7.5µm Width w/ Fillet.

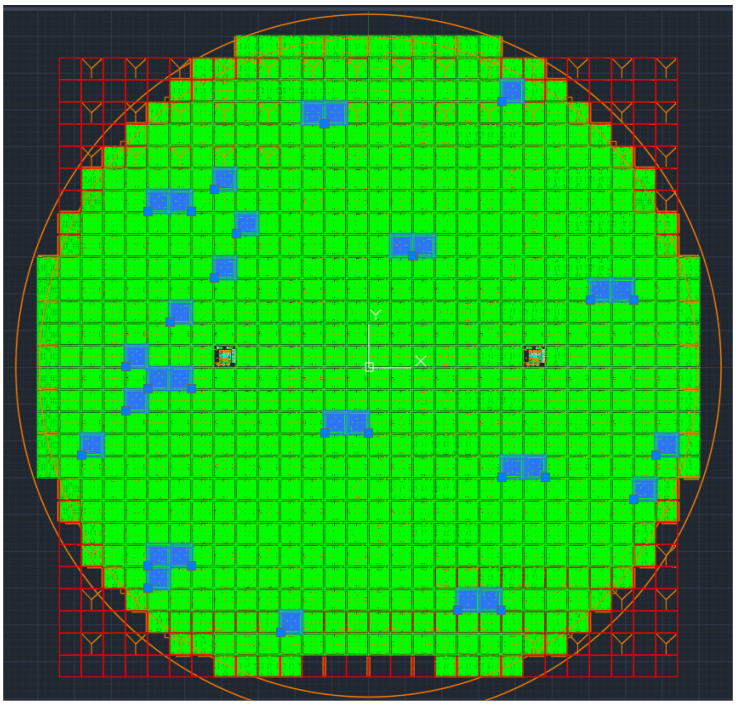

Figure C.33 Experiment 2 Design 3 Locations on Wafer, 10µm Width No Fillet.

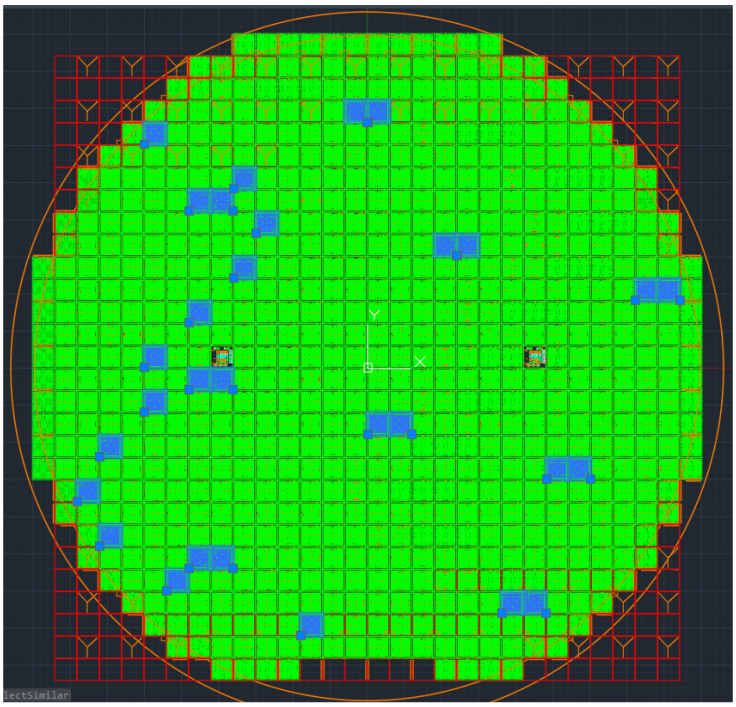

Figure C.34 Experiment 2 Design 4 Locations on Wafer, 10µm Width w/ Fillet.

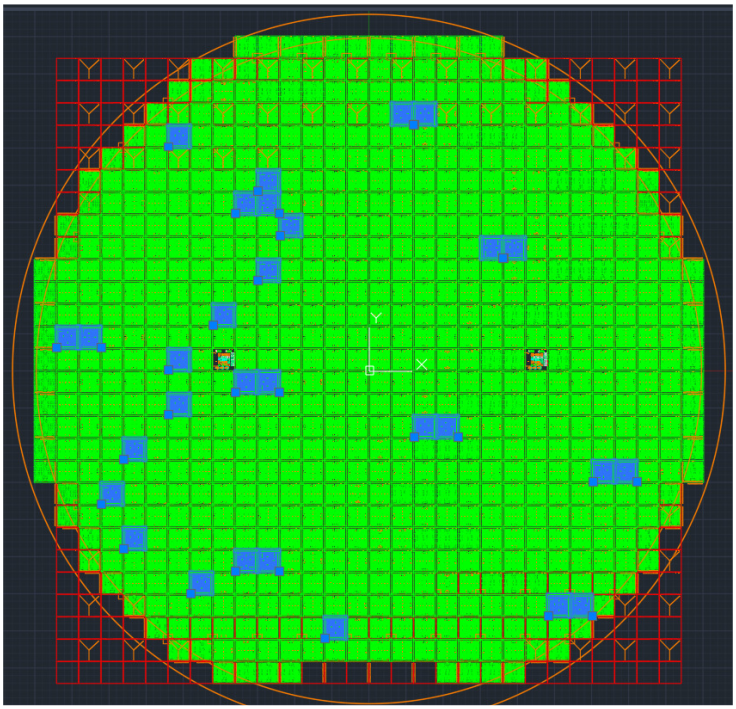

Figure C.35 Experiment 2 Design 5 Locations on Wafer, 15µm Width No Fillet.

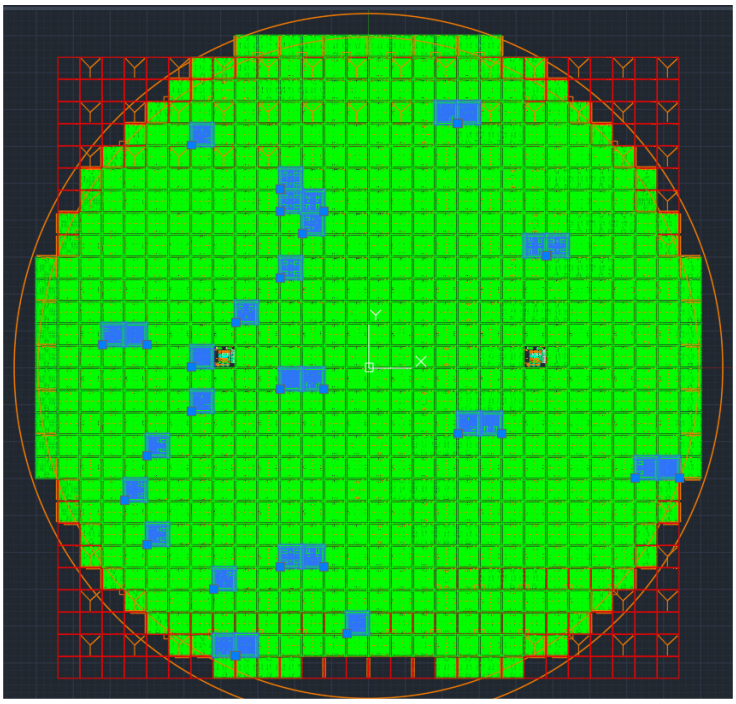

Figure C.36 Experiment 2 Design 6 Locations on Wafer, 15µm Width w/ Fillet.

The locations on the wafer of the individual design configurations for dual-mass resonator Experiment 4 (L to d ratio experiment) are shown for all designs in Figure C.37 through Figure C.40. These figures demonstrate a relatively even distribution of the design instances across the wafer.

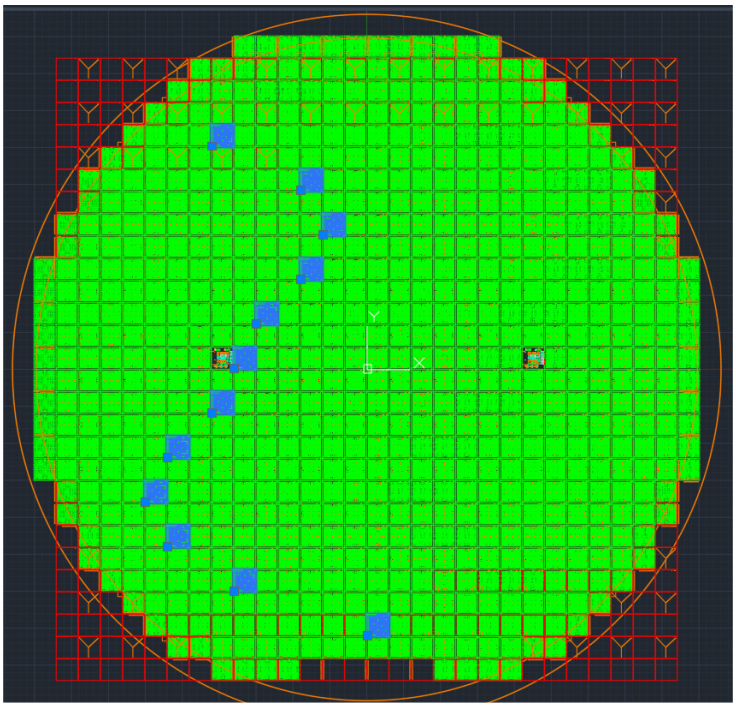

Figure C.37 Experiment 4 Design 1 Locations on Wafer, $L/d = 2$.

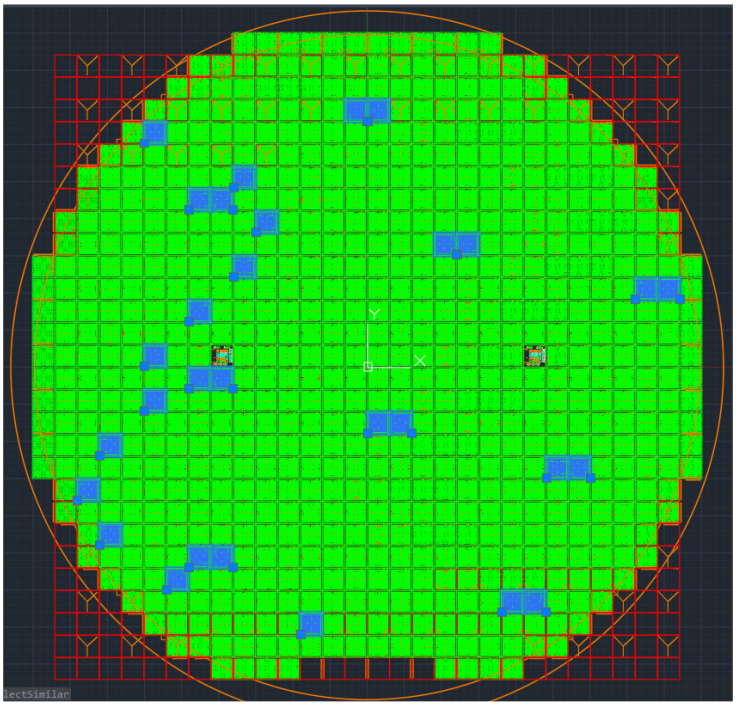

Figure C.38 Experiment 4 Design 2 Locations on Wafer, $L/d = 3$.

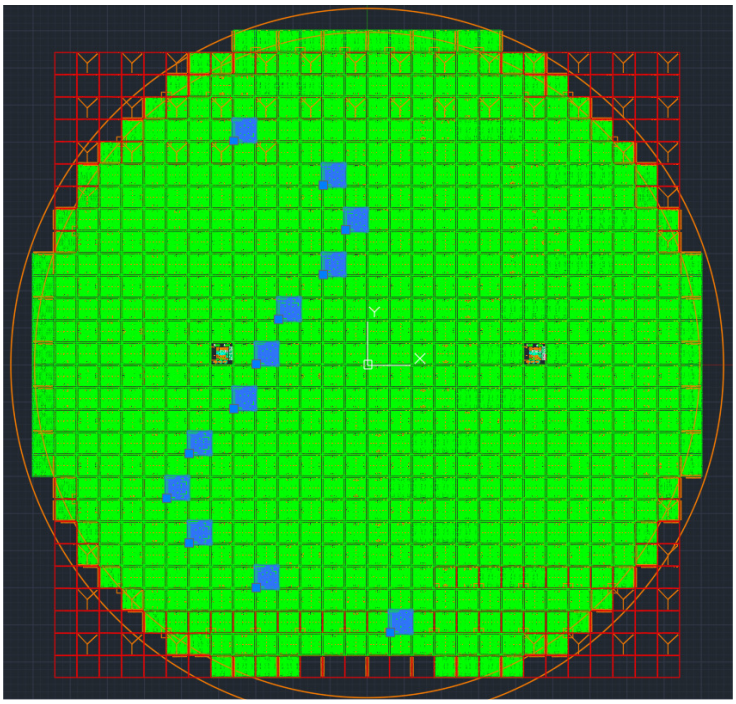

Figure C.39 Experiment 4 Design 3 Locations on Wafer, $L/d = 4$.

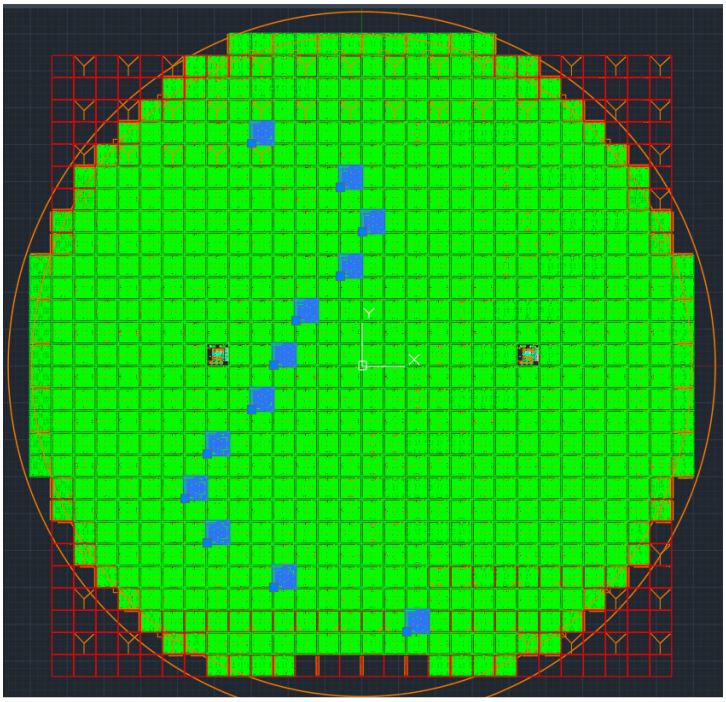

Figure C.40 Experiment 4 Design 4 Locations on Wafer, $L/d = 5$.

The locations on the wafer of the dual-mass resonator design of Experiment 5 (tapered flexure lever APLM) are shown in Figure C.41. The figure indicates a relatively even distribution of the design instances across the wafer.

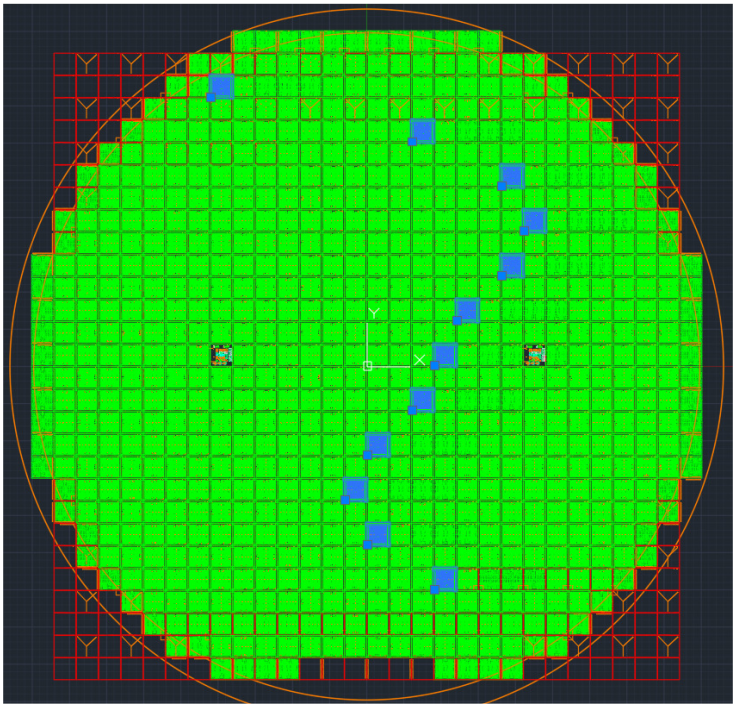

Figure C.41 Experiment 5 Design Locations on Wafer.

The locations on the wafer of the individual design configurations for dual-mass resonator Experiment 6 ("control" designs) are shown for all designs in Figure C.42 through Figure C.45. All Experiment 6 devices were x-axis devices so there are no double-block items in this experiment. These figures demonstrate a relatively even distribution of the design instances across the wafer.

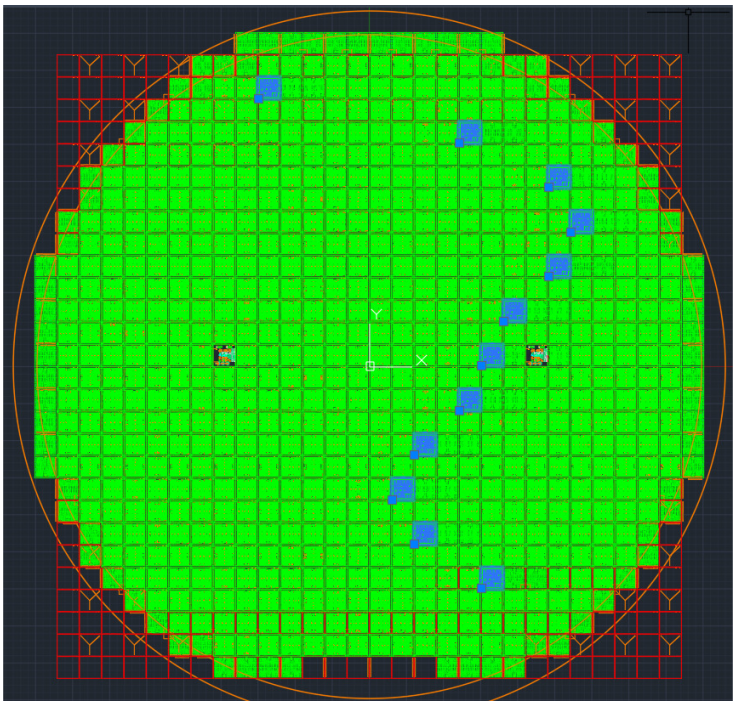

Figure C.42 Experiment 6 Design 1 Locations on Wafer.

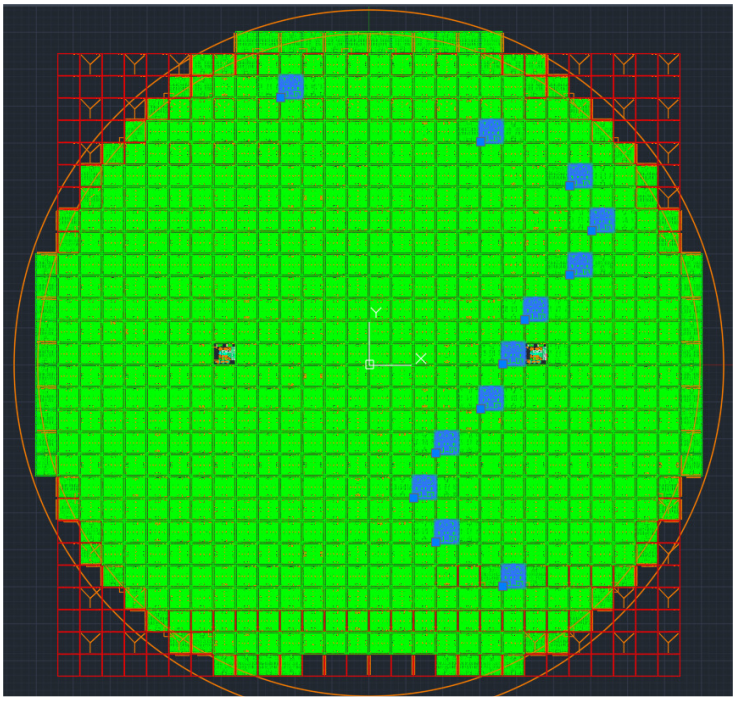

Figure C.43 Experiment 6 Design 2 Locations on Wafer.

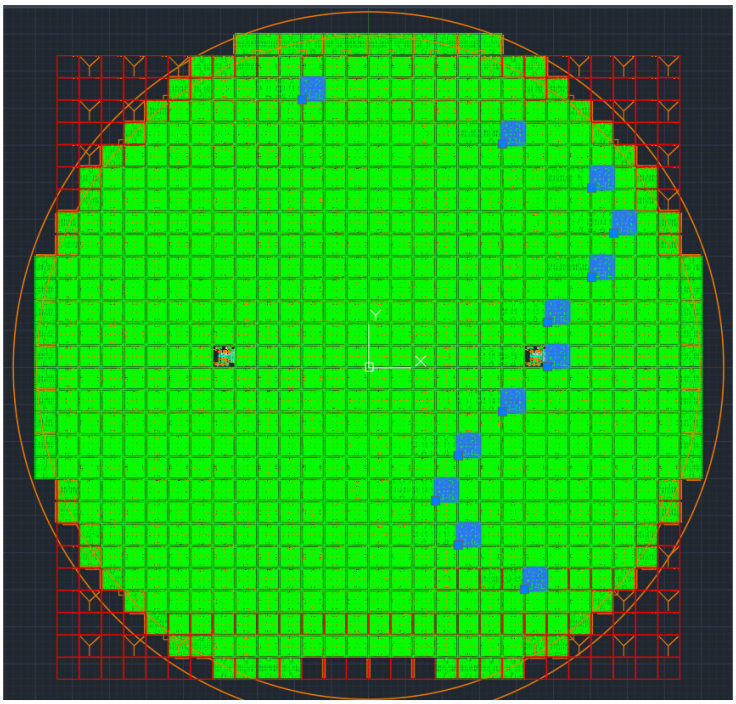

Figure C.44 Experiment 6 Design 3 Locations on Wafer.

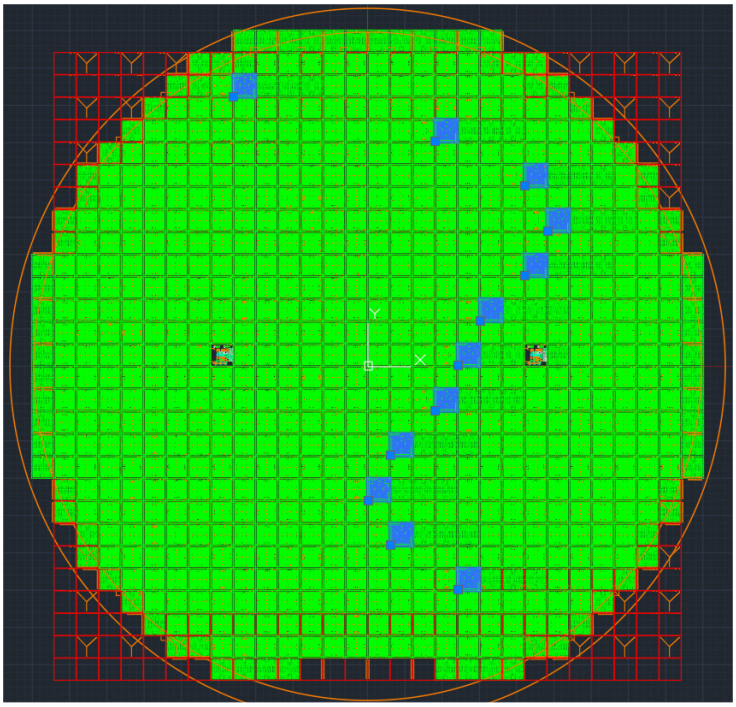

Figure C.45 Experiment 6 Design 4 Locations on Wafer.